UCRL-20426
c.2

NUCLEAR CHEMISTRY
Annual Report
1970

Lawrence Radiation Laboratory
University of California
Berkeley, California

UCRL-20426

UCRL-20426
UC-4 Chemistry
TID-4500 (57th Ed.)

NUCLEAR CHEMISTRY
Annual Report
1970

Lawrence Radiation Laboratory
University of California
Berkeley, California

Work done under
U.S. Atomic Energy Commission
Contract No. W-7405-eng-48

May 1971

Printed in the United States of America
Available from
National Technical Information Service
U.S. Department of Commerce
5285 Port Royal Road
Springfield, Virginia 22151
Price: Printed Copy $6.00; Microfiche $0.95

Contents

IV. INSTRUMENTATION AND SYSTEMS DEVELOPMENT

I. Nuclear Structure and Nuclear Properties

Nuclear Spectroscopy and Radioactivity

The Alpha Decay of ^{240}Am †

D. J. Gorman* and F. Asaro

We have observed for the first time alpha decay in the odd-odd nucleus ^{240}Am.

The main alpha group was first detected as a broadening of the 5.389 MeV alpha group of ^{241}Am during the course of experiments on the alpha decay of ^{239}Am.[1,2] In an effort to produce a better sample of ^{240}Am, we bombarded 200-300 mg of ^{239}Pu fluoride (99.973% ^{239}Pu; 0.0001% ^{241}Pu) with 18 MeV deuterons in the 88-inch cyclotron at the Lawrence Radiation Laboratory, Berkeley.

After purification of the americium by standard techniques,[2] the alpha spectrum was obtained using a 6-mm Au-Si surface barrier detector with a resolution (FWHM) of 20 keV, and recorded by a 400-channel pulse-height analyzer. The resultant spectrum is shown in Fig. 1. The decay of the two larger ^{240}Am peaks was followed for several days, and they were found to decay with a half-life of approximately 51 hours.

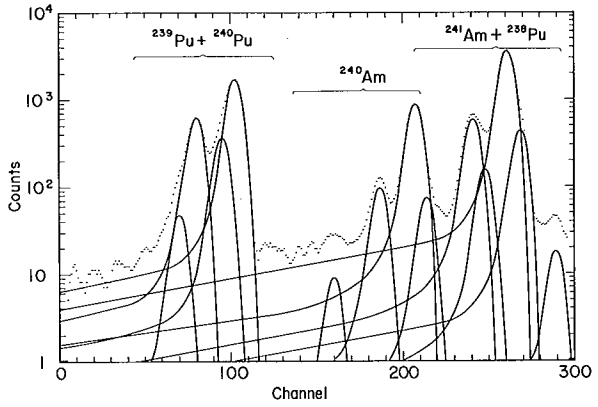

Fig. 1. ^{240}Am alpha spectrum--smoothed by computer. (XBL 708-3644)

The gamma spectrum of ^{240}Am exhibits K x rays and two strong γ rays with energies of 888.8 and 987.5 keV[3] coming from the electron capture decay. Assuming that all electron captures give rise to one of these γ rays[3,4,5] the branching ratio of the three observed alpha groups is 1.9×10^{-4}%.

The energies, abundances, and hindrance factors[6] for the observed alpha groups are given in Table I. The small magnitude of the hindrance factors is indicative of favored alpha decay.[7]

Table I. ^{240}Am alpha groups

Alpha particle energy (MeV)[a]	Intensity (%)	Hindrance factor
5.378±0.001	86.8±1.0	2.0
5.337±0.002	12.0±0.4	8.1
5.286±0.003	1.23±0.10	39

[a] Relative to ^{241}Am (5.486 MeV) and ^{240}Pu (5.168 MeV).

To determine the nature of the states populated in the favored alpha decay, we calculated the rotational constants and the energy differences between the ground and first excited states for the different combinations of Nilsson proton and neutron states available. In only one case did the calculated energy difference match the measured one of 41 keV. We therefore assign the ground state of ^{240}Am as a $K\pi I = 3^-3$ state composed of Nilsson $5/2^-[523]$ proton and $1/2^+[631]$ neutron orbitals.

The Q value for the ^{240}Am alpha decay, as estimated from closed decay-energy cycles, is 5.6 MeV.[8] This is substantially higher than that indicated by the highest energy alpha group we detected. Further decay-scheme studies on the γ ray transitions following the favored alpha decay should lead to a definite Q value.

Footnotes and References

† Condensed from UCRL-19953, August 1970, submitted to Phys. Rev.

* Present address: Bureau International des Poids et Mesures, Pavillon de Breteuil, 92 Sèvres, France.

1. Lawrence Radiation Laboratory Annual Report 1969, UCRL-19530, p. 1.

2. D. J. Gorman and F. Asaro, "Energy Levels in ^{235}Np," UCRL-19946, submitted to Phys. Rev.

3. D. J. Gorman, C. M. Lederer, and F. Asaro, unpublished data.

4. R. A. Glass, R. J. Carr, and W. M. Gibson, J. Inorg. & Nucl. Chem. 13, 181 (1960).

5. L. P. Bilbin, G. Aurov, and A. Albov, Isv. Akad. Nauk. SSSR Ser. Fiz. 30, 217 (Feb. 1966).

6. H. V. Michel, "Hindrance Factors for Alpha Decay," UCRL-9229, 1960.

7. A. Bohr, P. O. Fröman, and B. R. Mottelson, K. Dansk. Vid. Selsk. Mat. Fys. Medd. 29, 10 (1955).

8. C. M. Lederer, J. M. Hollander, and I. Perlman, Table of Isotopes (John Wiley & Sons, Inc., New York, 1967), 6th edition.

The Electron-Capture Decay of ^{240}Am †

C. M. Lederer, D. Gorman, and F. Asaro

The electron-capture decay of ^{240}Am has been studied with Ge(Li) γ-ray spectrometers (singles and Compton supression), a Si(Li) electron spectrometer, and an x-ray γ-ray coincidence system employing two NaI(Tl) detectors. The γ-ray spectrum (Table I) is dominated by two strong lines from a state at 1030.67 keV in ^{240}Pu. Conversion coefficients and subshell ratios (Table II) establish their multipolarities as E2 with very little M1 admixture. From the multipolarities and the absence of other transitions, the state is assigned spin-parity 3^+. Table III shows some additional results derived from x-γ coincidences and intensity balance considerations.

Figure 1 shows the decay scheme. The ground state of ^{240}Am has been assigned IπK 3-3 and a Nilsson configuration $5/2^-[523]_p\ 1/2^+[631]_n$.[1] Almost 100% of the decay populates the 1030.67-keV state. The energy of this state and log ft for the EC transition (5.8) are consistent with the assignment $1/2^+[631]_n\ 5/2^+[622]_n$. The capture transition is analogous to the strong transition observed in the decay of ^{239}Am,

$$5/2^-[523]_p \rightarrow 5/2^+[622]_n$$

(log ft ≈ 5.9).[2]

According to this interpretation, transitions between the 1033.67-keV state and the ground-state band of ^{240}Pu should be analogous to the principal γ-ray transitions in ^{239}Pu following ^{239}Am electron capture decay:

$$5/2^+[622]_n \xrightarrow{M1+E2} 1/2^+[631]_n ,$$

except that in ^{240}Pu there is an additional order of K-forbiddenness. On this basis, allowing for the higher transition energies in

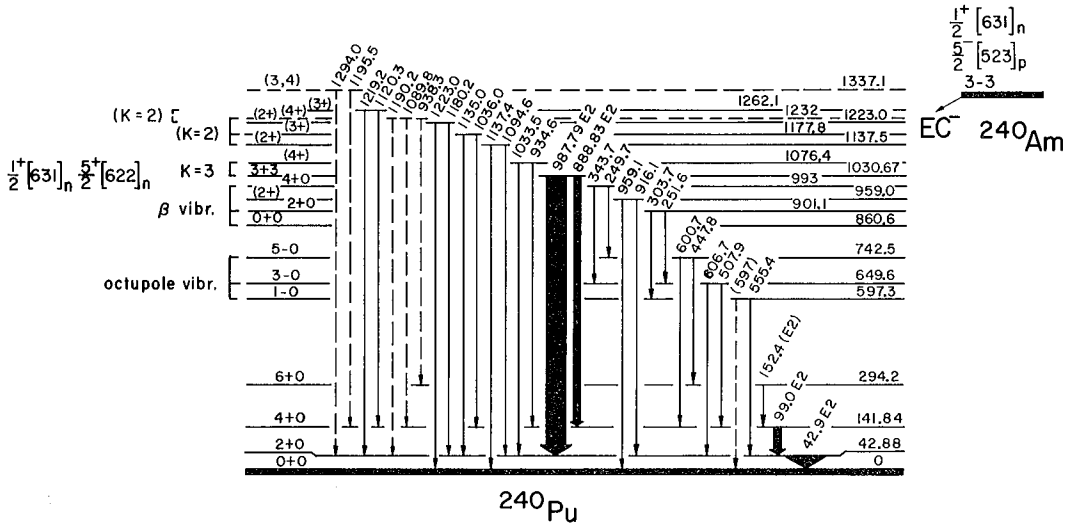

Fig. 1. Decay scheme of ^{240}Am.
(XBL712-2946)

Table I. Gamma-ray spectrum of ^{240}Am.

E_γ (keV)	I_γ [a] (%)	$I_{transition}$ [b] (%)
42.9[c]		112±14
99.0[c]		30±3
152.4±1.0	0.012(3)	0.04
249.7±1.0	0.020(3)	
251.8±1.0	0.005(2)	
303.7±1.0	0.009(2)	
343.7±1.0	0.049(5)	
382.1±1.0	0.053(5)	
447.8±1.0	0.013(4)	
507.9±1.0	0.072(6)	
555.4±1.0	≈0.01	
600.7±1.0	0.014(6)	
606.7±1.0	0.070(8)	
697.8	0.035(8)	
888.83±0.05	25.1(4)	25.5
916.1±0.2	0.087(6)	
934.6±0.5	0.025(3)	
938.0±0.6	0.007(3)	
959.1±0.5	0.037(4)	
987.79±0.06	73.2(10)	74.1
1033.5±0.3	0.010(1)	
1036.0±0.3	0.015(2)	
1089.8±1.0	0.0031(6)	
1094.6±0.3	0.016(1)	
1120.3±0.4	0.011(1)	
1135.0±0.3	0.048(3)	
1137.4±0.5	0.0073(20)	
1180.2±0.3	0.0101(8)	
1190.0±1.0	0.0005±0.0003	
1195.5±0.4	0.0026(5)	
1219.2±0.3	0.035(2)	
1223.0±0.3	0.007(1)	
1294.0±0.3	0.009(1)	

a. Normalized to 100% for the total EC decays, with the assumption that there is no direct EC decay to the ground-state band (see text).
b. From the measured γ-ray and electron spectra and some theoretical conversion coefficients.[5] Approximately equal to I_γ where not given.
c. Not seen in the γ-ray spectrum.

^{240}Pu and assuming that the additional K-forbiddenness hinders both E2 and M1 components by a factor of ≈ 100, one expects the transitions to be an equal mixture of M1 and E2, with lifetimes on the order of 5 nsec. This prediction obviously disagrees with the observed multipolarities (<3% M1) and lifetimes (≲ 1 nsec).

The disagreement in the mixing ratios must be ascribed to enhancement of the E2 components, since retardation of the M1 components would widen the discrepancy between the observed and predicted lifetime of the state. A probable mechanism for E2 enhancement would be admixture of the $I\pi K = 3+2$ member of the gamma-vibrational band into the 3+3 state. If the vibrational E2's have a strength of ≈ 5 single-particle units, an admixed amplitude of ≳ 0.3% would be required to explain the strength of the observed E2 transitions. However, if the 3+3 and 3+2 states are mixed to this extent, it is difficult to explain the apparent lack of EC feeding to the (unobserved) 3+2 state in the same amount.

Another difficulty with the proposed interpretation is the extreme weakness of the electron-capture branch to the 4+3 state. It is noteworthy that a parallel anomaly, failure of the

$$5/2^-[523]_p \rightarrow 5/2^+[622]_n$$

transition to populate the spin-7/2 member of the band, occurs in ^{239}Am decay.[2]

Other states of ^{240}Pu are inferred from energy differences between the very weak γ rays. The $K\pi = 0-$ and 0+ bands are well established from the decay of ^{244}Cm[3] and ^{240m}Np.[4] Transitions between the latter band and the ground-state band are too weak to have been observed in the present experiments.

Some additional new states are grouped into tentative bands in Fig. 1. The highest observed level, at 1337.1 keV, lies above the EC decay energy calculated from the K/total capture ratio by two standard deviations; either the decay energy is slightly higher, or the γ rays are incorrectly assigned.

A puzzling problem, bearing on the proposed admixture in the 3+3 state, is the location of the gamma-vibrational band in ^{240}Pu. A state of 938.1 keV populated by ^{240m}Np decay, assigned as 2^+ (K=2) in Ref. 4, seems more likely from its decay properties to be a 2-2 state. The 959.0-keV state observed in our experiments is a possible candidate for the 2+2 state, although the branching ratios differ slightly from the systematics of γ bands. A state at the same energy, seen in the decay of ^{240m}Np,[4] appears to have very different branching ratios from those observed in our experiments; it would seem that either the transitions involved (916.1 and 959.1 keV) are complex or have been placed incorrectly in the ^{240m}Np and/or ^{240}Am decay schemes.

Table II. Conversion coefficients and multipolarity assignment for ^{240}Am transitions.

Transition	Coefficient	Measured value	Theoretical value E1	E2	E3	M1	M2	Assigned multipolarity
42.9	(L1+L2)/L3	1.2±0.1	1.64	1.21	1.26	207	2.3	E2
	L/M	3.7±0.3	3.97	3.60	2.65	4.10	3.44	
99.0	(L1+L2)/L3	1.67±0.15	3.03	1.61	1.90	225	4.12	E2
152.4	α_M	0.47±0.13	0.00837	0.482	8.88	0.332	3.26	(E2)
888.83	α_K	0.0112±0.0004	0.000405	0.0114	0.0260	0.0544	0.118	E2(<4%M1)
	K/L3	39±20	112	60	41	1480	316	
987.79	α_K	0.00952[a]	0.00338	0.00952	0.0212	0.0412	0.0886	E2(<3%M1)
	K/L	3.77±0.11	5.77	3.82	2.50	5.15	4.42	
	L1/L2	$1.5^{+1.0}_{-0.5}$	7.84	2.18	1.18	7.96	6.34	
	(L1+L2)/L3	20±2	20.1	18.7	20.8	286	84.0	

a. Theoretical E2 value assumed. The maximum M1 content (3%) is derived from the measured K/L and (L1+L2)/L3 ratios. Assuming this limit, the calculated value of α_K(987.79) is $0.00952^{+0.00095}_{-0}$

Table III. Results derived from γ-K-x ray coincidences and intensity balance

$^{+}{}_{1/2}$ (1030.6 level): < 7×10^{-10} sec

E_γ keV	K x rays/γ ray: Coincidence	Singles
888.83	0.561±0.015	2.52±0.07
987.79	0.566±0.015	0.81±0.03

Calculated[a] EC(K)/EC(K+L+···) to 1030.6 level: 0.588±0.015

Q_{EC}, ^{240}Am → ^{240}Pu 1030.6 level: 273±15[b]

→ ^{240}Pu ground state: 1304±15 keV

K vacancies/decay not accounted for by EC transitions to states above g. s. band or K conversion of γ rays: 0.04±0.03

Net EC to g. s. band from K vacancies: < 10%

Feeding of ground-state band from intensity balance

02+ state: 12^{+14}_{-12}%

04+ state: 4±3 %

a. Assuming a K-fluorescence yield of 0.96

b. Calculated for an allowed or first-forbidden nonunique transition from the formulas of Brysk and Rose[6,7]

References

1. D. Gorman and F. Asaro, UCRL-19953 (1970), to be published in Phys. Rev.

2. W. G. Smith, W. M. Gibson, and J. M. Hollander, Phys. Rev. 105, 1514 (1957).

3. S. Bjornholm, C. M. Lederer, F. Asaro, and I. Perlman, Phys. Rev. 130, 2000 (1963); C. M. Lederer, unpublished data (1967).

4. M. R. Schmorak, C. E. Bemis, Jr., M. J. Zender, F. E. Coffman, A. V. Ramayya, and J. H. Hamilton, Phys. Letters 24, 1507 (1970); Nuclear Data B4, 663 (1970).

5. R. S. Hager and E. C. Seltzer, Nuclear Data A4, 1 (1968).

6. H. Brysk and M. E. Rose, ORNL-1830 (1955).

7. A. H. Wapstra, G. J. Nijgh, and R. Van Lieshout, Nuclear Spectroscopy Tables (North-Holland Publishing Company, Amsterdam 1959).

Energy Levels of ^{249}Bk

M. D. Holtz and J. M. Hollander

The results of an experimental and theoretical study of the levels of ^{249}Bk populated by the alpha decay of ^{253}Es have been discussed previously.[1,2] In those studies a detailed examination of the conversion electron spectra of ^{249}Bk was made, but only preliminary gamma spectra were taken. Recently a detailed examination of the gamma spectrum of ^{249}Bk from 0-1500 keV was made with the use of a 10 cm^3 planar Ge(Li) detector.

The ^{253}Es source was obtained from the Lanthanide, Actinide Chemistry Group at this laboratory. The meticulous chemistry done by this group, combined with the fact that the Es fraction was obtained from a milking of ^{253}Cf done at the Oak Ridge National Laboratory, resulted in a source practically free of impurities, and with a very high (5000:1) ratio of ^{253}Es to ^{254}Es.

A series of spectra was taken over a four month period and analyzed with the use of the SAMPO program of Routti and Prussin.[3] The experimental results are shown in Tables I and II. The level scheme of ^{249}Bk is shown in Fig. 1. Although many new transitions were observed, very few new levels have been found. The higher energy transitions observed in this study were related to the levels postulated by Lederer in his study of α-γ coincidences[4] in the decay of ^{253}Es.

From a theoretical point of view, the most interesting transitions newly observed are the interband transitions from the $K = 5/2^+$ band to the $K = 3/2^-$ band, and from the $K = 5/2^+$ band to the $I = \pm 2$ levels in the ground state $7/2^+$ band. The former are the previously unobserved E1 transitions while the latter are expected to be pure E2 transitions. Previously only the stronger, predominantly M1, transitions between the $K = 5/2^+$ and $K = 7/2^+$ bands have been seen. Thus, we observe in these experiments M1, E1, and E2 transitions from single states in the $K = 5/2^+$ band to several states in the $K = 7/2^+$ and $K = 3/2^-$ bands. We can, therefore, test the consistency of theoretical formulas for M1, E1, and E2 transition probabilities. From Nilsson,[5] the probability for a γ transition of multipole order λ is

$$T(\lambda) = \frac{8\pi(\lambda+1)}{\lambda[(2\lambda+1)!!]^2}\ \frac{1}{\hbar}\left(\frac{\omega}{C}\right)^{2\lambda+1} B(\lambda),$$

where ω is the frequency and $B(\lambda)$ is the reduced transition probability. For a comparison of M1 and E2 γ transitions to the same state, this equation reduces to

$$\frac{T(M1)}{T(E2)} = \frac{37\,c^2}{\omega^2}\ \frac{B(M1)}{B(E2)}\ .$$

The B(M1)'s and the B(E2)'s may also be obtained from Nilsson.[6] Using Nilsson's formulas and assuming no mixing between the $K = 5/2^+$ and $K = 7/2^+$ bands, we calculate, as an example,

$$\frac{T(M1)_{428.9}}{T(E2)_{335.1}} = 3000\ .$$

Experimentally we find that the ratio is 40. If we allow the $K = 5/2^+$ and $K = 7/2^+$ bands to mix via a Coriolis interaction, however, there should be a collective B(E2) between a level in the $K = 5/2^+$ band and its admixed component in the $K = 7/2^+$ band, and vice

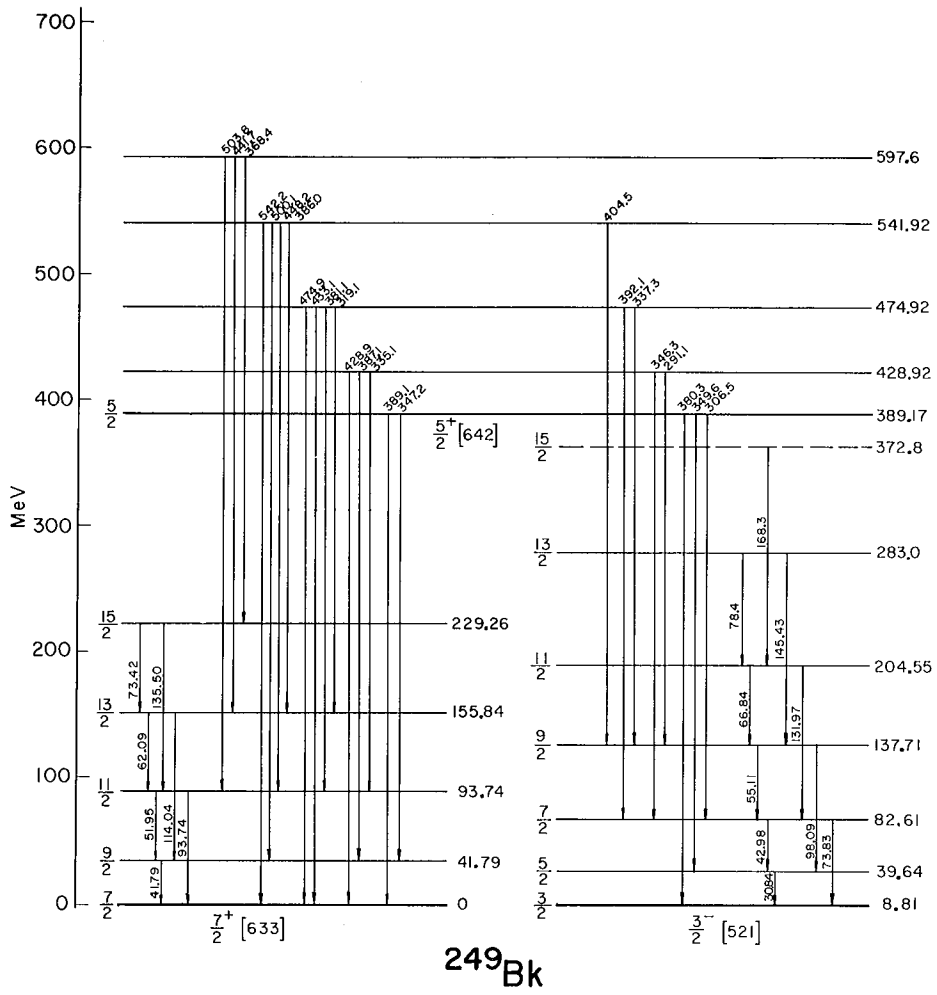

Fig. 1. Level scheme of ^{249}Bk.
(XBL712-2947)

versa. These B(E2)'s are calculated from the formula[7]

$$B(E2) = 5/16\ e^2 Q_0^2 \langle I2k0 | I' K' \rangle^2 ,$$

where Q_0 is the intrinsic quadrupole moment. The Coriolis mixing is determined from the energy spacings of the levels.[1] Q_0 was taken to be 11.5 b, as calculated by Szymanski.[8] Using this formula,

$$\frac{T(M1)_{428.9}}{T(E2)_{335.1}} = 26,$$

which is in much better agreement with observation. This indicates that the E2 transitions are collective and arise from the Coriolis mixing of the bands. Similar results were obtained for all of the T(M1)/T(E2) ratios.

The experimental T(M1)/T(E1) ratios are in suprisingly good agreement with the theoretical ratios one obtains using Nilsson's formulas.[5] As an example, experimentally

$$\frac{T(M1)_{389.1}}{T(E1)_{349.6}} = 189 .$$

Using Nilsson's formulas we calculate the ratio to be 87. Coriolis mixing of like parity bands does not significantly affect the result.

Thus, considering only Nilsson's first order contributions to the M1 and E1 moments and assuming collective E2's, there is good general agreement between the theory and the experimental data. The Weisskopf hinderance factors for the E1 transitions are between 10^{-3} and 10^{-4}.

Table I. Gamma-ray energies and intensities, K-conversion coefficients and multipolarities for interband transitions between known levels in ^{249}Bk.

Assignment $K_i I_i \rightarrow K_f I_f$	E_γ	γ Intensity per α ($\times 10^7$)	Experimental α_K	Theoretical M1	Theoretical E2	Calculated multipolarity
5 5 → 7 7*	389.1	2640	0.64**	0.64	0.054	100% M1**
5 5 → 7 9	347.2	18.0		0.88	0.065	
5 5 → 3 3	380.3	38±12		0.69	0.056	
5 5 → 3 5	349.6	14.0		0.87	0.064	
5 5 → 3 7	306.5	2.7		1.3	0.080	
5 7 → 7 7	428.9	604	0.45±0.03	0.50	0.045	M1 + (11 ± 7) % E2
5 7 → 7 9	387.1	1810	0.65±0.08	0.66	0.054	predominantly M1
5 7 → 7 11	335.1	14.9		0.97	0.069	
5 7 → 3 7	346.3	17.2		0.89	0.065	
5 7 → 3 9	291.1	3.5		1.4	0.086	
5 9 → 7 7	474.9	34.9	0.34±0.04	0.38	0.048	M1 + (12 ± 12) % E2
5 9 → 7 9	433.1	289	0.49±0.03	0.48	0.045	predominantly M1
5 9 → 7 11	381.1	555	0.66±0.06	0.68	0.055	predominantly M1
5 9 → 7 13	319.1	3.7		1.1	0.075	
5 9 → 3 7	392.1	13±10		0.63	0.053	
5 9 → 3 9	337.3	5.4		0.96	0.068	
5 11 → 7 7	541.9	2.4		0.26	0.031	
5 11 → 7 9	500.1	16.8	0.30±0.10	0.33	0.035	predominantly M1
5 11 → 7 11	448.2	69.5	0.35±0.04	0.44	0.042	M1 + (23 ± 12) % E2
5 11 → 7 13	386.0	130±50	0.59±0.20	0.66	0.054	predominantly M1
5 11 → 7 15	312.8	0.4±0.2		1.2	0.078	
5 11 → 3 9	404.5	0.56		0.58	0.050	
5 13 → 7 11	503.8	2.0		0.32	0.035	
5 13 → 7 13	441.7	8.5	0.47±0.14	0.46	0.043	predominantly M1
5 13 → 7 15	368.4	35.0	0.45±0.15	0.72	0.058	M1 + (41 ± 25) % E2

*5 5 → 7 7 means 5/2 5/2 → 7/2 7/2, etc.

**Normalized to give pure M1.

Table II. Gamma-ray energies and intensities for all observed gamma-ray lines not included in Table I.

E_γ (keV)	γ Intensity per α (x 10^7)	E_γ (keV)	γ Intensity per α (x 10^7)	E (keV)	γ Intensity per α (x 10^7)
41.9	479*			585.2	3.7
43.0	80	189.9	0.60**	616.3	0.42
51.8	476			621.5	0.17**
55.1	191	283.4	0.69		
62.1	104	312.7	0.4**		
66.9	97	421.3	10.6		
73.3	83	425.1	24.2	653.0	0.2**
74.7	52**	456.7	1.7**	663.8	0.35
78.4	28	468.8	8.7	669.4	0.49**
84.6	17**	477.2	12		
		487.7	0.2**	761.9	0.42**
93.7	69	494.2	0.7**	768.2	2.9
98.1	97	514.4	0.7	900.2	0.83
113.4	56	518.5	11	932.3	4.6
121.8	67	524.0	5.7	946.3	0.76
135.4	15			1040.4	0.28
145.2	28			1075.0	0.52
		549.4	3.2		
162.6	1.4			1106.4	0.14
168.3	5.2	560.4	4.0	1266.5	1.6**
180.2	1.4**	567.0	5.1		

*The intensities of transitions below 200 keV are unreliable because of absorbtion of low energy gamma rays in the source and in its double walled container.

**The existence of this transition in ^{249}Bk is in doubt.

References

1. Nuclear Chemistry Division Annual Report, 1963, UCRL-11213, Feb. 1964.

2. Nuclear Chemistry Division Annual Report, 1964, UCRL-11878, Jan. 1965.

3. J. T. Routti and S. G. Prussin, Nucl. Instr. Methods 72, 125 (1969).

4. C. M. Lederer, (Ph. D. thesis), UCRL-11028.

5. S. G. Nilsson, K. Danske Vidensk. Selsk. Mat. -fys. Medd. 29, 31 (1955).

6. S. G. Nilsson, K. Danske Vidensk. Selsk. Mat. -fys. Medd. 29, 33 (1955).

7. A. Bohr and B. R. Mottelson, K. Danske Vidensk. Selsk. Mat. -fys. Medd. 27, 109 (2nd edition, 1957).

8. Z. Szymanski, Nucl. Phys. 28, 63 (1961).

In-Beam Studies of Mo and Ru Isotopes with (α, xn) Reactions (concluded)

C. M. Lederer, J. M. Jaklevic, and J. M. Hollander

The most recent report of this project[1] included extensive level schemes of ^{96,97,99,101,102}Ru and ^{94}Mo. New level schemes for ^{95,96,97,98}Mo and ^{98,100}Ru are shown in the accompanying figures. They are based on data obtained from γ-ray singles, beam-γ delay, beam-γ angular correlations, and γγ-coincidence measurements.

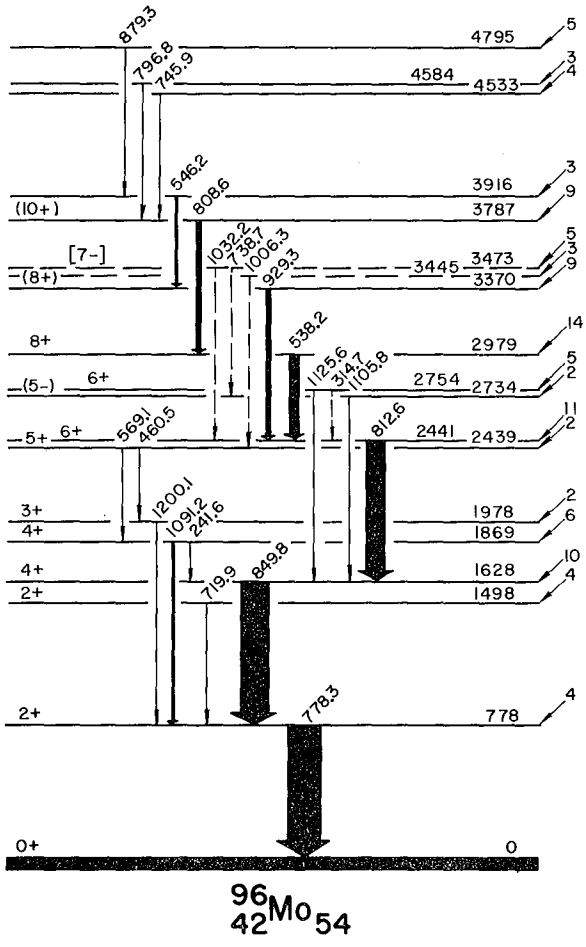

Fig. 1. Level scheme of ^{96}Mo studied via the (α, 2nγ) reaction. (XBL7010-3958)

A more complete description of the results and analysis of the level schemes in terms of systematics and shell-model calculations are contained in two papers submitted to Nuclear Physics.

Reference

1. J. M. Jaklevic, C. M. Lederer, and J. M. Hollander, Nuclear Chemistry Division Annual Report, 1969, UCRL-19530, pp. 48, 49, and 51.

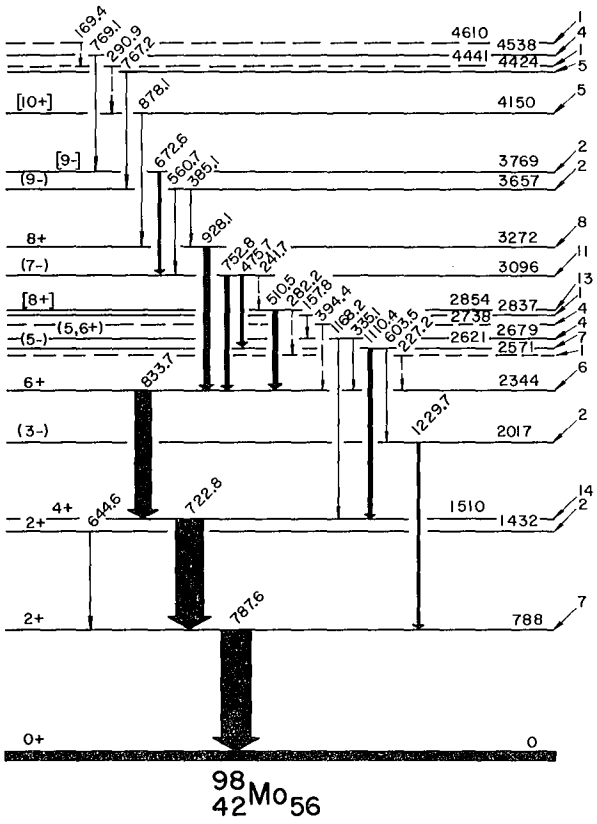

Fig. 2. Level scheme of ^{98}Mo studied via the (α, 2nγ) reaction. (XBL7010-3957)

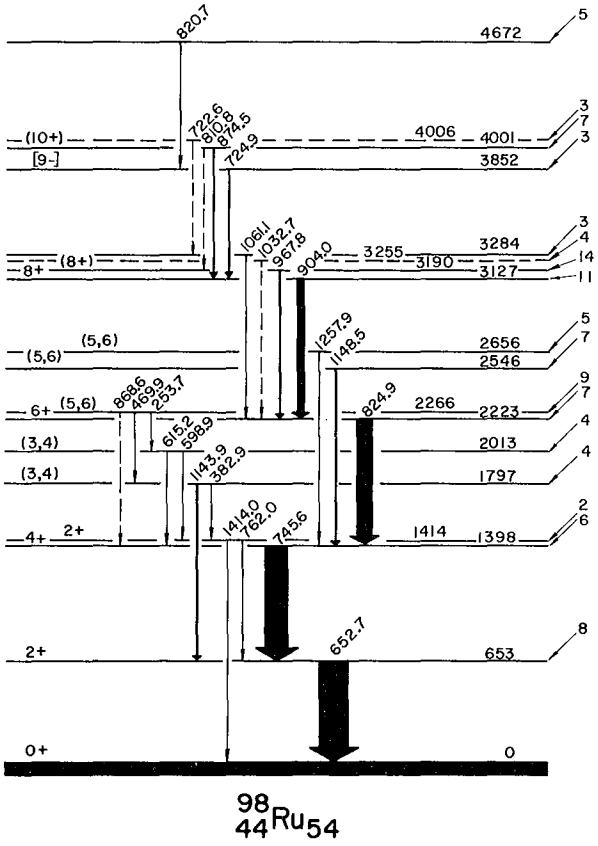

Fig. 3. Level scheme of ^{98}Ru studied via the (α, 2nγ) reaction. (XBL7010-3955)

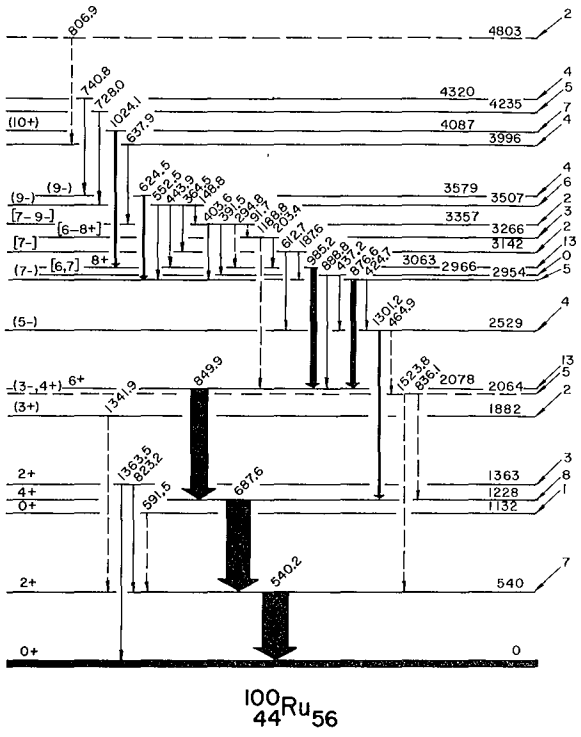

Fig. 4. Level scheme of ^{100}Ru studied via the (α, 2nγ) reaction. (XBL7010-3954)

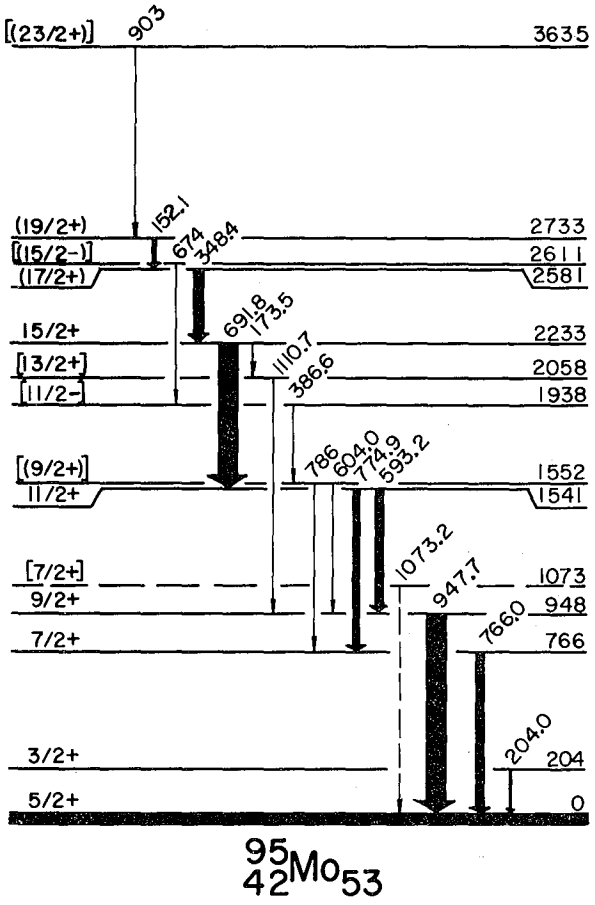

Fig. 5. Level scheme of ^{95}Mo studied via the (α, 3nγ) reaction. (XBL7010-3998)

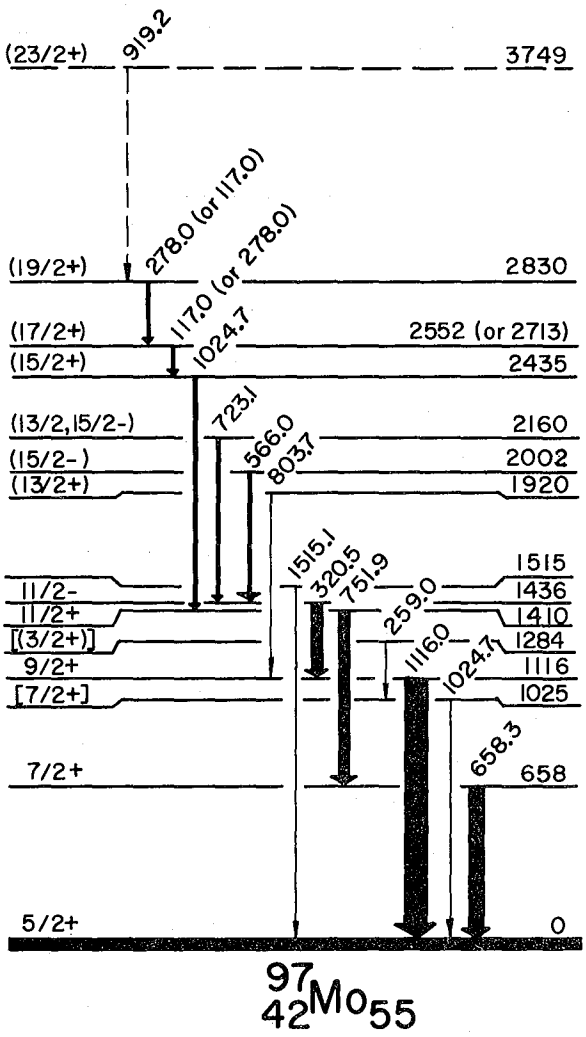

Fig. 6. Level scheme of ^{97}Mo studied via the (α, 3nγ) reaction. (XBL7010-3967)

Quadrupole Moment of the First Excited State in ^{36}Ar

K. Nakai,† F. S. Stephens, and R. M. Diamond

A series of experiments[1,2] has been carried out at the Berkeley Hilac to measure quadrupole moments of the first excited states of even-even nuclei in the 2s-1d shell. The method used was to measure the reorientation effect[3] in projectile Coulomb excitation; the sensitivity to the effect is a factor of five or more greater than in the usual target reorientation method, so that the uncertainties in the results are correspondingly reduced. The nuclei whose first-excited-state quadrupole moments were previously measured using this method[1,2] are ^{20,22}Ne, ^{28}Si, ^{32}S, and ^{40}Ar. Recently a number of Hartree-Fock calculations have been published for the 4n nuclei in the 2s-1d shell.[4] The experimental results on the shapes of ^{20}Ne, ^{24}Mg (prolate shape $Q_0 > 0$) and ^{28}Si (oblate shape $Q_0 < 0$) are reasonably well reproduced by the calculations, but the result on ^{32}S ($Q_0 > 0$) is not.

Table I. Summary of the least-squares fitting.

^{206}Pb target values		Result for ^{36}Ar	
B(E2, $0^+ \rightarrow 2^+$) $e^2 \times 10^{-50}$ cm^4	$Q(2^+)$ b	B(E2, $0^+ \rightarrow 2^+$) $e^2 \times 10^{-50}$ cm^4	$Q(2^+)$ b
	$+0.5\|Q_r\|$	3.2 ± 0.5	$+0.091 \pm 0.052$
9.1 ± 0.6[a]	0.0	3.2 ± 0.5	$+0.107 \pm 0.052$
	$-0.5\|Q_r\|$	3.2 ± 0.5	$+0.124 \pm 0.052$
9.1 ± 0.6[a]	$0.0 \pm 0.5\|Q_r\|$[b]	3.2 ± 0.5*	$+0.11 \pm 0.06$*

[a]Reference 5.

[b]Assumption: $|Q_r|$ is the value calculated from the B(E2) using the rigid-rotor model.

*Possible systematic errors of (±5%) have been included.

The change of sign of Q_0 between ^{28}Si and ^{32}S appears to indicate a difficulty in predicting deformations of nuclei in this region of the 2s-1d shell. We then became interested in ^{36}Ar, and so measured the static quadrupole moment of the first 2^+ state of this nucleus by the same method as in the previous experiments. The details of the method are described in Ref. 1.

The ^{36}Ar beam was accelerated to ≈ 150 MeV in the Hilac and then struck a ^{206}Pb target (≈ 1.5 mg/cm^2). Gamma-ray spectra, in coincidence with a ring counter for particles scattered at 160°, and with a circular particle counter at 90°, have been taken simultaneously. The ratio of the γ-ray yields of the projectile, ^{36}Ar(2^+, 1.970 MeV), to those of the target, ^{206}Pb(2^+, 0.803 MeV), at each angle (R^{90}, R^{160}) were obtained, together with the double ratio $\Re = R^{160}/R^{90}$, as shown in Fig. 1. The solid lines in the figure are the best fits obtained by least-squares fitting using the deBoer-Winther Coulomb excitation program. The two parameters determined in the fitting were: 1) the intrinsic quadrupole moment Q_0 from the B(E2, $0^+ \rightarrow 2^+$), and 2) the ratio of the static quadrupole moment Q of the 2^+ state to the rotational moment Q_r deduced from Q_0. For the target excitation, the B(E2, $0^+ \rightarrow 2^+$) in ^{206}Pb is known,[5] but the static moment of the 2^+ state is not, so that we assumed $Q(^{206}\text{Pb}, 2^+) = 0.0 \pm 0.5 |Q_r(^{206}\text{Pb}, 2^+)|$. This assumption introduces some uncertainty into the result; however, as discussed in the previous paper,[1] this method of comparing with target excitation measured simultaneously has a number of advantages.

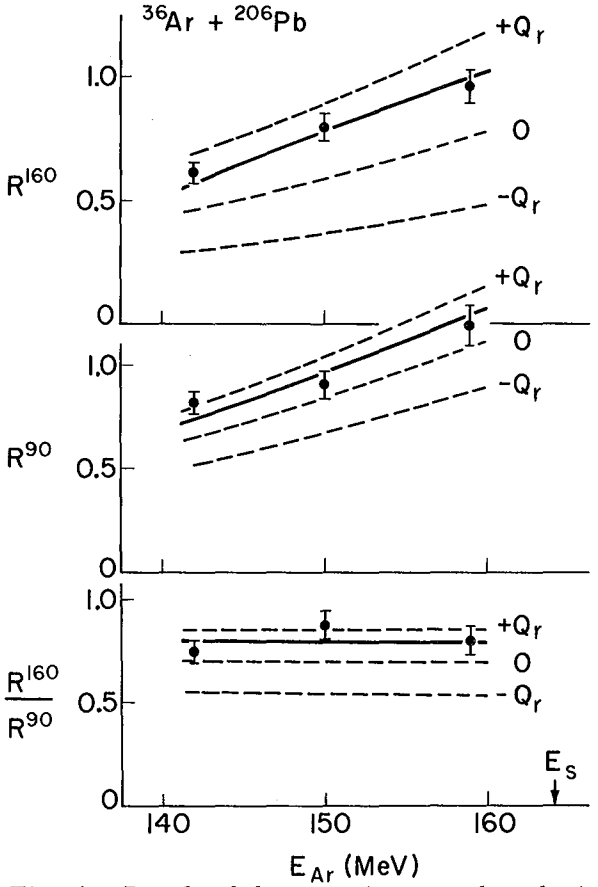

Fig. 1. Result of the experiment and analysis. The solid lines are the best fits and the dashed lines show the curves for Q = 0 or ± $|Q_r|$. The arrow indicates the safe energy, E_s, defined in Ref. 3. (XBL 706-3184)

Corrections have been made for: 1) the attenuation of the γ-ray angular distribution; 2) the finite solid angles of both particle and γ detectors; and 3) the change of detection efficiency of γ rays due to the recoil motion. The lack of data on the transition probabilities between the ground or first excited state and the other low-lying states in ^{36}Ar made the correction for effects due to those states ambiguous. These effects were estimated using deformation parameters determined from inelastic scattering experiments,[6] and rather conservative errors were included for these corrections. The static quadrupole moment obtained is

$$Q(^{36}\mathrm{Ar},\ 2^+) = (+0.11 \pm 0.06)\mathrm{b},$$

with the positive value of the moment indicating an oblate shape for the nucleus.

In Fig. 2 we have added the new point to a model-dependent plot of Q_0 in 2s-1d shell nuclei which was published previously.[2] Three noticeable features in this plot are the remarkably similar magnitudes of $|Q_0|$ obtained from the values of B(E2, $0^+ \rightarrow 2^+$) measured for the seven doubly-even nuclei, the rather large positive static moment Q_0 of ^{32}S, and the fact that the static moments are ≈ 30% larger than the rotational value for the light nuclei, ^{20,22}Ne, ^{24}Mg.

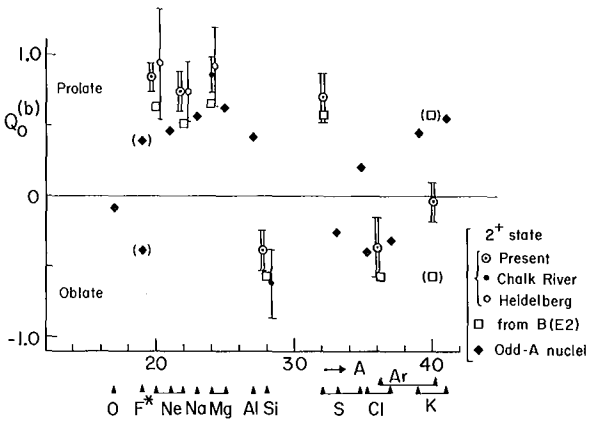

Fig. 2. Intrinsic quadrupole moments, Q_0, in the 2s-1d shell nuclei. The present result on ^{36}Ar has been added to the figure from Ref. 2. The circles indicate the Q_0 of the first-excited 2^+ states deduced from measured static quadrupole moments by: the present method (double circles), the method of the Chalk River group[7] (closed circles) and that of the group at Heidelberg[8] (open circles). The squares indicate the values calculated from measured B(E2, $0^+ \rightarrow 2^+$) values. The intrinsic moments of odd-A nuclei deduced from the spectroscopic quadrupole moments--assuming K = I except for ^{19}F* (K = 1/2, I = 5/2)--are shown by the diamonds. (XBL 701-2137)

Footnote and References

†On leave from Osaka University, Toyonaka, Osaka, Japan.

1. K. Nakai, F. S. Stephens, and R. M. Diamond, Nucl. Phys. A150, 114 (1970).

2. K. Nakai, J. L. Québert, F. S. Stephens, and R. M. Diamond, Phys. Rev. Letters 24, 903 (1970).

3. J. deBoer and J. Eichler, in Advances in Nuclear Physics, ed. by M. Baranger and E. Vogt (Plenum Press, New York, 1968), Vol. 1.

4. G. Ripka, in Advances in Nuclear Physics, edited by M. Baranger and E. Vogt (Plenum Press, New York, 1968), Vol. 1; J. Bar-Touv, A. Goswami, A. L. Goodman, and G. L. Struble, Phys. Rev. 178, 1670 (1970); S. J. Kriger, Phys. Rev. C 1, 76, (1970), and references therein.

5. J. L. Québert, K. Nakai, R. M. Diamond, and F. S. Stephens, Nucl. Phys. A150, 68 (1970).

6. M. C. Mermaz, C. A. Whitten, Jr., and D. A. Bromley, Phys. Rev. 187, 1466 (1970); R. R. Johnson and R. J. Grifiths, Nucl. Phys. A117, 273 (1968).

7. O. Häusser, B. W. Hooton, D. Pelte, T. K. Alexander, and H. C. Evans, Phys. Rev. Letters 22, 359 (1969) and Phys. Rev. Letters 23, 320 (1969).

8. D. Schwalm and B. Povh, Phys. Letters 29B, 103 (1969); A. Bamberger, P. G. Bizzeti, and B. Povh, Phys. Rev. Letters 21, 1599 (1968).

Electric Hexadecapole Transition Moment in ^{152}Sm†

F. S. Stephens, R. M. Diamond, N. K. Glendenning, and J. de Boer*

The present study of an E4 transition moment in ^{152}Sm began as the evaluation of a correction to measurements[1] of B(E2; $2^+ \rightarrow 4^+$) from Coulomb-excitation studies. It became apparent that this particular correction was not very well known and could be rather large, especially when light projectiles were used so that double-E2 excitation is weak. The accurate determination of the B(E2; $2^+ \rightarrow 4^+$) value from lifetime measurements[2] made it possible to combine that result with the Coulomb excitation measurements and determine the E4 moment.

The experiment consisted of an accurate determination of the intensity of the $4^+ \rightarrow 2^+$ γ-ray transition in ^{152}Sm relative to those of the $2^+ \rightarrow 0^+$ transitions in ^{152}Sm and ^{150}Sm following Coulomb excitation with ^4He ions. Targets of both natural samarium and enriched ^{152}Sm were measured at each bombarding energy. This method provides accurately known standard peaks (122 and 334 keV). Gamma-ray spectra were simultaneously stored as singles events and as coincidences with ^4He ions backscattered through an angle of about 160 deg. These two types of measurement are about equally sensitive to the effect of an E4 transition moment, but differ markedly in their sensitivity to many other effects. Thus the agreement of the singles and backscatter results greatly reduces the probability that an important effect has been overlooked.

An overall view of the possibilities for measuring E4 transition moments using this method is contained in Fig. 1. We have used the following notation:

$$\langle 0^+ \| \mathcal{M}(E4) \| 4^+ \rangle = \int \rho r^4 Y_{40} d^3 r$$

$$= \sqrt{B(E4;\ 0^+ \rightarrow 4^+)}\ ,$$

where ρ is the nuclear charge density. The effect of an E4 moment on the cross section for populating the 4^+ level of ^{152}Sm in coincidence with backscattered ^4He ions ($d\sigma$) is shown, normalized to the cross section with no E4 moment ($d\sigma_0$). This behavior changes very little with projectile scattering angle, so that the corresponding curve for the singles measurements differs by only a few percent. The general shape of this curve is caused by the dominance of the direct E4 transition, which depends quadratically on the moment. The weaker interference term (linear) causes

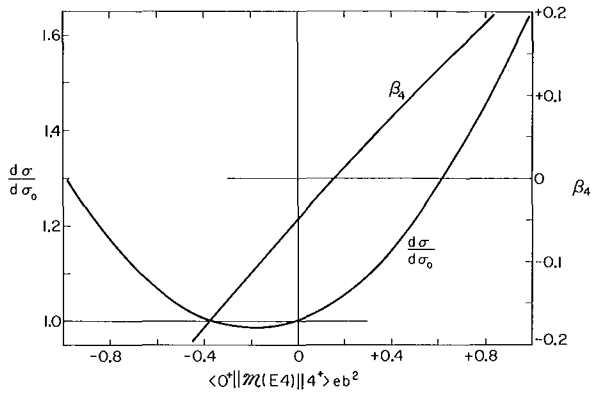

Fig. 1. Relationship between the E4 moment and a) the normalized cross section (backscatter) for populating the 4^+ state of ^{152}Sm with 10.4 MeV ^4He ions, and b) the deformation parameter, β_4, using a radius of $R_0 = 1.2\ A^{1/3}F$ (see text). (XBL 703-2496)

the asymmetry about zero. Also shown in Fig. 1 is the relationship of the E4 moment to the deformation parameter, β_4, which will be defined below. This curve has been constructed by adjusting β_2, for each value of β_4, so that the measured B(E2; $0^+ \rightarrow 2^+$) value in ^{152}Sm is reproduced. The asymmetry of this curve relative to zero is caused by the positive second-order contribution to the E4 moment from β_2. The asymmetries in these two curves make it unlikely that one can measure negative E4 moments by this technique, since reasonable values[3] of β_4 (≥ -0.2) do not give rise to sufficiently large negative E4 moments to cause measurable deviations in the cross section. This situation renders improbable one of the two possibilities for the moment that would otherwise result from a given cross-section measurement. Small positive values of β_4, however, should produce readily measurable effects in the cross section.

The experimental details and corrections have been given in a fuller report of this work.[4] An effect that has not yet been evaluated is the possibility of quantal corrections to the semiclassical calculations used. These would be expected to lower the calculated cross sections[5] (increase our E4 moment) and could be as large as a few percent. In Fig. 2 we have plotted the ratio of the observed cross section, (σ), against the bombarding energy. The error bars on the data

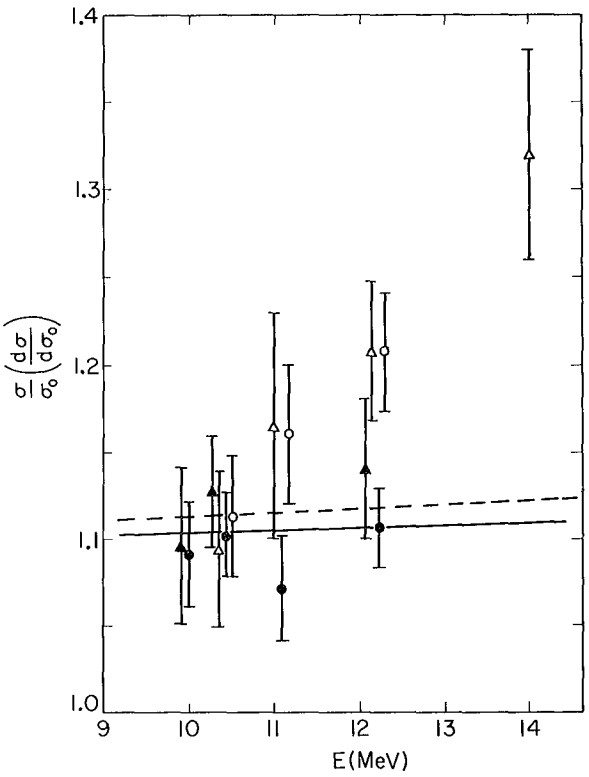

Fig. 2. The measured cross sections for populating the 4^+ level of ^{152}Sm normalized to the appropriate calculated value with no E4 moment, plotted against the bombarding energy. The solid points are for enriched ^{152}Sm targets and the open ones are for natural samarium targets. The triangles and circles are backscatter and singles results, respectively. The dashed and solid lines are the calculated results for backscatter coincidences and singles, respectively, with $\langle 0^+ \| \mathfrak{M}(E4) \| 4^+ \rangle = +0.35$ eb^2.

(XBL 703-2495)

points do not include any of the systematic uncertainties involved in the analysis. The dashed and solid lines show the values for the backscatter and singles data, respectively, corresponding to an E4 moment of $+(0.35 \pm 0.11)$eb^2, which is the best fit to the data below 11 MeV.

If we assume the nucleus to be a rigid, uniformly-charged rotor with a sharp surface defined by:

$$R = R_0 (1 + \beta_2 Y_{20} + \beta_4 Y_{40}),$$

we can evaluate β_2 and β_4 from the measured E2 and E4 transition moments. Taking the charge radius to be $R_0 = 1.2\ A^{1/3}$F, we find $\beta_2 = (+)\ 0.259$ and $\beta_4 = +0.058 \pm 0.032$ in ^{152}Sm. The sign of β_2 has been assumed to be positive in this analysis. These values of β_λ depend on the radius used and change roughly as $R_0^{-\lambda}$. The inclusion of still higher moments would probably affect the deduced deformation parameters slightly. It is interesting to try to compare this shape of the charge field with the shape of the nuclear field measured by Hendrie et al.,[6] who found $\beta_2 = +0.246$ and $\beta_4 = +0.048$ for the above value of R_0. These appear to be quite similar, but it is not really clear that this is the proper way to compare these two sets of results. The present value of β_4 is also in reasonable accord with theoretical estimates[3] of nuclear shapes.

Footnotes and References

†Condensed from Phys. Rev. Letters 24, 1137 (1970).

*Rutgers University, New Brunswick, New Jersey 08903 and Universität München, München, Germany.

1. F. S. Stephens, David Ward, R. M. Diamond, J. de Boer, and R. Covello-Moro (to be published).

2. R. M. Diamond, F. S. Stephens, R. Nordhagen, and K. Nakai, Proceedings of the International Conference on Properties of Nuclear States, Montreal, Canada (University of Montreal Press, 1969), p. 653; Phys. Rev. C 3, 344 (1971)

3. S. G. Nilsson, C. F. Tsang, A. Sobiczewski, Z. Szymanski, S. Wycech, C. Gustafson, I. -L. Lamm, P. Möller, and B. Nilsson, Nucl. Phys. A131, 1 (1969); P. Möller, to be published.

4. F. S. Stephens, R. M. Diamond, N. K. Glendenning, and J. de Boer, Phys. Rev. Letters 24, 1137 (1970).

5. K. Alder and H. K. Pauli, Nucl. Phys. A128, 193 (1969).

6. D. L. Hendrie, N. K. Glendenning, B. G. Harvey, O. N. Jarvis, H. H. Duhm, J. Saudinos, and J. Mahoney, Phys. Letters 26B, 127 (1968).

Lifetime of Ground-Band States in ^{154}Sm

R. M. Diamond, G. Symons,† J. Québert,* K. Nakai,‡
K. H. Maier,†† J. R. Leigh, and F. S. Stephens

It is well known that the energy spacings of the first few ground-band levels of doubly-even deformed rare-earth nuclei are, to a first approximation, in agreement with the rigid-rotor expression,

$$E_I = AI(I + 1); \quad (1)$$

however, in detail, they diverge from this simple formula to a greater or lesser degree. There seems to be a number of causes for this behavior, the most prominent being Coriolis antipairing, centrifugal stretching, and fourth-order cranking model corrections.[1] These effects should also cause deviations of transition probabilities from the expectations of the simple rigid-rotor formula,

$$B_0(E2;I \rightarrow I\text{-}2) = B_0(E2;2 \rightarrow 0) \frac{\langle I\,200 | I2\,I\text{-}20\rangle^2}{\langle 2\,200 | 2\,200\rangle^2}. \quad (2)$$

For centrifugal stretching the deviations in the transition probabilities may be directly related to those in the energy-level spacings, but for the other two effects the relationships are not known. For them even the sign of the deviations is not known. So it is not clear overall whether the transition probability differences will be larger, smaller, or similar in magnitude, or even of which sign, compared with the differences in the energy spacings.

For good rotors, both sets of differences are expected to be small. This makes the deviations in B(E2) values particularly difficult to observe. We have chosen to study the ground-band transition probabilities in ^{154}Sm by the direct-distance Doppler-shift method,[2,3] because we believe that it currently gives the most accurate values of the B(E2)'s.

A schematic drawing of the experimental arrangement is shown in Fig. 1; it is essentially the same as in previous studies.[3] A collimated beam of 146 MeV ^{40}Ar ions from the Berkeley Hilac passes through the aperture in a Si-ring counter and strikes a 1 mg/cm^2 target of ^{154}Sm metal which has been stretched tight and flat. The recoiling (Coulomb -) excited nuclei gamma cascade to ground, either while in flight or after stopping in the lead-covered plunger. The γ rays are observed in a Ge(Li) detector placed behind the plunger at 0° to the original beam direction and operated in coincidence with backscattered (148°- 160°) ^{40}Ar projectiles detected in the ring counter. Since the velocity of the recoiling Sm nuclei is $\approx$ 3.4% that of light, the Doppler-shifted transition is moved to a sufficiently high energy to be clearly resolvable from the unshifted line. Changes in the distance between the target and the plunger can be measured to 0.003 mm. Such changes vary the relative intensities of the shifted and unshifted transitions, allowing determination of the mean lifetime of the (upper) state involved, if the average recoil velocity is also known.

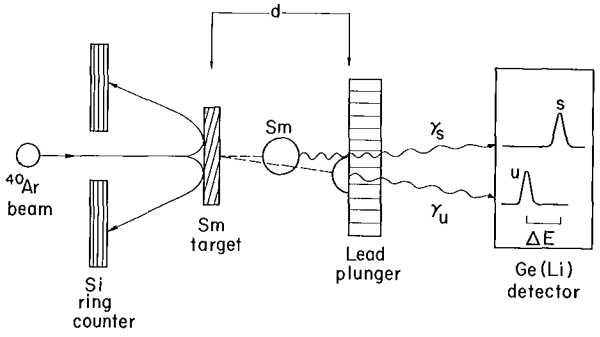

Fig. 1. Schematic representation of direct-difference Doppler-shift arrangement; γ_s and γ_n represent the shifted and unshifted gamma transitions, respectively. (XBL 708-3633)

At each distance the intensities of the unshifted and shifted transitions have been integrated and corrected for accidental coincidences and for background. Additional small corrections have been made for the small changes in solid angle at the Ge counter due to the change in position of the lead plunger; for the variation in the Ge counter efficiency with shifted γ-ray energy; and for the change in the angular distribution and in the solid angle at the Ge counter caused by the motion of the recoiling nucleus.

A semilogarithmic plot is shown in Fig. 2 of the fraction of unshifted intensity for the $8^+ \rightarrow 6^+$, $6^+ \rightarrow 4^+$, and $4^+ \rightarrow 2^+$ transitions vs the target-plunger distance. Actually, two further corrections must be applied in the data analysis: one for the feeding of the level

Table I. B(E2) Values for ^{154}Sm

Transition	Energy (MeV)	$T_{1/2}$ (p sec)	α_T	B(E2; I → I-2) (c^2 b^2)	
				experiment	rotor
2 → 0	81.99	3017±38	5.003	0.843±0.021	(0.843)
4 → 2	184.9	172.7±5.0	0.277	1.186±0.037	1.205
6 → 4	277.4	23.34±0.69	0.074	1.374±0.047	1.328
8 → 6	359.1	6.17±0.62	0.032	1.49±0.15	1.391

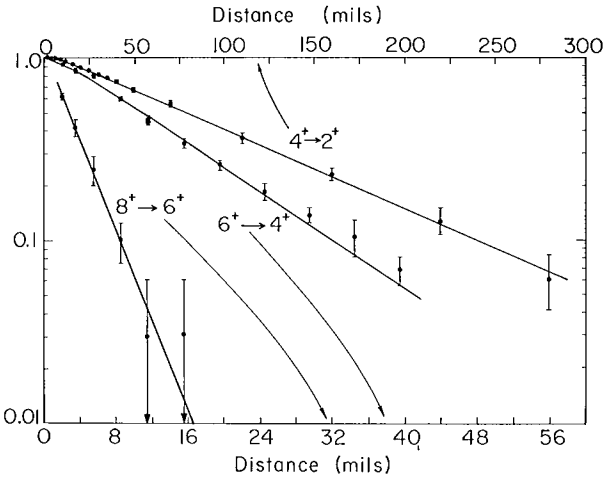

Fig. 2. The fraction of each transition in ^{154}Sm which is unshifted in energy vs the distance between target and plunger. The symbols are the experimental points; the lines are the computer best fits allowing for one stage of feeding.
(XBL711-2569)

of interest by transitions from a higher-lying state; and another for the attenuation of the angular distribution of the γ rays by the hyperfine field of the unpaired electrons of the recoiling ion. The results of a computer least-squares fit are shown as the solid line in Fig. 2, and the deduced half-lives are given in Table I. It should be noted that the lifetime of the 2^+ level has not been measured in this study, but is taken as the mean value of two direct electronic measurements,[4,5] which agree to within 1%.

From Table I it can be seen that the presently measured B(E2) values fit the $2^+ \rightarrow 0^+$ transition moment, and within their experimental errors are in agreement with the expectations of the rigid-rotor formula, Eq. (2). Still better accuracy would be needed to see if the deviations are consistent with a small degree of centrifugal stretching, as a comparison of the deviations in the energy-level spacings for ^{154}Sm and ^{152}Sm suggest that the former are ≈ 4 times smaller than the latter. When this factor is carried over to the B(E2) measurements, the expected deviations are just the order of the present experimental errors.

Footnotes and References

†Summer visitor, 1969; present address: Department of Nuclear Physics, The Australian National University, Canberra, Australia.

*Present address: C. E. N. Bordeaux-Gradignan, France.

‡Present address: Niels Bohr Institute, Copenhagen, Denmark.

††Permanent address: Hahn Meitner Institute for Nuclear Research, Berlin, Germany.

1. See, for example, C. W. Ma and J. O. Rasmussen, Phys. Rev. C 2, 798 (1970) or E. R. Marshalek, Phys. Rev. 158, 993 (1967), and the references listed therein.

2. See, for example, T. K. Alexander and R. W. Allen, Can. J. Phys. 43, 1563 (1965) or K. W. Jones, A. Z. Schwarzschild, E. K. Warburton, and D. B. Fossan, Phys. Rev. 178, 1773 (1969), and the references listed therein.

3. R. M. Diamond, F. S. Stephens, K. Nakai, and R. Nordhagen, Phys. Rev. C 3, 344 (1971); J. L. Québert, K. Nakai, R. M. Diamond, and F. S. Stephens, Nucl. Phys. A150, 68 (1970).

4. F. W. Richter, J. Schütt, and D. Wiegandt, Z. Physik 213, 202 (1968).

5. P. J. Wolfe and R. P. Scharenberg, Phys. Rev. 160, 866 (1967).

Levels in ^{157,159}Er

J. R. Leigh, R. M. Diamond, K. H. Maier,† R. Nordhagen,* and F. S. Stephens

The isotopes of ^{157,159}Er have been studied following (^{12}C, 3n) and (^{40}Ar, 3n) reactions on isotopically enriched targets of ^{148,150}Sm and ^{120,122}Sn, respectively. Gamma-gamma coincidence measurements have been performed and establish the schemes shown in Figs. 1 and 2. Singles Ge(Li) spectra have been recorded in-beam and following the beam on time scales ranging from ≃ 100 nsec to ≃ 100 msec.

The prompt de-excitation proceeds predominantly by E2 transitions between members of a positive parity band, considered to arise from strong Coriolis mixing between the states of the i 13/2 Nilsson orbit. The $13/2^+ \rightarrow 9/2^+$ transition has not been observed in either isotope due to its low energy, though it is determined in ^{159}Er by the decay

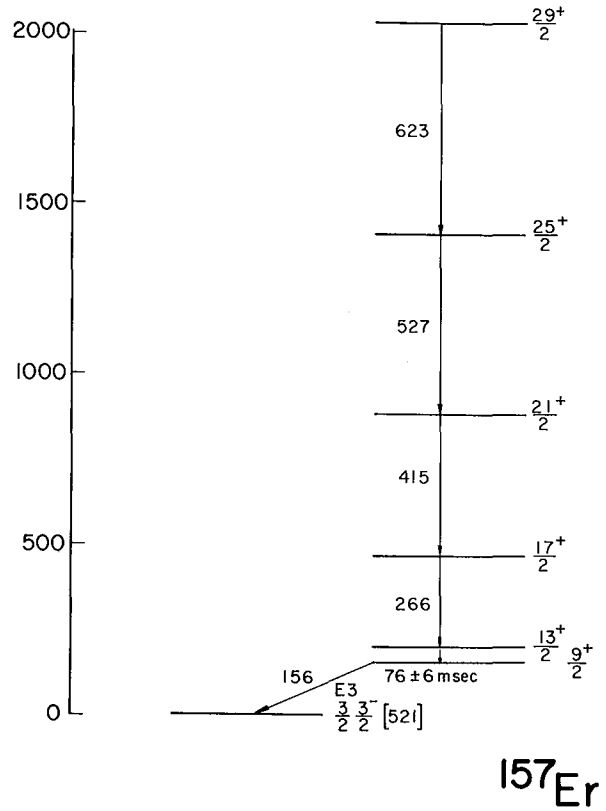

Fig. 1. Partial level scheme for ^{157}Er. (XBL712-2948)

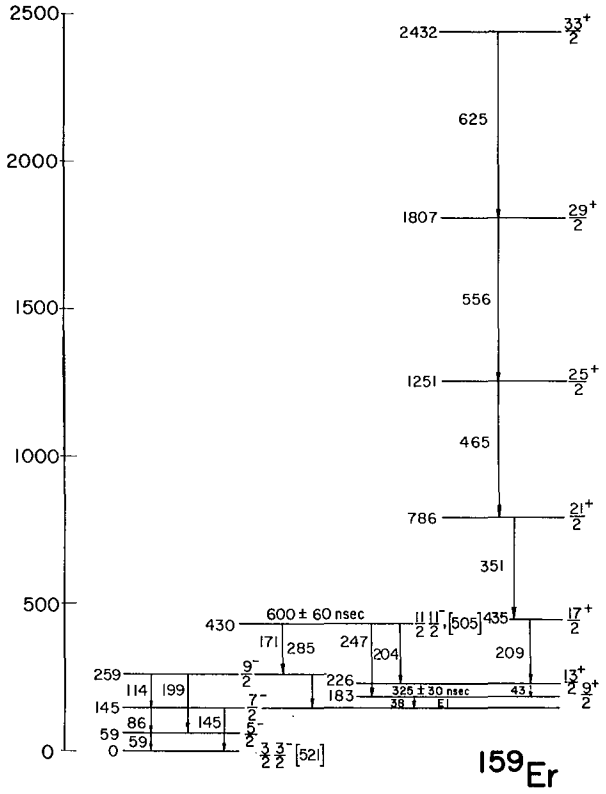

Fig. 2. Partial level scheme for ^{159}Er. (XBL712-2949)

of the $11/2^-$ [505] state to both the $9/2^+$ and $13/2^+$ levels. The energy of this transition is expected to be approximately the same in both isotopes.

The ground-state spins of both nuclei have been measured as 3/2.[1] In ^{157}Er the $9/2^+$ member of the mixed positive parity band decays via an E3 transition to the ground-state, assigned as $3/2^-$ [521]. The half-life of the $9/2^+$ state has been measured in a solenoid electron-spectrometer, the decay being observed between the Hilac beam bursts (every 200 msec for this purpose). Only one transition was observed. Its E3 nature being established by the K/L/M ratios of the conversion electrons. The absence of an M2 transition to the $5/2^-$ member of the ground-state band might imply a rotational constant $\gtrsim$ 30, approximately 2.5 times that of ^{159}Er. The ^{159}Er level scheme is very similar to that of ^{161}Er,[2] the

Table I.

Isotope	State	Transition	Multipolarity	Hindrance factor
^{157}Er	$9/2^+$	76±6msec		
		$9/2^+ \rightarrow 7/2\ 3/2^-[521]$	E3	4
^{159}Er (^{161}Er)	$9/2^+$	325±30nsec (70±20nsec)		
		$9/2^+ \rightarrow 7/2\ 3/2^-[521]$	E1	1.9×10^5 (0.6×10^5)
	$11/2^-[505]$	600±60nsec (7.5±0.7μsec)		
		$11/2^- \rightarrow 9/2\ 3/2^-[521]$	M1	3.0×10^5 (49×10^5)
		$11/2^- \rightarrow 7/2\ 3/2^-[521]$	E2	2.0×10^3 (24×10^3)
		$11/2^- \rightarrow 13/2^+$	E1	3.4×10^8 (9.5×10^8)
		$11/2^- \rightarrow 9/2^+$	E1	4.2×10^8 (24×10^8)
		$11/2^- \rightarrow 11/2^+$	E1	----- (3.7×10^8)

$9/2^+$ state decaying only to the 7/2 $3/2^-$ [521] level. The $11/2^-$ [505] level is also populated in the reaction and, as in ^{161}Er,[2,3] decays to members of the ground band and the positive parity band. The half-lives of both the $9/2^+$ and $11/2^-$ states have been measured using a chopped beam and standard time-to-amplitude conversion techniques.

The half-life results are summarized in Table I, and the decay characteristics of the $11/2^-$ and $9/2^+$ levels of ^{159}Er and ^{161}Er are compared. The hindrance factors relative to the single particle estimate, associated with the same transitions in these two isotopes would be expected to be similar. The most significant difference involves the decay of the $11/2^-$ [505] state to the ground band. Both the M1 ($11/2^- \rightarrow 9/2^-$) and E2 ($11/2^- \rightarrow 7/2^-$] transitions of ^{159}Er are more than an order of magnitude faster than those in ^{161}Er. The difference is possibly indicative of changes in the Coriolis mixing in all these states, which arise from high-j Nilsson orbits where the mixing might be significant.

Coriolis coupling calculations are being performed to fit the positive parity states. Similar calculations have been performed[2] for the heavier isotopes of Er, and it will be interesting to see how well this description applies to the less well-deformed isotopes studied here.

Footnotes and References

†NATO fellow on leave from Hahn-Meitner Institute, Berlin.

*Present address: Institute of Physics, University of Oslo, Norway.

1. C. Ekström, T. Noreland, M. Olsmats, and B. Wannberg, Nucl. Phys. A135, 289 (1969).

2. S. A. Hjorth, H. Ryde, K. A. Hagemann, G. Løvhøiden, and J. C. Waddington, Nucl. Phys. A144, 513 (1970).

3. J. Borggreen and G. Sletten, Nucl. Phys. A143, 255 (1970).

Rotational Bands in Odd-Odd Holmium Isotopes †

J. R. Leigh, F. S. Stephens, and R. M. Diamond

The following reactions have been used to populate high-angular-momentum states in ^{160}Ho and ^{162}Ho; ^{154}Sm(^{11}B, 5n)^{160}Ho, ^{159}Tb(^{4}He, 3n) ^{160}Ho and ^{160}Gd(^{7}Li, 5n) ^{162}Ho. The schemes presented in Fig. 1 are established by γ-γ coincidence measurements. Angular distribution measurements indicate a series of cascading M1-E2 transitions, where the E2 admixture is a few percent. Excitation functions indicate increasing angular momentum up the band.

The 6^- state of ^{162}Ho has been assigned as the p 7/2$^-$ [523] n 5/2$^+$ [642] configuration.[1] Comparison of the band intensity and that of the decay of the 106 keV 6^- level suggests that the observed band is based on this 6^- state. In ^{164}Ho, three rotational levels have been attributed[2] to this same 6^- configuration, and the similarity of that band to the one discussed here lends support to the present assignment. (The similarity of these two bands would be even more striking using an alternative assignment discussed in Ref. 2.) This 6^- configuration should also occur in ^{160}Ho and the band observed there is most probably also based on this state. The 169 keV level is tentatively assigned as the 6^- state; with this assignment a possible configuration for the 118 keV would be 5^-, p 7/2$^-$ [523] n 3/2$^+$ [402].

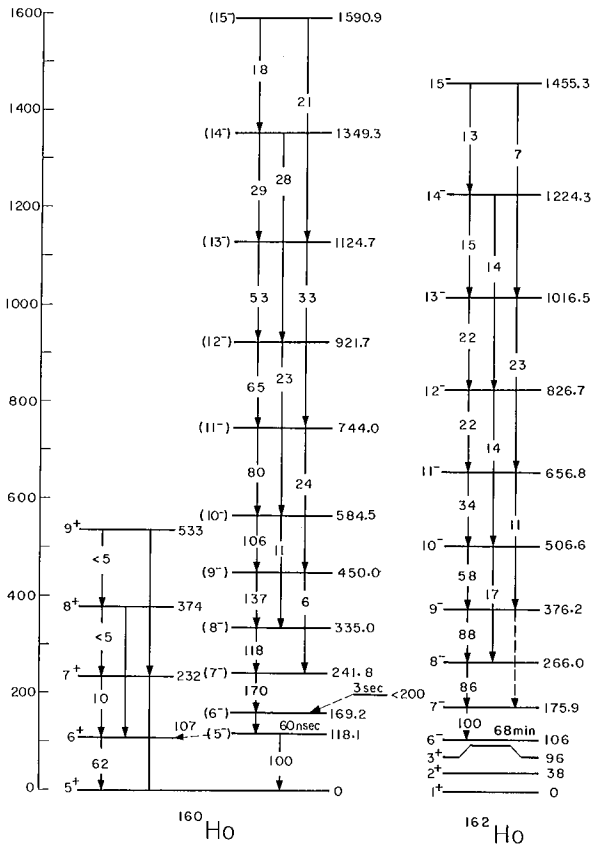

Fig. 1. Level schemes for ^{160}Ho and ^{162}Ho. Relative transition intensities are indicated and are those obtained following ^{154}Sm(^{11}B, 5n)^{160}Ho and ^{160}Gd(^{7}Li, 5n) ^{162}Ho reactions. (XBL 707-3363)

The rotational sequence has been fitted with the expression

$$E_I = E_0 + AI(I+1) + BI^2(I+1)^2 + CI^3(I+1)^3 + (-1)^{I+K} A_{2K} \frac{(I+K)!}{(I-K)!} \quad (1)$$

The band has three rather striking properties: 1) an apparent moment of inertia approximately twice the rigid-body value (A = 3.3 keV for ^{162}Ho and 3.5 keV for ^{160}Ho); 2) a positive rotation-vibration interaction term (B = +22 eV for ^{162}Ho and +21 eV for ^{160}Ho); and 3) a small oscillating term of order 10^{-14} keV for both. This is precisely the behavior expected from highly Coriolis-mixed bands, and is not surprising in this case since bands based on the proton and neutron states involved in this configuration show large Coriolis mixing in neighboring odd-A Ho[3] and Er[4] isotopes respectively.

Coriolis mixing in odd-A nuclei has been treated rather comprehensively[4, 5] and the largest effects come from the unique-parity, high-j Nilsson orbits within each shell. In the odd-odd case, coupling can take place through both proton and neutron states and many more states become important. For the present band in $^{162, 160}$Ho, both the proton and neutron occupy the above mentioned orbitals for their respective shells, namely the $h_{11/2}$ and $i_{13/2}$ orbits.

The lowest-order effect of the mixing on the level spacing is to increase the apparent moment of inertia in the band. Thus, neutron states associated with the $i_{13/2}$ orbit in odd-A nuclei in this region have moments of inertia close to the rigid-body value[6] or above in special cases.[7] Likewise, the $h_{11/2}$ proton states have exceptionally large mo-

ments of inertia, though less dramatic than those of the above neutron states. The coupling of these two states in the 6^- band combines the contributions to the moment of inertia due to each one, producing the enormous effective moment observed. In such highly compressed bands there is a general higher-order effect leading to positive B terms, in accordance with the observations on the present bands.

The oscillation in the energy levels observed in strongly Coriolis-mixed odd-A bands can be described as due to the successive coupling of states with K, K - 1 $\cdots$, etc. back to the 1/2 band; the decoupling parameter of this band being responsible for the oscillation. The magnitude of the oscillation is reduced at each stage and hence is smallest for highest K. In the odd-odd case, K = 0 bands generally exhibit a displacement of the even-spin levels relative to the odd-spin ones[8] which can be transmitted to the K = 6 band. In the case of $\Omega_n = \Omega_p = 1/2$, the Coriolis mixing of the K = 0 and K = 1 bands gives a contribution to this displacement. For the $\Omega = 1/2$ bands of interest here, namely n $1/2^+[660]$ and p $1/2^-[550]$, the Coriolis effects will be large and likely to dominate other sources of displacement. If so, one can predict A_{2K} (Eq. 1) to be negative. This is, indeed, in accordance with the observed sign. However, the last term of Eq. 1 does not reproduce the observed I dependence of the oscillation very well, probably due to contributions from other bands and from higher-order terms.

Footnote and References

†Condensed from Phys. Letters 33B, 410 (1970).

1. C. Ekström, T. Noreland, M. Olsmats, and B. Wannberg, Nucl. Phys. A135, 289 (1969); M. Jørgensen, O. B. Nielsen, and O. Skilbreid, Nucl. Phys. 24, 443 (1961).

2. H. D. Jones and R. K. Sheline, Nucl. Phys. A150, 497, (1970).

3. R. M. Diamond and F. S. Stephens, unpublished data.

4. K. A. Hagemann, S. A. Hjorth, H. Ryde, and H. Ohlsson, Phys. Letters 28B, 661 (1969); S. A. Hjorth, H. Ryde, K. A. Hagemann, G. Løvhøiden, and J. C. Waddington, Nucl. Phys. A144, 513 (1970).

5. F. S. Stephens, D. M. Holtz, R. M. Diamond, and J. O. Newton, Nucl. Phys. A115, 129 (1968).

6. O. Nathan and S. S. Nilsson, Alpha-, Beta-, and Gamma-Ray Spectroscopy, edited by K. Siegbahn, (North-Holland Publishing Co., Amsterdam, Vol. 1), Chap. X.

7. O. Schult, et al., Phys. Rev. 154, 1146 (1967).

8. N. D. Newby, Jr., Phys. Rev. 125, 2063 (1962).

The Ground-State Bands of the N = 126 Nuclei ^{212}Rn and ^{214}Ra Studied by (HI, xn) Reactions

K. H. Maier, J. R. Leigh, R. M. Diamond, and F. S. Stephens

Of the even nuclei with the magic neutron number N = 126 above ^{208}Pb, only the level scheme of ^{210}Po has been studied.[1] According to the shell model, the configuration $(h9/2)^{2n}$ (n = 1, 2, 3) should be most important for the 0^+, 2^+, 4^+, 6^+, 8^+ levels of the "ground-state band" in these three nuclei. In ^{210}Po the lifetimes of all the levels except for the 2^+ are long enough to be measured electronically, so we could expect to be able to measure not only energies, but also lifetimes and possibly magnetic moments, thus gathering enough data for a more detailed understanding of these nuclei.

^{212}Rn: An excitation function of the reaction ^{209}Bi (^{7}Li, 4n) ^{212}Rn showed three strong γ rays at 138.2, 227.6, and 1273.7 keV. The maximum yield lies between 42 and 46 MeV ^{7}Li energy, which agrees with the expected value for a 4n reaction. A γ-γ coincidence measurement for the same reaction showed all three lines to be in coincidence. The order of the sequence (Fig. 1) could be established through the relative intensities of the lines. Preliminary measurements showed all three lines to have a common half-life of about 1 μsec. The delayed conversion electrons from the ^{205}Tl (^{11}B, 4n) ^{212}Rn were then examined with a pulsed beam. Their intensities together with those of the delayed γ-lines established the 138 and 227 keV transi-

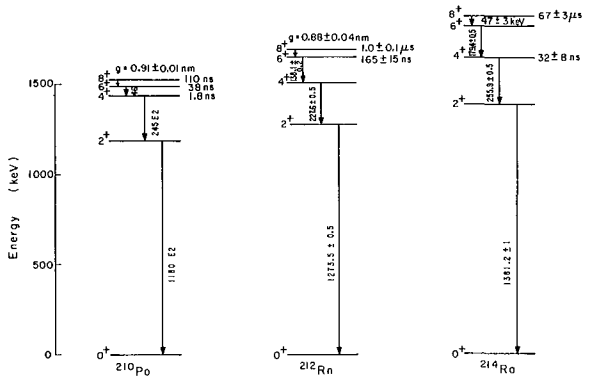

Fig. 1. The ground-state bands of the N = 126 nuclei ^{210}Po (Ref. 1), ^{212}Rn, and ^{214}Ra. (XBL 712-2815)

tions to be of E2 multipolarity. The $8^+ \rightarrow 6^+$ transition could not be seen, setting an upper limit of 60 keV to its energy. But since the lifetime is unreasonably long for a 138-keV E2 transition, we assume the reaction has to proceed to a large extent through the (unseen) low energy $8^+ \rightarrow 6^+$ transition. A time differential measurement of the g factor using the ^{204}Hg (^{12}C, 4n) ^{212}Rn reaction with a pulsed beam gave $g(8^+, {}^{212}\text{Rn}) = (0.88 \pm 0.04)$ μ_N and $T_{1/2} = (1.0 \pm 0.1)$ μsec. Simultaneously, it showed that the A_2 coefficients of the 227 keV and 1274 keV lines agree with the values for stretched E2 transitions.

^{214}Ra: This nuclide was produced by means of the ^{206}Pb (^{12}C, 4n) reaction. An excitation function taken simultaneously for γ rays and for the known α particles from its decay showed the three strongest lines in the spectrum at 180, 256, and 1381 keV to belong to ^{214}Ra. A common half-life $T_{1/2}=67 \pm 3$ μsec was found in a pulsed-beam measurement. All three lines are in coincidence, too. A delayed conversion electron spectrum revealed one more strong transition of 47 ± 3 keV and is consistent with E2 assignments to all lines, although it does not determine the multipolarities unambiguously. An attempt failed to make ^{214}Ra via ^{204}Hg (^{16}O, 4n), in order to preserve the alignment and measure the magnetic moment and the angular distributions. This seems to be due mainly to the fact that the compound nucleus decays mostly by fission. The striking feature here is the 67 μsec half-life of the $8^+ \rightarrow 6^+$ transition which corresponds to less then 10^{-3} single particle units. We therefore have to convince ourselves that the half-life is really connected with this transition. The 47 keV transition is limited to E2 or M2 multipolarity from its energy, half-life, and the intensity of the L and M conversion electrons. We can eliminate M2, as the 8^+ level should be populated strongly and we find no prompt or much faster component (< 10%). This same fact makes it unlikely that the delay is connected with a transition into the 8^+ level. Such a transition would have to be below 45 keV to escape detection, and most likely M2 to explain the lifetime, and there is no reason to expect such a transition.

One very similar case is known. In ^{94}Ru an $8^+ \rightarrow 6^+$ transition of 145 keV shows a half-life of 71 μsec.[2] ^{94}Ru is 6 protons short of the doubly magic ^{100}Sn and the proton holes are mainly in the $g_{9/2}$ shell. ^{214}Ra consists of 6 protons in the $h_{9/2}$ shell added to the ^{208}Pb core. So the explanation probably is the same in both cases. The seniority scheme allows prediction of the E2 moments of ^{212}Rn and ^{214}Ra from those in ^{210}Po (Ref. 3)

$$3\langle (h_{9/2}{}^4)_I \,|\, \mathcal{M}(E2) \,|\, (h_{9/2}{}^4)_{I'} \rangle$$

$$= \langle (h_{9/2}{}^2)_I \,|\, \mathcal{M}(E2) \,|\, (h_{9/2}{}^2)_{I'} \rangle$$

$$= -3\langle (h_{9/2}{}^6)_I \,|\, \mathcal{M}(E2) \,|\, (h_{9/2}{}^6)_{I'} \rangle,$$

for the seniority v = 2. Indeed, the lifetime of the 8^+ level in ^{212}Rn is about 9 times that found in ^{210}Po as predicted. Though neither transition energy is measured, they cannot significantly influence the lifetimes (as long as they are high enough for L conversion to take place) as the transitions proceed predominantly by electron conversion.

The g factors of the 8^+ levels in ^{210}Po and ^{212}Rn coincide within the small errors, being $0.91 \pm 0.01\ \mu_N$ and $0.88 \pm 0.04\ \mu_N$,[4] respectively. So the 8^+ level in ^{212}Rn seems to be well described by a $(h_{9/2}{}^4)$ configuration with seniority v = 2.

The lifetime found in ^{214}Ra, however, is 50 times that predicted for an $(h_{9/2}{}^6)$ configuration from the ^{210}Po lifetime. If we assume the wave function for ^{214}Ra to be

$$\chi = A \,|\, (h_{9/2}{}^6)_{I=8^+,\ v=2} \rangle + B \,|\, (h_{9/2}{}^4)_{I=8^+,\ v=2} \; (j^2)_{I=0} \rangle,$$

with j standing for any other orbit such as $i_{13/2}$ or $f_{7/2}$ or a mixture, we can get a complete cancellation of the two matrix elements for $A = \pm B = 1/2$. The pairing interaction is likely to admix such components. The spacing between the 0^+ and 2^+ levels and, in fact, the increasing spacing in this series of nuclei, indicates the importance of the pairing interaction. It is, however, very striking that the

cancellation is so complete in ^{214}Ra and in ^{94}Ru; especially as the lifetimes of the 6^+ level in ^{94}Ru and of the 4^+ level in ^{214}Ra are much less, though still very significantly, retarded. One also expects the same type of admixture to occur in ^{212}Rn, but its magnitude should be smaller and it should have considerably less effect on the half-life due to the like signs of the moments in this case. There should be no effect on the magnetic moment. So the agreement with the simple prediction is quite reasonable.

An attempt to look at ^{216}Th, the next nucleus in the sequence, with the ^{204}Pb (^{16}O, 4n) reaction was unsuccessful. We saw only a smooth background in the γ-ray spectrum. By looking at fission products directly and their characteristic x rays, it became clear that the reason for this was that fission dominated the decay of the compound nucleus.

References

1. T. Yamazaki, Phys. Rev. C1, 290 (1970).
2. J. M. Jaklevic, C. M. Lederer, and J. M. Hollander Physics Letters 29B, 179 (1969).
3. Amos de-Shalit and Igal Talmi, Nuclear Shell Theory (Academic Press, New York and London, 1963) formula (28.40), p. 315.
4. T. Yamazaki, T. Nomura, U. Katou, T. Inamura, A. Hashizume, and Y. Tendou, Phys. Rev. Letters 24, 317 (1970).

Some Limitations in the Production of Very Neutron-Deficient Nuclei †

F. S. Stephens, J. R. Leigh, and R. M. Diamond

Heavy-ion reactions have been used for a number of years as a means of producing and studying neutron-deficient nuclei. The fusion of a target and projectile nucleus inevitably tends to produce a neutron-deficient compound system due to the increasing neutron excess of heavier nuclei along the valley of beta stability. These compound systems are produced with considerable excitation energy, which usually results in the evaporation of a few particles. For heavier nuclei, the Coulomb barrier inhibits the evaporation of charged particles resulting (normally) in a strong preference for evaporating neutrons. This tends to produce still more neutron-deficient products. As the compound system becomes very neutron-deficient, however, proton evaporation competes with, and eventually dominates over, neutron evaporation, resulting in products which are less neutron-deficient. This competition constitutes a limit on our ability to produce very neutron-deficient products using this method, and the present work has explored the nature and location of this limit in the region of the periodic table between tin and lead. Above Pb, fission begins to compete with particle evaporation from the compound system and this changes the situation rather completely.

In order to find the limit in producing neutron-deficient products nuclei, we must evaluate two things. These are (1) which compound system can be produce and (2) what particles will be evaporated from this system. The first of these is easy to evaluate under any given conditions for a particular projectile-target combination. Since accelerators will soon be available that can accelerate any nucleus, we have chosen, as a reasonable condition, only that both target and projectile must exist in nature. This is not an ultimate limit, but seems likely to be the best achievable in the near future. One can then easily determine the lightest compound nucleus (LCN) that can be produced for each element. In Fig. 1 this limit is shown as the heavy line.

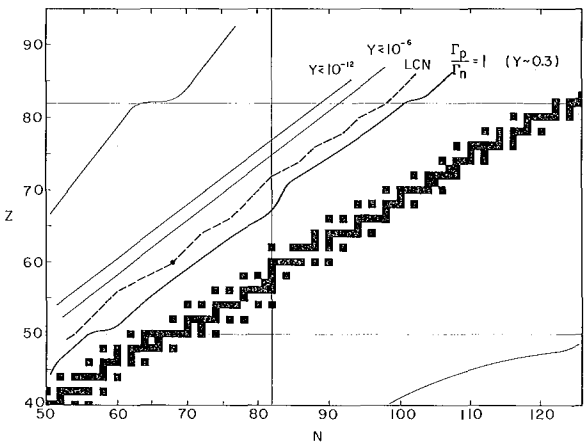

Fig. 1. Section of the chart of nuclides showing the location of the various lines discussed in the text. (XBL 706-3153)

The question of which particles are evaporated from a compound nucleus clearly depends on the relative effective binding energies. For neutrons, these effective binding energies do not differ from the usual binding energy,[2] but for protons they must include an effective Coulomb barrier. We believe this effective barrier can be best determined empirically from the proton-neutron relative evaporation rates near the point where they are equal. We have used the very simple relationship[1]

$$P_n/P_p = e^{-\left(\frac{B_n - B_p^*}{T}\right)} \qquad (1)$$

where P_n and P_p are the probabilities of evaporating a neutron and proton respectively, B_n is the neutron binding energy, B_p^* is the effective proton binding energy, and T is the nuclear temperature. One can see that B_p^* can be determined from P_n/P_p since B_n is available from the mass tables and T is not very important if $P_n/P_p \approx 1$. We then obtain the effective Coulomb barrier, E_c^*, from

$$B_p^* = B_p + E_c^* , \qquad (2)$$

where B_p is the proton binding energy from the mass tables. We can then scale E_c to other elements on the assumption that

$$E_c^* = k \frac{Z}{1 + A^{1/3}} , \qquad (3)$$

where k is a number (presumably near one) that is evaluated from the measured E_c^*. This method has the enormous advantage that errors in B_n, B_p, or Eq. (3) are normalized out at the point where P_n/P_p is measured, and only relative errors from this point are important. For the region we are interested in, around $P_n/P_p \approx 1$, the value chosen for T is not very important, but it is critical for calculating P_n/P_p far from this region. We have used T = 1.5 MeV. For alpha evaporation, we have used the simple empirical values $P_p/P_\alpha = 3$ for the Ce region and $P_p/P_\alpha = 2$ for the Os region.

In the Ce and Os regions, we have measured the relative yields of two or more reaction products, from about 10 different compound nuclei. These determine k to be 0.85 ± 0.05, where the uncertainty in k reflects the rms deviation between the calculated and experimental results. This value of k determines the point of equal probability of emission of a proton and a neutron to about $\pm$ 1.5 amu, and this line is shown in Fig. 1. Also indicated in Fig. 1 are lines where the maximum yields obtainable have fallen to 10^{-6} and 10^{-12} of the compound nucleus cross section. The proton and neutron drip lines are the two widely-spaced lines.

In Fig. 2 are shown calculations which are relevant to producing Ce product nuclei. We show here the cross sections (relative to those of the compound nucleus) to be expected from several types of reactions which produce Ce product nuclei of various mass

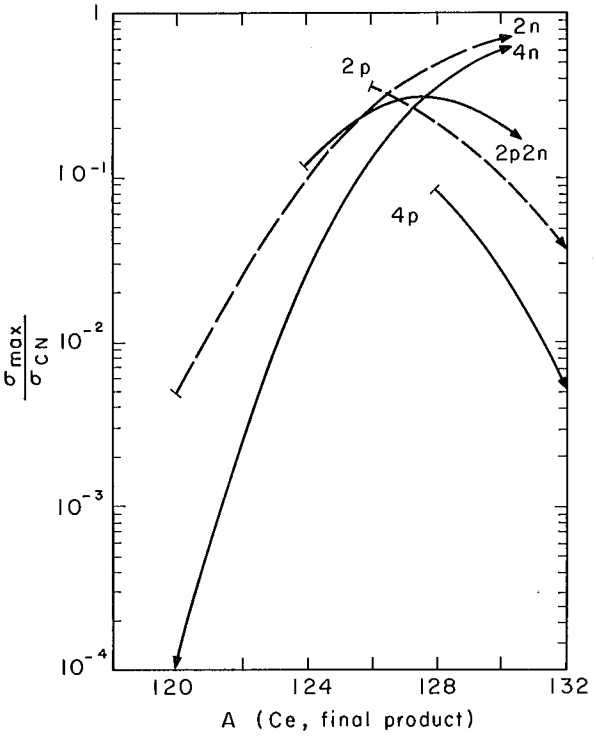

Fig. 2. Expected yields (see text) of Ce nuclei resulting from various reactions. (XBL 706-3148)

numbers. Several conclusions may be drawn from this plot. The first is that above mass 128 the HI, xn reactions are the best, and should give yields of 50% or higher. A second is that the HI, xp reactions never have large yields because sufficiently neutron-deficient compound nuclei cannot be made. (The short vertical bars terminating a line indicate the limit in producing compound nuclei for that reaction.) If one wants to make a particular Ce nucleus, ^{126}Ce for example, then Fig. 2 immediately shows that the best reactions to try are 2p, 2n, or 2p2n (p2n should also be in this group, but the three-particle-out reactions have been omitted for the sake of clarity). In fact, the 2n reaction has recently been found to work very well in this case. We further see that ^{124}Ce can only be produced in $\approx$ 3 times poorer yield - by 2n or 2p2n (or p2n) reactions. Such knowledge is

extremely useful in trying to identify these products. Figure 2 also illustrates the important fact that the highest possible yields for producing the Ce nuclei begin to drop off rather sharply below mass ≈ 126. Below mass 120, there is no significantly better way to produce the Ce nuclei than by the 4n reaction, and the highest possible yield is less than 0.01%. This is already well below the yield required for in-beam spectroscopic studies of the type currently being made (≈ 10%), so that such studies can only be made down to mass about 124. However, some types of out-of-beam experiments, such as those using on-line isotope separators or the study of alpha or proton emitters, can work with much lower yields, so it is useful to extend these calculations to lower yields, and this has been done in the full report of these results.

In conclusion, we believe it is now possible to estimate rather reliably the expected yields for very neutron-deficient products of compound-nucleus reactions. Preliminary investigation also gives results that are in accord with data in the Kr region, so that this rather simple approach seems to have validity over a large portion of the periodic table.

Footnote and References

†Condensed from UCRL-20422, December 1970; submitted to Nucl. Phys.

1. See for example: G. Rudstam, Arkiv för Fysik 36, 9 (1966).

2. We have used: W. D. Meyers and W. J. Swiatecki, UCRL-11980, May 1965.

Alpha Decay of Neutron-Deficient Osmium Isotopes†

Jørn Borggreen* and Earl K. Hyde

Alpha decay is energetically possible in elements below lead, but in general the alpha decay energies are so low that this mode of decay is not observed. The most neutron-deficient isotopes have larger alpha decay energies, and alpha emission has been observed to compete with electron capture or positron emission in the decay of light isotopes of iridium, platinum, gold, and mercury produced by heavy ion reactions[1,2,3] or by high-energy proton spallation.[4] Many more cases of alpha decay remain to be discovered among the neutron-deficient isotopes of these and lighter elements. The present study is a contribution to this task. Guided by the predictions of Siivola,[5] we investigated the alpha decay of ^{172}Os, ^{173}Os, and ^{174}Os produced by bombardment of ^{164}Er with beams of ^{16}O. Gamma-ray measurement techniques were used to measure the extent of competitive decay by electron capture or positron emission. The contribution of alpha emission is less than 0.3% in all cases even though these nuclei have 10, 11, and 12 fewer neutrons, respectively, than ^{184}Os--the lightest of the beta stable isotopes of osmium. Nonetheless, the slight probability for alpha emission is important for testing the reliability of published mass predictions for nuclei far from beta stability.

The experiments were performed at the heavy ion linear accelerator. The primary reaction used was ^{164}Er(^{16}O, xn)$^{180-x}$Os at bombarding energies between 160 and 110 MeV, a range which allows evaporation of up to eight or nine neutrons. The maximum available beam energy was 10.3 MeV/amu; lower beam energies were obtained by inserting stacks of 1.72 mg/cm^2 aluminum foils in front of the target. Targets of 2.5 mg/cm^2 thickness were prepared by molecular plating of erbium oxides onto 1.7 mg/cm^2 Ni foils, starting with erbium oxide of varied isotopic composition.

The targets were mounted in a small helium-filled reaction cell. The recoiling product nuclei were stopped in helium, rapidly transported out of the reaction zone in a stream of helium, and collected on a plate positioned in front of an alpha detector made of semiconducting silicon. The helium-jet transfer technique and the associated techniques for control of data recording are described in our previous articles.[6,7]

The range of the recoil atoms in erbium for the energy region of interest was calculated[8] to lie between 1.1 and 1.6 mg/cm^2. The recoil ranges in He of 2.2 atm pressure were estimated from measured ranges of Dy recoils[13] to cover the region 1.6 - 2.2 cm, which is larger than the actual chamber length of 1.3 cm. These ranges, compared with the target thickness and the path length in He, assure that the recoils which are stopped in the helium are produced in the same effective thickness of target material independent of bombarding energy.

In the initial series of experiments, activity was collected on a foil positioned directly in front of a stationary detector and α-particle spectra were measured continuously, except that data recording was blocked during the 4-msec beam bursts. Figure 1 shows an alpha spectrum recorded during the bombardment of ^{164}Er with 134 MeV ^{16}O. The error in the determination of the energy of the unknown groups was estimated to be 10 keV. Spectra from the products of the $^{164}Er + ^{16}O$ reaction were recorded at many beam energies for equivalent amounts of integrated beam, and the yield of specific alpha peaks was determined as a function of ^{16}O energy. Yield curves for three of the alpha groups are shown in Fig. 2.

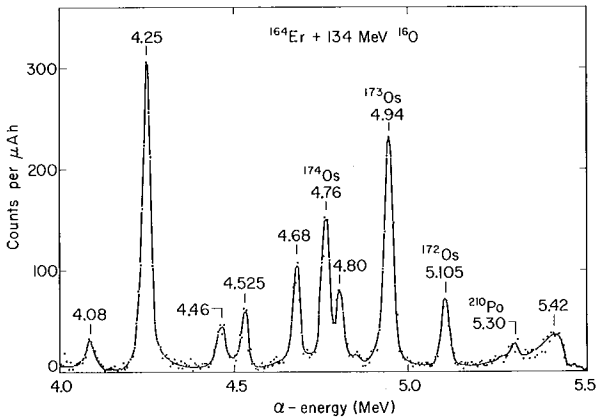

Fig. 1. Spectrum of alpha particles emitted by products isolated from ^{164}Er target bombarded with ^{16}O. The ^{210}Po peak at 5.30 MeV is due to a contamination of the detector surface from other reactions.
(XBL 705-2894)

The significant half-lives in this study fell in the range of seconds. For their measurement we used a technique discussed previously[7] in which a two-position collector plate was employed. Alpha active products were collected for some preselected number of seconds at one collector position after which the collector was flipped with a solenoid-activated drive in order to position the sample in front of an α detector. Alpha pulses were then recorded in eight time periods. At the end of the 8th period, the collector was flipped back to its original position and a second sample was counted while the first was receiving new activity from the helium jet. Decay curves for two alpha groups measured by this method at a beam energy of 154 MeV are shown in Fig. 3. In addition, a decay curve was determined for the 4.76-MeV α group at a bombardment energy of 120 MeV.

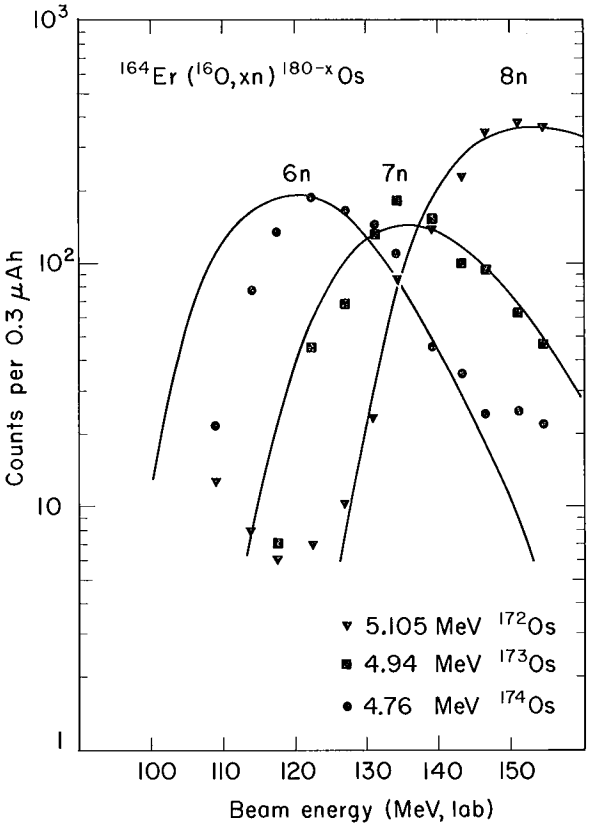

Fig. 2. Points are yields of individual α groups for different bombarding energies. The curve is the result of a neutron evaporation calculation.
(XBL 705-2891)

To obtain sufficient information for the assignment of the observed alpha groups, measurements were made with the following target-projectile combinations: $^{164}Er + ^{16}O$, $^{166}Er + ^{16}O$, and $^{164}Er + ^{14}N$.

In order to confirm the mass assignments and to measure the extent of partial decay by orbital-electron electron capture and/or positron emission, γ-ray measurements were made of the daughter and granddaughter products in the beta-decay chains. These measurements are described in the more complete report.

The isotopic assignments were made by a comparison of the experimental yield curves for the 5.105, 4.94, and 4.76 MeV alpha groups with theoretical curve shapes calculated with the aid of Sikkeland's formula[9] for the evaporation of 6,7, and 8 neutrons from the compound nucleus (See Fig. 2). These assignments were confirmed by the analysis of the γ-ray data, which showed a maxima in

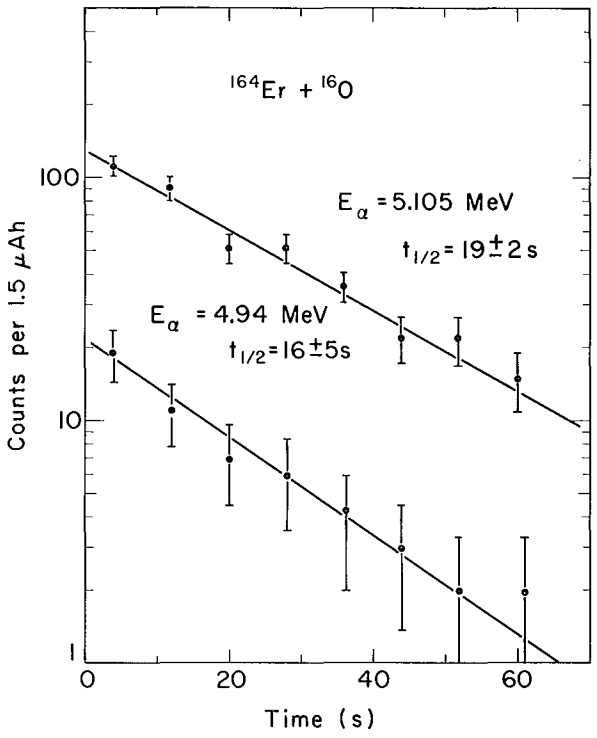

Fig. 3. Decay curves for the 5.105 MeV and 4.94 MeV α groups obtained at a bombarding energy of 154 MeV.
(XBL 705-2893)

the yields of products of electron-capture decay chains at the proper energy. The possibility of proton emission was considered.

A summary of the data on three new osmium isotopes is given in Table I.

Table I. Summary of data on Os isotopes.

Nuclide	α energy (MeV)	Half-life (s)	α-branch (%)
^{172}Os	5.105±0.010	19±2	≤ 0.3
^{173}Os	4.94±0.01	16±5	0.021±0.006
^{174}Os	4.76±0.01	45±5	0.020±0.004

Footnotes and References

†Present address: Niels Bohr Institute, Risø, Denmark.

*Condensed version of report UCRL-19596, July 1970; to be published in Nucl. Phys.

1. A. Siivola, Nucl. Phys. A92, 475 (1967).
2. A. Siivola, Nucl. Phys. 84, 385 (1966).
3. A. Siivola, UCRL-11828, 1965.
4. P. G. Hansen et al., Phys. Letters 28B, 415 (1969).
5. A. Siivola, Arkiv Fysik 36, 413 (1967).
6. J. Borggreen, K. Valli, and E. K. Hyde, Phys. Rev. C 2, 1841 (1970).
7. K. Valli and E. K. Hyde, Phys. Rev. 176, 1377 (1968).
8. P. G. Steward, Ph. D. thesis, University of California, UCRL-18127, 1968.
9. T. Sikkeland, Arkiv Fysik 36, 539 (1967).

On-Line α-γ and γ-γ Study of 26-msec ^{220}Ac

Richard E. Eppley and Earl K. Hyde

This study was initiated as part of a continuing study at the Hilac of neutron-deficient α emitters in that portion of the heavy element isotope chart lying just above the 82-proton and 126-neutron shells. The helium transport technique has played an indispensable role in gaining information on α-decay energies, nuclear half-lives, and excitation functions for the heavy-ion reactions involved. However, few decay schemes have been developed for nuclei in this region other than the placement of energy levels based on the α-decay energies. In most instances this is due to the fact that there are only one or two α groups, so that the decay schemes are quite simple. Another reason is the difficulty of studying species with very short half-lives. The recent successes of the helium transport technique for on-line studies of α decay has prompted us to explore this technique in the acquisition of γ singles, α-γ coincidence, and γ-γ coincidence spectra for the decay of short-lived nuclei in the same region.

^{220}Ac was picked since its alpha spectrum has at least eight α groups, which hold promise of an interesting decay scheme. These α groups have been reported recently

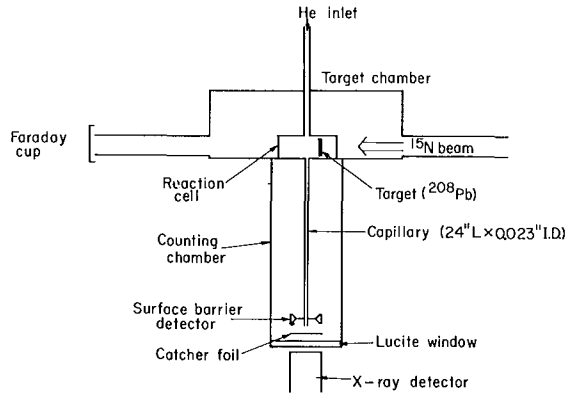

Fig. 1. Schematic of α-γ coincidence apparatus. The beam recoil products are slowed by the 2-atm He pressure in the reaction cell, swept through the capillary tube, and deposited on the catcher foil where they are counted.

(XBL712-2953)

by Børggreen, Valli, and Hyde[1] and are listed together with their relative intensities in Table I. The same experimental apparatus was used except that the recoil products were transported over a longer distance (24 in.) before they were collected and counted. Figure 1 is a schematic representation of this apparatus. In brief, the recoil products were thermalized in the reaction cell by helium at a pressure of 2 atm, swept through the capillary tube (I. D. = 0.023 in.) into an evacuated chamber, and collected on a metal plate. The collected activity was counted, between beam bursts, by an annular surface barrier detector in the case of α particles and by a Ge(Li) detector for the γ activity. More details can be found in Ref. 1.

From the α study previously reported,[1] the ^{208}Pb (^{15}N, 3n)^{220}Ac reaction at 75 MeV of beam energy was chosen for the present experiments. As expected, the major experimental difficulty was the γ-ray background. Owing to the experimental arrangement, the γ detectors were located close to the beam. Beam scattering caused a large flux of both fast and slow neutrons in the vicinity of the detectors. Even though counts were registered only between beam bursts, this flux proved to be large enough to preclude any chance of obtaining significant γ-ray singles spectra on ^{220}Ac. This background was reduced considerably by use of shielding in the form of cadmium sheets, lead bricks, and borax bricks.

It was found, however, that the vast majority of these unwanted events were rejected by an α-γ coincidence circuit. The electronics consists of a fairly standard setup. The coincidence events were determined by a time-to-amplitude converter (TAC) whose start and stop pulses were derived from the preamplifier pulses via fast discriminators. The computer hardware and data-taking program allowed the storage of the coincidence events from each detector, along with the TAC output as a single event on magnetic tape. This tape was later sorted, event by event, to determine which γ rays were in coincidence with particular α transitions, and vice versa. Some results of an ^{220}Ac α-γ coincidence run are shown in Figs. 2 and 3. The integral γ spectrum is shown in Fig. 2 along with a gated spectrum resulting from sorting on the 7.85 MeV α peak and the prompt time peak. Figure 3 shows the integral α spectrum along with the spectrum resulting from sorting on the 154 keV γ peak and prompt time. The γ energies shown on Fig. 2 are preliminary, but should be correct to $\pm$1 keV.

These spectra represent 11.5 hours of beam time and point up a difficulty with this type of on-line experiment. The coincidence rate is low and a compromise must be reached between beam time expended and the minimum statistics required. By analysis of the time spectrum resulting from such a run, those transitions in prompt coincidence can be separated from those in delayed coincidence. In this manner we have determined that the 134-keV γ transition originates from a state having a 71 $\pm$ 5 nsec half-life. Single particle estimates for proton transitions of this energy yield half-lives of 49 and 122 nsec for E2 and M2 transitions, respectively, after correction for internal conversion.

The integral γ spectrum shows this 134-keV γ transition to be the most intense. This suggests placing the transition as proceeding

Table I. ^{220}Ac α energies and intensities

α-particle energy[a]	Relative intensity[a]
7.61 $\pm$ 0.02	23 $\pm$ 5
7.68 $\pm$ 0.02	21 $\pm$ 5
7.790 $\pm$ 0.010	13 $\pm$ 2
7.850 $\pm$ 0.010	24 $\pm$ 2
7.985 $\pm$ 0.010	4 $\pm$ 2
8.005 $\pm$ 0.010	5 $\pm$ 3
8.060 $\pm$ 0.010	6 $\pm$ 1
8.195 $\pm$ 0.010	3 $\pm$ 1

[a]Taken from Reference 1.

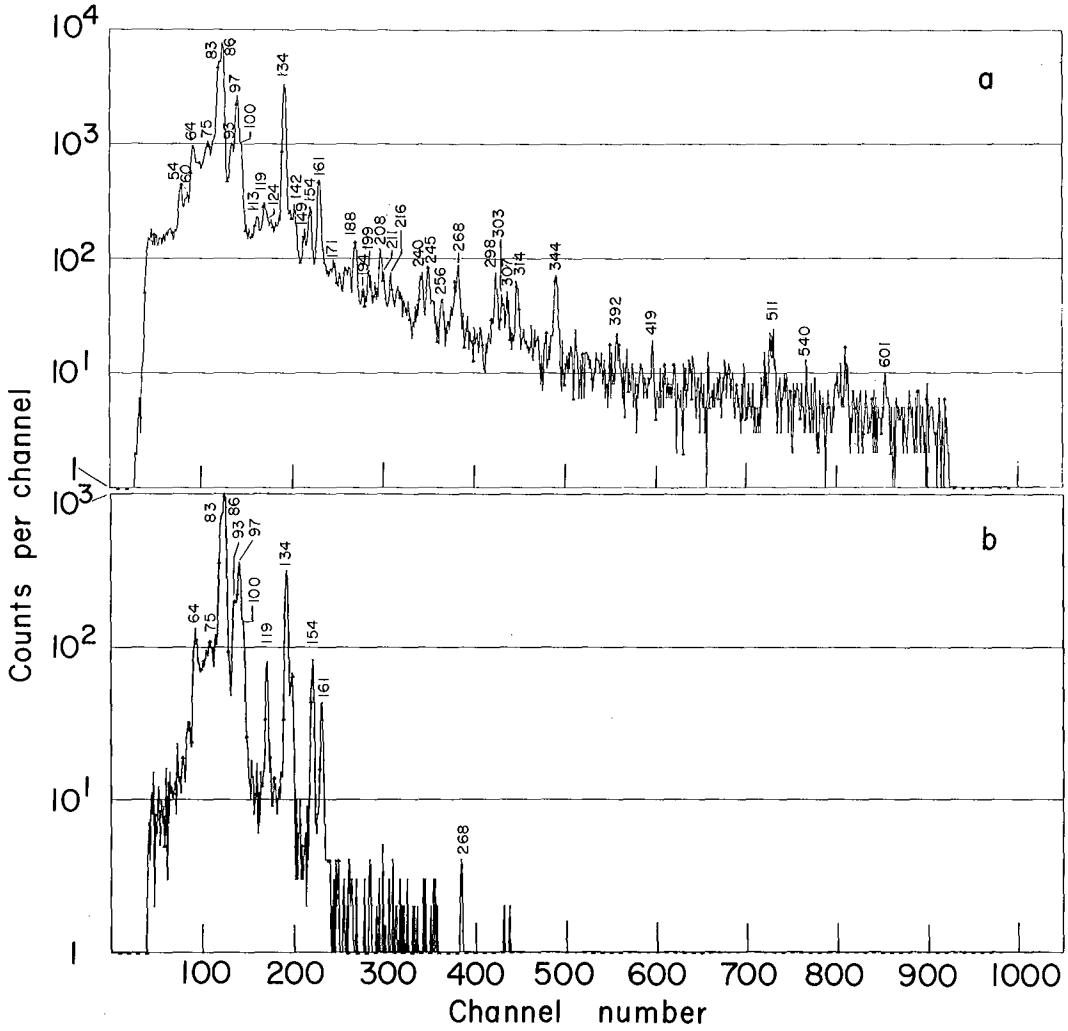

Fig. 2. γ-ray coincidence spectra:
a) Integral spectrum, b) spectrum resulting from sorting on the 7.85-MeV α group and prompt time.
(XBL712-2932)

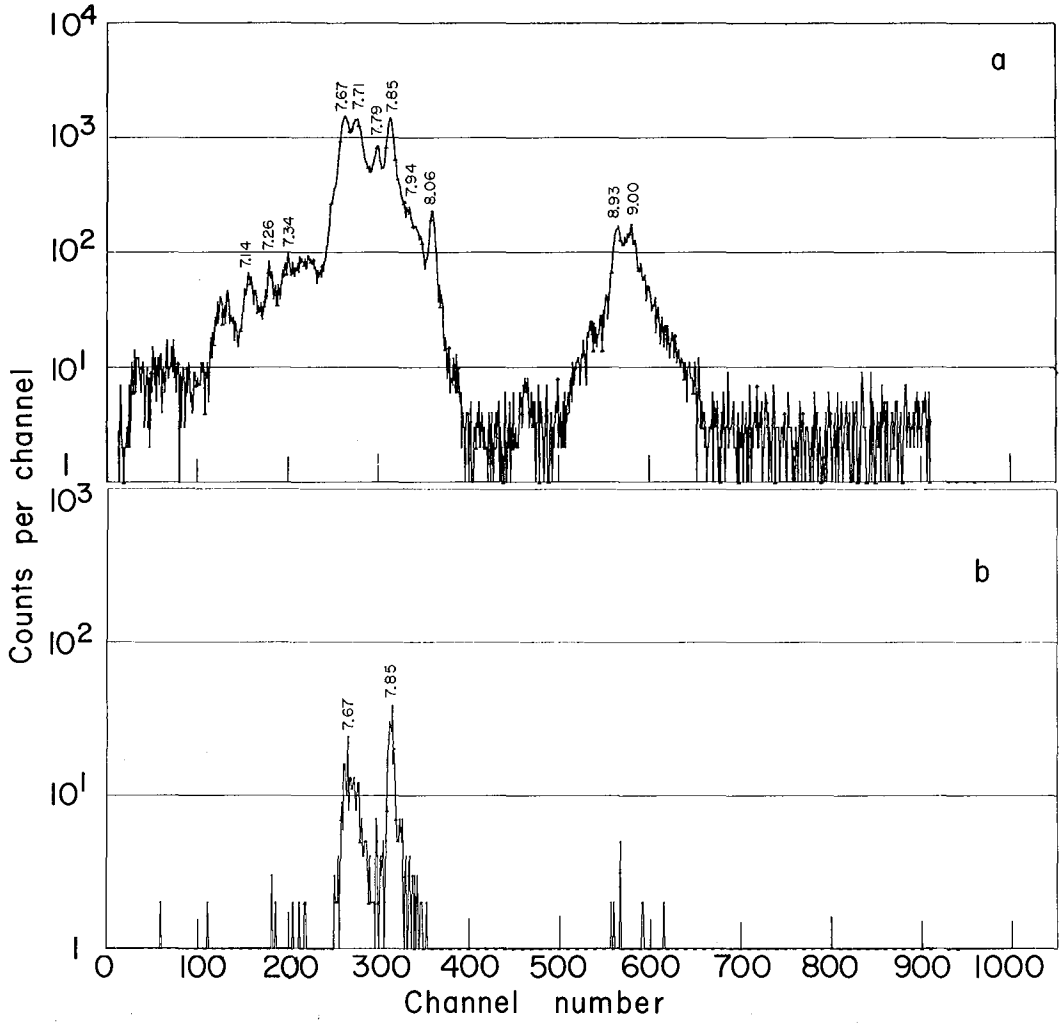

Fig. 3. α coincidence spectra: a) Integral spectrum, b) spectrum resulting from sorting on the 154-keV γ ray and prompt time. (XBL712-2931)

from the first excited state of ^{216}Fr, a conclusion which is consistent with the α decay results in Reference 1. Another prominent feature of the integral γ spectrum is the presence of very intense francium K x rays. This implies that a sizable fraction of the Fr deexcitations are accomplished by low energy transitions having appreciable internal conversion.

The bulk of our data is yet to be analyzed, so we do not present a decay scheme at this time. In addition to the α-γ experiments, we are presently analyzing results of γ-γ coincidence experiments. Our preliminary results convince us of the applicability of the helium transport technique to coincidence studies of short-lived nuclei.

Reference

1. Jørn Borggreen, Kalevi Valli, and Earl K. Hyde, Phys. Rev. C 2, 1841 (1970).

Characteristics of Fragments Produced in the Interaction of 5.5 GeV Protons with Silver

Earl K. Hyde, Gilbert W. Butler,† and A. M. Poskanzer

Fragments ejected from silver targets inserted in the 5.5 GeV external proton beam of the Bevatron were detected by a telescope of silicon semiconductor detectors incorporated in a power-law particle-identifier system. Individual isotopes of the elements from hydrogen to nitrogen were resolved (see Fig. 1).

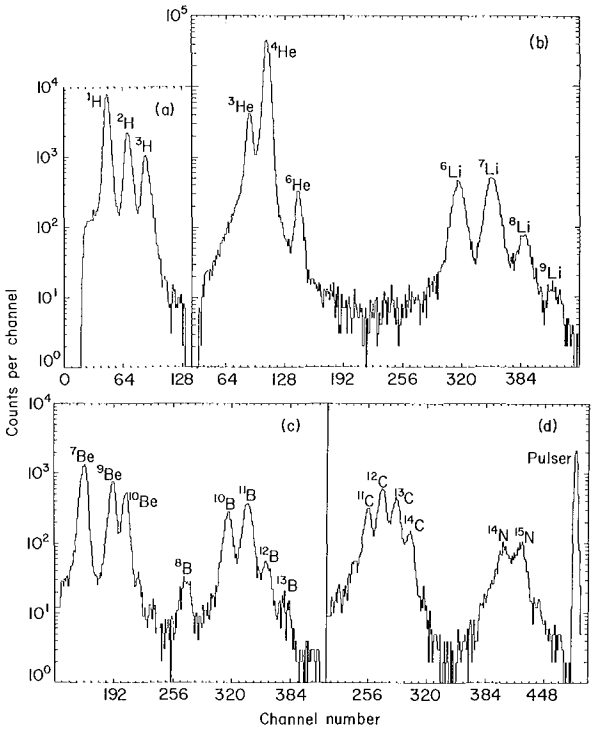

Fig. 1. Typical particle spectra of fragments ejected from silver targets bombarded with 5.5-GeV protons. The telescope for part (a) consisted of a 100 μm ΔE detector and a 1500 μm E detector. The telescope for parts (b), (c), and (d) consisted of a 61 μm E detector and a 250 μm E detector. (XBL 705-2837)

Above nitrogen, isotopic resolution was lost, but it was possible to resolve elements up through silicon (see Fig. 2). The energy spectra of individual isotopes were determined. This required the use of several telescopes containing detectors of different thicknesses. Some extrapolation of the data was required at the lower energies because of an

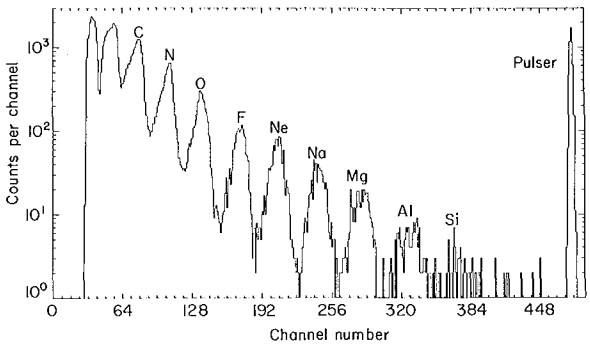

Fig. 2. Spectrum of elements ejected from a 7.1 mg/cm^2 silver target and measured in a telescope with a 20 μm ΔE detector. (XBL 705-2846)

instrumental cutoff. Some typical energy spectra showing curves derived from data taken at 90° to the proton beam are displayed in Fig. 3. Similar sets of data were taken at 20°, 45°, 135°, and 160°. The energy spectra were extrapolated and integrated to obtain the angular distributions of the fragments, and the results are given in Fig. 4. The integration of these curves in turn resulted in the set of total cross sections given in Table I.

This study has resulted in a detailed set of data on the energy, angular distribution, and yield characteristics of 13 light fragments from the breakup of the silver nucleus. The data are being examined to obtain insight on the nature of nuclear reactions between GeV protons and complex nuclei. The results are being compared with a similar set of data previously obtained by us[1] on uranium targets. The data are also being compared with those obtained previously by numerous investigators by means of nuclear emulsion techniques. These literature reports deal principally with the hammer tracks of ^{8}Li, but some heavier fragments were studied by the track-area method of identification.

Many of the fragment characteristics are superficially like those expected from nuclear evaporation. However, our attempts to fit the observed properties to a simple evaporation model incorporating isotropic emission from a moving system were not successful. The analysis required multiple choices of nu-

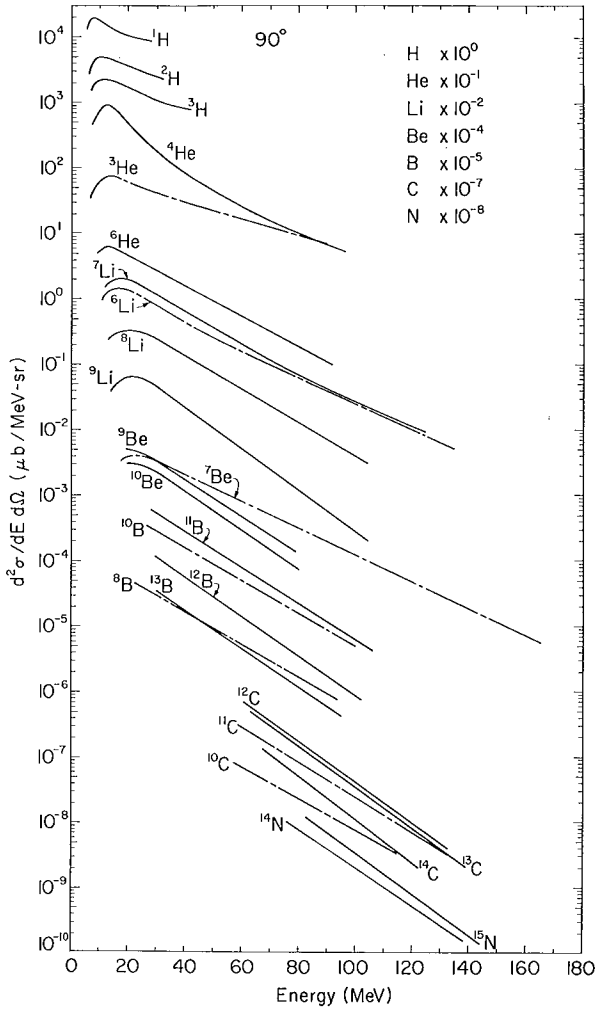

Fig. 3. Composite figure showing energy spectra of isotopes of H through N at 90° to the beam. Curves are displaced by the scale factors listed at the upper right of the drawing. (XBL 705-2845)

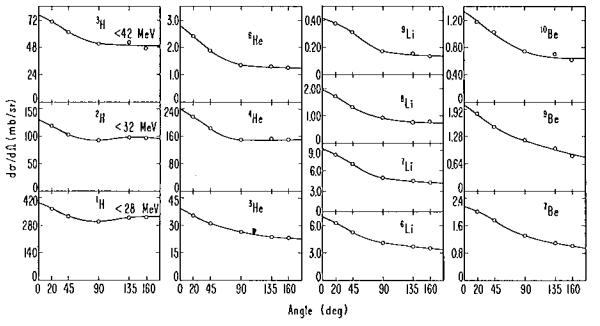

Fig. 4. Laboratory angular distributions of isotopes of H, He, Li, and Be obtained by integration of energy spectra taken at five angles to the proton beam. (XBL 705-2843)

Table I. Total cross sections and forward-to-backward ratios for fragments from silver irradiated by 5.5-GeV protons

Fragment	σ (mb)	F/B
^{1}H	3993[a]	
^{2}H	1239[a]	
^{3}H	687[a]	
^{3}He	345[b]	1.23
^{4}He	2031	1.16
^{6}He	19.2	1.36
^{6}Li	55.1	1.30
^{7}Li	68.6	1.38
^{8}Li	12.8	1.50
^{9}Li	2.6	1.74
^{7}Be	17.4[c]	1.42
^{9}Be	15.4	1.39
^{10}Be	10.1	1.38

[a]Hydrogen yields refer only to that part of the spectrum lying below 28, 32, and 42 MeV for the isotopes ^{1}H, ^{2}H, and ^{3}H, respectively.

[b]In the ^{3}He case, a correction of 8.8% was applied for the unmeasured part of the spectrum lying above 90 MeV.

[c]Absolute value determined by radiochemistry (see appendix of Ref. 1); all other values in this table are normalized to this value.

clear temperature, and no choice of parameters provided a satisfactory description of the spectra at all angles. The discrepancies were particularly bad for Li, Be, and B. Some mechanism causes pronounced favoring of emission in the forward hemisphere. The Coulomb barrier parameters derived from the analysis were quite low--approximately half of the expected values.

Comparison of our data with literature data on ^{8}Li showed rough agreement, but a similar comparison with data on heavier isotopes obtained by the track-area identification method revealed some gross discrepancies.

Footnote and Reference

†Present address: Chemistry Division, Argonne National Laboratory.

1. A. M. Poskanzer, G. W. Butler, and E. K. Hyde, Phys. Rev. C 3, 882(1971); see also UCRL-18996, 1970.

Spontaneous-Fission Half-Life of ^{258}Fm and Nuclear Instability†

E. K. Hulet,* J. F. Wild,* R. W. Lougheed,* J. E. Evans,* B. J. Qualheim,* M. Nurmia, and A. Ghiorso

As shown in Fig. 1, the spontaneous-fission half-lives of nuclei with neutron numbers greater than 152 decrease rapidly with increasing N (nuclei with more than 157 neutrons were unknown until now). Because of the perturbation introduced by the 152-neutron subshell, theoretical extrapolations of spontaneous-fission (SF) lifetimes for nuclei with neutron numbers above 156 are contradictory and allow the possibility of a recovery of stability at this level. Since theory was hopeful while the trend of experimental half-lives was pessimistic, it became important to search for an even-even nuclide well past the 152-neutron subshell.

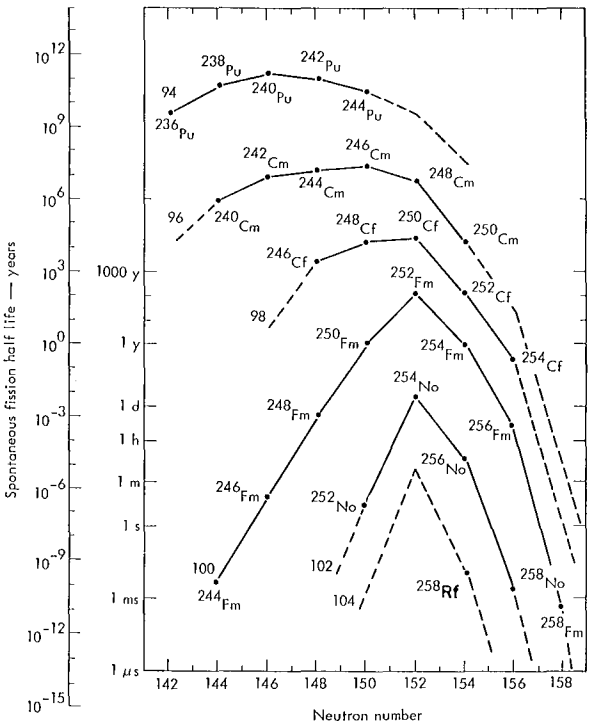

Fig. 1. Systematics of the spontaneous-fission half-lives of even-even isotopes of the heaviest elements.

(XBL712-2952)

Our search centered upon ^{258}Fm, since we believed the fissionability of a nucleus containing 158 neutrons would not be influenced by the localized effect of the 152-neutron subshell. Thus, the SF half-life of ^{258}Fm would serve as an important guide to the nuclear stability of even heavier nuclei. We expected the principal mode of decay of ^{258}Fm to be spontaneous fission, since we estimated the SF half-life to be less than two hours, whereas systematics indicated a 70-200 day partial half-life for α decay.

Many experiments designed to identify ^{258}Fm were performed over a period of five years. Previously we made attempts to detect the spontaneous-fission decay of this nuclide in fermium, chemically separated from the debris of thermonuclear explosions,[1] in reactor-produced fermium, after electron-capture decay of ^{258}Md,[2] and from short neutron irradiations of ^{257}Fm.[3] No fission events assignable to ^{258}Fm could be detected in these experiments, although it was shown that the half-life was greater than 50 years or less than 0.2 sec if formed with a 1 b cross section from ^{257}Fm.[3]

In the experiments we are now reporting, ^{258}Fm was produced in the (d, p) reaction by the bombardment of ^{257}Fm with 12.5 MeV deuterons. The quantities of ^{257}Fm needed to make such bombardments successful were

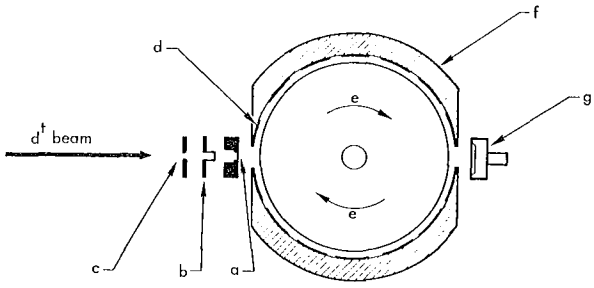

Fig. 2. Schematic of target and drum-mica system. Deuterons strike the ^{257}Fm target (a) after passing through aluminum degrading foils (b) and tantalum collimator (c). The atoms of ^{258}Fm recoiling from the target are caught on the surface of rotating drum (e), and their decay by SF is recorded in short strips of mica (d) attached in a continuous band to drum housing (f). An α detector (g) was used for monitoring the recoil efficiency of the targets.

(XBL712-2951)

unavailable until the Hutch thermonuclear test, which produced a total of 0.25 mg of ^{257}Fm.[4,5] A very small fraction, 5×10^9 atoms of ^{257}Fm, was chemically separated from ≈ 10 kg of rock debris after the explosion. After extensive chemical purifications, a weightless sample was isolated which was electroplated onto 0.013-mm-thick beryllium foil giving a 2.2-mm-diameter target.

The fermium target, facing away from the incoming beam, was clamped into a water-cooled collimating assembly containing aluminum degrading foils which reduced the energy of the Berkeley Hilac deuteron beam from 20.4 to 12.5 MeV. The target assembly together with the detection system, schematically shown in Fig. 2, were enclosed in an evacuated box connected with the Hilac beam tube.

The technique[6] for detecting spontaneous-fission events from the decay of ^{258}Fm required the collection of ^{258}Fm recoil atoms on the rim surface of a large drum rotating at high speed. Surrounding and facing the drum-surface were stationary strips of mus-

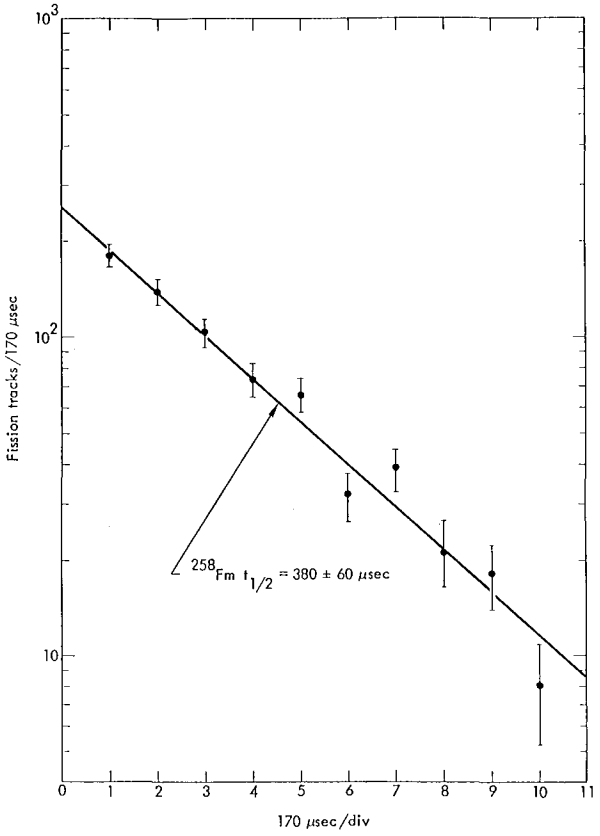

Fig. 3. Decay curve for spontaneous fissions assigned to ^{258}Fm. Net fission tracks from five bombardments have been summed. (XBL712-2950)

covite mica, in which only fission tracks are recorded. The atoms of ^{258}Fm were caught and carried on the surface of the drum until they decayed, leaving a track in the mica which was readily identified at 200 X magnification, after etching in hot hydrofluoric acid. In these experiments, we used a 25-cm-diameter drum rotating at a preset frequency between 1500 and 3275 rpm with a gap of 0.8 mm between the surfaces of the mica and drum.

A total of 680 net fissions was counted in five bombardments (see Fig. 3). In every experiment, the half-life was found to be within 380 ± 40 μsec although the drum speed was changed from one experiment to the next; the lowest speed was 1500 rpm and the highest was 3275 rpm. No fissions other than background were observed at 75 rpm. Between the fourth and fifth bombardment, the target was chemically repurified from all actinide elements, and the 380 μsec SF activity was found again in undiminished yield. We have concluded this activity can belong only to ^{258}Fm, since it was produced from the ^{257}Fm targets and not from a similar target containing 10^{10} atoms each of ^{257}Fm daughters (^{249}Bk, ^{249}Cf, and ^{253}Es) mixed with 42 ng of uranium and 0.1 ng of ^{239}Pu.

A cross section of 35 mb was measured for the formation of ^{258}Fm with 12.5 MeV deuterons. This cross section is consistent with known (d, p) cross sections for fissile targets which average ≈ 50 mb when bombarded with 11-13 MeV deuterons.[7] It is also 10-30 times larger than cross sections expected for compound nucleus reactions with deuterons, thereby excluding products from reactions such as (d, n), (d, 2n), etc. Lastly, we believe fission isomers are very unlikely since their formation cross sections by (d, p) reactions are typically less than 2 μb.[7,8]

The exceedingly short half-life of ^{258}Fm has led us to conclude that heavier even-even nuclei are becoming catastrophically unstable toward fission. Therefore, it seems unlikely that many such nuclei with N > 158 will be identified in the future until a region is reached where filling of the next proton or neutron shell (^{298}114 ?) will add a necessary measure of stability. We further conclude that reactor production of heavy isotopes will cease at ^{257}Fm and that although thermonuclear explosions, such as the Hutch experiment, may have produced heavier nuclides, these were not detected in the debris[4,5] because of their excessively short SF lifetimes. Finally, we note that theoretical predictions of SF lifetimes fail to forecast the severe shortening of half-lives for neutron-rich isotopes. Figure 1 shows that the experimental fission half-lives, at a constant Z, attain a

maximum at or near beta stability and decrease symmetrically with decreasing or increasing neutron numbers. The divergence between theoretical and measured values becomes especially serious for even-even nuclei well beyond the 152-neutron subshell. As an example, the difference amounts to $\geq 10^8$ for ^{258}Fm, when our half-life is compared to the estimates of Johansson,[9] Viola,[10] and of S. G. Nilsson.[11] In view of such large discrepancies, we conclude that the fission barriers calculated from single-particle effects superimposed upon the liquid-drop model are not realistic for estimating half-lives. In particular, the neutron number seems to have little influence upon the barrier heights (deformation energy) of the heavier isotopes of the transplutonium element. This lack of strong neutron dependency, within the Nilsson formulation,[11] may arise from misplacing the position of the neutron levels or from underestimating the reduction in surface energy of a liquid-drop caused by neutron-proton asymmetry at the nuclear surface.

We are pleased to acknowledge the excellent support of the Hilac staff and operating crew, and to thank Christina Jung for scanning many of the mica strips for fission tracks. We would especially like to acknowledge the vital work by Roland Quong, Hugh Wilson, Wesley Hayes, John Cowles, and Melvin Coops in separating ^{257}Fm from the bulk of the Hutch rock debris.

Footnote and References

†Condensed from a paper submitted to Phys. Rev. Letters 26, 523 (1971).

*Lawrence Radiation Laboratory, Livermore, California.

1. Combined Radiochemistry Group, Phys. Rev. 148, 1192 (1966).

2. E. K. Hulet, A. Ghiorso, R. W. Lougheed, J. E. Evans, J. D. Brady, R. W. Hoff, R. E. Stone, and B. J. Qualheim, Bull. Am. Phys. Soc. 13, 604 (1968).

3. E. K. Hulet, C. E. Bemis, and R. W. Lougheed (1969), unpublished data.

4. S. F. Eccles and E. K. Hulet, UCRL-50767, 1969.

5. R. W. Hoff and E. K. Hulet, in Proceedings of the ANS Meeting, Eng. with Nucl. Explo., 1970, CONF-700101, Vol. 2, pp. 1283-1294.

6. M. Nurmia, T. Sikkeland, R. Silva, and A. Ghiorso, Phys. Letters 26B, 78 (1967).

7. N. L. Lark, G. Sletten, J. Pedersen, and S. Bjørnholm, Nucl. Phys. A139, 481 (1969), Table 2.

8. S. Bjørnholm and V. M. Strutinsky, Nucl. Phys. A136, 1 (1969).

9. S. A. E. Johansson, UCRL-10474, 1962.

10. V. E. Viola, Jr. and B. D. Wilkins, Nucl. Phys. 82, 65 (1966).

11. S. G. Nilsson, C. F. Tsang, A. Sobiczewski, Z. Szymanski, S. Wycech, G. Gustafson, I. Lamm, P. Moller, and B. Nilsson, Nucl. Phys. A131, 1(1969).

New Isotopes of Mendelevium and Einsteinium

Pirkko Eskola

Four new alpha-active mendelevium isotopes with masses 248-251 have been produced by bombarding ^{241}Am and ^{243}Am targets with ^{12}C and ^{13}C ions. The apparatus used was the same as the one described in our study of hahnium[1] or in some more detail in Ref. 2. The half-lives, α-particle energies and the target-projectile combinations are given in Table I. The mass number assignments of the activities are mostly based on excitation functions. In the case of 24-sec, 8.03-MeV ^{249}Md, a genetic relation with the daughter, 1.3-min, 7.70-MeV ^{245}Es, has also been established. Such genetic links have not been as readily observed for other isotopes because of large electron capture branching in the daughter or parent atoms, or in both.

A comparison of the observed alpha-decay energies with those predicted by Wapstra[3] shows that the former are consistently lower by some 300 keV. This can be understood in terms of the single-particle level scheme of Nilsson et al.[4] According to the scheme, there is a fairly large gap between the 101st ($7/2^-[514\downarrow]$) and the 99th ($7/2^+[633\uparrow]$) proton levels. Alpha decay from the $7/2^-[514\downarrow]$ state, the predicted ground state of odd Md

Table I

	Half-life	α-particle energy [MeV]	Ways of production
^{243}Es	20 ± 2 sec	7.90 ± 0.04	^{233}U+^{15}N
^{244}Es	40 ± 5 sec	no alpha	^{233}U+^{15}N
^{248}Md	6 ± 2 sec	8.32 ± 0.02	^{241}Am+^{12}C
^{249}Md	24 ± 3 sec	8.03 ± 0.02	^{241}Am+^{12}C ^{243}Am+^{12}C
^{250}Md	53 ± 5 sec	7.73 ± 0.02	^{243}Am+^{12}C, ^{13}C
^{251}Md	4.0 ± 0.3 min	7.53 ± 0.02	^{243}Am+^{12}C, ^{13}C

isotopes, to the 7/2+[633 ↑] state, the ground state of odd Es isotopes, is greatly hindered because of a change of both parity and relative orientation of intrinsic spin. Therefore, the favored alpha decay from the 7/2 [514 ↓] state of Md to that of Es is much preferred even if the level in the latter lies several hundreds of keV above the ground state.

The previously unknown einsteinium isotopes ^{244}Es and ^{243}Es were produced in bombardments of a ^{233}U target with ^{15}N ions. The 40-sec ^{244}Es was observed only indirectly through the decay of its EC daughter ^{244}Cf. The excitation function for the ^{244}Cf activity, recoiled onto the detectors as a result of the decay of the 40-sec activity, is consistent with that of a 4n-reaction. The assignment of 20-sec, 7.90-MeV alpha activity assigned to ^{243}Es is also based on an excitation function measurement.

The results given in Table I are preliminary; further details will be published after a more thorough analysis of the data.

References

1. A. Ghiorso, M. Nurmia, K. Eskola, J. Harris, and P. Eskola, Phys. Rev. Letters 24, 1498 (1970).

2. A. Ghiorso, The Robert A. Welch Foundation Conferences on Chemical Research, XIII. The Transuranium Elements--The Mendeleev Centennial, Houston, Texas, 1969 (to be published); UCRL-18633, 1970.

3. A. Wapstra, Proceedings of the Third International Conference on Atomic Masses, Winnipeg, Canada, 1967, edited by R. C. Barber (University of Manitoba Press, 1967) p. 153.

4. S. G. Nilsson, C. F. Tsang, A. Sobiczewski, Z. Szymanski, S. Wycech, C. Gustafson, I. Lamm, P. Moller, and B. Nilsson, Nucl. Phys. A131, 1 (1969).

Evidence for Isomeric Transitions in ^{254}No and ^{250}Fm

A. Ghiorso, K. Eskola,*P. Eskola, and M. Nurmia

During our studies[1] of ^{257}Rf we noticed that two nuclides, ^{254}No and ^{250}Fm, were being mysteriously transferred from the wheel, where they were deposited by the gas jet, to the "mother" crystals.[2] After eliminating other possible explanations, we have come to the conclusion that the transfer is probably caused by nuclear recoil imparted by isomeric transitions in these nuclides, the half-lives being 1.8 ± 0.3 sec for ^{250m}Fm (Fig. 1) and 0.20 ± 0.05 sec for ^{254m}No. These isomers apparently decay predominantly by gamma transitions to their ground states; so far we have seen no evidence for other modes of decay.

Footnote and References

*On leave of absence from Department of Physics, University of Helsinki, Helsinki, Finland.

1. A. Ghiorso, M. Nurmia, J. Harris, K. Eskola, and P. Eskola, Phys. Rev. Letters 22, 1317 (1969).

2. For a description of the crystal-shuttle system see A. Ghiorso, UCRL-18633 (to be published).

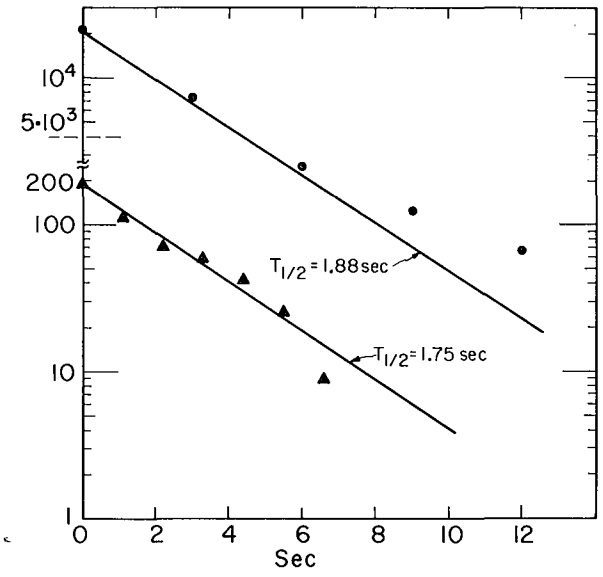

Fig. 1. Formation of ^{250m}Fm in bombardment of ^{249}Cf with ^{12}C. In this experiment, five mother-crystal stations were used and the wheel was stepped from one station to the next every 3 sec. The points indicate the number of counts from ^{250g}Fm recorded while the mother crystals were shuttled off the wheel (●). Formation of ^{250m}Fm from the ^{249}Cf (^{4}He, 3n)^{250m}Fm reaction. Seven crystal stations were used and the wheel was stepped every 1.06 sec (▲).
(XBL712-2954)

^{259}No, A Long-Lived Nobelium Isotope

A. Ghiorso, K. Eskola, P. Eskola, and M. Nurmia

Following a report[1] that a long-lived nobelium activity assignable to ^{259}No had been chemically isolated at ORNL, we have bombarded ^{248}Cm with ^{18}O in order to obtain further nuclear spectroscopic information on this interesting nuclide. We used the seven-station crystal-shuttle system described earlier[2] at a wheel-cycling rate of 30 minutes per station.

The series of alpha-particle spectra displayed in Fig. 1 resulted from bombardment of ^{248}Cm with 94-MeV ^{18}O ions. The somewhat broad peak centered at 7.52 MeV is due to ^{259}No; it excitation function is consistent with the ^{248}Cm(^{18}O, α3n)^{259}No reaction. A least-squares analysis of data from several bombardments gave a half-life of 57 ± 10 min.

References

1. Robert Silva, private communication.
2. A. Ghiorso, UCRL-18633 (to be published).

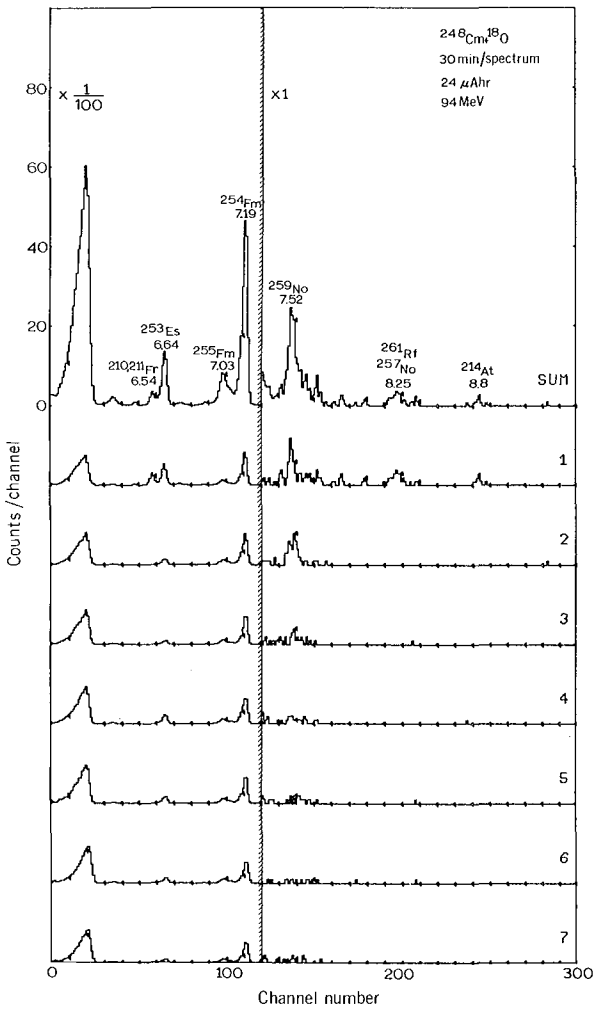

Fig. 1. A series of alpha-particle spectra from a bombardment of ^{248}Cm with ^{18}O at a wheel-cycle rate of 30 min/station. The sum of the seven spectra is plotted topmost.
(XBL713-6318)

Studies of Lawrencium Isotopes with Mass Numbers 255 through 259 †

K. Eskola,* P. Eskola, M. Nurmia, and A. Ghiorso

The Lr isotopes were produced by bombarding a ^{249}Cf or a ^{248}Cm target with heavy ions from the Berkeley Hilac. The 290-μg/cm^2 ^{249}Cf target had 60 μg of isotopically pure ^{249}Cf electrodeposited from isopropyl alcohol solution in an area of 0.21 cm^2 on a 2.2-mg/cm^2 Be foil, on which 80-μg/cm^2 Pd had been sputtered. The 41-μg ^{248}Cm target was also prepared by the molecular plating method and had an area of 0.18 cm^2. The isotopic composition of the target was as follows: ^{244}Cm(2.0%), ^{245}Cm(0.06%), ^{246}Cm (3.4%), ^{247}Cm (0.007%), and ^{248}Cm (94.5%). The crystal-shuttle system used in the experiments has been described elsewhere.[1-3]

^{255}Lr

Preliminary results on the decay characteristics of ^{255}Lr have been reported by Druin.[4] His studies of alpha activities produced by bombarding ^{243}Am target with ^{16}O ions indicated that ^{255}Lr has a half-life of about 20 sec and an α-particle group at 8.38 MeV.

We have produced a 22-sec alpha activity with an α-particle group at 8.37 MeV by bombarding the ^{249}Cf target with ^{10}B and ^{11}B ions, and a ^{243}Am target with ^{16}O ions. The series of α-particle spectra displayed in Fig. 1 resulted from bombardment of ^{249}Cf with 65-MeV ^{10}B ions. The use of the SAMPO computer program[5] made it possible to resolve the 8.37-MeV group into two components of 8.35±0.02 MeV (~ 50%) and 8.37±0.02 MeV (~ 50%). A least-squares analysis gave a half-life of 22±5 sec for the activity. Most of the other activities present belong to well-established isotopes of No and Fm, or were induced by a lead impurity in the target. The alpha group at 7.75 MeV is too prominent to be due to ^{255}No only, and it has been tentatively assigned to 45-sec ^{250}Md known to have a group at this energy. It is also most difficult to distinguish between the contributions of ^{249}Fm and ^{251}Md in the 7.54-MeV peak. The latter has been found to have a half-life of about 4 min and the most prominent α-particle group at 7.53 MeV by bombarding ^{243}Am target with both ^{12}C and ^{13}C ions.[6]

The α-particle spectra shown in Fig. 1 were recorded by the movable detectors when facing the wheel. The combined spectra recorded by these same detectors when in off-

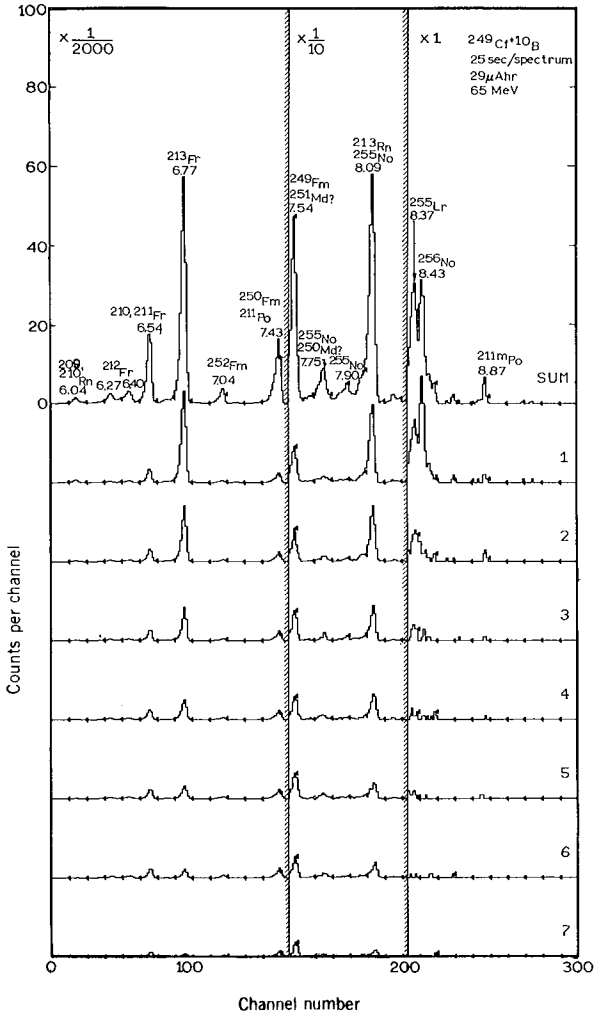

Fig. 1. A series of α-particle spectra produced by bombardments of ^{249}Cf with ^{10}B ions. The individual spectra show the total counts recorded at each of the seven stations by the two movable detectors when facing the wheel. The sum of the seven spectra is plotted topmost. The wheel-cycle rate, the integrated beam reading and the bombardment energy are indicated in the figure. (XBL 7011-6266)

wheel position, and by the stationary detectors facing them, were analyzed to find out if there were counts that arose from the decay of ^{251}Md, the alpha-recoil daughter of ^{255}Lr. All together six alpha-decay events were ob-

served between 7.5 and 7.6 MeV; the total number of counts assigned to ^{255}Lr was 129. The calculated ratio of detected mother events to detected daughter events is 2.5, which is approximately one-tenth of the observed ratio. Thus ^{251}Md seems to decay predominantly by electron capture, which is also borne out by greatly reduced apparent reaction cross sections, as measured by alpha decay.

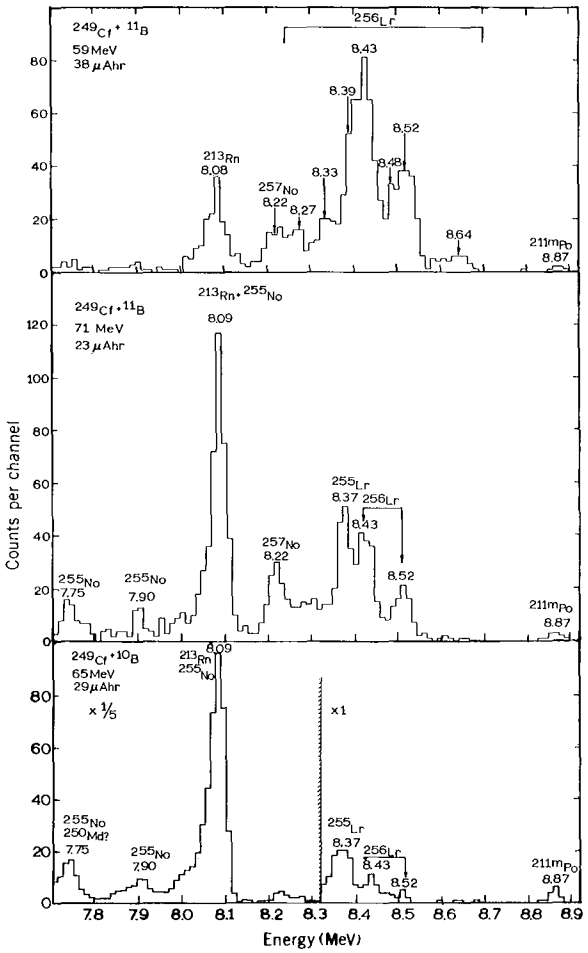

Fig. 2. A comparison of α-particle spectra resulting from bombardments of ^{249}Cf with 59-MeV and 71-MeV ^{11}B ions, as well as 65-MeV ^{10}B ions. In each case the first two time subgroups (12.5 sec following the end of each collecting period) have been excluded to eliminate short-lived activities, such as the 3.2-sec ^{256}No. (XBL 7011-6267)

Further proof that the 8.37-MeV α-particle activity arises from the decay of ^{255}Lr was furnished by excitation function studies. In Fig. 2, the α-particle spectra from bombardments of ^{249}Cf by ^{11}B ions at 59 MeV and 71 MeV and by ^{10}B ions at 65 MeV are plotted for comparison. The spectra represent the sum of the spectra recorded by the detectors in the on-wheel position, and in all cases the first 12.5 sec (the two first time subgroups out of the four at the first detector station) have been excluded to reduce interference from short-lived activities.

The excitation functions for the activities resulting from bombardments of ^{249}Cf with ^{11}B ions and characterized by half-lives of 22 sec, 31 sec and 0.6 sec, and the most prominent α-particle groups at 8.37, 8.43, and 8.87 MeV, respectively, are plotted in Fig. 3. The relatively large uncertainties for the 8.37-MeV alpha activity (^{255}Lr) reflect the difficulty of separating it from the complex α-particle spectrum of ^{256}Lr. The facts that the excitation functions for the 8.87 and 8.43-MeV activities reach their maxima at about the same energy, and that the maximum for the 8.37-MeV activity is about 10 MeV higher, are consistent with the activities being produced by 3n, 4n, and 5n reactions, respectively.

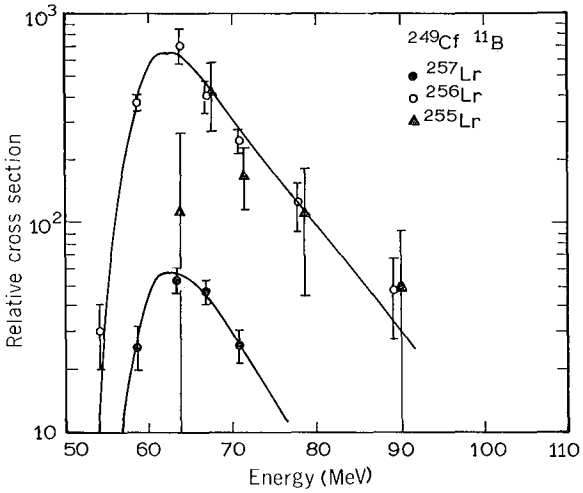

Fig. 3. Excitation curves for Lr activities produced in bombardments of ^{249}Cf with ^{11}B ions. The error bars indicate an uncertainty of one standard deviation. (XBL 706-6221)

^{256}Lr

We have produced a 31-sec alpha activity assignable to ^{256}Lr by bombarding ^{249}Cf with ^{11}B ions. The α-particle spectra displayed in Fig. 4 results from a bombardment of the ^{249}Cf target with 59-MeV ^{11}B ions. The sum spectrum is shown in Fig. 2 (excluding the first 12.5 sec following an irradiation, as discussed earlier). An analysis of the spectrum by the SAMPO computer program[5] gives the

Table I

	Half-life [sec]	α-particle energy [MeV]	Intensity (%)	α-decay hindrance factor	Upper limit for EC (%)	Ways of production
^{255}Lr	22 ± 5	8.37 ± 0.02	~ 50	2.4	30	^{243}Am+^{16}O
		8.35 ± 0.02	~ 50	2.0		^{249}Cf+^{10}B, ^{11}B
^{256}Lr	31 ± 3	8.64 ± 0.02	3 ± 2	490	20	^{246}Cm+^{15}N
		8.52 ± 0.02	19 ± 3	30		^{249}Bk+^{12}C
		8.48 ± 0.02	13 ± 3	36		^{249}Cf+^{11}B
		8.43 ± 0.02	34 ± 4	8.8		
		8.39 ± 0.02	23 ± 5	9.7		
		8.32 ± 0.02	8 ± 2	1.6		
^{257}Lr	0.6 ± 0.1	8.87 ± 0.02	81 ± 2	2.1	15	^{246}Cm+^{15}N
		8.81 ± 0.02	19 ± 2	6.0		^{249}Bk+^{12}C
						^{249}Cf+^{11}B, ^{12}C, ^{13}C, ^{14}N, ^{15}N
^{258}Lr	4.2 ± 0.6	8.68 ± 0.02	7 ± 2	55	5	^{246}Cm+^{15}N
		8.65 ± 0.02	16 ± 3	19		^{248}Cm+^{15}N
		8.62 ± 0.02	47 ± 3	5.4		^{249}Bk+^{12}C
		8.59 ± 0.02	30 ± 4	6.8		^{249}Cf+^{15}N
^{259}Lr	5.4 ± 0.8	8.45 ± 0.02	100	1.1		^{248}Cm+^{15}N

energies and intensities shown in Table I for the α-particle groups of ^{256}Lr. A least-squares analysis of the decay data yielded a value of 31 ± 3 seconds for the half-life.

^{257}Lr

The 8.6-MeV, 8-sec α-particle activity discovered in Berkeley in 1961,[7] and shown to be an isotope of element 103, was tentatively assigned to mass number 257. Subsequent work in Dubna failed to confirm such an assignment, and experiments carried out by bombarding a ^{243}Am target with ^{18}O ions suggested that ^{257}Lr has decay properties very similar to those of ^{256}Lr with $8.5 < E\alpha < 8.6$ MeV and $T_{1/2} = 35$ sec.[8,9]

In our bombardments of the ^{249}Cf target with ^{15}N ions, with the primary goal of making isotopes of element 105, a pronounced 8.87-MeV, 0.6-second α-particle group appeared in the spectra. By producing this activity using five different projectiles--^{11}B, ^{12}C, ^{13}C, ^{14}N and ^{15}N--on the ^{249}Cf target, we have concluded that the activity must be due to ^{257}Lr. The excitation function for the ^{257}Lr activity produced by ^{11}B ions is shown in Fig. 3. It is the unexpectedly low peak cross section of about 7 nb for the ^{249}Cf(^{11}B, 3n) ^{257}Lr reaction that helped the 0.6-sec activity to escape identification in earlier experiments. The excitation functions for the 0.6-sec, 8.87-MeV and the 4.2-sec, 8.6-MeV alpha activities produced by ^{15}N ions on ^{249}Cf are displayed in Fig. 5. In addition two measured cross sections, one for each activity, are plotted and labeled ^{257}Lr and ^{258}Lr. These are results from a 36-μA-h bombardment of ^{249}Cf with 81-MeV ^{14}N ions. It is evident that the ratio of the cross sections changes drastically when ^{15}N is substituted by ^{14}N. Such a behavior is in accordance with the assignments of the activities to ^{257}Lr and ^{258}Lr; for then in one case the reactions would be ^{249}Cf(^{15}N, α3n)^{257}Lr and ^{249}Cf(^{15}N, α2n)^{258}Lr, and in the other ^{249}Cf(^{14}N, α2n)^{257}Lr and ^{249}Cf(^{14}N, αn)^{258}Lr.

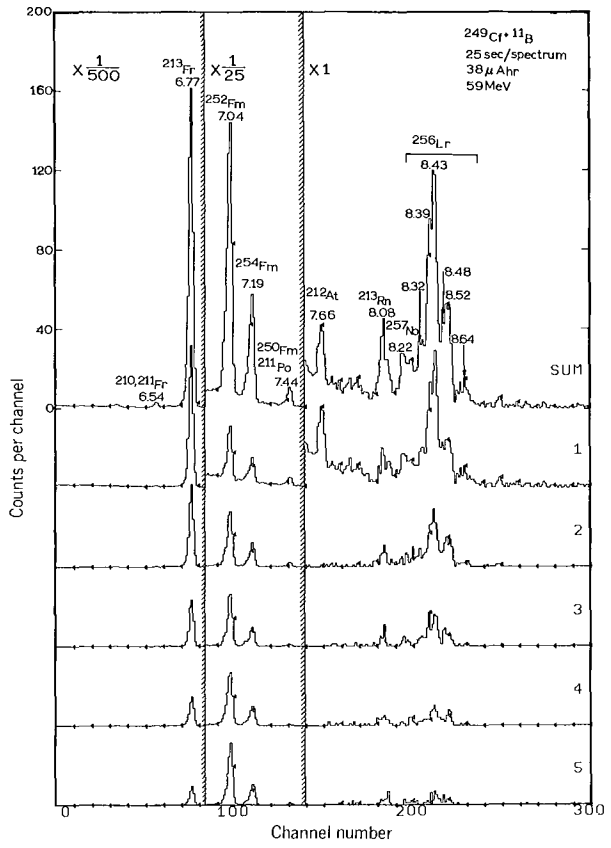

Fig. 4. A series of α-particle spectra produced by bombardments of ^{249}Cf with ^{11}B ions. Both the arrangement of the spectra and the data pertinent to the bombardment correspond to those in Fig. 1. (XBL 706-6220)

The complete display of the series of α-particle spectra produced by bombardments of ^{249}Cf with ^{15}N ions is presented in Ref. 1. Results of an analysis of the complex α-particle groups at 8.6 MeV and 8.87 MeV by the SAMPO computer program are shown in Fig. 6 and are given in numerical form in Table I as energies and intensities of the α-particle groups assigned to ^{257}Lr and ^{258}Lr.

^{258}Lr

Bombardments of both ^{249}Cf and ^{248}Cm by ^{15}N ions produced an 8.6-MeV, 4-sec alpha activity assignable to ^{258}Lr. A series of α-particle spectra from the latter target-projectile combination (^{248}Cm, ^{15}N) is displayed in Fig. 7. The excitation curves for the 8.6-MeV and 8.45-MeV activities produced in bombardments of ^{248}Cm by ^{15}N ions are shown on the right-hand side of Fig. 5. The peak cross section for the 8.6-MeV activity is attained about 8 MeV higher than that for the

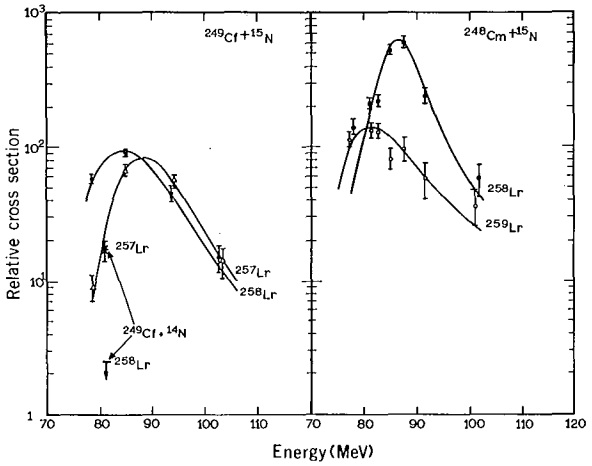

Fig. 5. Excitation curves for the activities assigned to ^{257}Lr, ^{258}Lr, and ^{259}Lr produced from either bombarding ^{249}Cf or ^{248}Cm with ^{15}N ions. The asterisk and the arrow, labeled ^{257}Lr and ^{258}Lr respectively, indicate the cross section and an upper limit for the cross section for producing the activities by bombarding ^{249}Cf with ^{14}N ions. (XBL 7010-6259)

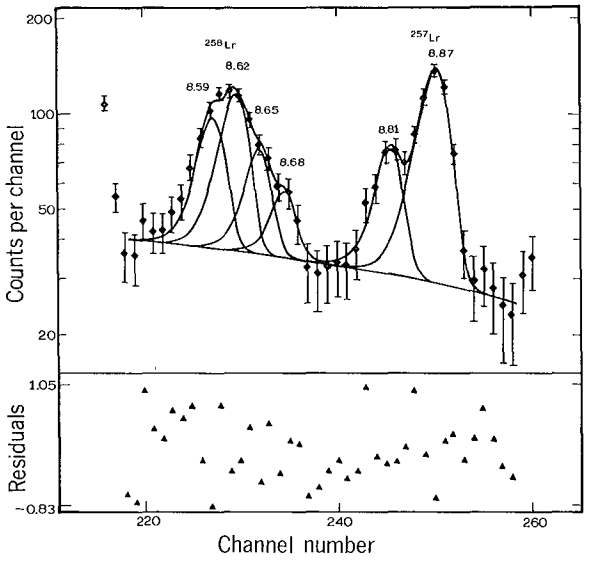

Fig. 6. A fit by SAMPO computer program to the 8.5 - 9.0 MeV α-particle energy region in the sum spectrum resulting from bombardments of ^{249}Cf with ^{15}N ions. The quadruplet at about 8.6 MeV is assigned to ^{258}Lr and the doublet at about 8.85 MeV to ^{257}Lr. The peaks at 6.538 MeV (^{210,211}Fr) and 6.773 MeV (^{213}Fr) were used for both shape and energy calibrations. (XBL7012-6272)

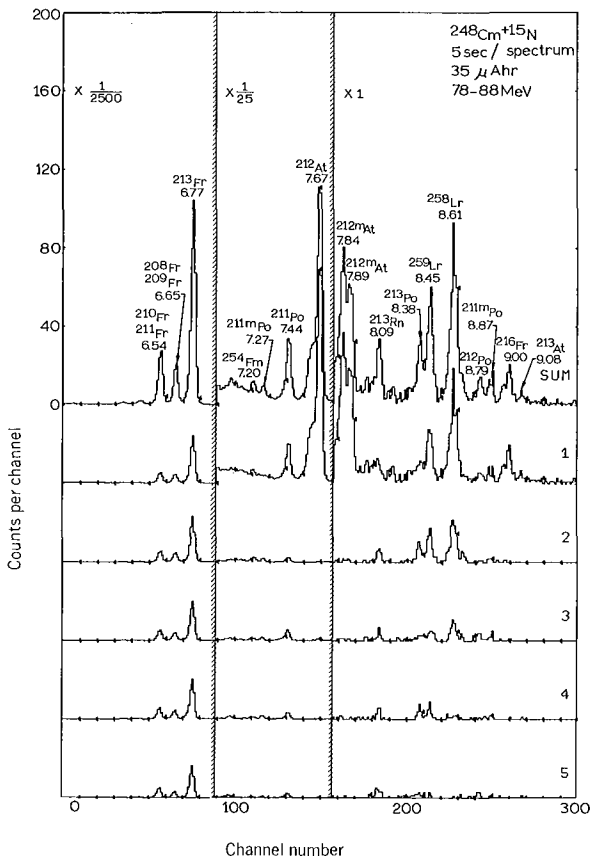

Fig. 7. A series of α-particle spectra produced by bombardments of ^{248}Cm with ^{15}N ions. Both the arrangement of spectra and the data pertinent to the bombardment correspond to those in Fig. 1.
(XBL 7010-6260)

8.45-MeV activity, which is compatible with the former being produced in a 5n reaction. This activity was also observed in bombardments of ^{249}Cf with ^{12}C and ^{13}C ions[2,3] and in a bombardment of a ^{244}Pu target with ^{19}F ions.

Because decay properties of the α-particle daughter ^{254}Md are unknown, but one expects it to decay predominantly by electron capture, we looked for the α-particles emitted by 3.2-h ^{254}Fm in the off-wheel position. For 620 observed decays of ^{258}Lr, some 300 decays in the 7.13-7.22 MeV range were observed. Accounting for the losses due to decay and to geometry factors, as well as for the fact that each movable detector only spends half of its time in the off-wheel position, one would expect to detect some 200 decays of ^{252}Fm atoms corresponding to the ^{258}Lr atoms. The excess of daughters is probably due to direct production of ^{254}Md, the electron-capture daughter at which then transfers onto the detectors with low efficiency.

^{259}Lr

The 8.45-MeV, 5.4-sec alpha activity was produced in bombardments of ^{248}Cm with ^{15}N ions, as shown in Fig. 7. The excitation function of this activity presented in the right half of Fig. 5 does not exclude the possibility that the activity could be assigned to ^{260}Lr. However, one would then be puzzled by the absence of ^{259}Lr, which as a 4n-reaction product should have a cross section of the same order of magnitude as a 5n reaction. That a 3n-reaction product does not show up in the spectrum is understandable in the light of the small cross sections observed for 3n reactions in this region in general.

A summary of experimental data obtained in this study is presented in Table I. Alpha-decay hindrance factors have been calculated using the spin-independent (ℓ=0) equations of Preston.[10] Because we have not done any γ-ray spectroscopy to support the level scheme information, only qualitative discussion of finer details of nuclear structure is possible. A cursory glance at alpha-decay hindrance factors in Table I shows that for each isotope there are transitions with a hindrance factor of less than 10. Such low hindrance factors for odd nuclei are characteristic of favored alpha decay, which leaves the last odd particle in the same orbital in the daughter as in the parent. According to the single-particle level scheme of Nilsson et al.,[11] the 103rd proton should occupy the $9/2^+[624\uparrow]$ level in the region of $250 < A < 270$, and for deformation parameter $\epsilon \approx 0.24$ and ϵ_4 distortion of 0.04. A transition from the $9/2^+[624\uparrow]$ level to the $7/2^-[514\downarrow]$ level--which seems to be the ground state for several Md isotopes--is strongly hindered because of a change in parity as well as in relative orientation of orbital and intrinsic spin components Λ and Σ.

In the case of ^{255}Lr it is possible that the broadness of the 8.37-MeV α-particle peak, which has been interpreted as being caused by two α-particle groups of approximately equal intensity, may instead be due to summation of γ rays or conversion electrons coincident with the α particles.

Assuming that the 8.81-MeV α-particle group of ^{257}Lr populates the $11/2^+[624\uparrow]$ state, i.e., is the first member of the rotational band built on $9/2^+[624\uparrow]$ Nilsson level, one obtains a reasonable value of 5.5 keV for the rotational constant $\hbar^2/2\mathfrak{I}$. Both of the odd-odd isotopes ^{256}Lr and ^{258}Lr have complex α-particle spectra. However, it is dif-

ficult to give even speculative Nilsson assignments to any of the levels populated in Md daughter isotopes on the basis of hindrance factors. Assuming that the odd proton is in $9/2^+[624\uparrow]$ state, the 153rd neutron is in $1/2^+[620\uparrow]$ state, and 155th neutron is in $7/2^+[613\uparrow]$ state, an application of the Gallagher-Moszkowski rule gives a ground-state spin of 5^- and 8^- to ^{256}Lr and ^{258}Lr, respectively.

An upper limit to EC branching for most of the Lr isotopes studied is given in Table I. These limits have been obtained by comparing the number of observed alpha-decay events resulting from the decay of Lr and No isotopes of the same mass number. It has been assumed that none of the No atoms were produced directly by pxn-type reaction. Also it has been assumed that the EC branchings of the No isotopes are negligible. In the case of ^{259}Lr, no meaningful limit could be set for EC branching because ^{259}No was highly discriminated against under the experimental conditions used.

The alpha-decay energies plotted in Fig. 8, as a function of neutron number, represent either an estimate of Wapstra[12] or an experimental value obtained by taking the energy of the highest observed α-particle group and correcting it for recoil energy loss. In addition to the new data discussed earlier in the text, tentative values for ^{248}Md, ^{249}Md, and ^{259}No have been plotted.

Perhaps the most interesting general trend discernible in the plotted experimental alpha-decay energies is the apparent reduction in the spacing of curves for successive Z values above nobelium. It is most evident for the N = 155 isotopes, for which data are available up to hahnium. Although all the evidence for decrease in the rate of change for alpha-decay energies when going from No to Ha is based on odd-A isotopes, the phenomenon seems general enough to suggest that it is real and may be caused by a local shell effect or by a fringe effect of a more remote major shell. The latter could manifest itself as a transition region from a deformed nuclear shape to a spherical one.

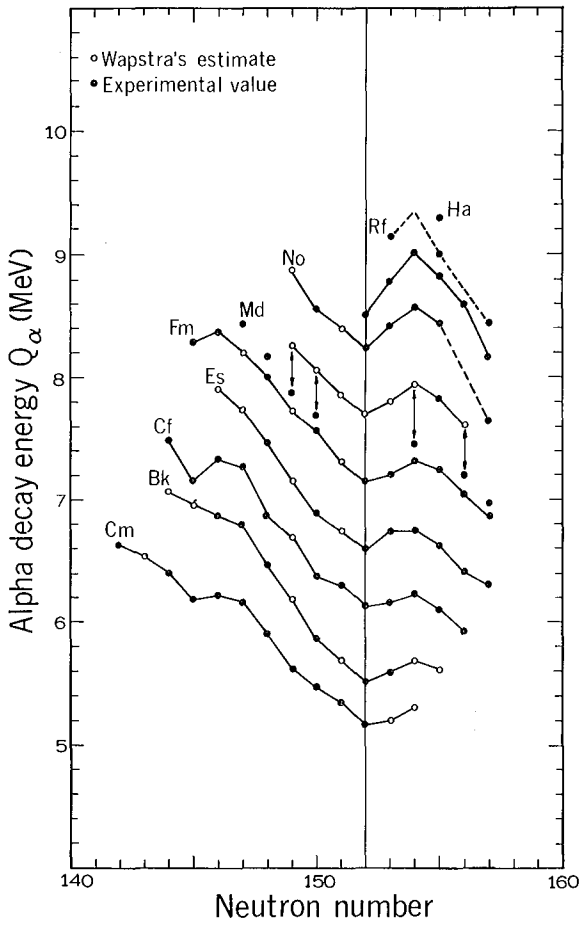

Fig. 8. Alpha-decay energy as a function of neutron number. The black circles correspond to the highest known α-particle group, and the open circles are those estimated by Wapstra by interpolation and α - β decay chains. It is seen that the influence of the N = 152 subshell on alpha-decay energies persists up to highest-known Z values. (XBL 7012-6271)

Footnotes and References

†Condensed from a preliminary version of UCRL-20442 (submitted to Phys. Rev.).

*On leave of absence from Department of Physics, University of Helsinki, Helsinki, Finland.

1. A. Ghiorso, M. Nurmia, K. Eskola, J. Harris, and P. Eskola, Phys. Rev. Letters 24, 1498 (1970).

2. A. Ghiorso, M. Nurmia, J. Harris, K. Eskola, and P. Eskola, Phys. Rev. Letters 22, 1317 (1969).

3. A. Ghiorso, UCRL-18633, 1970 (to be published).

4. V. A. Druin, Yadern. Fiz. 12, 268 (1970).

5. J. T. Routti and S. G. Prussin, Nucl. Instr. Methods 72, 125 (1969).

6. This report, New Isotopes of Mendelevium and Einsteinium; UCRL-20441 (to be published).

7. A. Ghiorso, T. Sikkeland, A. E. Larsh, and R. M. Latimer, Phys. Rev. Letters 6, 473 (1961).

8. G. N. Flerov, Yu. S. Korotkin, V. L. Mikheev, M. B. Miller, S. M. Polikanov, and V. A. Schegolev, Nucl. Phys. A106, 476 (1967).

9. E. D. Donets, V. A. Druin, and V. L. Mikheev, Ann. Phys. 3, 332 (1968).

10. M. A. Preston, Phys. Rev. 71, 865 (1947).

11. S. G. Nilsson, C. F. Tsang, A. Sobiczewski, Z. Szymanski, S. Wycech, C. Gustafson, I. Lamm, P. Moller, and B. Nilsson, Nucl. Phys. A131, 1 (1969).

12. A. Wapstra, Proceedings of the Third International Conference on Atomic Masses, Winnipeg, Canada, 1967, edited by R. C. Barber (University of Manitoba Press, 1967), p. 153.

New Element Hahnium, Atomic Number 105 †

A. Ghiorso, M. Nurmia, K. Eskola,* J. Harris, and P. Eskola

Using the same target of ^{249}Cf that was instrumental in the discovery of the alpha-emitting isotopes of element 104,[1] rutherfordium,[2] we have produced with moderate yield a 1.6-sec, 9.1-MeV α-particle activity by bombardment with ^{15}N ions at the heavy-ion linear accelerator (Hilac). By the alpha-recoil milking of a known isotope of element 103 we have obtained evidence that assigns this new radioactivity unambiguously to an isotope of element 105.

The procedures used in these new experiments were similar to those described in our previous communications.[1-3]

The element-105 reaction recoils were ejected from the target a short distance into helium gas at 620 Torr. They were pumped through a small orifice into a rough vacuum to impinge upon the periphery of a vertically mounted wheel which acted as a carrier. The wheel was periodically rotated to place the collected transmutation products next to a series of solid-state Si-Au surface-barrier detectors in order to measure their alpha-particle spectra. Half-life information was derived both from the relative numbers of counts detected at each station and from the decay of the activities while the wheel was stationary at each position.

To measure the alpha-recoil daughters of these activities, each detecting crystal facing the wheel was periodically shuttled to a position opposite another similar detector, where at high geometry the two detectors together could analyze the daughter α-particle activity which had recoiled off the wheel into the crystal. At each detecting station there were four detectors, two "mother" crystals which alternately faced the wheel and two "daughter" crystals to alternately face the "mother" crystals when they were shuttled off the wheel. Five stations were arranged at 39° intervals so that the same position on the 45-cm diameter wheel would not be reexamined by the detectors until all steps of the digital motor had been used.

The information from each of the many detectors was amplified by modular units developed in our laboratory and processed and stored by a PDP-9 computer and ancillary devices. Alpha-particle spectra were analyzed in 512-channel segments covering the range from 6 to 12 MeV with spontaneous-fission discriminators set to detect pulses greater than 30 MeV. The spurious count level was essentially eliminated by the use of judicious shielding and electronic-gating techniques.

The α-particle spectra displayed in Fig. 1 resulted from a series of bombardments of the ^{249}Cf target with ^{15}N ions. The individual spectra show the total counts recorded at each of the five stations by the two movable detectors when facing the wheel. The sum of the five spectra is plotted topmost. The wheel-cycle rate was 1 sec and the shuttle period 50 sec.

The complex group of peaks above 9 MeV is assigned to ^{260}105; by use of the SAMPO computer program[4] it can be resolved into α-particle groups at 9.06 (55%), 9.10 (25%), and 9.14 MeV (20%). For alpha-energy calibration, the 6.773-MeV peak of ^{213}Fr and the 7.443-MeV peak of ^{211}Po were used. The absolute accuracy of the energy values is estimated to be 0.02 MeV. Calculations based on spin-independent ($\ell = 0$) equations of Preston[5] give hindrance factors 7, 20, and 33, respectively, for these transitions. The half-life of this activity is 1.6 ± 0.3 sec. The branching by spontaneous fission is less than 20%, or

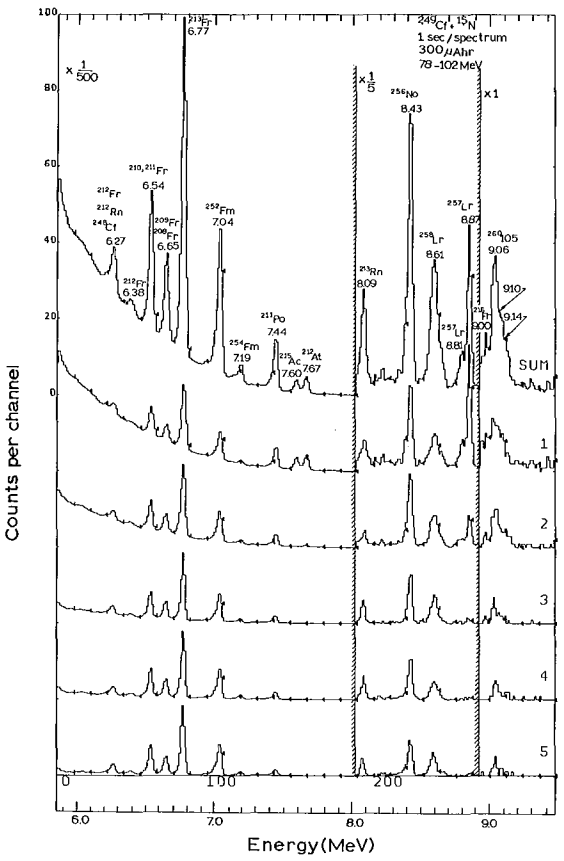

Fig. 1. A series of α-particle spectra produced by bombardments of ^{249}Cf with ^{15}N ions. The alpha peak at 9.00 MeV is that of ^{216}Fr, the daughter of 23-msec ^{220}Ac produced from the lead impurity in the target. Most of the ^{211}Po derives from electron-capture of 7.2-h ^{211}At.
(XBL 704-6171)

alternatively, assuming that ^{260}Rf is a very short-lived fission emitter, the electron-capture branching is less than 20%.

The 8.87-MeV peak as well as its 8.81-MeV satellite belong to 0.7-sec ^{257}Lr, and the complex peak at 8.6 MeV belongs to 4.0-sec ^{258}Lr.[6-8] Several of the peaks with a lower alpha energy are present because of lead and mercury impurities in the target. Bombardment of lead and mercury targets with ^{15}N ions ensured that the new activity was not produced by these impurities.

The measured relative cross sections for the 9.1-, 8.87-, and 8.6-MeV alpha activities at four different bombarding energies are plotted in Fig. 2. The peak production rate of the 9.1-MeV activity is about 1.5 alpha counts per microampere-hour which corresponds to a cross section of 3×10^{-33} cm^2 assuming a recoil-collection yield of 50%. The dashed curve in Fig. 2 is a calculated excitation function for the reaction ^{249}Cf(^{15}N, 4n)^{260}105. It was calculated using the formalism of Sikkeland[9] and the same parameter values as in Ref. 9.

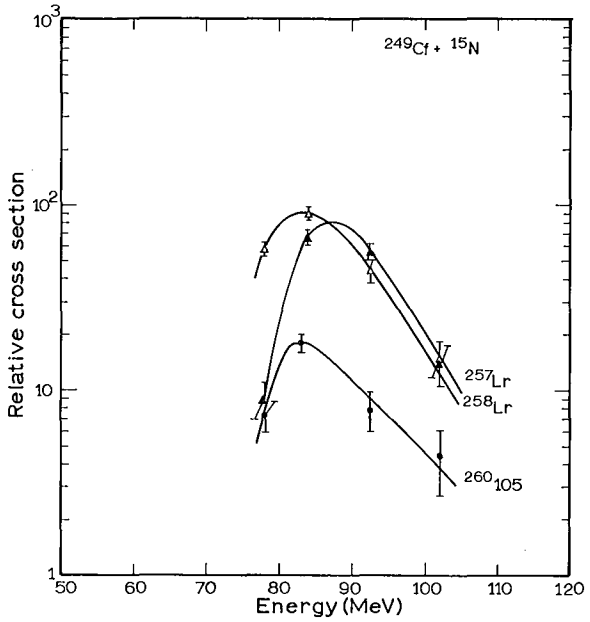

Fig. 2. Excitation curves for Lr and element-105 activities produced in bombardments of ^{249}Cf with ^{15}N ions.
(XBL 704-6170)

The α-particle spectra shown in Fig. 3 were recorded simultaneously with those displayed in Fig. 1, but by the detectors in the off-wheel position, i.e., they arose from the decay of alpha-recoil-daughter atoms embedded in the movable detectors. We believe that the α-particle events with an energy of 8.2 to 8.6 MeV belong to the daughter of the 1.6-sec, 9.1-MeV activity for the following reasons: (1) The number of recorded events at successive detector stations diminishes with a half-life of 2 ± 1 sec; and (2) the ratio of counts in the 9.1-MeV peak in the mother spectrum to those between 8.2 and 8.6 MeV in the daughter spectrum is 234:84 = 2.8 ± 0.4 and agrees well with the calculated value 2.7. The 8.4-MeV daughter activity decays with a half-life of 30 ± 10 sec, which value is based on the distribution of counts in the four 12.5-sec time subgroups of the 50-sec shuttle period. In the inset above the sum spectrum in Fig. 3 there is shown an alpha spectrum of 30-sec ^{256}Lr produced by the reaction ^{249}Cf (^{11}B, 4n)^{256}Lr.[6] Because of the similarity of the sum spectrum with the spectrum in the inset, and the good agreement of the half-lives, the daughter activity is assigned to

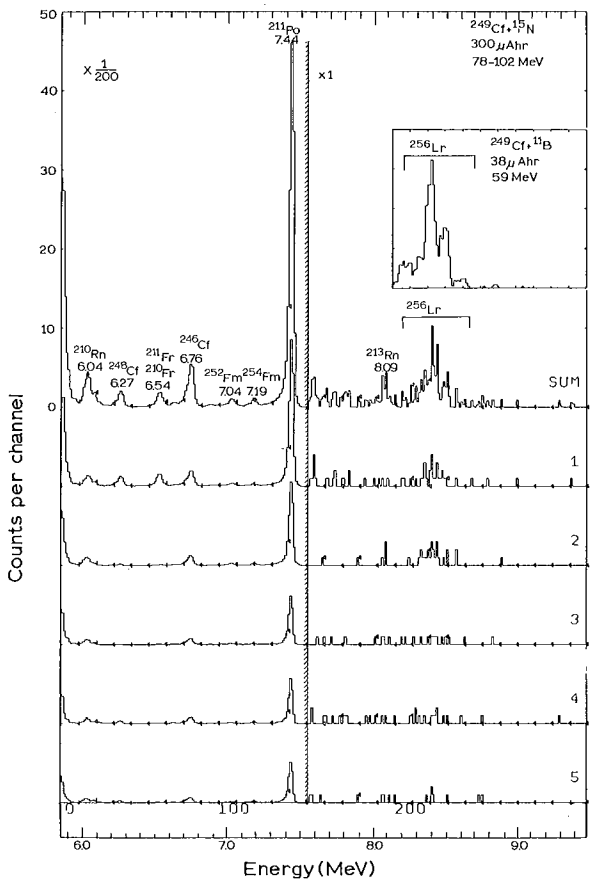

Fig. 3. A series of α-particle spectra from the same bombardment as those in Fig. 1, but recorded by the detectors in the off-wheel position. The spectrum in the inset is that of ^{256}Lr produced by the reaction ^{249}Cf(^{11}B, 4n)^{256}Lr. The energy scale in the inset is the same as that in the main figure, but the full scale for counts per channel is 100.

(XBL 7046-6172)

^{256}Lr and therefore the 9.1-MeV mother activity has to be ^{260}105. We find, in accordance with the Dubna group,[10] that the main feature of the α-particle spectrum of the 20-sec ^{255}Lr is a predominant group at 8.37 MeV. It would be very difficult to explain the spectrum in Fig. 3 on the basis of the genetic sequence ^{259}105 → ^{255}Lr. Another argument against the mother-daughter pair being ^{259}105 → ^{255}Lr is that we did not observe the 9.1-MeV activity in a 36-μA-h bombardment of ^{249}Cf with ^{14}N ions.

In 1968 there was published a paper by Flerov et al.,[11,12] which purported to show the discovery of two alpha-emitting isotopes of element 105 produced by the bombardment of ^{243}Am with ^{22}Ne ions. The transmutation products were carried by a gas stream through an annular solid-state detector to a collecting surface. In the gross spectrum they observed peaks with energies of 8.3, 8.7, 9.0, and 11.6 MeV which were ascribed to known reaction products from lead and americium. Delayed coincidences were observed between α-particle pulses of 8.8 to 10.3 MeV with those from 8.35 to 8.6 MeV, a region which is occupied by ^{256}Lr and, supposedly, ^{257}Lr. In particular they seemed to find a statistically meaningful correlation for "peaks" at 9.4 and 9.7 MeV. They came to a preliminary conclusion that they might be detecting ^{261}105 with E_α = 9.4 ± 0.1 MeV, $0.1 < T_{1/2} < 3$ sec, and ^{260}105 with E_α = 9.7 ± 0.1 MeV, $T_{1/2} > 0.01$ sec. The rate of production of these events was extremely low; only ten delayed coincidences were observed in 400 μA-h. We have shown in Fig. 4 a compilation of their data on the coincident events arranged according to their energy range. Their gross alpha spectrum is also shown and for comparison we have plotted the high-energy part of some of our data on the same energy scale. There appear to be similar continua above 9.2 MeV in both cases, but they are not necessarily due to the same effect. In our experiments this high-energy tail for the most part is due to one or more very light nuclides produced by the interaction of the ^{15}N ions with the Be substrate of our target. We have searched for delayed coincidences between these high-energy α-par-

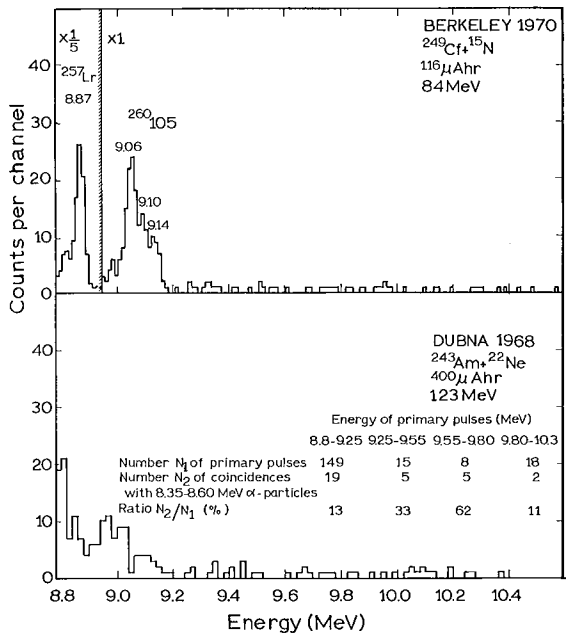

Fig. 4. A comparison of the alpha-particle spectra produced in the Dubna experiments (Refs. 11 and 12) with those reported in this paper. (XBL 704-6169)

ticles and the various lawrencium peaks. We found none that was statistically significant.

In addition to these negative findings it is unlikely that the 9.4- and 9.7-MeV "groups" can be due to $^{260}105$ or $^{261}105$ for the following reasons: (1) Our present work shows that $^{260}105$ has an energy of ca. 9.1 MeV and (2) the daughter of $^{261}105$, ^{257}Lr, was excluded from the Dubna delayed-coincidence measurements because its energy and half-life are not the same as ^{256}Lr, as assumed. In view of these considerations it is difficult for us to ascribe any significance to the meager data of the Dubna group regarding alpha-emitting isotopes of element 105.

In honor of the late Otto Hahn we respectfully suggest that this new element be given the name hahnium with the symbol Ha.

In a complicated research effort such as this we obviously are indebted to many people, but in particular we would like to express our gratitude for the continued essential and patient assistance provided by R. G. Leres, A. A. Wydler, C. A. Corum, A. E. Larsh, and D. F. Lebeck. The experiments were made possible by the excellent performance of the accelerator and for this we must thank F. S. Grobelch and the Hilac operating and maintenance staffs. As always we appreciate the interest and suggestions of G. T. Seaborg.

Footnotes and References

†Condensed from Phys. Rev. Letters 24, 1498 (1970).

*On leave of absence from Department of Physics, University of Helsinki, Helsinki, Finland.

1. A. Ghiorso, M. Nurmia, J. Harris, K. Eskola, and P. Eskola, Phys. Rev. Letters 22, 1317 (1969).

2. A. Ghiorso, UCRL-18633, 1970 (to be published).

3. A. Ghiorso, M. Nurmia, K. Eskola, and P. Eskola, Phys. Letters 32B, 95 (1970).

4. J. T. Routti and S. G. Prussin, Nucl. Instr. Methods 72, 125 (1969).

5. M. A. Preston, Phys. Rev. 71, 865 (1947).

6. A. Ghiorso, M. Nurmia, K. Eskola, and P. Eskola, to be published.

7. A. Ghiorso, T. Sikkeland, A. E. Larsh, and R. M. Latimer, Phys. Rev. Letters 6, 473 (1961).

8. A. Ghiorso, M. Nurmia, K. Eskola, and P. Eskola, UCRL-19530, 1970 (unpublished).

9. T. Sikkeland, A. Ghiorso, and M. Nurmia, Phys. Rev. 172, 1232 (1968).

10. I. Zvara, private communication.

11. G. N. Flerov, J. Phys. Soc. Japan Suppl. 24, 237 (1968).

12. G. N. Flerov, V. A. Druin, A. G. Demin, Yu. V. Lobanov, N. K. Skobelev, G. N. Akapiev, B. V. Fefilov, I. V. Kolesov, K. A. Gavrilov, Yu. P. Kharitonov, and L. P. Chelnokov, Joint Institute for Nuclear Research Report No. JINR-P7-3808, 1968 (unpublished.)

In Defense of the Berkeley Work Concerning the Alpha-Emitting Isotopes of Element 104†

A. Ghiorso, M. Nurmia, J. Harris, K. Eskola,* and P. Eskola

Introduction

Certain questions have been raised regarding the validity of our work reported in Physical Review Letters[1] concerning the discovery of two alpha-emitting isotopes of element 104, rutherfordium. Doubt was first expressed by V. A. Druin in the International Conference on Nuclear Reactions Induced by Heavy Ions[2] at Heidelberg, Germany in July, 1969. These doubts were repeated in a paper submitted to Yadernaya Fizika[3] in November, 1969 by Akapiev et al. In this same month the Robert A. Welch Foundation Conference on Transuranium Elements-the Mendeleev Centennial was held at Houston, Texas and the issues were discussed at length following the presentation of papers[4] by A. Ghiorso and by I. Zvara. Apparently this discussion did not sufficiently clarify the matter because strong doubts were again published in Atomnaya Energiya by G. N. Flerov.[5]

In our paper[6] on the discovery of an alpha-emitting isotope of element 105, hahnium, we carefully included answers to the major criticisms, but in view of the continued charges made by the Dubna group we feel that

a detailed rebuttal is in order. This paper will attempt to perform this function and in addition will present new evidence in support of our original work.

Criticism and Rebuttal

We will first present what we believe to be a fair statement of the major charges raised by the paper of Akapiev et al.,[3] and then follow it with our answer. To help the reader follow the arguments we have produced two figures (Figs. 1 and 2) along with their captions from the original publication.

1. The Berkeley group did not present alpha spectra of background activities that would be produced by the bombardment of lead impurities with carbon ions and did not discuss any background effects.

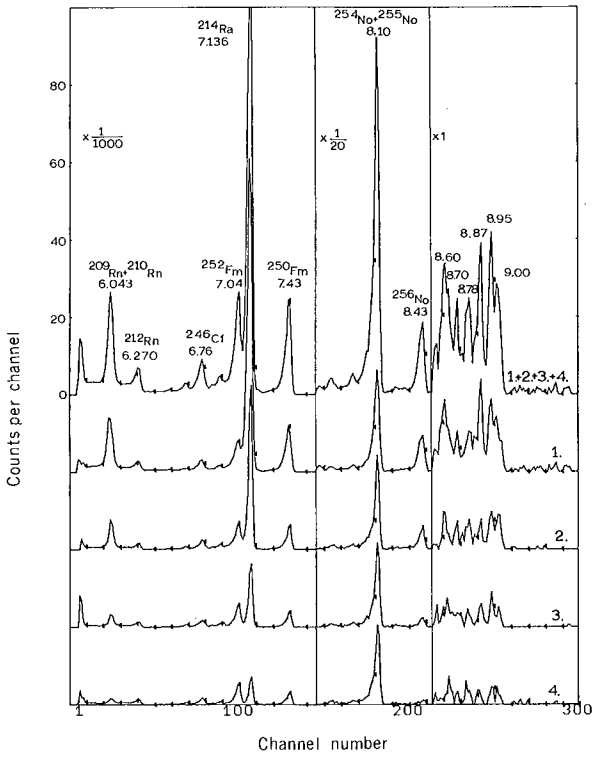

Fig. 1. A series of alpha spectra of the activities produced by bombardment of ^{249}Cf with 71-MeV ^{12}C ions. The top spectrum is the sum of the individual spectra from the four detectors. The 8.60-MeV peak is probably due to ^{258}Lr; the peaks above that energy belong to ^{257}104, with the exception of the one at 8.87 MeV whose origin is uncertain.[1] (See text of this paper; this peak is now known to be due to ^{257}Lr and ^{211m}Po.) (XBL694-4816)

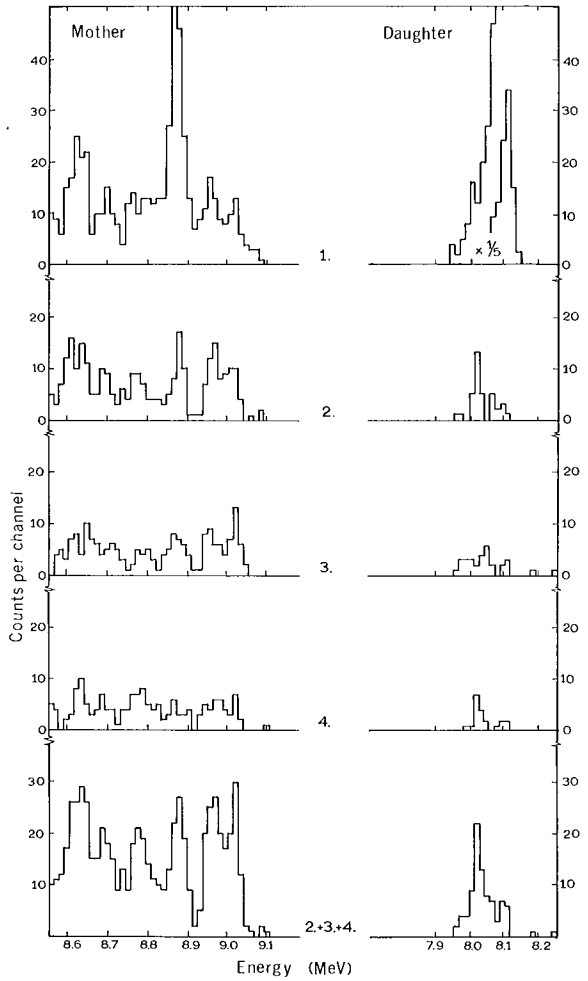

Fig. 2. A set of spectra from the mother-daughter experiment which demonstrates the genetic relationship between ^{257}104 and ^{253}No. The spectra recorded by the individual crystal pairs are shown on top with the sum of the last three pairs at the bottom.[1] (XBL694-4813)

These statements are both true. Because of the stringent word and figure limitations set by Physical Review Letters there was no detailed discussion of this aspect of the experiments. Note, however, that we carefully stated that we had made bombardments with other ions and thus implied that suitable background checks had been made. The fact that certain Pb-produced peaks in the alpha spectra, such as ^{214}Ra and 209, 210, ^{212}Rn, were labeled also implies that we were clearly aware of background effects that are caused by a lead impurity. The simple fact is that the element-104 alpha activities were so clearly above the background usually encountered that this problem was almost irrelevant. Thus we devoted the limited amount

of space available to other more important phases of the experiment.

2. Well-known Pb-produced nuclides do not decay with their proper half-lives, e.g., 30-min ^{209}Rn and 2.7-hour ^{210}Rn.

The main activity in the 6.043 MeV-labeled peak is due to ^{210}Rn and arises as the alpha-recoil daughter of 2.6-sec ^{214}Ra, which is produced from a tiny lead impurity in our californium target. Thus the 6.043-MeV peak appeared to decay in the successive alpha spectra with a 2.6-second half-life, since it was controlled by ^{214}Ra. There must have been some ^{209}Rn (which has the same alpha energy) present in this peak, since it is produced as the daughter of 2.75-min ^{213}Ra, but it was a minor component.

3. The alpha-particle peak at 8.87 MeV can only be due to the 25-sec ^{211m}Po and thus cannot decay with a 3-second period.

We were very careful to point out that the origin of the 8.87-MeV peak was uncertain, and we did not claim that it was due to ^{257}104. From recent results we find that there are several sources that can contribute to this peak in the alpha spectra.

a) One obvious source, of course, is 25-sec ^{211m}Po, as demonstrated in Fig. 4, where a lead target with some 50,000 ng/cm^2 has been substituted for the ^{249}Cf target, which contains about 20 ng/cm^2 Pb impurity. The polonium activity has a 25-second half-life, both as measured from the relative amounts of activity observed at each station and by the decay while the crystals are stationary.

b) We now know that ^{257}Lr has a half-life of 0.7 seconds and a most prominent alpha group at 8.87 MeV, as opposed to the Dubna group's[7] claim that it had a half-life of 35 seconds and an alpha energy of 8.5-8.6 MeV. By resolving the 8.87-MeV peak of the repeat experiment (to be discussed later) into two components, we find that about one-half of the activity is due to 0.7-sec ^{257}Lr and the other half to 25-sec ^{211m}Po.

c) It is conceivable that 5-sec ^{257}104 can have a weak alpha group at this energy, but this can not be resolved easily because of the interfering activities.

4. All Berkeley half-lives in the heavy element region must be questioned because the apparent half-life of 30-min 7.43-MeV ^{250}Fm is obviously only a few seconds.

We now have fairly good evidence[8] that ^{250}Fm has an isomeric state with a half-life of 1.8 seconds, and that some of the ^{250}Fm will thus be transferred to the crystals in our measuring system because of the recoil associated with the isomeric transition.

With only the evidence afforded by this unusual transfer phenomenon, the Dubna group suggested that all of our half-life measurements could be in error because of some undiscovered artifact of our system. Suffice it to say that we have obtained the same values for many nuclides as they have and most of these half-lives were measured before their published work. These measurements vary in range from 3.2 seconds[9] for ^{256}No (which from 1963 to 1967 was quoted as 8 seconds by its Russian discoverers![10]) to 200 seconds[11] for ^{255}No. Aside from statistical considerations we have found no reason to question our decay periods.

5. The construction and geometry of our setup causes "3 seconds" to be a characteristic value in our measurements. In particular, activity may be collected directly on the detector faces by gas-jet leakage around the wheel.

To determine whether a small amount of activity could bypass the wheel and be collected on the detector faces, we have performed an experiment to measure such an effect. Under our normal conditions some 2×10^5 alpha counts of ^{214}Ra were observed from carbon-ion bombardment of a lead target, with the wheel being cycled at a rate of 3 seconds per detecting station. The wheel was then stopped and the measurement repeated for an identical integrated-beam charge. Not one count which could be ascribed to ^{214}Ra was observed in any of the detectors. This was not particularly surprising to us since the volume through which the wheel is rotated is carefully shielded internally by lead sheets to reduce the fast-neutron degradation damage of the silicon detectors. We feel we can state categorically that in our system there is no significant direct transfer by a gas-leakage path. Our "3-second half-lives" can only be the result of nuclear characteristics beyond our control.

6. The half-lives of ^{257}104 and ^{259}104 could be much shorter because there is an excess of ^{253}No and ^{255}No on the first detector.

This criticism must be answered in two ways.

a) If there was such an excess of these two isotopes on the first detector, then why would not the alpha particles from their presumed parents also be observed in this same detector?

b) We never said that there was an excess of either ^{253}No or ^{255}No in the first detector. The excess activity was identified as ^{254}No (from its decay on the detector with a

55 ± 20-second half-life). We used this isotope of nobelium as a monitor of the amount of "self-transfer" in the daughter-measuring experiment. It now appears that this transfer was accomplished by the decay of another new isomer, ^{254m}No, with a 0.2-second half-life.[8]

7. The Berkeley experiment can be compared with a background run made at Dubna with a lead-plus-carbon-ion bombardment and this shows an overwhelming ratio of ^{211m}Po to ^{214}Ra.

The Russian experiment is by no means a suitable standin for our experiments on element 104. Our experiment has been carefully tailored to maximize the heavy nuclide yield and reduce that of interfering activities, so it should not be too surprising if our ratio of ^{211m}Po to ^{214}Ra is lower than in their experiment. We do know that there is some ^{211m}Po in the 8.87-MeV peak, but it has not affected the interpretation of the nearby alpha groups which belong to ^{257}104. It is clear that the Dubna system operates differently from ours because of the large amount of ^{213}Rn (8.09-MeV peak) visible in their spectrum. It appears to us that this can only be observed by decay from gaseous atoms of radon in the vicinity of the detectors, since the amount is hundreds of times larger than that which could come via electron-capture branching from the 6.77-MeV ^{213}Fe, no trace of which is visible in their spectrum.

New Experiments

The above statements with their rebuttals we believe to be a fair summary of the criticisms leveled at our experiments. A more satisfying answer, perhaps, is furnished by the following.

We have repeated the ^{249}Cf(^{12}C, 4n) ^{257}104 → ^{253}No experiment with a higher efficiency and better resolution. A background experiment was also performed with a 50-μg/cm^2 lead target. This was not exactly a standin for the californium experiment, serving only as a reasonable approximation, but showed that ^{211m}Po was not an important problem. The new element-104 experiment gave statistically better information than the previous run, even though it was run in a shorter time.

The results of the repeat experiments are presented in Figs. 3, 4 and 5. The first one displays a series of alpha-particle spectra of the activities produced in bombardments of the ^{249}Cf target with 74-MeV ^{12}C ions. The experiment was done with the 20-detector system, and the spectra shown are from the detectors in the on-wheel position. The wheel-cycle rate was 3 seconds per detecting station. In cases where two activities contribute to the same peak, the approximate ratio of the two is shown below the peak label. It should be noted that the 6.26-MeV peak is predominantly due to ^{248}Cf, not due to ^{212}Rn as indicated in Fig. 1. The 6.04-MeV ^{210}Rn peak has the apparent half-life of its mother, ^{214}Ra, because the observed events are mostly due to the decay of ^{210}Rn atoms recoiled into the detectors as a result of the alpha decay of ^{214}Ra atoms.

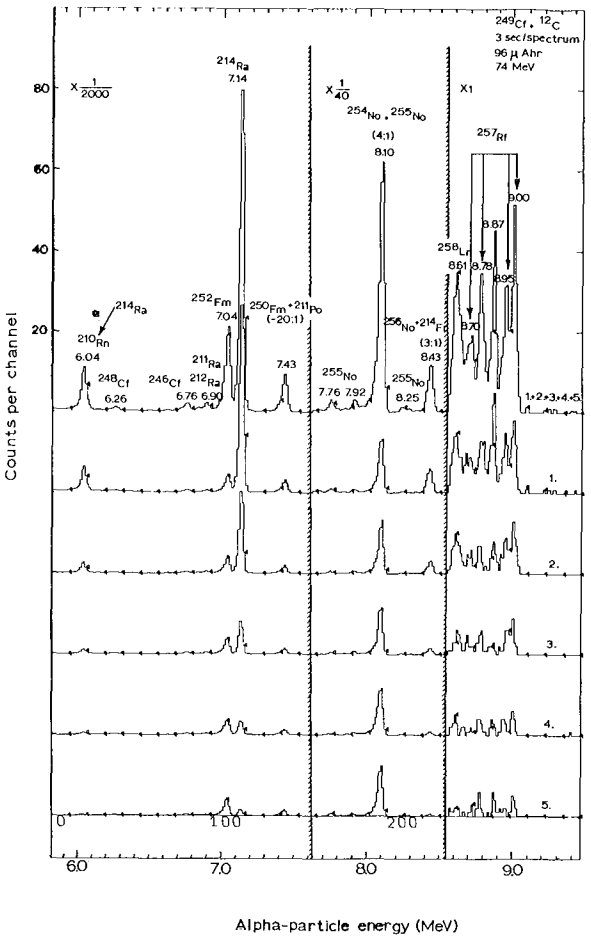

Fig. 3. A series of alpha-particle spectra of the activities produced in repeat experiments when bombarding ^{249}Cf target with 74-MeV ^{12}C ions. A 20-detector system was used instead of the 8-detector one employed in the experiments resulting in the spectra shown in Fig. 1. The wheel-cycle rate was 3 seconds in both series of experiments. (XBL702-6141)

The peak at 8.87 MeV results from the decay of ^{257}Lr and ^{211m}Po, both of which contribute about equal amounts. The assignment of the 0.7-sec component to ^{257}Lr was

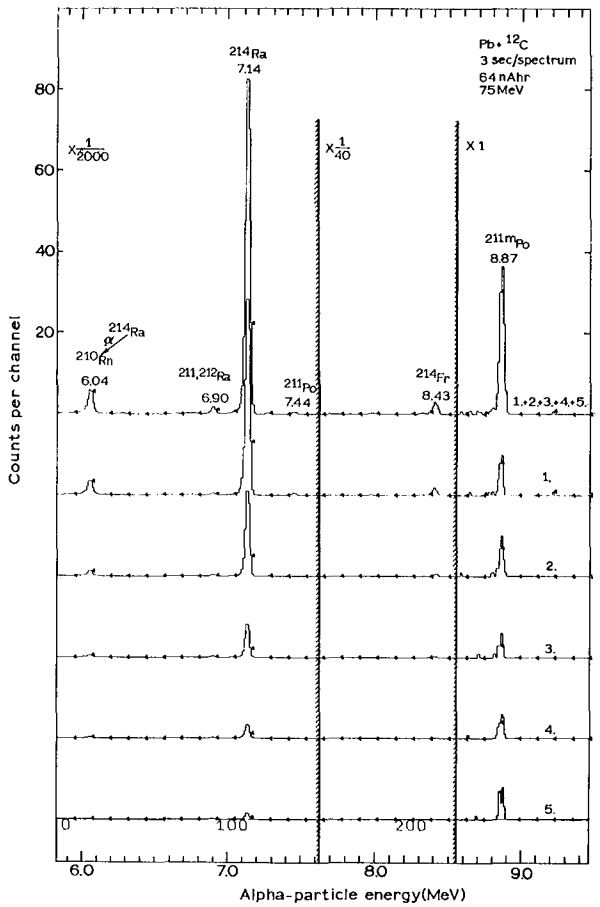

Fig. 4. Alpha-particle spectra resulting from an experiment where the ^{249}Cf target was replaced by a lead target. (XBL702-6139)

confirmed in connection with the experiments on element 105 by a cross bombardment utilizing the ^{249}Cf(^{11}B, 3n)^{257}Lr reaction.

Figure 4 displays a series of alpha-particle spectra of the activities produced in bombardment of a natural lead target by ^{12}C ions under similar conditions to those in Fig. 3. The ratio of ^{210}Rn/^{214}Ra is smaller than in Fig. 3 because the decay of ^{210}Rn was not followed equally long after the bombardment. Because of the differences in target thicknesses and beam intensities, and about 1.5-MeV difference in the bombarding energy of the ^{12}C ions, the ratio of ^{211m}Po(8.87 MeV) to ^{214}Ra(7.14 MeV) is higher by a factor of two in the lead spectrum.

The series of alpha spectra from the same experiment as in Fig. 3, but recorded by the crystals in the off-wheel position, is shown in Fig. 5. The on-wheel off-wheel cycle, or shuttle period, was 100 seconds, whereas the wheel-cycle rate was 3 seconds. The presence of ^{250}Fm and ^{254}No alpha-particle peaks with apparent half-lives of 2 sec and 0.2 sec, respectively, is believed to be caused by isomeric states of these isotopes, as explained previously. The other peaks in the spectrum are caused by the decay of alpha-recoil atoms on the movable detectors.

The apparent half-life of ^{253}No obtained by measuring the amount of ^{253}No recoiling at each detector station is 4.4 ± 1.0 seconds. This is in agreement with the value 4.8 ± 0.5 seconds for ^{257}104 as measured directly by the amount of activity observed at each station. Summing the detected daughter events by the four 25-second time subgroups of the 100-second shuttle period, one obtains a half-life of 90 ± 30 seconds for the 8.01-MeV alpha-particle group, which is consistent with the 105-second half-life[9] of ^{253}No. The ratio of

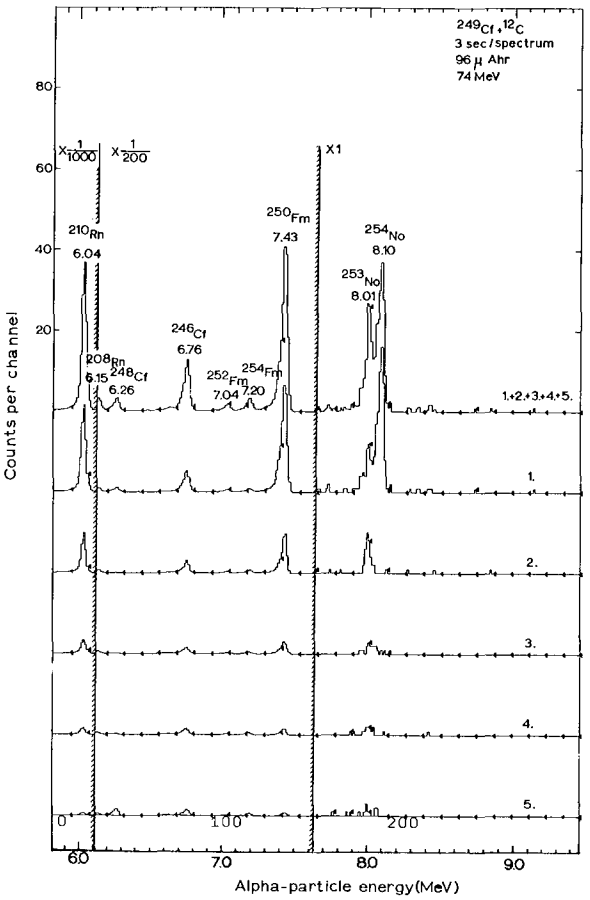

Fig. 5. A series of alpha-particle spectra from the same experiments as in Fig. 3 but recorded by the crystals in off-wheel position. These spectra correspond to those displayed in Fig. 2, but show a wider range of alpha-particle energies. (XBL702-6140)

counts in the alpha-particle peaks assigned to $^{257}104$ to those in the 8.01-MeV peak in Fig. 5 is 506:137 = 3.5. A calculation taking into account geometry and timing conditions gives a value 2.5. This difference could possibly be an indication of some 20-30% electron-capture branching in the decay of ^{253}No.

The same equipment was used to discover another isotope of rutherfordium. This work[12] characterized the 65-second alpha emitter, ^{261}Rf, and showed conclusively that its 26-second daughter, ^{257}No, was observed as the result of alpha-particle recoil-transfer from its mother. This discovery was confirmed chemically when it was shown[13] by fast aqueous-chemistry experiments utilizing this isotope that rutherfordium was a transactinide element. More recently this system was used in the discovery[6] of an alpha-emitting isotope of element 105, the 1.6-sec ^{260}Ha. The fact that the radiations detected in these two sets of experiments were completely different shows that there is no built-in constant background effect that could conceivably mislead us in our interpretations of other results.

Summary

We feel that we can safely draw the following conclusions:

1) The additional experiments with ^{257}Rf which have been described above fully confirm our original findings.

2) The puzzling transfer phenomenon has been explained as the result of previously unknown isomeric transitions in the even-even nuclides, ^{250}Fm and ^{254}No.

3) The unknown 0.7-sec 8.87-MeV activity has been determined to be due to ^{257}Lr.

4) There is no gas leakage effect in our system that can transfer activity directly to the detector faces.

5) Our system does not have a "characteristic half-life due to some unexplained artifact."

In our opinion the performance and reliability of our experimental system is beyond reproach. The present multidetector shuttle apparatus is quite a complicated instrument which has required a great deal of development and testing, and its value as a research tool has been proven by the quality of the nuclear spectroscopic data obtained for the seven isotopes of nobelium, five of lawrencium, three of rutherfordium, and one of hahnium which have been characterized up to the present time.

We would like to express our appreciation to S. Bjørnholm, E. K. Hyde, and G. T. Seaborg for comments which were very helpful in the preparation of this manuscript.

Footnotes and References

†Condensed from Nature 229, 603 (1971).

*On leave of absence from Department of Physics, University of Helsinki, Helsinki, Finland.

1. A. Ghiorso, M. Nurmia, J. Harris, K. Eskola, and P. Eskola, Phys. Rev. Letters 22, 1317 (1969).

2. V. A. Druin, in Proceedings of the International Conference on Nuclear Reactions Induced by Heavy Ions, Heidelberg, 1969, ed. by R. Bock and W. R. Hering (North-Holland Publishing Company, Amsterdam, 1970), p. 657.

3. G. N. Akapiev, V. A. Druin, V. I. Rud, and Sun-Tsin Yan, Joint Institute for Nuclear Research Report No. JINR-P7-4772, 1969 (unpublished).

4. Proceedings of the Robert A. Welch Foundation Conferences on Chemical Research XIII. The Transuranium Elements - The Mendeleev Centennial, Houston, 1969 (to be published).

5. G. N. Flerov, At. Energ. (USSR) 28, 302 (1970).

6. A. Ghiorso, M. Nurmia, K. Eskola, J. Harris, and P. Eskola, Phys. Rev. Letters 24, 1498 (1970).

7. E. D. Donets, V. A. Druin, V. L. Mikheev, Ann. Phys. 3, 332 (1968).

8. A. Ghiorso, K. Eskola, P. Eskola, and M. Nurmia, UCRL-20431.

9. A. Ghiorso, T. Sikkeland, and M. J. Nurmia, Phys. Rev. Letters 18, 401 (1967).

10. G. N. Flerov, S. M. Polikanov, V. L. Mikheev, V. I. Ilyushchenko, V. F. Kushniruk, M. B. Miller, A. M. Sukhov, and V. A. Shchegolev, Yadern. Fiz. 5, 1186 (1967) [Soviet J. Nucl. Phys. 5, 848 (1967), translated from Russian].

11. P. Eskola, K. Eskola, M. Nurmia, and A. Ghiorso, Phys. Rev. C 2, 1058 (1970).

12. A. Ghiorso, M. Nurmia, K. Eskola, and P. Eskola, Phys. Letters 32B, 95 (1970).

13. R. Silva, J. Harris, M. Nurmia, K. Eskola, and A. Ghiorso, Inorg. Nucl. Chem. Letters 6, 871 (1970).

Nuclear Reactions and Scattering

Beta-Delayed-Proton Decay of ^9C

John E. Esterl, David Allred, † J. C. Hardy, * R. G. Sextro, and Joseph Cerny

Observation of peaks in the delayed-proton spectrum of ^9C could determine energy levels in ^9B, a nucleus whose lower levels are still not well characterized.[1] These levels, in particular those of negative parity, are of interest because they can be compared to the predictions of intermediate coupling calculations,[2] which have proved quite successful elsewhere in the 1p shell. Fortunately, β decay from ^9C should preferentially populate the levels of interest, since ^9C should have $J^\pi = 3/2^-$, as does its mirror ^9Li.

The methods of target preparation, activity transport, particle identification, and data collection were described in detail previously.[3] Oxygen swept the ^9C, which was produced by a 43-MeV proton beam via the $^{10}B(p, 2n)^9C$ reaction, to a shielded counting chamber. Protons were detected by a counter telescope consisting of a 14-μm phosphorous-diffused silicon ΔE counter and a 1.5-mm lithium-drifted silicon E counter, and identified by a Goulding-Landis identifier.

Figure 1 shows the proton spectrum following the beta decay of ^9C. Other data taken with a thicker (50-μm) ΔE detector show more intense peaks at 9.28 and 12.30 MeV because higher energy protons deposited insufficient energy in the 14-μm detector to operate the electronics reliably. All peaks decayed with the same half-life, 126.5 ± 1.0 msec, and therefore are believed to result from the decay of ^9C. This half-life agrees well with earlier work[4] and results in an average value of 126.5 ± 0.09 msec. Any contribution to the spectrum from ^{13}O produced from a nitrogen contaminant in the sweeping gas is eliminated by its short half-life, 9 msec, since counting began about 100 msec after bombardment.

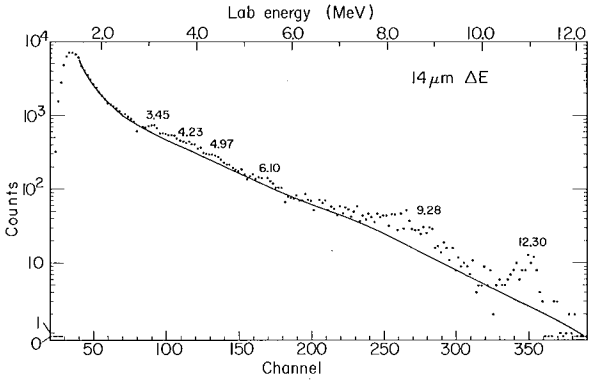

Fig. 1. Spectrum of delayed protons following the beta decay of ^9C taken with a counter telescope employing a 14-μm ΔE detector.
(XBL 7010-4059)

The peak energies were fixed by calibrating the three higher energy peaks against the known[3] spectrum of ^{17}Ne using the 50-μm ΔE counter. These peaks were then used to calibrate the data taken with the thinner ΔE counter. The line on Fig. 1 shows the continuum level assumed in the extraction of peak widths and energies. Since previous delayed-proton experiments[3] with virtually identical apparatus had very low background levels, the continuum must be composed almost entirely of protons.

Table I lists the energies of all proton peaks observed, and tentatively correlates them with known states in ^9B. The 4.97-MeV proton group has been assumed to result from decay of the positive parity state of 4.85 MeV. Beta decay to this state is first forbidden and therefore would not be expected to be observable. However, the log ft values for allowed beta decays in the mirror nucleus ^9Li are known[5] to range from 5 to 6, whereas first forbidden transitions in ^{15}C and ^{11}Be have comparable log ft values ranging from 6 to 6.8. From experiments[6] in which ^9B was populated in the $^{10}B(He^3, \alpha)^9B$ reaction and α-p coincidences were observed, the 2.80-MeV state ($J^\pi = 3/2^+, 5/2^+$) in ^9B was found to decay almost entirely via proton emission to the ground state of ^8Be, whereas the 2.33-MeV state ($J^\pi = 5/2^-, 1/2^-$) has less than a 0.5% branch via this channel. This selectivity in decay channel, if characteristic of all low-lying states, would make it much easier to detect protons from positive parity levels even if their feeding via beta decay was rather weak. Similarly, since no states of spin $(1/2, 3/2, 5/2)^-$ in the region of 6 MeV are predicted[2] by intermediate coupling, the 6.10-MeV proton group may follow the decay of an unknown positive parity state formed via first forbidden beta decay.

The 3.45-MeV proton group could result from decay of a ^9B state at 3.2 MeV. In fact, intermediate coupling calculations[2] predict a hitherto unassigned $3/2^-$ state at about 4.8 MeV, but are unable to provide a reliable estimate for the strength of the beta decay to this state. Predictions[2] of the ft value range over two orders of magnitude, depending on

Table I. Delayed protons following the beta decay of $^{9}C(J^{\pi} = 3/2^{-})$.

Proton energy[a] (MeV)	Γ[b] (keV)[a]	Corresponding state in ^{9}B (MeV)		Known state	
		If decaying to ^{8}Be(g.s.)	If decaying to ^{8}Be(2.9 MeV)	(MeV)	J^{π}
3.45 ± 0.25	200 ± 100	3.26 ± 0.25	c	(3.2)	$(3/2^{-})$
4.23 ± 0.25	1000 ± 200	4.04 ± 0.25	6.94 ± 0.25	4.05	$(5/2^{-})$
4.97 ± 0.15	400 ± 150	4.78 ± 0.15	c	4.85	$(3/2, 5/2)^{+}$
6.10 ± 0.10	400 ± 100	5.91 ± 0.10	c		
9.28 ± 0.24[d]	1800 ± 200	9.09 ± 0.24	11.99 ± 0.24	12.06	$(1/2, 3/2)^{-}$
12.30 ± 0.10[d]	450 ± 100	12.11 ± 0.10	c	12.06	$(1/2, 3/2)^{-}$

[a]Energies and widths are given in the center-of-mass system.

[b]The width given is the full width at half maximum.

[c]The relatively narrow width indicates that the proton group does not lead to the first excited state of $^{8}Be(\Gamma = 1.4$ MeV).

[d]The ratio of the intensities of the 9.28- and 12.30-MeV groups is 1.0 ± 0.2.

the parameter set used to determine the wave function. Even though Clough et al.[1] have tentatively assigned $J^{\pi} = 3/2^{-}$ to a level at 3.2 MeV, the existence of a state at this energy has not been definitely established.[1,7] Though further work is clearly necessary, our data are also consistent with a state at 3.2 MeV.

The strong proton continuum probably results from two sources. First, the levels of ^{9}B are quite broad, as is the first excited state of ^{8}Be (1.4 MeV), so the combination of many broad peaks tends to produce a featureless spectrum. Second, a level in ^{9}B may emit an α particle to form states in ^{5}Li which, in turn, break up into a proton and another α particle resulting in an extremely broad distribution of proton energies. There may be some contribution to the continuum from direct three-body decay. The existence of a large continuum and the suggestion from the work of Wilkinson et al.[6] that those states fed most strongly in beta decay may prefer to decay via ^{5}Li have prevented the determination of ft values and level energies from the delayed-proton spectrum.

Footnotes and References

†Present address: Brigham Young University, Provo, Utah.

*Present address: Chalk River Nuclear Laboratories, Chalk River, Ontario, Canada.

1. K. Gul, B. H. Armitage, and B. W. Hooton, Nucl. Phys. A153, 390 (1970); A. S. Clough, C. J. Batty, B. E. Bonner, and L. E. Williams, Nucl. Phys. A143, 385 (1970); and references therein.

2. S. Cohen and D. Kurath, Nucl. Phys. 73, 1 (1965); F. C. Barker, Nucl. Phys. 83, 418 (1966).

3. J. C. Hardy, J. E. Esterl, R. G. Sextro, and J. Cerny, Phys. Rev. C 3, 700 (1971).

4. J. M. Mosher, R. W. Kavanagh, and T. A. Tombrello, Phys. Rev. C 3, 438 (1971); J. C. Hardy, R. I. Verrall, R. Barton and R. E. Bell, Phys. Rev. Letters 14, 376 (1965).

5. Y. S. Chen, T. A. Tombrello, and R. W. Kavanagh, Nucl. Phys. A146, 136 (1970).

6. D. H. Wilkinson, J. T. Sample, and D. E. Alburger, Phys. Rev. 146, 662 (1966).

7. J. D. Anderson, C. Wong, B. A. Pohl, and J. W. McClure, Phys. Rev. C 2, 319 (1970) and R. J. Slobodrian, H. Bichsel, J. S. C. McKee, and W. F. Tivol, Phys. Rev. Letters 19, 595 (1967).

Beta-Delayed-Proton Decay of ^{13}O: A Violation of Mirror Symmetry †

John E. Esterl, J. C. Hardy,* R. G. Sextro, and Joseph Cerny

Recent work[1,2] has called attention to the existence of deviations from mirror symmetry in beta decay. In the case of the well-studied mass-12 nuclei, the magnitude of electromagnetic, second-forbidden, isospin-mixing, and binding-energy effects have been evaluated[1] and found insufficient to explain the observed deviation. This lends support to the proposal[3] that there is an induced tensor term in beta decay. Since such a term is expected to cause the ratio $(\overline{ft})^+/(\overline{ft})^-$ to increase linearly[2,3] with $(W_0^+ + W_0^-)$, it is of particular interest to examine cases with large decay energies.

We have investigated the decay of ^{13}O and compared it with that[4] of its mirror ^{13}B, since $(W_0^+ + W_0^-)$ for these nuclei is ≈ 30 MeV. ^{13}O is a beta-delayed-proton emitter for which all the allowed β^+ decays, except those to the ground state, lead to proton unbound levels in ^{13}N.

A target of N_2 gas was bombarded with a 43-MeV proton beam from the Berkeley 88-inch cyclotron. At ≈ 1/2-sec intervals the gas was swept with helium into a shielded counting chamber. There, protons from ^{13}O, produced by the $^{14}N(p, 2n)^{13}O$ reaction, were detected and identified in a cooled ΔE-E counter telescope, which fed a Goulding-Landis particle identifier. The signal from the 14-μm ΔE detector was required to be < 1 MeV to eliminate background coincidences between α particles and multiply scattered β particles from the decay of ^8B. Identified protons were time-sorted into four groups in a pulse height analyzer, thus providing both lifetime and energy data. In addition, the decay of a selected proton peak was recorded with a 400-channel multiscalar.

A proton spectrum from the decay of ^{13}O is shown in Fig. 1. All peaks shown have half-lives of less than 50 msec--much less than any light delayed-proton emitter other than ^{13}O. The proton groups can be assigned to known[5] states in ^{13}N as is shown in Fig. 2 and Table I. The widths of all assigned peaks were extracted and found compatible with the known[5] widths after correcting for the broadening due to nuclear recoil following beta decay.

Our results for the higher energy peaks of Fig. 1 can be compared with proton resonance data. For the 8.92- and 9.52-MeV states, the fraction of proton decays that leads to the ground state of ^{12}C is 0.70 ± 0.07 and 0.65 ± 0.12, respectively. This compares well with the values of Γ_{el}/Γ of 0.66 and 0.58 derived[6] from elastic and inelastic proton scattering on ^{12}C. The energy of the decay branch of the 7.39-MeV state to the first excited state of ^{12}C is too low for us to observe. Therefore the total number of proton decays from this state was calculated using the decay we observed to the ^{12}C ground state together with the known[6,7] Γ_{el}/Γ of 0.09 ± 0.02. Similarly, the total number of decays from the 10.35-MeV level was calculated using the measured[8] Γ_{el}/Γ of 0.27 ± 0.02. Arrow B in Fig. 1 shows the expected location of the ground state branch. Arrows A and C indicate the predicted location of protons from the known $J^\pi = 1/2^-$, 10.78-MeV state.

The half-life of ^{13}O deduced from a least-squares analysis of the data is 8.95 ± 0.20 msec. Our result agrees with the previous[9] value of 8.7 ± 0.4 msec, so a weighted average of 8.9 ± 0.2 msec was used for further analysis.

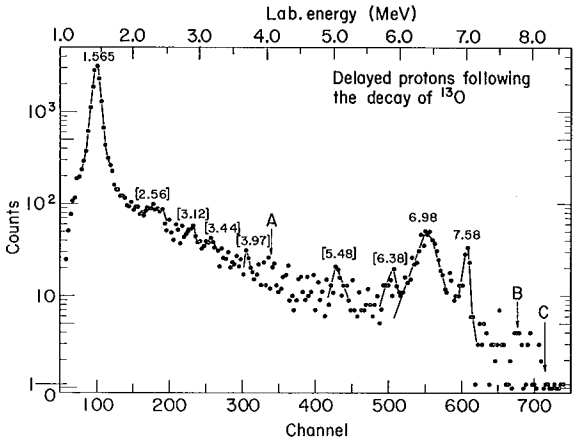

Fig. 1. Delayed-proton spectrum following the decay of ^{13}O. The unbracketed energies were used to calibrate the spectrum. The arrows indicate the location of allowed but unobserved decays. All peak energies explicitly shown are in the center-of-mass system.

(XBL708-3605)

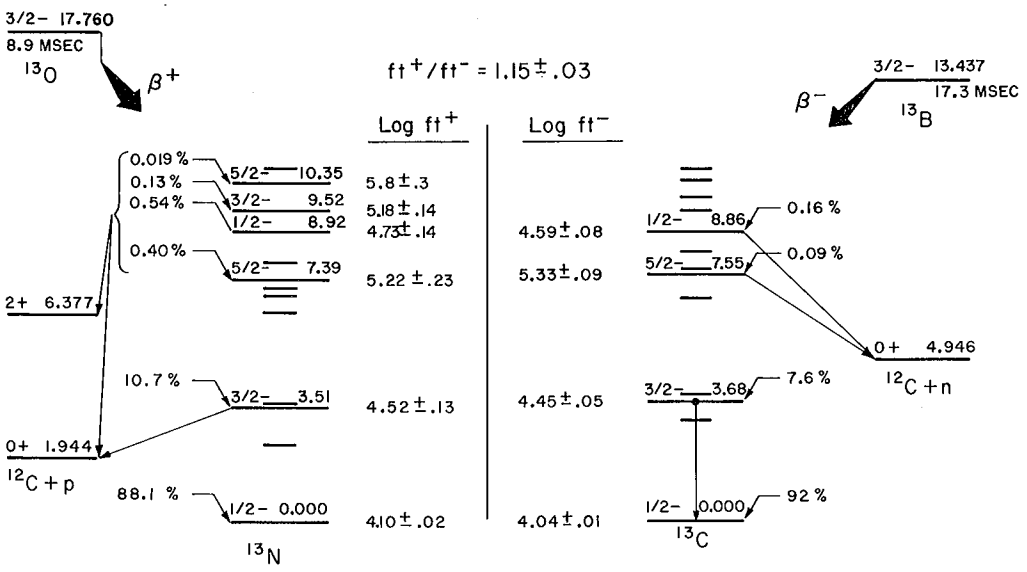

Fig. 2. Comparison of the decay schemes of the mirror nuclei ^{13}O and ^{13}B. The spins, parities, and energies are taken from previous work as are the half-life and decay of ^{13}B. The log ft values for the excited states of ^{13}O were obtained using the ratio of ground state ft's indicated in the figure. (XBL708-3604)

The ft values for ^{13}B decay were calculated from the relative intensities of Jones et al.[4] and the recently measured[10] half-life of 17.33 ± 0.17 msec. The results are listed in Table I. Assuming perfect mirror symmetry for these transition rates and correcting for additional observed decay branches, the half-life of ^{13}O is predicted to be 7.74 ± 0.16 msec. The ratio of the true half-life to the predicted one is 1.15 ± 0.03, indicating a significant departure from mirror symmetry. It also reflects the ratio $(ft)^+/(ft)^-$ providing that the effects causing asymmetry are state independent.[3]

Individual ft values to all observed states in ^{13}N were calculated from the measured proton intensities and the half-life, assuming that the ratio of the mirror ground state ft values was 1.15. The results are compared with ft values from ^{13}B decay in Table I; they compare well with the relevant mirror decays. However, the contrary assumption of equal ground-state ft's yields a partial half-life for the ground state branch alone of 8.78 ± 0.11 msec, a value incompatible with the observed half-life of ^{13}O. The ratio of $(ft)^+/(ft)^-$ required by our results agrees well with that predicted by a linear fit[2] to $(W_o^+ + W_o^-)$ in 11 light mirror nuclei.

Allowed log ft values have been observed for all known[5] $J^\pi = 5/2^-$, $3/2^-$, and $1/2^-$ levels through 10.35 MeV in ^{13}N. This fixes the J^π of ^{13}O as $3/2^-$ in agreement with the prediction of the simple shell model.

Footnotes and References

†Condensed from Phys. Letters, 33B, 287 (1970).

*Present address: Chalk River Nuclear Laboratories, AECL, Chalk River, Ontario, Canada.

1. R. J. Blin-Stoyle and M. Rosina, Nucl. Phys. 70, 321 (1965); R. J. Blin-Stoyle in Isospin in Nuclear Physics, edited by D. H. Wilkinson (North-Holland Publishing Co., Amsterdam, 1969), p. 115.

2. D. H. Wilkinson, Phys. Letters 31B, 447 (1970).

3. J. N. Huffaker and E. Greuling, Phys. Rev. 132, 738 (1963).

4. K. W. Jones, W. R. Harris, M. T. McEllistrem, and D. E. Alburger, Phys. Rev. 186, 978 (1969).

Table I. Beta decay of ^{13}O and a comparison with its mirror, ^{13}B.

^{13}N State (MeV) [a]	J^π	E_p(c.m.) (MeV)	Relative intensity	% of all β decays [b]	^{13}O log ft [b]	^{13}B log ft [c]
g.s.	$1/2^-$	———	———	88.1 ± 3.4	4.10 ± 0.02	4.04 ± 0.01
3.509	$3/2^-$	1.565 [d]	100	10.7 ± 3.1	4.52 ± 0.13	4.45 ± 0.05
7.387	$5/2^-$	1.010 [e] 5.48 ± 0.05	3.4 ± 1.4 [f] 0.33 ± 0.10	0.40 ± 0.19	5.22 ± 0.23	5.33 ± 0.09
8.92	$1/2^-$	2.56 ± 0.05 6.98 [d]	1.5 ± 0.3 3.5 ± 0.3 [g]	0.54 ± 0.16	4.73 ± 0.14	4.59 ± 0.08
9.52	$3/2^-$	3.12 ± 0.05 7.58 [d]	0.43 ± 0.15 0.8 ± 0.1 [g]	0.13 ± 0.04	5.18 ± 0.14	> 5.0
10.35	$5/2^-$	3.97 ± 0.05 8.41 [e]	0.13 ± 0.07 0.05 ± 0.03 [f]	0.019 ± 0.012	5.8 ± 0.3	———
		3.44 ± 0.05 [h]	0.3 ± 0.1	0.030 ± 0.016		
		6.38 ± 0.05 [h]	0.46 ± 0.10	0.050 ± 0.018		

a. Energies, spins, and parities taken from Ref. 5, except as noted.

b. The ground state ft was taken to be 1.15 times that of ^{13}B.

c. Calculated from the data of Ref. 4 using a ^{13}B half-life of 17.33 ± 0.17 msec.

d. Used to determine the energy calibration.

e. Calculated value, unobserved in this experiment.

f. Calculated using the known ratio of the elastic and inelastic widths.

g. Our relative intensities agree with those of Ref. 9 for the two peaks observed in that work.

h. Weak proton groups observed in this work, but not positively attributed to ^{13}O decay.

5. F. Ajzenberg-Selove, Nucl. Phys. A152, 1 (1970).

6. A. C. L. Barnard, J. B. Swint, and T. B. Clegg, Nucl. Phys. 86, 130 (1966).

7. G. G. Shute, D. Robson, V. R. McKenna, and A. T. Berztiss, Nucl. Phys. 37, 535 (1962); F. C. Barker, G. D. Symons, N. W. Tanner, and P. B. Treacy, Nucl. Phys. 45, 449 (1963); N. Nikolic, L. J. Lidofsky, and T. H. Kruse, Phys. Rev. 132, 2212 (1963).

8. E. M. Bernstein and G. E. Terrell, Phys. Rev. 173, 937 (1968); J. B. Swint, J. S. Duval, Jr., A. C. L. Barnard, and T. B. Clegg, Nucl. Phys. A93, 177 (1967).

9. R. McPherson, R. A. Esterlund, A. M. Poskanzer, and P. L. Reeder, Phys. Rev. 140, B1513 (1965).

10. D. E. Alburger and D. H. Wilkinson, private communication.

The Reactions $^{11}B(p, {}^3He)\,^9Be$ and $^{11}B(p,t)\,^9B$: Is There Strong Isospin Mixing in Mass 9?†

J. C. Hardy,* J. M. Loiseaux,‡ Joseph Cerny, and Gerald T. Garvey††

If it is assumed that two-body forces are responsible for charge dependence in nuclei then, to first order, the masses of members of an isobaric multiplet are related by the so-called isobaric-multiplet mass equation (IMME).

$$M(A, T, T_z) = \underset{\sim}{a}(A, T) + \underset{\sim}{b}(A, T)T_z + \underset{\sim}{c}(A, T)T_z^2. \quad (1)$$

By using second-order perturbation theory the IMME can be extended to include[1] the additional terms $\underset{\sim}{d}T_z^3 + \underset{\sim}{e}T_z^4$, where the coefficients $\underset{\sim}{d}$ and $\underset{\sim}{e}$ are functions only of off-diagonal matrix elements.

Experimentally it is possible, by measuring the masses of all four members of a $T = 3/2$ quartet, to determine the magnitude of the coefficient $\underset{\sim}{d}$. What light this may shed on the extent of isospin mixing is illustrated by considering the interaction between two states--one with $T = 3/2$ and the other with $T = 1/2$--which appear in a $|T_z| = 1/2$ nucleus. The perturbed energy of the $T = 3/2$ level can be expanded in powers of T_z, where the coefficient of the T_z^3 term is[2]

$$\underset{\sim}{d} = -\left[\sqrt{15}\,(E_{3/2} - E_{1/2})\right]^{-1} \langle T = \tfrac{3}{2} \,||H_{CD}^{(1)}|| \tfrac{1}{2}\rangle \langle \tfrac{3}{2} \,||H_{CD}^{(2)}|| \tfrac{1}{2}\rangle . \quad (2)$$

Here $H_{CD}^{(i)}$ is the i^{th} rank tensor component of the charge-dependent part of the Hamiltonian and E_T is the excitation energy of the state with isospin T. The corresponding amplitude α of the $T = 1/2$ component admixed into the $T = 3/2$ analogue-state wave function is

$$\alpha(T_z = \pm\tfrac{1}{2}) = (E_{3/2} - E_{1/2})^{-1} \left\{ \frac{1}{\sqrt{6}} \langle \tfrac{3}{2} \,||H_{CD}^{(1)}|| \tfrac{1}{2}\rangle \pm \frac{1}{\sqrt{10}} \langle \tfrac{3}{2} \,||H_{CD}^{(2)}|| \tfrac{1}{2}\rangle \right\}, \quad (3)$$

where the $\pm$ signs correspond to $T_z = \pm 1/2$. Under these restrictive limits of only two-state mixing, it is now possible to derive from Eqs. (2) and (3) several relationships which are otherwise model independent:

$$\alpha^2(\pm\tfrac{1}{2}) \pm (E_{3/2} - E_{1/2})^{-1}\,\underset{\sim}{d} \geq 0 \quad (4)$$

$$\alpha^2(-\tfrac{1}{2}) - \alpha^2(+\tfrac{1}{2}) = 2\underset{\sim}{d}(E_{3/2} - E_{1/2})^{-1}. \quad (5)$$

Thus, it is evident that even if the $\underset{\sim}{d}$ coefficient is measured to be zero, isospin mixing cannot be precluded; and conversely, a significant $\underset{\sim}{d}$ coefficient is compatible with no isospin mixing in <u>one</u> of the $|T_z| = 1/2$ nuclei but not in both.

Recent results on measurements of $\underset{\sim}{d}$ coefficients are given in Refs. 2 and 3. It appears that the only quartet which displays a significantly nonzero $\underset{\sim}{d}$ coefficient is in mass 9--this involves the ground states of ^9C and ^9Li, and the lowest $T = 3/2$ states in ^9B and ^9Be. It is then of particular interest to study the mass-9 system with a view to isospin mixing so as to discover what special circumstances have determined the size of its $\underset{\sim}{d}$ coefficient.

In probing this question previously, Jänecke[1] has pointed out that two $T = 1/2$ states of uncertain spin lie at $\approx$ 500 keV and $\approx$ 2500 keV below the $3/2^-$ ($T = 3/2$) analogue states in both ^9B and ^9Be; if one of these states were also $3/2^-$, then it might well mix with the analogue state, perturbing its energy sufficiently to cause the observed $\underset{\sim}{d}$ value. However, by assuming such two-state mixing, he requires very large off-diagonal Coulomb matrix elements and predicts isospin impurities in the analogue state of $\approx$ 16% if mixing occurs with the nearer $T = 1/2$ state or $\approx$ 4% if it is with the other.

It now seems unlikely from the measured widths of the levels involved that such large isospin impurities in the analogue state could occur, particularly in ^9Be. All excited states in ^9Be are unstable to neutron emission and consequently almost all known $T = 1/2$ states have $\Gamma \gtrsim$ 100 keV. The lowest $T = 3/2$ state, if it had pure isospin, would be

bound to isospin-conserving particle decay and its width would be determined by radiative decay. Certainly some impurity must be present since its width is known to be 0.4 keV[4], but the size of the impurity will be approximated by $0.4/\Gamma_{1/2}$, where $\Gamma_{1/2}$ is the width of the T = 1/2 state with which it is assumed to mix. For $\Gamma_{1/2} \gtrsim 100$ keV, the corresponding impurity must be less than 0.5%. Since both T = 1/2 states suggested by Jänecke have widths of more than 400 keV, such large impurities as he suggests are improbable.

It was hoped that two-nucleon transfer reaction studies might clarify some of these points. As such, representative (p, t) and (p, ^{3}He) spectra are shown in Fig. 1. Below the T = 3/2 analogue states at ≈ 14.5 MeV in both nuclei, these schemes are the same as those which appear in Ref. 4 and we see no evidence for additional states. However, above this energy we observe new T = 1/2 states at 15.96 ± 0.04 MeV in ^{9}Be and at 15.29 ± 0.04 MeV and 15.58 ± 0.04 MeV in ^{9}B; in addition there is a possible state or states at ≈ 15.13 MeV in ^{9}Be.

In discussing the possibility of two-state mixing, between the analogue state and a nearby T = 1/2 state, it is convenient to divide the approach between two possibilities: $E_{1/2} < E_{3/2}$ and $E_{1/2} > E_{3/2}$. Considering the first possibility, the most intense T = 1/2 level within a few MeV below the analogue state is that at 12.06 MeV, but even it is a factor of four weaker than the analogue state. Hence we can rule out the possibility of significant isospin mixing with T = 1/2 levels at lower excitation (see extended discussion in original paper).

The experimental data imply that the possibility of mixing with the two pairs of T = 1/2 levels at higher excitation energy than the analogue must be considered. For these levels $E_{1/2} - E_{3/2} \approx 750$ keV and ≈ 1.5 MeV. Where $E_{1/2} > E_{3/2}$, Eq. (5) indicates that the mixing in ^{9}Be must be greater than in ^{9}B, and since the width of the T = 1/2 levels is approximately independent of T_z, this means that the width of the T = 3/2 state in ^{9}B must be $\Gamma < 0.4$ keV, which is the width of its analogue in ^{9}Be. At present only an experimental upper limit has been set[5] and it is too high to test this hypothesis. Further, Eq. (4) can now be written:

$$\alpha^2(^9\mathrm{Be}) \geq d(E_{1/2} - E_{3/2})^{-1},$$

or

$$\frac{0.4}{\Gamma_{1/2}} \geq \frac{9.1}{E_{1/2} - E_{3/2}}, \qquad (6)$$

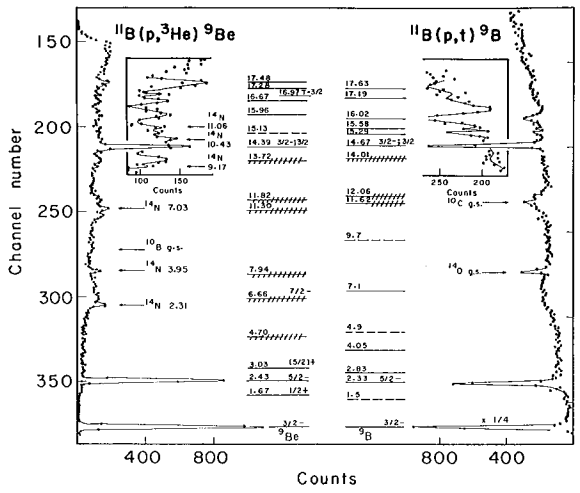

Fig. 1. Spectra of tritons and ^{3}He particles from the reactions ^{11}B(p, ^{3}He)^{9}Be and ^{11}B(p,t)^{9}B recorded at 31.5° for 1940 μC. The energy level diagram is taken from Ref. 4 with additional levels at ≈ 15 MeV from this work. The slight difference in the energy scale between ^{9}Be and ^{9}B is due to the effects of energy loss by the reaction products in the target and counter dead-layers. (XBL702-2350)

where $\Gamma_{1/2}$ is the width of the T = 1/2 state. This indicates that, if mixing with the 15.13-MeV "state" is to explain the observed d coefficient, then its width must be $\Gamma \lesssim 40$ keV, while if the 15.96-MeV state is responsible, $\Gamma \lesssim 80$ keV. In either case, the impurity in the analogue state might be as little as 1%. It does seem unlikely, though, that a 3/2$^-$ (T = 1/2) level at this excitation energy would be narrower than 40 keV, and in fact our data determine the width of the 15.96-MeV level to be ≈ 300 keV. Thus it is improbable that strong isospin mixing occurs with T = 1/2 levels at higher excitation energy than the analogue state.

The present results, taken together with previously measured level-energies and widths in ^{9}B and ^{9}Be, make the possibility of very significant isospin mixing in the lowest-energy T = 3/2 analogue states rather remote.

Footnotes and References

†Condensed from Nucl. Phys. A162, 552 (1971).

*Present address: Chalk River Nuclear Laboratories, AECL, Chalk River, Ontario, Canada.

‡NATO Fellow; permanent address: I. P. N., Orsay, France.

††Present address: Joseph Henry Laboratories, Princeton University, Princeton, N. J. 08540.

1. J. Jänecke, Nucl. Phys. A128, 632 (1969).

2. G. T. Garvey in Nuclear Isospin, ed. by J. D. Anderson, S. D. Bloom, J. Cerny, and W. W. True, (Academic Press, New York, 1969) p. 703.

3. J. Cerny, Ann. Rev. Nucl. Sci. 18, 27 (1968).

4. T. Lauritsen and F. Ajzenberg-Selove, Nucl. Phys. 78, 1 (1966).

5. $\Gamma_{T=3/2}$ is < 15 keV from the reaction ^{7}Li(^{3}He, n)^{9}B, E. Adelberger, private communication; see also F. S. Dietrich, Nucl. Phys. 69, 49 (1965).

Spin Dependence in the Reactions ^{16}O(p,t) ^{14}O and ^{16}O(p, ^{3}He) ^{14}N†

D. G. Fleming,* J. C. Hardy,‡ and Joseph Cerny

Two-nucleon transfer reactions have proved to be a useful method for determining the spins, parities and isospins of nuclear states. We have studied the reactions ^{16}O(p,t)^{14}O, ^{16}O(p, ^{3}He)^{14}N, and ^{16}O(d, α) ^{14}N. Recent assignments for states in ^{14}O, resulting from (^{3}He, t) reaction[1] studies, are confirmed and predictions using the (1p)-shell wave functions of Cohen and Kurath[2] are compared with the data.

Following the distorted-wave Born approximation (DWBA), the differential cross section for a two-nucleon pickup reaction A(a, b)B can be expressed in the following form if the effects of spin-orbit coupling are included:[3]

$$\frac{d\sigma}{d\Omega} = \frac{\mu_a \mu_b}{(2\pi\hbar^2)^2} \frac{k_b}{k_a} \frac{2s_b+1}{2s_a+1} \sum_{M\sigma_a\sigma_b} \times \left| \sum^{NLST} b_{ST}(T_B T_{z_B} \; T T_z \,|\, T_A T_{z_A}) \; D(S,T) \; G_N(LSJT) B^{NLSJT}_{M\sigma_a\sigma_b} \right|^2 . \quad (1)$$

The notation is discussed in Ref. 3.

In the calculations presented here we will assume that the interaction has zero range[4] but we will examine the strength of the spin- and isospin-exchange terms in the interaction potential. If the two-body interaction V_{ij} is written as

$$V_{ij} = U(r_{ij})[W + BP^{\sigma}_{ij} - HP^{\tau}_{ij} - MP^{\sigma\tau}_{ij}] , \quad (2)$$

where P^{σ}_{ij} and P^{τ}_{ij} are the operators which exchange the spin and isospin coordinates of nucleons i and j, then it has been shown[5] that D(S, T) in Eq. (1) can be expressed as follows:

$$D(S,T) = 1 - (0.5 + \delta_{S,1})(B + H) . \quad (3)$$

Thus, the larger the exchange terms, the more the S = 1 term in Eq. (1) is reduced relative to that for which S = 0.

An examination of the ^{16}O(p, ^{3}He)^{14}N reaction provides a sensitive measure of the strength of the exchange terms. Since the ^{16}O ground state has T = 0, the isospin of the final states (T = 0 or 1) determines uniquely the spin transferred by this reaction (S = 1 or 0, respectively). By comparing the relative strengths of transitions with S = 0 and 1, and making use of Eq. (4) it will be possible to extract a value for (B + H). Actually the quantity which will be determined experimentally is R [see Eq. (1)], where

$$R \equiv \left| \frac{D(1,0)}{D(0,1)} \right|^2 = \left| \frac{1 - 1.5(B+H)}{1 - 0.5(B+H)} \right|^2 . \quad (4)$$

Obviously, an accurate determination of R depends upon the reliability of the wave functions used for the initial and final states.

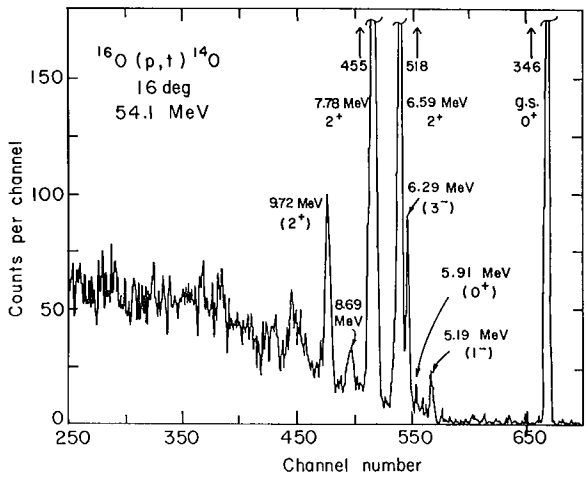

Fig. 1. Energy spectrum of the ^{16}O(p,t)^{14}O reaction. (XBL678-3969)

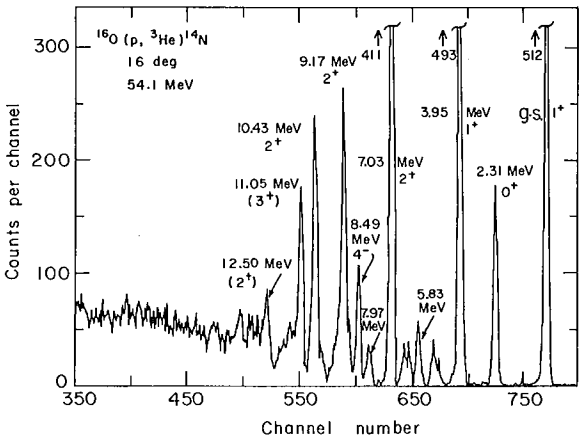

Fig. 2. Energy spectrum of the ^{16}O(p, ^{3}He) ^{14}N reaction. (XBL678-3968)

Here ^{14}N is particularly advantageous since the wave functions of its ground and first two excited states have recently been examined extensively[6] as to their efficacy in reproducing a variety of experimental data.

Those states produced by the (p,t) reaction in ^{14}O have T = 1 and their analogues in ^{14}N will be produced by T = 1 transfer using the (p, ^{3}He) reaction. Since these are now analogous reactions, the (p,t) and (p, ^{3}He) reactions leading to T = 1 analogue states will have angular distributions with the same shape and relative magnitudes related by

$$A \equiv \frac{d\sigma/d\Omega\ (p,t)}{d\sigma/d\Omega\ (p,\ ^{3}He)} = \frac{2}{2T-1}\ \frac{k_t}{k_{^{3}He}} = \frac{2k_t}{k_{^{3}He}}\ . \qquad (5)$$

Figures 1 and 2 present energy spectra taken at 54.1 MeV for the ^{16}O(p,t)^{14}O and ^{16}O(p, ^{3}He)^{14}N reactions, respectively; both were recorded simultaneously. The L = 0 and 2 triton angular distributions are shown on the left-hand side of Fig. 3. On the right-hand side of the same figure are shown the (p, ^{3}He) angular distributions to their known or suspected T = 1 analogues in ^{14}N; the latter have been multiplied by $(2k_t/k_{^{3}He})$ to facilitate the comparison suggested by Eq. (5). The shapes of the dashed curves provide the best fit to the triton data. The same curves, but renormalized, were then drawn through the corresponding (p, ^{3}He) angular distributions. For two states which are analogues, the dashed curve should fit the (p, ^{3}He) data, and the magnitudes of the distributions as they appear in the figure should be the same. These conditions are satisfied for the four pairs of states shown in the figure, thus

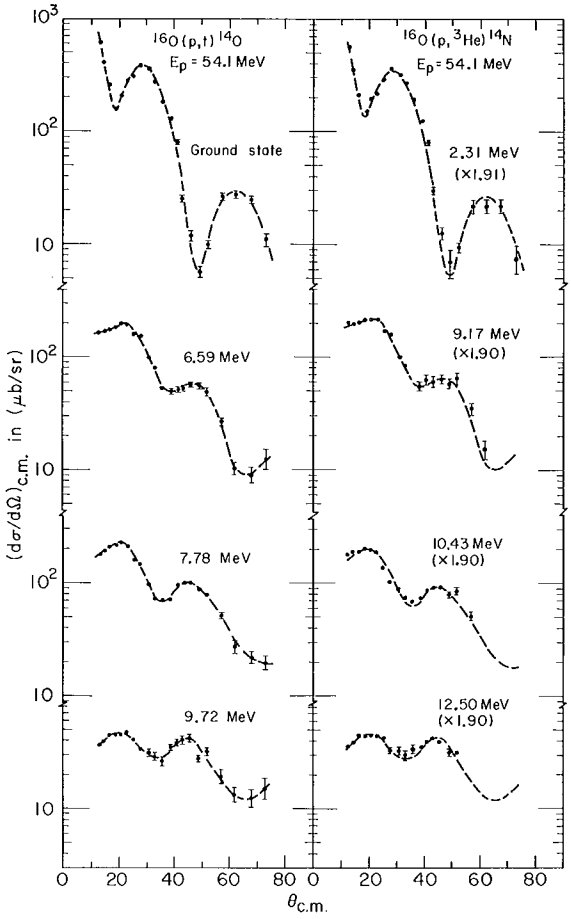

Fig. 3. Angular distributions for the reactions ^{16}O(p,t)^{14}O and ^{16}O(p, ^{3}He)^{14}N at 54.1 MeV leading to analogue T = 1 states. The ^{3}He points have been multiplied by $(2k_t/k_{^{3}He})$. See text for a discussion of the dashed curves. (XBL708-3776)

Table I. Values for the ratio $[D(1,0)/D(0,1)]^2$ determined from experiments at two different bombarding energies, assuming various sets of wave functions and optical-model parameters.

Wave function set[a]	$[D(1,0)/D(0,1)]^2$				Average
	E_p = 43.7 MeV		E_p = 54.1 MeV		
	1[b]	2[b]	1[b]	2[b]	
I	0.19	0.19	0.14	0.15	0.17
II	0.19	0.19	0.15	0.15	0.17
III	0.26	0.27	0.21	0.22	0.24
IV	0.30	0.31	0.25	0.26	0.28
V	0.33	0.32	0.25	0.26	0.29
VI	0.33	0.33	0.26	0.27	0.30

[a]The references for these wave functions appear in Table V of the original paper.

[b]These numbers refer to the ^{3}He optical-model parameters given in Table III of the original paper. The appropriate proton parameters were used for both bombarding energies.

confirming them as analogues.

The relative magnitudes of the angular distributions of the first four strong states produced in the (p, ^{3}He) reaction are affected not only by the details of the wave functions, but also by the form of the interaction potential or specifically by D(S, T). Since each transition is characterized by a unique value of S, then, $[D(S, T)]^2$ appears as a simple multiplicative factor in the expression for the cross section, and the ratio R [see Eq. (4)] can be determined directly by comparison with the data. The results appear in Table I where they are tabulated as a function of wave function, optical-model parameters and bombarding energy. Except for wave-function sets I and II, which were deemed generally less successful[6] in fitting experimental data, the range of R values is not large, although R is systematically lower for the higher bombarding energy. A best value of R would be ≈ 0.28. The resultant $B + H \approx 0.4$ is not significantly different from the force mixtures frequently used in shell-model calculations[5]

Footnotes and References

†Condensed from Nucl. Phys. A162, 225 (1971).

*Present address: Niels Bohr Institute, Copenhagen, Denmark.

‡Present address: Chalk River Nuclear Laboratories, AECL, Chalk River, Ontario, Canada.

1. G. C. Ball and J. Cerny, Phys. Rev. 155, 1170 (1967).

2. S. Cohen and D. Kurath, Nucl. Phys. 73, 1 (1965); D. Kurath, private communication.

3. I. S Towner and J. C. Hardy, Advan. Phys. 18, 401 (1969).

4. N. K. Glendenning, Ann. Rev. Nucl. Sci. 13, 191 (1963); N. K. Glendenning, Phys. Rev. 137B, 102 (1965).

5. J. C. Hardy and I. S Towner, Phys. Letters 25B, 98 (1967).

6. H. J. Rose, O. Häusser, and E. K. Warburton, Rev. Mod. Phys. 40, 591 (1968).

$^{53}Co^{m}$: A Proton-Unstable Isomer †

K. P. Jackson, C. U. Cardinal, H. C. Evans, N. A. Jelley, and Joseph Cerny

A recently reported experiment[1] has demonstrated the feasibility of using heavy-ion induced reactions to produce new nuclides of the A = 4n + 1, $T_Z = (N-Z)/2 = -3/2$ series of beta-delayed-proton emitters. Protons emitted from the lowest T = 3/2 state in ^{49}Mn were observed following the $^{40}Ca(^{12}C, 3n)^{49}Fe$ reaction. As a natural extension of this program a similar experiment was designed to produce ^{53}Ni via the $^{40}Ca(^{16}O, 3n)$ reaction. This communication reports an unforeseen result of these experiments--the observation of a proton activity for which the most plausible explanation is direct proton decay of an unbound isomer in ^{53}Co produced in the $^{40}Ca(^{16}O, 2np)$ reaction.

In the initial experiments designed to produce ^{53}Ni, a natural calcium target was bombarded with a pulsed beam of ≈ 0.5 μA of $^{16}O(4+)$ ions at energies up to 81 MeV produced by the Harwell variable-energy cyclotron. Delayed protons were detected and their lifetimes were measured with the same system as that described in Ref. 1, except that the semiconductor telescope consisted of a 23-μm ΔE counter followed by a 100-μm E detector and these fed a particle identifier.[2] As shown in Fig. 1(a), the identified proton spectra from this reaction were dominated by a strong group near the minimum energy (≈ 1.3 MeV) required for reliable detection. In order to obtain energy spectra unaffected by the telescope cutoff, this low energy activity was also measured using a single 50-μm, totally depleted, silicon detector as shown in Fig. 1(b).

Both detection systems always gave identical results for this activity which can be summarized as follows: (a) the energy of the protons after correction for energy loss in the target is 1.53 ± 0.04 MeV and their half-life is 245 ± 20 msec; and (b) their excitation function indicates a threshold below an ^{16}O bombarding energy of 39 MeV with a peak cross section ≈ 8 μb occurring in the region of 53 MeV (laboratory). The low threshold eliminates ^{53}Ni as a source of these protons, and irradiation of other targets indicated that the observed activity could not be attributed to any likely contaminant.

In order to investigate further the reactions of ^{16}O on ^{40}Ca, delayed γ-ray spectra were recorded with a Ge(Li) detector following the bombardment of a calcium target with pulses of ^{16}O ions at energies below

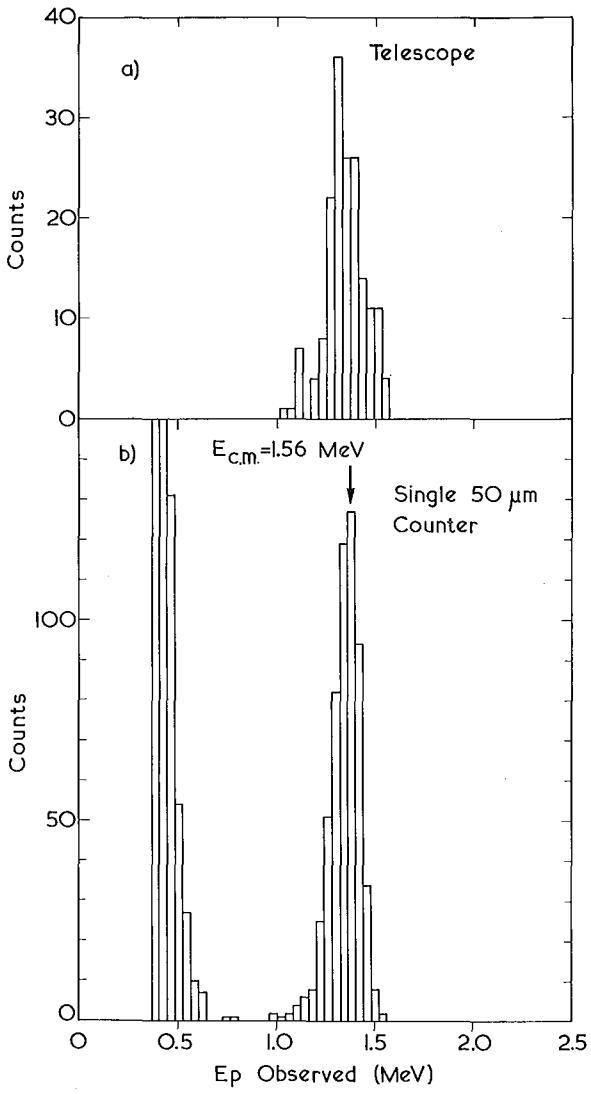

Fig. 1. (a) An identified proton spectrum arising from the bombardment of calcium by ^{16}O at 49 MeV. Protons between 1.3 and 3.6 MeV could be linearly detected.

(b) A spectrum recorded in a single 50-μm detector of the activity arising from bombardment of calcium by 49 MeV ^{16}O. The center of mass energy shown results from assuming $^{53}Co^{m}$ to be the origin of this activity. Events below 0.6 MeV arise from the high beta background and those below 0.4 MeV are not shown.

(XBL708-6442)

50 MeV produced by the coupled injector and EN tandem facility at Oxford. As was anticipated, prominent peaks were observed corresponding to the known[3] cascades in ^{54}Fe and ^{50}Cr following β^+ decay of the high-spin isomers $^{54}Co^m$ and $^{50}Mn^m$. Gamma rays were also observed which indicated a cross section of ≈ 50 mb for the (^{16}O, 2pn) reaction leading to $^{53}Fe^m$--a 2.5-min isomer at an excitation of 3.04 MeV.[4] This isomer is presumed to be $19/2^-$, T = 1/2 on the basis of its observed properties and shell-model predictions for high-spin states with the configuration $(f_{7/2})^{-3}$.

Considering the observed yield of $^{53}Fe^m$ from the (^{16}O, 2pn) reaction, it is reasonable to expect a significant population of its isobaric analogue state in ^{53}Co from the (^{16}O, 2np) reaction. The mass excess of the ^{53}Co ground state is predicted to be -42.64 MeV from the known mass of ^{53}Fe[5] and the Coulomb displacement energy calculations of Harchol et al.[6] From the known mass of ^{52}Fe,[7] the binding energy of a proton in ^{53}Co is then estimated to be 1.6 MeV and thus, $^{53}Co^m$, the isobaric analogue state of $^{53}Fe^m$, must be unbound. If the observed proton group is attributed to the direct decay of $^{53}Co^m$ to ^{52}Fe, one obtains a value of 8.42 MeV for the mass difference between the analogue isomers. This result is in adequate agreement with the value 8.30 MeV calculated in Ref. 6 for the corresponding ground states.[8] The calculated threshold for the $^{40}Ca(^{16}O, 2np)^{53}Co^m$ reaction is 33.0 MeV, consistent with the experimental observations, and its excitation function agrees well with that expected from simple statistical model calculations.[9]

Based on $^{53}Co^m$ as the origin of the proton activity, the probable decay scheme presented in Fig. 2 is consistent with our data. The observed 245 msec half-life implies that the dominant mode of decay is by positron emission to $^{53}Fe^m$.

Proton emission apparently arises only as a weak branch in the decay of $^{53}Co^m$. A rough order of magnitude estimate of the partial lifetime for this branch can be obtained from the statistical model calculations;[9] at an ^{16}O energy of 47 MeV the predicted ratio of

$$\frac{\sigma(^{16}O, 2pn)}{\sigma(^{16}O, 2np)} \text{ is } \approx \frac{70}{1} ,$$

while the observed ratio of

$$\frac{\sigma(^{53}Fe^m)}{\sigma\left(\begin{matrix}\text{proton}\\ \text{activity}\end{matrix}\right)} \text{ is } \approx \frac{15000}{1} ,$$

implying a partial half life ≈ 50 sec. Since penetration through the Coulomb and $\ell = 9$ centrifugal barriers leads to an expected half-life of ≈ 0.3 μsec for $\gamma_p^2 = 1$, this rough estimation implies $\gamma_p^2 \approx 6\times10^{-9}$ for this very complex decay. A 0.7 MeV (c. m.) proton group leading to the first excited (2^+) state[10] of ^{52}Fe is also energetically possible (with a barrier penetrability 50 times less), but could not have been observed in these experiments.

The best alternative explanation for this activity is of course to attribute it to beta-delayed-proton emission. In this vein one must consider the ground states and isomers of all other nuclei for which the emission of beta-delayed protons of 1.53 MeV is energetically possible. Of these the most reasonable example follows the assumption that the parent nuclide is still the isomer $^{53}Co^m$, but that its direct proton decay is too weak to be observed. One would then attribute the observed activity to delayed-proton emission following β^+ decay to a level in the region of 9.08 MeV in ^{53}Fe, as shown in Fig. 2. In the unlikely event that such a state were populated by β^+ decay from $^{53}Co^m$ having a log ft as low as 3.8, such a branch would represent only 4×10^{-4} of all decays of the isomer. This would imply that the ratio $\sigma(^{53}Co^m)/\sigma(^{53}Fe^m)$ was at least one order of magnitude higher than expected on the basis of statistical model calculations.[9] Similar arguments and the excitation function data make it improbable that any other T_Z = - 1/2, -1, or -3/2 nuclide below ^{56}Ni is the origin of this activity. In conclusion, it is our opinion that the best explanation for the observed activity is the weak proton radioactivity of $^{53}Co^m$.[11]

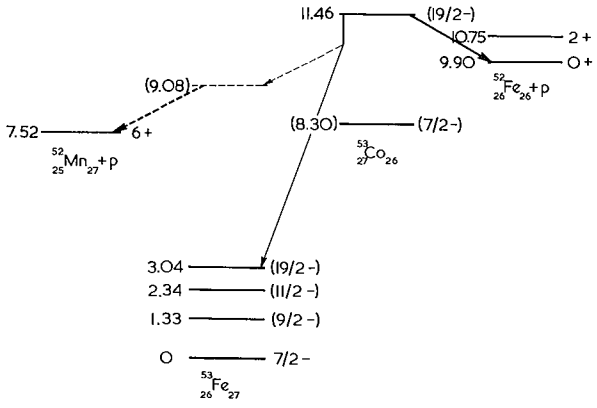

Fig. 2. The proposed decay scheme for the proton-unstable isomer $^{53}Co^m$. Energies are given in MeV. The probable decay modes are given by solid arrows while the less-likely production of beta-delayed protons is indicated by dashed lines. (XBL708-6441)

Footnote and References

†Condensed from Phys. Letters 33B, 281 (1970); written at Nuclear Physics Laboratory, Oxford University, England, supported in part by a grant from the Science Research Council. During part of this work, one of the authors (J. C.) was a J. S. Guggenheim Fellow (1969-1970) at Oxford University.

1. J. Cerny, C. U. Cardinal, H. C Evans, K. P. Jackson, and N. A. Jelley, Phys. Rev. Letters 24, 1128 (1970).

2. P. S. Fisher and D. K. Scott, Nucl. Instr. Methods 49, 301 (1967).

3. C. M. Lederer, J. M. Hollander, and I. Perlman, Table of Isotopes (John Wiley and Sons, 1967).

4. K. Eskola, Phys. Letters 23, 471 (1966); I. Dernedde, Zeit. für Physik 216, 103 (1968).

5. A. Trier, L. Gonzalez, J. Rapaport, T. A. Belote, and W. E. Dorenbusch, Nucl. Phys. A111, 241 (1968).

6. M. Harchol, A. A. Jaffe, J. Miron, I. Unna, and J. Zioni, Nucl. Phys. A90, 459 (1967).

7. J. H. E. Mattauch, W. Thiele, and A. H. Wapstra, Nucl. Phys. 67, 1 (1965).

8. Some difference in Coulomb displacement energies might be expected due to the differing seniorities of the ground states and the isomers.

9. M. Blann, University of Rochester, private communication. The calculations follow the model discussed in Nucl. Phys. 80, 223 (1966). We wish to thank Professor Blann for performing these computations for us.

10. G. Bassini, N. M. Hintz, and C. D. Kavaloski, Phys. Rev. 136, B1006 (1964).

11. V. I. Goldanskii, Ann. Rev. Nucl. Sci. 16, 1 (1966); J. Jänecke, Nucl. Phys. 61, 326 (1965).

Confirmed Proton Radioactivity of $^{53}Co^{m}$ †

Joseph Cerny, John E. Esterl, R. A. Gough,* and R. G. Sextro

Reactions of ^{16}O ions on ^{40}Ca have produced an activity[1] whose most plausible origin is the proton radioactivity of $^{53}Co^{m}(19/2^{-})$ (see Fig. 2 of Ref. 1). However, (a) these heavy-ion experiments could not without question attribute the activity to this nuclide, and (b) the possibility that the observed decay in fact arises through beta-delayed-proton emission was not conclusively eliminated. This paper reports further experiments which definitely establish the direct proton radioactivity of $^{53}Co^{m}$.

In order to confirm $^{53}Co^{m}$ as the parent nuclide, the external proton beam of the Berkeley 88-inch cyclotron was used to induce the $^{54}Fe(p, 2n)$ reaction. Protons were detected in a counter telescope, consisting of a 14-μm ΔE detector followed by a 50-μm E detector, which fed a Goulding-Landis particle identifier, as well as in a single 50-μm E detector. These systems were mounted behind a slotted, rotating wheel, which controlled the duration of the beam pulse and protected the counters during the beam-on interval. Pulsing was achieved by modulating the voltage on the cyclotron dee; proton beam intensities of up to 8 μA on target were utilized.

An identified proton spectrum resulting from bombardment of an 840-$\mu g/cm^2$ ^{54}Fe target with 31.8-MeV protons is shown on the top of Fig. 1. An analyzed beam of 3.39-MeV H_2^+ ions was used for energy calibration of both detection systems. From this calibration the energy of the proton group was determined to be 1.57 ± 0.03 MeV. Half-life information was obtained by using a 400-channel multiscaler whose address was advanced by a quartz-crystal oscillator; the half-life of the protons was determined to be 242 ± 15 msec. Both the energy and the half-life found in the ^{54}Fe + p reaction agree excellently with those found in Ref. 1.

An excitation function for the production of this proton activity is shown on the bottom of Fig. 1. Proton-beam energies were measured using the high-resolution analysis magnet of the cyclotron. The threshold for this activity is determined to be 26.3 ± 0.4 MeV and the observed peak cross section is ≈ 0.5 μb. This threshold agrees well with the expected one of 26.14 ± 0.04 MeV,[2] based on a $^{53}Co^{m}$ mass-excess of -39.44 ± 0.04 MeV constructed from the mass of ^{52}Fe (g. s.) plus a 1.60-MeV (c. m.) proton. Since this fairly low threshold precludes formation of any other nuclide

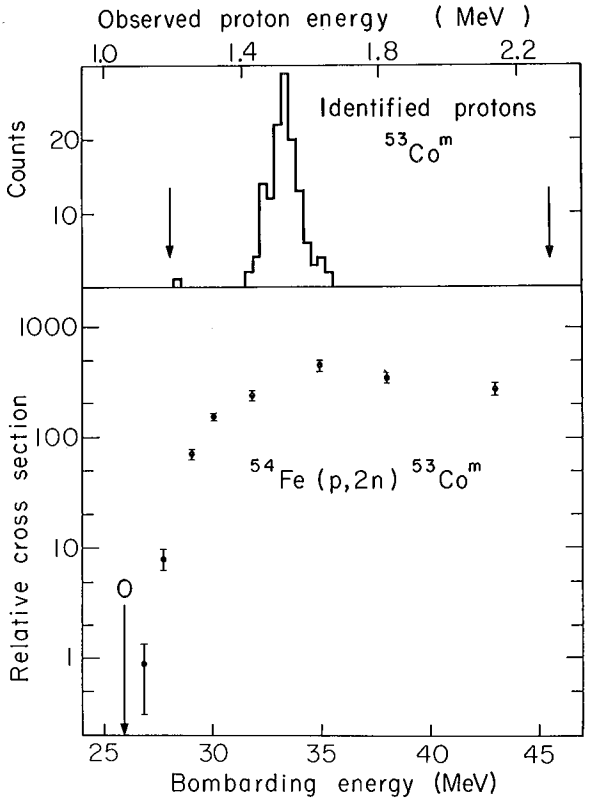

Fig. 1. Top: An identified proton spectrum arising from the bombardment of ^{54}Fe by 31.8-MeV protons. The arrows denote the energy region over which protons could be observed.
Bottom: The excitation function for the $^{54}Fe(p,2n)^{53}Co^{m}$ reaction. The scale on the ordinate approximates the absolute cross section in nb. (XBL709-3834)

energetically capable of beta-delayed-proton emission, the excitation function data establish $^{53}Co^{m}$ as the parent nuclide.

In order to confirm the proton radioactivity of $^{53}Co^{m}$, the possibility of beta-delayed-proton emission must be eliminated. The only avenue for delayed-proton decay of this isomer that can be considered remotely possible would be allowed beta decay--with a quite small log $\overline{ft}$--to a state near 9.08 MeV in ^{53}Fe (see Fig. 2 of Ref. 1). This β^{+} decay (end point $\approx$ 1.36 MeV) must then be followed by proton decay to the 6^{+} ground state of ^{52}Mn; in this case a short lifetime for proton emission from the intermediate state would be expected due to the available low ℓ values and an anticipated larger reduced width (see Ref. 1). In order to determine whether such beta-delayed-proton emission occurs, a search for positron-proton coincidences in the decay of $^{53}Co^{m}$ was conducted.

In this experiment, positrons were detected in a 0.5-cm-thick plastic scintillator which subtended a solid angle of 0.12 sr, while protons were detected in the single 50-μm detector. An isotropic angular correlation is expected following normal allowed beta decay. [3]

The coincidence experiments were conducted at a proton energy of 35 MeV. In order to monitor the correct operation of the coincidence electronics, positron - alpha-particle coincidences resulting from the decay of ^{20}Na, produced via the $^{24}Mg(p,\alpha n)$ reaction, were observed at intervals throughout the bombardment of ^{54}Fe. The observed α-particle decay spectrum of ^{20}Na shown in the top of Fig. 2 agrees with earlier work. [4] Coincidences were observed between positrons and α particles (or protons) in the fixed energy range indicated by the arrows in Fig. 2. A coincidence resolving time of 4 nsec was obtainable over this narrow energy interval. The observed coincidence data corrected for chance-coincidence background for this ^{20}Na decay are shown in the bottom of Fig. 2; ex-

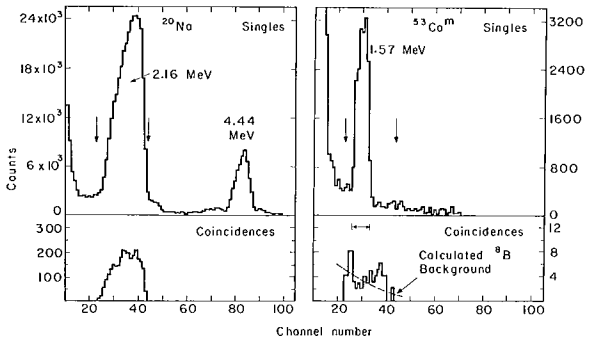

Fig. 2. Left: Alpha-particle energy spectra arising from the decay of ^{20}Na produced via the $^{24}Mg(p,\alpha n)$ reaction on a 0.5-mg/cm^{2} natural Mg target. The energies indicated are the undegraded values. The data in the lower spectrum arise from coincidences between positrons and those α particles in the energy region limited by the arrows in the singles spectrum.
Right: Composite energy spectra arising from the bombardment of a 3-mg/cm^{2} ^{54}Fe target and its ^{12}C contaminant. The upper spectrum shows the 1.57-MeV (undegraded value) proton peak arising from the decay of $^{53}Co^{m}$ astride a background of α particles from ^{8}B decay. The data in the lower spectrum arise from coincidences between positrons and protons or α particles in the energy region limited by the arrows in the singles spectrum. The horizontal arrow in the coincidence spectrum indicates the expected position of the 1.57-MeV peak if preceded by positron emission. (XBL709-3836)

cellent agreement was found with the expected efficiency.

The proton spectrum following the decay of $^{53}Co^{m}$ observed in the 50-μm detector is also shown in the top of Fig. 2. Since the low yield of the isomer prevented employment of the counter telescope due to its reduced solid angle, the proton peak rides on a background of α particles from ^{8}B decay produced in reactions on the ^{54}Fe target and on the ^{12}C target impurity. Various subsidiary experiments established that the vast majority of the background events between the arrows in the $^{53}Co^{m}$ singles spectrum arise from ^{8}B decay and are not due to multiply-scattered β particles. As such, β^{+}-α coincidences due to this ^{8}B background are to be expected.

Composite results for the coincidence runs corrected for chance-coincidence background from 37 hours of observation of the decay of $^{53}Co^{m}$ are shown in the bottom of Fig. 2. The calculated coincidence background arising from ^{8}B decay is indicated in the figure. No peak resulting from β^{+}-p coincidences--which should lie in the region denoted by the horizontal arrows--is observable in this spectrum. After making all the efficiency corrections including allowance for 12% loss due to electron capture[5] in this hypothetical decay, we would expect 65 ± 8 β^{+}-p coincidence events in the denoted region of interest, whereas we observe 0 ± 15 events after correction for the β^{+}-α background due to ^{8}B. The absence of this peak establishes the fact that the 1.57-MeV proton group arising in the decay of $^{53}Co^{m}$ is not preceded by positron emission.

A review of the various modes of radioactive decay involving proton emission has been given by Goldanskii[6] in which the possibility of decay from isomeric states was also considered. Our results and those in Ref. 1 defining the properties of $^{53}Co^{m}$ establish it to be the first example[6] of radioactive nuclear decay by direct proton emission.

Footnotes and References

†Condensed from Phys. Letters 33B, 284 (1970).

*National Research Council of Canada Postdoctoral Fellow.

1. K. P. Jackson, C. U. Cardinal, H. C. Evans, N. A. Jelley, and J. Cerny, Phys. Letters 33B, 281 (1970); (preceding paper, this report).

2. The threshold for $^{53}Co^{g}$ would be approximately 3 MeV lower, based on the equivalent $^{53}Fe^{m}$ - $^{53}Fe^{g}$ separation. See K. Eskola, Phys. Letters 23, 471 (1966); I. Dernedde, Zeit. für Physik 216, 103 (1968).

3. H. Frauenfelder and R. M. Steffen in, Alpha-, Beta-, and Gamma-Ray Spectroscopy, ed. by K. Siegbahn (North-Holland Publishing Company, Amsterdam, 1965) p. 997.

4. R. M. Polichar, J. E. Steigerwalt, J. W. Sunier, and J. R. Richardson, Phys. Rev. 163, 1084 (1967); N. S. Oakey and R. D. Macfarlane, Phys. Rev. Letters 25, 170 (1970).

5. E. J. Konopinski and M. E. Rose in, Alpha-, Beta-, and Gamma-Ray Spectroscopy, ed. by K. Siegbahn (North-Holland Publishing Company, Amsterdam, 1965) p. 1327.

6. V. I. Goldanskii, Ann. Rev. Nucl. Sci. 16, 1 (1966).

Isospin Purity and Delayed-Proton Decay: ^{17}Ne and ^{33}Ar†

J. C. Hardy,* John E. Esterl, R. G. Sextro, and Joseph Cerny

The $T_Z = -3/2$ nuclei ^{33}Ar and ^{17}Ne are both delayed-proton precursors. That is, many of their β^{+}-decay branches lead to states above the proton separation energy of the appropriate daughter nucleus, resulting in proton emission with the half-life characteristic of the preceding β^{+} decay. Measurement of the energies and intensities of these proton groups determines energy levels in the daughter nuclei. It can also yield the ft values for β^{+} decay to these levels if it is possible to determine the intensity of β^{+} transitions to those states below the proton separation energy.

For the case of ^{17}Ne, decay to the only two states below the proton separation energy is first-forbidden and therefore quite weak. In the case of ^{33}Ar, there are two allowed transitions that lead to bound states. The ft

for the allowed ground-state decay was calculated from that of the mirror decay, viz. $^{33}P \xrightarrow{\beta^-} {}^{33}S$ with a six percent correction for the deviation from mirror symmetry caused by a possible induced tensor coupling.[1] The intensity of the other allowed branch, that to the first excited state at 810 keV, was determined by observing its γ decay to the ground state.

In both ^{17}Ne and ^{33}Ar, one of the decay branches observed is the superallowed transition to the T = 3/2 analogue state in the daughter T = 1/2 nucleus. The log ft for such transitions can be calculated quite accurately since the strength of the decay is determined predominantly by the Fermi matrix element, which in the case of T = 3/2 states is given by $a\sqrt{3}$, where a is the amplitude of the T = 3/2 part of the analogue-state wave function in the daughter nucleus. Thus any isospin impurity in the analogue state will cause the ft value to increase. Therefore, accurate measurements of ft values for these transitions are fairly sensitive tests for isospin purity.

External ^{3}He beams from the Berkeley 88-inch cyclotron produced ^{17}Ne and ^{33}Ar via $(^{3}He, 2n)$ reactions on oxygen and sulfur targets, respectively. Figure 1 shows a diagram of the system used to collect and count ^{33}Ar in a low-background environment. In this arrangement CS_2 vapor was bombarded for a time, and then helium was used to sweep the activity past the traps and up to the counting chamber. Then the line between the target and counting chambers was pumped out and the target was refilled. This process was repeated every second. For the production of ^{17}Ne, either the CS_2 source was replaced by an oxygen cyclinder or a stack of TiO_2 foils was used in a slightly different target chamber.

The active volume of the counting chamber was conical with a counter telescope placed at the apex. The telescope consisted of a 1.0-mm lithium-drift E counter and a phosphorous-diffused silicon ΔE detector which ranged from 14 to 50 μm in thickness depending on the experiment. Identified protons were time-sorted into eight groups of a pulse-height analyzer to provide simultaneous energy and lifetime information.

In both decay studies, γ-ray measurements were required. A 2 in. × 2 in. NaI(Tl) crystal was mounted externally at the base of the conical counting volume and was used to detect p-γ coincidences (2τ = 50 nsec) occurring in the decay of ^{17}Ne. A 45-cc Ge(Li) detector was mounted in a similar position to detect γ rays following the decay of ^{33}Ar.

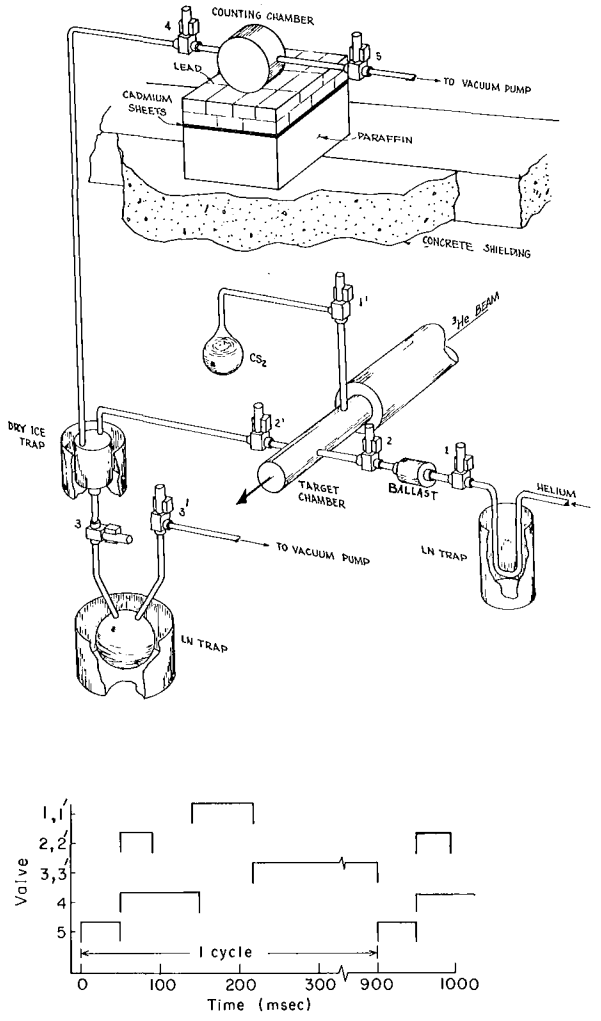

Fig. 1. A schematic diagram of the apparatus used for the production of ^{33}Ar. The sequence of valve operation is shown at the bottom; valve on times are indicated. (XBL708-3569)

Figure 2 shows a sample proton spectrum. All peaks shown follow the decay of ^{33}Ar except the two labelled ^{17}Ne, which resulted from an oxygen contaminant, and peak 11, which does not have the same relative intensity at higher bombarding energies. Energy calibration was obtained from another spectrum taken at a higher bombarding energy such that ^{29}S was produced via the $^{32}S(^{3}He, \alpha 2n)^{29}S$ reaction. Since the excitations of the T = 3/2 analogue states in ^{33}Cl and ^{29}P are well known,[2] the positions of the two peaks resulting from these states provided an excellent energy calibration.

The proton group energies were then used to establish the location of states in ^{17}F and ^{33}Cl as shown in Fig. 3 and Table I. The

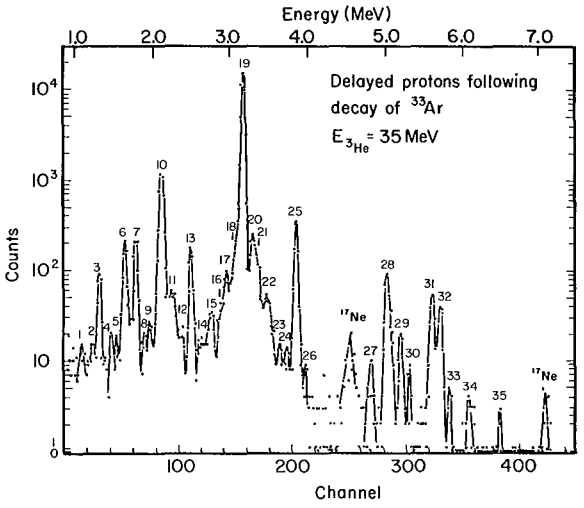

Fig. 2. Spectrum of delayed protons observed in a counter telescope with a 14-μm ΔE counter. The proton laboratory energy is indicated at the top.
(XBL707-3451)

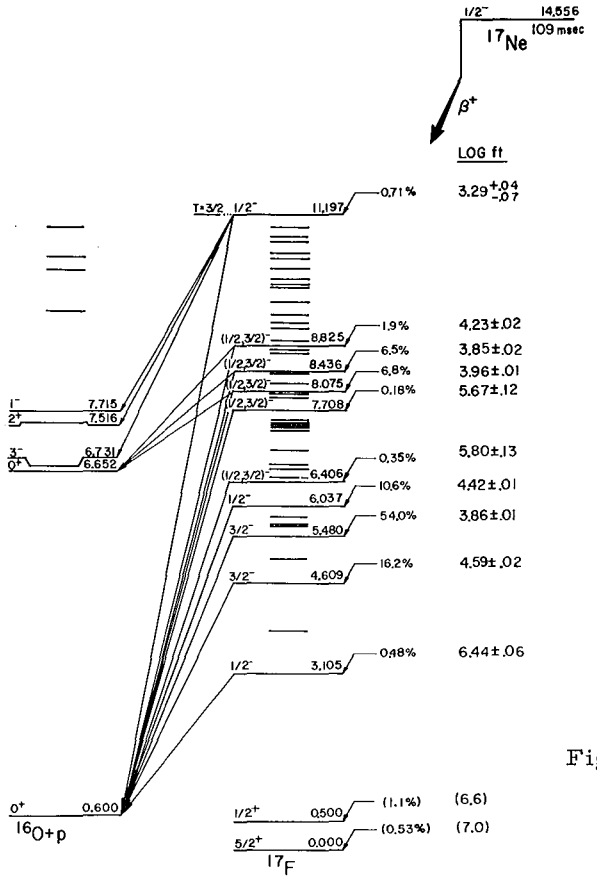

Fig. 3. Proposed decay scheme of ^{17}Ne. The ^{17}F level energies above 4 MeV are the values determined from the present experiment (except the 11.197-MeV state).
(XBL701-2187)

Table I. β^+ branching ratios and ft values for ^{33}Ar $\xrightarrow{\beta^+}$ ^{33}Cl.

Energy level[a] in ^{33}Cl (MeV)	Branching ratio from ^{33}Ar (%)	log ft[b] (sec)
0.000	18.1 ± 1.9[c]	5.03 ± 0.05
0.810	48.1 ± 3.6	4.44 ± 0.03
3.983	0.40 ± 0.04	5.71 ± 0.05
4.123	0.43 ± 0.05	5.64 ± 0.05
4.442	2.50 ± 0.26	4.76 ± 0.05
4.751	0.047 ± 0.008	6.39 ± 0.08
4.838	0.31 ± 0.04	5.54 ± 0.05
5.111	0.081 ± 0.013	6.03 ± 0.07
5.455	0.57 ± 0.06	5.05 ± 0.05
5.550	26.7 ± 2.7	3.34 ± 0.05
5.675	0.55 ± 0.06	4.97 ± 0.05
5.744	0.37 ± 0.04	5.12 ± 0.05
5.882	$0.23^{+0.13}_{-0.07}$	5.26 ± 0.18
6.034	0.027 ± 0.007	6.13 ± 0.12
6.125	0.017 ± 0.007	6.29 ± 0.22
6.254	0.58 ± 0.06	4.70 ± 0.05
7.228	0.041 ± 0.008	5.35 ± 0.09
7.475	0.29 ± 0.03	4.35 ± 0.06
7.595	0.25 ± 0.03	4.34 ± 0.06
7.767	0.010 ± 0.003	5.62 ± 0.14
8.084	$0.23^{+0.13}_{-0.07}$	4.05 ± 0.20
8.183	$0.14^{+0.13}_{-0.07}$	4.17 ± 0.30
8.310	0.017 ± 0.004	4.98 ± 0.10
8.609	0.017 ± 0.004	4.71 ± 0.12
8.969	0.003 ± 0.0015	5.09 ± 0.25

[a] The values below 6 MeV are averages with other work. Above that energy they are from the present work only.

[b] The ft values are calculated using (-9.400 ± 0.050) MeV as the mass excess of ^{33}Ar and (173.0 ± 2.0)msec as its half-life.

[c] This ratio is calculated by comparison with the mirror ^{33}P decay.

Table II. Isospin purity of lowest T = 3/2 states in ^{17}F and ^{33}Cl.

Nucleus	Superallowed ft value feeding analogue state: Experimental (sec)	Calculated[a] (sec)	Limit (i. e. $\langle \sigma \rangle^2 = 0$) (sec)	Isospin purity ($= 100a^2$) (%)
^{17}F	$(1.93^{+0.17}_{-0.29})\times10^3$	1.96×10^3	$\leq 2.06\times10^3$	> 95
^{33}Cl	$(2.18\pm0.24)\times10^3$	1.82×10^3	$\leq 2.06\times10^3$	81 ± 9 [95^{+5}_{-10}][b]

[a] See Ref. 5.

[b] The bracketed value applies if $\langle \sigma \rangle^2 = 0$.

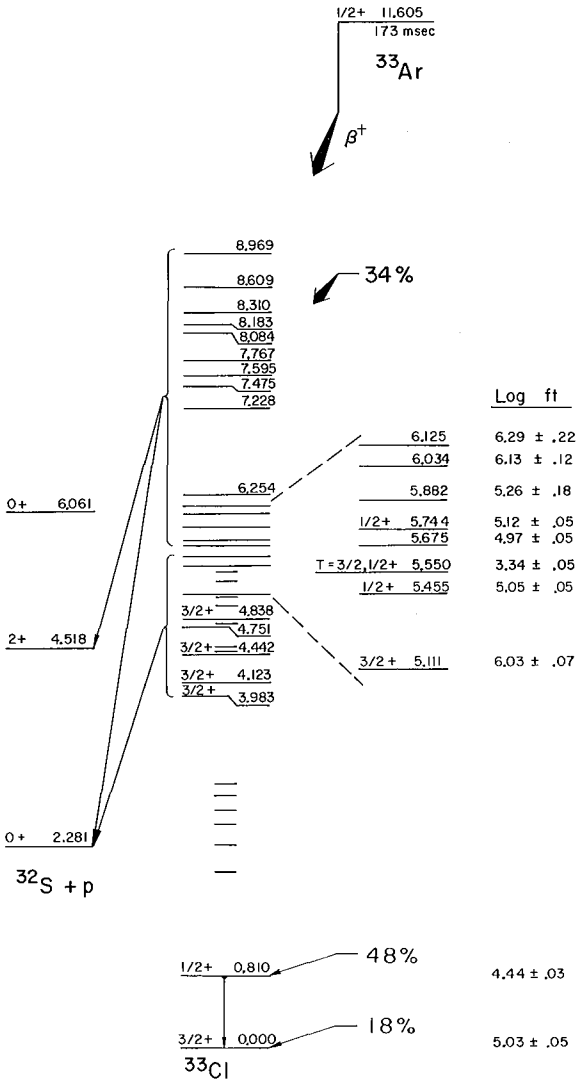

Fig. 4. Proposed decay scheme of ^{33}Ar. The ^{33}Cl level energies below 6 MeV are averages of present and earlier work. Above that energy the values are from the present work only. (XBL709-3885)

results for the case of ^{17}Ne resolve the previous discrepancy[3] in the lower energy levels of ^{17}F in favor of the results of Harris et al. In the case of ^{33}Ar decay, the lower energy levels in ^{33}Cl agreed well with the known levels whereas several new levels at higher excitation were found.

Analysis of the time-decay data yielded half-lives of 109.0 ± 1.0 msec and 173.0 ± 2.0 msec for ^{17}Ne and ^{33}Ar, respectively. Absolute ft values were calculated using this information as well as the relative intensities of the proton groups, ft values from mirror decays as described earlier, and, in the case of ^{33}Ar, the ratio of protons to 810 keV γ rays. The results are shown in Fig. 3 and Table I.

Our results for ^{17}Ne decay agree well with calculations[4] of the levels in ^{17}F which included up to two particles in the (2s, 1d) shell and one hole in the 1p shell. They predict ten $1/2^-$ or $3/2^-$ levels below 10 MeV while we observe nine. These calculations along with our measured log ft value for decay to the 3.105-MeV state in ^{17}F predict that between 80% and 85% of the antianalogue configuration resides in that state.

Table II compares our results for superallowed ft values to those predicted by a calculation[5] which used the Nilsson model to calculate the Gamow-Teller matrix elements. In the case of ^{17}Fe there seems to be no isospin impurity, but for ^{33}Cl a considerable impurity is indicated if the calculations are correct, while an impurity is possible even in the limit

$\langle\sigma\rangle^2 = 0$. The expanded section in Fig. 4 shows another indication of isospin mixing. The states near the analogue state in ^{33}Cl exhibit increasing log ft values as the states move farther away in energy from the analogue state. If the amount of mixing in the four nearest levels is calculated by assuming $\langle\sigma\rangle^2 = 0$ for these states, each state is found to have about 1% to 2% T = 3/2 strength. This is about the right amount to account for the observed isospin impurity. Further, if the charge-dependent matrix elements for these states are calculated using second-order perturbation theory, they are found to vary from 13 to 35 keV, in the range of the known[6] examples for 0^+ states. This evidence is only circumstantial, however, and the observed clustering of log ft values may be coincidental. In addition only two of the nearby states are known to have $J^\pi = 1/2^+$, which is required for mixing to occur; the other states can only be restricted to $J^\pi = (1/2, 3/2)^+$.

Footnotes and References

†Condensed from Phys. Rev. C 3, 700 (1971).

*Present address: Chalk River Nuclear Laboratories, Chalk River, Ontario, Canada.

1. D. H. Wilkinson, Phys. Letters 31B, 447 (1970).

2. R. Van Bree, H. Ogata, and G. M. Temmer, Bull. Am. Phys. Soc. 13, 1402 (1968); D. H. Youngblood, G. C. Morrison, and R. E. Segel, Phys. Letters 22, 625 (1966).

3. G. R. Salisbury and H. T. Richards, Phys. Rev. 126, 2147 (1962); R. W. Harris, G. C. Philips, and C. M. Jones, Nucl. Phys. 38, 259 (1962).

4. B. Margolis and N. de Takacsy, Can. J. Phys. 44, 1431 (1966), and Phys. Letters 15, 329 (1965).

5. J. C. Hardy and B. Margolis, Phys. Letters 15, 276 (1965).

6. S. D. Bloom in Isobaric Spin in Nuclear Physics, ed. by J. D. Fox and D. Robson (Academic Press Inc., New York, 1966) p. 123.

The Mass of ^{13}O and the Isobaric Multiplet Mass Equation†

Robert Mendelson, G. J. Wozniak, A. D Bacher, J. M. Loiseaux,* and Joseph Cerny

Although the level energies of several isobaric multiplets with T = 3/2 have been determined,[1] only the A = 9 quartet has been measured with sufficient accuracy to observe a significant deviation from the quadratic form of the isobaric multiplet mass equation, $\Delta M = a + bT_z + cT_z^2$. If this deviation is parameterized by an additional term dT_z^3 in the mass equation, then d has a value[2] of (9.2 ± 3.7) keV. The nonzero value for d indicates that a first-order perturbation treatment of the isospin-nonconserving operator (assuming charge-dependent forces of tensorial rank two or less) is inadequate to describe the A = 9 quartet.

In order to investigate systematics that might appear in the d coefficient, we have accurately remeasured the mass of ^{13}O, and we report new or improved values for the masses of ^{17}Ne, ^{21}Mg, and ^{25}Si.

The experiments were performed with ^{3}He and ^{4}He beams from the Berkeley 88-inch variable-energy cyclotron. The ^{13}O mass measurement employed semiconductor counter-telescopes to observe the ^{16}O(^{3}He, ^{6}He)^{13}O reaction and the calibration reactions ^{12}C(^{3}He, ^{6}He)^{9}C and ^{12}C(α, ^{6}He)^{10}C. Since the peaks due to ^{9}C and ^{13}O were separated by approximately 1.4 MeV, the known mass[2] for the ^{9}C ground state provided an accurate energy calibration. The slope of the energy scale was determined by observing the ground state and first-excited state (E_x = 3.3527 MeV)[3] in ^{10}C produced by α-particle bombardment of ethane.

Two similar four-counter telescopes (consisting of 114-μ, 90-μ, 300-μ, and 500-μ counters) and electronic systems were employed simultaneously at equal angles on opposite sides of the beam axis.[4] Two particle-identifications were performed and compared using the signals from the two successive differential-energy-loss (ΔE) detectors and the third E detector. Subnanosecond pulse-shape

Table I. Completed 4n + 1, T = 3/2 multiplets. Values of a, b and c are obtained from a least-squares fit to $\Delta M = a + bT_z + cT_z^2$; d is the coefficient of an additional T_z^3 term in ΔM. Errors, in parentheses, are in keV.

A	$T_z = -3/2$ Mass excess (MeV)	IMME Prediction[c] (MeV)	a (MeV)	b (MeV)	c (MeV)	χ^2	d (keV)
9	28.906 (4)[a]	28.961 (22)	26.343 (4.0)	-1.315 (2.0)	0.263 (2.4)	6.16	9.2 (3.7)
13	23.107 (15)[b]	23.102 (14)[d]	19.257 (2.2)	-2.181 (3.4)	0.256 (2.7)	0.06	-0.8 (3.4)
17	16.479 (50)[b]	16.508 (23)[e]	11.651 (3.7)	-2.878 (5.4)	0.238 (8.1)	0.28	4.8 (9.2)
21	10.889 (40)[b]	10.940 (24)	4.897 (4.8)	-3.658 (6.8)	0.241 (6.4)	1.18	8.5 (7.8)
25	3.839 (45)[b]	3.796 (42)	-3.262 (8.1)	-4.387 (10.6)	0.216 (10.8)	0.10	-3.5 (10.9)
37	-13.230 (50)[c]	-13.198 (91)	-22.886 (11.6)	-6.181 (14.6)	0.174 (14.6)	0.10	5.3 (17.3)

[a] Ref. 2.

[b] Present work. For the ^{25}Si measurement we have assumed that only the ground state is populated.

[c] Ref. 1.

[d] An improved value for the ^{13}N state [M. J. Levine and P. D Parker, Phys. Rev. 186, 1021 (1969)] and for the ^{13}C state [K. A. Snover, E. G. Adelberger and F. Riess, Bull. Am. Phys. Soc. 13, 1662 (1968)] has been included in the weighted average.

[e] A new value for the ^{17}O state [C. Detraz and H. H. Duhm, Phys. Letters 29B, 29 (1969)] has been included in the weighted average.

discrimination was employed to reduce pileup due to ^{3}He's and deuterons from the same beam burst, which can produce a false signal in the ^{6}He region of the particle-identifier spectrum.

Five parameters were recorded for each event: the total energy, two ΔE losses, particle identification, and pileup. Corrections were made and limits were placed on these parameters using an off-line computer. A typical set of spectra is shown in Fig. 1. The resolution was 200-300 keV.

The ^{13}O mass was obtained by averaging the Q values measured in each detector system. Two independent runs at $E_{^3He} = 62.6$ MeV, $\theta_{Lab} = 11.65$ deg and at $E_{^3He} = 66.3$ MeV, $\theta_{Lab} = 12.19$ deg were combined to yield an ^{13}O mass excess of (23.107 ± 0.015) MeV, based on a ^{9}C mass excess of (28.906 ± 0.004) MeV.[2] The mass excess obtained is in excellent agreement with the previously measured value, (23.110 ± 0.070) MeV.[5]

The masses of ^{17}Ne, ^{21}Mg and ^{25}Si, measured using similar techniques but with less precision, are given in Table I.[6] For the ^{17}Ne measurement, a gas target containing a mixture of 97% -enriched ^{20}Ne gas and CO_2 was used. Carbon-backed ^{24}Mg

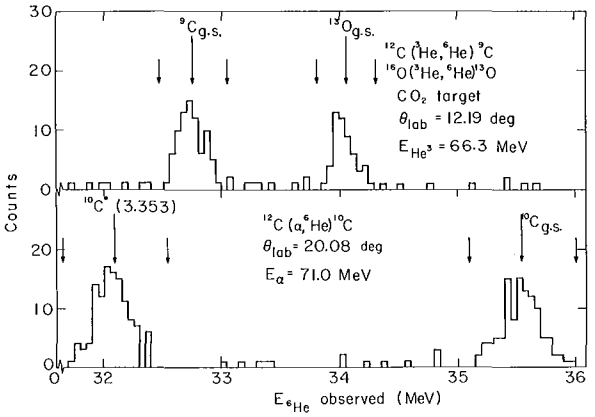

Fig. 1. Typical spectra representing approximately 25% of the total data. The short arrows indicate the region used in calculating the centroids of the peaks. The long arrows mark the positions of these centroids. (XBL706-3042)

(99% enriched) and natural SiO_2 targets were used for the ^{21}Mg and ^{25}Si measurements, respectively. The overall resolution for the solid targets was ≈ 175 keV.

The mass of ^{17}Ne (16.479 ± 0.050 MeV) is found to be in good agreement with a previous

value[7] of (16.47 ± 0.25) MeV. The new mass of ^{21}Mg, (10.889 ± 0.040) MeV, supersedes the previous measurement of (10.62 ± 0.12) MeV from this laboratory.[8] For the ^{25}Si measurement, the group observed could be composed of both the ground and first-excited states which are expected to lie ≈ 30 keV apart. If the first-excited state is populated to a significant extent, the d coefficient will be slightly more positive than that given in Table I, but it will still be consistent with zero. Values of a, b, c, and χ^2 determined by a linear-least-squares fit to the quadratic mass equation are also given in Table I. With the exception of A = 9, all are consistent with a value of $\chi^2 \lesssim 1$. Values for d are given in the last column of Table I.

Our value for d, (-0.8 ± 3.4) keV, for the A = 13 quartet is significantly less than the value, (9.2 ± 3.7) keV, previously determined for A = 9. Since additional values of d for the quartets with A > 13 are also essentially consistent with zero, there does not appear to be a systematic increase in d with increasing average charge of the multiplet. This suggests that the nonzero d coefficient for the A = 9 quartet is not due primarily to charge-dependent forces of tensorial rank 3 or higher.

Footnotes and References

†Condensed from Phys. Rev. Letters 25, 533 (1970).

*NATO Fellow; permanent address: I. P. N., Orsay, France.

1. J. Cerny, Ann. Rev. Nucl. Sci. 18, 27 (1968). All values of masses and excitation energies are those given by G. T. Garvey, in Nuclear Isospin, ed. by J. D. Anderson, S. D. Bloom, J. Cerny, and W. W. True (Academic Press, New York, 1969), p. 703, unless explicitly stated otherwise.

2. J. M. Mosher, R. W. Kavanagh and T. A. Tombrello, Bull. Am. Phys. Soc. 14, 1167 (1969).

3. R. A. Paddock, S. M. Austin, W. Benenson, I. D. Proctor, and F. St. Amant, Phys. Rev. 182, 1104 (1969).

4. The system used, with the exceptions discussed in the text, was identical to that reported in J. Cerny, R. A. Mendelson, Jr., G. J. Wozniak, John E. Esterl, and J. C. Hardy, Phys. Rev. Letters 22, 612 (1969).

5. J. Cerny, R. H. Pehl, G. Butler, D. G. Fleming, C. Maples, and C. Detraz, Phys. Letters 20, 35 (1966).

6. The values of the measured masses are relevant to the possibility of an induced isotensor interaction in beta decay as discussed by D. H. Wilkinson, Phys. Letters 31B, 477 (1970). Although the values we obtain are essentially the same as those used by Wilkinson, the somewhat smaller errors obtained here reinforce his thesis.

7. R. A. Esterlund, R. McPherson, A. M. Poskanzer, and P. L. Reeder, Phys. Rev. 156, 1094 (1967); A. M. Poskanzer, private communication.

8. G. W. Butler, J. Cerny, S. W. Cosper, and R. L. McGrath, Phys. Rev. 166, 1096 (1968).

Two-Nucleon Transfer Reactions Induced by Polarized Protons†

J. C. Hardy,* A. D. Bacher,‡ G. R. Plattner,†† J. A. Macdonald, and R. G. Sextro

The two-nucleon transfer reactions, (p, t) and (p, ^{3}He), have been used in the past not only to determine spins, parities and isospins of nuclear energy levels,[1] but also to investigate wave functions for the states involved.[2,3] Such studies have always used unpolarized projectiles. We present here a partial report on the asymmetries produced when these reactions are initiated by polarized protons; of particular interest is whether these asymmetries are characteristic of the quantum numbers of the transferred nucleons. We have investigated the (p, t) and (p, ^{3}He) reactions at 43.8 MeV on ^{16}O and ^{15}N gas targets. The external beam from the Berkeley 88-inch cyclotron was 30-50 nA, with polarization $|P| \approx 0.75$. Emitted particles were detected in two ΔE - E counter telescopes positioned symmetrically on opposite sides of the incident beam.

In general, at forward angles ($\theta_{lab} \leq 60°$) the angular distributions of differential cross sections for (p, t) and (p, ^{3}He) reactions are characteristic of the transferred orbital angular momentum L and are reasonably well reproduced by DWBA calculations. In our experiment sixteen transitions were observed,

of which eleven corresponded to unique sets of transferred quantum numbers. Since all L values, $L \leq 3$, were represented, it was hoped that these unique transitions might define characteristic shapes for angular distributions of the analyzing power so that the ability of the DWBA calculations to reproduce them could be tested.

However, a very striking result has emerged. Five (p,t) transitions were observed for which the transferred quantum numbers are L = 2 and S = 0. Although these quantum numbers are the same for all five cases, the measured analyzing powers do not have the same angular distributions. They appear instead to be of two distinct types, one which agrees well with DWBA calculations (we shall refer to this as the "normal" type) and one which does not ("anomalous" type). This is particularly surprising in light of the success we have had in reproducing the shapes of the analyzing-power angular distributions for transitions with other L values, and in fitting cross sections for all transitions, including the "anomalous" ones.

The observed cross-section angular distributions for the five, L = 2, (p,t) transitions are shown in Fig. 1, together with the distribution for the L = 0 ground state transition, $^{16}O(p,t)^{14}O$. Measured analyzing powers for the same transitions appear in Fig. 2. The DWBA calculations, whose results appear in both figures, utilized optical model parameters taken from elastic scattering data which, for the protons, included polarization measurements. The results of two separate zero-range calculations are shown. They differ only in the choice of the form factor used to describe the radial wave function of the transferred nucleons; the solid line is the result of using harmonic oscillator wave functions and the dashed line represents calculations which use Woods-Saxon wave functions.

The agreement between calculation and experiment is seen to be good for the differential cross section data in Fig. 1, and there is also reasonable success in fitting those observed transitions which are not shown. Similar agreement is seen in Fig. 2 for the L = 0 and "normal" L = 2 transitions, and again this is typical of the fits for all of the unique transitions. This success makes the disagreement with the analyzing powers for the "anomalous" L = 2 transitions all the more striking. It must be emphasized that this is not simply a disagreement with theory, but that there is a significant discrepancy--virtually opposite phase in their analyzing powers--observed between transitions in the same nucleus which are characterized by the same transferred

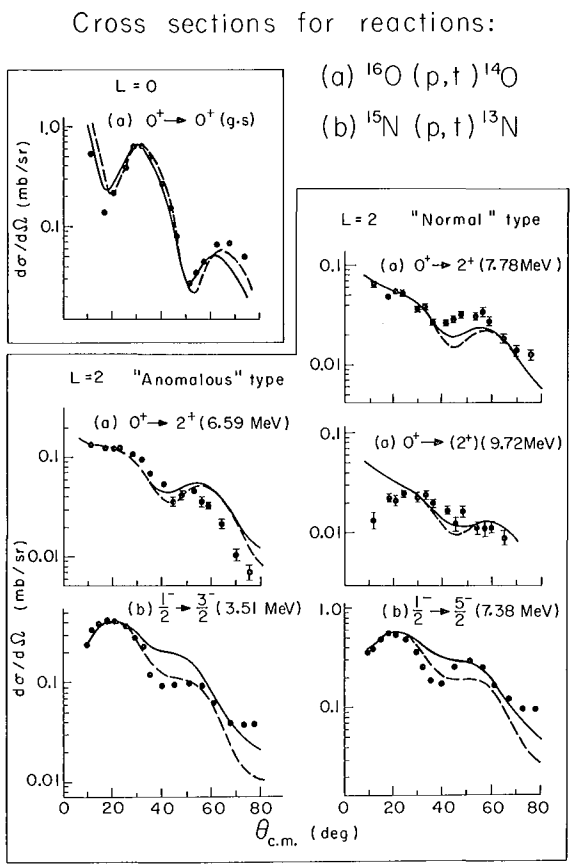

Fig. 1. Differential cross sections for some transitions from the reactions $^{16}O(p,t)^{14}O$ (labeled a) and $^{15}N(p,t)^{13}N$ (labeled b). Each transition is denoted by the spin and parity of its initial and final states and the excitation energy of the latter. The results of DWBA calculations are shown with each angular distribution; the solid line corresponds to the use of harmonic oscillator wave functions for the transferred nucleons, while the dashed line indicates Woods-Saxon wave functions were used. (XBL706-3058)

quantum numbers. In attempting to understand the "anomalous" transitions, we have examined whether it is possible to reproduce their analyzing powers by making variations in (i) optical-model parameters, (ii) bound-state parameters, and (iii) nuclear wave functions (i.e. introducing sd-shell admixtures into the assumed p-shell wave functions). No improvement in the fitting of "anomalous" transitions could be effected.

It does not appear possible within the context of the simple DWBA to explain both types of L = 2 transitions. Based on the ^{15}N data, it is tempting to postulate coupling to the spin

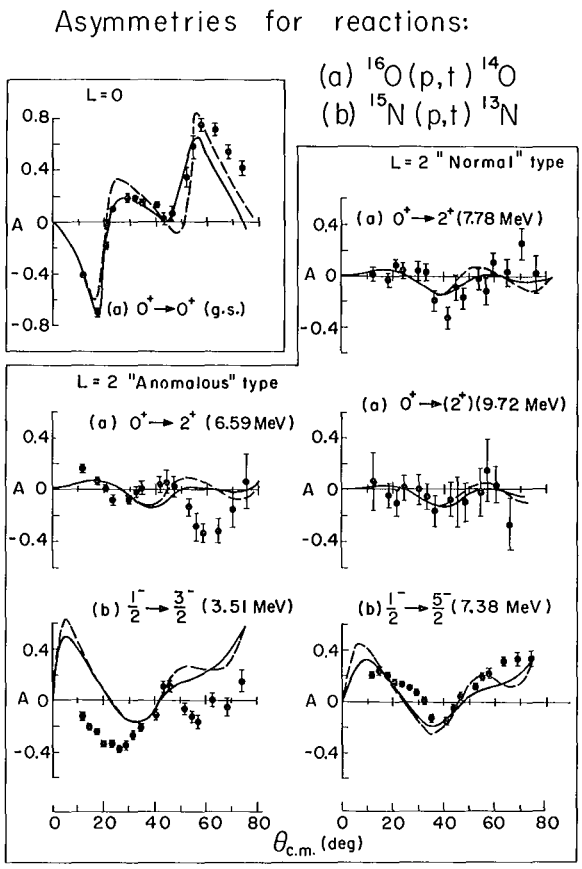

Fig. 2. Angular distributions of analyzing powers for the same transitions as in Fig. 1. The curves and labels have the same significance. (XBL706-3059)

of the residual nucleus, since the two final states in ^{13}N differ in that respect ($3/2^-$ and $5/2^-$). However no such explanation could apply to the three 2^+ states in ^{14}O. Dependence on the L-S coupling of the transferred nucleons cannot play a significant role either, since the transferred nucleons in the (p,t) reaction must have predominantly S = 0. The explanation may lie in the use of a more realistic interaction potential than the delta function assumed in calculations of the type followed here, or it may lie in a more complicated reaction mechanism--i.e., two-step, knock-out, etc. But for these refinements to be effective, the basic terms which we have considered must be reduced considerably in the "anomalous" transitions relative to the "normal" ones. In ^{13}N, where p-shell wave functions adequately account for the number of states observed, the relative magnitudes of the ground, $3/2^-$, and $5/2^-$ states are reliably predicted by our calculations. Thus, there is no a priori indication that the normally dominant processes should be reduced or forbidden for the "anomalous" transitions.

The (p, ^{3}He) transitions observed proceed by more than one set of transferred quantum numbers (L, S and J), and the process is described by the coherent sum of transition amplitudes characterized by the same J but different values of L and S. The extent of the interference between these amplitudes depends upon the strength of spin-orbit coupling in the entrance and exit channels. The observed asymmetries are sensitive to these effects and have been used in their investigation.

Footnotes and References

†Condensed from Phys. Rev. Letters 25, 298 (1970).

*Present address: Chalk River Nuclear Laboratories, Chalk River, Ontario, Canada.

‡Present address: Physics Department, Indiana University, Bloomington, Indiana.

††Present address: Physics Department, University of Basel, Switzerland.

1. e.g., J. Cerny and R. H. Pehl, Phys. Rev. Letters 12, 619 (1964); H. Brunnader, J. C. Hardy, and J. Cerny, Nucl. Phys. A137, 487 (1969).

2. e.g., D. G. Fleming, J. Cerny, C. C. Maples, and N. K. Glendenning, Phys. Rev. 166, 1012 (1968).

3. I. S. Towner and J. C. Hardy, Advan. Phys. 18, 401 (1969).

Polarization and Cross-Section Measurements in p-^{4}He Scattering from 20 to 40 MeV †

A. D. Bacher,* G. R. Plattner,‡ H. E. Conzett, D. J. Clark, H. Grunder, and W. F. Tivol††

The scattering of protons from ^{4}He has been particularly useful as a proton polarization analyzer since it produces large polarizations over a wide range of energies. Also, analysis of resonance effects corresponding to states in ^{5}Li above the deuteron threshold are simplified if observed in the proton channel because of the single channel-spin available. In particular, a broad anomaly near an excitation energy of 20 MeV, which has been seen in the ^{3}He(d, p)^{4}He reaction[1] and in d-^{3}He elastic scattering,[2] has not yet been explained unambiguously. Even though no effect has been seen in p-^{4}He cross-section excitation functions,[3] the ^{3}He(d, p)^{4}He data show that if the anomaly results from a state in ^{5}Li, the state must have a proton width. Thus, because of the greater sensitivity to small changes in a partial-wave amplitude that is possible to polarizations than to cross sections, p-^{4}He polarization excitation functions could provide information important to the explanation of this anomaly.

We have used the new axially-injected polarized proton beam from the 88-inch cyclotron to supplement and to improve previous p-^{4}He elastic scattering data between 20 and 40 MeV. External beams of 80-120 nA with polarization ≈ 0.75 were available. Angular distributions of cross sections and polarizations were measured at 2 MeV intervals at 20 laboratory angles between 17.5° and 150°. At each energy the relative uncertainty of the polarization is less than ± 0.010. An absolute normalization with an uncertainty of less than 3% at all energies has been obtained by using the analyzing power of p-^{4}He scattering near 14.5 MeV.[4] Absolute cross sections were obtained by normalizing to the data of Ref. 3. As examples, Fig. 1 shows our results near 24 and 26 MeV. Additional measurements of comparable precision were made in the region between 20 and 30 MeV to search for an effect corresponding to the anomaly discussed above.

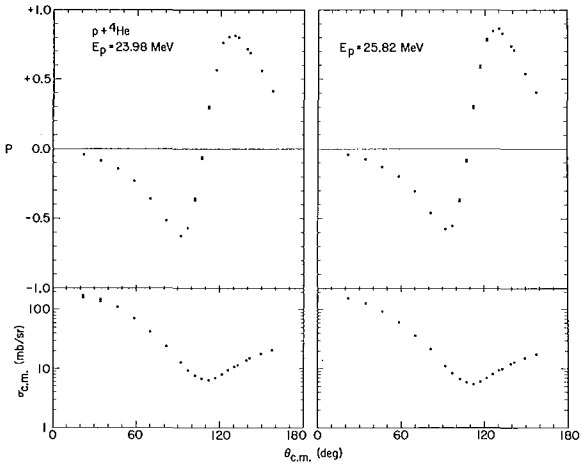

Fig. 1. Differential cross sections and polarizations in p-^{4}He scattering hear 24 and 26 MeV. (XBL705-2763)

A contour plot of the experimental proton polarization is shown in Fig. 2. Measurements for the region between 16 and 20 MeV are taken from Ref. 4. The effect of the 16.65 MeV $3/2^+$ state of ^{5}Li is clearly seen near 23 MeV. Excitation functions were taken across this resonance to provide data for an improved determination of the resonance parameters[5] and to aid in the continuation of a phase-shift analysis to the higher energies. With the exception of this narrow resonance region, the analyzing power near θ_{lab} = 120° - 130° remains large, and these measurements provide an accurate proton polarization analyzer up to 40 MeV. A broad bump between 26 and 32 MeV is apparent in the contour plot at backward angles. This can be seen more clearly in Fig. 3, which shows an excitation function of the proton polarization at θ_{cm} = 102.2° (87.5° lab). The

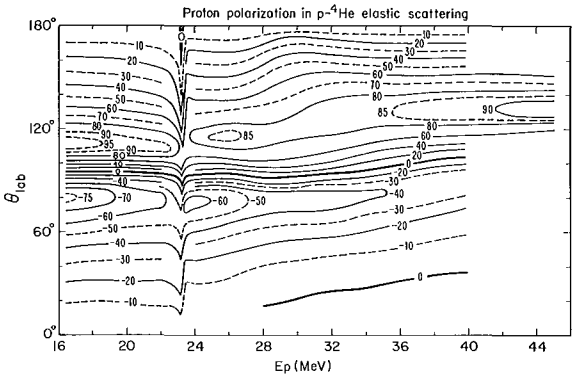

Fig. 2. Contour plot of the experimental polarization in p-^{4}He scattering. The numbers on the contour lines are polarizations in percent. (XBL703-2603)

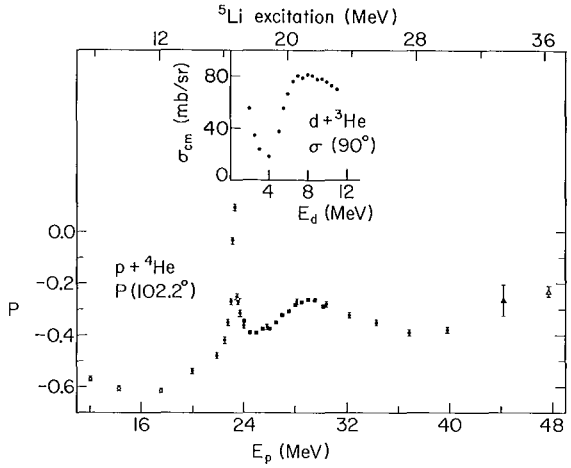

Fig. 3. Polarization excitation function at θ_{cm} = 102.2°. The insert shows the d-^{3}He elastic scattering cross-section excitation function at θ_{cm} = 90°. (XBL703-2605)

sharp structure near 23 MeV is due to the $3/2^+$ level, and the broad anomaly between 26 and 32 MeV is seen to correspond in energy to that seen in the d-^{3}He elastic scattering cross-section data[2] at θ_{cm} = 90°, which is plotted in the insert of Fig. 3.

Preliminary phase-shift analyses of these data have been made. Above 30 MeV the phase shifts, as expected, vary quite smoothly with energy, and the addition of at least a small $g_{9/2}$ contribution provides significantly better fits to the data than are possible with analyses limited to f waves. In the region 26 to 32 MeV we have not yet found satisfactory fits to the data, indicating a nonsmooth behavior of phase shift(s) with energy. Finally, the 23-MeV resonance is a $d_{3/2}$ proton resonance, and our analysis shows the behavior of the $d_{3/2}$ phase shift there to be characteristic of an inelastic resonance for which Γ_p/Γ, the ratio of the proton width to total width, is less than 0.5. The ratio, Γ_d/Γ_p, of the deuteron to proton widths at the resonance energy, E_r can be calculated from the value of the $d_{3/2}$ phase-shift parameter

$$\eta_2^{3/2}(E_R) = 0.55 - 0.60 .$$

Since

$$(\Gamma_d/\Gamma_p)_{E_R} = (P_d\gamma_d^2/P_p\gamma_p^2)_{E_R} = [(1+\eta)/(1-\eta)]_{E_R} ,$$

calculation of the penetrabilities P_d and P_p gives the ratio of the reduced widths

$$\gamma_d^2/\gamma_p^2 = 52$$

for η = 0.60. Analyses[5] of previous p-^{4}He scattering data over this resonance had given a value near 70 for this ratio. Our more extensive and more accurate data provide this lower value, and it agrees well with the ratio of deuteron-to-neutron reduced widths for the mirror state in ^{5}He,[6] as would be expected on the basis of charge symmetry.

Footnotes and References

†Condensed from UCRL-19943, July 1970; contribution to the Third International Symposium on Polarization Phenomena in Nuclear Reactions, Madison, Wisconsin, September 1970.

*Present address: Physics Department, Indiana University, Bloomington, Indiana.

‡Present address: Physics Department, University of Basel, Switzerland.

††Present address: Sealy Mudd Laboratory, University of Southern California, Los Angeles, California.

1. L. Stewart, J. E. Brolley, and L. Rosen, Phys. Rev. 119,1649 (1960).

2. T. A. Tombrello, R. J. Spiger, and A. D. Bacher, Phys. Rev. 154, 935 (1967).

3. P. W. Allison and R. Smythe, Nucl. Phys. A121, 97 (1968); S. N. Bunker et al., Nucl. Phys. A133, 537 (1969).

4. D. Garreta, J. Sura, and A. Tarrats, Nucl. Phys. A132, 204 (1969); P. Schwandt, private communication.

5. W G. Weitkamp and W. Haeberli, Nucl. Phys. 83, 46 (1966); P. Darriulat, D. Garreta, A. Tarrats, and J. Testoni, Nucl Phys. A108, 316 (1968).

6. B. Hoop, Jr. and H. H. Barschall, Nucl. Phys. 83, 65 (1966).

The $^{38}Ar(^{3}He,t)^{38}K$ Reaction at 40 MeV

G. Bruge,† M. S. Zisman, A. D. Bacher,* and R. Schaeffer

In recent years, increasing use has been made of the $(^{3}He,t)$ reaction as a spectroscopic tool.[1] The emphasis of these studies has generally been to attempt a microscopic description of the reaction in mass regions near closed shells, where comprehensive shell-model calculations are available. From previous attempts[2] at a microscopic treatment of the $(^{3}He,t)$ reaction, it is known that a tensor term is required[3,4] in the effective interaction in order to reproduce the observed[1] preference for the higher L value in the experimental angular distributions for unnatural parity transitions.

Recent calculations have also suggested that there are two distinct types of $(^{3}He,t)$ transitions which should show different sensitivity to the tensor term. These types are characterized by the shell-model states (j and j') involved in the transition:

$$\left.\begin{aligned} j &= \ell + 1/2 \rightarrow j' = \ell' + 1/2 \\ j &= \ell + 1/2 \rightleftarrows j' = \ell' - 1/2 \end{aligned}\right\} \text{ Type 1}$$

$$j = \ell - 1/2 \rightarrow j' = \ell' - 1/2 \qquad \text{Type 2}$$

For Type 1 transitions (e. g. , $f_{7/2} \rightarrow f_{7/2}$), the calculated angular distributions for unnatural-parity states depend almost entirely on the tensor strength, although comparison with the experimental data does determine an upper limit for the central term.[4] For Type 2 transitions (e. g. , $p_{1/2} \rightarrow p_{1/2}$ or $d_{3/2} \rightarrow d_{3/2}$) on the other hand, the calculated angular distributions[4] depend mainly on the central force, although the tensor force contribution is not negligible.

Unfortunately, the only Type 2 transitions studied experimentally,[5] $p_{1/2} \rightarrow p_{1/2}$ in $^{14}C(^{3}He,t)^{14}N$ and $^{14}N(^{3}He,t)^{14}O$, indicated that neither a pure central[5] nor a central plus tensor[6] force could reproduce the shape of the observed angular distributions. Whether the fault lies with the optical-model treatment or with an inadequate discription of the transition operator is not clear. However, the measurements do suggest[6] that the central force required for Type 2 unnatural-parity transitions is about four times stronger than the upper limit determined[4] from Type 1 transitions. In order to investigate further this apparent difference between the two types of $(^{3}He,t)$ transitions, we have studied the $^{38}Ar(^{3}He,t)^{38}K$ reaction.

The experiment was performed with a 40 MeV ^{3}He beam from the Berkeley 88-inch cyclotron. The target was argon gas (enriched to 94.4% ^{38}Ar) at a pressure of 120 Torr, which was contained in a cell having a thin (0.68 mg/cm^2) nickel entrance foil and a

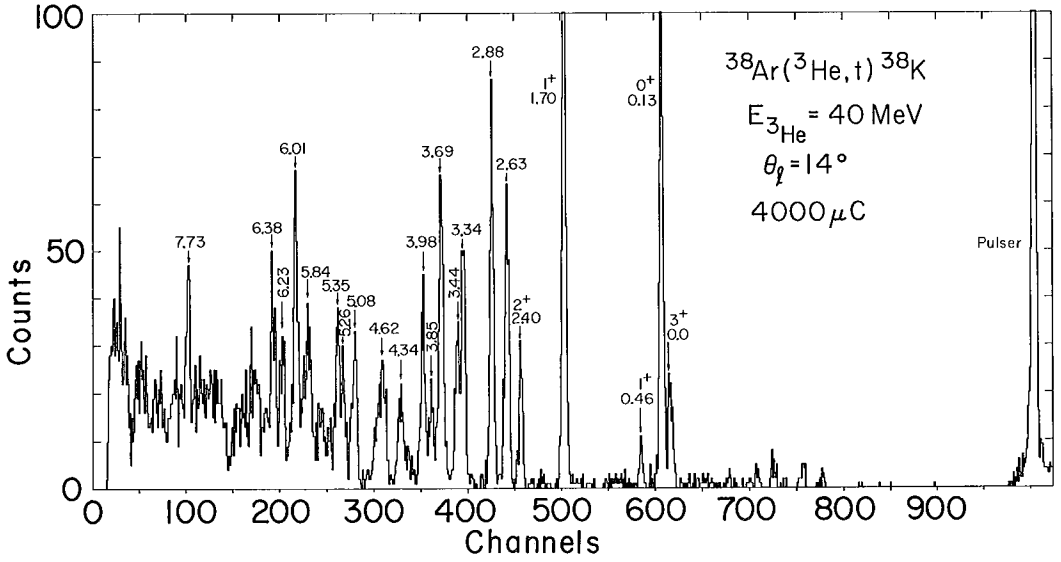

Fig. 1. Triton energy spectrum from the $^{38}Ar(^{3}He,t)^{38}K$ reaction at θ_ℓ = 14°.
(XBL713-3082)

2.1 mg/cm^2 Havar exit foil. Tritons were detected with telescopes consisting of 0.25-mm ΔE and 3-mm E detectors which fed a Goulding - Landis particle identifier.[7] A triton spectrum at $\theta_\ell = 14°$ is shown in Fig. 1. The overall resolution is 75 keV FWHM. Angular distributions for the first five levels of ^{38}K from $\theta_{c.m.} = 11°$ to 50° are shown in Fig. 2.

According to the wave functions of Dieperink and Glaudemans,[8] which reproduce the observed β-transition rates rather well, three of the five ^{38}K levels below 2.40 MeV [3^+ (g. s.), 0^+ (0.13 MeV), and 2^+ (2.40 MeV)] are built mainly from the $(d_{3/2}^{-2})$ configuration, while the other two levels [1^+ (0.46 MeV) and 1^+ (1.70 MeV)] are composed of $(d_{3/2}^{-2})$, $(d_{3/2}^{-1}, s_{1/2}^{-1})$ and other components. As can be seen in Fig. 2, the angular distributions of the two 1^+ levels are quite different. Preliminary DWBA calculations using the formalism of Ref. 4 indicate that these differences are probably not due to the wave functions, but rather to an inadequate description of the transition operator. Such differences in (^{3}He, t) angular distributions leading to states of the same spin and parity have also been reported recently in other nuclei.[9,10] Results of preliminary calculations for the 3^+ (g. s.) indicate that it is necessary to use a stronger central force for the Type 2 unnatural-parity transitions.

Further calculations are being performed in an effort to find a force mixture which can be used for both types of unnatural-parity transitions.

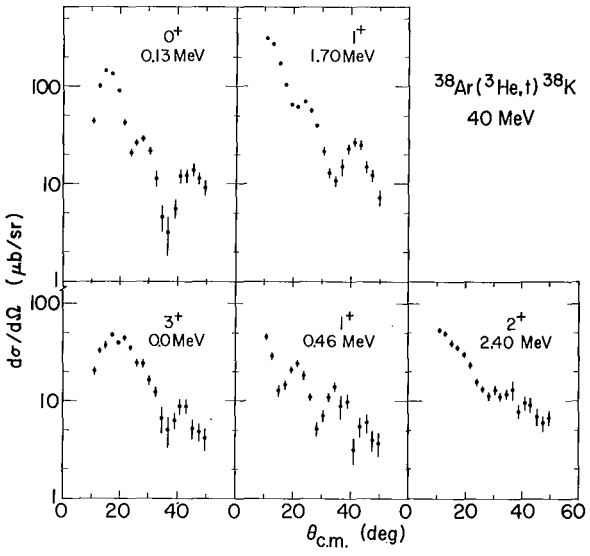

Fig. 2. Angular distributions of tritons leading to the 0.0, 0.13, 0.46, 1.70, and 2.40 MeV levels in ^{38}K. Statistical errors are indicated for each point.
(XBL713-3070)

Footnotes and References

† Present address: CEN Saclay, 91 Gif - sur - Yvette, France

* Present address: Physics Department, Indiana University, Bloomington, Indiana.

1. See, for example, Argonne National Laboratory Informal Report No. PHY - 1970A, January 1970 (unpublished), and references contained therein.

2. P. Kossanyi-Demay, P. Roussel, H. Faraggi, and R. Schaeffer, Nucl. Phys. A148, 181 (1969).

3. E. Rost and P. D. Kunz, Phys. Letters 30B, 231 (1969).

4. R. Schaeffer, UCRL-19927; submitted to Nucl. Phys.

5. G. C. Ball and J. Cerny, Phys. Rev. 177, 1466 (1969).

6. R. Schaeffer, unpublished calculations based on the data in Ref. 5.

7. F. S. Goulding, D. A. Landis, J. Cerny, and R. H. Pehl, Nucl. Instr. Methods 31, 1 (1964).

8. A. E. L. Dieperink and P. W. M. Glaudemans, Phys. Letters 28B, 531 (1969).

9. R. A. Hinrichs, R. Sherr, G. M. Crawley, and I. Proctor, Phys. Rev. Letters 25, 829 (1970).

10. J. E. Holden, H. T. Fortune, D. P. Balamuth, and R. W. Zurmühle, Phys. Rev. Letters 25, 1677 (1970).

The $^{14}N(\alpha,d)\,^{16}O$ Reaction at 40 MeV†

M. S. Zisman, E. A. McClatchie,* and B. G. Harvey

For many years it has been suggested[1] that certain states in ^{16}O exhibit a rotational-band structure based on the 6.05 MeV 0^+ level. This result has been reproduced with various calculations,[2-5] which indicate that the nature of the lowest even-parity band is mainly 4p-4h. The 4p-4h nature of the rotational states is also indicated by their strong population in the four-nucleon transfer reactions $^{12}C(^7Li,t)\,^{16}O$[6-8] and $^{12}C(^6Li,d)\,^{16}O$,[7-9] which should preferentially populate 4p-4h states if the reaction corresponds to a direct α-particle transfer. However, the 6^+ member of the band, at 16.2 MeV,[1] was found to be essentially degenerate with a state observed in the $^{14}N(\alpha,d)\,^{16}O$ experiment[10] at 16.16 ± 0.10 MeV and believed to be one member of a triplet of states whose dominant configuration is

$$\left[{}^{14}N(1^+) + (d_{5/2})^2_{5^+}\right] 4^+, 5^+, 6^+.$$

(The strong population of these states is expected from the systematics[10,11] of the (α,d) reaction in this mass region.) Since the ground state of ^{14}N is mainly 0p-2h,[12] a 4p-4h state should not be populated strongly in the $^{14}N(\alpha,d)\,^{16}O$ reaction. In order to help remove this ambiguity from the previous results, it was decided to reinvestigate the $^{14}N(\alpha,d)\,^{16}O$ reaction with better resolution that the 250 keV attained in that work.[10] In this way we could improve the accuracy of both the positions and widths of the three states.

The experiment was performed with a 40- MeV α-particle beam from the 88-inch cyclotron. Energy analysis of the beam was provided by two uniform-field 110° bending magnets. Object and image slit widths of 1 mm produced a beam resolution, $\Delta E/E$, of 0.04%. The target gas was natural nitrogen (99.6% ^{14}N) at a pressure of about 30 Torr, which was contained in a cell having a thin (0.22 mg/cm^2) nickel entrance foil and a 2.1 mg/cm^2 Havar exit foil covering 315°. Deuterons were identified with a Goulding – Landis particle identifier.[13]

A deuteron spectrum at $\theta_\ell = 10°$ is shown in Fig. 1. The resolution was 66 keV FWHM for the sharp states of ^{16}O. A biased amplifier was used to look selectively at the high-excitation region of ^{16}O, so the ground state does not appear at any angle, and the 6.05 - 6.13 MeV doublet appears only at the more backward angles. Even with the

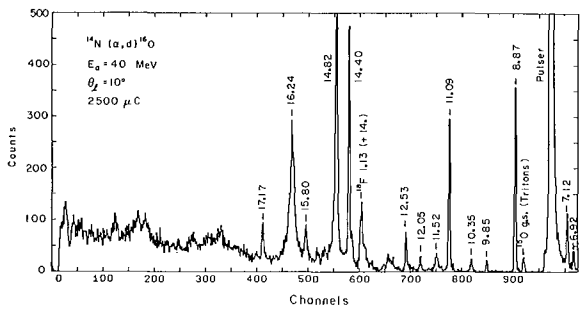

Fig. 1. Deuteron energy spectrum from the $^{14}N(\alpha,d)\,^{16}O$ reaction at $\theta_\ell = 10°$. (XBL706-3087)

improved resolution, the three members of the previously observed triplet still appear as single states. The energies determined from this work for the three largest states are 14.40 ± 0.03, 14.82 ± 0.03, and 16.24 ± 0.04 MeV. Angular distributions for these levels are shown in Fig. 2. The widths for the states, with the experimental resolution subtracted in quadrature, are 30 ± 30, 69 ± 30, and 125 ± 50 keV, respectively.

As can be seen in Fig. 1, the states which are believed to be members of the rotational band (2^+, 6.92 MeV; 4^+, 10.35 MeV) are populated very weakly. Also, the width of the 16.24 MeV level seen in the (α,d) reaction is much smaller than the 320 keV reported for the 16.2 MeV 6^+ state observed in the α - ^{12}C resonance work of Carter et al.[1,14] On this basis we feel that the strong level observed in the $^{14}N(\alpha,d)\,^{16}O$ experiment at 16.24 ± 0.04 MeV is not the same as the rotational 6^+ level at this energy observed in the α - ^{12}C resonance[1] and four-nucleon transfer[6-9] experiments. Additional support for the existence of two different states at this energy comes from the $^{13}C(^6Li,t)\,^{16}O$ data of Bassani et al.[15] The peak at 16.2 MeV observed in the $(^6Li,t)$ reaction[15] is much sharper than that observed at the same excitation energy in the $^{12}C(^6Li,d)\,^{16}O$ reaction.[16] If the three-nucleon transfer proceeds by a direct reaction, the states which are populated would be mainly 1p-1h, 2p-2h, and 3p-3h. Thus, neither the $(^6Li,t)$ or (α,d) reaction would easily populate the rotational (4p-4h) states, but both could reach 1p-1h and 2p-2h levels.

A recent investigation of the $^{12}C(\alpha,\alpha_0)$ and $^{12}C(\alpha,\alpha')$ reactions[17] has shown that a

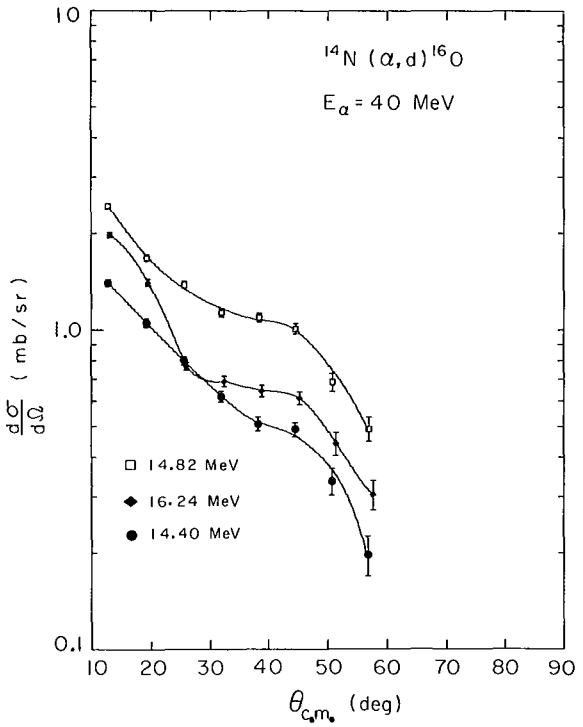

Fig. 2. Angular distributions of deuterons from the $^{14}N(\alpha,d)^{16}O$ reaction leading to the 14.40, 14.82, and 16.24 MeV levels. Statistical errors are indicated for each point. The curves have no theoretical significance. (XBL706-3086)

6^+ assignment is preferred for the 14.79-MeV level of ^{16}O, in contrast with the previous low-spin assignment.[1] The strong population of the 14.82 ± 0.03 MeV state in the $^{14}N(\alpha,d)^{16}O$ experiment suggests that it is this level whose dominant configuration is

$$\left[^{14}N(1^+) + (d_{5/2})^2_{5^+}\right]_{6^+}.$$

If our interpretation of the 14.40, 14.82, and 16.24 MeV states as a

$$\left[^{14}N(1^+) + (d_{5/2})^2_{5^+}\right]_{4^+,\,5^+,\,6^+}$$

triplet is correct, then the 16.24 MeV level seen in the (α,d) experiment should be a 4^+ or 5^+. The latter spin may account for the apparent absence of this level in the $^{12}C + \alpha$ reactions, since unnatural parity states should not be populated.

Footnotes and References

†Condensed from Phys. Rev. C 2, 1271 (1970).

*Present address: ARKON Scientific Laboratories, Berkeley, California.

1. E. B. Carter, G. E. Mitchell, and R. H. Davis, Phys. Rev. 133, B1421 (1964); G. E. Mitchell, E. B. Carter, and R. H. Davis, Phys. Rev. 133, B1434 (1964).

2. W. H. Bassichis and G. Ripka, Phys. Letters 15, 320 (1965).

3. I. Kelson, Phys. Letters 16, 143 (1965).

4. G. E Brown and A. M. Green, Nucl. Phys. 75, 401 (1966).

5. L. S. Celenza, R. M. Dreizler, A. Klein, and G. J. Driess, Phys. Letters 23, 241 (1966).

6. V. I. Chuev, V. V. Davidov, A. A. Ogloblin, and S. B. Sakuta, Arkiv Fysik 36, 263 (1967).

7. K. Bethge, K. Meier-Ewert, K. Pfeiffer, and R. Bock, Phys. Letters 24B, 663 (1967).

8. J. R. Comfort, H. T. Fortune, G. C. Morrison, and B. Zeidman, in Proceedings of the International Conference, Heidelberg, July, 1969 (North - Holland Publishing Company, 1970), p. 303.

9. K. Meier-Ewert, K. Bethge, and K. O. Pfeiffer, Nucl. Phys. A110, 142 (1968).

10. E. Rivet, R. H. Pehl, J. Cerny, and B. G. Harvey, Phys. Rev. 141, 1021 (1966).

11. C. C. Lu, M. S. Zisman, and B. G. Harvey, Phys. Rev. 186, 1086 (1969).

12. W. W. True, Phys. Rev. 130, 1530 (1963).

13. F. S. Goulding, D. A. Landis, J. Cerny, and R. H. Pehl, Nucl. Instr. Methods 31, 1 (1964).

14. E. B. Carter, private communication.

15. G. Bassani, J. H. Kruse, N. Saunier, and G. Souchere, Phys. Letters 30B, 621 (1969).

16. G. Bassani, private communication.

17. T. R. Ophel, S. D. Cloud, Ph. Martin, and J. M. Morris, Phys. Letters 32B, 101 (1970).

Nuclear Reaction Study of ^{140}Ce via the (p,t), (p,p') and ^{138}Ce by the (p,t) Processes

Joseph D. Sherman, Bernard G. Harvey, David L. Hendrie, and Michael S. Zisman

In the last few years it has become evident that pairing theory in the framework of pairing vibrations[1] is providing an explanation for strong L = 0 transitions observed in (t, p) and (p, t) reactions. The essential idea is that the nuclear pairing field gives rise to collective modes which are selectively populated by the two-nucleon transfer reaction. These modes are defined with respect to a vacuum state and are specified by the notation (n_1, n_2); n_1 equals the number of pairs removed and n_2 is the number of pairs added to the vacuum, (0, 0). The vacuum state is usually associated with a closed-shell nucleus. The configuration (1, 0) applies to a nuclear ground state two particles lighter than the vacuum, whereas (0, 1) refers to a nuclear ground state two particles more massive. The configuration (1, 1) refers to an excited state of the closed-shell nucleus and is known as the pairing vibration. In the harmonic approximation (no interaction between the (1, 0) and (0, 1) quanta), the pairing vibration energy is equal to the sum of the (1, 0) and (0, 1) energies. These ideas are expanded in Ref. 1; more quantitative detail can be found in Ref. 2.

The experimental status up to 1968 has been summarized by O. Nathan.[3] Further experimental work is desirable to search for the predicted collective and noncollective[4] modes of excitation. We have chosen to study the (p, t) reaction on the ^{142}Ce and ^{140}Ce targets. Experimental information obtained from the (p, t) reaction in this region (N = 82) is accumulating;[5] (t, p) and (p, t) reactions on most of the stable Ce isotopes are also being studied by the Los Alamos group.[6]

Self-supporting metallic-Ce foils were prepared. The ^{142}Ce and ^{140}Ce targets were 400 and 790 $\mu g/cm^2 \pm 20\%$ thick, respectively. A momentum-analyzed 30-MeV proton beam from the 88-inch cyclotron and a ΔE-E particle-identifying telescope were utilized to study the reactions. Deuteron and triton spectra were stored for the ^{142}Ce target. Proton, deuteron, and triton spectra from the ^{140}Ce target were stored. Resolution attained in the two experiments was approximately 30 keV (^{142}Ce) and 50 keV (^{140}Ce).

Figure 1 shows a triton spectrum from ^{142}Ce(p, t). The ground state is strongly

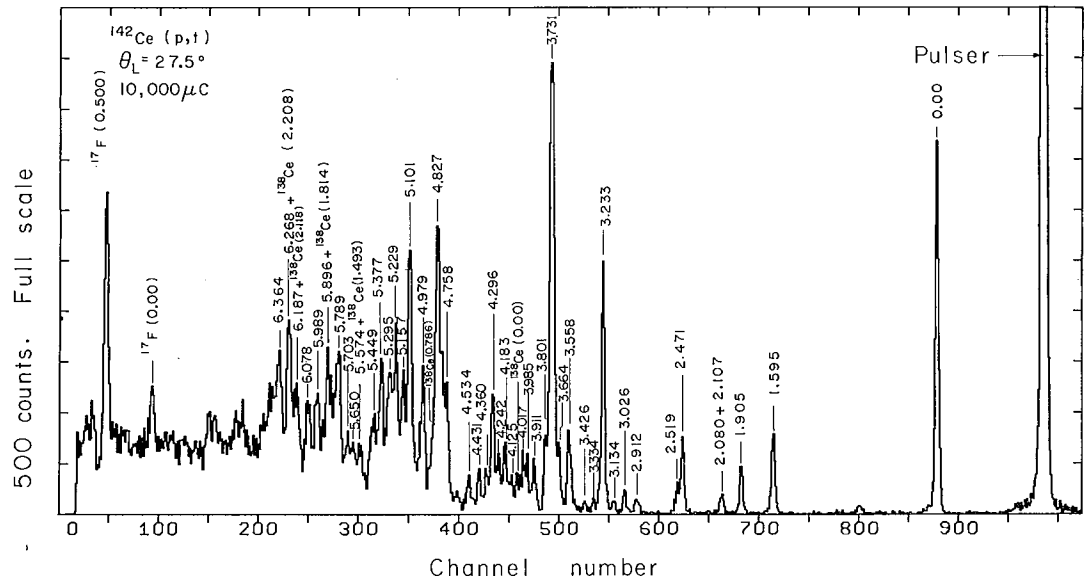

Fig. 1. A triton spectrum obtained from ^{142}Ce target. The proton-beam energy is 30 MeV and laboratory scattering angle is 27.5°. (XBL7012-4216)

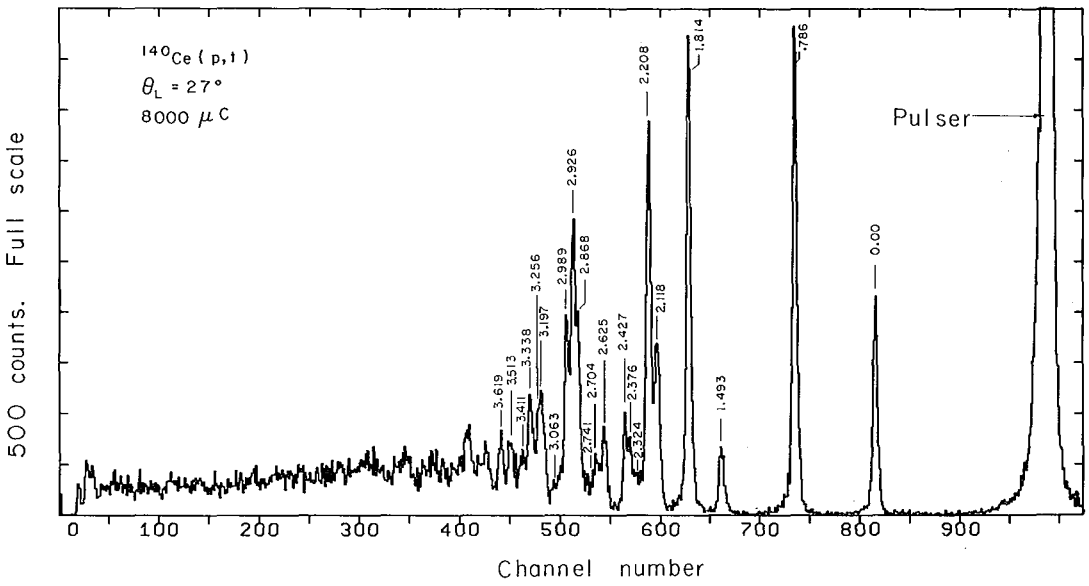

Fig. 2. A triton spectrum obtained from ^{140}Ce target. The proton-beam energy is 30 MeV and the laboratory scattering angle is 27.0°. (XBL7012-4215)

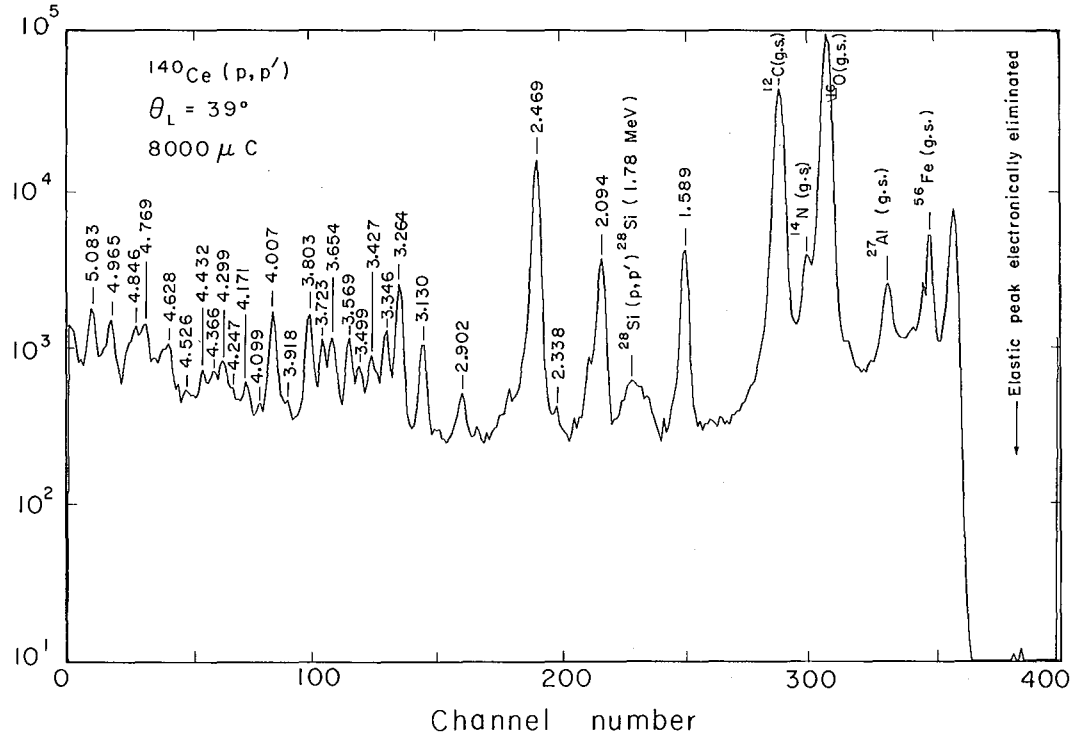

Fig. 3. A proton inelastic-scattering spectrum obtained from ^{140}Ce. The proton-beam energy is 30 MeV and the laboratory scattering angle is 39°. (XBL7012-4217)

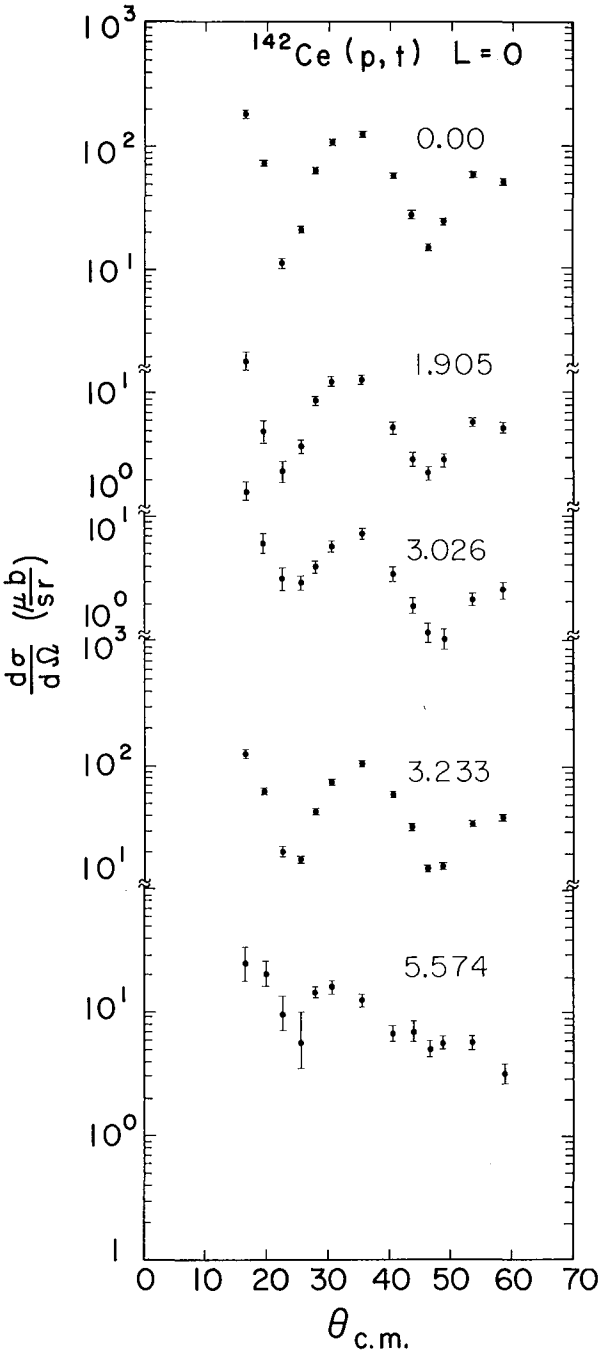

Fig. 4. Differential cross sections for the L = 0 transitions deduced in the (p,t) reaction of ^{142}Ce. (XBL7012-4219)

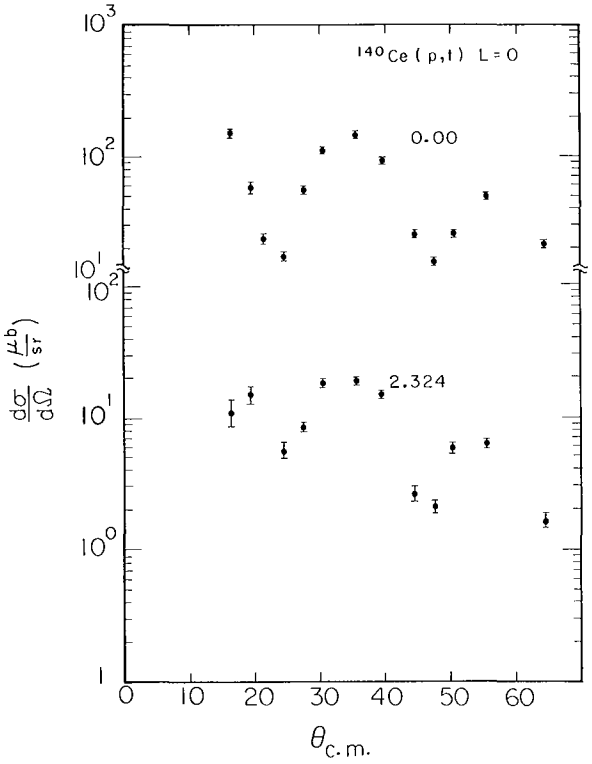

Fig. 5. Differential cross sections for the L = 0 transitions deduced in the (p,t) reaction of ^{140}Ce. (XBL7012-4218)

populated, as is the 3.23 MeV state. These show an L = 0 angular distribution. Most of the excitation strength, other than the ground state, lies at an energy of 3.23 MeV or greater. The state at 3.73 MeV shows a typical L = 2 angular distribution. The only other state seen in this experiment with an energy greater than 3.23 MeV which could possibly be assigned $J^\pi = 0^+$ is at 5.57 MeV.

Figure 2 is a ^{140}Ce(p,t) spectrum. The ground state is heavily excited, as are most of the low-lying states in ^{138}Ce. The 0.786 MeV exhibits an L = 2 pattern. Besides the ground state transition, the only remaining state to reveal an L = 0 pattern is the weakly excited 2.32-MeV level.

A ^{140}Ce(p,p') spectrum is displayed in Fig. 3. The strongly excited states in ^{140}Ce are the 1.59(2^+), 2.09(4^+), and the 2.47(3^-) states. The level at 3.26 MeV has moderate strength; the (p,p') angular distribution suggests an L transfer greater than 4. Inelastic alpha scattering[7] on ^{140}Ce indicates that a state at 3.25 MeV has $J^\pi = 5^-$. By comparing the (p,p') and (p,t) reactions leading to the excited states of ^{140}Ce, one notices that the two reactions populate different final states. The (p,p') strongly populates those states

which are associated with instabilities toward deformation, i. e., low-lying vibrational states. In distinction to these, the (p,t) preferentially excites states whose structure is based on pair correlations.

Figures 4 and 5 show the L = 0 differential cross sections deduced from the ^{142}Ce (p,t) and ^{140}Ce(p,t) experiments. The strongly excited 0^+ level at 3.23 MeV in ^{140}Ce can be associated with the predicted pairing vibration state. The ground-state transitions are enhanced as predicted by the pairing vibration model. The 5.57-MeV level in ^{140}Ce does not yield an unequivocal L = 0 pattern. Extracting this state was difficult due to background and an impurity peak. The anharmonic calculations of B. Sørensen[4] predict the weakly excited 0^+ states to lie above the pairing vibration in ^{140}Ce and the ground state in ^{138}Ce. The latter may be associated with the 2.32-MeV level. The 0^+ states at 1.90 and 3.03 MeV in ^{140}Ce currently do not have an explanation based on neutron pairing states.

References

1. A. Bohr, in Proceedings of the International Symposium on Nuclear Structure, Dubna (1968).

2. Hartwig Schmidt, Zeitschrift für Physik 181, 532 (1964); D. R. Bes and R. A. Broglia, Nuclear Physics 80, 289 (1966).

3. O. Nathan, Proceedings of the International Symposium on Nuclear Structure, Dubna (1968).

4. B. Sørensen, Nuclear Physics A134, 1 (1969).

5. J. B. Ball, R. L. Auble, J. Rapaport, and C. B. Fulmer, Physics Letters 30B, 533 (1969); K. Yagi, Y. Aoki, J. Kawa and K. Sato, Physics Letters 29B, 647 (1969); and K. Yagi, Y. Aoki, and K. Sato, Nuclear Physics A149, 45 (1970).

6. O. Hansen and T. Mulligan, private communication.

7. F. T. Baker and R. S. Tickle, University of Michigan Annual Report (1970) p. 39.

The Reaction: ^{12}C(^{16}O, ^{12}C) ^{16}O

B. G. Harvey, J. Mahoney, J. R. Meriwether,† and D. L. Hendrie

Recent experiments[1] on the four-nucleon transfer reaction (^{16}O, ^{12}C) are interpreted as a direct transfer of the nucleons to populate selectively four-particle n-hole states of high symmetry. The process is loosely called α transfer.

It is therefore important to test the proposed reaction mechanism by forming a final-state nucleus in which there are well-known four-particle states. The best candidate is ^{16}O, which has a rotational band of 4p-4h states[2] based on the 0^+ state at 6.05 MeV. The reactions ^{12}C(^{16}O, ^{16}O)^{12}C (elastic and inelastic scattering of ^{16}O from ^{12}C) and ^{12}C(^{16}O, ^{12}C)^{16}O (α transfer) were therefore studied with a 70-MeV beam of ^{16}O ions from the 88-inch cyclotron. Particles were detected with a ΔE(11μ)-E counter telescope. A PDP-5 on-line computer identified the particles by computing the function $\Delta E(E + E_0 + K\Delta E)$, where E_0 and K are adjustable parameters. Energy resolution was about 400 keV.

Figure 1 shows the spectrum of particle types obtained at 25°(lab). The height of the C and Ne peaks compared with those of B, N and F shows the high probability for transfer

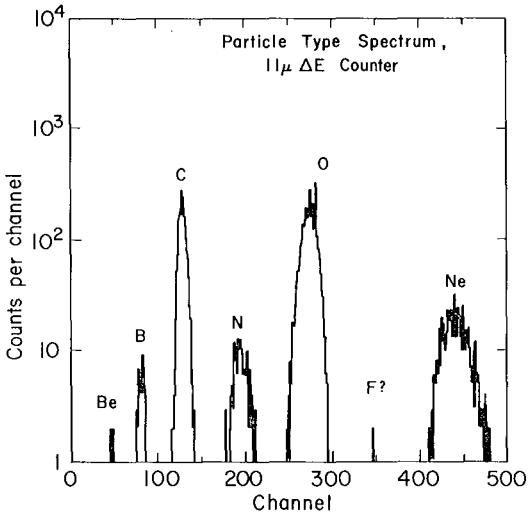

Fig. 1. Particle-type spectrum from reaction of 69.5-MeV ^{16}O ions on ^{12}C at 30°(lab). (XBL713-3075)

of two protons (probably as an α particle) to or from the beam particles. A short run with a thicker ΔE counter and a 75-MeV beam,

permitting resolution of individual mass numbers in the particle-type spectrum, showed that the carbon peak consisted entirely of ^{12}C. The range of the Ne ions was too small to permit identification in this experiment.

Figure 2 shows the spectrum of ^{12}C ions at 30°(lab). The ^{12}C 4.43-MeV peak is broadened by recoil from the γ-ray emission in flight. The spectra of ^{16}O are similar, but decay in flight broadens all peaks (except the double ground state and the peak corresponding to ^{12}C 4.43 MeV) so much that resolution of the 6.05 - 6.92 and 10.34 - 11 MeV doublets is not possible.

The Q = 0 and -4.43 MeV peaks in the ^{12}C spectra were least-squares fitted to a three-parameter energy scale, which showed that the peaks at Q ≈ -7 MeV and -10 MeV were due to the ^{16}O levels at 6.92 MeV and 10.34 MeV, respectively. A least-squares fit of 50 values, including the Q = 0, -4.43, -6.92 and -10.34 MeV points, was then used to identify additional peaks of the spectra. The peak at Q ≈ -6 MeV gave E_{ex} = 6.081 ± 0.023 MeV, slightly favoring identification with the 6.05-MeV α^+ level rather than the 6.13-MeV 3^- level. The narrowness of the peak at 10.34 MeV shows that it cannot be entirely due to the double excitation, ^{12}C 4.43 MeV + ^{16}O 6.05 MeV. A peak corresponding to an excitation of 14.7 MeV in ^{16}O was observed at small ^{12}C angles; at larger angles it was broad, perhaps containing a contribution from the double excitation, ^{12}C 4.43 MeV + ^{16}O 10.34 MeV.

Careful analysis of the peak at Q ≈ 11 MeV leaves its identification in doubt--it appears only in the neighborhood of 30°(lab). The corresponding excitation energy in ^{16}O is 10.95 ± 0.09 MeV, but the two closest known states (at 10.952 and 11.080 MeV) have spins 0^- and 3^+, so that neither of them should be excited. In spite of its narrowness, the 11-MeV peak could be due to the double excitation ^{12}C 4.43 MeV + ^{16}O 6.05 + 6.13 MeV if the γ-ray direction were strongly correlated with the ^{12}C particle direction.

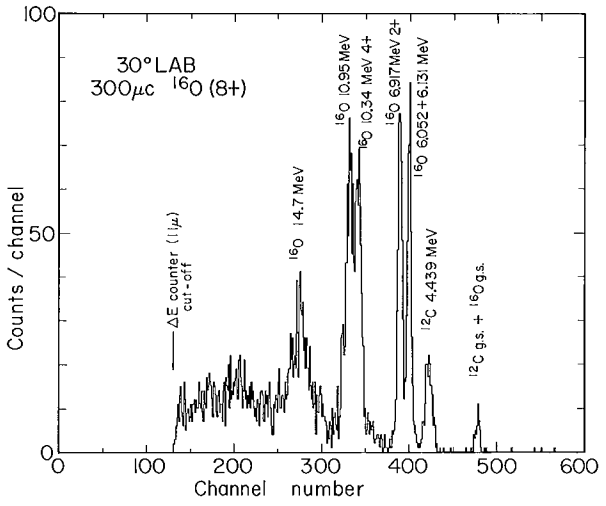

Fig. 2. Energy spectrum of ^{12}C ions at 30°(lab). (XBL713-3015)

At no angle was the 16.2-MeV 6^+ member of the rotational band observed. However, the Coulomb barrier for ^{12}C + ^{16}O may be responsible for its absence. The center of mass outgoing ^{12}C energy is 7.77 MeV while the Coulomb barrier height is $14.37/r_{int}$ MeV, where r_{int} is the interaction radius parameter in fermis. The barrier is therefore higher than the ^{12}C energy unless r_{int} is greater than 1.84 F. This is an unreasonably large value.

Figure 3 shows the ^{12}C angular distributions for Q = 0 and Q = - 4.43 MeV. The clear break at ≈ 90°(c. m.) separates the scattering reaction (^{12}C backward angles, ^{16}O forward angles) from the transfer reaction (^{12}C forward angles, ^{16}O backward angles). ^{12}C angular distributions at forward angles for Q = - 6.08 and Q = - 6.92 MeV are somewhat featureless.

The α-transfer reaction probably excites the ^{16}O 6.05-MeV 0^+ ground state of the 4p-4h rotational band, and certainly excites the 2^+ and 4^+ band members at 6.92 and 10.34 MeV. Excitation of the 14.8 MeV level in this reaction as well as in (Li^6, d) and (α, d) is not well understood; there are too many levels in the vicinity, and the resolution of the experiments is inadequate to be certain that the same level is excited by each reaction.

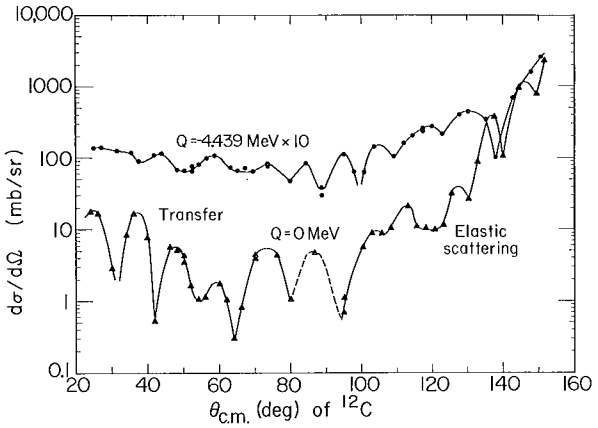

Fig. 3. Angular distributions for Q = 0 and Q = - 4.43 MeV. The angles are for ^{12}C in the center-of-mass system; therefore, ^{16}O scattering appears at back angles. (XBL713-3014)

Footnote and References

†Present address: University of Southwestern Louisiana, Lafayette, Louisiana.

1. J. C. Faivre, H. Faraggi, J. Gastebois, B. H. Harvey, M. C. Lemaire, J. M. Loiseaux, M. C. Mermaz, and A. Papineau, Phys. Rev. Letters 24, 1188 (1970); Annals of Physics, de Shalit Memorial Volume, to be published.

2. See for example A. P. Zucker, B. Buck, and J. B. McGrory, Phys. Rev. Letters 21, 39 (1968).

Deformation of ^{182}W

D. L. Hendrie, B. G. Harvey, J.-C. Faivre, and J. Mahoney

Recent work at this laboratory[1] has determined in some detail the shapes of several rare earth nuclei. In addition to the previously known large quadrupole moments, precision measurements were made of hexadecapole moments and, with less precision, some even higher moments. For this work, rather than directly specify the moments, it was convenient to parameterize the shape of the axially symmetric nuclear surface by

$$R = R_0(1 + \beta_2 Y_{20} + \beta_4 Y_{40} + \beta_6 Y_{60}),$$

where the betas are deformation parameters determined from the experiment. Data were taken which showed a systematic trend of β_4 ranging from +0.048 in ^{152}Sm to -0.072 in ^{178}Hf. It would be more restrictive on those nuclear structure calculations which describe this effect if the range of nuclei species were extended. At the low mass end of the range, the onset of quadrupole deformations occurs sharply upon the inclusion of 90 neutrons, so that measurements are not possible below ^{152}Sm or ^{154}Gd. However, at the high end, the deformation decreases only slowly with mass, so that measurements in W, Os, Pt, and even Hg are possible. In particular, it is of interest to determine whether β_4 continues to go even more negative in the W, Os nuclei or (as some models predict) levels off and starts to go positive.

We have performed the ^{182}W(α,α') reaction at 60 MeV, exciting the known levels of the ground-state rotational band up to the 8^+ level.

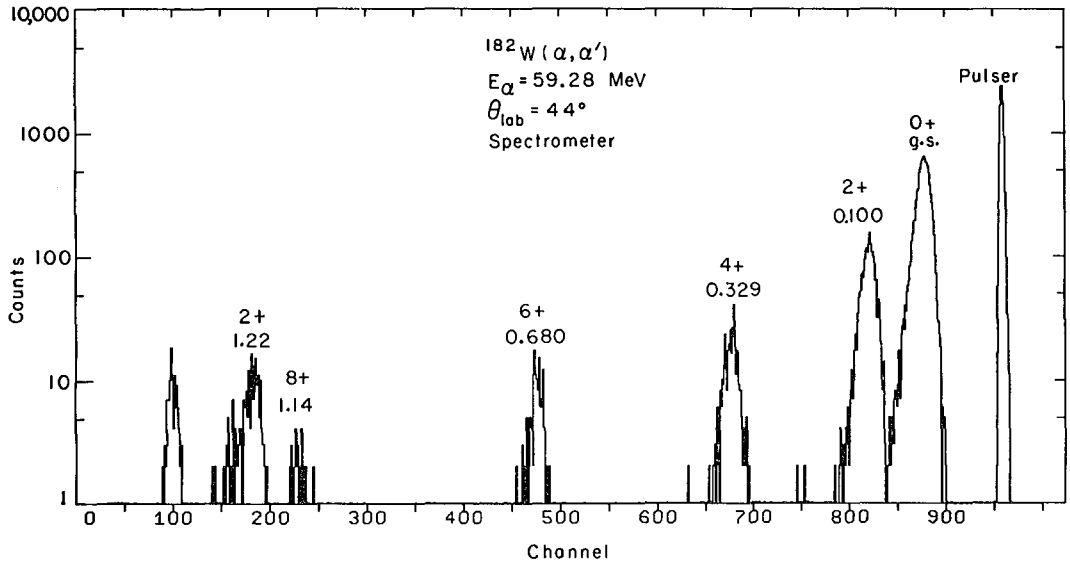

Fig. 1. Sample spectrum of the ^{182}W(α,α') reaction showing the separation and lack of background for the ground-state rotational band. (XBL7011-4152)

Data were taken with the 88-inch cyclotron magnetic spectrometer. The resolution of 19-26 keV permitted the extraction of the 2^+ states into 15°, the smallest angle measured. Absolute cross sections to about 3% were obtained by normalizing the data to calculations at small angles, where the predominantly Coulomb scattering is quite insensitive to assumptions about nuclear parameters. The target was a 75-$\mu g/cm^2$ isotopic metallic evaporated foil; its only contaminant of significance was ^{54}Fe, which obscured the ^{182}W peaks at a few angles. The focal-plane detector was a 5-cm long by 1-cm high nuclear-triode position-sensitive solid-state detector. A sample spectrum is shown in Fig. 1.

A preliminary analysis of the data is shown in Fig. 2, using the coupled-channels code of Glendenning.[2] The optical parameters used were identical to those of Ref. 1; β_2 was scaled in the manner of Ref. 1 from the table of Stelson and Grodzins.[3] From this preliminary fit we can see that β_4 will not significantly increase from that of ^{178}Hf, and that little, if any, β_6 deformation will be needed to reproduce the data.

References

1. D. L. Hendrie, N. K. Glendenning, B. G. Harvey, O. N. Jarvis, H. H. Duhm, J. Saudinos, and J. Mahoney. Phys. Letters 26B, 127 (1968).

2. N. K. Glendenning, Proc. Intern. School of Physics "Enrico Fermi" Course XL (Academic Press, 1967).

3. P. H. Stelson and L. Grodzins, Nuclear Data 1, 42 (1965).

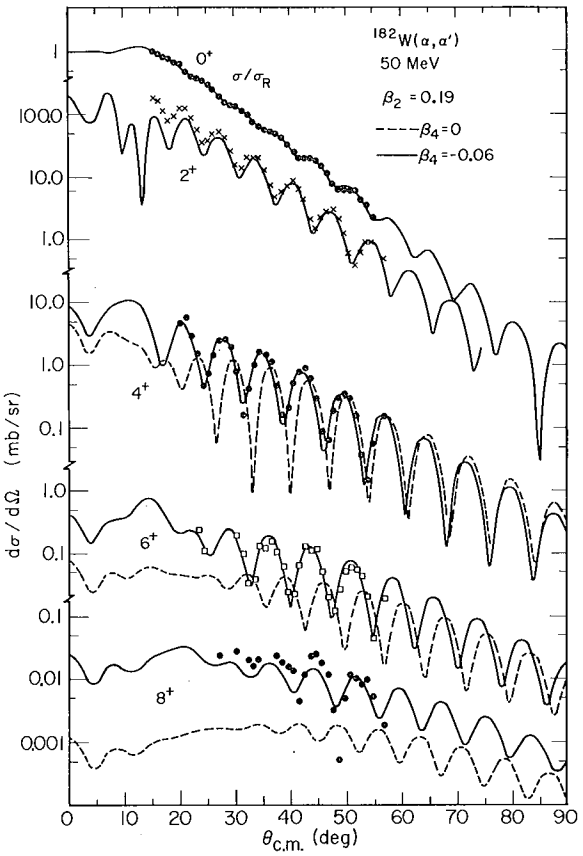

Fig. 2. Cross sections for levels in the ground-state rotational band excited by the $^{182}W(\alpha,\alpha')$ reaction at 60 MeV. The solid and dashed curves are two calculations using the coupled-channels code of N. K. Glendenning.

(XBL713-3078)

Evidence for the Full Thomas Form of the Spin-Orbit Potential from the Scattering of Polarized Protons on ^{20}Ne and ^{22}Ne

A. D. Bacher,† R. de Swiniarski,* D. L. Hendrie, A. Luccio,‡ G. R. Plattner,†† J. Raynal,** F. G. Resmini,‡‡ and J. Sherman

It has been shown that a large hexadecapole deformation (β_4) was needed[1] to reproduce both the shape and the magnitude of the 2^+, 4^+, and 6^+ cross sections in ^{20}Ne corresponding to the ground-state rotational band in this nucleus. In the coupled-channels calculations, the intrinsic deformation of the states was parameterized according to the following definition of the nuclear radius

$$R = R_0 \left[1 + \beta_2 Y_{20}(\theta) + \beta_4 Y_{40}(\theta)\right].$$

With the newly installed Berkeley polarized-proton source, the analyzing power of the $^{20}Ne(\vec{p},p')^{20}Ne$ and the $^{22}Ne(\vec{p},p')^{22}Ne$ reactions leading to the first few excited states in these targets has been measured. The experimental aspects of this experiment have already been discussed[2] and will not be presented. The measured asymmetries for ^{20}Ne

and ^{22}Ne (0^+, 2^+, and 4^+ states) are shown in Figs. 1 and 2. They exhibit the similarities between the asymmetries for the 0^+ and 2^+ states in ^{20}Ne and ^{22}Ne, and the large difference for the 4^+ measurements.

Preliminary coupled-channels (rotational-model) calculations using the code of A. Hill have failed to reproduce the measured asymmetries in ^{20}Ne[2] when the parameters and deformations of Ref. 1 were used. This program included a deformed spin-orbit term either of the so-called Saclay type or or the Oak-Ridge type, which both give very similar results.[3] The failure of the collective model may indicate that the nuclear model may be too simple. However, since the cross sections are reproduced so well, the discrepancy might well be due to simplifications of the description of the spin-orbit interaction in the optical potential.[3] Recently, H. Sherif and J. Blair[4] have obtained significant improvements for asymmetries when using DWBA collective-model form factors with the full Thomas form of the spin-dependent optical potentials. Such a deformed L. S. coupling has now been introduced in a coupled-channel program[5] which has been adapted to the University of Grenoble IBM 360-67 computer. The coupled-channel calculations with full Thomas term using the deformation of Ref. 1 are shown in Fig. 1 for ^{20}Ne, and a new calculation for ^{22}Ne is shown in Fig. 2, together with some previously reported calculations.[2]

As can be seen from Fig. 2, only the full Thomas terms are able to reproduce the

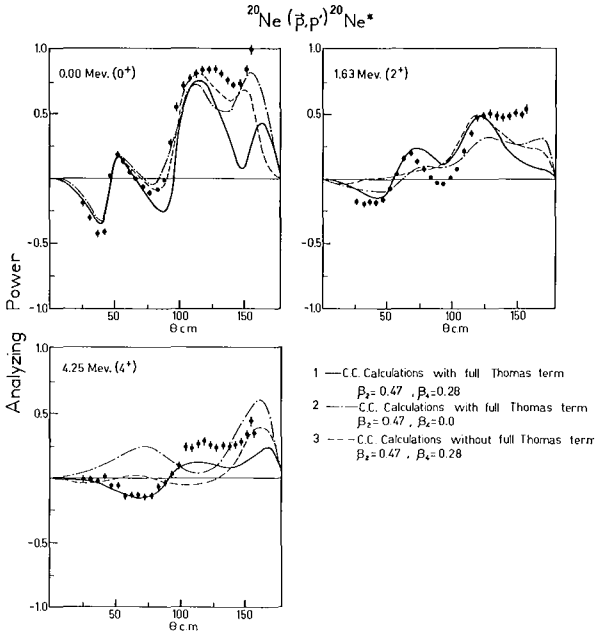

Fig. 1. (XBL713-3056)

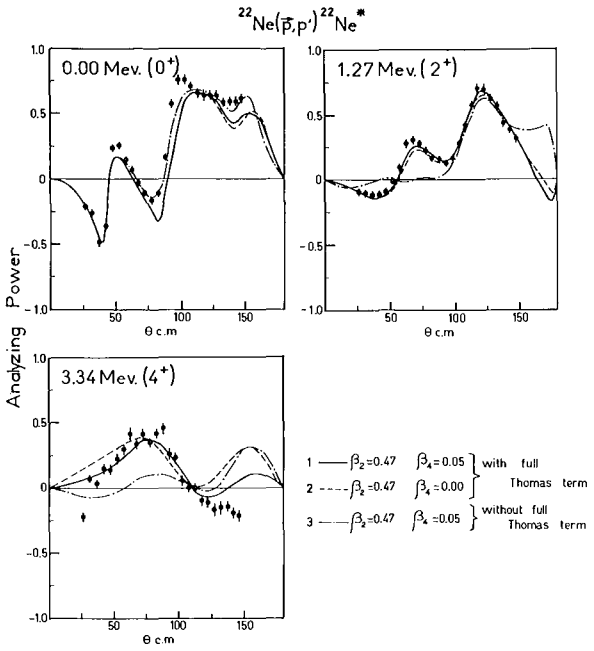

Fig. 2. (XBL713-3054)

shape of all asymmetries for the 0^+, 2^+, and 4^+ states in ^{20}Ne. The agreement with the data is now very good at least up to 130°; the good agreement already obtained for the corresponding cross sections still remains. On the other hand, this good agreement is completely destroyed when β_4 is set equal to zero. Such sensitivity of the asymmetries to the β_4 deformation is much less pronounced when the distorted spin-orbit term is not of the full Thomas form.[2] Figures 2 and 3 show good fits for the 0^+, 2^+, and 4^+ cross sections and analyzing powers in ^{22}Ne with β_2 = 0.47, and with only a very small value of β_4, equal to 0.05.

In conclusion, we can say that the values of β_2 and β_4 determined from the ^{20}Ne cross sections are still the best values for these deformations even when polarizations data are included. Moreover, the asymmetry data emphazise strongly the need of a Y_4 deformation for the ^{20}Ne ground-state rotational band. It is, on the other hand, extremely interesting to point out that the ground-state rotational band in ^{22}Ne is very well fitted (cross sections as well as asymmetries) with β_2 = 0.47, whereas the β_4 deformation needed is very small and is equal to 0.05.

Since these data were not able to be fit with DWBA, including the full Thomas term, or by coupled-channels calculations without it, our results are strong evidence for the inadequacy of the more simple treatments of

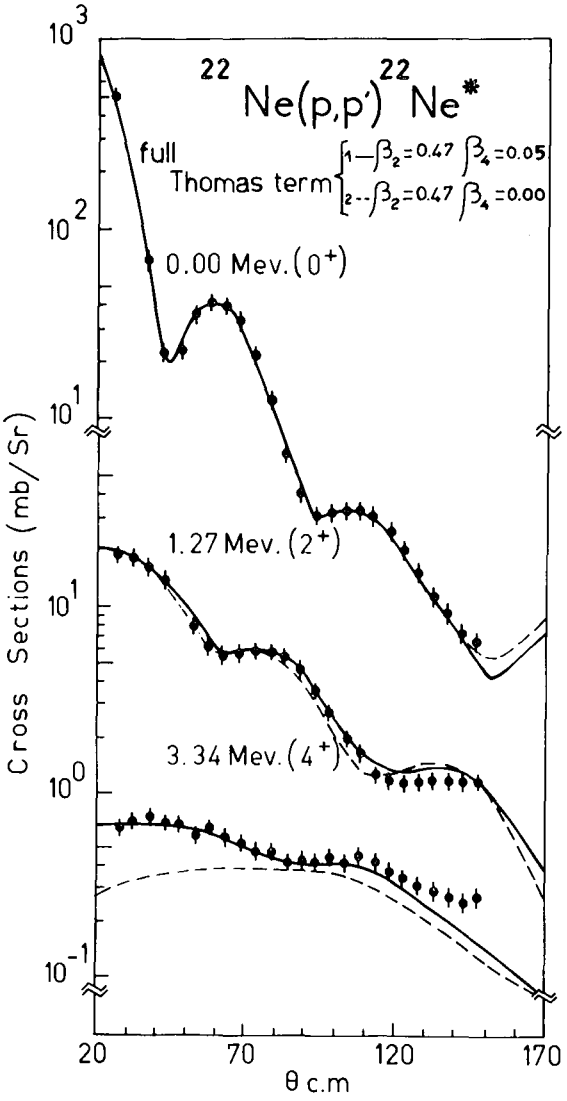

Fig. 3. (XBL713-3055)

the spin-orbit interaction and of DWBA calculations.

Footnotes and References

†Present address: University of Indiana, Bloomington, Indiana.

*Present address: Institut des Sciences Nucléaires, Grenoble, France.

‡Present address: Institut für Plasma Fysik, Munich, Germany.

††Present address: University of Basel, Switzerland.

**CEN, Saclay, France

‡‡Present address: University of Milan, Italy.

1. R. de Swiniarski, C. Glashausser, D. L. Hendrie, J. Sherman, A. D. Bacher, and E. A. McClatchie, Phys. Rev. Letters 23, 317 (1969).

2. A. D. Bacher, R. de Swiniarski, D. L. Hendrie, A. Luccio, G. R. Plattner, F. G. Resmini, and J. Sherman, Third International Symposium on Polarization Phenomena in Nuclear Reactions, Madison (Sept. 1970); Nuclear Chemistry Division Annual Report, 1969, UCRL-19530.

3. A. G. Blair et al., Phys. Rev. C, 1, 444 (1970); M. P. Fricke, Ph. D. thesis, Oak Ridge National Laboratory.

4. H. Sherif and J. S. Blair, Phys. Letters 26B, 489 (1968); H. Sherif and R. de Swiniarski, Phys. Letters 28B, 96 (1968); and H. Sherif, Ph. D. thesis, University of Washington.

5. J. Raynal, Proceedings of the Symposium on Nuclear Reactions Mechanisms and Polarization Phenomena, Quebec, 1969, p. 73.

Excitation of a Strong Feature by the Scattering of Alpha Particles from Heavy Nuclei

D. L. Hendrie, C. Glashausser,† G. Chenevert,* I. Halpern,* and N. Chant*

As part of a study of direct reaction spectra to very high excitation energies in residual nuclei, we report here some observations on the α, α' reaction in the heavy nuclei, Ta, Au, and Pb. The incident α-particle energies were 42, 50, 65, and 90 MeV and the outgoing spectra were recorded for the full energy range extending from the incident energy down to $\approx$ 15 MeV, i.e., to well below the Coulomb barrier for α particles. The detection was carried out with solid-state counter telescopes which permitted us to distinguish α particles

from all other particles, including ^{3}He.

The spectra observed in forward directions all showed the expected excitations of individual low-lying levels in each of the nuclei. At excitation energies above a few MeV, it becomes difficult to resolve individual levels and the spectra are found to be rather smooth and amorphous, except for a conspicuous, broad, mesalike structure that appears in all spectra at forward angles. This mesa is perhaps most striking in the 65 MeV bombardments on ^{208}Pb. (The spectra seen with Au and Ta are very similar, but the cross sections are slightly smaller.) The integral over angle and energy of the Pb differential cross sections corresponding to the mesa is about 90 mb. The total (α, α') direct cross section is between 300 and 400 mb at the energies investigated, and constitutes an appreciable fraction ($\approx$ 1/6) of the reaction cross section.

It is seen that the edges of the mesa (in Fig. 1) are moderately sharp and that they appear to remain more or less fixed in energy as the angle of observation is varied. The halfway point on the low-excitation energy edge comes at about 9 MeV of excitation and the higher excitation edge is at roughly 25 MeV. When the incident energy is raised to 90 MeV, the low excitation edge remains at 9 MeV, but the higher edge is found to more up to 31 MeV. The mean cross section (in mb/sr MeV) in the region of the mesa is almost twice as large, at 30°, as the average cross section to excitations which lie below the mesa. The events of the mesa must be produced by some sort of direct interaction. This can be appreciated from the extreme forwardness of the observed angular distribution and from evidence that the yield of evaporated α particles is entirely negligible in the region of the mesa. [1]

Our attempts to understand the nature of the mesa events have led us to consider (1) the excitation of nuclear surface oscillations by the α particles, (2) the collisions of incident α particles with individual nuclear nucleons, and finally as a special case of (2), (3) the possibility that at least some of the observed events might be due to pickup reactions in which ^{5}He and ^{5}Li are formed. [2] Since these two nuclei are particle-unstable in their ground states, they quickly decay to α + p, and we detect the breakup α.

The in-flight decay of ^{5}He and ^{5}Li have approximate kinematical features that fit some of the spectral characteristics of Fig. 1 in a very natural way. Thus if we assume that these nuclei are formed only in their ground states, that these states are narrow

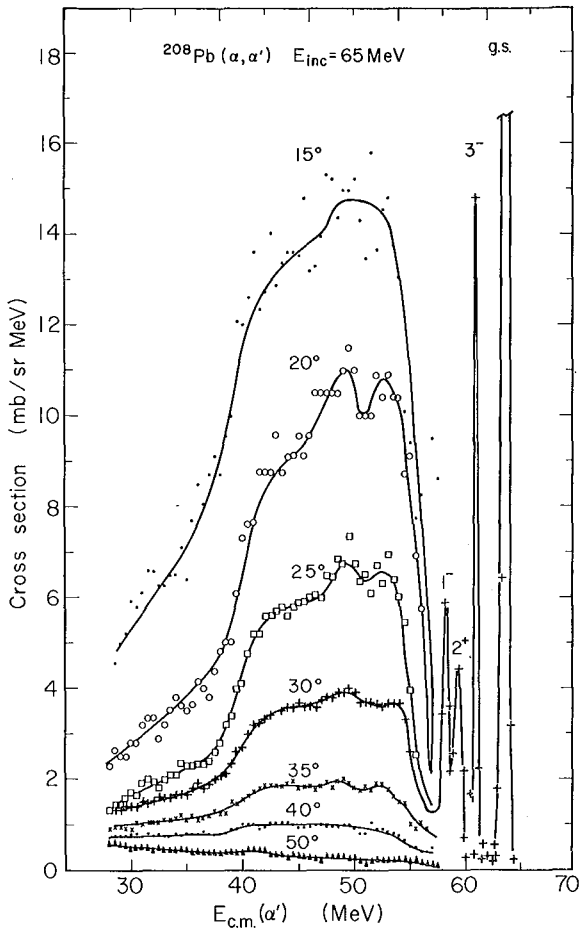

Fig. 1. Integrated cross section for the ^{208}Pb(α, α') reaction over an excitation range of 35 MeV for several forward-scattering angles showing the prominent "mesa" at forward angles. The discrete low-lying states of ^{208}Pb are shown for one typical scattering angle for comparison purposes.
(XBL713-3057)

and that they break up isotropically, it follows that the breakup α particles will have a mesalike spectrum. Further, if the outgoing kinetic energies, E_0, of the ^{5}He and ^{5}Li are equal to within a few MeV at all angles (as expected if the alphas tend to pick up mainly the least-bound nucleons), it follows that the observed α-particle spectra would be very nearly the same at all angles. With E_R (the energy of the ^{5}He ground state) $\simeq$ 1 MeV and $E_0 \simeq$ 55 MeV (corresponding to an incident α-particle energy of 65 MeV), we find that the minimum α-particle energy from the decay of ^{5}He will be $\approx$ 38 MeV. This corresponds in Fig. 1 to an "excitation energy" of $\approx$ 26 MeV. At an incident energy of 90 MeV, the excitation energy at the same edge of the

mesa, computed in the same way, is found to be 31 MeV. These values are in good agreement with the observed values mentioned earlier. Had we used for E_R, the ^{5}Li ground state energy ($\approx$ 2 MeV) rather than that of ^{5}He, the agreement would have been somewhat less. This may mean that more pickups lead to ^{5}He than to ^{5}Li.

The pickup model does not, however, give the observed location ($\approx$ 9 MeV) for the low-excitation edge of the mesa. With the values of E_0 and E_R given earlier, the width of the mesa would be 12 and 14-1/2 MeV for incident energies of 65 and 90 MeV, respectively. The observed spectra are half again as wide. Our tentative view is that we are dealing with two separate phenomena. The high-excitation portion of the mesa spectrum is presumably due to the pickup process, whereas the low-energy portion is due to some other process, yet to be identified.

This view is given some semiquantitative support by the following facts. Along with the study of the α,α' reaction involving large energy transfers, parallel studies were carried out for the ^{3}He, ^{3}He' reaction at comparable bombarding energies.[3] It is found in the ^{3}He studies that the cross section rises sharply at $\approx$ 9 MeV of residual excitation to about the same values as in the α,α' bombardments. In the ^{3}He, ^{3}He' spectra there is, however, no mesa. The pickup mechanism would not be expected to play a role here because of the lack of unstable but narrow states in ^{4}He and ^{4}Li. Upon subtracting a constructed pickup spectrum from the full observed (α, α') spectrum, there is a remainder which resembles the measured(^{3}He, ^{3}He') spectrum both in shape and in magnitude. This portion of both spectra presumably arises from the scattering of ^{3}He (or α particles) from either single particles or from collective degrees of freedom. Some calculations based on both kinds of models have been carried out, but so far they have not been successful in reproducing this sharp striking structure in the observed spectra.

Footnotes and References

†Present address: Rutgers University, New Brunswick, New Jersey.

*Present address: University of Washington, Seattle, Washington.

1. G. Chenevert, I. Halpern, B. G. Harvey, and D. L. Hendrie, Nucl Phys. A122, 481 (1968).

2. We are indebted to Prof. H. Morinaga for calling this process to our attention.

3. G. Chenevert, Ph. D. thesis, University of Washington, 1969.

Ground- and Gamma-Vibrational Bands in Even Os Isotopes from (α,xnγ) and (p,xnγ) Reactions

T. Yamazaki,† K. Nishiyama,† and D. L. Hendrie

In this paper we report on a systematic study of the ground bands and the gamma-vibrational bands of even osmium isotopes (A = 182 - 188) by means of the in-beam γ-ray spectroscopy following (α,xnγ) and (p,xnγ) reactions. Previous experiments by (α,xnγ) reactions,[1,2] (HI, xnγ) reactions,[3] and (p,2nγ) reactions,[4] as well as by the radioactive decays,[5] have revealed transitional aspects of the collective levels in this region. The aim of the present work was to investigate the gamma-vibrational bands in the neutron-deficient isotopes, ^{184}Os and ^{182}Os, which were not known earlier. To this purpose, alpha- and proton-induced reactions were useful, since these reactions populate more side-band levels than (HI,xnγ) reactions do.

Gamma rays of ^{182}Os, ^{184}Os, ^{186}Os, and ^{188}Os were measured by use of (p,2nγ) and (p,4nγ) reactions on ^{185}Re and ^{187}Re, and (α,2nγ) reactions on ^{182}W, ^{184}W, and ^{186}W. The external beams from the 88-inch cyclotron were used to induce the reactions. Typical bombarding energies were 14 MeV for (p,2n), 37 MeV for (p,4n), and 30 MeV for (α,2n).

A Ge(Li) detector of 30 cc coaxial-type was placed at a distance of 20 cm from the target and could be moved for angular distribution measurements. The targets were prepared by depositing enriched-Re or W metallic powder onto 800-μg/cm^2-thick mylar film. They were about 20 mg/cm^2 thick. In order to search for isomeric levels, both prompt and delayed γ-ray spectra were taken by the use of natural beam bursts.

Since the lowest-lying excited band in even Os nuclei is the K = 2 gamma-vibrational band, we expect in (p, xn) or (α, xn) reactions a γ-ray spectrum in which the ground-band transitions appear equidistantly in the low energy region, and the intertransitions from the members of the K = 2 band will form a complicated pattern in the higher energy region. The $2_\gamma \rightarrow 2_g$, $4_\gamma \rightarrow 4_g$, ----, transitions should be located as a cluster, as well as the $2_\gamma \rightarrow 0g$ and $3_\gamma \rightarrow 2g$ transitions. However, since the $I_\gamma \rightarrow Ig$ transition should always associate with the $I_\gamma \rightarrow (I-2)g$ transition, and these two should be spaced by the known energy of the $Ig \rightarrow (I-2)g$ transition, it is still possible to assign each line reasonably well. Comparison of the γ-ray intensities in the different reactions were used to confirm the identifications.

For a sample of the data, Fig. 1 shows γ-ray spectra in the $^{184}W(\alpha, 2n)$ and ^{187}Re (p, 2n) reactions, where the known interband transitions are identified. The branching ratios of γ rays from one level populated in these reactions agree with those observed in the ^{186}Ir decay.

The present experiment has revealed the K = 2 gamma-vibrational bands in ^{182}Os and ^{184}Os up to the 5^+ members. The energy systematics together with previous information[6] is summarized in Fig. 2. The 2_g^+ energy decreases as the mass number, whereas the 2_γ^+ energy increases. At A = 184, the 2_g^+ energy reaches a minimum, whereas the 2_γ^+ energy reaches a maximum. Thus a unique relation between the 2_g^+ energy and the 2_γ^+ energy throughout the Os region is observed of:

$$E_2^g \cdot E_2^\gamma \approx \text{const.}$$

This relation is characteristic of the Os isotopes.

The K = 4 gamma-vibrational state is known in ^{190}Os. The 1353 keV level of 4^+ spin in ^{186}Os is presumably the K = 4 band

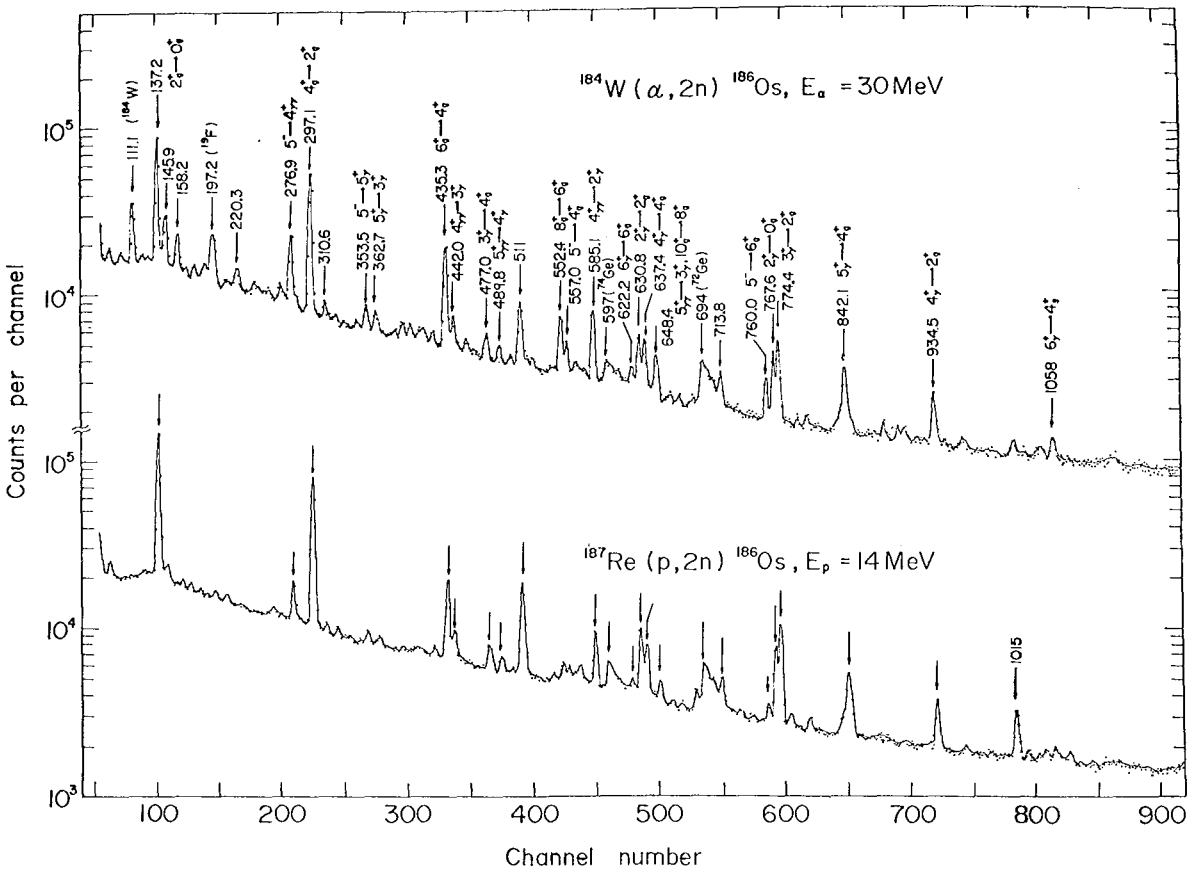

Fig. 1. Gamma-ray spectra in the $^{184}W(\alpha, 2n)^{186}Os$ and $^{187}Re(p, 2n)^{186}Os$ reactions. (XBL713-3053)

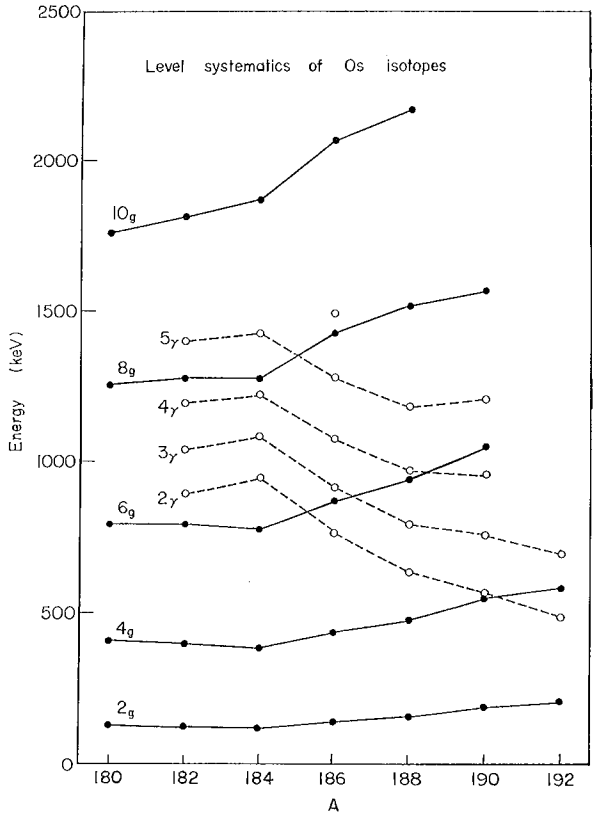

Fig. 2. Level systematics of even Os isotopes revealed in the present work together with the previous data. (XBL713-3052)

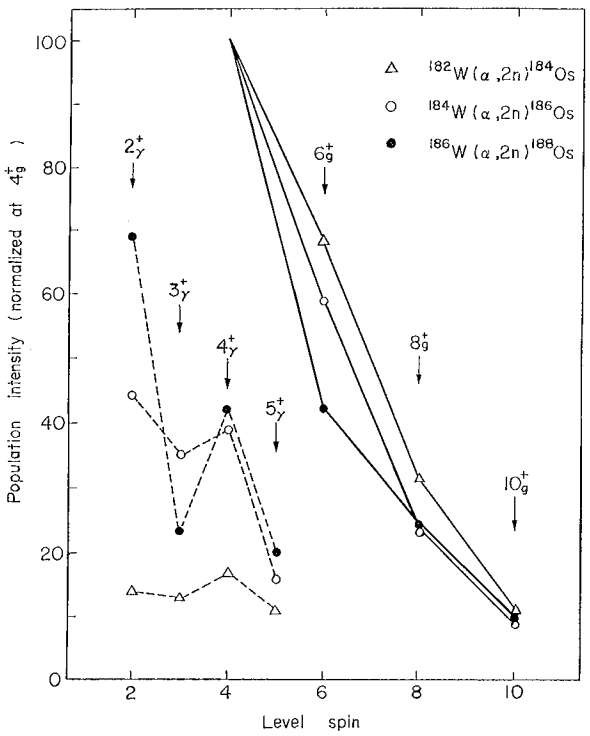

Fig. 3. Observed population intensities of the ground and the gamma-vibrational band levels in $(\alpha, 2n)$ reaction. They are normalized to the intensity of the $4_g^+ \rightarrow 2_g^+$ transition. (XBL713-3051)

head, since it proceeds only to the K = 2 band. The tentative level at 1280 keV in ^{188}Os may also be the K = 4 band head, because it is populated by the decay of the isomeric state, which is supposed to have a large K quantum number. The fact that the K = 4 band lies about twice as high as the K = 2 band supports the interpretation of these levels in terms of the gamma vibration.[7] The asymmetric-rotor model[8] postulates the K = 4 energy to be four times larger than the K = 2 energy.

The Os region provides a good test field to investigate the dependence of the population intensities of the $(\alpha, 2n\gamma)$ reactions on the level sequences. Figure 3 summarizes the observed population intensities in $(\alpha, 2n\gamma)$ reactions normalized to the 4_g level. A characteristic feature is that as the mass number increases, the ground-band levels receive less intensity and the gamma-band levels more. This fact can be ascribed to the change of the level sequence. In ^{188}Os, the gamma-band levels are lower lying and the level spacings within a band are larger so that the gamma-band levels take more feeding from above and lose less to the ground band. A similar tendency has been observed in the Gd region.[9]

Footnote and References

†Present address: Department of Physics, University of Tokyo, Bunkyo-ku, Tokyo, Japan.

1. N. L. Lark and H. Morinaga, Nucl. Phys. 63, 466 (1965).

2. J. O. Newton, F. S. Stephens, and R. M. Diamond, Nucl. Phys. A95, 377 (1967).

3. J. Burde, R. M. Diamond, and F. S. Stephens, Nucl. Phys. A92, 306 (1967).

4. M. Sakai, T. Yamazaki, and H. Ejiri, Nucl. Phys. 74, 81 (1965).

5. T. Yamazaki and D. L. Hendrie, International Physics Conference, edited by R. L. Becker, C. D. Goodman, P. H. Stelson, and A. Zucker (Academic Press, New York, 1967) p. 894.

6. C. M. Lederer, J. M. Hollander, and I. Perlman, Table of Isotopes (John Wiley and Sons, New York, 1967) 6th ed.

7. T. Yamazaki, Nucl. Phys. 49, 1 (1963).

8. A. S. Davydov and G. F. Filippov, Nucl. Phys. 8, 237 (1958); A. S. Davydov and A. A. Chaban, Nucl. Phys. 20, 499 (1960).

9. H. Ejiri, M. Ishihara, M. Sakai, K. Katori, and T. Inamura, J. Phys. Soc. Japan 24, 1189 (1968).

Nuclear Theory

Extension of Two-Nucleon Transfer Theory to Include Inelastic Processes†

R. J. Ascuitto* and Norman K. Glendenning

The existent treatments of the two-nucleon transfer reaction all neglect the effect of inelastic processes. There are two circumstances where this neglect is not justified. The first concerns a question of parentage. If in the reaction

$$t + (A) \rightarrow p + (A + 2),$$

the configuration of the group of (A) nucleons is the same in the residual state of interest as in the target ground state, then the usual treatment may be valid. However, if the state of motion of any of the core nucleons is different, then a description of the inelastic processes that produced this difference becomes essential, if in fact the state is excited in the reaction.

The second circumstance when inelastic processes are crucial for a correct description arises when some inelastic transitions in either the target or residual system, or both, are so strong as to produce significant deexcitation back into the elastic channel. In this circumstance the usual one-channel optical potential will not provide a good description of the relative motion in the vicinity of the nucleus, just where it is important for the description of the transfer reaction.

In this paper we present the formalism by which inelastic processes can be incorporated into the theory of two-nucleon transfer reactions. The method that we use was described and justified in an earlier publication,[1] and may be referred to briefly as the source-term method. The theory is formulated in such a way that the particular structure of the nuclear states enters the description of the reaction only through certain generalized two-particle coefficients of fractional parentage. As an example these are calculated for a particular nuclear model, namely one in which the ground state is the BCS vacuum, and which has excited two-quasiparticle states as well as a "two-phonon" triplet which is built from the operator which describes the collective 2_1^+ state.

For definiteness our notation refers to the (p, t) reaction, but the results are general, and we indicate at appropriate places how to interpret the formalism for other two-nucleon transfer reactions.

The method consists of writing down the coupled equations which describe the inelastic scattering of the projectile by the target, and a second system of coupled equations which would describe the scattering in the residual partition, in this case the triton and final nucleus, except that the second system is coupled to the first by a source term which describes the transfer process. Thus the inelastic processes are carried to all orders among the retained channels, but the asymmetric way that the source appears means that the reaction itself is treated as a weak process only in first order. This corresponds to the fact that (p, t) cross sections are typically an order of magnitude smaller than the strongest inelastic ones.

We will describe the scattering in the initial partition of the system consisting of proton plus nucleus (A + 2) by a system of N equations which includes the strongly coupled channels and any others of interest. For each parity π and total angular momentum I of the system, they are

$$(T_{p'} + U_p(r) - E_{p'})u_{p'}^{p\pi I}(r) + \sum_{p'' \neq p'} V_{p'\,p''}^{\pi I}(r)u_{p''}^{p\pi I}(r) = 0. \qquad (1)$$

The rationale for use of such a system for a microscopic description of inelastic scattering has been discussed in detail elsewhere.[2] Here U stands for a complex optical potential, which is a parametrization of the diagonal matrix elements of the effective interaction which enters the problem because we intend to solve it in a highly truncated space of nuclear states, and V is the direct interaction between the nuclear nucleons and the exterior particle. Matrix elements are taken with respect to the channel wave functions

$$\phi^{M}_{p\pi I}(\hat{r}, A+2) = [Y_{l_p s_p j_p}(\hat{r}, \sigma)\Phi_{\alpha_p J_p}(A+2)]^{M}_{I}, \tag{2}$$

where Φ is a nuclear wave function, Y is a spin-orbit function for the scattered proton,[1] and the square bracket denotes vector coupling. We use p to denote the whole collection of quantum numbers defining a proton channel

$$p \equiv l_p s_p j_p \alpha_p J_p . \tag{3}$$

When both p and p' appear in an equation, p is understood to refer to an entrance channel, and p' to any channel. The superscript p on u in Eq. (1) signifies that the system is subject to the boundary condition that only channels p, in which the nucleus is in its ground state, have incoming waves.

The equations describing the final partition of the system are

$$[T_{t'} + U_t(R) - E_{t'}]w^{p\pi I}_{t'}(R) + \sum_{t'' \neq t'} V_{t' t''}^{\pi I}(R) w^{p\pi I}_{t''}(R) = \sum_{p'} \rho_{p', t'}^{p\pi I}(R), \tag{4}$$

which are to be solved subject to the condition that there are only outgoing waves in triton channels. These equations differ in structure from the preceding ones only in the addition of the source term ρ which represents the appearance of tritons in the channel t' due to the transfer process in the various channels p' of the initial partition. The rest of the paper is essentially devoted to the description of how this source is constructed, given the detailed microscopic structure of the states in the target and residual nuclei.

The source for tritons in the channel t' is equal to the sum of matrix elements describing the transfer processes leading to it from the various channels p',

$$\rho^{p\pi I}_{t'}(R) = \sum_{p'} \rho_{p', t'}^{p\pi I}(R), \equiv R \sum_{p'} \left\langle \phi_{t'\, \pi I}^{M}(\hat{R}, A)\phi_0 \,|v|\, \phi_{p'\pi I}^{M}(\hat{r}, A+2) \frac{u^{p\pi I}_{p'}(r)}{r} \right\rangle . \tag{5}$$

All coordinates in the matrix element are integrated except R. Here v represents the stripping interaction. In Ref. 1 we showed that this form for the source leads precisely to the usual distorted-wave Born approximation (DWBA) in the event that in our equations, the off-diagonal matrix elements of V describing the inelastic processes are dropped, and it leads to the result of Penny and Satchler[3] when they are kept.

We will evaluate the matrix elements appearing in the source term under the assumptions usually made in two-nucleon transfer theory.[4] The result can be written in the form

$$\rho^{\pi I}_{p, t}(R) = \frac{A+2}{A} D_0 \sum_{LSJ} A_{LSJ}(p, t) u^{\tilde{\alpha}_p \alpha_t}_{LSJ}(R) u^{\pi I}_{p}\left(\frac{A}{A+2} R\right). \tag{6}$$

This is written more generally than required for the (p,t) reaction (where only S = 0 transfer is allowed) so that we can cover other two-nucleon transfer reactions. Here L, S, J, denote the orbital, intrinsic, and total angular momentum carried by the transferred pair. The quantity A_{LSJ} is a geometrical factor defined by

$$A_{LSJ}(p,t)=(-)^{l_t+j_p+J_p+I}\left(\frac{\hat{j}_t\hat{l}_p\hat{J}_p\hat{L}}{4\pi}\right)^{1/2}\begin{pmatrix} l_p & L & l_t \\ 0 & 0 & 0\end{pmatrix}\begin{Bmatrix} j_p & J & j_t \\ J_t & I & J_p\end{Bmatrix}\begin{bmatrix} l_p & s_p & j_p \\ L & S & J \\ l_t & s_t & j_t\end{bmatrix}\Lambda_s(p,t), \tag{7}$$

where $\hat{l} = 2l + 1$. This factor is general for any particle transfer reaction when p is interpreted to refer to the lighter and t to the heavier of the light nuclides.[5] D_0 is a constant which collects together two normalization factors,

$$D_0 = g\left[\phi_{10}(4\eta^2\rho^2)\right]_{\rho=0} = g\left(\frac{4\eta^2}{\pi}\right)^{3/4}, \tag{8}$$

Λ_S is the overlap matrix element for spins

$$\Lambda_S = \left\langle \chi_{s_t}^{m_t}(\vec{\sigma}_p\vec{\sigma}_1\vec{\sigma}_2)\,|\,[\chi_{s_p}(\vec{\sigma}_p)\chi_S(\vec{\sigma}_1\vec{\sigma}_2)]_{s_t}^{m_t}\right\rangle. \tag{9}$$

Here χ_{s_t} and χ_{s_p} are the spin functions of the triton and the proton and

$$\chi_S(\vec{\sigma}_1\vec{\sigma}_2) = [\chi_{1/2}(\vec{\sigma}_1)\chi_{1/2}(\vec{\sigma}_2)]_S \tag{10}$$

is the singlet or triplet spin function of the two transferred particles. For other reactions, see the original paper.

The function $\tilde{u}_{LSJ}^{\alpha_p\alpha_t}(R)$ in (6) is a projected wave function which defines the radial motion of the center of mass of the transferred pair in the state α_p of the nucleus (A + 2) when their correlation corresponds to that in the triton, given that the remaining nucleons are in the state α_t of nucleus (A). It can be written in general as

$$\tilde{u}_{LSJ}^{\alpha_p\alpha_t}(R) = \sum_{a\le b}\beta_{ab}(\alpha_p,\alpha_t)\tilde{u}_{LSJ}^{ab}(R), \tag{11}$$

where $\beta(\alpha_p,\alpha_t)$ are generalized two-particle parentage factors.[4]

In this way of formulating the problem, the structure of the nuclei (A) and (A + 2) enters the description of the reaction only through the values of the parentage coefficients $\beta(\alpha_p,\alpha_t)$. For a complicated structure calculation, these would depend upon intimate details of the calculation. However, for a simple model they can be exhibited explicitly, as we do now.

The parentage coefficient given in Ref. 4 (there in L-S coupling) may be expressed in second-quantization notation, for equivalent particles, as

$$\beta_{abJ}(\alpha_p,\alpha_t) \equiv [\hat{J}_p(1+\delta_{ab})]^{-1/2}\left\langle \Phi_{\alpha_p J_p}(A+2)\,||\,[d_a^\dagger d_b^\dagger]_J\,||\,\Phi_{\alpha_t J_t}(A)\right\rangle. \tag{12}$$

Here $d_{am_a}^\dagger$ creates a particle in the state $n_a l_a j_a m_a$. The definition adopted for reduced matrix elements is that of Racah.[6] However for transfer of a neutron and proton pair, when the isospin formalism is not used, the δ_{ab} factor should be omitted and $d_a^\dagger$ and $d_b^\dagger$ commute.

If the structure of the nuclear states is defined in terms of quasiparticles $\alpha^\dagger$ related to particles through,[7]

$$d^\dagger_{am} = U_a \alpha^\dagger_{am} + V_a \tilde{\alpha}_{am}, \qquad \tilde{\alpha}_{am} = (-)^{j_a - m} \alpha_{a,-m}, \tag{13}$$

where U and V are coefficients of the Bogolyubov-Valatin transformation, then

$$[d^\dagger_a d^\dagger_b]^M_J = -U_a U_b A^\dagger_{JM}(a,b) + (-)^{J+M} V_a V_b A_{J-M}(a,b)$$

$$-U_a V_b N^\dagger_{JM}(a,b) - (-)^{J+M} V_a U_b N_{J-M}(a,b) + V_a U_b (\hat{j}_a)^{1/2} \delta_{ab} \delta_{J0}, \tag{14}$$

where

$$A^\dagger_{JM}(a,b) = -[\alpha^\dagger_a \alpha^\dagger_b]^M_J, \qquad N^\dagger_{JM}(a,b) = (-)^{j_a - j_b + M} N_{J-M}(b,a) = -[\alpha^\dagger_a \tilde{\alpha}_b]^M_J. \tag{15}$$

As an example of the calculation of the parentage coefficients, we consider a simple model. If the ground state is described as the BCS vacuum, and excited states as two-quasiparticle states, then four types of parentage coefficients enter the problem, illustrated by Fig. 1. We write the two-quasiparticle wave functions for nucleus (A) as

$$|\alpha(A)JM\rangle = \frac{1}{2} \sum_{a,b} \eta^{\alpha J}_{ab}(A) A^\dagger_{JM}(a,b) |\omega_A\rangle, \tag{16}$$

where the sum on a, b is not ordered (i.e., both a, b and b, a occur). Here $|\omega_A\rangle$ is the BCS vacuum, and similarly for nucleus (A + 2). Then the parentage coefficients for the four types of transitions numbered in Fig. 1 are[8]

$$\beta_{abJ}(1) = (\tfrac{1}{2} \hat{j}_a)^{1/2} V_a(A+2) U_b(A) \delta_{ab} \delta_{J0}, \tag{17}$$

$$\beta_{abJ}(2) = \left(\frac{\hat{J}}{1+\delta_{ab}}\right)^{1/2} \eta^{\alpha_t J_t}_{ab}(A) V_a(A+2)\, V_b(A+2) \delta_{JJ_t}, \tag{18}$$

$$\beta_{abJ}(3) = -\left(\frac{1}{(1+\delta_{ab})}\right)^{1/2} \eta^{\alpha_p J_p}_{ab}(A+2)\, U_a(A) U_b(A) \delta_{JJ_p}, \tag{19}$$

$$\beta_{abJ}(4) = (\hat{j}_a/2)^{1/2} \theta(\alpha_p, \alpha_t) V_a(A+2)\, U_b(A) \delta_{ab} \delta_{J0} \delta_{J_p J_t} + \left(\frac{\hat{J}\hat{J}_t}{1+\delta_{ab}}\right)^{1/2} (-)^{J_t + J - J_p}$$

$$[U_a(A) V_b(A+2) X_{ab}(\alpha_p, \alpha_t) + (-)^{j_a - j_b + J} U_b(A) V_a(A+2) X_{ba}(\alpha_p, \alpha_t)], \tag{20}$$

where

$$\theta(\alpha_p, \alpha_t) = \frac{1}{2} \sum_{cd} \eta^{\alpha_p J_p}_{cd}(A+2) \eta^{\alpha_t J_t}_{cd}(A), \tag{21}$$

$$X_{ab}(\alpha_p, \alpha_t) = \sum_d \eta^{\alpha_p J_p}_{da}(A+2) \eta^{\alpha_t J_t}_{bd}(A) \begin{Bmatrix} J_t & J & J_p \\ j_a & j_d & j_b \end{Bmatrix}. \tag{22}$$

Note that θ represents the overlap of a two-quasiparticle state in (A) with one in (A+2). For the lowest collective 2_1^+ states in adjacent nuclei, this overlap will usually be close to unity.

In analogy with the vibrational model, we may use the collective operator

$$Q^\dagger_{\alpha 2M}(A) \equiv \frac{1}{2} \sum_{a,b} \eta^\alpha_{ab}(A) A^\dagger_{2m}(a,b) \tag{23}$$

corresponding to the lowest 2_1^+ state to generate a triplet of "two-phonon" states

$$|\alpha_p(A) J_p M_p\rangle = \frac{1}{\sqrt{2}} [Q^\dagger_2(A) Q^\dagger_2(A)]^{M_p}_{J_p} |\omega_A\rangle , \tag{24}$$

and similarly for the nucleus (A + 2). The quasiboson commutation relations are approximately [assuming identical BCS vacuum for (A) and (A + 2)] ,

$$[Q_{\alpha_p J_p M_p}(A+2),\ Q^\dagger_{\alpha_t J_t M_t}(A)] \cong \theta(\alpha_p, \alpha_t) \delta_{J_p J_t} \delta_{M_p M_t} . \tag{25}$$

The two-particle operator $[d^\dagger d^\dagger]$ does not connect the vacuum ground state to the two-phonon states. The additional parentage factors needed are illustrated in Fig. 2. They computed in the quasiboson approximation to be

$$\beta_{abJ}(5) = [(2\hat{J}_t)^{1/2}/\hat{J}] \theta \beta_{col}(2) \delta_{J_2} \delta_{J_p 2} , \tag{26}$$

$$\beta_{abJ}(6) = \sqrt{2}\, \theta \beta_{col}(3) \delta_{J2} \delta_{J_t 2} , \tag{27}$$

$$\beta_{abJ}(7) = \theta_{col}{}^2 \beta(1) \delta_{J_p J_t} , \tag{28}$$

where the subscripts "col" denote that these quantities involve the amplitudes η of the collective 2_1^+ states in (A) and (A + 2). In (26) and (27), θ is the overlap between the two-quasiparticle state and the collective 2_1^+ state from which the two-photon states are built, whereas in (28) it is the overlap between the collective 2_1^+ states in the two nuclei. Therefore the coupling is weak except with another two-phonon state or with the collective 2_1^+ state, in which cases $\theta \simeq 1$.

To summarize, a theory of two-nuclear transfer reactions which includes the effects of inelastic processes has been formulated. In addition to the direct production of the final state from the target ground state, these processes allow for its production through intermediate states produced by the inelastic scattering of the incoming or outgoing particle. The reaction is treated as the weak process it is, only in first order, but the inelastic processes are treated to all orders among the retained channels. The theory can be applied easily to microscopic calculations of nuclear structure, because the entire content of such descriptions can be inserted into our formulation very concisely through reduced matrix elements of two types of operators; namely, the transfer operators $[d^\dagger_a d^\dagger_b]_J$ and the scattering $[d^\dagger_a \tilde{d}_b]_J$, evaluated between the nuclear states for the various configurations a,b entering the structure calculation. This obviously makes all structure calculations readily accessible to use in calculations of transfer and scattering. However, for many-particle shell-model calculations the job requires an intimate knowledge of the conventions employed, and generally can be done best (or only) by the structure theorist himself.

Footnotes and References

†Condensed from Phys. Rev. C 2, 415 (1970).

*Now at Physics Department, Yale University, New Haven, Connecticut.

1. R. J. Ascuitto and N. K. Glendenning, Phys. Rev. 181, 1396 (1969).

2. N. K. Glendenning, in Proceedings of the International School of Physics "Enrico Fermi," Course XL, 1967, edited by M. Jean (Academic Press Inc., New York, 1969), p. 332; and Nucl. Phys. A117, 49 (1968).

3. S. K. Penny and G. R. Satchler, Nucl. Phys. 53, 145 (1964).

4. N. K. Glendenning, Phys. Rev. 137, B102 (1965).

5. The square bracket is a recoupling coefficient related to the 9-j symbol, cf. Eq. (3.4) of Ref. 4.

6. We use Racah's original definition, cf. A. R. Edmonds, Angular Momentum in Quantum Mechanics (Princeton University Press, Princeton, New Jersey, 1957), p. 75.

7. Condon-Shortley phases are used with a consequence that $UV(-)^1 \geq 0$.

8. The first three results were given, aside from the configuration amplitude, by S. Yoshida, Nucl. Phys. 33, 685 (1962).

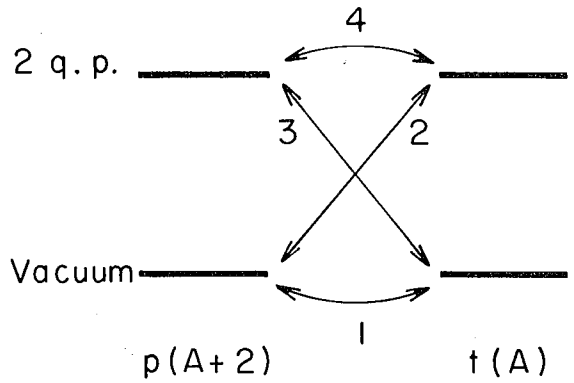

Fig. 1. Four types of parentage coefficients occur in a nucleus with the vacuum ground state and two-quasiparticle excited states. (XBL694-2537)

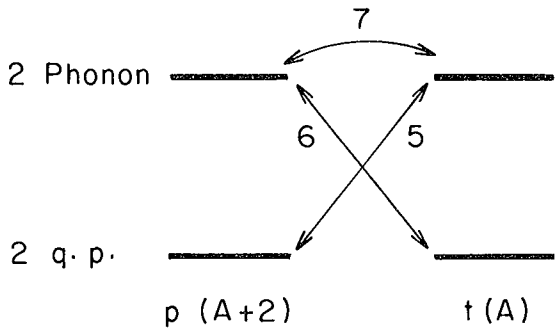

Fig. 2. Microscopic two-phonon states have parentage coefficients connecting them to other two-quasiparticle states or to each other. (XBL694-2538)

Assessment of Two-Step Processes in (p,t) Reactions†

R. J. Ascuitto* and Norman K. Glendenning

Particle transfer reactions have been treated customarily as proceeding directly from the target ground state to the final state by a simple deposit or pickup of the transferred particle (simple or composite) which leaves the other nucleons undistributed. [1] Undoubtedly this is the dominant mechanism by which most low-lying levels are produced. However some nuclear levels, even at low excitation, will have a parentage that is based more on an excited state of the target rather than on the ground state. If this excited state is produced with appreciable cross section in inelastic collisions, then alternate modes of producing the final state in the transfer reaction are possible. These are the two-step modes that proceed through the intermediate state produced by inelastic collisions with the incoming or outgoing particle.

The primary purpose of this investigation is to assess whether higher-order processes are likely to be significant in two-nucleon transfer reactions, and if so, whether there are any special characteristics by which they can be distinguished from direct transitions. While this question would seem largely academic as long as attention was focused on the lowest-lying states, it acquires ever more importance as improving experimental techniques allow detailed investigations of higher-lying levels whose parentage is expected to be more complicated. It is already evident that a number of interesting new phenomena involving second-order processes will be uncovered. [2]

It has been customary to compute by use of the distorted-wave Born approximation (DWBA) the cross section for those states that can be produced directly. [1,3] In this approximation, the wave function for the relative motion between the nucleus and free particle in the entrance and exit channels is generated by a one-channel optical potential. However when inelastic processes are very strong, the usual optical potential may not provide a sufficiently accurate representation for these

wave functions within the nuclear interior, just where they have their largest overlap with the nuclear wave functions appearing in the DWBA integrals. Since the optical parameters are chosen so as to reproduce the observed elastic cross section, this assures that the wave function is correct in the external region. However if a particular inelastic transition is very strong, the population of the excited state becomes large enough that deexcitation back to the ground state becomes significant. The process cannot be described by a one-channel optical potential and it produces changes in the wave function in the nuclear interior, just where it is needed in the reaction calculation. In this circumstance the inelastic processes play a role even for states that are produced directly in the transfer reaction. Therefore, as a secondary purpose of this investigation, we examine at what point the strength of inelastic transitions leads to significant errors in the usual DWBA for direct single-step transitions.

The method that we use to include the multiple-step processes (sometimes referred to as core excitation) that proceed through excited states of either target or residual nucleus has been described in previous publications.[4,5] (See also preceding report.)

To carry out the investigation described above, we adopt a model for a nucleus having a collectivity typical of spherical nuclei, which we refer to nominally as Ni. The ground state is taken to be a BCS vacuum. There are excited states of two-quasiparticle configurations, the lowest of which is the collective 2_1^+ state.[6] In addition we construct a triplet of two-phonon states by using the operator that creates the collective 2^+ state. This state, which we sometimes call the one-phonon state, has the structure,

$$|2_1^+\rangle = B_2^\dagger |\mathrm{BCS}\rangle , \tag{1}$$

$$B_{2,M}^\dagger = \frac{1}{2} \sum_{a,b} \eta_{ab} [\alpha_a^\dagger \alpha_b^\dagger]_{2,M}, \tag{2}$$

where $a \equiv nlj$, and $\alpha_a^\dagger$ creates a quasiparticle in the state a. The η_{ab} are the configuration mixing amplitudes, and the square bracket denotes vector coupling. The two-phonon states are

$$|J\rangle = \frac{1}{\sqrt{2}} [B_2^\dagger B_2^\dagger]_J |\mathrm{BCS}\rangle , \quad J = 0, 2, 4. \tag{3}$$

They have the special significance that they cannot be produced directly by the two-nucleon transfer reaction. This follows because they are four-quasiparticle states and therefore cannot be connected to the ground-state vacuum by a two-particle process. Presumably, in real nuclei ideal two-phonon states do not exist. In terms of quasiparticles, they would also have two quasiparticle components (and others). We shall comment on this again later after presenting our results for the idealized model described here. The main parent of the two-phonon states is, in any case, the collective 2^+, and the two-nucleon transfer reaction connecting them to this state is enhanced in the same sense as the transition from the ground to the one-phonon state is enhanced. (The parentage amplitudes in the two cases are equal within a statistical factor.)

Our model therefore possesses three kinds of states: the ground and 2_1^+, which have a strong direct transition; the remaining two-quasiparticle states (0^+, 2^+, 4^+), which have weaker direct transitions (however, the ground state is their main parent); and finally the two-phonon states, which have a strong transition from the collective 2_1^+ but which are not fed directly at all.

To assess the effect of inelastic processes on the two-nucleon transfer reaction, we consider the (p,t) reaction on a moderately collective nucleus, nickel, at a typical bombarding energy of $E_p = 30$ MeV. A complete body of data would consist of the elastic and inelastic cross sections of the 2^+ collective state (since it is the most important intermediate state for those included in our model) in both the initial and final nuclei, at the appropriate energies of the (p,t) reaction. This body of data does not exist, but fortunately there is data on neighboring nuclei which is sufficient to define the parameters realistically for our model calculations.

The reaction we consider is

$$^{62}\mathrm{Ni}(p,t)^{60}\mathrm{Ni}, \quad E_p = 30 \text{ MeV}. \tag{4}$$

The Q of the reaction is -10 MeV. There exist proton data[7] at 30 MeV on ^{60}Ni and triton data[8] at 20 MeV on ^{62}Ni. These data we use to define the optical-model parameters for protons and tritons in Eq. (4), and it is shown in Fig. 1. The elastic cross sections were computed by solving the coupled equations for the set of states described above. The corresponding optical-model parameters are labeled C. C. in Table I. (The parametrization of the Oak Ridge group is employed.[9] We also used an optical-model search routine to obtain parameters of the one-channel optical potential that reproduce the same elastic

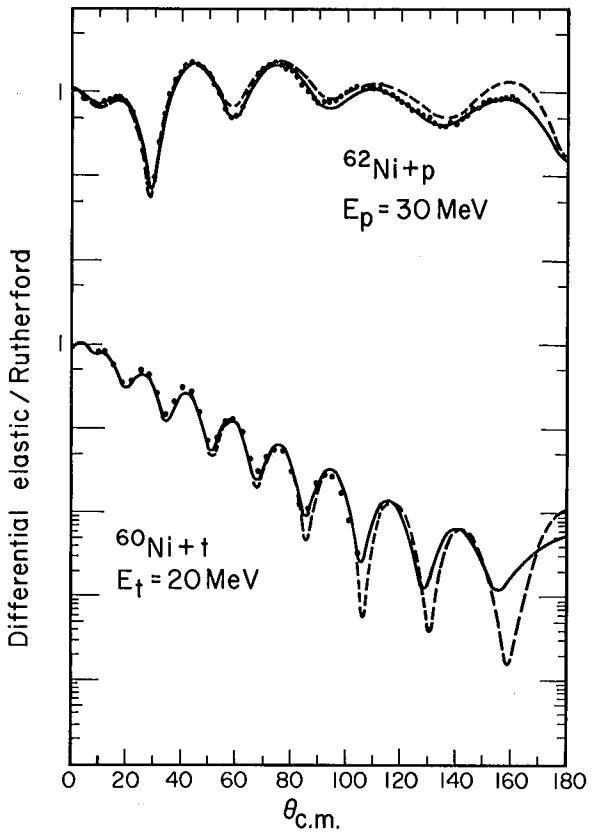

Fig. 1. Elastic cross sections are shown. The solid line represents two calculations: (1) a coupled-channel one involving all the states described previously and using the optical parameters labeled C. C. in Table I; and (2) a usual one-channel optical-model calculation using adjusted parameters labeled "elastic" in Table I which reproduce the same elastic cross section as the coupled-channel calculation. The dashed lines are also one-channel optical-model calculations but use the same parameters as the coupled-channel calculation. The differences show the effect of coupling to other states. Proton data is for ^{60}Ni (Ref. 7) and triton data for ^{62}Ni (Ref. 8).
(XBL695-2749)

cross section as obtained in the coupled-channel calculation. These are needed for comparison of our results for the (p, t) reaction with those predicted by the usual DWBA. The solid line in Fig. 1 represents both these calculations. The dashed line corresponds to the usual one-channel optical potential using the same parameters as in the coupled-channel calculation. The difference shows the effect of the coupling of other channels of which the collective 2^+ is the most important. Figure 1 illustrates the importance of backward-angle scattering for determining the effect of the coupling on the optical-model parameters.

In the calculations reported here, we did not include a spin-orbit term in the triton optical potential. The strength of this term is expected, on theoretical grounds, to be about one third that of the nucleon spin-orbit strength. We did include it in several calculations, but its effect on the (p, t) reaction was very small.

The strength of the inelastic transition to the 2^+ collective state in both target and final nucleus is vital in our analysis because it is the parent of the two-phonon states. Again we have to rely on an extrapolation from other situations, but this is quite adequate for our purposes. For tritons,[10] the cross section to the 2^+ state has been measured in ^{64}Ni at 20 MeV. For protons,[11] we do not have data at the appropriate energy, but the reaction has been studied at 18 and 40 MeV, and we use the strength of the direct interaction obtained there. We are able to handle a direct interaction of the form

$$V(r) = [V_0 + V_1(\sigma_1 \cdot \sigma_2)]e^{-(r/r_0)^2} . \qquad (5)$$

However, since the V_1 part is so unimportant for the excitation of the collective state, we have set it equal to zero in these calculations. The remaining two parameters V_0 and r_0 for protons and tritons are shown in Table II. The range parameter for tritons bears the kind of relationship to that for protons as described for other composite particles elsewhere.[12] It is larger because of the finite extension of the triton.

The strength of the interaction causing the (p, t) reaction is unimportant in our calculations because we treat the reaction in first order. Thus all our calculated (p, t) cross sections scale as the square of this strength. However, we belive our arbitrary units are approximately millibarns.

Finally the single-particle bound-state wave functions, in terms of which the nuclear wave functions are expressed, are harmonic-oscillator functions having a constant $\nu = 0.25\ F^{-2}$ $\left(\psi \sim e^{-\frac{1}{2}\nu r^2}\right)$. We confirmed (see later) that as concerns an evalulation of the role of inelastic processes, correction of the asymptotic behavior of the oscillator functions is not necessary.

The complete calculation for the ^{62}Ni(p, t) ^{60}Ni reaction at 30 MeV is shown in Fig. 2. All the inelastic couplings between the eight

Table I. Optical-model parameters. The "elastic" ones yield the same elastic cross section as obtained in the coupled-channel calculation which uses the C. C. parameters.

	V	W	W_D	r_V	r_W	r_C	a_V	a_W
				triton				
C. C.	-158.35	-22.9	1.094	1.22	1.506	1.25	0.695	0.8
elastic	-149.04	-27.	4.313	1.274	1.576	1.25	0.6559	0.8828
				proton				
C. C.	-54.	-2.	-5.2	1.09	1.3	1.2	0.772	0.64
elastic	-54.087	-3.239	-5.367	1.099	1.295	1.2	0.772	0.601

V_{so}	r_{so}	a_{so}
-5.74	1.022	0.688

Table II. Parameters of the direct interaction causing inelastic transitions [see Eq. (5)].

	V_0	r_0
Proton	-55	1.85
Triton	-70	2.3

states in each nucleus that are implied by their microscopic structure are included to all orders.[13] All the particle-transfer couplings leading from all target states to all final states are included with the strengths prescribed by their structure.[5,14] The features that determine the strength of this coupling between a pair of states are (1) the fraction of parentage of the state in the heavier nucleus that is based on the other nucleus, and (2) the degree to which the extra pair of neutrons are correlated in the way they exist in the triton. As expected, the ground and collective 2^+ states have the largest cross sections. Two very surprising facts can be learned from Fig. 2. First, the two-phonon states, which, as discussed above, can be excited only through higher-order processes, nonetheless have cross sections just as strong as the other noncollective states, running about one tenth that of the collective 2^+ state. Second, the angular distributions are largely characterized by the multipolarity of the transition, independent of whether the state was produced directly, or through an intermediate state. The polarizations of outgoing tritons from this reaction are shown in Fig. 3 and, like the angular distributions, are characterized by the multipolarity of the overall transition. Thus we find that under the typical circumstances of this calculation there is nothing about the angular distributions or polarizations that can be used to distinguish multiple processes from direct ones, and the probability of the higher-order transitions is as large as typical noncollective ones.

In Fig. 2 we also compare a DWBA calculation of those states that can be produced in a single step with the full calculation. The DWBA cross sections were computed according to the usual prescription. For this comparison, that means that the optical parameters were chosen to reproduce the same proton and triton elastic cross sections as emerged from the coupled-channel calculation as shown in Fig. 1. One sees in Fig. 2 discrepancies of up to a factor of 5 in absolute cross sections and up to nearly 2 in relative cross sections. The DWBA in every case underestimates cross sections. Thus, even for a nucleus no more strongly collective than nickel, application of the usual DWBA leads to large errors in relative cross sections. The higher-order processes do, in fact, play a very important role. This is shown in more detail in Fig. 4, where the cross sections of individual paths leading to the final states are shown. One sees that the direct route, if it alone were present, accounts for about half the cross section of the collective 2^+ state. The other major contributions are the transition through the collective 2^+ state of the target (not shown), and through the ground state of the final nucleus. Although the cross section of this latter process is only about 1/6 that of the direct, its amplitude is about 40% of the direct process. Of course the cross section for exciting a state which can be reached in several distinct ways is obtained by squaring the sum of the amplitudes for the individual ways.

Concerning the noncollective two-quasiparticle states (0_2, 2_2, 4_1) shown in Fig. 2, their main parent is the ground state, and they are produced almost exclusively through

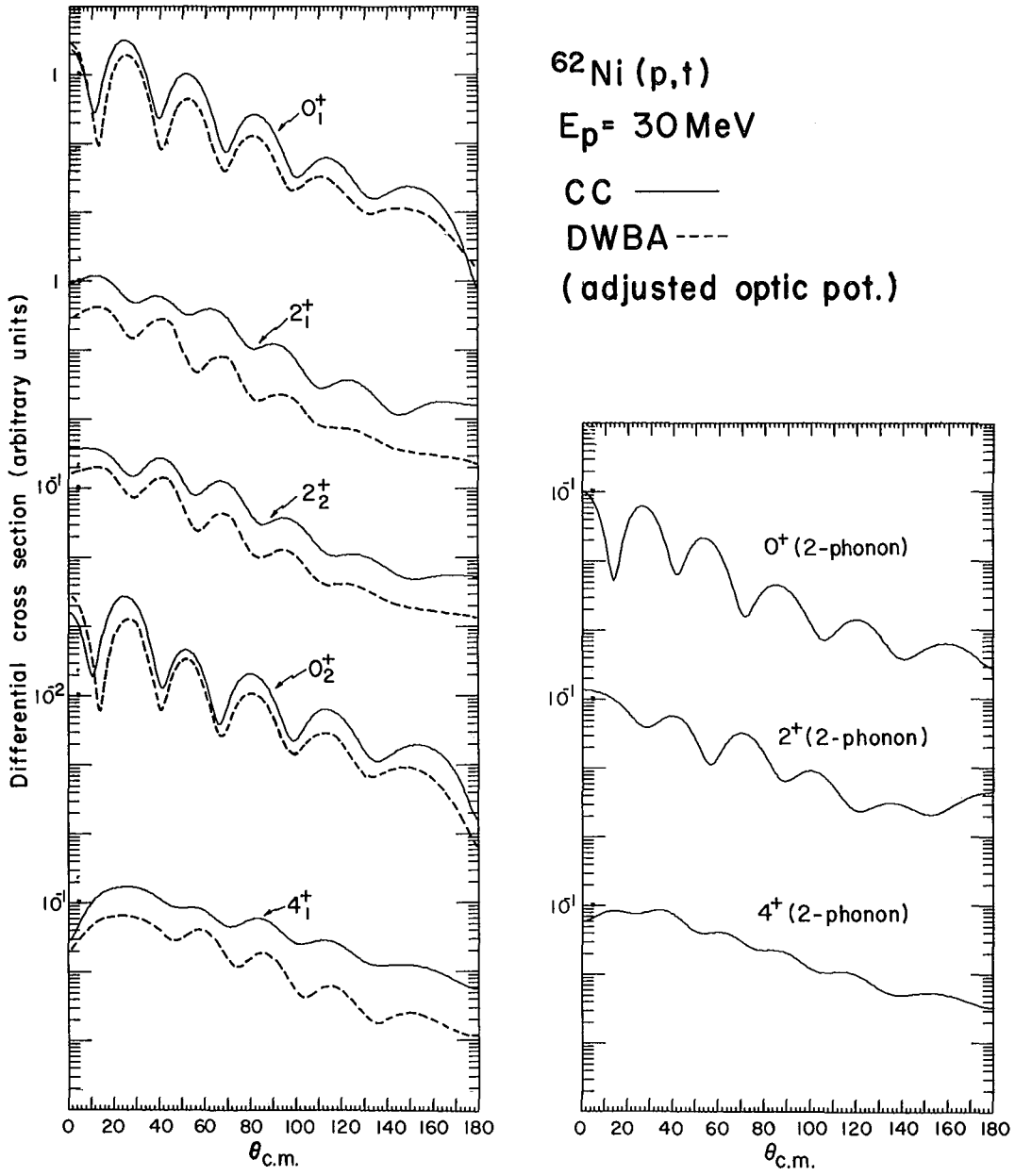

Fig. 2. Calculated cross sections of the ^{62}Ni(p,t) reaction to ground and two-quasiparticle states are shown on the left, and "microscopic" two-phonon states on the right. Solid lines include multiple-step processes. Optical parameters are labeled C. C. in Table I. Microscopic structure of the states was described previously. Dashed lines show DWBA calculations, using optical parameters, labeled "elastic" in Table I, which reproduce the same triton and proton elastic cross sections as the coupled-channel calculation.

(XBL704-2712)

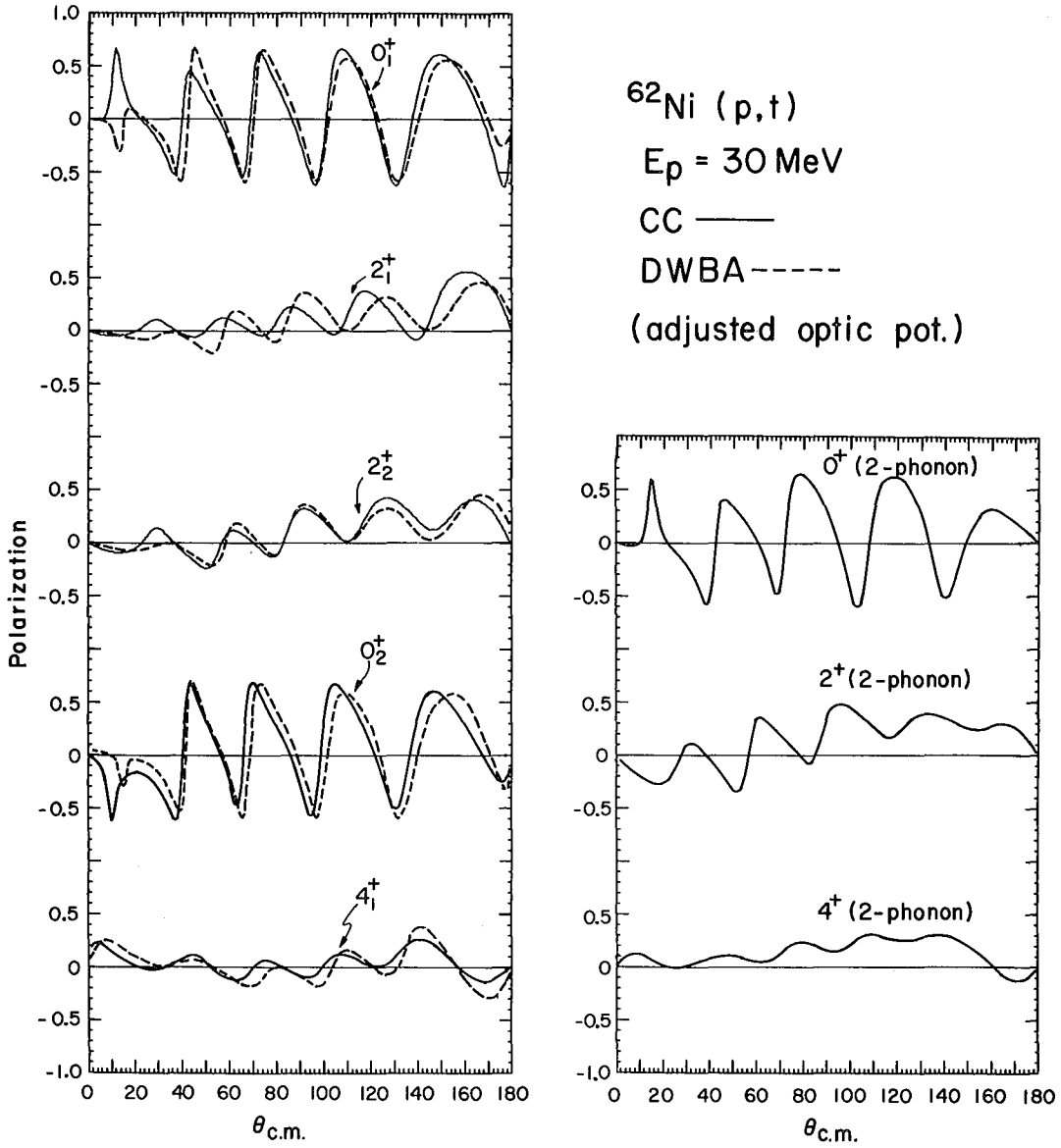

Fig. 3. Polarization of outgoing tritons of the ^{62}Ni-(p,t) reaction corresponding to the cross sections of Fig. 2.
(XBL704-2717)

the direct transition from the ground state. Even so, we see that the DWBA underestimates their cross sections. The cause for this, as discussed in the introduction, is the modification of the wave function in the elastic channel due to coupling to the 2^+ collective state. This is an important effect even in such moderately collective nuclei as these.

If it is true that in a nucleus as mildly collective as nickel the DWBA underestimates cross sections by as much as a factor of 5, and fails in relative cross sections by a factor of 2 or so, one may ask how weak must the collectivity of the intermediate state in the two-step process be before the errors are suitably reduced. In Fig. 5 we show a calculation analogous to that of Fig. 2 except that the strength of the direct reaction causing inelastic transitions has been reduced by $\sqrt{2}$. This cuts the inelastic cross section to the collective state by about 2, so that two-step processes are correspondingly weaker. The DWBA calculation was again carried out by

adjusting the optical parameters so that the elastic cross sections of the coupled-channel calculations for both protons and tritons were reproduced. The DWBA still underestimates the (p,t) cross sections but does considerably better than for the case of stronger collectivity in Fig. 2. The relative cross sections are, however, in very good agreement with the full calculation, so that we may conclude that if the collectivity of an intermediate state in a two-step (p,t) reaction is about half as strong as it is in nickel, then the DWBA works very well for those states that have the target ground state as their main parent. The cross sections to the two-phonon states, which can be produced only by multiple processes, are reduced by almost a factor of 2. In other words they scale, as expected, with the collectivity of the parent intermediate state.

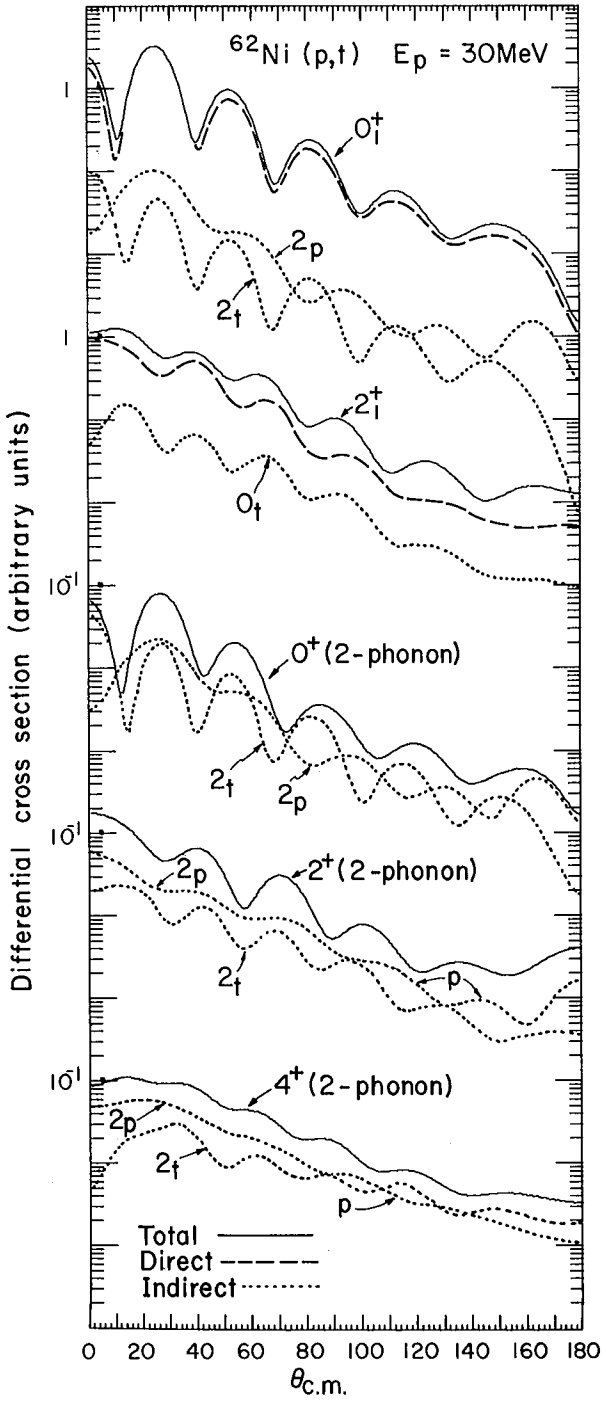

To summarize, we have studied two-step processes in (p,t) reactions in a model which contains some states (a triplet) which have as their parent a state which has an enhanced inelastic transition from the ground state, namely the collective 2^+ state. We found that although these states can be produced only indirectly by two-step transitions through the parent state, their cross sections are comparable in magnitude with other noncollective states which can be produced directly. This finding holds for a nucleus, namely nickel, in which the collectivity of the intermediate state is only moderate. The two-step processes scale as the strength of the inelastic transition from the ground to the intermediate parent state. Therefore, since most nuclei are more collective than nickel, our result probably indicates a widespread phenomenon. Moreover, both angular distributions and polarizations are characterized mainly by the multipolarity of the overall transition and not by the multiplicity of the reaction process. The two-step processes therefore do not have a special fingerprint, at least not under the typical conditions of our calculation.

Presumably, in real nuclei, ideal two-phonon states such as we studied do not exist. Some of their character persists, since the radiative selection rules hold approximately, but they most likely possess admixtures in their wave function other than the two-phonon

Fig. 4. Dashed lines represent cross sections for ground and collective 2^+ states corresponding to the direct (p,t) transition from the ground to final state, if it alone were possible, while dotted lines represent two-step processes going through the collective 2^+ state in either the proton or triton system or through the ground state of the triton system as marked by subscripts. The idealized two-phonon states do not have a direct transition, as explained previously. Solid lines represent cross sections in which all inelastic and transfer processes allowed by the structure of the states take place. Amplitudes of the individual processes add. (XBL704-2713)

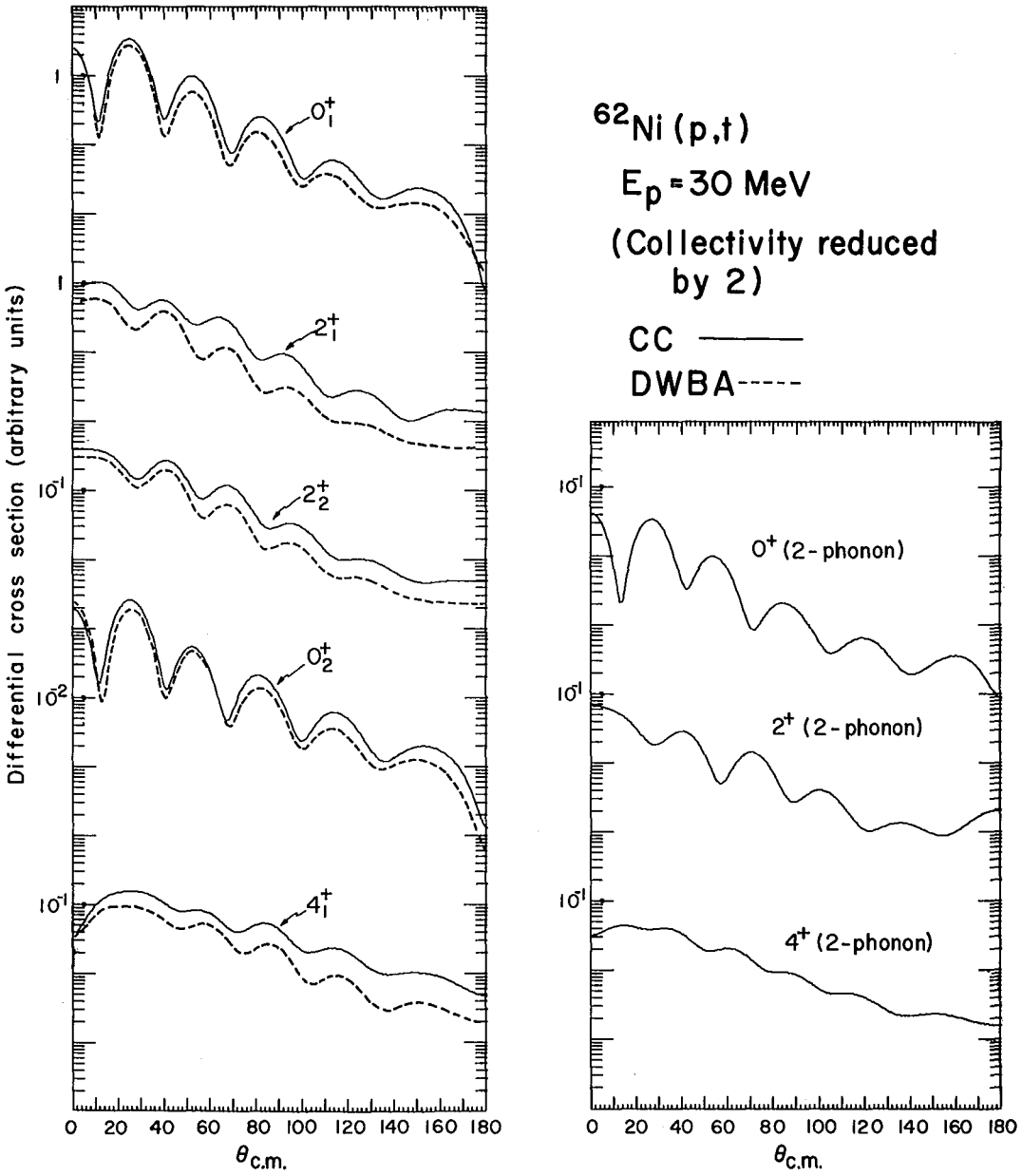

Fig. 5. The same calculation as Fig. 2 except that the strength of the interaction causing inelastic transitions is reduced by $\sqrt{2}$. For our purposes this corresponds to a collectivity of the 2_1^+ state of about $\frac{1}{2}$ that of Fig. 2.

(XBL704-2715)

component of Eq. (3). Conversely, other near-lying states share the two-phonon character. Suppose that a noncollective state has a 10% admixture of two-phonon character. Previously one would have ignored this component and calculated the cross section to this state on the basis of those components that can be produced directly. Let us denote by F the amplitude that can be produced directly. Then in this approximation the cross section is F^2. However, since we now know that the two-phonon state is excited as strongly as a typical noncollective state and that its angular distribution is nearly the same, then corresponding to the 10% admixture we should add $F/\sqrt{10}$ to the above amplitude. The phase could vary anywhere from -1 to +1 with the result that the cross section for the admixed state could be anywhere from 0.4 to 1.6 times the result based on the neglect of the 10% two-phonon admixture.

Concerning those states which are produced dominantly by the direct transition from the ground, the DWBA does underestimate their cross sections also, and seriously. This is due to changes in the wave function in the elastic channel induced by inelastic coupling to the collective 2^+ state. We see no reason to believe that this effect is exclusive to the (p,t) reaction and suggest therefore that the DWBA also underestimates (d,p) cross sections more or less, depending on the degree of collectivity. Thus it appears that single-particle spectroscopic factors may be overestimated in the usual DWBA analysis.

Although our findings give cause for pessimism, we do point out that the so-called source-term method that we have used to include higher-order processes in particle transfer reactions does provide a feasible means of incorporating these previously neglected processes. Moreover, if one suspects that special parentage relations exist among certain states, one can now explicitly compute the results of such relations. Two interesting examples have already been studied at this laboratory.[2]

Footnotes and References

†Condensed from Phys. Rev. C 2, 1260 (1970).

*Present address: Wright Nuclear Structure Laboratory, Yale University, New Haven, Connecticut 06520.

1. See, e.g., N. K. Glendenning, Ann. Rev. Nucl. Sci. 13, 191 (1963), and references therein.

2. R. J. Ascuitto and B. Sørensen, unpublished work performed at Lawrence Radiation Laboratory.

3. G. R. Satchler, Nucl. Phys. 55, 1 (1964).

4. R. J. Ascuitto and N. K. Glendenning, Phys. Rev. 181, 1396 (1969).

5. N. K. Glendenning, in Proceedings of the International Conference on Properties of Nuclear States, Montréal, Canada, 1969, edited by M. Harvey et al. (Presses de l'Université de Montréal, Montréal, Canada 1969); R. J. Ascuitto and N. K. Glendenning, Phys. Rev. C 2, 415 (1970).

6. R. Arvieu and M. Veneroni, Compt. Rend. 250, 922, 2155 (1960); 252, 670 (1960); R. Arvieu, Ann. Phys. (Paris) 8, 407 (1963); R. Arvieu, E. Salusti, and M. Veneroni, Phys. Letters 8, 334 (1964).

7. The proton data are for ^{60}Ni at 30 MeV from B. W. Ridley and J. F. Turner, Nucl. Phys. 58, 497 (1964).

8. The triton data are for ^{62}Ni at 20 MeV from J. C. Hafele, E. R. Flynn, and A. G. Blair, Phys. Rev. 155, 1238 (1967).

9. The Oak Ridge parametrization of the optical potential is adopted, cf. F. G. Perey, Phys. Rev. 131, 745 (1963).

10. E. R. Flynn and collaborators, Los Alamos, private communcation.

11. The analysis of the 40-MeV data is unpublished, while for the 18-MeV analysis see N. K. Glendenning, in Nuclear Structure and Nuclear Reaction, Proceedings of the International School of Physics "Enrico Fermi," Course XL, 1967, edited by M. Jean (Academic Press Inc., New York, 1969).

12. Cf. Appendix of N. K. Glendenning and M. Veneroni, Phys. Rev. 114, 839 (1966), and V. A. Madsen, Nucl. Phys. 80, 177 (1966).

13. N. K. Glendenning, Nucl. Phys. A117, 49 (1968), and Ref. 11.

14. N. K. Glendenning, Phys. Rev. 137, B102 (1965).

Confirmation of Strong Second-Order Processes in (p,t) Reactions on Deformed Nuclei†

R. J. Ascuitto,* Norman K. Glendenning and Bent Sorenson‡

Direct nuclear reactions are thought usually to proceed in a single step from the ground state of the target to the final state. However, in our earlier investigations[1] on spherical nuclei it was found that it was important to include higher order processes involving the production of an intermediate state, either before or after the transfer reaction, and involving an inelastic scattering event to complete the transition to the final state. No firm evidence one way or the other can be developed for spherical nuclei at this time. However, recent (p,t) experiments performed at Minnesota[2] on rotational nuclei have stimulated our interest in investigating these questions where the inelastic cross sections are strongly enhanced, compared with the moderate collectivity characteristic of the vibrational nuclei.

We adopt the Bohr-Mottelson adiabatic hypothesis for the rotational wave functions of the ground-band members[3]

$$|JM\rangle = \left(\frac{2J+1}{8\pi^2}\right)^{1/2} D^J_{MO} X_o. \qquad (1)$$

We describe the internal wave function, X_o, as a BCS state[4] constructed from 20 levels around the Fermi surface. A pairing force of such a strength as to yield a gap parameter estimated by the Nilsson-Prior formula[5] was employed. The single-particle wave functions from which the BCS state is constructed are eigenfunctions of a deformed Woods-Saxon potential. These eigenfunctions were obtained on a harmonic-oscillator basis comprising 15 oscillator shells ($0 \leq 2n + \ell \leq 15$). This large basis ensures a good representation of the single-particle radial wave functions and the use of the oscillator basis facilitates the calculation of the projected center-of-mass wave function of the transferred neutron pair.[6] The nuclear wave functions being thus defined, the (p,t) transitions between various rotational states of (A) and (A+2) are determined by the parentage factors[6,7]

$$\beta_{(ab)LSJ}(J_p, J_t) \equiv [(2J_p+1)(1+\delta_{ab})]^{-1/2} \langle J_p || [d_a^+ d_b^+]^{Lab}_{LSJ} || J_t \rangle$$

$$= (-)^J C^{J_p\ J\ J_t}_{o\ o\ o} \langle X_o(A+2) | [d_a^+ d_b^+]_{LSJ}^{o} | X_o(A) \rangle . \qquad (2)$$

Here "a" denotes single-particle quantum numbers and d_a^+ creates a particle in such a state. In the first line the operators are expressed in the laboratory frame of axis, and in the second line, in the intrinsic frame. Note the factorization of the parentage amplitude into a Clebsch-Gordan coefficient depending on the spin of the states, and a matrix element depending only on the multipolarity and the intrinsic structure of the nuclear states. This means that all (p,t) transitions are proportional to the direct transition of the corresponding multipole (i.e., the form factor for the 4-pole transition connecting $2^+_p \rightarrow 2^+_t$ is proportional to the $0^+_p \rightarrow 4^+_t$).

Inelastic transitions in deformed nuclei can be very accurately described in terms of a deformed optical potential.[8] The nucleus is treated as a rigid rotor that can be set into rotation by interaction of the free particle with the deformed field. The optical potential in this case is an effective interaction which replaces an explicit treatment of intrinsic nuclear excitations, but the rotations are treated explicitly through solution of the appropriate system of coupled equations.[9] As discussed in detail elsewhere, the appropriate optical potential parameters will be those of nearby spherical nuclei.[9,10] For protons we use the average potential of Becchetti and Greenlees,[11] since only spherical nuclei were used in that analysis. For tritons we extrapolated the average potential of Flynn et al.,[12] with an assumed energy dependence of $dV/dE = -0.33$ and $dW/dE = 0$. These optical potentials together with the neutron potential for the bound states[13] are given in Table I.

The shape of deformed nuclei in the rare earth region were determined very accurately through a careful analysis of alpha inelastic scattering[8] and that information is used here. Thus we have left ourselves with no adjustable parameters save a single normalization constant that scales all reaction cross sections. (No adjustments in relative cross sections are allowed.)

The method used to incorporate the various indirect reactions with the direct single-step transition from the ground state is called the source term method and is described elsewhere.[1,7,15] The results of the complete calculation are compared in Fig. 1 with data of the Minnesota group.[2] The agreement is very good especially for the 0^+ and 2^+ states. This agreement would not be surprising inasmuch as the conventional DWBA treatment of the (p, t) reaction is usually successful. However, for these deformed nuclei, DWBA calculations are shown in Fig. 2. The same normalization was used as for Fig. 1. Now we see that whereas the 0^+ and 4^+ angular distributions are in fair agreement with experiment, the 2^+ is in complete disagreement. If these calculations were renormalized to the ground state, the cross sections of the 2^+ state would still be much too large. Evidently for this state, indirect processes are very large and interfere destructively with the direct amplitude so as to alter the angular distribution shown in Fig. 2 and reduce the cross section to bring about the agreement shown in Fig. 1. Indeed this is borne

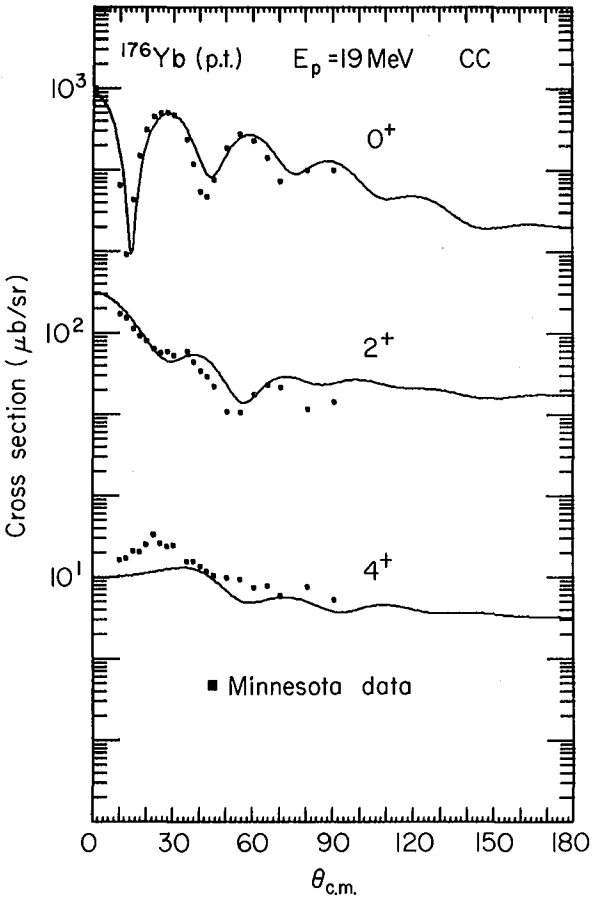

Fig. 1. Cross sections for members of the ground-state rotational band in ^{174}Yb produced by 19 MeV protons in the (p, t) reaction. Calculations include the indirect modes of excitation due to inelastic excitation of rotational states in both the target and final nucleus, as well as the direct transition. The only adjusted parameter was an overall normalization which does not alter the computed relative cross sections. The experimental data is from the Minnesota Group (see Ref. 2).
(XBL7010-4069)

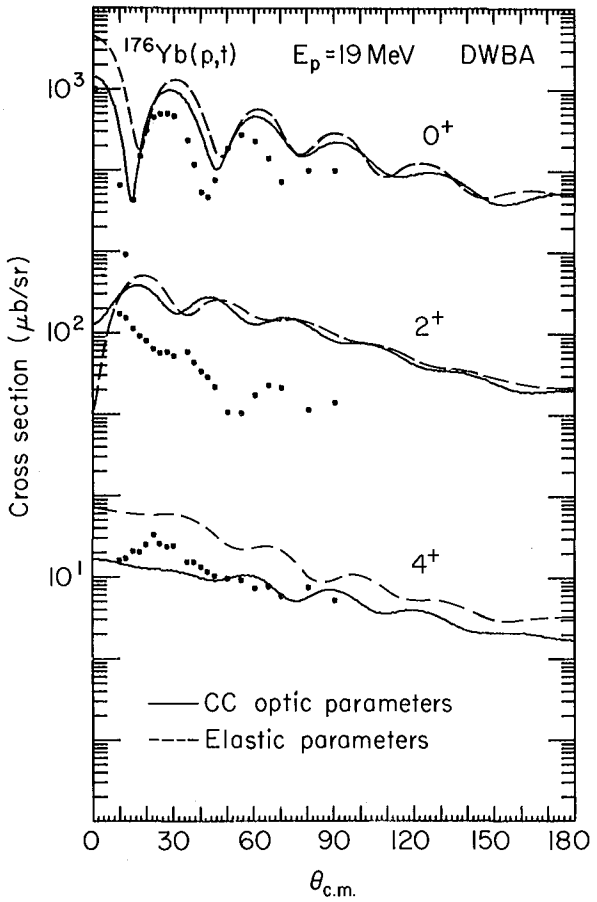

Fig. 2. Two DWBA calculations without inelastic processes are compared with experiment using the same normalization as Fig. 1. Note that the relative cross sections are in disagreement and the 2^+ angular distribution does not resemble experiment. The solid curves correspond to the same optical model parameters that were used in the coupled-channel calculation of Fig. 1, while the dashed curves correspond to adjusted parameters that reproduce the proton and triton elastic scattering obtained in the coupled-channel calculation, and therefore correspond to the conventional DWBA.
(XBL7010-4068)

Table I. Potential parameters. Those labeled "C. C." were used in the coupled-channel calculation and are derived from Refs. 11 and 12. Those labeled "elastic" yield the same elastic cross sections obtained in the coupled-channel calculation.

	V	W	W_D	r_v	r_w	r_c	a_v	a_w	V_s	r_s	a_s
						Proton					
C. C.	-57.83	-1.48	- 9.5	1.17	1.32	1.125	0.75	0.653	-6.2	1.01	0.75
elastic	-54.65	-1.48	-10.4	1.2	1.27	1.125	0.698	0.893	-6.2	1.01	0.75
						Triton					
C. C.	-169.	-12.6	0	1.16	1.498	1.125	0.752	0.817	0		
elastic	-248.	-13.6	0	0.938	1.346	1.125	0.846	1.141	0		
						Neutron					
bound	-46.4			1.241			0.66		-8.23	1.241	0.66

out by the calculations shown in Fig. 3. Cross sections corresponding to the three most important amplitudes feeding the 2^+ state are shown. It can be seen that the direct amplitude is not much stronger than the indirect amplitudes going through the target 2^+ state and the residual nucleus ground state.

We are accustomed to thinking that second-order direct reactions are considerably weaker than allowed first-order ones, if not entirely negligible. Can these unexpected results be made plausible? The answer is yes. First it is necessary to consider the meaning of the transfer of a pair of nucleons from one rotational state to the other. The cross section for the direct pickup of a pair of neutrons from the ground state to produce the rotational state J^+ measures the probability that all of the rotational motion is possessed by the pair. (This statement is more transparent for the stripping reaction.) This probability clearly ought to decrease with increasing angular momentum, and indeed it does as can be seen by the decreasing cross sections for higher rotational levels in Fig. 2. Now the reaction branch of the two indirect routes in Fig. 3 can go by the J = 0 transition, whereas the direct one has to be J = 2. Of course, the indirect routes have at least two branches, the other consisting of an inelastic transition. But these are enhanced in deformed nuclei. Moreover the crucial point is that the probability for an indirect transition is not given by the disjoint product of the probabilities for the individual branches, but by the conditional probability that one step having been taken, the second is more probable since the free particle is already in the vicinity of the nucleus.

We summarize our results. The cross

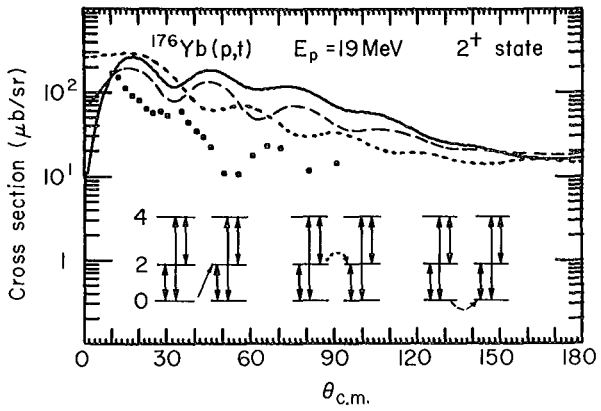

Fig. 3. Cross sections for production of the 2^+ rotational state corresponding to the individual transfer processes shown. The solid curve is the direct processes while the other two proceed through an intermediate level, the 2^+ in the target, and the ground state of the final nucleus, respectively. Note that all three processes acting alone overestimate the observed cross section, relative to the ground-state cross section. It is the interference among these various modes which produces the agreement with experiment shown in Fig. 1. (XBL7010-4067)

section for the direct two-nucleon pickup leading to the ground state has the correct angular dependence, but that for the 2^+ rotational state is much too large relative to the ground state and has a grossly incorrect angular dependence. However, when the amplitudes for indirect modes of producing the 2^+ are allowed to interfere with the direct, the resulting cross section is much reduced and strongly altered in angular dependence. This

alteration comes about because each of the three most important amplitudes has a different angular shape (see Fig. 3), and it is magnified since they interfere destructively (which we know since the resultant cross section, Fig. 1, is smaller than that due to any one of these three processes). That the destructive interference between three such different amplitudes results in agreement with experiment, we consider to be very hard evidence for the accuracy of each of them. To our knowledge this is the firmest confirmation of second-order direct reactions. In this instance they are almost as strong as the allowed first-order reaction.

We are very much indebted to N. M. Hintz for an early communication which stimulated our interest in the (p,t) reaction on deformed nuclei.

Footnotes and References

†Condensed from UCRL-20402, October 1970; to be published in Phys. Rev. Letters.

*Present address: Wright Nuclear Structure Laboratory, Yale University, New Haven, Connecticut 06520.

‡Present address: The Niels Bohr Institute, University of Copenhagen, Denmark.

1. R. J. Ascuitto and N. K. Glendenning, Phys. Rev. C 2, 1260 (1970); N. K. Glendenning, in Proceedings International Conference on Properties of Nuclear States, ed. by M. Harvey (University of Montreal Press, Montreal, 1969).

2. M. Oothoudt, N. M. Hintz, and P. Vedelsby, Phys. Letters 32B 270 (1970); M. Oothoudt, private communication, University of Minnesota.

3. A. Bohr and B R. Mottelson, Dan. Mat. Fys. Medd. 27, No. 16 (1953).

4. S. T. Belyaev, Mat. Fys. Medd. Dan. Vid. Selsk. 31, No. 11 (1959).

5. S. G. Nilsson and O. Prior, Mat. Fys. Medd. Dan. Vid. Selsk. 32, No. 16 (1961) see Eq. 44.

6. N. K. Glendenning, Phys. Rev. 137B, 102 (1965).

7. R. J. Ascuitto and N. K. Glendenning, Phys. Rev. C 2, 415 (1970).

8. D. L. Hendrie, N. K. Glendenning, B. G. Harvey, D. N. Jarvis, H. H. Duhm, J. Savdinos, and J. Mahoney, Phys. Letters 26B, 127 (1968).

9. N. K. Glendenning, in Proceedings International School of Physics, "Enrico Fermi" Course XL, 1967, ed. by M. Jean (Academic Press, New York, 1969).

10. N. K. Glendenning, D. L. Hendrie, and O. N. Jarvis, Phys. Letters 26B, 131 (1968).

11. F. D. Becchetti, Jr. and G. W. Greenlees, Phys. Rev. 182, 1190 (1969), see Eq. 8.

12. E. R. Flynn, D. D. Armstrong, J. G. Beery, and A. G. Blair, Phys. Rev. 182, 1113 (1969).

13. The neutron potential has the geometry suggested by Myers (Ref. 14), but the well depths are adjusted slightly so that $V r_o^2$ has the value used in the study of lead by J. Blomqvist and S. Wahlborn, Arkiv für Fysik 16, 545 (1960).

14. W. D. Myers, Nucl. Phys. A145, 387 (1970).

15. R. J. Ascuitto and N. K. Glendenning, Phys. Rev. 181, 1396 (1969).

The Microscopic Analysis of a Charge-Exchange Reaction: ^{42}Ca(h,t)^{42}Sc

Richard Schaeffer

The microscopic description of the (h, t) reaction is used[1] as a spectroscopic tool. First, an effective interaction is derived and its parameters are deduced from some simple transitions. The transition operator has very different properties depending on whether the transition is of natural parity or not. For natural parity states, a pure central force is able to reproduce the observed angular distributions and the contribution of the tensor interaction is seen to be small. The strength of the force, however, has to be adjusted for each spin transfer J, but is independent[1,2] of the peculiar nucleus considered (Fig. 1). For unnatural parity states, two types of transitions have to be considered: Type 1 transitions, like $f_{7/2} \rightarrow f_{7/2}$ (and more generally from an orbital $j = \ell + 1/2$ to $\ell' \pm 1/2$),

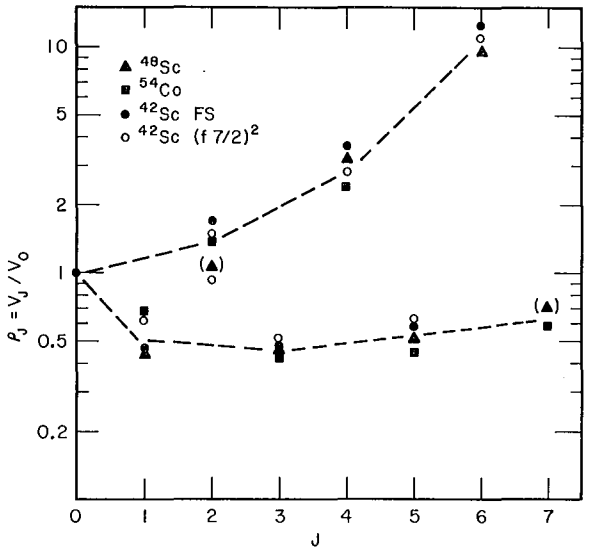

Fig. 1. V_J is the strength needed in order to fit the experimental cross-section normalization relative to the transition $0^+ \rightarrow J^+$ as a function of the angular momentum transfer J. The ratio $\rho_J = V_J/V_0$ is considered for various nuclei and is shown to be typical for each momentum transfer J. The fits are made to the states that contain most of the $f_{7/2}^2$ (or $f_{7/2}\, f_{7/2}^{-1}$, or $f_{7/2}^{-2}$) strength. For ^{42}Sc, the states have been described either by a pure $f_{7/2}^2$ configuration or by the wave functions of Flowers and Skouras[7] (FS). For the 2^+ of ^{42}Sc, the lower value is obtained when considering only the lowest 2^+ state, and the higher when summing the experimental cross sections of the two lowest 2^+ states. The parentheses indicate that the 2^+ and 7^+ states of ^{48}Sc were an unresolved doublet. (XBL707-3275)

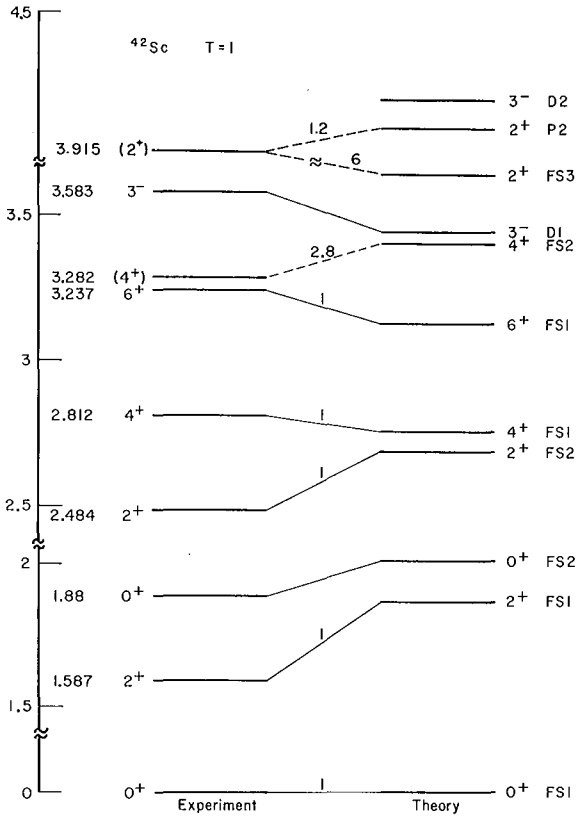

Fig. 2. Level scheme of the T = 1 states of ^{42}Sc. The first column refers to the (h, t) experiment and the second to the theoretical predictions of Flowers and Skouras[7] (FS), of Pülhofer[6] (P), and Dieperink et al.[8] (D). The lines between the levels indicate the various possible matchings of theoretical and experimental levels, and the numbers refer to the normalization factor σ_{exp}/σ_{th} between experimental and theoretical cross sections when the strength of the force is taken from Fig. 1. (XBL707-3276)

where the tensor force is very strong[1,3] and ensures that the angular momentum transfer L = J + 1 dominates in the transition; and Type 2 transitions, like $d_{3/2} \rightarrow d_{3/2}$ (and more generally from $j = \ell - 1/2$ to $j' = \ell - 1/2$), where the central force predicts a dominating L = J + 1 transfer and the tensor force is weak. Different force parameters are used for Type 1 and Type 2 transitions, and it is not yet known[4] if a unified description of both types of transitions can be made within the central + tensor force model.

The ^{42}Ca(h, t)^{42}Sc data[5] are analyzed using the previously defined transition operator and various nuclear models[6,7,8] for the ^{47}Sc wave functions. The simplest states in ^{42}Sc are built with two particles in the $f_{7/2}$ shell. The (h, t) reaction can, however, hardly decide among the different nuclear models for the $f_{7/2}^2$ states, provided one sums up the $(f_{7/2}^2)^{2+}$ strength, which is obviously split over two states by 4p-2h admixtures. The model of Flowers and Skouras[7] is the only one which includes such admixtures. It reproduces very nicely the splitting ratio of the $(f_{7/2}^2)^{2+}$ strength, and generally gives a very good agreement for the T = 1 angular distributions and cross-section strengths[1] (Fig. 2). Moreover, this model[7] for the nuclear structure of ^{42}Sc is absolutely necessary in order to account for the large number of states seen in the T = 0 spectrum (Fig. 3). The magnitudes of the cross sections are however, in this case, only approximately reproduced. A discussion of the uncertainty in the force parameters

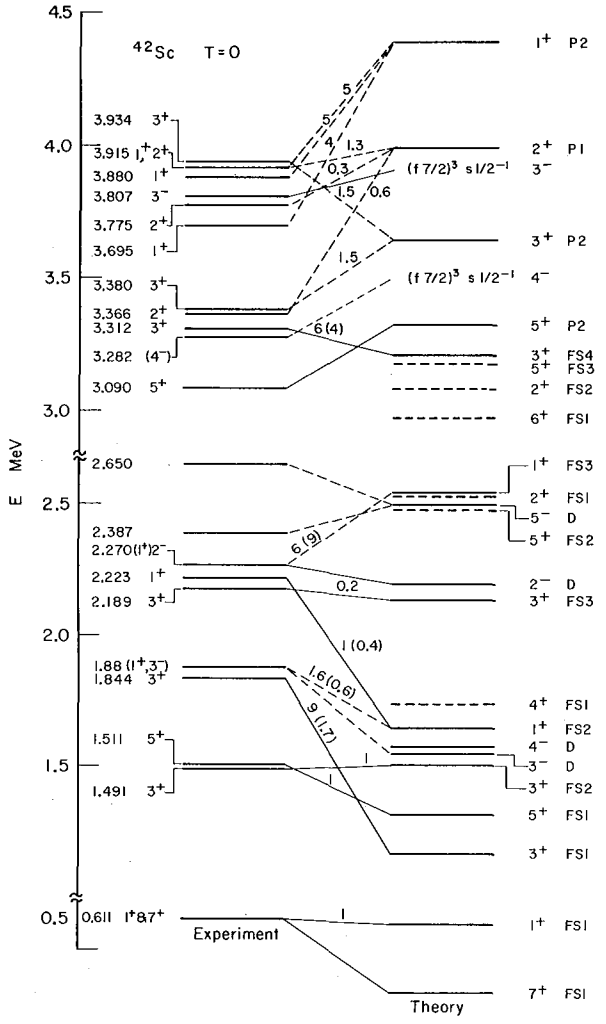

Fig. 3. Level scheme for the T = 0 states of ^{42}Sc (see Fig. 2). (XBL707-3277)

shows that this might be due to the bound-state wave function rather than to the assumed transition operator. For instance, the two lowest 3^+, T = 0 states as predicted by Flowers and Skouras[7] (who are, on the other hand, the only ones to predict two states) should be inverted.

A discussion is given for the excitation of negative parity states in ^{42}Sc by the (h, t) reaction. As for the $f_{7/2}{}^2$ states, some negative parity states are expected to have a simple shell-model structure--for instance, $f_{7/2}{}^3\, d_{3/2}{}^{-1}$ or $f_{7/2}{}^3\, s_{1/2}{}^{-1}$--and should be seen according to this picture. There is, however, no unambiguous evidence in the T = 0 spectrum for these states to be populated as expected from the ^{40}Ca(h, t)^{40}Sc experiment and from their assumed structure. The lowest T = 1, 3^- state has probably been identified. Its weak cross section has been explained in terms of the mixing of various 3p-1h components. The same explanation might hold for the inhibition of the T = 0 negative parity states and, more generally, of cross-shell transitions.

References

1. R. Schaeffer, Lawrence Radiation Laboratory Report UCRL-19551, presented at Argonne (^{3}He, t) Symposium, Argonne Physics Division Informal Report PHY-1970A, January 1970; R. Schaeffer, UCRL-19927, to be published in Nucl. Phys.

2. P. Kossanyi-Demay, P. Roussel, H. Faraggi, and R. Schaeffer, Nucl. Phys. A148, 181 (1970).

3. E. Rost and P. D. Kunz, Phys. Letters 30B, 231 (1969).

4. G. Bruge, M. S. Zisman, A. D. Bacher, and R. Schaeffer, this report.

5. R. Sherr, T. S. Bhatia, D. Cline, J. J. Schwartz, to be published.

6. F. Pühlhofer, Nucl. Phys. A116, 516 (1968).

7. B. M. Flowers and L. D. Skouras, Nucl. Phys. A136, 353 (1969).

8. A. E. L. Dieperink and P. J. Brussaard, Nucl. Phys. A106, 177 (1968).

Study of the $^{40}Ca(h,t)^{40}Sc$ Reaction at 30.2 MeV †

J. M Loiseaux,* P. Kossanyi-Demay,‡ Ha Duc Long,‡
A. Chaumeaux,‡ H. Faraggi,‡ G. Bruge, and R. Schaeffer

In the last few years, the (h, t) reaction has been systematically used to investigate odd-odd nuclei, especially near the closed shells. In most cases, the members of low-lying spin multiplets, corresponding to the lowest shell-model configurations in the residual nucleus, have been identified using very simple empirical rules[1] for spin assignments. In these experiments, the in-shell transitions were mostly studied. It was, however, rather difficult to study the higher lying levels corresponding to cross-shell configurations, since often no shell-model calculation was available. Nevertheless, the general trends of the (h, t) reaction were carefully tested on almost all the lighter nuclei, confirming the previously established properties, and some evidence seemed to appear[1,2] that the cross-shell transitions with parity change were inhibited. It was also shown[3] that a tensor force is needed in order to explain the angular distributions of the unnatural parity states.

Besides the question of whether or not cross-shell transitions with parity change are allowed, it is interesting to study, in a simple case, the interference of the central and tensor parts that these transitions allow, in order to better determine the force responsible for the (h, t) transition. We have therefore analyzed the $^{40}Ca(h,t)^{40}Sc$ data which were taken at Saclay, using a microscopic description and a transition operator including both central and tensor components

$$v = V(f(r)\ (1 - \vec{\sigma}_1\vec{\sigma}_2) - g(r)S_{12})\vec{\tau}_1\vec{\tau}_2.$$

Except for the strength V, all the force parameters are taken from Ref. 4.

By comparison with the ^{40}K levels, the four lowest states can be identified as 4^-(g. s), 3^-(0.034), 2^-(0.772), and 5^-(0.892) and are mainly built with the $f_{7/2}\ d_{3/2}^{-1}$ configuration. For the 3^- and 5^- natural parity states, the contribution of the tensor force is seen to be small. It is, however, not negligible and improves the fits.

For the unnatural parity states 2^- and 4^-, a pure central force gives angular distributions which are in total disagreement with the experimental ones. This is as expected for (h, t) reactions to unnatural parity states, where a tensor force is known to be necessary.[3] Rather good fits are obtained, and indeed, the contribution of the central term

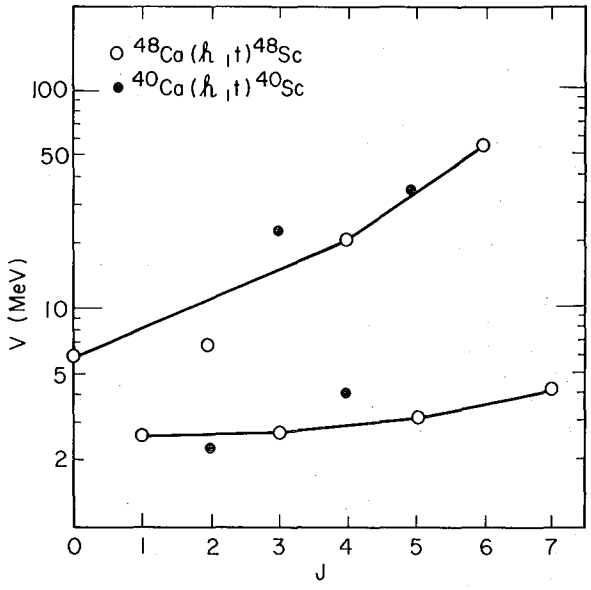

Fig. 1. The effective force strengths V are represented as a function of the transferred spin J. The upper curve is relative to the transitions leading to natural parity states and the lower to unnatural parity states. For ^{48}Ca, the strengths for the natural parity states are taken from Ref. 5 and for the unnatural parity states from Ref. 4. The same force, including the OPEP tensor term (averaged over the projectile density), has been used in the analysis of both experiments. (XBL713-2977)

is small compared with the tensor contribution. Increasing the central contribution with respect to the tensor, one will probably not drastically change the fit for the 4^- state (which is already good), but may improve the fit for the 2^- state at large angles.

The strengths V needed to explain the experimental magnitude of the cross sections relative to the

$$\left\{(f_{7/2})_p\ (d_{3/2})_n^{-1}\right\}_{J^-}$$

multiplet are very similar (Fig. 1) to those needed for the

$$\left\{(f_{7/2})_p\ (f_{7/2})_n^{-1}\right\}_{J^+}$$

multiplet in ^{48}Sc (Refs. 4 and 5). Some suggestions have recently been made[1,2] that the excitations involving a parity change should be inhibited in the (h,t) reaction. We have shown that, for the simple case we consider, the excitations presumably occur through the same mechanism, whether or not there is a parity change.

The most important consideration is whether or not the transition is of natural parity. This has already been explained since, in the first case, the excitation occurs mainly through the central term of the force and, in the second case, the tensor term dominates the transition.

Higher levels are tentatively identified 3^- (1.799), mainly $p_{3/2}\, d_{3/2}^{-1}$, 4^-(2.38), and 3^-(3.05), mainly $f_{7/2}\, s_{1/2}^{-1}$. Even when assuming pure shell-model structure, the strengths V needed to reproduce the experimental cross sections are in nice agreement with the strength needed for the lower 3^- and 4^- states.

Cross-shell transitions occur, therefore, with the same strength as in-shell transitions, at least when the final states can be assumed to be made of a single proton-particle neutron-hole excitation.

Footnotes and References

†Condensed from UCRL-19558 and Proceedings of the Argonne (He^3,t) Symposium, Argonne Physics Division, February 1970, PHY-1970A.

*Present address: I. P. N. Orsay, France

‡Present address: C. E. N. Saclay, France

1. G. Bruge, A. Bussiere, H. Faraggi, P. Kossanyi-Demay, J. M. Loiseaux, P. Roussel, and L. Valentin, Proceedings of the Dubna International Symposium on Nuclear Structure 1968; Nucl. Phys. A129, 417 (1969).

2. J. J. Schwartz, Bull. Am. Phys. Soc. AE3, 1207 (1969).

3. P. D. Kunz and E. Rost, Phys. Letters 30B, 231 (1969).

4. R. Schaeffer, UCRL-19551 and Proceedings of the Argonne (He^3,t) Symposium, Argonne Physics Division PHY-1970A; R. Schaeffer UCRL-19927, to be published in Nucl. Phys.

5. P. Kossanyi-Demay, P. Roussel, H. Faraggi, and R. Schaeffer, Nucl. Phys. A148, 181 (1970).

Investigation of the States of 2s-1d Shell Nuclei Based on the Four-Particle-Four-Hole State in ^{16}O †

S. N. Tewari* and G. L. Struble

It is well known that the 0^+ state at 6.06 MeV in ^{16}O is the beginning of a rotational band. Stephenson and Banerjee[1] have successfully explained this state on the basis of the Hartree-Fock (HF) theory. It is identified as the lowest member of a triaxial 4-particle-4-hole HF state. Further, one of the 0^+ states around 7 MeV in ^{20}Ne cannot be explained using the space of the 2s-1d shell alone. It is our opinion that it may be an 8-particle-4-hole state, the analog of the 4-particle-4-hole state in ^{16}O. In view of these results we have been tempted to calculate the analogous n-particle-4-hole states in N = Z even-even nuclei of the 2s-1d shell.

The ground and excited intrinsic states have been assumed to be Slater determinants and the wave functions and energies have been calculated by solving HF equations. We have assumed that there is no parity admixture in our solutions and that they are invariant under time reversal. For the two-body Hamiltonian, we have chosen a Gaussian radial dependence and assumed a Rosenfeld mixture. The single-particle energies were chosen to fit the experimental levels in ^{17}O and ^{15}O. We have also calculated the properties of the intrinsic states using the realistic Yale t matrix.[2]

In order to compare with experiment we must calculate the energy and the wave function of the band head and the several rotational states of good angular momentum. In a previous publication[3] we did this using the adiabatic assumption and calculating the inertial parameter in first-order cranking.[4] The more correct procedure of projecting states of good angular momentum from the intrinsic state is followed in this study. Further, we compute the overlap of the calculated state with the exact eigenstate by evaluating the quantity

$$E/C = \frac{\langle \psi^J | H | \psi^J \rangle}{[\langle \psi^J | H^2 | \psi^J \rangle]^{1/2}} . \qquad (1)$$

This quantity is a measure of the accuracy of our approximations.

In Table I we give shapes of the intrinsic states as calculated by HF. These are in agreement with predictions based on overlap arguments first proposed by Banerjee et al.[5] The excitation energies of the band heads of these intrinsic states are plotted in Fig. 1. It can be seen that these states will not be of importance after ^{24}Mg. In Fig. 2 we compare the calculated and experimental energy levels. On the whole there is good agreement, although it is difficult to make a one-to-one correspondence for levels above 7 MeV in excitation energy. In ^{20}Ne we predict that one of the excited 0^+ states $\approx$ 7 MeV is predominantly an 8-particle-4-hole state, whereas the other is a 1-particle-1-hole state built on the ground intrinsic state.

Table I. Predicted shapes of the most stable np-4h solutions of the HF equations for N = Z even-even nuclei in the s-d shell.

Nucleus	Hole-particle structure	Shape
^{16}O	4p-4h	triaxial
^{20}Ne	8p-4h	triaxial
^{24}Mg	12p-4h	oblate axial
^{28}Si	16p-4h	triaxial
^{32}S	20p-4h	oblate axial
^{36}Ar	24p-4h	oblate axial

In Table II we illustrate that our solutions are very close to eigenstates of the Hamiltonian by listing the overlaps defined in Eq. (1) for the 12-particle-4-hole state in ^{24}Mg.

Our calculations show that the adiabatic approximation is not reliable for light deformed nuclei. In Table III we compare the results from angular momentum projection with the results of the adiabatic model of Ref. 3. The adiabatic model clearly predicts too small a moment of inertia.

Our calculations show the importance of n-particle-4-hole states in the first part of

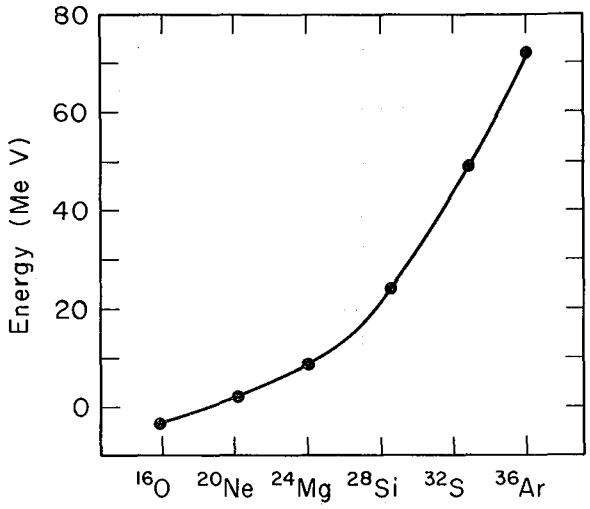

Fig. 1. Excitation energies of np-4h intrinsic states in the N = Z even-even nuclei of the s-d shell. (XBL699-3783)

Table II. A tabulation of the results from a calculation of the energy fluctuation for the states of good angular momentum projected from the intrinsic 12p-4h HF state for ^{24}Mg. Since the ratios in column 4 are nearly unity, the projected solutions are a good approximation to the exact eigenstates of the Hamiltonian.

J	$\langle J\|H\|J\rangle^2$ (MeV)^2	$\langle J\|H^2\|J\rangle$ (MeV)^2	$\frac{E}{C} = \frac{\langle J\|H\|J\rangle}{\langle J\|H^2\|J\rangle^{1/2}}$
0	31469.2344	31475.9764	0.9999
2	31070.0905	31106.8366	0.9994
4	30162.4846	30265.1558	0.9983
6	28799.9567	28996.9486	0.9966

Table III. A comparison of excitation energies relative to the band head for states of good angular momentum obtained from HF intrinsic states by exact angular momentum projection and using the Davydov-Filipov model.

	^{16}O		^{20}Ne	
J	Projection (MeV)	DF model (MeV)	Projection (MeV)	DF model (MeV)
0^+	0.0	0.0	0.0	0.0
2^+	1.28	2.35	1.26	1.66
2^+	2.81	4.59	2.52	2.62
3^+	3.99	6.94	3.69	4.29
4^+	4.07	7.81	2.40	5.27
4^+	5.48	10.14	3.87	6.94
4^+	10.30	16.77	5.71	9.24

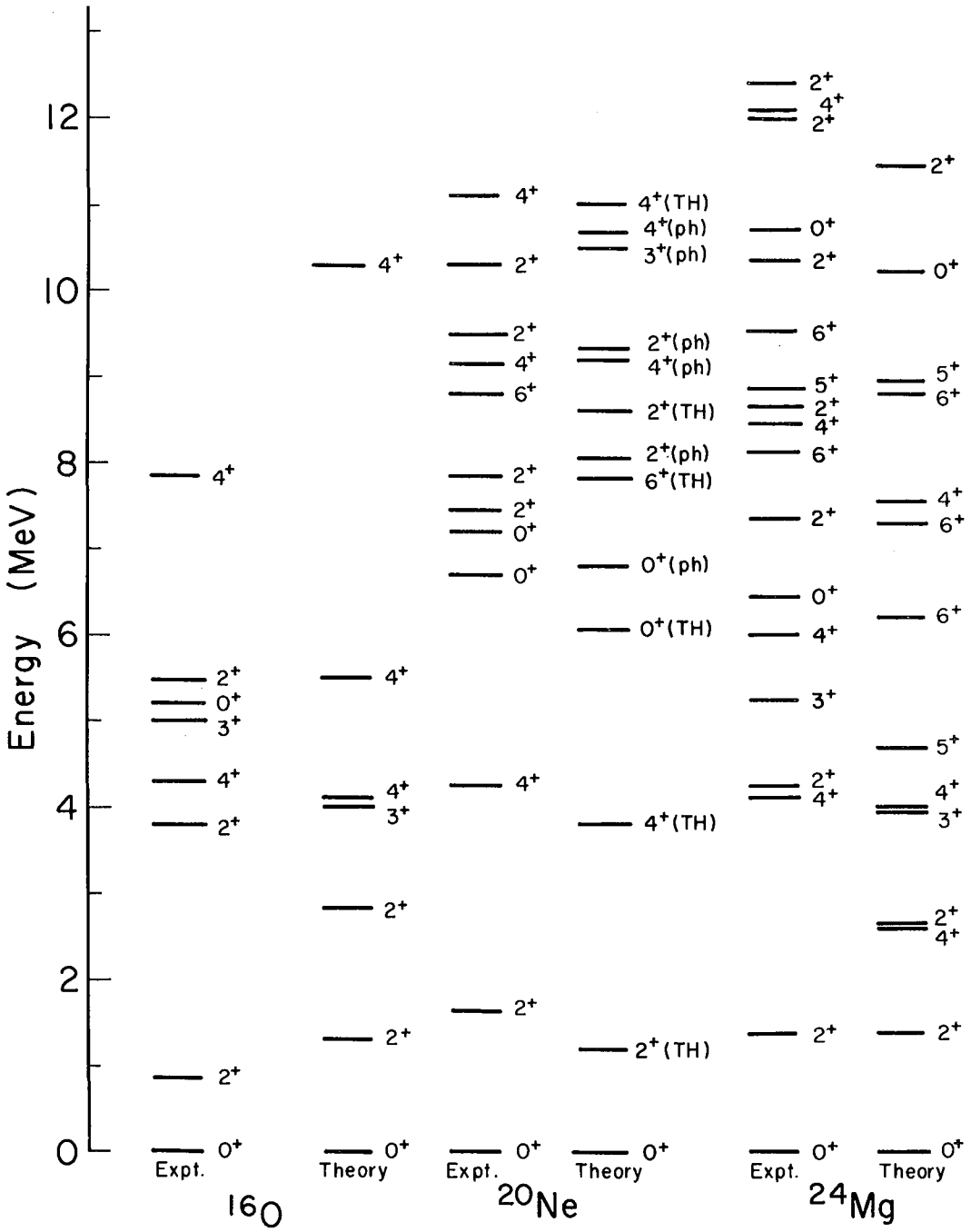

Fig. 2. A comparison of experimental and calculated energies in ^{16}O, ^{20}Ne, and ^{24}Mg. The zero of energy in ^{16}O has been taken at the first excited 0^+ state. For ^{20}Ne and ^{24}Mg the zero of energy corresponds to the ground state. In ^{20}Ne, $J^+(ph)$ corresponds to the projected state from the 8p-4h intrinsic state while $J^+(TH)$ is a linear combination of projected states from the HF and TDA intrinsic states. (XBL698-3507)

the 2s-1d shell. In order to increase the accuracy of these results, the influence of the (n-2)-particle-2-hole states must be considered.

Footnotes and References

†Condensed from Phys. Rev. C 1, 1156 (1970).

*Present address: Department of Physics, University of Arizona, Tucson, Arizona.

1. G. J. Stephenson and M. K. Banerjee, Phys. Letters 24B, 209 (1966).

2. C. M. Shakin, Y. R. Waghmare, and M. H. Hull, Jr., Phys. Rev. 161, 1006 (1967).

3. G. L. Struble and S. N. Tewari, in Proceedings of the International Nuclear Physics Conference, Montreal, Canada, 1969, edited by M. Harvey (Le Presses de l'Université de Montreal).

4. D R Inglis, Phys. Rev. 96, 1059 (1954).

5. M. K. Banerjee, C. R. Levinson, and G. J. Stephenson, Jr., Phys. Rev. 178, 1709 (1969).

Solution of Hartree-Fock-Bogoliubov Equations with Realistic Forces and Comparison of Different Approximations †

A. L. Goodman,* G. L. Struble, J. Bar-Touv,‡ and A. Goswami††

In an earlier publication,[1] we have shown how to generalize the BCS transformation to include both T = 0 and T = 1 pairing by using a complex BCS transformation. The purpose of the present work is to study the effect of generalized pair correlations on the underlying Hartree-Fock (HF) field using the Hartree-Fock-Bogoliubov (HFB) formalism. The generalized HFB transformation may be written

$$a^{+}_{\alpha\mu} = \sum_{i\nu} (u_{\alpha\mu,i\nu}\, c^{+}_{i\nu} + v_{\alpha\mu,i\nu}\, c_{i\nu}), \qquad (1)$$

where $u_{\alpha\mu,i\nu}$ and $v_{\alpha\mu,i\nu}$ are complex coefficients of the HFB transformation; $a^{+}_{\alpha\mu}$ and $c^{+}_{i\nu}$ are creation operators quasiparticles and shell-model particles respectively; and α, i refer to quantum numbers associated with the space-spin coordinates, while μ, ν are quantum numbers associated with the charge coordinates. The coefficients are determined by solving the Euler-Lagrange equations obtained by minimizing the total energy.

The general BCS transformation [Eq. (1)] can be written as the product of three transformations:[2]

(1) a transformation D in particle space, which defines the canonical basis and is obtained by diagonalizing the density matrix;

(2) a generalized BCS transformation B_{SP}; and

(3) a transformation R in the quasiparticle space,

$$B_{gen} = R\, B_{sp}\, D\,. \qquad (2)$$

The well-known BCS approximation consists of assuming that we know a priori the canonical basis, and that the Euler-Lagrange matrix equations break into 4×4 blocks. The approximation that we used in an earlier work[3] was to take the coupled Hartree-Bogoliubov[4] and BCS equations, which are equivalent to the HFB equations up to a unitary transformation, and note that if the off-diagonal elements of the pairing potential Δ are small, they reduce to coupled generalized HF and BCS equations. Although this might intuitively seem a better approximation than BCS, it still depends on Δ being diagonal in the canonical basis.

The HFB equations were solved using a basis of harmonic-oscillator wave functions. A number of symmetries were assumed for the HFB wave function. The ground states were assumed to be axially symmetric, invariant under inversion, and invariant under time reversal. The oscillator basis was truncated after the N = 2 or, in a few cases, the N = 3 oscillator shells. The calculations were performed with the Yale t matrix,[5] the Nestor-Davies-Krieger (NDKB) potential,[6] and the Rosenfeld-Yukawa effective interaction.

The results of our calculations clearly show that Δ is not diagonal in the canonical basis, and so any calculation making this assumption will be subject to large error. This is illustrated in Table I. Here we compare the contributions to the total energies in the HFB approximation, in the HF + BCS approximation, and the approximate HFB of Ref. 3. It is observed that the pairing energy is very much larger in the HFB because the canonical basis can change to enhance the pairing energy. This effect is not nearly as pronounced for T = 1 pairing in heavy nuclei.

The effects of pairing correlations on the nuclear shape and, in particular, the tendency toward higher symmetry due to pairing is illustrated in Figs. 1 and 2 by comparing the density distribution of the prolate HF solution and the prolate HFB solution for ^{24}Mg. In this case it can be seen that there is an α particle clustering the HF solution, and this effect is reduced in the HFB solution.

We attempt to describe the lowest intrinsic state of the N = Z even-even nuclei in the s-d shell with our HFB solutions. Arguments

Table I. A comparison of pairing theories. E_{HF}, E_{PAIR} and E_{TOTAL} denote the Hartree-Fock, pairing, and the total energies in MeV.

Method	E_{HF}	E_{PAIR}	E_{TOTAL}
	^{24}Mg		
HF + BCS	-126.02	-6.31	-132.33
Approx. HFB	-126.53	-5.58	-132.11
HFB	-124.73	-7.80	-132.53
	^{32}S		
HF + BCS	-219.01	-4.75	-223.76
Approx. HFB	-218.94	-4.88	-223.83
HFB	-215.32	-9.21	-224.53
	^{36}Ar		
HF + BCS	-283.71	-3.39	-287.10
Approx. HFB	-282.76	-3.92	-286.68
HFB	-282.24	-9.52	-291.76

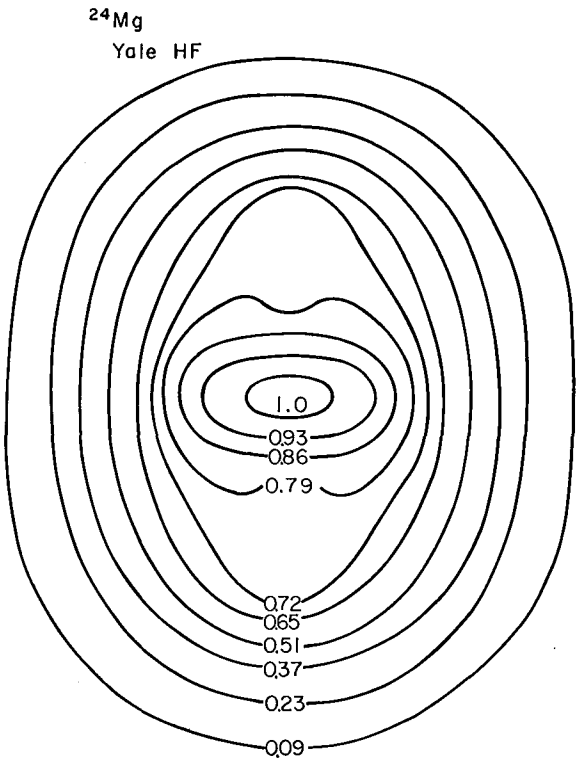

Fig. 1. Constant density contour plot for the prolate HF solution of ^{24}Mg obtained with the Yale potential. Rms radius = 2.853 fm. The densities are given in units of 0.240 fm^{-3}. (XBL6912-6345)

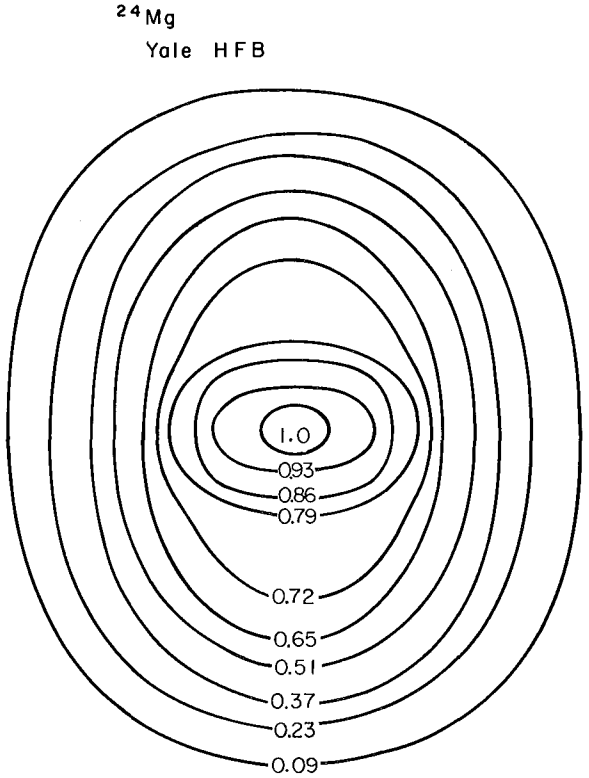

Fig. 2. Constant density contour plot for the prolate HFB solution of ^{24}Mg obtained with the Yale potential. Rms radius = 2.856 fm. The densities are given in units of 0.246 fm^{-3}. (XBL6912-6349)

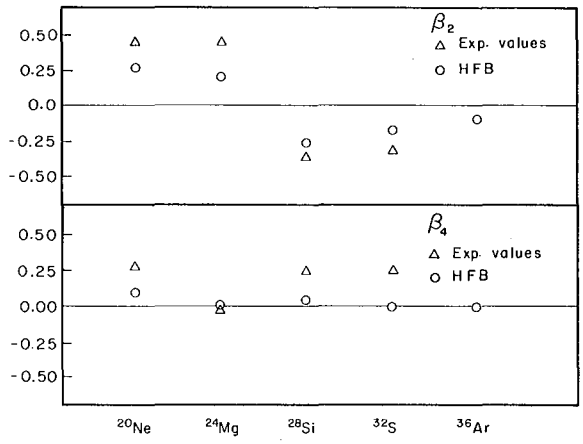

Fig. 3. The calculated values of distortion parameters β_2 and β_4 are compared with the experimental values of de Swiniarski et al.[7] For ^{20}Ne and ^{28}Si the theoretical value corresponds to the HF value.
(XBL6912-6352)

based on the total energy suggest that the paired solutions should give a good description of these nuclei. A recent paper by de Swiniarski et al.[7] has used a coupled-channel analysis of inelastic scattering data to determine the β_2 and β_4 values for the N = Z even-even nuclei. In Fig. 3 we compare our calculated values with the results of their analysis. In Fig. 4 we compare the inertial parameters calculated with these wave functions with the values obtained from experiment. It should be noted that the inertial parameter in HFB is greater than the HF + BCS approximation by 20%. This is caused by an increase in the energy gap in HFB, indicating that these solutions are more stable.

Footnotes and References

†Condensed from Phys. Rev. C 2, 380 (1970).

*Present address: Argonne National Laboratory, Argonne, Illinois.

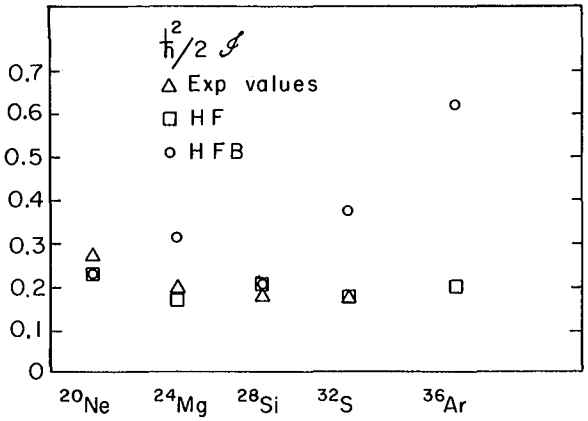

Fig. 4. The theoretical values of the moment-of-inertia parameter $\hbar/2\mathcal{I}$ (in MeV) are compared with the experimental values. For ^{20}Ne and ^{28}Si the HFB value corresponds to the HF value.
(XBL6912-6343)

‡Present address: Department of Physics, University of the Negev, Beersheba, Israel.

††Present address: University of Oregon, Eugene, Oregon, 97403.

1. A. L. Goodman, G. L. Struble, and A. Goswami, Phys. Letters 26, B260 (1968).

2. A. L. Goodman, Ph. D. thesis, UCRL-19514.

3. J. Bar-Touv, A. Goswami, A. L. Goodman, and G. L. Struble, Phys. Rev. 178, 1670 (1969).

4. K. Dietrich, H. T. Mang, and J. Pradhal, Z. Physik. 190, 357 (1966).

5. C. M. Shakin, Y. R. Waghmare, and M. H. Hull, Phys. Rev. 161, 1006 (1967).

6. C. W. Nestor, K. T. R Davis, S. J. Kreiger, and M. Baranger, Nucl. Phys. A113, 14 (1968).

7. R. de Swiniarski, C. Glashausser, D. L. Hendrie, J. Sherman, A D. Bacher, and E. A. McClatchie, Phys. Rev. Letters 23, 317 (1969).

Quadrupole and Octupole States in Deformed Even-Even Nuclei

J. D. Immele and G. L. Struble

The low-energy excitations in even-even nuclei are often described as collective rotations and shape vibrations. During the past several years there have been several attempts to provide a microscopic description of the vibrational states using schematic models. These have given qualitative agreement with experiment. Starting with fundamental relations in many-body theory, we are attempting to give a quantitative phenomenological description of these states with special attention to the interaction of phonon and particle modes in even-even and odd-mass nuclei. This report describes the first results from this program.

Using the quasiparticle approximation and assuming the quasiparticle irreducible interactions are not retarded, the Bethe-Salpeter equation for superfluid nuclei may be written[1]

$$\omega Z^{\pm}_{\alpha\beta} = (E_\alpha + E_\beta) Z^{\mp}_{\alpha\beta} + \sum_{\gamma\delta} \sqrt{\frac{1}{1+\delta_{\alpha-\beta}}} \sqrt{\frac{1}{1+\delta_{\gamma-\delta}}} \Big[\xi^{\mp}_{\alpha\beta}\, \xi^{\mp}_{\gamma\delta} \left(\langle \alpha\beta | V_{pp} | \gamma\delta \rangle + \delta_{K,0} s_\gamma s_\delta \langle \alpha\beta | V_{pp} | -\delta-\gamma \rangle \right)$$

$$+ \eta^{\mp}_{\alpha\beta}\, \eta^{\mp}_{\gamma\delta} \left(s_\beta s_\delta \langle \alpha-\delta | V_{ph} | -\beta\gamma \rangle \pm s_\beta s_\gamma \langle \alpha-\gamma | V_{ph} | -\beta\delta \rangle \right) - \delta_{K,0}\, \eta^{\mp}_{\alpha\beta}\, \eta^{\mp}_{\delta\gamma} \left(s_\beta s_\delta \langle \alpha\gamma | V_{ph} | -\beta-\delta \rangle \right.$$

$$\left. \pm s_\beta s_\gamma \langle \alpha\gamma | V_{ph} | -\beta-\gamma \rangle \right) \Big] Z^{\mp}_{\gamma\delta} , \qquad (1)$$

where

$$\xi^{\mp}_{\alpha\beta} = (u_\alpha u_\beta \mp v_\alpha v_\beta), \quad \eta^{\pm}_{\alpha\beta} = (u_\alpha v_\beta \pm v_\alpha u_\beta), \quad s_\alpha = (-1)^{1/2-\Omega_\alpha}, \text{ and } \Omega_\alpha + \Omega_\beta = K.$$

In this notation, the Greek indices refer to a set of quantum numbers for a single particle in a deformed well[2] and u_α, v_α, E_α are determined by the BCS transformation.[3] ω is the excited-state energy of the system, and the amplitudes $Z^{\pm}$ measure participation in the phonon of two valiton(de) excitations on the ground state. The irreducible interaction is taken to be the density-independent delta potential with different parameters in the particle-particle and particle-hole channels.

$$V_{pp} = - G\, \delta(\vec{r}_1 - \vec{r}_2)$$

$$V_{ph} = - (F_1 + F_2 \mathbb{P}_\sigma)\, \delta(\vec{r}_1 - \vec{r}_2), \qquad (2)$$

where $\mathbb{P}_\sigma$ is the spin-exchange operator and G, F_1, F_2 are constants. In Fig. 1 and Fig. 2, we present the calculated energies and reduced transition probabilities for the gamma (2+) vibrations. In general, the agreement with experimental trends is quite good. Thus we find that the delta potential is a good approximation to the effective interaction and that the calculated phonon provides a good description of how the nucleus vibrates in the gamma mode.

A comparison of our results with those of

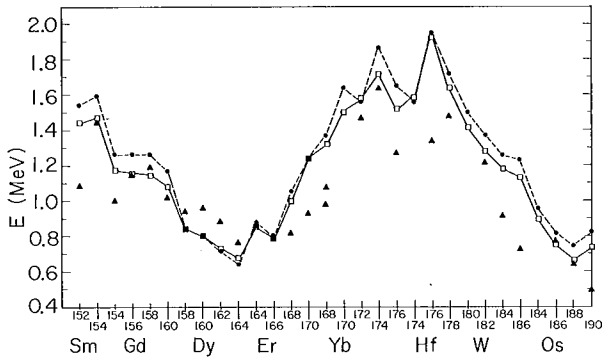

Fig. 1. 2+ states calculated using

(●) $G = F_2 = 0$, $F_1 = 473$ direct matrix element only;

(□) $G \approx 434$, $F_1 = 641$, $F_2 = 0$

(▲) experimental points.

(XBL713-2978)

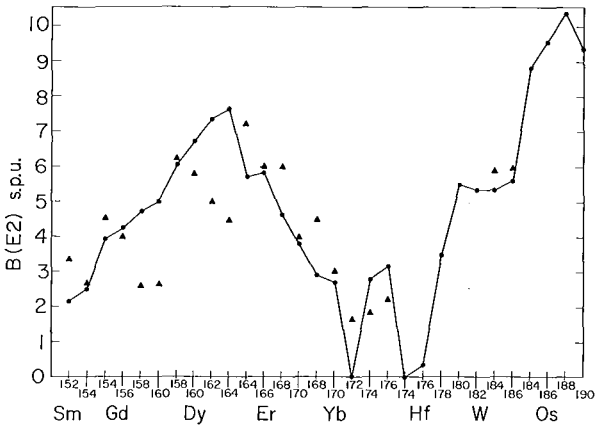

Fig. 2. B(E2) values calculated for G = 434, F_1 = 641, F_2 = 0. One effective change was taken to be $0.4 \approx Z/A$. Note that for B(E2) values greater than the experimental points (*), the energies calculated in Fig. 1 are too low. Agreement would be improved by fitting E_{theory} to E_{exp} before calculating the transition probability (XBL713-2979)

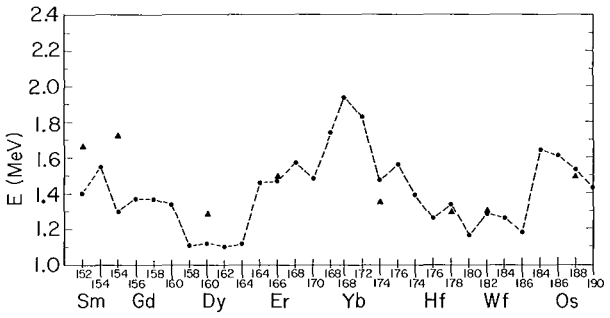

Fig. 3. 2- states calculated using
(●) G = 434, F_1 = 1112, F_2 = 0.
(▲) experimental points.
(XBL713-2980)

Faessler,[2] who used the quadrupole-quadrupole component of the surface delta interaction, suggests that the interaction inside the nucleus where the radial functions are incoherent is of considerably less consequence than surface interaction where radial functions are all positive in sign. Secondly, it supports the widely held notion that only the quadrupole motion is important in the vibration. It is seen from Fig. 1, where results using various components of the force are graphed, that including the exchange particle-hole matrix element contributes only to a renormalization of the force constant. Further, it is somewhat surprising that the interaction in the particle-particle channel not only leaves the spectrum almost identical, but also has little effect on renormalization (the G = 0, F_1 = 641 spectrum is not shown). This is in contrast with the prediction of the schematic model.[4] Finally, we note that a nonzero $\mathcal{H}_\sigma$ component has little effect on the calculated spectrum for reasonable values of F_2.

Calculations have also been carried out for the octupole states. Figure 3 shows the results for the 2- states. Coriolis coupling is not taken into account. Yet we again find good agreement with the experimental trend.

In general, we have found that using the delta force as effective interaction, Eq. (1) yields a fairly accurate picture of collective states in deformed even-even nuclei. The nature of these excitations has been established to be due to a particular multipole component of the interaction evaluated near the nuclear surface.

References

1. P. Nozières, Interacting Fermi Systems (Interscience Publishers, Inc. New York, (1959).

2. A. Faessler and A. Plastino, Nucl. Phys. A94, 580 (1967).

3. N. N. Bogoliubov, Soviet Phys. -Usp. 2, 236 (1959).

4. A. Faessler, A. Plastino, and S. A. Moszkowski, Phys. Rev. 156, 1064 (1967).

O^+ States in Deformed Even-Even Nuclei

J. D. Immele and G. L. Struble

Currently, the most interesting states in even-even deformed nuclei are the 0^+ excitations. Not only are quadrupole (beta) vibrations possible but also pairing vibrations[1] and spin-quadrupole vibrations.[2] Further, these states are characterized not only by their E2 transition rates but also their E0 rates and two-nucleon transfer cross sections.

Experimentally, one often observes as many as four 0^+ states below 2 MeV.[3] Among the lighter elements in this region, the lowest-lying state is beta-vibrational in character. Several nuclei, with a gap in the Nilsson spectrum, possess levels which are populated strongly in (p,t) reactions.[4] Such levels are classified as neutron-pairing vibrations.[1] However, the complexity of these spectra, in general, suggests coupling of the different non-rotational collective modes and has also encouraged the postulation of several new modes of coherent motion.

An outline of the theory we are employing is given in an earlier contribution;[5] however, there is an added difficulty in the exclusion of spurious state contributions to the 0^+ solutions. For a general two-body interaction in the particle-particle channel, the solutions of the Bethe-Salpeter equation are not automatically orthogonal to the spurious state. A projection-like matrix method has been derived to overcome this difficulty.[6] As before, a delta force is employed for the irreducible interactions. Equations for the E0 and E2 rates are given elsewhere.[7] The two-nucleon transfer probability between superfluid ground states is

$$S_g = \sum_\alpha u_\alpha v_\alpha, \quad (1)$$

where the sum is only over pairs of neutrons or protons in the two-quasiparticle configuration space. The probabilities for populating an excited state by two-nucleon stripping or pickup are

$$S_e = \frac{1}{2} \sum \left[Z^-_{\alpha\text{-}\alpha} \mp Z^+_{\alpha\text{-}\alpha} (u_\alpha^2 - v_\alpha^2) \right]. \quad (6)$$

The ratio of cross sections is $(S_e/S_g)^2$.

In Fig. 1, we present the two lowest 0^+ states calculated for various types of forces. In particular, we wish to analyze the effect of pairing and delta potentials in the particle-particle channel. It appears, in general, that the pairing vibration is not a distinct state but rather a component of the beta-vibration and, occasionally, other states. The additional terms in the delta force, which guarantee gauge invariance, affect only the diagonal energies. This causes all levels to be lower but does not bring down a new state (in particular, the pair fluctuation predicted by Belyaev.[8] The effect of introducing the spin-dependent term in the interaction was found to be negligible. We thus question the existence of spin-quadrupole vibrations.

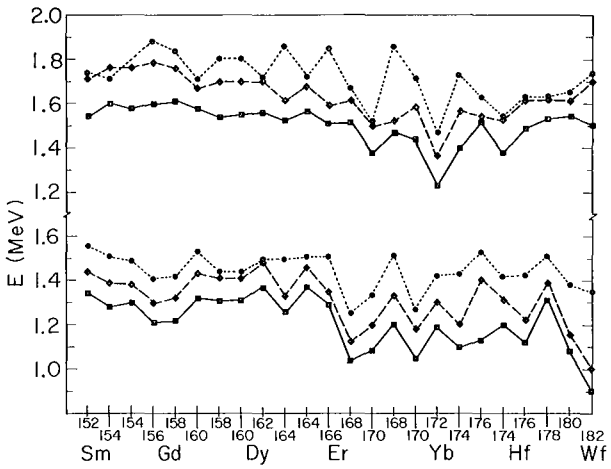

Fig. 1. First and second 0^+ states calculated using (●) G = 0, F_1 = 664. (◇) G = pairing force ≈ 26-28/A MeV, F_1 = 664; (□) G ≈ 411-489, F_1 = 664. (XBL713-2981)

We have also noted that combining a high degree of nonadiabaticity with the requirement of orthogonalization to the spurious state guarantees incoherency of 0^+ excited states. As a result, the calculated transition rates vary greatly from nucleus to nucleus, and the character of a vibration is often solely dependent on the sign of an off-diagonal matrix element. Such was not the case for the gamma and octupole vibrations. Another feature of the theory is that the equation for two-nucleon transfer cross sections gives rise to interference between pairing and beta-vibrational modes (due to a change in sign of $Z^\pm$ at the Fermi surface). The effect is that while a (p,t) reaction may be favorable, a (t,p) may not. There are still no experimental data to confirm this prediction.

References

1. D. R. Bes and R. A. Broglia, Nucl. Phys. 80, 289 (1966).

2. N. I. Pyatov, Arkiv Fysik 36, 667 (1968).

3. B. S. Dzhllepov and S. A. Shestopalova, Proceedings of the Dubna International Symposium on Nuclear Structure, 1968.

4. M. Oothovdt, et al., Phys. Letters 32B, 270 (1970).

5. G. L. Struble and K. D. Immele, Quadrupole and Octupole States in Even-Even Deformed Nuclei, preceding paper.

6. G. L. Struble and J. D. Immele, to be published.

7. A. A. Kuliev and N. I. Pyatov, Izv. Akad. Nauk. SSSR 32, 831 (1968).

8. S. T. Belyaev, Sov. J. Nucl. Phys. 4, 671 (1967).

Resonant Approximation for Single-Particle Resonances in the Renormalized RPA Problem †

M. Weigel*

In a previous work[1] we have given the equations for the renormalized RPA problem with inclusion of the single-particle continuum by extending Migdal's quasiparticle approach[2] to the continuum.[3] We designed a model in which the so called nuclear-structure problem (only bound single-particle orbits are included) was used as a zero-order solution. In this model, one could first solve the nuclear-structure problem with the full effective particle-hole force. The influence of the continuum was taken into account by approximating all matrix elements containing continuum single-particle states with a separable force, thus avoiding the original complicated Fredholm problem. This is due to the fact that the Fredholm determinant degenerates for a separable force. The details as well as further references can be found in Refs. 1 and 3.

The model implied the assumption that the solution for the nuclear-structure problem is already a good approximation for the corresponding "bound-state" solution with inclusion of the single-particle continuum. But in some cases it is well known that one has to include single-particle resonances--for instance the $1d_{3/2}$-resonance in ^{16}O--in order to obtain a satisfactory solution for the nuclear-structure problem. We have been able to overcome this difficulty by applying the method of Garside and MacDonald.[4,5] It turns out that the resulting equations are rather complicated, so one might try an approximate treatment by the use of a "resonant approximation" for the resonant single-particle states.[6,7]

The resulting system of equations for the bound and the scattering problem is therefore derived and discussed. In order to make the structure of the problem more transparent, a solvable model is presented, in which all matrix elements containing nonresonant continuum single-particle states are approximated by a separable force. One has only to use standard matrix methods and to perform integrations over known nonresonant functions.

Footnotes and References

†Condensed from UCRL-19578, April 1970; Z. Naturforsch. 25a, 1562 (1970).

*On leave from Sektion Physik der Universität München, Munich, Germany

1. M. Weigel, Phys. Rev. C 1, 1647 (1970).

2. A. B. Migdal, Theory of Finite Fermi Systems and Applications to Atomic Nuclei (Interscience Publishers, Inc., New York, 1967).

3. M. Weigel, Nucl. Phys. A137, 629 (1969).

4. L. Garside and W. M. MacDonald, Phys. Rev. 138, B582 (1965).

5. L. Garside and M. Weigel, Phys. Rev. C 2, 374 (1970).

6. V. V Balashov et al., Sov. J. Nucl. Phys. (Engl. Transl.) 2, 461 (1966).

7. H. J. Unger, Nucl. Phys. A104, 564 (1967).

Second-Order Corrections in the Dipole Sum Rule for Nonlocal Potentials

M. v. Borsig† and M. Weigel*

Nucleon-nucleon potentials are determined today by fitting the parameters of a suitable Ansatz to the experimental phase shifts and the deuteron data. Since one knows the scattering data only in a limited energy range, a unique selection of a potential is not possible. A further test might be the calculation of sum rules since local or nonlocal potentials behave differently with respect to sum rules. We therefore calculated for the Tabakin potential the second-order contribution to the dipole sum rule, since in first order a decisive statement could not be achieved.[1] It turned out that the second-order effect is as large as the first-order contribution, leaving the problem still unsettled. Up to second order one still has--as in first order--agreement with experimental results, which, unfortunately, are not well determined.

Footnotes and Reference

†Sektion Physik der Universität München, Munich, Germany

*On leave from Sektion Physik der Universität München, Munich, Germany.

1. M. Weigel, G. Süssmann, Z. f. Physik 193, 389 (1966).

The Nuclear Matter Problem in the Green's Function Approach†

M. Weigel* and G. Wegmann‡

In the last fifteen years several methods for the treatment of the quantum-mechanical many-body problem have been developed. Since the encountered problems--renormalization of one-particle motion in matter, (partial-) summation of the perturbation theory, etc. --are similar to those of the field theory, one utilizes methods already developed in elementary particle physics. Examples for such a treatment are the Brueckner theory and allied approaches, which are based on an analysis of the Feynman diagrams for the many-body systems.[1] Another approach is the treatment of the system within the scope of the so-called Green's functions, which are the reproduction of the vacuum expectation values of a time-ordered operator product in field theory. One can also conceive of them as quantum-mechanical generalizations of the distribution functions in statistical mechanics. A knowledge of them is sufficient for the description of the system.

The aim of this article is the representation of the theory of nuclear matter using the technique of many-body Green's functions, since they enable us to treat the problem in a relatively transparent manner. We have utilized the functional method to derive the relevant system of equations for Green's functions. This method is--in our opinion--a simpler way than the standard perturbational approach. The analytic properties of Green's functions and related quantities--for instance, the effective one-particle potential, the effective scattering amplitude, etc. --are given and the emerging dispersion relations are used to obtain the final set of equations for the nuclear matter problem, thus avoiding the use of thermodynamic Green's functions. Several approximations and results achieved today are discussed. Brueckner theory and related methods are not discussed further, since they are sufficiently known. We think one must choose such approximations, which fulfill the so-called Baym condition, i. e., the effective single-particle potential can be represented as a functional derivative of a function with respect to the single-particle propagator. This guarantees thermodynamic consistency and preservation of conservation laws. Fixation of equilibrium data by means of various relations (e. g., pressure = 0, $E = \mu N$, E/N = minimum) leads to the same result, which is not guaranteed in other approximations, however. This condition is

fulfilled in Hartree-Fock and $\Lambda^{(11)}$ approximation. The $\Lambda^{(11)}$ approximation has the disadvantage against the $\Lambda^{(00)}$ and Brueckner approximation that the spectral function in the relevant energy range is no longer represented by a δ-function; or otherwise expressed, the independent particle model holds true only approximately. This renders the numerical calculations more complicated.

Footnotes and Reference

†Condensed from UCRL-19999, to be published in Fortschritte der Physik.

*On leave from Sektion Physik der Universität München, Munich, Germany.

‡Permanent address: Sektion Physik der Universität München, Munich, Germany.

1. D. A. Kirshnits, Field Theoretical Methods in Many-Body Systems (Pergamon Press Limited, London, 1967).

Renormalization Constants in the Random-Phase Approach†

M. Weigel,* L. Garside, and P. K. Haug‡

In the last decade many calculations of certain excited states of even nuclei have been performed under the assumption that those states are describable as a superposition of particle-hole and hole-particle excitations (RPA-approximation). In most of the calculations one assumes that the one-particle propagation takes place with the experimental single-particle energy in a shell-model state approximated by a suitable harmonic oscillator potential. With this assumption a certain kind of force is connected, since a change in the single-particle propagation can result in a change of the effective forces. It is the aim of this paper to investigate the change of the force due to the use of Saxon-Wood functions instead of harmonic oscillator functions. In addition we tested Migdal's assumption that the renormalization constants can be kept approximately fixed throughout the periodic system. For this purpose we calculated the spectra of ^{16}O, ^{40}Ca, ^{48}Ca, and ^{208}Pb using harmonic oscillator wave functions, and determined the "best" renormalization constant in each case. At least for smaller nuclei, we were not able to confirm this assumption.

In order to make plain the assumptions involved in a renormalized RPA treatment, the renormalization procedure for the random-phase approximation has been discussed in detail in order to trace the different effects contributing to the renormalization. We calculated for ^{16}O and ^{40}Ca the renormalized effective particle-hole interaction using Saxon-Wood states for the quasiparticle description and compared the results with the outcome of the harmonic oscillator state description of quasiparticles. As expected we found an increase in the renormalization constant. In our calculations, the density dependence of the force was interpolated between the center value and the vacuum value according to the density distribution of the considered nucleus. For the effective particle-hole force we used the solutions for the Puff-Reynolds potential in the Λ^{00} approximation.

Footnotes

†Condensed from Phys. Rev. C 3, 563 (1971).

*On leave from the Sektion Physik der Universität München, Munich, Germany.

‡Present address: Project Symphonie, Bonn, Germany.

Supermultiplets of $(1p)^{10}$ for A = 14 and the New, Second Superallowed β Transition of O^{14}

Martin G. Redlich

The supermultiplet theory of Wigner[1] is based upon the assumption that the effect of spin- and isotopic-spin dependent two-nucleon interactions may be neglected. Recent experimental masses have given indications that the mass formula[1] of the supermultiplet theory is approximately valid for many nuclei.

An early, remarkable success of the theory is the differentiation between allowed favored and unfavored β transitions. All transitions occurring within a single supermultiplet should be favored, with $ft < 10^4$. For a long time, however, the decay of C^{14} and the mirror decay of O^{14}, both to the ground state of N^{14}, appeared to be an exception to this rule. The discovery of a new, superallowed β^+ transition[2] from O^{14} to N^{14}, 3.95 MeV, has led to the present calculations, which resolve the above difficulty. This transition occurs with very small probability, in addition to the well-known superallowed transition $O^{14} \rightarrow N^{14}$, 2.31 MeV, which is within the lowest T = 1 multiplet.

The calculations for the configuration $(1p)^{10}$ or $(1p)^{-2}$ have been made with the empirically determined effective-interaction matrix elements of Cohen and Kurath,[3] with a $1p_{3/2} - 1p_{1/2}$ single-hole energy difference determined by the data for A = 15. They show that within the framework of this shell-theoretical calculation, the supermultiplet theory is rather accurately valid. The theoretical and experimental energies of excitation E_x are given in Table I, together with the probability of the main supermultiplet state. This probability lies between 72% and 100%. Its average is 94% for the T = 0 states, and 84% for the T = 1 states. It may be expected that the $(1p)^{10}$ strength is divided among two or more states for some of the higher levels.

The results for the two Gamow-Teller β transitions of O^{14} follow:

$O^{14} \rightarrow N^{14}$, 0 MeV

ft(exp.) = 21,400,000 ± 300,000

ft(th.) = 326,000

$O^{14} \rightarrow N^{14}$, 3.95 MeV

ft(exp.) = 1,200 ± 150, ft(th.) = 921

It is now easy to see why the transition to the ground state is nearly forbidden: it is mainly $^1S_0 \rightarrow {}^3D_1$. The fact that the ft value for this transition is above the usual unfavored range is due to cancellation in the matrix element. A very small change in the wave functions would suffice to increase the theoretical ft value to the experimental one. The second transition and the one to the 2.31 MeV state are both within the S supermultiplet. They are $^1S_0 \rightarrow {}^3S_1$ and $^1S_0 \rightarrow {}^1S_0$, respectively.

The results give particularly striking evidence for the approximate validity of the supermultiplet theory. It appears very likely that it will be possible to find evidence for those states of $(1p)^{10}$ which are yet unknown by the investigation of appropriate reactions.

References

1. See, e.g., E. Feenberg and E. P. Wigner, Reports on Progress in Physics 8, 274 (1941).

2. F. Ajzenberg-Selove, Nucl. Phys. A152, 1 (1970).

3. S. Cohen and D. Kurath, Nucl. Phys. 73, 1 (1965).

Table I. The ten states of the configuration $(1p)^{10}$ for N^{14}, arranged according to the supermultiplets (P, P', P'') L, where P, P', P'' are the partition numbers. E_x = excitation energy in MeV. The column "Probability" gives the probability of the main supermultiplet state $(2S+1)L_J$. Two experimental states are listed for the theoretical state with E_x = 9.56 MeV; its strength was found to be divided between these two states.

(1,0,0)S				(1,0,0)D				(1,1,-1)P			
(T, J)	E_x(th.)	E_x(exp.)	Probability	(T, J)	E_x(th.)	E_x(exp.)	Probability	(T, J)	E_x(th.)	E_x(exp.)	Probability
(0,1)	3.87	3.95	92% $^3S_1$	(0,3)	10.03		100% $^3D_3$	(1,2)	17.58		87% $^3P_2$
(1,0)	2.46	2.31	72% $^1S_0$	(1,2)	9.56	10.43 9.17	87% $^1D_2$	(1,0)	16.11		72% $^3P_0$
				(0,2)	7.01	7.03	100% $^3D_2$	(0,1)	15.21		85% $^1P_1$
				(0,1)	0	0	92% $^3D_1$	(1,1)	11.93	13.75	100% $^3P_1$

A Study of Deformation Energy Surfaces Obtained from Single-Particle Energies

W. A. Bassichis,† A. K. Kerman,* C F. Tsang, D. R Tuerpe,‡ and L. Wilets††

The constrained Hartree-Fock (CHF) method[1] with the Tabakin potential[2] is used as a framework to understand the Strutinsky method[3] for obtaining nuclear deformation energy surfaces (DES) from single-particle energies.

The underlying foundation of the program is the Nilsson IPM.[4] We must obtain some physical interpretation of the model. No simple one exists! The only satisfactory interpretation we can proffer begins with some generalized Hartree-Fock approximation utilizing an effective interaction: Unconstrained Hartree-Fock yields a single point or isolated points which are local minimum in the energy (with respect to continuous variations in the wave function). If we wish to map out a DES, we must study the system as a function of deformation. This implies a constraint on the deformation (say the quadrupole moment). Hence we introduce a Lagrange multiplier or "Lagrange potential", λ.

As a function of deformation, the Lagrange multiplier is discontinuous. It is a monotonic function of deformation which vanishes at equilibrium points and is discontinuous at level switching. We will see that the Hartree-Fock eigenvalues are similarly discontinuous. The introduction of pairing can remove such discontinuities and certainly does so in real nuclei.

The single particle energies for ^{108}Ru as calculated[5] are shown in Fig. 1 as a function of quadrupole moment Q. The breaks in the orbitals occur where there is a change of configuration, and hence a change in the average field. Mathematically this is effected by having two different Hamiltonians on the two sides of the break: on the left, $\mathcal{H} = H + \lambda_L Q$ and on the right, $\mathcal{H} = H + \lambda_R Q$. The Hamiltonian on either side is solved self-consistently to obtain the configuration with the lowest HF energy, and different values are obtained in general for the two sides of the break.

A connection between CHF and the Strutinsky procedure has been studied. An essential element is the definition of a properly averaged field which yields average single-particle energies containing most of the shell effects. An explicit expression for the corrections to this procedure is obtained

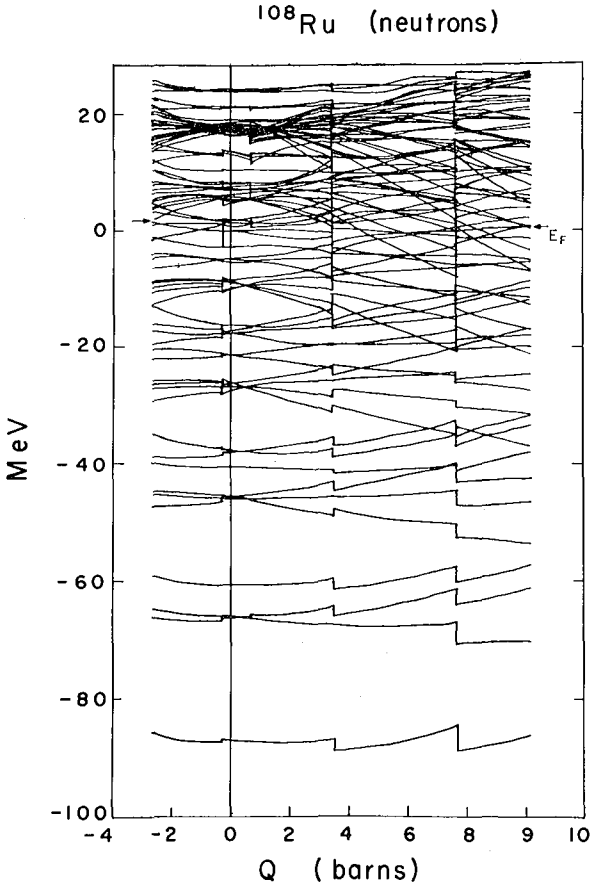

Fig. 1. CHF eigenvalues ϵ_n as a function of $\langle Q \rangle$ for $^{108}_{44}Ru_{64}$. The Fermi energy is indicated by arrows. Breaks occur at configuration changes; the configurations chosen yield the lowest $\langle H \rangle$.
(XBL7010-3948)

which could be used for a direct test of the Strutinsky method, although this procedure has not yet been carried out. Instead, we have applied the Strutinsky prescription directly to CHF single-particle energies.

Figure 2 shows our main results as a function of quadrupole moment Q. At the top of the figure is shown the Hartree-Fock total energy (designated $\langle H \rangle$); the adiabatic deformation energy surface is taken along the lowest curves of all the scallops. The curve designated E_{LD} is a freehand drawing of a

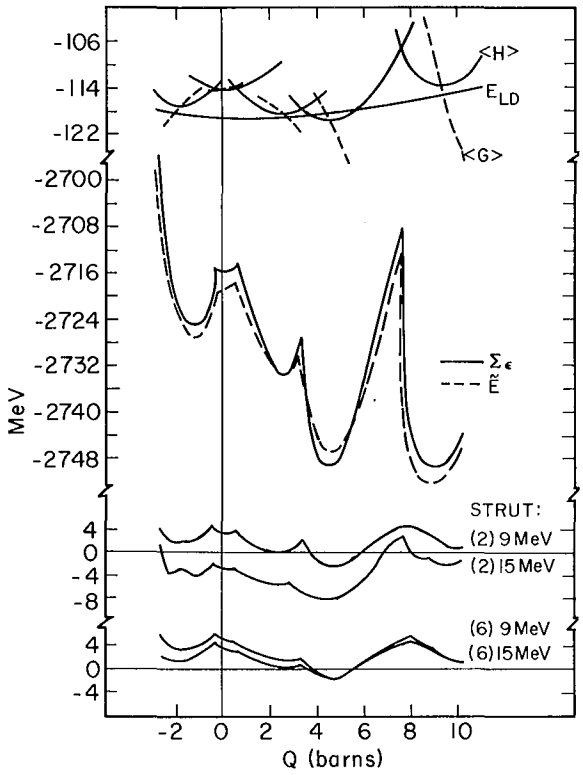

Fig. 2. Comparison of summation of eigenenergies, Strutinsky shell correction, and the Hartree-Fock energy for the case of $^{108}_{44}Ru_{64}$. Four sets of curves are displayed. The top set consists of the solid curve giving the Hartree-Fock binding energy $\langle H \rangle$, the dashed curve giving $\langle G \rangle = (1/2)\Sigma(\epsilon_n + t_n)$, and the light curve E_{LD} which is a freehand drawing of the smooth background of $\langle H \rangle$. The "Hartree-Fock shell correction" is, by definition, $\langle H \rangle - E_{LD}$. The second set of curves gives the summation of eigenenergies $\Sigma\epsilon$ (solid curves) and the Strutinsky smoothed energy $\tilde{E}$ (dashed curves). The third set gives the Strutinsky shell corrections calculated on the eigenenergies with p = 6 for two values of smearing parameter γ: 9 MeV and 15 MeV. The fourth set is the same as the third set, but with p = 2.
(XBL712-2914)

smooth background assumed to be given by some leptodermous (or liquid-drop) approach.[6] This curve has a generous bias toward the final results. The shell correction given by the Hartree-Fock model is then just the difference between $\langle H \rangle$ and E_{LD}. This is to be compared with the shell correction obtained by the Strutinsky method.

The next set of curves is the summation of Hartree-Fock single-particle energies for the appropriate nucleus. On top of these curves, indicated by a broken curve, is the Strutinsky smoothed energy ($\tilde{E}$) using p = 6 and γ = 15 MeV, where p and γ are Strutinsky order parameter and smearing parameter, respectively. The difference between the $\Sigma\epsilon$ curve and the smooth energy $\tilde{E}$ gives the Strutinsky shell correction.

In the lowest part of the figures are the two sets of Strutinsky shell corrections with p = 6 and γ = 9 MeV and 15 MeV. For comparison, the shell corrections of second order (p = 2) with the same values of γ are also plotted.

We can summarize the comparison between $\Sigma\epsilon$ and $\langle H \rangle$ in this figure as follows:

(1) The locations of the minima (as a function of $\langle Q \rangle$) for $\Sigma\epsilon$ are fairly close to the values given by $\langle H \rangle$. This result is more valid for the heavier (A = 108) nuclei than for light (A = 20) nuclei. The physical condition for the minima of $\Sigma\epsilon$ to be at the same Q values as those of $\langle H \rangle$ is found to be "perfect nuclear shielding"; that is, the change in the potential field induced by a small external field has an expectation at equilibrium which exactly cancels that of the external field.

(2) The relative heights of the $\Sigma\epsilon$ minima bear only slight relationship to those of $\langle H \rangle$.

(3) The curvature of $\Sigma\epsilon$ at a minimum is very much greater than that of $\langle H \rangle$.

In perspective it should be pointed out that there has been no valid justification in the literature of the conjecture that the Hartree-Fock energy surface should have the same variation with deformation as the summation of single-particle energies.

A study of the curves of Strutinsky shell correction with p = 6 in the figure shows the surprising result that they appear to give qualitatively reasonable Hartree-Fock shell correction ($\langle H \rangle - E_{LD}$). This is not yet fully understood, but in the manner the Strutinsky prescription is applied, we observe the following:

(i) The prescription averages vertically (over ϵ or N and Z), whereas the final result is expected to smooth horizontally (over Q).

(ii) The particle orbitals involved in the smoothing process are mainly within a region γ (9-15 MeV) of the Fermi surface, and orbitals in this region contribute the major part of the final shell correction.

(iii) The "smoothed" energy function $\tilde{E}$ preserves all systematic features (slope, curvature, etc.) in the $\epsilon_n(Q)$, and hence such features are obliterated in the final shell correction. For example, the high curvature in $\Sigma\epsilon$ is due to a systematic curvature present

in each $\epsilon_n(Q)$; the curvature in $\tilde{E}(Q)$ is very nearly equal to that in $\Sigma\epsilon$ (See Fig. 2), and indeed $\tilde{E}(Q)$ is nearly equal to $\Sigma\epsilon$. In this regard, we note that the Nilsson constant-volume condition gives rise to a systematic $\langle Q\rangle^2$ term in $\Sigma\epsilon$, and hence is obliterated by the prescription (and replaced by the liquid-drop surface term).

(iv) The discontinuities in the $\epsilon_n(Q)$ at the point of configuration switching are also nearly obliterated in the shell correction because the averaging is vertical. These discontinuities, of course, are not present in the Nilsson model.

(v) The net shell corrections appear to arise from those "few" particles near the Fermi surface whose properties deviate from the mean. As long as only a few particles are involved, one can use Koopmans' theorem[7] to relate total energy differences to differences in the single-particle eigenvalues. This, we believe, is the ultimate hope for justification of the qualitative and perhaps semiquantitative success of the Strutinsky prescription.

Footnotes and References

†Department of Physics, Texas A. and M. University, College Station, Texas 77843.

*Department of Physics, Massachusetts Institute of Technology, Cambridge, Massachusetts 02139

‡Lawrence Radiation Laboratory, Livermore, California.

††Department of Physics, University of Washington, Seattle, Washington 98105.

1. D. R. Tuerpe, W. H. Bassichis, A. K. Kerman, Nucl. Phys. A142, 49 (1970).

2. F. Tabakin, Ann. Phys. (N. Y.) 30, 51 (1964).

3. V. M. Strutinsky, Nucl. Phys. A95, 420 (1967); V. M. Strutinsky, Nucl. Phys. A122, 1 (1968); V. M. Strutinsky et al., R. M. P. (to be published).

4. B. R. Mottelson and S. G. Nilsson, Kg. Danske Videnskab. Selskab, Mat.-Fys; S. G. Nilsson, C. F. Tsang, A. Sobiczewski, Z. Szymanski, S. Wycech, C. Gustafson, I-L Lamm, P. Möller, and B. Nilsson, Nucl. Phys. A131, 1 (1969).

5. We have done the calculation for three nuclei: ^{20}Ne, ^{108}Ru (with Coulomb interaction) and ^{108}Xe (without Coulomb interaction). We present here the results for ^{108}Ru only. The results for the other two nuclei are consistent and lend further support to the discussions.

6. C. F. Tsang, Ph. D. thesis, UCRL-18899.

7. P. Koopmans, Physica 1, 104; A. Lande, Phys. Rev. Letters 18, 496 (1967).

Potential Energy Surfaces of Heavy Nuclei †

Chin Fu Tsang

Up to the present, the most successful method to calculate the potential energy surfaces of heavy nuclei in a deformation space is the two-part approach.[1] This is the approach that considers the energy to be composed of two parts: a smooth part given by the leptodermous (liquid-drop) expression,[2] which accounts for 99% of the potential energy, and a wiggly part, commonly known as the shell energy or shell correction, calculated on an independent-particle model. Figure 1 shows the potential-energy surfaces of four nuclei relative to their respective leptodermous energies at spherical deformation (E = 0). The broken curve is the smooth part of the energy and the solid curve is the total potential energy. Each plot is usually called the fission-barrier shape of the particular nucleus.

You will be surprised by how much one can learn from such plots of potential-energy surfaces. Not only does the calculation give very good agreement when compared with experiments, but it also affords a very clear picture to understand the results. We shall review below six different experimental areas in which an understanding can be achieved by the two-part approach.

A. Ground-State Nuclear Deformations

The ground-state nucleus is represented by the lowest minimum of the plot. The minimum occurs at an indentation made by the shell energy on the smooth part. Thus it is clear that the deformation of the ground state is qualitatively due to the shell energy. The effect of an incorrect smooth part as is present in the original Mottelson and Nilsson calculation,[3] will probably affect the deformation by a "small" amount (shifting the value from

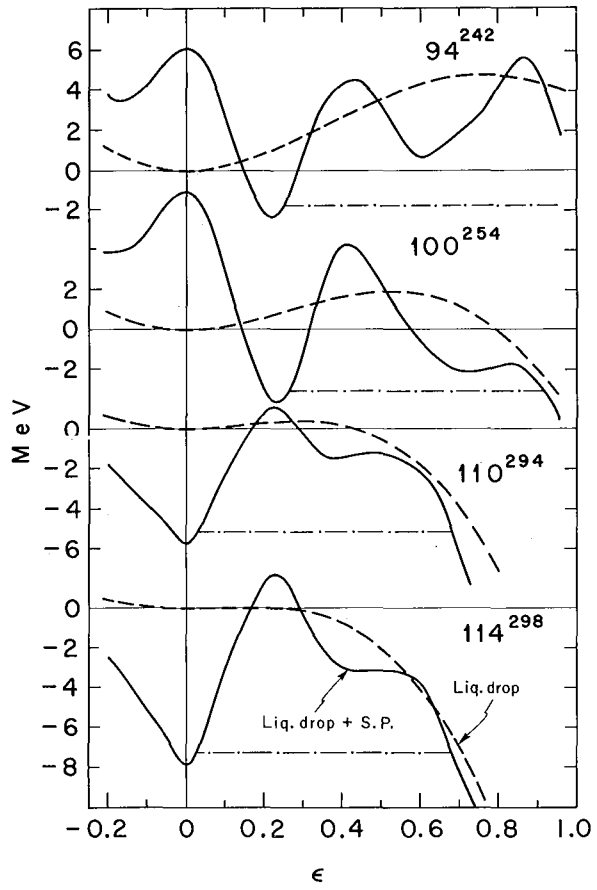

Fig. 1. Potential energy as a function of deformation. The broken curves correspond to the smooth energy given by the leptodermous (liquid-drop) approach. The solid curves are the potential energy after inclusion of shell and pairing effects. (XBL688-3679)

ϵ = 0.20 (say) to 0.23). This explains the success of Mottelson and Nilsson in their calculation of nuclear deformations.

B. Ground-State Nuclear Masses

The experimental ground-state nuclear mass is given very well (within 1-2 MeV) by the value at the lowest minimum. It is to be noted here that this value is always lower than the value of the smooth part at the same deformation. It is a general feature that at the minima in the barrier curve, the shell energy is always negative and at the maxima, it is always positive. One should be impressed by the surprising result that the shell energy which is extracted from single-particle spectrum with no obvious relation to nuclear masses should give the experimental values so well.

C. Fission-Barrier Heights and Detailed Comparison of the Fission Barrier with Experiments

In Fig. 1 the higher of the two peaks can be directly compared with experimental measurement of the spontaneous fission barrier. Bjørnholm[4] has attempted to make a comparison of the whole barrier shape for the actinide nuclei, including fission barrier. He was not only able to look at the ground-state mass and deformation and the fission barrier heights, but was also able to extract the excitation energy of the shape isomeric state (secondary minimum) and of the inner peak (which is the lower of the two peaks for these nuclei) from fission isomer and subthreshold neutron-resonance experiments. The relative energy heights are given very well by the theory. Experiments to determine the shapes at the peaks and isomeric state will be very valuable to test the theory further.

D. Trends of Decay Half-Lives Near a Magic Nucleus

On the two-part approach one is also able to understand the behavior of decay half-lives near a closed-shell (or magic) nucleus. If we look at the spontaneous-fission half-life in the neighborhood of a closed-shell nucleus (say Z = 114 and N = 184 as predicted by various authors), one is able to predict its qualitative behavior without any detailed calculations. In Fig. 2 the broken line indicates the spontaneous-fission half-life contours due to the smooth part of energy alone. The magic numbers Z = 114 and N = 184 will essentially make all nuclei around the nucleus $^{298}114_{184}$

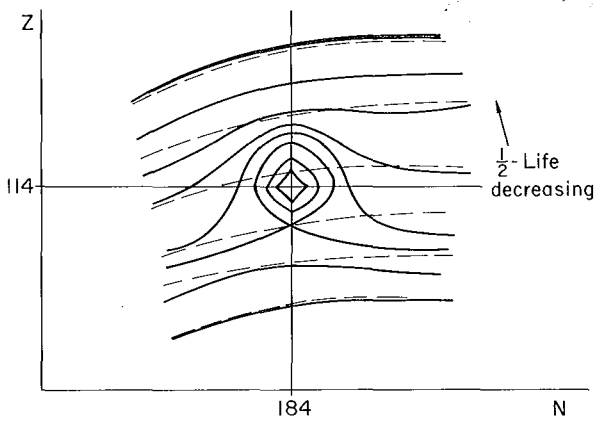

Fig. 2. Trends of spontaneous fission half-lives of nuclei near a closed shell (magic number). The broken curves indicate the half-lives if the closed shell is not present. The solid curves are obtained when the effects of the closed shell are included. (XBL713-2983)

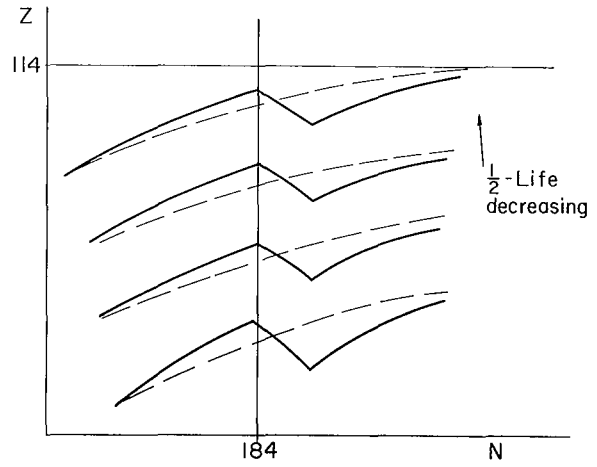

Fig. 3. Trends of alpha-decay half-lives of nuclei near a closed shell (magic number). The broken curves indicate the half-lives if the closed shell is not present. The solid curves are obtained when the effects of the closed shell are included. (XBL713-2982)

have a much longer half-life, forming an island out of the smooth background. The alpha-decay half-lives around a closed shell can also be understood in a similar way. In Fig. 3, the alpha-decay half-life contours without shell effects are indicated by broken lines. The value decreases as Z increases. A nucleus with a magic number has a particularly lower mass due to a negative shell energy. Thus the shell part will modify the contours in such a way that two kinks occur in the contours corresponding to the case when either the parent or the daughter nucleus is closed shell.

E. Possible Occurrence of Shape Isomers Over the Periodic Table

The shape-isomeric state is a metastable state of the nucleus with a different shape from the ground-state shape. It corresponds to the secondary minimum in the barrier plot of Fig. 1. By considering some well-known properties of the smooth part and the shell energy part, one is able to say something very simple but general on the necessary conditions for the occurrence of shape isomers. (See Nuclear Chemistry Annual Report 1969, UCRL-19530, p. 144.) Figure 4 shows the regions in the whole periodic table where the shape isomers may occur, based on this two-part approach.

F. Fission Asymmetry

A start for a quantitative explanation of the long-standing problem of fission asymmetry was made by Möller and Nilsson,[5] who

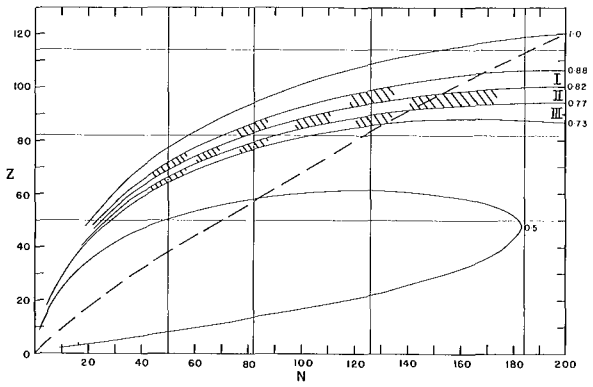

Fig. 4. The occurrence of shape isomers over the Z, N plane, indicated by shaded areas in bands. The broken line indicates the approximate line of beta stability. The vertical and horizontal lines indicate neutron and proton magic numbers, respectively. (XBL701-83)

used the two-part approach to study the potential energy surfaces in asymmetric as well as symmetric deformation coordinates. They have found an asymmetric fission saddle-point for ^{236}U.

In conclusion, it appears at the moment that the two-part approach is the only feasible method that can be used to calculate the potential energy surfaces of a large number of heavy nuclei. Its value lies very much in its simplicity (compared with other methods), and that not only is it able to give an understanding of many experimental results, but is also able to make rather general predictions regarding the stability of superheavy nuclei and the possible occurrence of shape isomers over the periodic table.

Footnote and References

†Condensed from the second part of an invited talk given at the Gordon Research Conference on Nuclear Structure Physics at Tilton, New Hampshire, July 1970; UCRL-19962.

1. W. D. Myers and W. J. Swiatecki, Nucl. Phys. 81, 1 (1966); V. M. Strutinsky, Nucl. Phys. A122, 1 (1968); Nilsson, et al., Nucl. Phys. A131, 1 (1969); and others.

2. C. F. Tsang, Ph. D. thesis, 1969; UCRL-18889.

3. B. R. Mottelson and S G. Nilsson, Mat. Fys. Skr. Dan. Vid. Selsk. 1, No. 8 (1959).

4. Sven Bjørnholm, Invited Talk at the Symposium on Transuranium Elements, Welch Foundation, Houston, Texas, November 1969.

5. Peter Möller and S G. Nilsson, Phys. Letters 31B, 283 (1970).

Smooth Trends and Shell Effects in Sums Over Single-Particle Energies

W. D. Myers, W. J. Swiatecki,† and C. F. Tsang

The total energy of a system of independent particles moving in a potential well shows variations about its average value when considered as a function of particle number or potential shape. These variations are called shell effects, and their origin is in the fluctuations in the level density near the Fermi surface.[1] When the energies of the single-particle states of the system are displayed in the conventional manner in a Nilsson diagram, the origin of the level density variations is obscured by the projection onto the one dimension of eigenenergy, of what is essentially a property of the three-dimensional quantum number space.

A substantial increase in our understanding of the origin, the frequency of occurrence, and the magnitude of shell effects can be obtained by examining the nature of the system's isoenergy surfaces in quantum number space. As an example, consider the eigenenergy expression in Cartesian coordinates for the harmonic oscillator, which is

$$E_{n_x, n_y, n_z} = \hbar\omega_x(n_x + 1/2) + \hbar\omega_y(n_y + 1/2) + \hbar\omega_z(n_z + 1/2). \quad (1)$$

In the space (n_x, n_y, n_z), where the lattice of points at the corners of unit cubes represents possible single-particle states of the system, the isoenergy surfaces are parallel planes whose orientation is determined by the relative magnitude of the $\hbar\omega$'s. Clearly, the striking shell effects displayed by the harmonic oscillator in Fig. 1 are a direct consequence of the fact that a planar isoenergy surface picks out a special symmetry existing in cubic lattices. As particles are added to such a system, the isoenergy plane representing the Fermi surface sweeps outward through the lattice. Regions where no points are encountered are gaps in the energy spectrum, and shells arise when a large number of points are encountered simultaneously.

Figure 2 shows the nature of the isoenergy surface of an isotropic harmonic oscillator when the eigenenergies are given in terms of spherical coordinates according to the expression

$$E_{n,\ell} = \hbar\omega(\ell + 2n + 3/2). \quad (2)$$

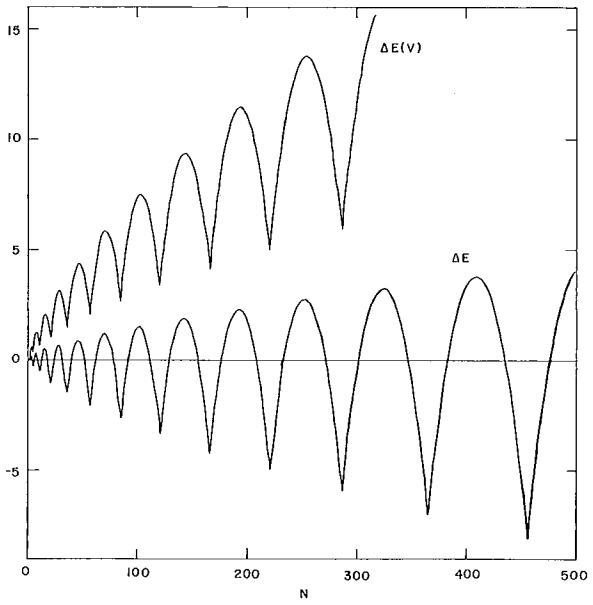

Fig. 1. This figure from Ref. 3 shows the shell effects ΔE for a harmonic oscillator potential as a function of particle number. (XBL713-2995)

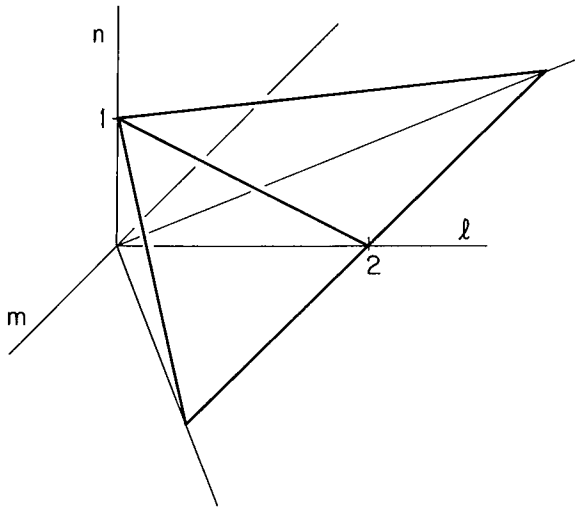

Fig. 2. The planar isoenergy surface in (n, ℓ, m) quantum number space for the harmonic oscillator potential. (XBL713-2985)

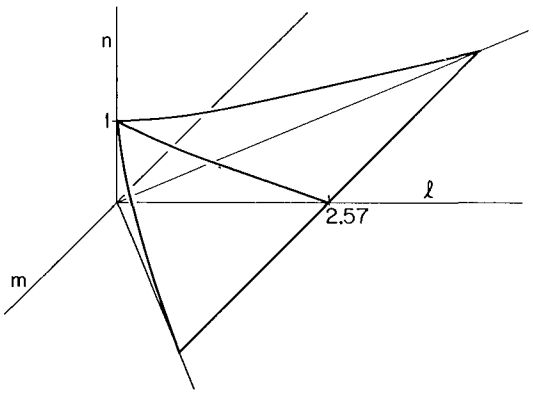

Fig. 3. The approximate isoenergy surface in (n, ℓ, m) quantum number space for a spherical square-well potential. (XBL713-2984)

Similarly, the expression for the eigenenergies of a hydrogen atom is given by

$$E_{n,\ell} = -(Me^4/2\hbar^2)/(n+\ell)^2, \qquad (3)$$

and we see that these isoenergy surfaces are also planar with a slope of 1:1 in contrast to the 2:1 slope in the harmonic oscillator case. Consequently, even greater degeneracies are encountered here than in the case of the harmonic oscillator.

Another interesting case is that of a spherical square-well potential where the eigenenergies are given by the approximate expression[2]

$$E_{n,\ell} = (\hbar^2/2MR)\left[(\ell + 2n)^2 \frac{\pi}{4} - \ell(\ell+1)\right]. \qquad (4)$$

These isoenergy surfaces, which are shown in Fig. 3, are approximately planar with a slope of 3.37:1 for large ℓ values and 2:1 for small ℓ values. The power of this approach to shell effects is seen when the magic numbers predicted by assuming an average slope of 3:1 are compared with the actual shells found in an exact calculation.

Predicted	1, 4, 9, 17, 29, 45, 66, 93, 126, 166
Exact	1, 4, 10, 17, 29, 46, 69, 93, 127, 169

Footnote and References

†Theoretical Physics Group, Lawrence Radiation Laboratory, Berkeley.

1. C. F. Tsang, Ph. D. thesis, 1969; UCRL-18899, and references listed therein.

2. M. L. Gursky, Nuclear Binding Energy From the Independent Particle Model, Ph. D. thesis Vanderbilt University 1958.

3. C. F. Tsang, UCRL-19962, August 1970.

Droplet-Model Shape Dependence*

William D. Myers and W. J. Swiatecki†

In order to extend the droplet-model mass formula of Ref. 1 to deformed nuclei and to the calculation of fission barriers, it was first necessary to establish its formal shape dependence. This was done and the following droplet-model mass formula was obtained:

$$M(N,Z;\text{shape}) = M_n N + M_H Z + \left[-a_1 + J\bar{\delta}^2 - \frac{1}{2}K\bar{\epsilon}^2 + \frac{1}{2}M\delta^{-4}\right] A + \left[a_2 + \frac{9}{4}(J^2/Q)\,\bar{\delta}^2\right] A^{2/3} B_s$$

$$+ a_3 A^{1/3} B_k + c_1 Z^2 A^{-1/3} B_c - c_2 Z^2 A^{1/3} B_r - c_3 Z^2 A^{-1} - c_4 Z^{4/3} A^{-1/3} - c_5 Z^2 B_w, \qquad (1)$$

where

$$\bar{\delta} = \frac{\left[1 + \frac{3}{16}(c_1/Q) Z A^{-2/3} B_v\right]}{\left[1 + \frac{9}{4}(J/Q) A^{-1/3} B_s\right]} \qquad (2)$$

$$\bar{\epsilon} = [-2a_2 A^{-1/3} B_s + L\delta^{-2} + c_1 Z^2 A^{-4/3} B_c]/K. \quad (3)$$

The B's which appear in these expressions are the shape dependences of various quantities of interest. There are now four new B's in addition to the two familiar ones, B_s and B_c. They are defined in the usual way so as to have the value unity for a sphere. In each case the quantity B_i is calculated by performing the indicated integral over the given shape and dividing by the value that the integral would have for a sphere of equal volume. As written here the denominators are in terms of R, the radius of the sphere of equal volume.

1. Surface

$$B_s = \iint_S d\sigma/(4\pi R^2) \quad (4)$$

2. Curvature

$$B_k = \iint_S \kappa \, d\sigma/(8\pi R), \quad (5)$$

where κ is the local curvature.
For notational convenience, we can define a quantity $W(\underset{\sim}{r}_1)$, which is proportional to the Coulomb potential, by the expression

$$W(\underset{\sim}{r}_1) = \iiint_V \frac{1}{r_{12}} \, dv_2, \quad (6)$$

$2\pi R^2 [1 - \frac{1}{3}(r/R)^2]$ for a sphere.

We can also define the average value $\bar{W}$ and the deviation from average $\tilde{W}$ by the expressions

$$\bar{W} = \iiint_V W(\underset{\sim}{r}) \, dv / \frac{4}{3}\pi R^3, \ \frac{8}{5}\pi R^2 \quad (7)$$

for a sphere,

$$\tilde{W}(\underset{\sim}{r}) = W(\underset{\sim}{r}) - \bar{W}, \ \frac{2}{5}\pi R^2 [1 - \frac{5}{3}(r/R)^2] \quad (8)$$

for a sphere,

With these definitions we can write the four Coulomb shape dependences in the following way:

3. Coulomb

$$B_c = \iiint_V W(\underset{\sim}{r}) \, dv/(\frac{32}{15}\pi^2 R^5) \quad (9)$$

4. Coulomb redistribution

$$B_r = \iiint_V [\tilde{W}(\underset{\sim}{r})]^2 \, dv/(\frac{64}{1575}\pi^3 R^7) \quad (10)$$

5. Surface Coulomb

$$B_v = \iint_S \tilde{W}(\underset{\sim}{r}) d\sigma/(-\frac{16}{15}\pi^2 R^4) \quad (11)$$

6. Surface Coulomb squared

$$B_w = \iint_S [\tilde{W}(\underset{\sim}{r})]^2 \, d\sigma/(\frac{64}{225}\pi^3 R^6). \quad (12)$$

A comment should probably be made with regard to the subscripts S and V used on many of the integrals which appear here. All integrals for the shape dependences (the quantities B_i) have such subscripts.

These subscripts imply that the integration is to be carried out over the surface (or volume) of a uniform body of the desired shape with a sharp surface and a total volume equal to $V = 4/3\,\pi\, r_0^3 A$. The actual droplet model prediction for the matter distribution of the nucleus in question will differ by a scale change from the object just described. In addition the neutron and proton density distributions will differ from the scaled shape by a displacement of their surfaces from the mean location of the surface of the matter distribution. This is because of the formation of a neutron skin. The neutron and proton density distributions and the matter distribution (which is their sum) will also vary throughout the central region because of the Coulomb repulsion. The influences of all of these effects are calculated in the model. Their influence on the total energy is included in the mass formula by means of analytic expressions involving only integrals over the originally specified shape.

The energy has been minimized analytically with respect to the new degrees of freedom introduced by the droplet model. They need not be varied explicitly. All that need be done in searching for stationary points in the total energy is to vary the shape.

The analytic dependence of the B's is given in Ref. 2 for spheroidal shapes, for tangent spheres, and for shapes which are described in terms of spherical harmonics. This work also contains extensive calculations of fission barriers using a simplified version of the droplet model.

Footnotes and References

†Condensed from UCRL-19543, January 1970.

*Theoretical Physics Group, Lawrence Radiation Laboratory, Berkeley.

1. William Don Myers, Ph. D. thesis, UCRL-18214, May 1, 1968; William D. Myers and W. J. Swiatecki, Ann. Phys. (N. Y.) 55, 395-505 (1969).

2. Rainer W Hasse, UCRL-19910, October 1970 (to be published).

Thomas-Fermi Calculations of Nuclear Properties

William D. Myers

The Thomas-Fermi statistical method is ideally suited to the study of average nuclear properties. Extensive use of this approach was made in Ref. 1, and references are given there to the large body of earlier work.

The phenomenological two-body interaction used in Ref. 1 was that of Seyler and Blanchard, which can be written

$$V(r,p) = -C_{\ell \text{ or } u}\,\frac{e^{-r/a}}{r/a}\,[1 - (p/b)^2], \quad (1)$$

where

- V = the potential energy of two particles,
- C = the strength of the interaction (different for "like" and "unlike" pairs),
- r = the distance between the particles,
- a = the range of the Yukawa force,
- p = the magnitude of the relative momentum of the particles, and
- b = the critical value of the relative momentum at which the attractive force (whose strength is decreasing for increasing relative momentum) vanishes and beyond which the force becomes repulsive.

The four quantities a, b, C_ℓ, and C_u were treated as adjustable parameters, and the four pieces of data that were used to determine them were the binding energy per particle of nuclear matter, the density of nuclear matter, the nuclear symmetry energy, and the nuclear surface energy.

When this force was used in a Thomas-Fermi calculation of nuclear properties, generally satisfactory results were obtained. However, the surface diffuseness -- given in terms of the 10-90% distance t -- was only 2 fm, as opposed to the generally accepted experimental value of 2.4 fm. In addition the nuclear compressibility coefficient K was found to have the value 295 MeV, which is larger than most other estimates. Both of these differences can be attributed to the rapid rate at which the interaction becomes weaker with increasing relative momentum.

To investigate this problem and perhaps obtain a more satisfactory nuclear model, an interaction was chosen that allows one to adjust the rate at which the interaction weakens. This interaction has the form

$$V(r,p) = -C_{\ell \text{ or } u}\,\frac{e^{-r/a}}{r/a} \times \left\{1 - (c/b)^2\left[1 - \frac{1}{1 + (p/c)^2}\right]\right\}. \quad (2)$$

It can also be written

$$V(r,p) = -C_{\ell \text{ or } u}\,\frac{e^{-r/a}}{r/a} \times \left\{(c/b)^2\left[\frac{1}{1 + (p/c)^2} - \kappa\right]\right\}, \quad (3)$$

where

$$\kappa = 1 - (b/c)^2. \quad (4)$$

The coefficients a, b, C_ℓ, and C_u are chosen as before, and the new coefficient κ can then be chosen so as bring the calculated surface diffuseness into agreement with the experimental value.

If $\kappa = 1$ in Eq. (3), then the quantity in the largest bracket becomes $1 + (p/b)^2$, which is identical to Eq. (1). On the other hand if $\kappa = 0$, the quantity in the bracket becomes $(c/b)^2/[1 + (p/c)^2]$, which has a very "soft" momentum dependence. Figure 1 illustrates the nature of the momentum dependence for different values of κ, where the other coefficients have been adjusted in each case so as to reproduce the properties of nuclear matter. Figure 2 illustrates the influence κ has

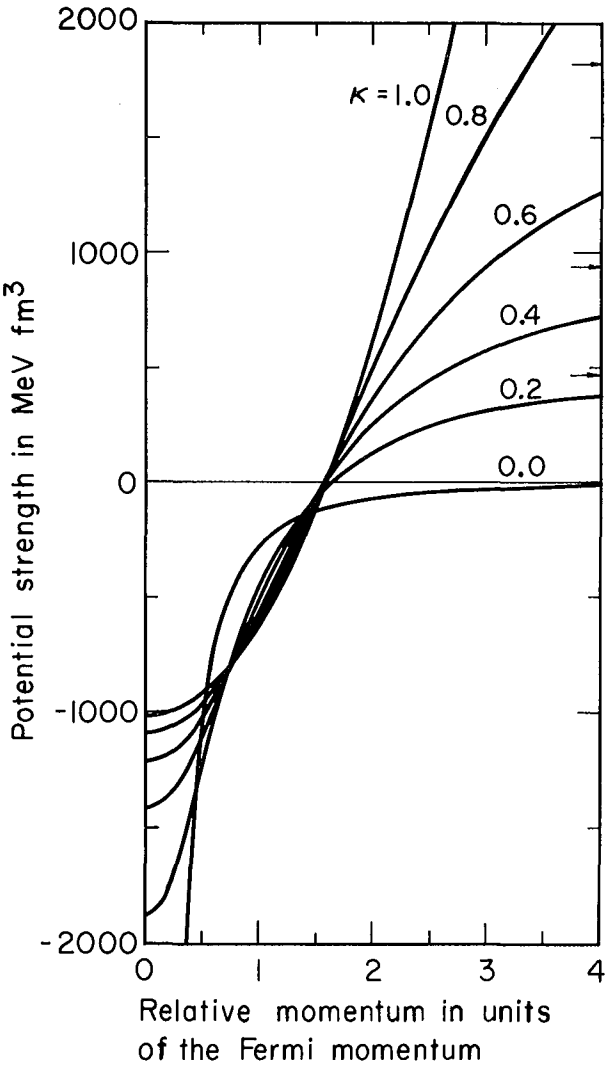

Fig. 1. The potential strength in MeV fm^3 is plotted against the relative two-body momentum for different values of κ. The strengths are not all the same for zero momentum since the other potential parameters have been adjusted in each case so as reproduce known properties of nuclear matter. The curve labeled κ = 0 corresponds to earlier work, and the arrows along the right side of the figure indicate the asymptotic values toward which the curves below them are tending.
(XBL713-2988)

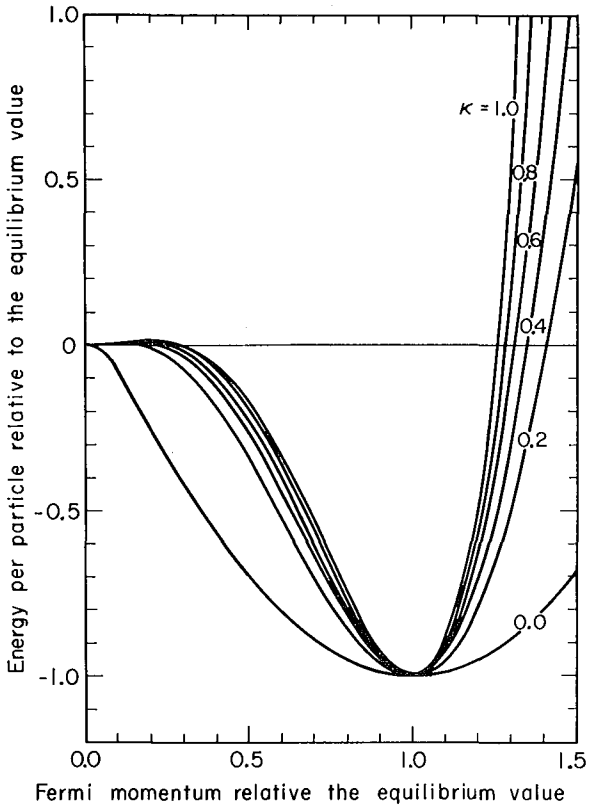

Fig. 2. The energy per particle of infinite nuclear matter in units of its equilibrium value is plotted against the Fermi momentum in units of its equilibrium value. (This later quantity is proportional to the cube root of the density.) Curves corresponding to different values of κ are so labeled, and one sees that the compressibility K, which is proportional to the second derivative of the curve at equilibrium, is an increasing function of κ.
(XBL713-2987)

on the density dependence of the energy per particle of nuclear matter. One easily sees in this figure that reducing the value of κ will bring a corresponding reduction in the value of the compressibility K. This relationship is shown in Fig. 3 where K is plotted as a function of κ.

A value of about 0.7 is required for κ in order to obtain the desired surface diffuseness. For this value of κ, the compressibility K is about 240 MeV. The other quantities of interest in the droplet model,[1] such as L, M, Q, and a_3, have also been calculated in this way. The results differ somewhat from the earlier calculations, but no large variations have been observed.

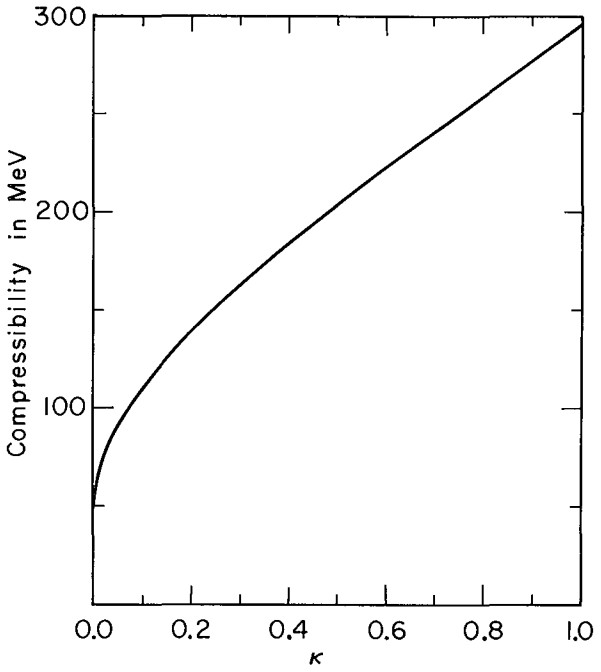

Reference

1. William Don Myers, Ph. D. thesis, UCRL-18214, May 1, 1968; William D. Myers and W. J. Swiatecki, Ann. Phys. (N. Y.) 55, 395 (1969).

Fig. 3. The compressibility of nuclear matter K is plotted as a function of κ for the interaction given in Eq. (3); all the other coefficients being adjusted in each case so as to reproduce known nuclear matter properties. (XBL713-2986)

Comparison Between the Truncated-Droplet Model and a Conventional Liquid-Drop Model Mass Formula

William D. Myers

The droplet-model mass formula of Ref. 1 has tentatively been truncated to a form which is believed to retain the most significant new features of the method. The new formula, which is considerably simpler and easier to use than the complete droplet model, can be written

$$
\begin{aligned}
M(N,Z;\text{shape}) = {} & M_n N + M_H Z - a_1 A \\
& + a_2 A^{2/3} B_s + a_3 A^{1/3} B_k + a_4 \\
& + JI^2 A/(1 + \zeta A^{-1/3} B_s) \\
& + c_1 Z^2 A^{-1/3} B_c - c_3 Z^2 A^{-1} \\
& - c_4 Z^{4/3} A^{-1/3} \\
& + W(|I| + \Delta) + \delta \\
& + S(N,Z)(1 - 2\theta^2) e^{-\theta^2}, \qquad (1)
\end{aligned}
$$

where the notation for the basic nuclear and Coulomb energies in the first five lines is the same as that of Ref. 1. The next to last line contains three terms found to be necessary for the description of real nuclei. The first is the so called Wigner term $W\cdot|I|$ and the second is a related correction (see Ref. 2) that has the value W/A for odd-odd $N = Z$ nuclei and is zero otherwise. The last term in this line δ is the usual even-odd mass difference whose origin is in the pairing force. The last line of Eq. (1) is the phenomenological shell correction of Ref. 3.

The shell correction method used here is provisional and improved corrections, such as those being developed by Nix at Los Alamos using the Strutinsky method, will be incorporated when they become available.

The droplet-model formula seems to differ substantially in its treatment of the nuclear symmetry energy from conventional liquid-drop model formulae, such as the one used in our own earlier work[4] or that of Seeger.[5] [See line 3 of Eq. (1).] The difference in predicted stability of neutron excess nuclei is of special interest in astro-

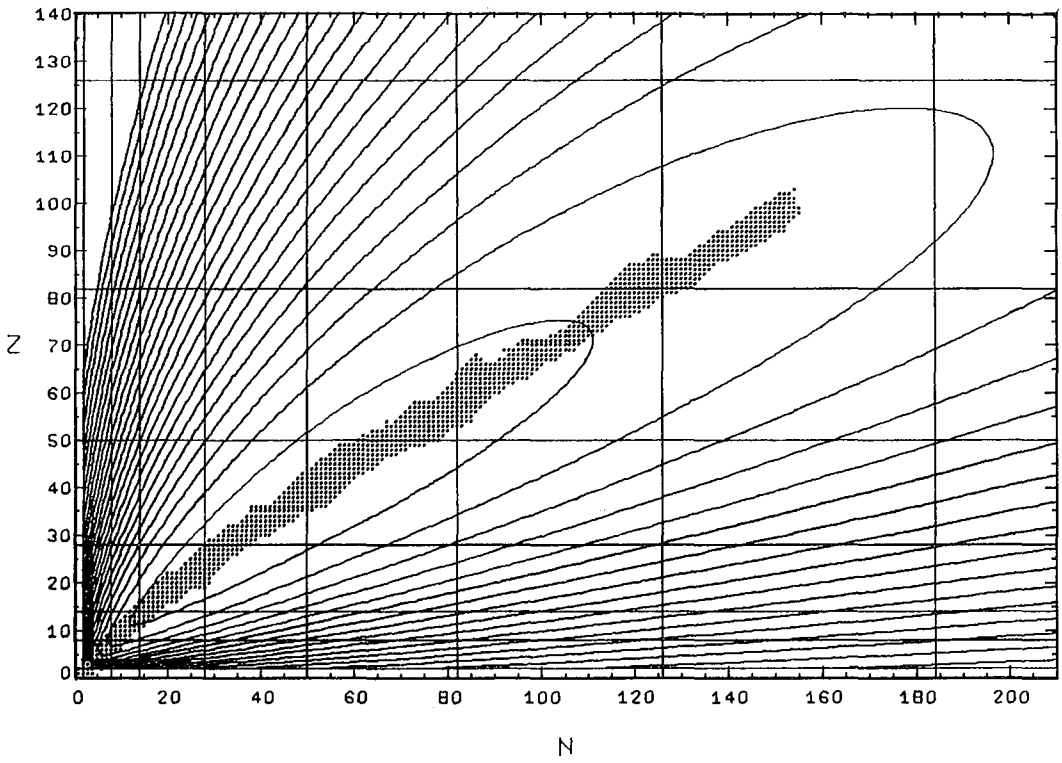

Fig. 1. Contours of the binding energy per particle according to the smooth part of the droplet-model mass formula for nuclei with N neutrons and Z protons. The innermost contour corresponds to 8 MeV and the other contours correspond to decreasing values with a spacing of 1 MeV. (XBL713-2996)

physical studies of the r process of nucleosynthesis. Consequently a preliminary set of droplet-model coefficients, determined by fitting the formula to nuclear masses, were used to assess the importance of this new term.

Figure 1 is a partial contour plot of the smooth part of the droplet-model binding energy per particle (i. e. the shell and even-odd terms have been dropped) for nuclei with N neutrons and Z protons. The innermost contour represents a binding of 8 MeV per particle and the other contours represent decreasing values with a contour spacing of 1 MeV. The straight lines indicate the position of magic numbers and the dots are the location of nuclei whose masses are known.

Figure 2 is a similar plot using the Seeger[5] liquid-drop model formula. A comparison of these two figures shows that there is very little difference in the two methods of calculation. Consequently, it is expected that the stability properties of neutron excess nuclei predicted by the droplet model will be essentially the same as those found in earlier work.

References

1. William D. Myers and W. J. Swiatecki, UCRL-19543, January 1970.

2. W. J. Swiatecki, unpublished notes; G. T. Garvey et al., Rev. Mod. Phys. S1, (1969).

3. W. D. Myers and W. J. Swiatecki, Ark. f. Fys. 36, 343 (1967).

4. W. D. Myers and W. J. Swiatecki, Nucl. Phys. 81, 1 (1966).

5. P. A. Seeger, Proceedings of the Third International Conference on Atomic Masses (University of Manitoba Press, 1967).

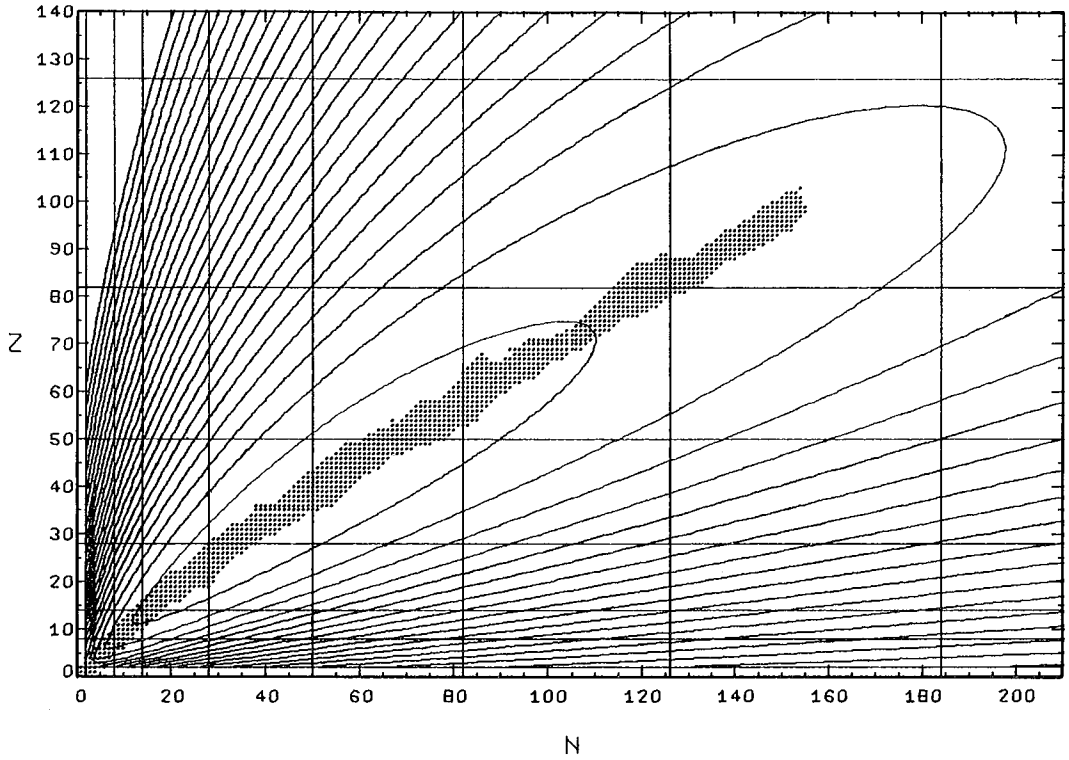

Fig. 2. The same as Fig. 1, but for the conventional liquid-drop model mass formula of Seeger.[5] (XBL713-2997)

Determination of the Nuclear Radius Constant and Surface Diffuseness Parameter from the Binding Energy Differences of Mirror Nuclei

William D. Myers

Since the binding energy differences of mirror nuclei are expected to be entirely due to Coulomb effects, they provide a simple and direct method for the determination of those parameters critical for the characterization of nuclear charge distributions, i. e., the radius constant and surface diffuseness parameter. These parameters are obtained by noting that a calculation of the binding energy difference using a conventional liquid-drop model mass formula, such as the one used in Ref. 1, yields the expression

$$\Delta E_b = c_1(\Delta Z^2/A^{1/3})[1 - (5/2)(b/r_o)^2 A^{-2/3}]. \quad (1)$$

If the experimental quantity F,[2] defined by the expression

$$F \equiv \Delta E_b (A^{1/3}/\Delta Z^2), \quad (2)$$

is plotted against $A^{-2/3}$ as in Fig. 1, and a straight line is passed through the points, then the intercept and slope of this line correspond to the quantities

$$\text{intercept} = c_1 , \quad (3)$$

$$\text{slope} = (5/2)(b/r_o)^2 c_1 . \quad (4)$$

The straight line could have been drawn through the points in Fig. 1, but since some unexplained periodic variation remains, the data were averaged over the four-point groups which seem to constitute each substructure

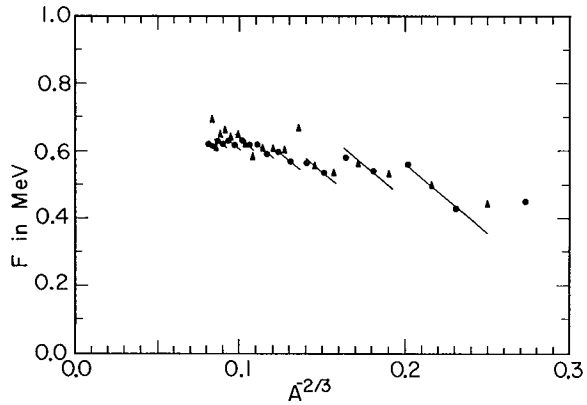

Fig. 1. The experimental quantity F defined in Eq. (2) is plotted against $A^{-2/3}$ for mirror nuclei corresponding to values of A from 7 to 43. The straight-line segments serve to identify groups of four points that seem to be members of some substructure. (XBL713-2990)

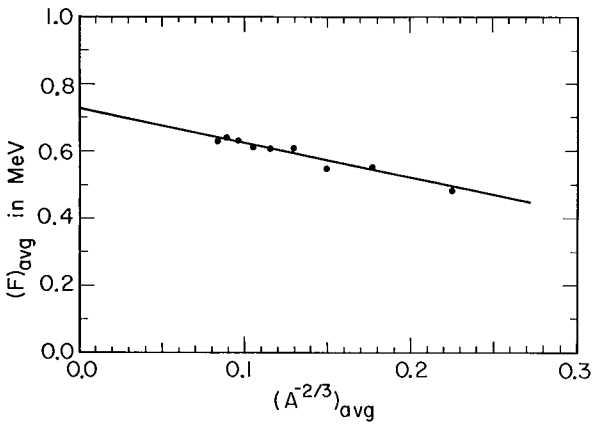

Fig. 2. The average value of F is plotted against the corresponding average value of $A^{-2/3}$, where the average has been carried out within the groups of four points identified in Fig. 1. The intercept and slope of the line drawn through these points are used to determine r_o and b, respectively. (XBL713-2989)

and the aesthetically more pleasing result was plotted in Fig. 2. The intercept of 0.727 MeV and slope of 1.027 MeV, which are obtained from the line in Fig. 2, correspond to

$$c_1 = 0.727 \text{ MeV} \quad \text{and} \quad (b/r_o) = 0.752. \qquad (5)$$

As used here c_1 corresponds to the Coulomb energy coefficient in the liquid-drop model mass formula of Ref. 1. It is related to the radius constant r_o by the expression $c_1 = (3/5) \cdot (e^2/r_o)$, where $e^2 = 1.4399784$ MeV fm. Hence,

$$r_o = 1.19 \text{ fm} \quad \text{and} \quad b = 0.89 \text{ fm},$$

where b is the surface "width,"[3] which -- for Fermi function density distributions -- is related to the diffuseness parameter z and 10-90% distance t by the expressions:

$$z = (\sqrt{3}/\pi) \cdot b \quad \text{and} \quad t = 4 \ln 3 \cdot z. \qquad (6)$$

Consequently, for these light nuclei, we find that the surface diffuseness is characterized by the values

$$z = 0.49 \text{ fm} \quad \text{and} \quad t = 2.16 \text{ fm}.$$

Earlier discussions of this type, such as Ref. 4, have been somewhat misleading because the influence of the surface diffuseness was not taken into account.

References

1. William D. Myers and W. J. Swiatecki, Nucl. Phys. 81, 1 (1966).

2. J. H. E. Mattauch, W. Thiele, and A. H. Wapstra, Nucl. Phys. 65, 1 (1965).

3. Georg Süssmann, UCRL-19960, August 1970.

4. O. Kofoed-Hansen, Rev. Mod. Phys. 30, 449 (1958).

A New Semiempirical Level Density Formula with Pairing and Shell Effects

A. Gilbert, R. C. Gatti, S. G. Thompson and W. J. Swiatecki

Bethe[1] developed the original Fermi gas formula for the nuclear level density ρ

$$\rho = C \exp(\sqrt{aU}),$$

where U is the excitation energy and a is

proportional to A, the number of nucleons.

Efforts to improve the Bethe formula have been concentrated in two regions of excitation energy.

A. Neutron Resonance Region

Using the Bethe formula to fit neutron resonance data, with a as an adjustable parameter, one finds systematic odd-even and shell effects in a. Specifically, even-even nuclei have systematically lower level densities than neighboring odd-A nuclei; also, in the region of closed shells, the value of a is reduced compared with the Fermi gas value.

Newton[2] found that the odd-even effect could be accounted for by replacing U in the Bethe formula by $U - U_o$, where U_o is the odd-even term in the semiempirical mass formula. He also related a to shell-model parameters.

A slightly different approach by Gilbert and Cameron[3] gave a relation between a and the shell-effect term in the nuclear mass formula.

B. High-Energy Limit

Rosenzweig[4] and Gilbert[5] have shown that for a periodic scheme of single-particle states the level density should have the form

$$\rho \sim \exp \left[2\sqrt{a(U - \Delta)}\right]$$

at high energies. The term Δ is related to shell structure and is largest at closed shells.

In order to incorporate all of these effects, we are developing a semiempirical level density formula with three adjustable parameters:

$$\rho = C \exp 2\sqrt{a[U - d(U)]},$$

where

$$a = \alpha A$$

and

$$d(U) = \frac{\Delta}{1 + \frac{k}{U}} .$$

The adjustable parameters are C, α and k. Both the odd-even and shell terms from the nuclear mass formula will be included in Δ. This level density formula can also be written as

$$\rho = C \exp \left(2\sqrt{a_{eff} U}\right),$$

where

$$a_{eff} = a \left(1 - \frac{\Delta}{U + k}\right),$$

so that we get a reduced value of a_{eff} particularly near closed shells.

In conjunction with this project we are updating the collection of neutron resonance data of Gilbert and Cameron,[3] using the Brookhaven compilation of neutron data (BNL-325) along with supplements to the Nuclear Data Sheets and their list of recent references.

This set of data will be used to determine the parameters of the level density formula. The formula will also be tested with data on nuclear levels near the ground state and on high-energy fission data.[6]

References

1. H. Bethe, Phys. Rev. 50, 332 (1936).

2. T. D. Newton, Can. J. Phys. 34, 804 (1956).

3. A. Gilbert and A. G. W. Cameron, Can. J. Phys. 43, 1446 (1965).

4. N. Rosenzweig, Phys. Rev. 108, 817 (1957); and Phys. Letters 22, 307 (1966).

5. A. Gilbert, UCRL-18095, February 1968.

6. A. Khodai-Joopari, Fission Properties of Some Elements Below Radium (Ph. D. thesis), UCRL-16489, July 1966.

Fission Barriers in the Droplet Model

Rainer W. Hasse†

The droplet model as given by Myers and Swiatecki[1] is investigated in its shape dependence. In order to calculate fission barriers, effective moments of inertia and related geometrical quantities of the symmetric saddle points, we parameterize the nuclear surface in terms of different families of shapes. As important results, it is noted that the curvature correction to the surface energy has the largest influence on the fission barriers and can produce a second minimum in the potential energy vs deformation (isomeric states). The Coulomb redistribution energy can produce a minimum in the potential energy of two tangent fragments vs their ratio of radii (asymmetric fission). We mostly confine ourselves to a truncated form of the droplet model, i. e., we neglect the effect of the Coulomb energy on the dilation of the nucleus and on the neutron skin thickness.

The droplet-model total energy of a nucleus as given by Myers and Swiatecki reads

$$E_{total} = [-a_1 + J\bar{\delta}^2 - \tfrac{1}{2}K\bar{\epsilon}^2 + \tfrac{1}{2}M\bar{\delta}^4]A + [a_2 + \frac{9J^2}{4Q}\bar{\delta}^2]A^{2/3}B_{surf} + a_3 A^{1/3} B_{curv}$$
$$+ C_1 Z^2 A^{-1/3} B_{Coul} - C_2 Z^2 A^{1/3} B_{red} - C_3 Z^2 A^{-1} - C_4 Z^{4/3} A^{-1/3} - C_5 Z^2 B_{sr2} \quad (1)$$

where

$$\bar{\delta} = \left[1 + \frac{3C_1}{16Q} ZA^{-2/3} B_{sr1}^{1/2}\right] \Big/ \left[1 + \frac{9J}{4Q} A^{-1/3} B_{surf}\right]$$
$$\bar{\epsilon} = \frac{1}{K}\left[-2a_2 A^{-1/3} B_{surf} + C_1 Z^2 A^{-4/3} B_{Coul} + L\bar{\delta}^2\right]. \quad (2)$$

The energy terms of Eq. (1) are in the respective order: volume energy, surface energy, curvature energy, Coulomb energy, Coulomb redistribution energy, diffuseness energy, exchange energy, and surface redistribution energy of second kind. The shape dependences B_{surf}, B_{curv} --- B_{sr1} which are defined to take the value of unity for a sphere, are plotted in Fig. 1 for spheroidal shapes.

The truncated-droplet model deformation energy, i. e., total energy for some deformation minus the total energy of the same but spherical nucleus reads

$$E_{Def} = a_2(1-b_3 I^2)A^{2/3}(B_{surf}-1) + a_3 A^{1/3}(B_{curv}-1)$$
$$-a_4 A^{1/3}(B_{comp}-1) + C_1 Z^2 A^{-1/3}(B_{Coul}-1) - C_2 Z^2 A^{1/3}(B_{red}-1)\,. \quad (3)$$

This formula apart from the liquid-drop model

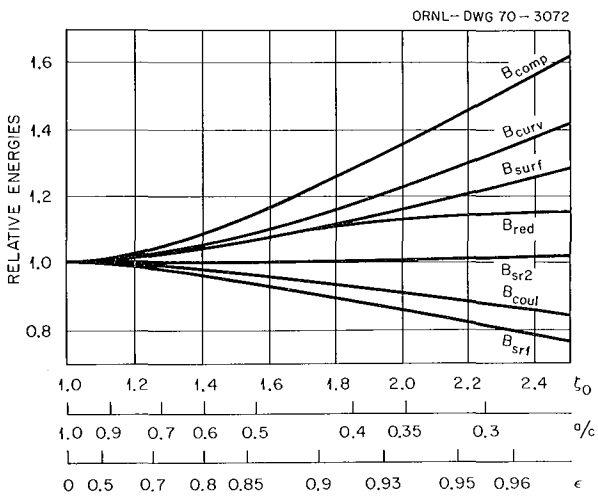

Fig. 1. The shape dependences of the droplet model evaluated for spheroidal shapes (ζ_0 = major semiaxis, a/c = ratio of minor to major semiaxes, ϵ = eccentricity). (XBL713-3183)

energies (surface and Coulomb) contains the droplet-model corrections (curvature, compressibility with $B_{comp} = B^2_{surf}$ and Coulomb redistribution) as additional energies. After having defined the relative strengths of the energies and an energy unit by

$$E^0 = E^0_{surf} + E^0_{curv} + 2\,E^0_{comp},$$

$$\xi = \left(\tfrac{1}{2} E^0_{Coul} - E^0_{red}\right)/E^0,$$

$$\eta = E^0_{curv}/E^0,$$

$$\zeta = -\,E^0_{red}/E^0,$$

$$\chi = -\,E^0_{comp}/E^0, \qquad (4)$$

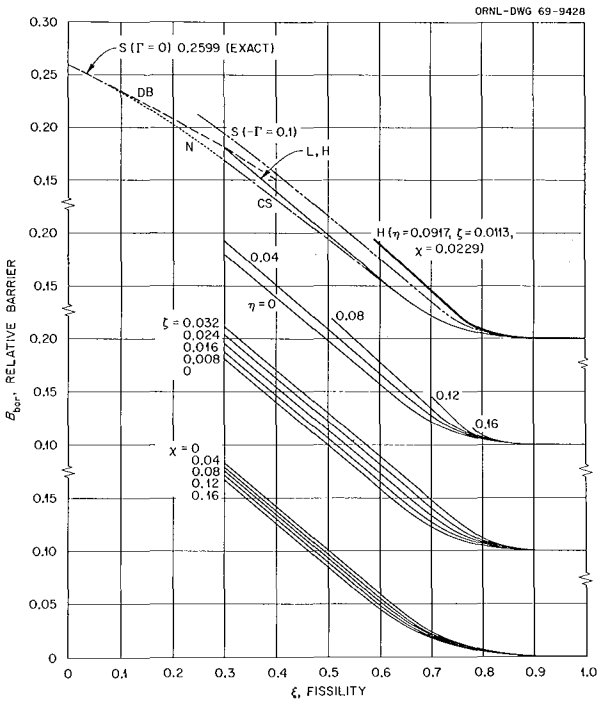

Fig. 2. Relative barriers in the truncated droplet model evaluated for generalized spheroids (η = relative curvature strength, ζ = relative Coulomb redistribution strength, χ = relative compressibility strength). For comparison, the upper bunch of curves gives relative barriers evaluated with other parameterizations of the nuclear surface [s(Γ = 0) and s(-Γ = 0.1), Strutinski without and with curvature energy, DB dumbbells, N Nix, CS Cohen and Swiatecki, L Lawrence, H this work]. (XBL713-3184)

where a superscript zero denotes the value for the spherical nucleus, a dimensionless barrier formula is obtained

$$B_{Bar} \equiv E_{Bar}/E^0 = (B_{surf}-1) + 2\xi\,(B_{Coul}-1)$$

$$+ \eta\,(B_{surf} - B_{curv}) - \zeta\,(2B_{Coul} + B_{red} - 3)$$

$$+ \chi\,(2B_{surf} - B_{comp} - 1)\,. \qquad (5)$$

The first line is the familiar liquid-drop model barrier formula with the fissility x replaced by the refined fissility ξ.

Figure 2 shows the relative liquid-drop model barriers obtained by using various parameterizations of the nuclear surface (see caption) and the droplet model barriers obtained with the parameterization of generalized spheroids,[2] and assuming different values for η, ζ, χ. One can see that the curvature correction has the largest influence on the barriers and that the compressibility and Coulomb

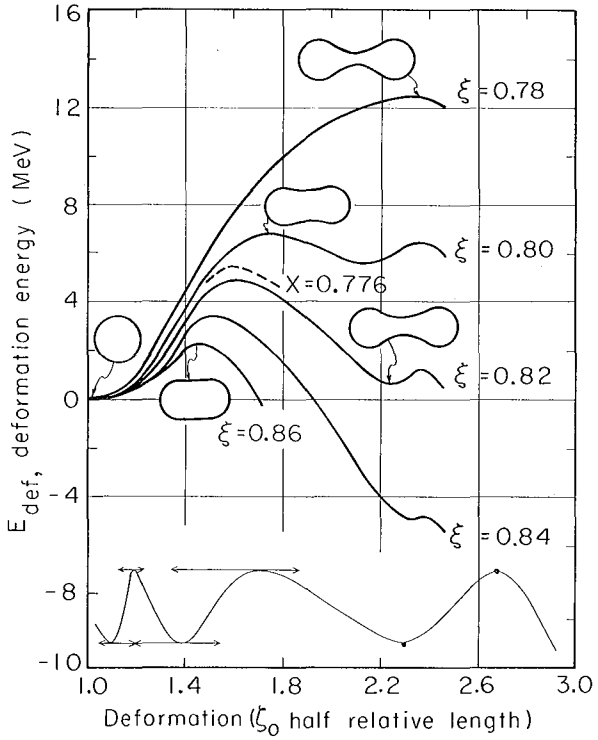

Fig. 3. Deformation energy of heavy nuclei evaluated by using the Nix parameterization and a relative curvature strength of η = 0.16. The solid line with ξ = 0.82 and the dashed line with x = 0.776 (pure liquid-drop model) correspond to the nucleus ^{232}U. The wiggly curve at the bottom indicates the presently known shell effects. (XBL707-3512)

redistribution energies are rather small.

Assuming a curvature tension of $a_3 = 15$ MeV, Fig. 3 shows the potential energies of heavy nuclei vs deformation. This large curvature correction introduces a second minimum into the barrier which is most pronounced for actinide nuclei like ^{232}U ($\xi = 0.82$ or $x = 0.776$).

The fission barriers obtained by using the full droplet model energy, Eq. (1) and Eq. (2), are plotted in Fig. 4 together with the experimental data. For medium-heavy nuclei, the theory predicts too large a barrier, whereas for heavy nuclei they come out to be too small. From these results one can conclude that the curvature tension of $a_3 = 9.34$ MeV, as calculated by Myers and Swiatecki with the Thomas-Fermi model, is too large to give reasonable fission barriers. The reciprocal effective moments of inertia as presented in Fig. 5, however, apart from the constant shift and the light nuclei region, seem to agree better.

In Fig. 6, the shape dependences of the droplet model are plotted against the ratio of

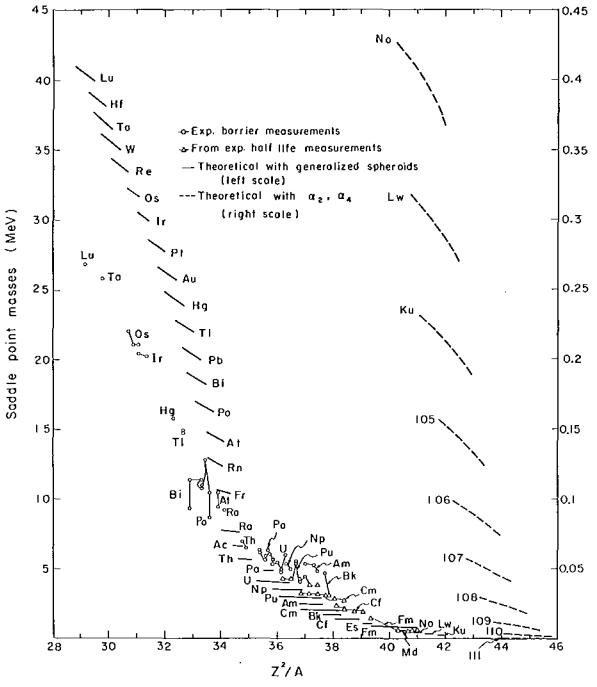

Fig. 4. Saddle-point masses in the truncated droplet model with a curvature coefficient of $a_3 = 9.34$ MeV. The curves are evaluated by using the parameterization of generalized spheroids (solid lines) or an expansion of the radius vector in P_2 and P_4 (dashed lines, scale enlarged ten times). (XBL707-3508)

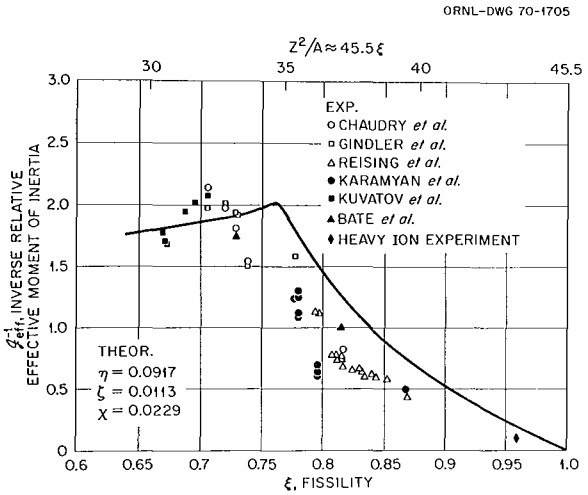

Fig. 5. Inverse relative effective moments of inertia in the truncated droplet model. (XBL713-3185)

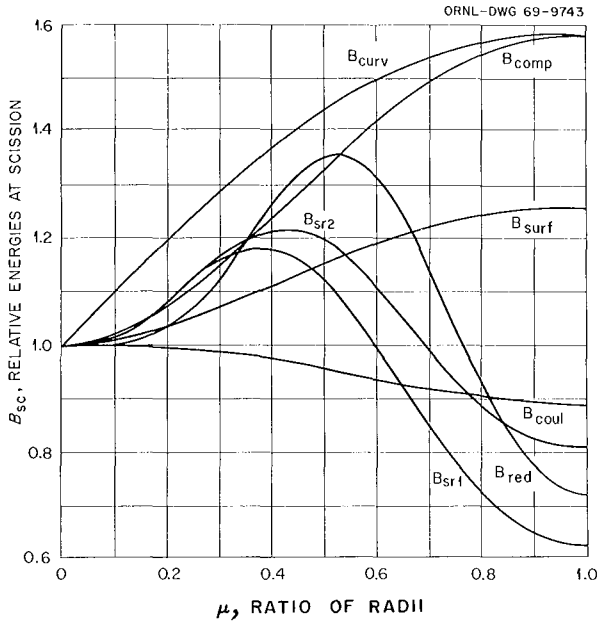

Fig. 6. The shape dependences of the droplet model evaluated for configurations of two tangent spheres with μ being the ratio of their radii. (XBL707-1627)

radii of two tangent spheres. The three redistribution functions B_{red}, B_{sr1}, and B_{sr2} do not have their maximum/minimum value at symmetry as the others do, but at a ratio of radii of about 0.5. This indicates the existence of a minimum in the potential energy vs asymmetry. The Coulomb redistribution strength C_2, however, in order to build up this minimum, must be larger than calculated by Myers and Swiatecki.

In conclusion of the studies in the shape-dependent droplet model, it turns out that the present knowledge of the constants does not allow for the existence of minima in the potential energy vs both symmetric and asymmetric deformation coordinates. The droplet-model corrections, however, flatten the potential energy. Consequently, the shell and pairing energies are expected to dominate at the barrier.

Footnote and References

†Summer guest from University of Würzburg Germany.

1. W. D. Myers and W. J. Swiatecki, Ann. Physics 55, 395 (1969); W D. Myers, UCRL-19543, 1970.

2. R. W Hasse, R. Ebert, and G. Süssmann, Nucl. Phys. A106, 117 (1968); R. W. Hasse, Nucl. Phys. A118, 577 (1968); Nucl. Phys. A128, 609 (1969).

Fission

Mass and Kinetic Energy of Fragments in Correlation with Specific Gamma Rays

E. Cheifetz,† R. C. Jared, S. G. Thompson, and J. B. Wilhelmy

In studies of prompt γ-ray emission from ^{252}Cf fission fragments, members of the ground-state bands of most of the even-even fragments have been identified. The identification was made possible by the systematic and simple way in which γ-ray deexcitation of even-even isotopes occurs and by finding through fragment kinetic energy measurements that the masses of the fragments in question were close (within 1 amu) to the assigned masses.[1,2]

The calculation of the mass associated with a specific γ ray was made by sorting all the measured multiparameter events into γ-ray spectra associated with 2 amu ranges of fragment masses. In determining the fragment mass of each event, the known neutron corrections and the Schmitt calibration procedure were incorporated. The line intensities in the complex γ-ray spectra were obtained by using the code of Routti et al.[3] in which a combination of predetermined line shapes and a straight-line background were fitted to segments of the γ-ray spectra. The mass distribution associated with a particular γ-ray transition is obtained from the distribution in intensities of that transition as a function of the various mass intervals. Typical mass distributions of several transitions are presented in Fig. 1. All of these transitions are in coincidence, and the two intense ones at 199.4 keV and 331.0 keV have been assigned as the 2 → 0 and 4 → 2 transitions in ^{144}Ba. The average masses associated with these transitions obtained by taking a simple average in the mass range 140-148 amu are 143.69 ± 0.023 (for the 199.4 keV 2 → 0 transition) and 143.61 ± 0.068 (for the 331.0 keV 4 → 2 transition). The cited standard deviations are obtained from the propagation of the statistical errors associated with the fitting procedure. The statistical errors of the mean masses are roughly the same as the difference between the two means. A similar situation occurs in most other intense transitions where the mean masses associated with various coincident γ rays differ by less than 0.1 amu. Such results confirm the validity of the fitting procedure as the lines were fitted independently in different energy regions of the spectra.

The mean masses associated with the even-even transitions were in general non-integer values, and transitions assigned to

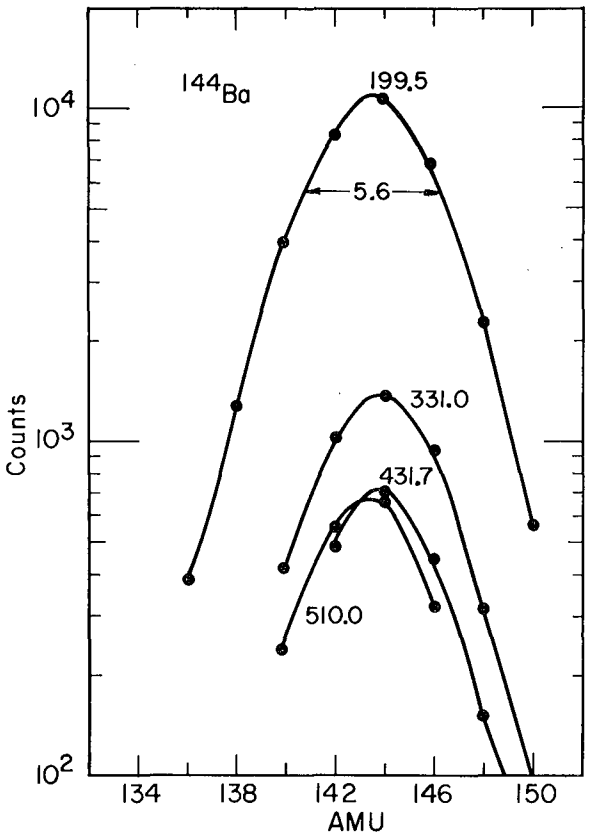

Fig. 1. Mass distributions associated with transitions in ^{144}Ba. The distributions associated with the 199.4-keV and 331.0-keV transitions were measured in the same experimental runs. The other two distributions were measured at different times. (XBL703-2398)

adjacent even-even isotopes had mean masses with less than 2 amu difference. This can be attributed mainly to the use of average neutron corrections. The average values of emitted neutrons, used in our mass calculations, were taken from the experiment of Bowman et al.[4] in which they correlated neutron emission with average masses. This procedure presumably gives mean masses which are too small for isotopes that are on the neutron-deficient side of the most probable isotope for a given element and conversely too large for isotopes on the neutron excess side. This results in a compression of the mean mass values of adjacent even-even isotopes of the

same element toward the most probable isotope as is indeed evident from the data.[1,2] The width of the mass distributions associated with specific γ rays is a direct measure of the experimental resolution of mass determination from fragment energies. The full width at half maximum varied in this experiment from ≈ 4 amu for palladium and tellurium isotopes to as much as 6 amu in the case of cerium isotopes. The width in the masses is due to experimental factors such as detector resolution and the variation in the energy loss in the dead layer of the detectors because of the large acceptance angle of the fission fragments; and it is also due to factors inherent in the fission process such as dispersion in the fragment energies caused by recoil of the fragments in the process of neutron emission and variation in neutron emission between the fragments. The experimental result indicates that this width cannot be considered to be a constant for all fragments.

The yield of specific isotopes was also correlated with the total kinetic energy of the fragments. This was done by sorting the γ-ray spectra into both mass intervals and kinetic energy intervals. The yield of three even-even ruthenium isotopes (108, 110 and 112) in three total kinetic regions is summarized in Table I. As is expected, the more neutron-deficient isotope, ^{108}Ru, is more abundant in the lower total kinetic energy group, which is consistent with its having increased neutron emission compared with ^{112}Ru, which is highly correlated with the high kinetic energy group.

The γ-γ coincidence data were used to correlate pairs of fragments with total kinetic energy release. Such correlations were studied for pairs of complementary fragments in which one of the fragments had a transition with sufficiently long lifetime (over 0.5 nsec),

Table I. Relative yield of even-ruthenium isotopes correlated with different intervals of the fragment total kinetic energy in the spontaneous fission of ^{252}Cf. The total fragment yield in the three kinetic energy intervals was normalized to unity.

	Total kinetic energy intervals in MeV		
Isotope	150 - 179	180 - 190	191 - 210
^{108}Ru	0.221	0.427	0.352
^{110}Ru	0.091	0.309	0.600
^{112}Ru	0.015	0.230	0.755

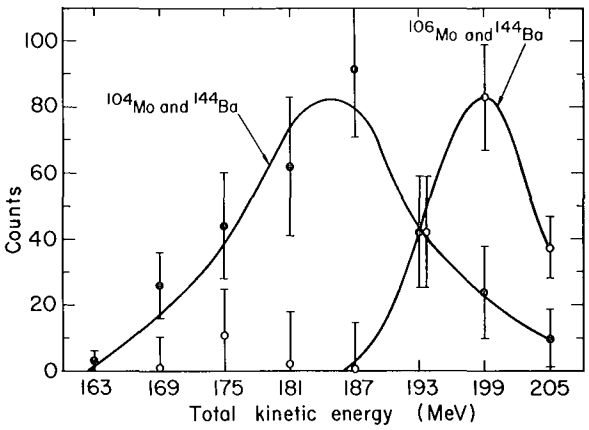

Fig. 2. The dependence of the yield of pairs of of complementary fragments on the total kinetic energy release. The pairs are ^{144}Ba - ^{104}Mo (represented by dots) and ^{144}Ba - ^{106}Mo (represented by open circles). The pairs were measured by observing coincidences of their specific γ rays. A large dispersion in the kinetic energy distribution is included in the presented results, but this does not affect the position of the means.
(XBL-713-3074)

so that a substantial part of the gamma decay occurred after the fragment traversed ≈ 10 mm in vacuum before it was stopped in the F_2 detector. Thus, the transition appeared non-Doppler shifted and sharp. The intensity dependence on the kinetic energy release for two pairs ^{104}Mo - ^{144}Ba and ^{106}Mo - ^{144}Ba is shown in Fig. 2. By identifying a pair of fragments, the total neutron emission associated with the events is determined. Although the statistical uncertainty is large (due to background subtraction), it is clear that events with emission of two neutrons (^{144}Ba - ^{106}Mo) are correlated with higher kinetic energy than events with four emitted neutrons (^{144}Ba - ^{104}Mo); furthermore, the difference in the mean kinetic energy of the two distributions is about 7 MeV/neutron, which is in very good agreement with the value of 6.6 MeV/neutron that Bowman et al.[4] found for the variation of total neutron emission as a function of total kinetic energy release.

Footnote and References

†On leave from the Weizmann Institute of Science, Rehovoth, Israel.

1. E. Cheifetz, R. C. Jared, S. G. Thompson, and J. B. Wilhelmy, Phys. Rev. Letters 25, 38 (1970).

2. J. B. Wilhelmy, S. G. Thompson, R. C. Jared, and E. Cheifetz, Phys. Rev. Letters 25, 1122 (1970).

3. J. T. Routti and S. G. Prussin, Nucl. Instr. Methods 72, 125 (1969).

4. Harry R. Bowman, J. C. D. Milton, Stanley G. Thompson, and Wladyslaw J. Swiatecki, Phys. Rev. 129, 2133 (1963).

Mass and Charge Distribution in the Fission of ^{252}Cf

J. B. Wilhelmy, E. Cheifetz,† R. C. Jared, and S. G. Thompson

For many years studies have been made to determine the charge distribution of products formed in fission. These studies have yielded information concerning detailed properties of the fission process. Historically most of the information has been acquired through radiochemical isolation of specific short-lived fission isotopes (for a review of these results, see Wahl et al. [1]). From these studies, independent and cumulative fission yields of several isotopes have been obtained. The limiting feature in the radiochemical analysis is that the majority of the high-yield prompt fission products have very short beta-decay half-lives. This makes the isolation of these isotopes quite difficult, and in general very little is known about their properties or yields. Therefore, much of the data which have been used to interpret the charge distribution have come from isotopes closer to beta stability. These isotopes have longer half-lives but have low independent yields as fission products. Since the interest is in the distribution at the time of fission, this makes the interpretation more difficult.

More recently with the advent of the high resolution solid-state photon detectors, it has become possible to study the prompt K x-ray spectra of the fission products.[2-6] Information concerning the charge and mass distribution of the products has been deduced from the measurements. This technique overcomes one of the main radiochemical difficulties in that the high-yield primary products are the ones that are sampled. However, there are still difficulties with this approach in that what is desired are the yields of the products and what is measured are the yields of the K x rays of the products. It is therefore necessary to make some approximation or justification showing that the x-ray yield follows the product yield. A further complication is in determining the dispersion of the charge and mass distributions. To obtain these values, an unfolding procedure has to be employed which removes the effects due to the relatively poor experimental resolution in the mass determination.

From our recent experimental studies of prompt γ rays from even-even fission products,[7-9] we have been able to develop a new technique which, for selected cases, overcomes the inherent difficulties of the radiochemical and x-ray determinations. It has been possible to determine the energies and intensities of the $2^+ \rightarrow 0^+$ ground-state transition for 32 of the highest independent-yield, even-even fission products. With the assumption that this ground-state transition reflects the yield of the isotope, it is possible to obtain information on the mass and charge distribution of the products. From considerations of the angular momenta of the prompt products,[10] it is possible to show that this is a reasonable assumption, especially when compared with the assumptions concerning conversion coefficients which are necessary for similar analysis of the x-ray spectra. Another advantage of the prompt γ-ray data is that information concerning the mass and charge dispersion is obtained directly without having to unfold the large dispersion introduced from the mass resolution.

The measured γ-ray intensities were analyzed by two separate methods to determine the fission-product distributions. The first analysis was to determine Z_p (the most probable charge for each mass chain) and σ_Z (the standard deviation of this distribution). The independent yields of the products, $Y(Z,A)$, are assumed to have, for each mass chain, a Gaussian distribution centered about Z_p,

$$Y(Z,A) = \int_{Z-\frac{1}{2}}^{Z+\frac{1}{2}} \frac{Y(A)}{\sqrt{2\pi}\,\sigma_Z} \exp - \left[(Z - Z_p)^2/2\sigma_Z{}^2\right]. \quad (1)$$

There are three parameters associated with this distribution: $Y(A)$, σ_Z, and Z_p. The parameter $Y(A)$, the total mass chain yield, has been measured independently[11] and therefore can be eliminated. The remaining two parameters can, in principle, be determined by a least-squares fitting procedure. Since

Table 1. Most probable charges for specific mass chains.

Mass chain	Isotopes used (independent yields)[a] [%/fission]	Mass chain[b] Yield [%/fission]	σ[c]	Z_p[d]	Wahl[e]	Watson[f]
94	Sr(0.51)	1.13	(0.623)	38.5 ± 0.2	37.67	
96	Sr(0.34)	1.47	(0.623)	38.9 ± 0.2	38.47	
98	Zr(0.3)	2.09	(0.623)	38.8 ± 0.2	39.26	
100	Zr(1.80)	3.15	(0.623)	40.1 ± 0.3	40.01	39.2 ± 0.3
102	Zr(1.43),Mo(0.46)	4.25	0.637	40.7 ± 0.1	40.75	40.6 ± 0.3
104	Mo(3.37)	5.40	(0.623)	42.0 ± 0.5	41.47	41.6 ± 0.2
106	Mo(3.37),Ru(0.16)	6.20	0.619	42.2 ± 0.2	42.29	42.5 ± 0.1
108	Ru(1.44)	6.00	(0.623)	43.1 ± 0.1	43.32	43.4 ± 0.1
110	Ru(3.49)	5.45	(0.623)	44.0 ± 0.5	44.08	44.4 ± 0.2
112	Ru(0.97),Pd(0.77)	3.65	0.829	44.9 ± 0.1	44.70	45.4 ± 0.2
114	Pd(1.48)	3.07	(0.623)	45.7 ± 0.1	45.31	46.0 ± 0.3
116	Pd(0.87)	1.60	(0.623)	46.2 ± 0.3	46.00	
118	Cd(0.32)	0.70	(0.623)	47.5 ± 0.2	46.69	
132	Te(0.2)	1.75	(0.623)	50.8 ± 0.2	51.21	
134	Te(1.5)	3.50	(0.623)	51.5 ± 0.1	52.12	
138	Xe(2.3)	4.94	(0.623)	53.5 ± 0.1	53.79	53.2 ± 0.2
140	Xe(1.5),Ba(0.52)	6.32	0.477	54.8 ± 0.1	54.59	54.4 ± 0.2
142	Ba(2.9)	6.00	(0.623)	55.6 ± 0.1	55.39	55.4 ± 0.1
144	Ba(3.6),Ce(0.2)	5.77	0.566	56.1 ± 0.3	56.18	56.3 ± 0.1
146	Ba(1.01),Ce(1.04)	5.15	0.609	57.0 ± 0.1	57.00	57.2 ± 0.1
148	Ce(2.31)	3.50	(0.623)	58.0 ± 0.5	57.88	58.1 ± 0.1
150	Ce(0.98)	2.34	(0.623)	58.6 ± 0.2	58.70	59.0 ± 0.2
152	Nd(0.6)	1.71	(0.623)	59.3 ± 0.1	59.49	59.8 ± 0.2
154	Nd(0.4)	1.11	(0.623)	60.7 ± 0.2	60.27	
156	Sm(0.1)	0.70	(0.623)	60.8 ± 0.3	60.96	
158	Sm(0.15)	0.39	(0.623)	62.6 ± 0.4	61.69	

[a] Refs. 7-9.

[b] Ref. 11.

[c] For mass chains having only one determined independent yield, the value of σ was fixed to be 0.623. This was the average of the values obtained from fitting to the chains having two independent yields ($\bar{\sigma}$ = 0.623 ± 0.116).

[d] The errors listed represent the propagation of the statistical errors associated with the independent yields of the individual isotopes.

[e] Ref. 1.

[f] Ref. 6.

the distributions are relatively narrow and the independent yields from the γ-ray analysis are only known for even-even isotopes, there were no mass chains for which more than two independent yields were found. Therefore Eq. (1) was analytically solved to give the values of Z_p and σ_Z. From the six mass chains analyzed (A = 102, 106, 112, 140, 144, 146), the average value of σ_Z was

$$\bar{\sigma}_Z = 0.623 \pm 0.116 .$$

Older radiochemical data for $^{235}U(n_{th}, f)$ have reported $\bar{\sigma}_Z = 0.59$,[12] while a more recent tabulation prefers $\bar{\sigma}_Z = 0.56 \pm 0.06$.[1] The γ-ray determined $\bar{\sigma}_Z$ is therefore in reasonable agreement with the radiochemical results. The somewhat higher value may be a dispersion effect reflecting difference associated with the evaporation of more neutrons in the fission of ^{252}Cf ($\bar{\nu} = 3.8$) than in the thermal neutron fission of ^{235}U($\bar{\nu} = 2.5$). There is however a large discrepancy in this value when compared with $\bar{\sigma}_Z = 0.467 \pm 0.064$, which is the unfolded preneutron emission value obtained by Glendenin et al.[5] from analysis of their x-ray data. Using the current value of $\bar{\sigma}_Z = 0.623$, it is possible to determine some information on the value of Z_p for mass chains in which only one independent yield is known. Using this one-point analysis, Z_p values were obtained for 20 additional mass chains. The results are presented in Table I along with the $^{235}U(n, f)$ radiochemical values tabulated by Wahl et al.[1] and the $^{252}Cf(sf)$ K x-ray values of Watson et al.[6] The errors quoted

Table 2. Most probable masses for specific charge numbers.

Z	Isotopes used (independent yields)[a] [%/fission]	σ[b]	Z yield[c] [%/fission]	A_p[c]	Watson[d]
38	94(0.51),96(0.34)	(1.512)	2.1 ± 0.4	94.5 ± 0.4	
40	98(0.3),100(1.80), 102(1.43)	1.376	7.4 ± 1.1	100.8 ± 0.3	100.6 ± 0.4
42	102(0.46),104(3.37), 106(3.37)	1.387	15.4 ± 2.4	105.0 ± 0.3	104.8 ± 0.3
44	106(0.16),108(1.44), 110(3.49),112(0.97)	1.333	12.0 ± 1.6	109.8 ± 0.2	109.3 ± 0.3
46	112(0.77),114(1.48), 116(0.87)	1.814	6.8 ± 1.4	114.1 ± 0.2	114.0 ± 0.5
52	132(0.2),134(1.5)	(1.512)	8.7 ± 2.9	135.4 ± 0.3	
54	138(2.3),140(1.5)	(1.512)	9.3 ± 1.2	138.5 ± 0.5	139.4 ± 0.3
56	140(0.52),142(2.9), 144(3.6),146(1.01)	1.612	16.2 ± 2.6	143.3 ± 0.2	143.2 ± 0.1
58	144(0.2),146(1.04), 148(2.3),150(0.98)	1.550	9.1 ± 1.3	148.0 ± 0.2	148.0 ± 0.1
60	152(0.6),154(0.4)	(1.512)	2.4 ± 0.5	152.5 ± 0.6	152.5 ± 0.3
62	156(0.1),158(0.15)	(1.512)	0.6 ± 0.2	157.5 ± 0.7	155.0 ± 0.5

[a] Refs. 7-9.

[b] For charge chains with only two independent yields, the value of σ was fixed to be 1.512 which was the average of the values obtained from fitting to the chains having more than two points ($\bar{\sigma} = 1.512 \pm 0.184$).

[c] The errors listed represent the propagation of the statistical errors associated with the individual parameters.

[d] Ref. 6.

on Z_p represent the propagation of the statistical errors associated with $\bar{\sigma}_Z$ and the independent yields. (Yields of greater than 1%/fission were estimated to have uncertainties of 15%, while those with yields less than 1% had estimated errors of 25%.) For the six mass chains having two independent yields, the current results are in good agreement with the radiochemical results and in each case closer to the radiochemical value than the x-ray-determined result.

The second method used to analyze the data was to determine information on fission-product distribution with respect to mass. In this representation the data are analyzed for constant Z values. The formalism used to define the distributions is analogous to that used for the charge distribution.

$$Y(Z,A) = \int_{A-\frac{1}{2}}^{A+\frac{1}{2}} \frac{Y(Z)}{\sqrt{2\pi}\sigma_A} \exp - \left[(A - A_p)^2/2\sigma_A^2\right]. \quad (2)$$

Again the distribution is assumed to be Gaussian. The three parameters are Y(Z) (the total prompt yield of each element), σ_A (the standard deviation of the distribution of individual isotopes for each Z value), and A_p (the mean of the distribution). They were determined by least-squares fitting the measured independent yields to Eq. (2). In a strict mathematical sense Eqs. (1) and (2) cannot, in general, both represent the distribution of the products. However, to the accuracy of this model, it is as a priori valid to assume that the distribution is Gaussian in the constant Z plane as in the constant A plane. There were six isotopic chains for which three or more yields were known, and for these the average value of $\bar{\sigma}_A$ was found to be

$$\bar{\sigma}_A = 1.512 \pm 0.184 .$$

By using this value, it was possible to obtain information on Y(Z) and A_p for five additional isotopic chains for which only two independent yields were known. The results are presented in Table II along with the values deduced from x-ray analysis.[6] The errors presented for the mean and yield of the various isotopic chains are calculated from the propagation of the statistical errors associated with $\bar{\sigma}_A$ and the independent yields. The values of A_p are in reasonable agreement with the x-ray results. The errors in the elemental yields are relatively large since this is a much more sensitive parameter to determine. A simple consistency check is to see the agreement between fit yields of complementary elements. For the five complementary pairs the values agree

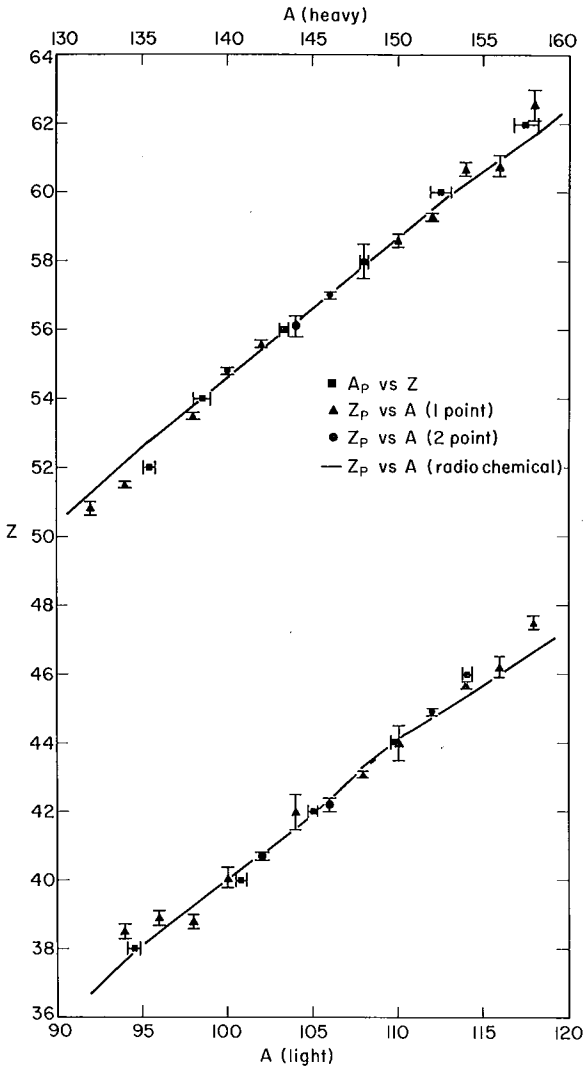

Fig. 1. A plot of the analyzed experimental data presenting (1) the most probable post-neutron-emission mass as a function of atomic number (A_p vs Z) and (2) the most probable atomic number as a function of the post-neutron-emission mass (Z_p vs A). The solid line represents the radiochemical results as tabulated in Ref. 1. (XBL-711-2525)

within their mutual error bars. Another check is the relationship between $\bar{\sigma}_Z$ and $\bar{\sigma}_A$. Simple arguments[5] suggest that these values should be approximately related by the post-neutron-emission charge-to-mass ratio of the fissioning nucleus

$$\frac{\bar{\sigma}_Z}{\bar{\sigma}_A} \approx \frac{98}{248} = 0.395 .$$

The experimental value for this ratio is

0.41 ± 0.09, which is in good agreement but with a large uncertainty. This implies that it has been possible to determine the true widths of the A_p distributions, which is very difficult in the x-ray experiments. The effect of the additional dispersion due to the mass determination can be shown by comparing our current value of $\bar{\sigma}_A = 1.51$ with the experimental value of $\bar{\sigma}_A = 2.86$ obtained from the x-ray analysis of Watson et al.[6]

A summary of the current results is presented in Fig. 1 along with the radiochemical results tabulated in Ref. 1. The agreement between the methods appears to be good with a possible systematic deviation around the more symmetric mass division. This region is near the Z = 50, N = 82 closed-shell region and is therefore an area where low-lying isomeric states are probable. Such states can cause problems in interpreting radiochemical results since the beta-decay chains can have several isomeric branches.

Footnote and References

†On leave from the Weizmann Institute of Science, Rehovoth, Israel.

1. A. C. Wahl, A. E. Norris, R. A. Rouse and J. C. Williams, Physics and Chemistry of Fission (International Atomic Energy Agency, Vienna, Austria, July 1969), p. 813.

2. L. E. Glendenin and J. P. Unik, Phys. Rev. 140, B1301 (1965).

3. S. S. Kapoor, H. R. Bowman, and S. G. Thompson, Phys. Rev. 140, B1301 (1965).

4. R. L. Watson, H. R. Bowman, and S. G. Thompson, Phys. Rev. 162, 1169 (1967).

5. L. E. Glendenin, H. C. Griffin, W. Reudorf, and J. P. Unik, Physics and Chemistry of Fission (International Atomic Energy Agency, Vienna, Austria, July 1969), p. 781.

6. R. L. Watson, R. C. Jared, and S. G. Thompson, Phys. Rev. C 1, 1866 (1970).

7. E. Cheifetz, R. C. Jared, S. G. Thompson, and J. B. Wilhelmy, Phys. Rev. Letters 25, 38 (1970).

8. J. B. Wilhelmy, S. G. Thompson, R. C. Jared, and E. Cheifetz, Phys. Rev. Letters 25, 1122 (1970).

9. E. Cheifetz, R. C. Jared, S. G. Thompson, and J. B. Wilhelmy, UCRL-19949, August 1970, and in Proceedings of the Conference on the Properties of Nuclei Far From the Region of Beta Stability, Leysin, Switzerland, 1970 (to be published).

10. Angular Momentum of Primary Fission Fragments, J. B. Wilhelmy, E. Cheifetz, R. C. Jared, S. G. Thompson, H. R. Bowman, and J. O. Rasmussen, this report.

11. W. E. Nervik, Phys. Rev. 119, 1685 (1960).

12. Andrew E. Norris and Arthur C. Wahl, Phys. Rev. 146, 926 (1966).

Gamma Transitions in Odd-A, Even-Z Fission Fragments

E. Cheifetz,† R. C. Jared, S. G. Thompson, and J. B. Wilhelmy

The x-ray and γ-ray radiations from fission fragments produced in the spontaneous fission of ^{252}Cf originate from more than 100 different neutron-rich nuclei, the most abundant of which appear with a yield of approximately 3% per fission. By studying these radiations in a multiparameter experiment, we have been able to identify several of the states in the ground-state bands of about 30 even-even fragments.[1-3] This was made possible by the fact that the deexcitation of even-even nuclei with 7 - 8 units of angular momentum is terminated by a cascade through the ground-state bands, the energies of which follow simple systematic relationships. A large number of transitions that were observed in the experiment did not fit into the systematics of the ground-state bands of the even-even nuclei as they presumably were emitted from the many even-odd, odd-even and odd-odd nuclei that comprise $\approx$ 75% of the species which are produced in spontaneous fission. The large number of decaying nuclei is in contrast to standard nuclear spectroscopy where single or at most very few decaying nuclei are studied. The first task in identifying the gamma transitions accompanying fission is to find out the atomic number and mass of the emitting fragment. The identity of the atomic number associated with individual transitions was deduced from three different coincidence approaches: (1) From γ rays emitted in coincidence with specific K x rays. For this to take place the decay sequence must include at least one highly converted transition with sufficient energy to emit an intense K x ray. This process is highly dependent on the nature of the

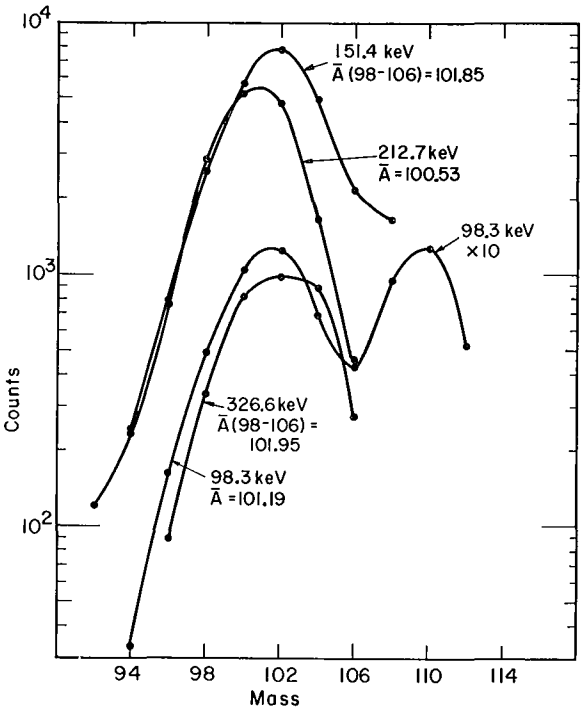

Fig. 1. Mass distributions associated with γ-ray transitions from zirconium isotopes. The value of Ā represents the average mass associated with the transition (the values in parentheses denote the region in which Ā was calculated). The lines have been assigned to the following isotopes: 151.4 keV 2 → 0 ^{102}Zr; 326.6 keV 4 → 2 ^{102}Zr; 212.2 keV 2 → 0 ^{100}Zr; 98.3 keV ^{101}Zr and ^{109}Ru (see text). (XBL-704-2748)

cascade, and the identity of the transition that undergoes conversion cannot be determined. (2) From γ rays emitted in coincidence with K x rays of the complementary fragment. Since the γ decays from complementary fragments are presumably independent of each other, a highly converted transition in one fragment appears in a nonselective coincidence with the transitions of the complementary fragment. (3) From γ-γ coincidence. This approach was used when one of the transitions had been assigned by using either of the first two methods. The Z identity of γ rays in the same nucleus or in the fragment having complementary Z was established by observing γ-ray coincidences with an already known γ ray.

The assignments of masses were based on the fact that definite mass assignments have been made for the even-even fragments. As we have described in another report in this volume,[4] the mean masses were not absolutely correct and the mean masses associated with

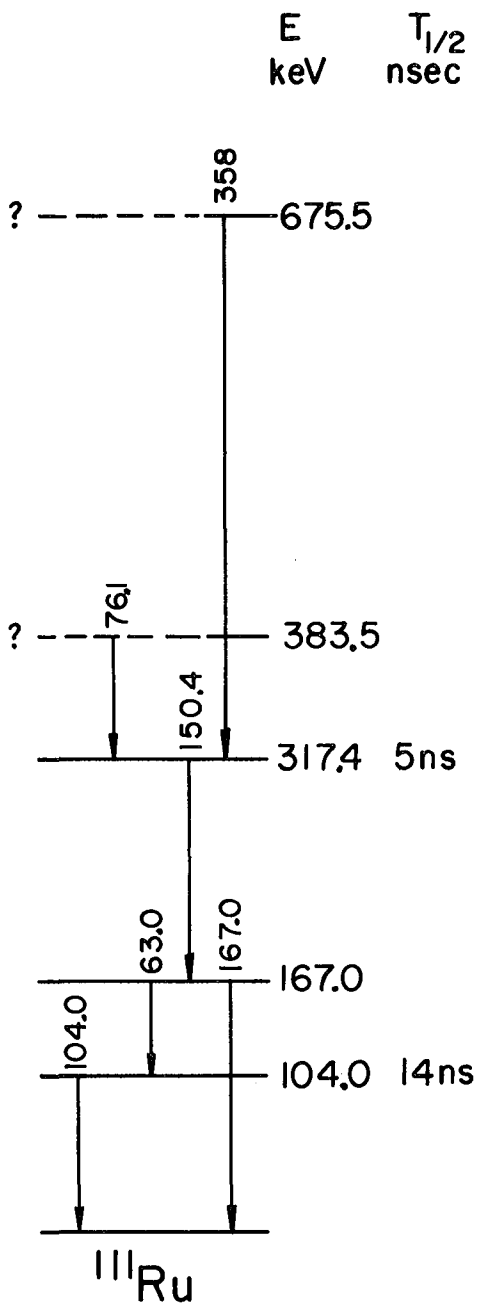

Fig. 2. Tentative decay scheme of ^{111}Ru. (XBL-713-3073)

transitions from adjacent even-even nuclei differed by less than 2 amu; nevertheless, the mean masses associated with γ rays of the same nucleus differed by less than 0.1 amu. The masses associated with transitions of even-Z, odd-A nuclei fell therefore in between the masses of the even-even nuclei.

An example of identifying a transition as

being associated with an even Z, odd A is shown in Fig. 1 for ^{101}Zr. The mass distributions associated with several transitions that appeared independently in coincidence with zirconium K x rays are presented. The 151.4-keV and 326.6-keV lines have been assigned as 2 → 0 and 4 → 2 transitions in ^{102}Zr. The mean masses associated with these transitions are 101.85 amu and 101.95 amu respectively. The 212.7-keV line has been assigned to ^{100}Zr and has a mean mass of 100.53. The 98.3-keV line has a double-peak mass distribution which is due to two lines, one associated with ^{109}Ru and the other with ^{101}Zr. Both ruthenium and zirconium K x rays have been observed in coincidence with these lines. The mean mass of the zirconium 98.3-keV line is 101.19, which is centered between the mean masses associated with the lines of ^{100}Zr and ^{102}Zr and therefore was assigned to ^{101}Zr.

In an attempt to find out the decay scheme of some even-Z, odd-A fission fragments, extensive sorting of the γ-γ coincidence data was undertaken. As an example we present in Table I a list of transitions assigned to ^{111}Ru. Some of these transitions have been observed, but not assigned to specific elements, by W. John et al.[5] in their study of delayed γ rays from ^{252}Cf fission. The results of that study are incorporated in the table. One of the transitions (150.4 keV) was also observed by Watson et al.[6] in x-ray, electron coincidence measurements and have been assigned to ruthenium.

A tentative and incomplete decay scheme is proposed in Fig. 2. The decay scheme is compatible with the measured half-life values and coincidence requirements. Both the 150.4-keV and 104.0-keV lines appear with high intensity in coincidence with a ruthenium K x ray, presumably produced from the conversion of the 63.1-keV transition which must have a conversion coefficient of at least five. Such a conversion coefficient is consistent with a strong E2 component. It would be of interest to establish the decay scheme, spin, and parities of levels in the light fission-fragment region as our studies of the even-even nuclei indicate the existence of large nuclear deformations in this region. The theoretical calculations of Nilsson et al.[7] predict this to be a region of oblate deformations. By studying the levels in these nuclei one could perhaps establish the positions of the Nilsson single-particle levels and establish whether the deformation in this region is prolate or oblate. At present not enough information is available to perform this task because no a priori simple relationships of energy-level spacings such as those of even-even nuclei can be applied to very limited sets of levels in even-odd nuclei; in addition, the angular momentum imparted to the fragments is perhaps not sufficiently high to create a situation in which easily detectable, very stretched cascades are fed.

Footnote and References

†On leave from the Weizmann Institute of Science, Rehovoth, Israel.

1. E. Cheifetz, R. C. Jared, S. G. Thompson, and J. B. Wilhelmy, Phys. Rev. Letters 25, 38 (1970).

2. J. B. Wilhelmy, S. G. Thompson, R. C. Jared, and E. Cheifetz, Phys. Rev. Letters 25, 1122 (1970).

Table I. Transitions in ^{111}Ru. E – energy of the transition; I – photon intensity in percent per fission; $\bar{A}$ – average mass associated with the transition.

This experiment			John et al.[5]			
E	I	$\bar{A}$	$\bar{A}$	I	$T_{\frac{1}{2}}$	Lines in coincidence
keV	%/Fiss	amu	amu	%/Fiss	nsec	in this experiment
63.0	0.18	111.0				
76.1	0.29	110.94				104.0, 150.5, 424
104.0	0.97	110.84	111	0.59	14	76.1, 139.2, 150.5, 358.1
150.4	0.94		111	0.80	6	76.1, 104.0, 167.0, 358.1
167.0	0.27		111	0.14	5	150.5, 358
358.1	0.6					104.0, 150.4

3. E. Cheifetz, R. C. Jared, S. G. Thompson, and J. B. Wilhelmy, UCRL-19949, August 1970, and in Proceedings of the Conference on the Properties of Nuclei Far From the Region of Beta Stability, Leysin, Switzerland, 1970 (to be published).

4. Mass and Kinetic Energy of Fragments in Correlation With Specific Gamma Rays, E. Cheifetz, R. C. Jared, S. G. Thompson, and J. B. Wilhelmy, this report.

5. W. John F. W. Guy, and J. J. Wesolowski, Phys. Rev. C 2, 1451 (1970).

6. R. L. Watson, J. B. Wilhelmy, R. C. Jared, C. Rugge, H. R. Bowman, S. G. Thompson, and J. O. Rasmussen, Nucl. Phys. A141, 449 (1970).

7. I. Ragnarsson and S. G. Nilsson, Lund Institute of Technology, Lund 7, Sweden, private communication (1969).

Prompt Neutrons from Spontaneous Fission of ^{257}Fm†

E. Cheifetz,* H. R. Bowman, J. B. Hunter, and S. G. Thompson

The average number of prompt neutrons $\bar{\nu}$ emitted in the spontaneous fission of ^{257}Fm has been measured to be 3.97 ± 0.13 (based on $\bar{\nu}$ = 3.72 for ^{252}Cf). A ^{257}Fm sample with an intensity of ≈ 0.5 fissions/min faced a solid-state detector that detected fission fragments. Both the solid-state detector and the fermium source were placed at the center of a large gadolinium-loaded liquid-scintillator tank.[1] The neutrons from the fission events underwent thermalization in the organic solvent in the tank and subsequently induced a cascade of thermal-neutron capture γ rays from the gadolinium. The cascade of γ rays produced signals in the photomultipliers that surrounded the tank. The fission fragment detector triggered a 35-μsec gate which started 0.5 μsec after fission, and during which the neutron-induced scintillations were counted and recorded in the form of a multiplicity distribution. For calibration, an identical system using a ^{252}Cf source with its own fission fragment detector was run simultaneously with the fermium source. The system was also triggered by a pulser to obtain the background multiplicity distribution. The efficiency of the system to detect neutrons was 51.5%. Altogether 1500 fission events of ^{257}Fm were recorded. The average values of the experimental multiplicity distributions were:

$$\bar{n}(^{257}Fm) = 2.168,$$

$$\bar{n}(^{252}Cf) = 2.040,$$

$$\bar{n}(\text{pulser}) = 0.124,$$

thus,

$$\bar{\nu}(^{257}Fm)/\bar{\nu}(^{252}Cf) = \left[\bar{n}(^{257}Fm) - \bar{n}(\text{pulser})\right]/\left[\bar{n}(^{252}Cf) - \bar{n}(\text{pulser})\right] = 1.067 \pm 0.036.$$

On the basis of $\bar{\nu}(^{252}Cf) = 3.72$,[2] we obtained $\bar{\nu}(^{257}Fm) = 3.97 \pm 0.13$.

The average prompt neutron yield from spontaneous fission is directly related to the average excitation energy of the fragments E_x by the equation

$$\bar{E}_x = \bar{\nu}(\bar{B}_n + \bar{E}_n) + \bar{E}_\gamma \cong (\bar{\nu} + 1)(\bar{B}_n + \bar{E}_n),$$

where

$\bar{B}_n$ = average neutron binding energy in the neutron emitting fragments,

$\bar{E}_n$ = average neutron kinetic energy in the frame of the reference of the moving fragment,

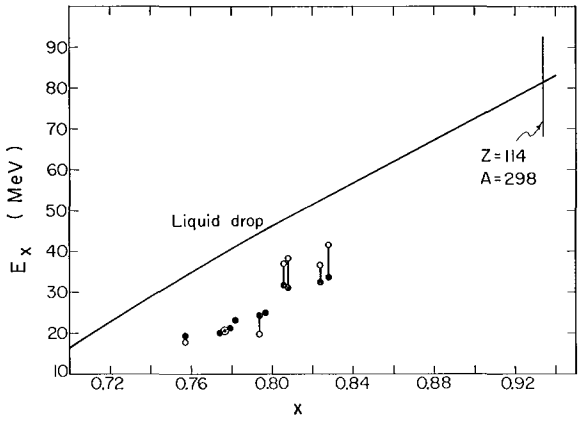

Fig. 1. The average excitation energy in spontaneous fission as a function of the fissionability parameter. Dots—values derived from experimental results of $\bar{\nu}$. Open circles—values derived from $\Delta\bar{M} - \bar{E}_K$. Values of $\bar{E}_x$ for the same isotope are connected by a line. The continuous line represents the liquid-drop estimate taken from Nix.[4]

(XBL-7012-4310)

$\bar{E}_\gamma$ = γ-ray energy emitted from the fragments.

We have evaluated the average excitation energy of the spontaneously fissioning nuclei with known values of $\bar{\nu}$ using the simplifying assumption that the mass division in all the cases results in asymmetric fission with a heavy fragment mass of 140 and equal Z/A in both fragments. The neutron binding energies of the Garvey et al.[3] tables were averaged over even-odd effects in both protons and neutrons. The average neutron kinetic energy in MeV was taken as $\bar{E}_n = 0.663 + 0.38\ \bar{\nu}^{1/2}$. This equation reproduces the known results for ^{252}Cf and thermal neutron fission of ^{235}U. Another approach, to obtain the average excitation energy in fission, is to consider the difference between the total energy release in fission obtained from mass formula tables and the average kinetic energy of the fragments. Some errors that can amount to 4 - 8 MeV were made in both approaches since in evaluating the excitation energy, a proper average of neutron binding energies and masses over all fission products was replaced by values averaged over only a few of the most probable species. The resultant excitation energies as a function of the fissionability parameter are shown in Fig. 1. In this figure we also show the behavior of the excitation energy as predicted by the dynamical calculations of Nix using the liquid-drop model.[4] Both the calculations and the experimental results show the same trend of increase in excitation energy with the fissionability parameter, but an absolute difference of ≈ 20 MeV is clearly seen. Better agreement between the calculations of the liquid-drop model regarding the kinetic energy of the fragments and the experimental results of fission induced by high energy projectiles has been obtained. Spontaneous fission and low-energy fission are unique in that they result in predominantly asymmetric mass distributions which are attributed to single-particle effects at the saddle point and (or) during the saddle-to-scission descent. During the saddle-scission descent some rearrangement of the cold deformed fragments into more nearly spherical shapes probably occurs, thus reducing the eventual excitation energy and increasing the kinetic energy.

Footnotes and References

†Condensed from UCRL-19988, December 1970; submitted to Phys. Rev.

*On leave from the Weizmann Institute of Science, Rehovoth, Israel.

1. V. J. Ashby, H. C. Canton, L. L. Newkirk, and C. J. Taylor, Phys. Rev. 111, 616 (1958).

2. A. De Volpi and K. G. Porges, Phys. Rev. C 1, 683 (1970).

3. G. T. Garvey, W. J. Gerace, R. L. Jaffe, I. Talmi, and I. Kelson, Rev. Mod. Phys. 41, S1 (1969).

4. J. R. Nix, Nucl. Phys. A130, 241 (1969).

Angular Momentum of Primary Fission Products

J. B. Wilhelmy, E. Cheifetz,† R. C. Jared, S. G. Thompson, H. R. Bowman, and J. O. Rasmussen*

Information concerning the angular momentum distribution of the primary-fission products formed in the spontaneous fission of ^{252}Cf has been deduced from our recent measurements[1-3] of the population of the members of ground-state bands in even-even fission products. We present here methods to extract information on the intrinsic-angular-momentum distribution of the fission fragments from the measured intensities of the prompt γ rays deexciting the ground-state band. The transitions observed within the ground-state band are the last stages of the dissipation of the large (≈ 15 MeV) internal excitation energy of the primary products. From the time of scission until the time of observation, the fragments have each emitted neutrons and various nonground-state-band transitions. To determine quantitative information on the primary angular momentum, we have utilized two independent methods of analysis.

The first method is based on an adaptation of the statistical-model-analysis methods developed by Huizenga and Vandenbosch[4,5] to explain isomeric yield ratios in neutron-capture and charged-particle reactions. This model has been extended by Warhanek and Vandenbosch[6] and by Sarantities, Gordon, and Coryell[7] to interpret information on angular momentum in fission from the population of certain isomeric levels in specific fission products. By observing the prompt γ rays we have three advantages when compared with

the previous methods: (1) It is not necessary to have a fission product which has a convenient isomer; (2) It is possible to obtain information on many high-yield prompt products; and (3) For each product we have population information on up to five spin levels (the 2^+, 4^+, 6^+ and 8^+ from the γ-ray intensities and the 0^+ ground state from the independent yields of the products), instead of just two in the isomer studies.

The statistical model used assumes that the level-density distribution of specific spin values is given by

$$P(J) \propto (2J + 1) \exp\left[-(J + \tfrac{1}{2})^2/2\sigma^2\right], \quad (1)$$

where P(J) is the probability distribution of spin levels, J is the value of the spin, and σ is treated as a parameter which limits the population of high-spin states. The spin level populated by a given transition (neutron or γ ray) is assumed to be proportional to the relative probability of the levels of allowed spin. With these assumptions it was shown[4,5] that a large variety of isomeric-yield data could be interpreted using for σ a value of three or four. We use this model not for its theoretical rigor, but for its empirical ability to give consistent interpretation of other experimental data.

To proceed with the statistical calculations, a further assumption is necessary regarding the angular momentum distribution of the primary fragments. Following Refs. 6 and 7, we assume the initial fission-fragment spin distribution is given by

$$P(J) \propto (2J + 1) \exp\left[-J(J + 1)/B^2\right], \quad (2)$$

where B is the parameter to be determined. In this representation B is used to limit the angular momentum and therefore serves a purpose similar to that of σ in Eq. (1). This distribution is analytically convenient and presents a smoothly varying, fairly wide distribution in J. It has some theoretical justification in that it is functionally quite similar to the expression derived by Nix[8] for the fission-product angular momentum based on the propagation of the amplitude of the normal asymmetric-bending mode evaluated at the equilibrium saddle point.

Using the above formalism we have evaluated the intensities of the members of the ground-state bands of the even-even fission products as a function of B, which is the only free parameter in the model. (B is approximately equal to the rms value of J plus one-half.) Explicitly the calculation procedure consists of: (1) determining the neutron multiplicity of each isotope by modifying with our current results[1-3] the neutron-emission table presented by Bowman et al.;[9] (2) evaluating the angular momentum removed by each neutron using transmission coefficients based on a simple square-well potential;[10] (3) assuming after neutron emission that there are three statistical E1 γ-ray transitions before the ground-state band is populated (the results are not very sensitive to the multiplicity or multipolarity of the preground-state-band transitions as long as they are assumed to be statistical); and (4) after the statistical γ-ray emission, feeding the ground state directly and evaluating the intensities of the cascading intraband transitions. The results of the statistical analysis for the isotope ^{144}Ba are shown in Fig. 1. The experimental data are within the band defined by the B = 6 and B = 8 lines and have as a mean value $\bar{B}$ = 7.2.

It was possible to extract similar information for 21 other even-even fission products for which members of the ground-state band were known.

A further application of this statistical model is a prediction of the nuclear alignment

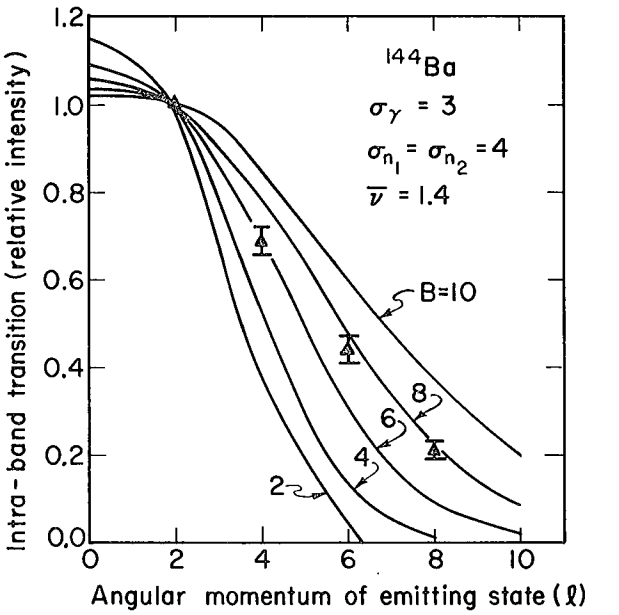

Fig. 1. Plot of the observed (▲) and calculated (—) ground-state-band transition intensities obtained in the deexcitation of the prompt-fission product ^{144}Ba. A family of calculated curves is presented as a function of the angular-momentum parameter B. All calculations were performed using the predetermined experimental parameters shown. $\bar{\nu}$ is the average number of neutrons emitted; σ_γ and σ_n are the statistical spin cutoff parameters associated with γ-ray emission and neutron evaporation, respectively. (XBL-711-2517)

of the populated spin levels. As an analogy to charged-particle-induced reactions, it is reasonable that the angular momentum of the primary-fission fragments is aligned in a plane perpendicular to the fission axis. The various neutron-evaporation and γ-ray-transition steps lead to a partial destruction of this alignment. This amount of disalignment can be quantitatively determined by using the spin-level distribution [Eq. (1)] and evaluating via Clebsh-Gordon coefficients the relative populations of the various magnetic states. For consistency with the Huizenga-Vandenbosch model,[4,5] it is necessary to interpret the preexponential factor in Eq. (1) as due to the 2J + 1 degeneracy of magnetic states for each spin level J. It should be pointed out that the alignment calculations involve no additional assumptions and can therefore be regarded as a further test for any statistical-model calculation. The results of the calculations for the predicted anisotropy for the $2^+ \rightarrow 0^+$ ground-state transition in ^{144}Ba are shown in Fig. 2 as a function of the parameter B. Also shown are the experimental data[11] and results fitted to those data. Again the experimental values lie within the B = 6 to B = 8 band and have a mean value of $\bar{B} = 6.3$. The analysis of the two sets of experimental data is thus in good agreement with regard to the prediction of the initial angular momentum.

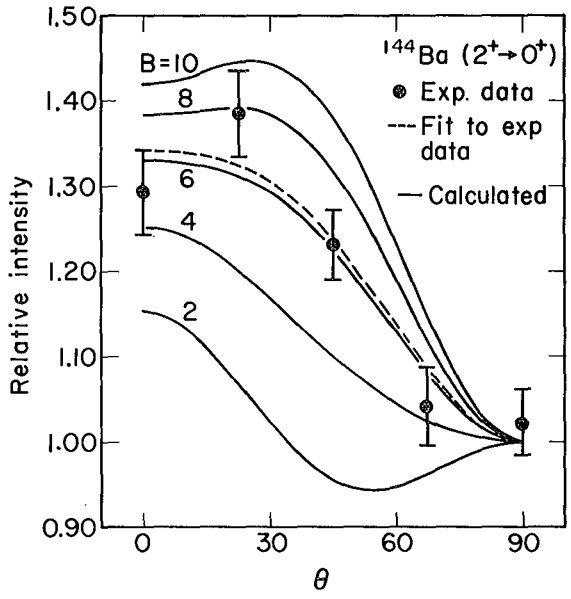

Fig. 2. Experimental and calculated angular distribution of the $2^+ \rightarrow 0^+$ ground-state transitions in the deexcitation of the prompt-fission product ^{144}Ba. The calculated curves are presented as a function of the angular-momentum parameter B. The experimental data were least-squares fitted to the function: $P(\theta) = N[1 + A_2P_2(\cos\theta) + A_4P_4(\cos\theta)]$. (XBL-711-2524)

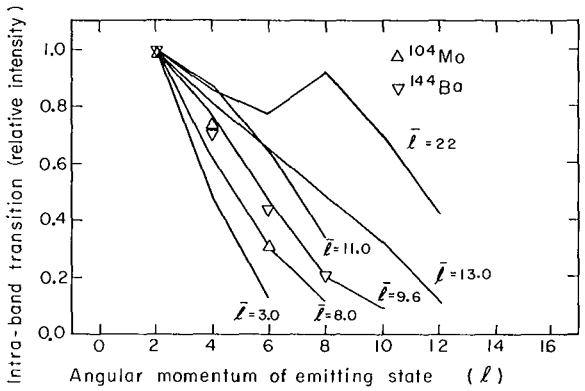

Fig. 3. A comparison of the observed relative ground-state-band transition intensities from the current experimental results (triangles) with those observed in various charged particle, xn reactions (lines). The reaction data are labeled with the average angular momentum of the reaction as calculated from optical-model codes. (XBL-706-3041)

The second method which was used to interpret the experimental data involved no theoretical analysis and simply consisted of a comparison of the intensities of the prompt-fission γ rays with those observed in in-beam γ-ray studies of charged particle, xn reactions. Figure 3 presents the results of such a comparison. The lines join observed experimental transition intensities as reported in the literature. The lines are labeled with the average angular momentum induced in the reaction as calculated from optical-model codes. Even though a variety of reactions are considered and the compound nuclei produced vary from what is nominally considered spherical to strongly deformed, there is good correlation with the intensity of the various spin members as a function of the initial angular momentum. The current experimental data presented are those for the complementary fission products, ^{104}Mo and ^{144}Ba. By direct interpolation, the average value of ℓ for ^{144}Ba would be ≈ 9.2.

The discrepancy between the two methods is probably due to inadequacies in the assumptions of the statistical model and also possibly due to the "resolution" available for interpolating such a wide variety of experimental data in the case of the reaction data comparison. Therefore, the absolute uncertainty of the determination of the magnitude of the angular momentum is implied by this discrepancy. However, the variation of the angular momentum as a function of products is essentially independent of the method of analysis as long as the supposition is valid that the intensities of the transitions in the ground-state band reflect the initial angular-momentum distribution. This variation in the mean angular

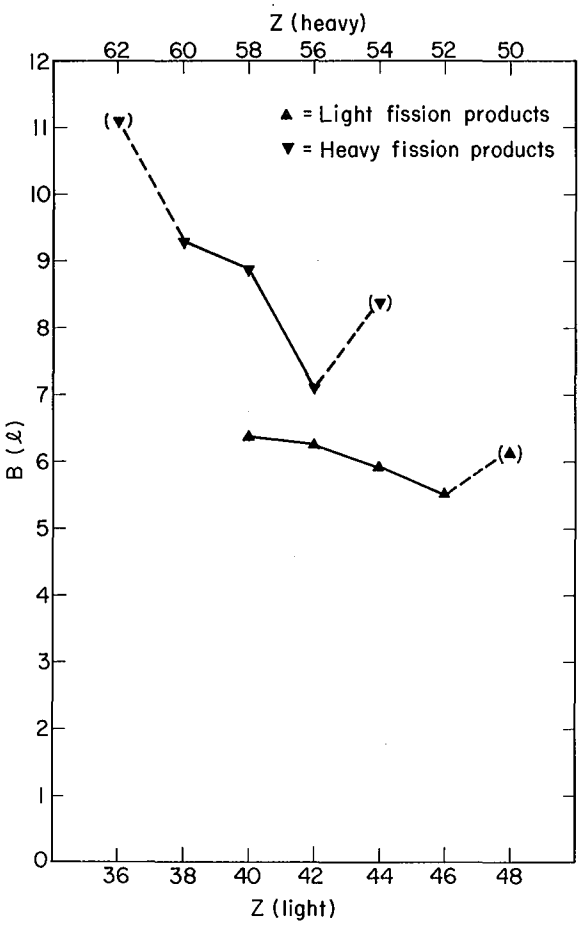

Fig. 4. A plot of the derived angular-momentum parameter B [$B \approx \text{rms}(J) + \frac{1}{2}$] as a function of atomic number. Each data point represents an average of the parameter B as determined from various measured isotopes of that element. The data in parentheses joined by dashed lines represent determinations from limited experimental data and are therefore taken to be less certain. The plot is presented such that complementary elements lie on the same abscissa.

(XBL-711-2523)

momentum between the products is presented in Fig. 4 using values derived in the statistical-model analysis. The data are plotted as a function of Z, and each experimental point represents the average of the parameter B as determined from the various measured isotopes of that element. The graph is presented such that complementary elements lie at the same abscissa value.

The most obvious features presented in Fig. 4 are: (1) the variation between products is not large; (2) the heavy fragments have somewhat larger angular momentum than the light products; and (3) the angular momentum appears to be slightly decreasing as symmetric division is approached. An important feature to note is that the angular momentum does not follow the internal excitation energy of the fragments. The palladium isotopes (Z = 46) which have the lowest values of B have essentially the highest internal excitation energy (as interpreted from the neutron multiplicity measurements[9]). A qualitative correlation which possibly does exist is the dependence of the angular momentum on the deformation of the nucleus. From our measured properties of the even-even fission products it has been possible to determine that the lightest fission products are apparently strongly deformed[1] in their ground states as are the heaviest fission products which are in the rare-earth region.[2] Taken individually the isotopes of both the light and heavy fission groups having the greatest softness to deformation also have the largest angular momentum.

Footnotes and References

†On leave from the Weizmann Institute of Science, Rehovoth, Israel.

*Present address: Sterling Chemical Laboratory, Yale University, 225 Prospect Street, New Haven, Connecticut 06520.

1. E. Cheifetz, R. C. Jared, S. G. Thompson, and J. B. Wilhelmy, Phys. Rev. Letters 25, 38 (1970).

2. J. B. Wilhelmy, S. G. Thompson, R. C. Jared, and E. Cheifetz, Phys. Rev. Letters 25, 1122 (1970).

3. E. Cheifetz, R. C. Jared, S. G. Thompson, and J. B. Wilhelmy, UCRL-19949, August 1970, and in Proceedings of the Conference on the Properties of Nuclei Far From the Region of Beta Stability, Leysin, Switzerland, 1970 (to be published).

4. J. R. Huizenga and R. Vandenbosch, Phys. Rev. 120, 1305 (1960).

5. R. Vandenbosch and J. R. Huizenga, Phys. Rev. 120, 1313 (1960).

6. H. Warhanek, and R. Vandenbosch, J. Inorg. Nucl. Chem. 26, 669 (1964).

7. Demetrios Sarantities, Glen E. Gordon, and Charles Coryell, Phys. Rev. 138B, 353 (1965).

8. J. R. Nix and W. J. Swiatecki, Nucl. Phys. 71, 1 (1965).

9. H. R. Bowman, J. C. D. Milton, S. G. Thompson, and W. J. Swiatecki, Phys. Rev. 129, 2133 (1963).

10. J. M. Blatt and V. M. Weisskopf, Theoretical Nuclear Physics (John Wiley & Sons, New York, 1952) pp. 342 - 365.

11. E. Cheifetz, H. R. Bowman and S. G. Thompson, in Nuclear Chemistry Division Annual Report 1968, UCRL-18667, p. 168.

Experimental Information Concerning Deformation of Neutron-Rich Nuclei in the A≈100 Region†

E. Cheifetz,* R. C. Jared, S. G. Thompson, and J. B. Wilhelmy

Experimental evidence has been found establishing rotational-like behavior in very neutron-rich even-even $_{40}Zr$, $_{42}Mo$, $_{44}Ru$, and $_{46}Pd$ isotopes. These results support recent theoretical studies by Ragnarsson and Nilsson[1] and by Arseniev et al.[2] which have predicted a new region of stable deformation which includes these nuclei. We have obtained systematic information on the ground-state bands of all the light even-even fission products formed in the spontaneous fission of ^{252}Cf which have independent yields[3] of greater than approximately 1% per fission. The experimental configurations and a discussion of the data reduction techniques are presented in another paper in this report[4] and therefore will not be discussed here.

Since it was to be expected that the radiations associated with even-even isotopes should come from low-lying states following a simple systematic behavior, our studies began with the investigation of these nuclei. From analysis of the data we have been able to assign transitions to 14 even-even isotopes for which previous assignments have not existed. The results of the investigation are summarized in Table I. For each isotope in the table we present two lines of information. The top line contains the experimental energies of the observed levels along with the ratio of the energies of the $4^+/2^+$, the measured half-life of the 2^+ level and the yield per fission of this transition. Also presented are the calculated B(E2;2 → 0) and β_2 values following the formalism of Stelson and Grodzins.[5] The criteria taken into account in making these assignments are summarized in Ref. 6. The second line for each isotope in Table I presents the corresponding predicted values. The predicted energies of the 6^+ and 8^+ states were determined from empirical "Mallmann" plots.[7] The predicted lifetimes were determined from considerations of the phenomenological variable moment-of-inertia model.[8] Single-particle B(E2;2 → 0) values and the theoretical deformation values of Arseniev et al.[2] are also presented below the corresponding quantities derived from the experimental data. The theoretical calculations predict this to be a region for which the equilibrium shape is an axially symmetric oblate spheroid. We have translated the reported ϵ_0 deformation to β_2 deformation, ($\beta_2 \cong \epsilon_0/0.95$).

The central question from these studies is whether the theoretical predictions for deformation can be verified. It is not possible to determine the existence of static deformations from observed energy-level spacings or

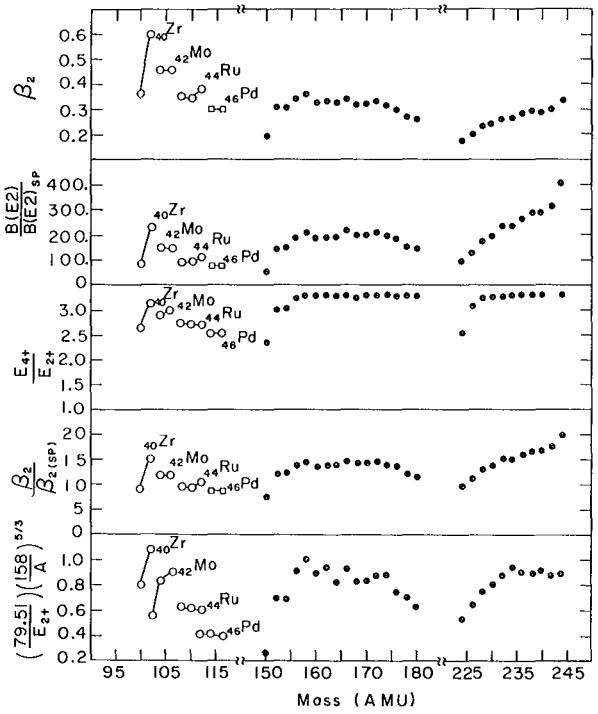

Fig. 1. A composite plot containing five indicators of deformation plotted as a function of mass. The mass intervals used contain only the current experimental region (100 - 116) and a representative sampling from the two major known regions of deformation. The rare earth and actinide data were taken from Refs. 5 and 8. The value of β_2, β_{2SP}, B(E2), and $B(E2)_{SP}$ were extracted from the relationships presented in Ref. 5; E_{2+} and E_{4+} are the experimental energies of the first 2^+ and 4^+ levels; the final indicator $(79.51/E_{2+}) \times (158/A)^{5/3}$ gives a relative comparison between the energies of the first 2^+ states on a basis which removes the inherent mass dependence from the moment of inertia. The open circles represent current results obtained using experimental energies and lifetimes. The open squares represent current results obtained using experimental energies and calculated lifetimes (Ref. 8). The closed circles represent literature values (Refs. 5 and 8).
(XBL-705-2752 with changes)

Table 1. Experimental results and phenomenological predictions for ground-state bands.

		Energy in keV				E4/E2	$t_{\frac{1}{2}}(2\rightarrow 0)$	Yield[a]	Mass	B(E2;2→0)		β_2[c]
		2^+	4^+	6^+	8^+		nsec	%/fiss		exp	s.p.	
^{94}Sr[d]	exp	837.4					<0.1	0.51	94.3			
	pred							0.57	94			
^{96}Sr[d]	exp	815.5					<0.1	0.34	96.0			
	pred							0.67	96			
^{100}Zr	exp	212.7	564.8	1062.7		2.65	0.52	1.80	100.5	233		0.364
	pred			1021	1563		0.29	1.82	100		2.74	-0.29
^{102}Zr	exp	151.9	478.5	964.5	(1551)	3.15	0.86	1.43	101.8	658		0.604
	pred			949	1533		0.94	0.82	102		2.81	-0.29
^{102}Mo	exp	296.0					<0.1	0.46	103.0	>241		>0.348
	pred							0.82	102		2.81	
^{104}Mo	exp	192.3	561.0	1081.0		2.92	0.45	3.37	104.7	430		0.459
	pred			1075	1681		0.45	3.12	104		2.88	-0.28
^{106}Mo	exp	171.7	522.5	(1034.3)		3.04	0.75	3.37	106.0	433		0.454
	pred			1008	1604		0.61	2.49	106		2.96	-0.27
^{108}Ru	exp	242.3	665.3			2.75	0.22	1.94	109.0	293		0.353
	pred			1240	1914		0.17	2.73	108		3.03	-0.26
^{110}Ru	exp	240.8	663.9	1240.0	(1947.7)	2.76	0.23	3.49	110.2	289		0.346
	pred			1238	1914		0.18	3.25	110		3.11	-0.25
^{112}Ru	exp	236.8	645.7			2.73	0.20	0.97	111.8	361		0.382
	pred			1200	1847		0.19	0.70	112		3.18	-0.25
^{112}Pd	exp	348.8					<0.1	0.77	112.9	>108		>0.199
	pred							0.71	112		3.18	
^{114}Pd	exp	332.9	853.6	1503.0		2.56	<0.1	1.48	114.4	>136		>0.221
	pred			1515	2304		0.052	1.77	114		3.26	
^{116}Pd	exp	340.6	878.6			2.58	<0.1	0.87	115.2	>121		>0.207
	pred			1570	2384		0.045	0.73	116		3.34	
^{118}Cd	exp	488.0	1165.3	(1970)		2.39	<0.1	0.32	117.7	>20		>0.080
	pred			1976	2952		0.012	0.20	118		3.41	

[a] Yield; exp. - no. of 2 → 0 transitions per fission corrected for internal conversion; pred. - radio-chemical yield of g.s. (Ref. 3).

[b] B(E2) are in units of $e^2\ cm^4 \times 10^{-51}$.

[c] The experimental β_2 values are derived from the B(E2) data following Ref. 5. The sign is undetermined.

[d] These transitions have also been reported by Ref. 10.

from measurements of B(E2;2 → 0). However, studies of such systematics are indicative of nuclear softness, and therefore it is of interest to compare these properties in this new region with the corresponding values for the rare earth and actinide regions, which are the two major areas of known permanent deformation. There are several different indicators of deformation and it is informative to compare each. Figure 1 is a composite plot containing five indicators associated with deformation [β_2, B(E2)/B(E2)SP, E_{4+}/E_{2+}, β_2/β_{2SP}, $(79.51/E_{2+})\times(158/A)^{5/3}$] plotted as a function of mass. The last indicator represents to a first approximation a mass-independent comparison of the energies of the first 2^+ states, using arbitrarily the deformed ^{158}Gd nucleus as a reference. The nuclei presented in the plot include the current region (100 - 116), and a representative sampling of isotopes in the rare earths (150 - 180) and in the actinides (224 - 244).

In this light fission-product region of the isotopes studied, ^{102}Zr appears as the most favorable candidate for deformation. Its

values for $\beta_2(0.604)$ and for the mass-independent energy parameter (1.08) are larger than any of the corresponding values found in the rare earth and actinide nuclei. Also its values for $B(E2)/B(E2)_{SP}(234)$ and β_2/β_{2SP} (15.2) are larger than for any of the rare earths though smaller than some of the actinides. The only parameter for which it has a lower value than obtained in the other regions is the E_{4+}/E_{2+} ratio, where the ^{102}Zr value of 3.15 is somewhat smaller than the limiting value for a perfect rotor (3.33), which is closely approached in both the rare earths and actinides. The other new isotopes for which we present information have smaller values for these deformation indicators than ^{102}Zr, but even they have, in several instances, values comparable or larger than those typically found in the rare earth and actinide regions and in all cases are larger than the values found for spherical nuclei near closed shells.

For the isotopes with higher masses, the decrease in the deformation indicators is believed to be due to the approach of the Z = 50 closed shell, and for the lighter isotopes the effect of the N = 50 shell should be important. The theoretical calculations of Arseniev et al.[2] imply that the regions of strongest deformation should be in the heavier isotopes of strontium (98 - 102) and of krypton (96 - 102), which are not produced in significant yield in the fission process. Recently (t, p) reactions leading to ^{98}Zr have verified the lowest 2^+ state to be at 1.223 MeV.[9] Therefore, the change in the energy of the lowest 2^+ states between ^{98}Zr and ^{100}Zr is larger than the well-noted change from ^{150}Sm to ^{152}Sm.

Footnotes and References

†Condensed from Phys. Rev. Letters 25, 38 (1970).

*On leave from the Weizmann Institute of Science, Rehovoth, Israel.

1. I. Ragnarsson and S. G. Nilsson, Lund Institute of Technology, Lund 7, Sweden, private communication (1969).

2. D. A. Arseniev, A. Sobieczewski, and V. G. Soloviev, Nucl. Phys. A139, 269 (1969).

3. R. L. Watson and J. B. Wilhelmy, UCRL-18632, 1969.

4. Analysis of Prompt Gamma and X-Ray Radiations of ^{252}Cf Fission Fragments, R. C. Jared, E. Cheifetz, S. G. Thompson, J. B. Wilhelmy, E. K. Quigg, and T. H. Strong, this report.

5. P. H. Stelson and L. Grodzins, Nucl. Data A1, 211 (1965).

6. E. Cheifetz, R. C. Jared, S. G. Thompson, and J. B. Wilhelmy, Phys. Rev. Letters 25, 38 (1970).

7. C. A. Mallmann, Phys. Rev. Letters 2, 507 (1959).

8. M. A. J. Mariscotti, Gertrude Scharff-Goldhaber, and Brian Buck, Phys. Rev. 178, 1864 (1969).

9. A. G. Blair, J. G. Beery, and E. R. Flynn, Phys. Rev. Letters 22, 470 (1969).

10. R. Foucher, Orsay, France, private communication.

Single-Particle and Pairing Effects in the Fission Probabilities of Nuclei Below Radium

L. G. Moretto,† J. T. Routti,* and S. G. Thompson

A very large amount of experimental data on the fission cross sections of nuclei below radium are available at present.[1,2] A simple analysis of such data has yielded rather accurate values for the fission-barrier heights, but so far it has been impossible to account completely for the overall energy dependence of the fission cross sections. The purpose of the present work is the analysis of the experimental data by means of statistical calculations performed on excited nuclei starting from current shell-model theories.

The ratio between the fission cross section σ_f and the compound nucleus cross section σ_c gives the total fission probability. Such probability is related to the "first chance" fission probability defined as the ratio of the fission width Γ_f and the total decay width Γ_T. In heavy nuclei, the charged-particle evaporation is highly hindered; therefore, the total decay width is essentially equal to the sum of the neutron width Γ_n and the fission width

$$\Gamma_f/\Gamma_T = \Gamma_f/(\Gamma_f + \Gamma_n) .$$

It follows that the analysis of the experimental

fission probabilities reduces to the evaluation of Γ_f/Γ_n.

On the basis of statistical assumptions the following expressions for Γ_f and Γ_n are obtained[3]

$$\Gamma_f = \frac{1}{2\pi\rho(E)} \int_0^{E-B_f} \rho_s(x)dx$$

and

$$\Gamma_n = \frac{2m}{\pi^2\hbar^2\rho(E)} \int_0^{E-B_n} \sigma(E - B_n - x)\rho_n(x)(E - B_n - x)dx$$

where

$\rho(E)$ is the compound-nucleus level density,
$\rho_s(x)$ is the saddle-point level density,
$\rho_n(x)$ is the level density of the nucleus after neutron emission,
$\sigma(E - B_n - x)$ is the inverse cross section for the process of neutron emission,
m is the neutron mass,
B_n is the neutron binding energy, and
B_f is the fission-barrier height.

In such formulas, the level densities are quantities which contain a large amount of information related to the nuclear structure. If the level density expressions obtained for a Fermi gas (a set of fermions populating a set of equally spaced single-particle levels) are used, it is difficult to fit the experimental ratio Γ_f/Γ_n over a large range of excitation energies. This is not too surprising since the Fermi gas level-density expression is based upon an oversimplified nuclear model.

In order to retain a larger amount of physical information, one needs to derive the level density from a reasonable shell model, which accounts also for the residual interactions between nucleons. At present formalisms have been developed which allow the numerical evaluation of level densities starting from an arbitrary sequence of single-particle levels.[4] It is also possible to include the residual interactions in a natural way by means of the B.C.S. Hamiltonian.[5]

For the evaluation of Γ_n we have used level densities based upon the Nilsson level sequence. Since most of the nuclei under study are close to ^{208}Pb, the level densities must show the onset of strong shell effects in a very dramatic way. Such effects are indeed seen[4] and reflect both the expectation and the experimental evidence that level densities should be lowest for nuclei closest to the doubly magic nucleus ^{208}Pb. In Fig. 1, a portion of the Nilsson single-particle spectrum

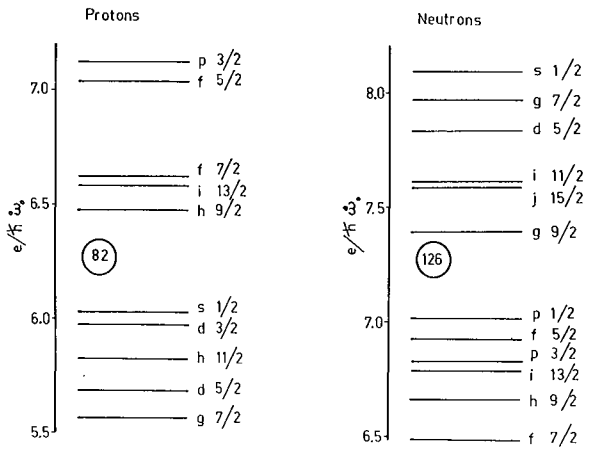

Fig. 1. Neutron and proton single-particle levels close to the 82 - 126 magic numbers. (XBL-713-3152)

used for the calculations is shown. In Fig. 2, the calculated level densities for nuclei around ^{208}Pb are presented. It appears from this figure that the level densities reflect nicely the details of the single-particle scheme used to calculate them.

We expect that the shell effects, which are here introduced in a most natural way from the shell model, will be adequate for a proper treatment of Γ_n.

For the evaluation of Γ_f no reasonable set of single-particle levels is available as yet from shell-model calculations. Therefore, we must rely at present upon the assumption that the actual sequence of single-particle levels can be adequately approximated by a uniform distribution of levels. Such an assumption may be justified by the expectation that, at the very large saddle-point deformations, the bunching and debunching of single-particle levels as a function of deformation (as can be observed in a Nilsson diagram) is reduced to a very unimportant level.

Pairing effects play an important role for ordinary nuclei and might play a more important one at the fission saddle point.[6] For this reason pairing effects are included both in Γ_f and Γ_n. In Fig. 3, we report the results of the statistical calculations performed on a ^{216}Rn nucleus based upon the Nilsson diagram and the B.C.S. Hamiltonian. The gap parameters for neutrons and protons decrease from their ground-state values and finally vanish, showing the transition from the superconducting phase to the ordinary one. The level-density denominator, which is a smooth function of the heat capacity of the nucleus, presents discontinuities typical of the superfluid transitions.

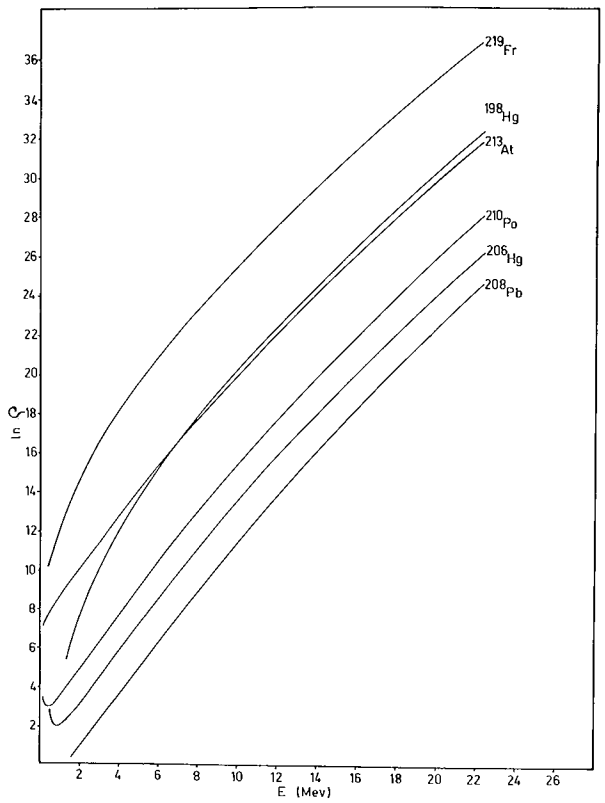

Fig. 2. Level densities for nuclei in the ^{208}Pb region calculated on the basis of the Nilsson diagram. Pairing is not included.
(XBL-713-3153)

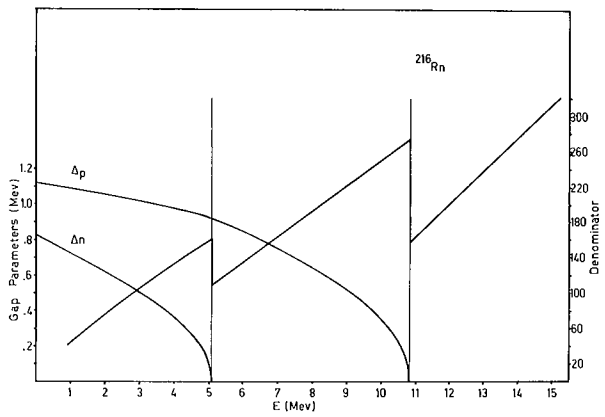

Fig. 3. Energy dependence of the neutron and proton gap parameters (left scale) and of the level-density denominator (right scale) for the nucleus ^{216}Rn. (XBL-713-3154)

Some level-density calculations, which include both the Nilsson diagram and the B. C. S. Hamiltonian, are shown in Fig. 4.

The resulting number of parameters in $\Gamma_f/(\Gamma_f + \Gamma_n)$ is rather small. Some of them

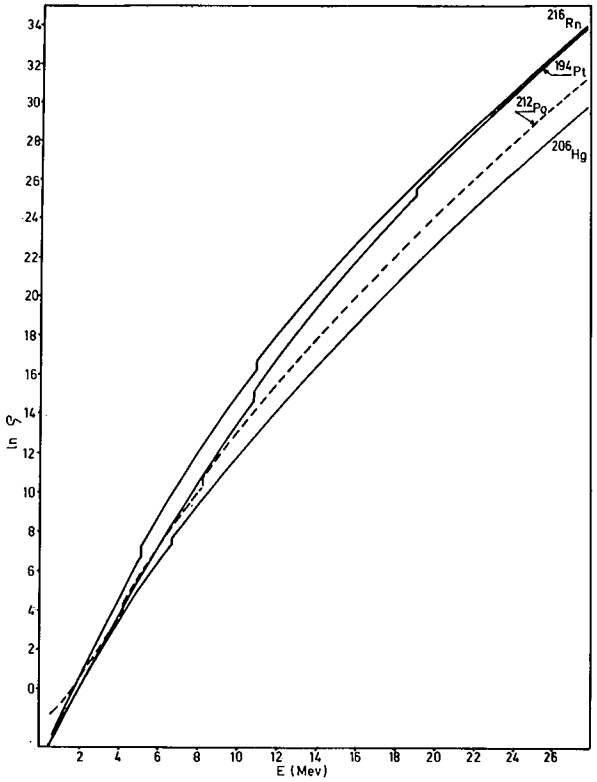

Fig. 4. Level densities for nuclei in the ^{208}Pb region calculated on the basis of the Nilsson diagram and of the B. C. S. Hamiltonian.
(XBL-713-3155)

are quite well known and therefore can be kept fixed--for instance, the neutron binding energy, the gap parameters for ground-state nuclei, etc. Some others, somewhat less certain, should be adjusted in such a way as to fit the experimental data--for instance, the fission-barrier height, the oscillator shell spacing $\hbar\omega_0$, the single-particle level density at the fission saddle point, etc.

The most complicated part of the numerical calculation is the evaluation of the level densities. For such a purpose, a subroutine (MOLOCH) has been written which calculates the level densities and excitation energies in tabular form as a function of the nuclear temperature. The input data are the single-particle levels and the mass and atomic numbers of the nucleus. The pairing strength is calculated in such a way as to reproduce the known gap parameters. The even-odd effects in the level densities are automatically accounted for. Such a code is used for the evaluation of Γ_n. Owing to the great simplification due to the uniform single-particle level spacing at the fission saddle point, a separate subroutine (BAAL) has been written for the evaluation of the saddle-point level

densities. Its structure is identical to that of MOLOCH, aside from the much simpler numerical procedures. The output of this subroutine is in tabular form also. Such a code is used for the evaluation of Γ_f. The tables of the level densities must be interpolated in order to obtain the level density at the required excitation energy. The overall program includes a minimization routine to fit the experimental data. The program can be alternatively operated on-line with the computer. The analysis of all the available experimental data is in progress.

Footnotes and References

†Present address: Instituto di Chimica Generale, Laboratorio di Radiochimica, Viale Taramelli 12, Pavia, Italy.

*Present address: CERN, IBR Division, 1211 Geneva 23, Switzerland.

1. A. Khodai-Joopari, Fission Properties of Some Elements Below Radium (Ph.D. thesis), UCRL-16489, July 1966.

2. S. G. Thompson, Arkiv Fysik 36, 267 (1967).

3. J. R. Huizenga, R. Chaudhry, and R. Vandenbosch, Phys. Rev. 126, 210 (1962).

4. L. G. Moretto, R. Stella, and V. Caramella Crespi, Energia Nucleare 17, 463 (1970).

5. P. Decowski, W. Groschulski, A. Marcinowski, K. Siwek, and Z. Wilhelmi, Nucl. Phys. A110, 129 (1968).

6. L. G. Moretto, R. C. Gatti, S. G. Thompson, J. R. Huizenga, and J. O. Rasmussen, Phys. Rev. 178, 1845 (1969).

Ground-State Bands in Neutron-Rich Even Te, Xe, Ba, Ce, Nd, and Sm Isotopes Produced in the Fission of ^{252}Cf †

J. B. Wilhelmy, S. G. Thompson, R. C. Jared, and E. Cheifetz*

We present new information concerning the energy levels of very neutron-rich even-even isotopes of $_{52}Te$, $_{54}Xe$, $_{56}Ba$, $_{58}Ce$, $_{60}Nd$, and $_{62}Sm$. These results were obtained in a series of experiments on the prompt γ-ray deexcitation of the fission fragments from spontaneous fission of ^{252}Cf. The data, which in some of the cases can be correlated with previously reported results, extend the knowledge about the systematic behavior of collective excitations to neutron-rich nuclei far from the β-stability line. The systematics of the energy levels in the ground-state bands for the heavier fragments are well fitted using the phenomenological variable-moment-of-inertia model of Mariscotti, Scharff-Goldhaber, and Buck.[1] One of the main features of the results is the evidence that the well-known abrupt discontinuity in the ratio $E4^+/E2^+$ for isotopes with 88 and 90 neutrons reaches its maximum effect in neodymium, samarium, and gadolinium isotopes and becomes much less abrupt in the cerium and barium nuclei. This smoother transition is similar to the behavior observed for isotopes with $Z > 66$.[2]

In the experiments x rays and (or) γ rays were measured in coincidence with pairs of fission fragments. The experimental techniques are presented in a previous paper in this report[3] and therefore will not be discussed here.

The experimental results are presented in Table I. For each isotope in the table, we present two lines of information. The top line contains the experimental energies of the observed levels along with the ratio of the energies of the 4^+ and 2^+ levels, the measured half-life of the 2^+ level, the yield per fission of this transition (corrected for internal conversion), and the mean experimental mass associated with the ground-state-band transitions. Also presented are $B(E2;2 \rightarrow 0)$ values. The second line contains corresponding predicted values. The energies of the 6^+ and 8^+ levels were obtained by interpolation using the standard Mallmann plots[5] of E_I/E_2 vs E_4/E_2 (I being 6 or 8). The ground-state-band data used for the curves were obtained from compilations of Mariscotti, Scharff-Goldhaber, and Buck.[1] The predicted half-life and B(E2) values are based on the phenomenological variable-moment-of-inertia model.[1] The predicted radiochemical yields are from the calculations of Watson and Wilhelmy.[6]

Criteria used in establishing the transitions presented in Table I are discussed in Ref. 7.

Table 1. Experimental results and phenomenological predictions for ground state bands.

		Energy in keV				E4/E2	$t_{\frac{1}{2}}(2\to0)$[a]	Yield	Mass[b]	B(E2; 2 → 0)[c]	
		2+	4+	6+	8+		nsec	%/fis		exp	s.p.
^{132}Te	exp	974				2.02		∿0.2	known		
	pred							0.42	132		3.96
^{134}Te	exp	1278	1575	1690		1.23		∿1.5[d]	133.99		
	pred							2.02	134		4.04
^{138}Xe	exp	589.5	1072.9			1.82		2.31	138.28		
	pred							2.25	138		4.21
^{140}Xe	exp	376.8	834.7			2.22		1.5	139.23		
	pred			1371	1940		0.04	3.18	140	185	4.29
^{140}Ba	exp	602.2						∿0.5	known		
	pred							0.2	140		
^{142}Ba	exp	359.7	835.4	1467.4		2.32		2.90	142.02		
	pred			1403	1996		0.04	2.08	142	226	4.37
^{144}Ba	exp	199.4	530.4	962.1	1472	2.66	0.49	3.60	143.58	314	
	pred			957	1455		0.35	3.33	144	454	4.45
^{146}Ba	exp	181.0	514			2.84	0.85	1.01	144.88	277	
	pred			959	1511		0.46	0.78	146	506	4.53
^{144}Ce	exp	397.5						∿0.2	known		
	pred							0.08	144		
^{146}Ce	exp	258.6	668.7	1171		2.59	0.29	1.04	146.40	157	
	pred			1186	1823		0.14	1.24	146	341	4.54
^{148}Ce	exp	158.7	454.4	840.9		2.86	0.9≈	2.31	147.80	445	
	pred			857	1341		0.70	2.11	148	578	4.61
^{150}Ce	exp	97.1	306.1	606.8	983.2	3.15	>0.9≈	>0.98	148.84		
	pred			607	976		2.14	0.56	150	956	4.70
^{152}Nd	exp	75.9	240.6	487.9	810.0	3.17	>2	>0.6	152.6		
	pred			478	782		2.76	0.99	152	1230	4.78
^{154}Nd	exp	72.8	235.2	483.9	812.0	3.23	>2	>0.4	153.5		
	pred			473	781		2.74	0.98	154	1280	4.87
^{156}Sm	exp	76	250.2	518		3.29		>0.1	155.8		
	pred			511	863		2.27	0.35	156	1220	4.95
^{158}Sm	exp	72.8	240.3	498.5	844.5	3.30		>0.15	157.2		
	pred			495	837		2.32	0.18	158	1280	5.04

[a] The life times were determined from two point decay curves and in principle could be shorter since there is a possibility of hold up from previous transitions. However the cases (denoted by ≈) for which the 4 transition had a measured delayed component with $T_{\frac{1}{2}} \geq 3$ nsec were corrected on the basis of the work of W. John et al.[4]

[b] In ^{132}Te, ^{140}Ba, and ^{144}Ce no reliable mass calculation was possible due to poor statistics. The γ transitions were known from previous work (Ref. 7). In general the calculated masses have a statistical error of less than 0.2 amu.

[c] The B(E2) values are in units of $e^2cm^4\ 10^{-51}$.

[d] The prompt yield of the 2^+ state is only ∿0.25% per fission. The balance is made up of delayed yield as taken from Reference 4.

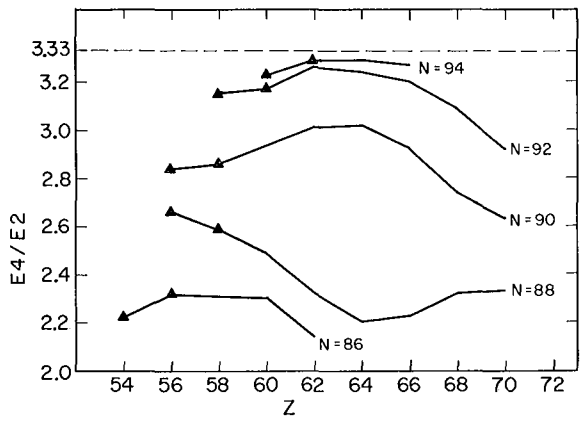

Fig. 1. Systematic behavior of the ratio E4/E2 as a function of proton number in the N = 86 - 92 region. Closed triangles are new data from this experiment. The other data are from Refs. 2 and 11. (XBL-706-3124)

An important feature shown by the data is that the 88 - 90 neutron discontinuity is smearing out as the proton number decreases below Z = 60. This is seen both for the energies of the 2^+ level and the $E4^+/E2^+$ ratio. A plot of the E4/E2 ratio of nuclei with $56 \leq Z \leq 70$ is presented in Fig. 1. This figure clearly shows that the maximum effect of the 88 - 90 neutron discontinuity occurs in the region $60 \leq Z \leq 66$. The nuclei with N = 92, Z = 58 and N = 92, Z = 68 have E4/E2 ratios and B(E2) values which indicate that they are as rotational as $^{152}_{62}Sm$, which is known to have permanent quadrupole deformation, even though for Z = 58 and Z = 68 the 88 - 90 neutron effect is relatively rather smooth. A similar effect has been shown to occur in the 76 - 80 proton-number region,[8] where a sharp discontinuity occurs for $106 \leq N \leq 112$, and a smooth behavior was observed outside this region. We can summarize then that the transition from a vibrational spectrum to a rotational one can be either abrupt or smooth depending probably on a delicate balance between proton- and neutron-pairing correlations. Calculations by Nilsson et al.[9] and by Ragnarsson and Nilsson[10] indicate that deformation is expected to occur abruptly between 86 and 88 neutrons for the nuclei discussed here. These calculations, which are based on the Nilsson model, combined with the Strutinsky normalization procedure, reproduce the general trend of decreased deformation for nuclei with 88 neutrons on both sides of Z = 62.

Footnotes and References

†Condensed from Phys. Rev. Letters 25, 1122 (1970).

*On leave from Weizmann Institute of Science, Rehovoth, Israel.

1. M. A. J. Mariscotti, G. Scharff-Goldhaber, and B. Buck, Phys. Rev. 178, 1864 (1969).

2. F. S. Stephens, D. Ward, and J. O. Newton, J. Phys. Soc. Jap., Suppl. 24, 160 (1968).

3. Analysis of Prompt Gamma and X-Ray Radiations of ^{252}Cf Fission Fragments, R. C. Jared, E. Cheifetz, S. G. Thompson, J. B. Wilhelmy, E. K. Quigg, and T. H. Strong, this report.

4. W. John, F. W. Guy, and J. J. Wesolowski, Phys. Rev. C 2, 1451 (1970).

5. C. A. Mallmann, Phys. Rev. Letters 2, 507 (1959).

6. R. L. Watson and J. B. Wilhelmy, UCRL-18632, 1969.

7. J. B. Wilhelmy, S. G. Thompson, R. C. Jared, and E. Cheifetz, Phys. Rev. Letters 25, 1122 (1970).

8. J. Brude, R. M. Diamond, and F. S. Stephens, Nucl. Phys. A92, 306 (1967).

9. S. G. Nilsson, C. F. Tsang, A. Sobiczewski, Z. Szymanski, S. Wycech, G. Gustafson, I. Lamm, P. Möller, and B. Nilsson, Nucl. Phys. A131, 1 (1969).

10. I. Ragnarsson and S. G. Nilsson, private communication.

11. C. M. Lederer, J. M. Hollander, and I. Perlman, Table of Isotopes (John Wiley and Sons, New York, 1967) 6th edition.

The Influence of Various Approximations on the Calculation of First-Chance Fission Probabilities

R. C. Gatti and S. G. Thompson

Excitation functions have been measured for the induced fission of about 12 nuclei lighter than radium. These data have been analyzed with standard theoretical expressions in order to determine the fission-barrier heights (B_f). Most earlier authors[1-3] have analyzed only the low energy data (up to about 40 MeV of excitation energy) and have neglected the influence of barrier penetration, pairing, shell effects and angular momentum. The level-density expressions themselves and the parameters used have some effect on the values of fission-barrier heights which are extracted. However, in general, when experimental fission barriers and level-density parameters which give good fits at low energies are used to calculate first-chance fission probabilities at higher energies, the resulting values are much larger than the experimental results. As the first step in trying to understand this discrepancy, we studied the separate influences on the calculated first-chance fission probability of a number of previously neglected effects.

The theoretical expression for the competition between first-chance fission and neutron emission used here is similar to one derived by Wheeler[4]

$$\frac{\sigma_f}{\sigma_R} = \frac{\Gamma_f}{\Gamma_f + \Gamma_n} ,$$

where σ_f is the measured fission cross section of the compound nucleus, σ_R is the calculated total reaction cross section, Γ_f is the fission probability, and Γ_n is the neutron evaporation probability ($\Gamma_n >> \Gamma_\gamma + \Sigma\Gamma_{\text{charged particle}}$). The total reaction cross section was calculated using the procedure of Huizenga and Igo.[5] For the fission width, Γ_f, we start with the expression derived from standard reaction rate theory[6] and incorporate the Hill and Wheeler[7] fission-barrier penetrability B_p to obtain the expression

$$\Gamma_f = \frac{1}{2\pi\rho(E_x)} \int_0^{E_x} B_p \rho^*(X) dX ,$$

where

$$B_p = \frac{1}{1 + e^{-\frac{2\pi}{\hbar\omega}(T_f)}}$$

T_f is the energy in the fission degree-of-freedom above the height of the fission barrier, $\hbar\omega$ is a measure of the thickness of the fission barrier, $\rho(E_x)$ is the level density in the compound nucleus at a given excitation energy E_x, and the level density at the saddle point is $\rho^*(X)$--where the excitation energy in the nonfission degree-of-freedom is X. The relation of the excess energy in the fission degree-of-freedom to the excess energy in the nonfission degree-of-freedom is given by

$$E_x = B_f + X + T_f$$

and

$$B_f = B_f^{LD} - S ,$$

where B_f^{LD} is the liquid-drop fission barrier,[8] S is the experimental shell effect in the ground state of the compound nucleus, and B_f is the experimental fission-barrier height.

The calculations of Cohen et al.[9] can be used to estimate the lowering of the fission barrier ΔB_{fR} caused by the angular momentum brought in by the bombarding projectile. To calculate the effect of pairing energy in the ground state Δ on the excitation energy, we use the method of Newton,[10] and subtract from the excitation energy the empirical value given in the Myers and Swiatecki mass formula[8] $\Delta = 11/\sqrt{A}$. For odd-A nuclei we subtract Δ, for even-even we subtract 2Δ, and for odd-odd there is no correction. Thus, the excess energy in the nonfission degree-of-freedom is given by

$$X = E_x - (B_f^{LD} - S) - \Delta - \Delta B_{fR} - T_f .$$

The basic expression given by Weisskopf[11] for the neutron-emission width Γ_n is

$$\Gamma_n = \frac{\frac{2gm}{\pi\hbar^2}}{2\pi\rho(E_x)} \int_0^{\max} T_n[\sigma(E_x, T_n)]\rho^{**}(x) dT_n ,$$

where g is the number of states for the spin

of a neutron, m is the mass of the neutron, T_n is the kinetic energy of the evaporated neutron, $\sigma(E_x,T_n)$ is the inverse formation cross section of the compound nucleus,[12] and $\rho^{**}(x)$ is the level density of the residual nucleus at an excitation energy of x. Corrections to the excitation energy of the residual nucleus are made for the shell effect S_r using Ref. 13, the pairing effect Δ_r, and the angular momentum left in the residual nucleus after correcting for the amount of angular momentum carried away by the evaporated neutron. From the angular momentum one calculates the rotational-energy correction of the residual nucleus ΔE_R. Corrections are also made for the neutron-separation energy from the compound nucleus B_n and the recoil of the residual nucleus due to the neutron evaporation. The equation for neutron-emission probability thus becomes:

$$\Gamma_n = \frac{2gmr^2\left(\frac{m_r}{M}\right)^2}{2\pi\rho(E_x)} \int_0^{max} \sigma(E_x, T_n) \cdot (E_x - B_n - \Delta_r + S_r - \Delta E_R - x)\rho^{**}(x)dx \ ,$$

where m_r is the mass of the residual nucleus, M is the mass of the compound nucleus, and r is the radius of the residual nucleus.

The level density was calculated using the expression given by Lang[14] which is

$$\rho(E,N,Z) = \left(\frac{1}{2\pi\sigma^2}\right)^{1/2} \left(\frac{\sqrt{\pi}}{12}\right) \cdot \left(\frac{1}{a}\right)^{1/4} \left(\frac{1}{E+t}\right)^{5/4} \exp\left(2\sqrt{aE}\right) ,$$

where

$$E = at^2 - t$$

$$\sigma^2 = \frac{6}{\pi} a(\langle m^2\rangle) t$$

$$\langle m^2\rangle = 0.24 A^{2/3}.$$

This formula eliminates the difficulty at low energies. Here t is the temperature, $\langle m^2\rangle$[15] is the average value of the square of the projection of the total angular momentum for states around the Fermi level, C is a constant, and a is a parameter proportional to A.

The experimental data for the reaction

$$^{197}_{79}Au + ^{4}_{2}He \rightarrow ^{201}_{81}Tl$$

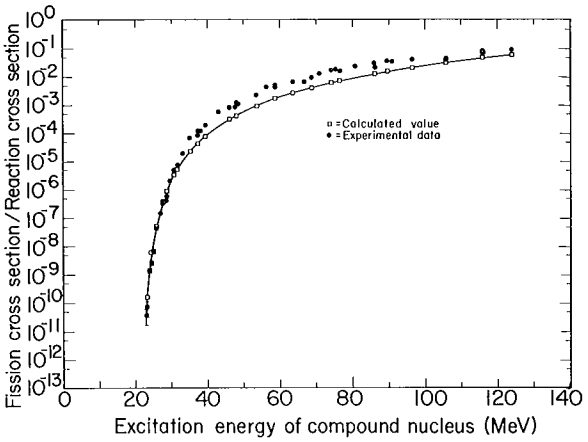

Fig. 1. Experimental data and calculated first-chance fission probability with all the various corrections as a function of excitation energy of the compound nucleus.
(XBL-713-3071)

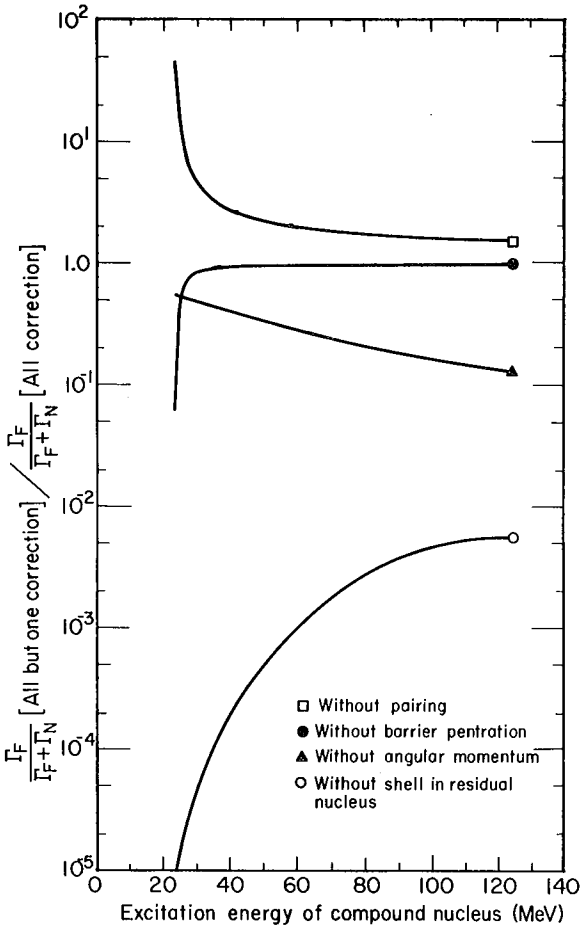

Fig. 2. The ratio of corrected to uncorrected first-chance fission probability for the four most important corrections as a function of the excitation energy of the compound nucleus.
(XBL-713-3072)

were analyzed using Lang's level-density expression. Some preliminary results with a fission barrier ≈ 22.2 MeV, a barrier penetration ≈ 1 MeV, $a_f \approx 33$ MeV^{-1}, and $a_n \approx 32$ MeV^{-1} are shown in Fig. 1. In this case, one finds that at low energies the effect of barrier penetration, pairing in the ground-state nucleus, and the shell correction are most critical. At the higher energies the angular momentum effects have a large influence on the results of the calculations. These effects are shown in Fig. 2. Since the calculated points are lower than the experimental points, one can probably also take into account the effects of higher order fission.

References

1. A. Khodai-Joopari, Fission Properties of Some Elements Below Radium (Ph.D. thesis), UCRL-16489, July 1966.

2. G. M. Raisbeck and J. W. Cobble, Phys. Rev. 153, 1270 (1967).

3. L. G. Moretto, R. C. Gatti, and S. G. Thompson, in Nuclear Chemistry Division Annual Report 1967, UCRL-17989, January 1968, p. 141.

4. J. A. Wheeler, in Fast Neutron Physics, edited by J. B. Marion and J. L. Fowler (Interscience Publishers, New York, 1963), Part II, p. 2051.

5. J. R. Huizenga and C. J. Igo, Nucl. Phys. 29, 462 (1962).

6. N. Bohr and J. A. Wheeler, Phys. Rev. 56, 426 (1939).

7. D. L. Hill and J. A. Wheeler, Phys. Rev. 89, 1102 (1953).

8. W. D. Myers and W. J. Swiatecki, UCRL-11980, May 1965.

9. S. Cohen, F. Plasil, and W. J. Swiatecki, UCRL-10775, April 1963.

10. T. D. Newton, Can. J. Phys. 34, 804 (1956).

11. V. Weisskopf, Phys. Rev. 52, 295 (1937).

12. Z. Fraenkel, I. Dostrovsky, and G. Friedlander, Phys. Rev. 116, 683 (1959).

13. N. Rosenzweig, Phys. Rev. 108, 817 (1957).

14. J. N. B. Lang and K. J. Le Couteur, Proc. Phys. Soc. (London) A67, 586 (1954).

15. U. Facchini and E. Saetta-Menichella, Energia Nucleare 15, 54 (1968).

II. Chemical and Atomic Physics

Atomic and Molecular Spectroscopy

Observation of the Magnetic-Dipole Decay of the 2^3S_1 State of Heliumlike Si XIII, S XV, and Ar XVII†

R. Marrus and R. W. Schmieder

The possibility of magnetic dipole decay from the metastable states of hydrogenlike and heliumlike atoms was first noted by Breit and Teller.[1] They pointed out that, although the transition rate (A_{M1}) for the decay of the 2s state of hydrogen and the 2^3S_1 state of helium by this mode would vanish in a nonrelativistic theory, a finite decay rate results if the Dirac theory is employed. Because of the long lifetime associated with this decay, it has so far not been experimentally possible to observe it in the light atoms. Recently, however, an observation in the solar soft x-ray spectrum, which has been attributed to the 2^3S_1-1^1S_0 decay in heavy heliumlike ions, has been reported.[2]

In this article we report the first laboratory observation of the magnetic dipole transition 2^3S_1-1^1S_0 in the heliumlike atoms Si XIII, S XV, and Ar XVII. A schematic diagram of our apparatus is shown in Fig. 1. The ions emerge from the Berkeley heavy-ion linear accelerator (Hilac) with an energy of about 10.2 MeV/nucleon. A bending magnet deflects the beam into our apparatus. The beam is well focused and, in order to obtain ions in the desired charge state, it is passed through a thin metallic foil. (For an experimental discussion of charge equilibrium achieved by passage of beams through thin foils, see Ref. 3.) At the beam energies appropriate to this experiment, essentially all the particles leave the foil either fully stripped or as hydrogenlike and heliumlike atoms. These atoms are distributed among the atomic levels, but rapidly decay to the ground and metastable levels with a sizeable fraction of the heliumlike atoms appearing in the 2^3S_1 state.[4] (For a review of prior work on hydrogenlike and heliumlike metastable states, see Ref. 4.) It is these atoms which are of interest and give rise to the decay reported here.

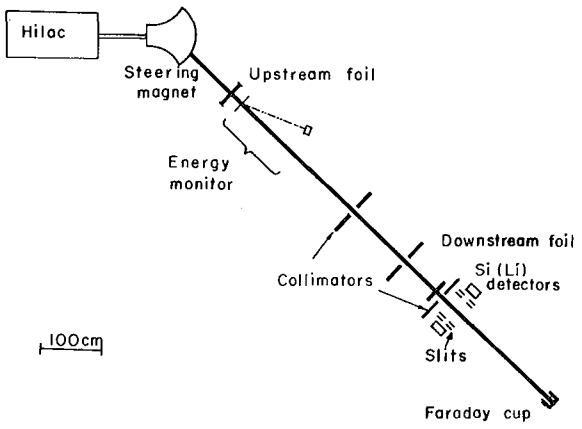

Fig. 1. Schematic of the apparatus. (XBL-712-2927)

The detector is a high-resolution silicon detector that views the beam through a narrow aperture which is adjustable. The detector is calibrated in place by exciting the K x rays of Mn, P, and Ca by fluorescence, using the x rays from an iron-55 source.

The x-ray spectrum in the energy range 500 eV to 7 keV observed with the silicon, sulfur, and argon beams, and the upstream foil in position, is shown in Fig. 2. To demonstrate that the x rays arise from a decay in flight of a beam atom, the aperture position in front of the detector was varied to observe the Doppler shift of the emitted x ray. The observed shift is in good agreement with the beam velocity $\beta = v/c = 0.14$. Several foil materials were used to demonstrate that the observed peaks are independent of foil material. To avoid collision processes between beam atoms and background gas atoms, the spectrum was shown to be pressure-independent. Finally, we note that when the foil is removed, the observed spectrum disappears.

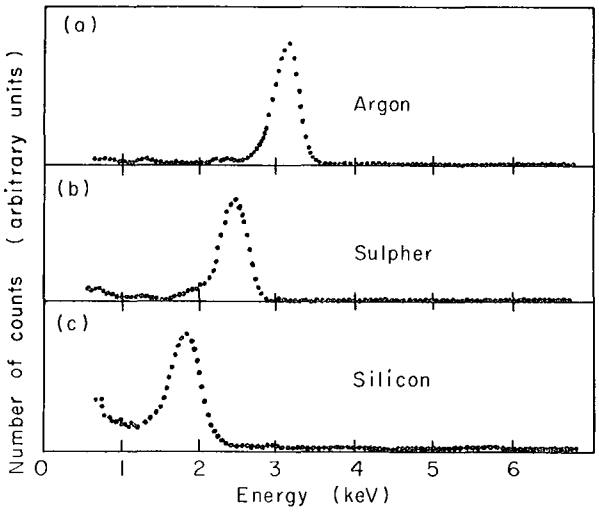

Fig. 2. Spectra observed in energy interval 500 eV-7 keV with (a) argon beam, (b) sulfur beam, (c) silicon beam. (XBL-712-2926)

The foregoing observations lead us to the conclusion that the x rays arise from a long-lived decay mode of ions formed when the beam passes through the foil. Our assignment of these x rays to the 2^3S_1-1^1S_0 transition is based on the following:

(a) For each of the three elements the observed x-ray energy is higher than the ionization energy of any atom having three or more electrons. Moreover, the fraction of such atoms present in the beam should be negligible.

(b) The only states of hydrogenlike and heliumlike atoms with lifetime long enough to be seen at the detector are the $2^2S_{1/2}$ state of hydrogenlike atoms, and the 2^1S_0 and 2^3S_1 states of heliumlike atoms. However, the primary mode of decay of the $2^2S_{1/2}$ and 2^1S_0 states is the two-photon mode, which gives rise to a continuous spectrum unlike the discrete lines observed here.

(c) The observed energies are in good agreement with a calculation of the 2^3S_1-1^1S_0 energy difference by Knight and Scherr[5] in a $1/Z$ expansion. These energies are compared in Table I.

Table I. Observed and predicted energies (2^3S_1-1^2S_0), in keV.

	Si XIII	S XV	Ar XVII
Observed	1.85 (0.10)	2.46 (0.10)	3.13 (0.10)
Predicted[4]	1.84	2.42	3.09

Footnote and References

†Taken from Phys. Letters 32A, 431 (1970).

1. G. Breit and E. Teller, Astrophys. J. 91, 215 (1940).

2. A. H. Gabriel and C. Jordan, Nature 221, 947 (1969).

3. H. H. Heckman, E. L. Hubbard and W. G. Simon, Phys. Rev. 129, 1240 (1963).

4. Beam Foil Spectroscopy, edited by S. Bashkin (Gordon and Breach, New York, 1968) Vols. I and II.

5. R. E. Knight and C. E. Scherr, Rev. Mod. Phys. 35, 431 (1963).

Relativistic Magnetic Dipole Emission: Lifetime of the 1s2s $^3S_1$ State of Heliumlike Argon†

Robert W. Schmieder and Richard Marrus

Until recently it was believed that the primary decay mode for the 1s2s $^3S_1$ state of two-electron atoms would be spin-orbit-induced double electric-dipole (2E1) emission. This process was first suggested by Breit and Teller,[1] and has been accurately calculated by Drake, Victor, and Dalgarno[2] and Bely and Faucher.[3] However, in 1969 Gabriel and Jordan[4] reported the observation of solar coronal lines corresponding to the 1s2s $^3S_1$-1s^2 $^1S_0$ energy separation for the helium isoelectronic sequence C V-Mg XI, and the Fe XXV line has been reported by Neupert and Swartz,[5] indicating that the primary decay mode is single-photon emission. Single-photon emission also was discussed by Breit and Teller,[1] who pointed out that relativistic effects can lead to magnetic-dipole radiation (this is identically zero in the nonrelativistic approximation). More recently Schwartz[6] and Drake[7] have studied this process and conclude that, to relative accuracy Z^{-1}, the dominant contributions come from kinetic-energy and finite-wavelength corrections to the magnetic-dipole moment, which have nonzero matrix elements between the 1^1S_0 and 2^3S_1 states. Schwartz[6] has calculated the rate of this process using hydrogenic wave functions and energies. He obtains the asymptotic (to large Z) result $A_{M1}(2^3S_1\text{-}1^1S_0) = 1.66\times10^{-6}Z^{10}\ \text{sec}^{-1}$, which yields, for argon (Z = 18), $\tau_{M1}(2^3S_1) = 169$ nsec. More accurate calculations have been performed by Drake[7] using correlated wave functions and energies, with the result for argon $\tau_{M1}(2^3S_1) = 194$ nsec.

We report the measurement of the lifetime of the 1s2s $^3S_1$ state of Ar XVII, using the beam-foil method. The result is

$$\tau(2^3S_1) = 172 \pm 30 \text{ nsec.}$$

The apparatus used in this measurement is illustrated in Fig. 1. Argon-40 ions in the +14 charge state having an energy of 10.3 MeV/nucleon ($\beta = 0.148$) are obtained from the Berkeley heavy-ion linear accelerator (Hilac) and are magnetically deflected into the high-vacuum region, where the pressure is a few microtorrs. The beam is passed through a 100-$\mu g/cm^2$ Be foil mounted on a movable track, emerging with the approximate charge

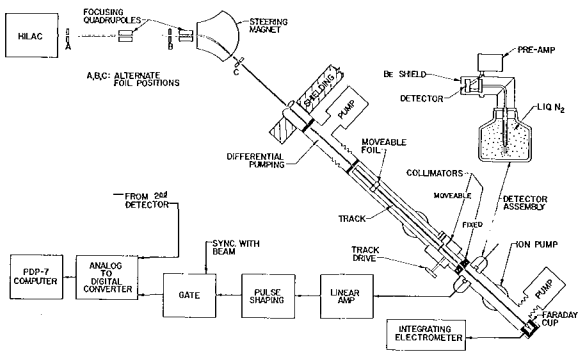

Fig. 1. Schematic diagram of the apparatus. (XBL708-1790)

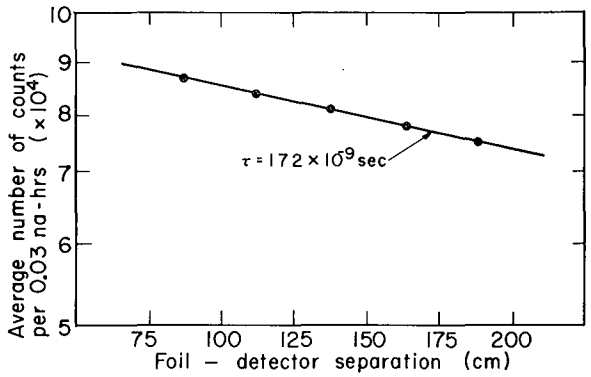

Fig. 2. Typical decay curve (semilog scale). The line represents the mean lifetime determined by least squares from several such plots, obtained independently. The statistical error on each point is roughly the size of the points. (XBL-712-2924)

distribution +16 (25%), +17 (50%), +18 (25%). Some of the ions emerging with +16 or +17 charge will be excited, and will quickly de-excite to the 1S ground states or the 2S metastable states. Ions in the 1s $^2S_{1/2}$ (hydrogenlike) and 1s2s $^1S_0$ (heliumlike) states decay to their ground states with 1/e decay lengths of a few centimeters (for our beam velocity v = 0.148c), and at distances over 75 cm, only the 1s2s $^3S_1$-1s^2 $^1S_0$ decay (with 1/e length $\cong$ 750 cm) is appreciably present. The photons (E $\cong$ 3.1 keV) emitted in flight are detected with a windowless Si(Li) x-ray detector of the type normally used for nuclear gamma spectroscopy. The resolution of this device (cooled to 77°K) is about 200 eV at 3 keV, but we purposefully permitted a large Doppler broadening so that the detector would have a large angular field of view. The broadening is of no consequence to this measurement, since only the total number of counts within the peak was used in determining the lifetime.

Pulse shaping and timing is performed with conventional electronics, and pulse-height analysis is performed with an analog-to-digital converter and a PDP-7 computer. Signal (number of counts within full width at 0.1-maximum of peak) was normally 50 to 100 times background (number of counts within equal width, away from peak).

The lifetime was determined by plotting the counting rate (peak minus background) for several foil-detector distances between 75 and 200 cm. The rates were normalized to a total charge of beam passing the detector (0.030 nA h), as measured by an integrating electrometer driven by the Faraday cup which stops the beam. In order to compensate for slow variations in the beam and/or apparatus, the data were accumulated in short time intervals (~3 min), moving the foil cyclically through five or six positions. Successive counts for each position were then averaged. Also two independent detectors (facing each other) were used, and the results averaged. In each of six independent runs, about 10^5 photons were recorded for each foil-detector distance.

A typical decay curve obtained in this way is shown in Fig. 2. Although the total decay is small, the counting rate appears to decay exponentially. The lifetime was computed by performing a least-squares fit of the data with the function ae^{-bx}, determining b, and thus $\tau = 1/bv$. The final result, $\tau(2^3S_1) = (172 \pm 30) \times 10^{-9}$ sec, was obtained as a weighted average of the results of the independent runs. The error quoted here is 2 times the mean error, or roughly 95% confidence. The main contributions to the mean error are believed to be due to slow drifts in beam and/or foil properties, and other systematic errors such as foil tracking, beam current integration, and detector efficiency (nominally 80%). The beam velocity, necessary for converting the mean decay length to a mean lifetime, is known from time-of-flight measurements to within 2%. Correction for velocity degradation by the foil has been made. Background corrections were typically 1%.

In order to test the pressure dependence of the measurements, the pressure was increased by a factor of 2.5. No significant deviations in the counting rates were observed, implying that collisions quenching between the foil and detector (typically ~ 10^{13} residual gas atoms per cm^2) is negligible. We have also shown that these results are independent of foil material (a 15-μg/cm^2 C foil and a 600-μg/cm^2 Ni foil were also used), beam current, counting rate, detector operation, etc.

Footnote and References

†Condensed from Phys. Rev. Letters 25, 1245 (1970).

1. G. Breit and E. Teller, Astrophys. J. 91, 215 (1940).

2. G. W. F. Drake, G. A. Victor, and A. Dalgarno, Phys. Rev. 180, 25 (1969).

3. O. Bely and P. Faucher, Astron. Astrophys. 1, 37 (1969).

4. A. H. Gabriel and C. Jordan, Nature 221, 947 (1969).

5. W. M. Neupert and M. Swartz, Astrophys. J. 160, L189 (1970).

6. C. Schwartz, private communication.

7. G. W. F. Drake, to be published.

Two-Photon Decay and Lifetime of the $2^2s_{1/2}$ State of Hydrogenlike Argon†

Robert W. Schmieder and Richard Marrus

The decay of the $2^2s_{1/2}$ state of hydrogenlike atoms has been a subject of long-standing theoretical interest. It was first shown by Breit and Teller[1] in 1940 that this state should decay to the $1^2s_{1/2}$ ground state primarily by the simultaneous emission of two photons. In this process, which we designate 2E1, the emission spectrum is a continuum, and the sum of the energies of the two photons equals the 1s-2s energy separation. Spitzer and Greenstein[2] invoked this mechanism to explain the continuous spectrum of planetary nebulae, and using nonrelativistic theory, they accurately computed the predicted spectrum and lifetime of metastable hydrogen. Later, Shapiro and Breit[3] obtained the decay rate for a hydrogenlike atom of atomic number Z:

$$A_{2E1}(2^2s_{1/2} - 1^2s_{1/2}) = 8.226\,Z^6\ \text{sec}^{-1}, \quad (1)$$

which agrees with Spitzer and Greenstein for Z = 1. Recently, a closed-form expression for the spectral distribution has been obtained[4] and several authors[5] have theoretically treated the two-photon decay mode in the 2^1S_0 and 2^3S_1 states of the helium isoelectronic sequence.

All of these calculations are nonrelativistic, and consequently are accurate only for small Z. Relativisitic effects make it possible for the $2^2s_{1/2}$ state to decay to the $1^2s_{1/2}$ state by magnetic dipole (M1) radiation a process that vanishes in the nonrelativistic approximation. This mechanism also was first noted by Breit and Teller, and recent calculations by Drake[6] and by Schwartz[7] reveal that to relative accuracy 1/Z, the M1 rate is

$$A_{M1}(2^2s_{1/2} - 1^2s_{1/2}) = 2.50\times10^{-6}\,Z^{10}\ \text{sec}^{-1}, \quad (2)$$

and hence for Z = 18 contribute about 4% of the total decay probability of the $2^2s_{1/2}$ state.

Experimentally, the two-photon decay mode was first observed in He II by Lipeles, Novick, and Tolk,[8] who reported detection of coincidences and angular distribution measurements consistent with the $1 + \cos^2\theta$ prediction. Rough spectral measurements made with broad-band crystal filters also have been reported.[9] A continuous spectrum observed in a plasma[10] has been attributed to the two-photon decay of the 2^1S_0 state of heliumlike atom Ne IX. The relativistic magnetic-dipole mode has been observed recently in the solar corona[11] and in the laboratory.[12,13] Two recent measurements of the 2^1S_0 lifetime in He I, which presumably decay by two-photon emission have been reported,[15] but there has so far been no measurement of the lifetime of the $2^2s_{1/2}$ state of any hydrogenlike atom.

We report the direct observation of the two-photon decay mode in the hydrogenlike atom Ar XVIII using coincident-photon counting techniques and the measurement of the lifetime of the $2^2s_{1/2}$ state, using the beam-foil time-of-flight method. The result is

$$\tau(2^2s_{1/2}) = 3.54(25)\times10^{-9}\ \text{sec}, \quad (3)$$

where the error indicates 95% confidence.

The apparatus used in this measurement

has been described in previous communications,[12-14] and only a brief summary is given here. Ions of ^{40}Ar in the +14 charge state are accelerated in the Berkeley Hilac to an energy of 412 MeV ($\beta = v/c = 0.148$) and passed through a thin foil, from which they emerge distributed among the +16 (heliumlike), +17 (hydrogenlike), and +18 (fully stripped) charge states. A significant fraction of the +16 and +17 ions may emerge highly excited, but they undergo fast radiative or nonradiative deexcitation to the ground or metastable states. The (forbidden) radiative decay of the metastable states is detected in flight a few tens of centimeters downstream from the foil by a pair of Si(Li) solid state x-ray detectors placed symmetrically perpendicular to the beam and about 2 cm from it. The photons were detected both singly and in coincidence, using standard high-rate coincidence circuitry with a resolving time of $2\tau \sim 1$ μsec. In the singles mode, the energy E1, E2 of every detected photon in each detector was recorded. In the coincidence mode, the detection of two photons in separate detectors with a time interval $|T1-T2| \lesssim 5$ μsec was defined as a "coincidence," and resulted in the storage of E1, E2, E1 + E2, and T1 - T2. With a typical beam current of 1 nA, single counting rates were typically 10^2 - 10^3 sec^{-1}, and coincidence rates were 0.1 - 1 sec^{-1}.

Since the lifetimes and spectra of the two-photon decays from 2^1S0 and $2^2s_{1/2}$ states are similar, it was necessary to discriminate against the heliumlike atoms in favor of the hydrogenlike atoms of interest here. To this end, a two-foil technique was used. A thick (> 100 μg/cm^2) beryllium foil capable of producing near charge equilibrium in the beam was placed ahead of the steering magnet (at position A in Fig. 1 of Ref. 14). The steering magnet was then set so that only fully-stripped ions were passed into our apparatus. The beam was then passed through an extremely thin (< 10 μg/cm^2) carbon foil, much thinner than is necessary to produce charge equilibrium. Since the capture of two or more electrons in this thin foil is a less likely process than the capture of one electron, the resulting beam has a substantially higher ratio of +17/+16 than with the near charge-equilibrated beam.

A typical singles spectrum taken in this way, using a foil-detector separation of 25 cm, is shown in Fig. 1. It consists of a broad continuum between the detector threshold and E ~ 3 keV, in general agreement with the predictions.[2,4] The observed spectrum also includes the composite effects of absolute detector efficiency (the step at 1.84 keV is due to absorption in the detector at the K-edge of silicon), detector resolution (≅ 0.2 keV),

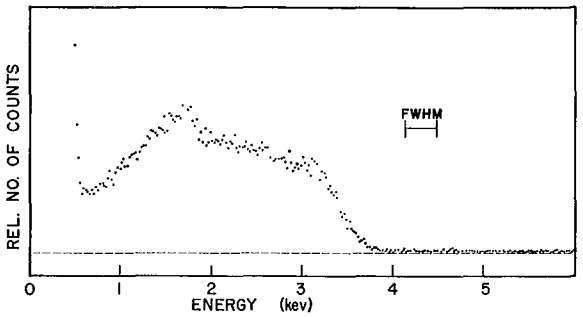

Fig. 1. Typical energy spectrum observed in singles mode. This uncorrected spectrum is predominantly the two-photon decay of metastable Ar XVIII. The edge at 1.84 keV is an instrumental effect (see text). The detector resolution is indicated. (XBL 709-6648)

doppler broadening due to the large acceptance angle of the detectors, low energy x rays, electronic noise, high energy background, and contributions from the decays of any heliumlike ions that might be present. Although the correction of the data for all these effects is not yet complete, these data clearly verify the qualitative nature of the two-photon spectrum.

To further verify the two-photon nature of the observed continuum, the detectors were operated in the coincidence mode, so that only coincident events (defined above) were stored. Figure 2a is a plot of the number of events versus the time delay T1 - T2 between the two photons. The zero in this plot was generated by introducing a fixed delay in one detector; it was calibrated using a pulse generator to simulate a true coincidence. The peak in the time spectrum of Fig. 2a is strong evidence that real coincident events are being observed.

The spectra observed in coincidence are shown in Figs. 2b and 2c. These spectra represent only the true coincidences appearing under the peak of the time spectrum in Fig. 2a.

The spectrum of the sum energy E1 + E2 observed as true coincidence is shown in Fig. 2c. The spectrum is a single strong peak with a width roughly equal to the system resolution, indicating that this peak represents a single line. That this line falls at 3.3 keV is also strong evidence of the two-photon mode in Ar XVIII and not Ar XVII. The fact that the singles spectrum observed in singles mode (Fig. 1) is the same as that observed in coincidence mode (Fig. 2b), and the association of the latter (via Figs. 2a, 2c) with the 2E1 decay mode in Ar XVIII, permits measuring the lifetime in the singles mode.

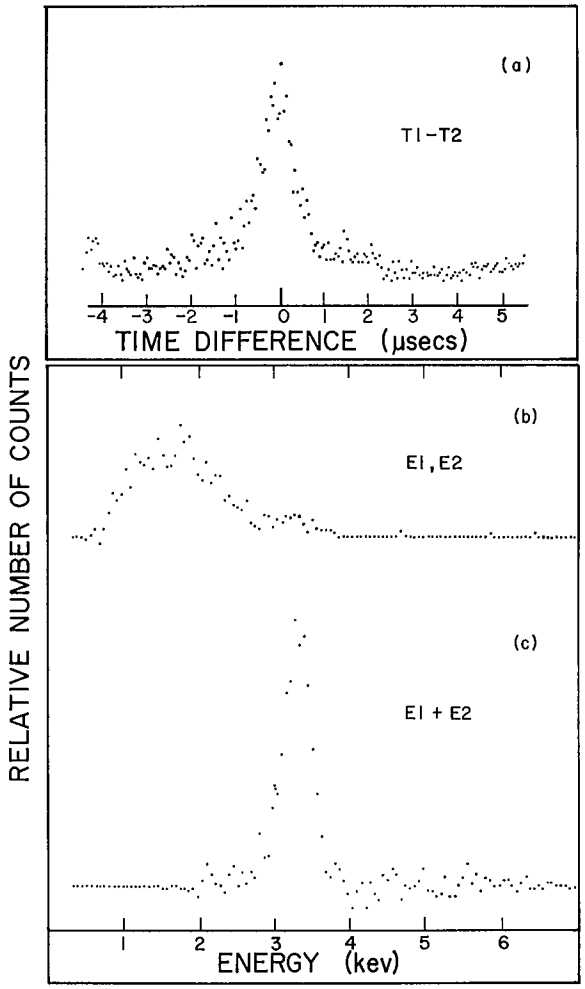

Fig. 2. Spectra observed in coincidence mode: (a) Time difference between coincident photon pairs. (b) Single-photon energy spectrum, including only events which participated in a true coincidence. (c) Sum of energies of photons participating in a true coincidence. (XBL 709-6650)

The decay of the $2^2s_{1/2}$ state was observed by varying the separation between the foil and the detectors. A set of spectra like Fig. 1 was taken for various separations (normalized to a fixed amount of integrated beam current), and the total number of counts in the interval $0.75 \leq E \leq 2.5$ keV was obtained. A plot of the normalized count rate versus distance is shown in Fig. 3. At large distances the count rate levels off due to background; this is subtracted to leave the pure $2^2s_{1/2}$ decay. From the measured decay length and known beam velocity, the mean (1/e) lifetime was determined. After a 1% correction for the relativistic time dilation, the proper mean lifetime was found to be $\tau(2^2s_{1/2}) = 3.54(25)\times10^{-9}$ sec.

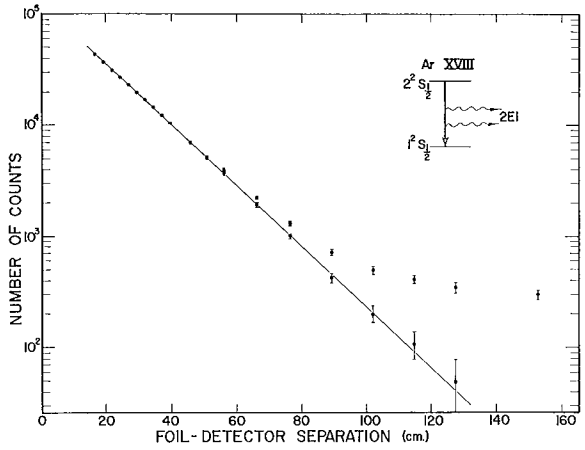

Fig. 3. Decay curve obtained by recording the singles count rate versus foil-detector separation. At large distances the observed counts level off to a constant value, which was subtracted from each point to give the two-photon counts. The error bars indicate the statistical error. (XBL 709-6649)

This result is in excellent agreement with the theoretical predictions. The nonrelativistic equation (1) predicts the value $\tau(2^2s_{1/2}) = 3.57\times10^{-9}$ sec. If we combine this result with Eq. (2) for the relativistic magnetic-dipole decay using

$$\frac{1}{\tau} = A_{2E1} + A_{M1} , \qquad (4)$$

the result $\tau(2^2s_{1/2}) = 3.47\times10^{-9}$ sec is obtained. Thus, our experimental results are in good agreement with the nonrelativistic calculation.

Footnote and References

†Condensed from UCRL-19978, September 1970; to be published in Phys. Rev. Letters.

1. G. Breit and E. Teller, Astrophys. J. 91, 215 (1940).

2. L. Spitzer and J. L. Greenstein, Astrophys. J. 114, 407 (1951).

3. J. Shapiro and G. Breit, Phys. Rev. 113, 179 (1959).

4. B. A. Zon and L. P. Rapoport, JETP Letters 7, 52 (1968).

5. G. A. Victor and A. Dalgarno, Phys. Rev. Letters 18, 1105 (1967); G. W. F. Drake and A. Dalgarno, Astrophys. J. 152, L121 (1968); G. W. F. Drake, G. A. Victor, and A. Dalgarno, Phys. Rev. 180, 25 (1969); O. Bely, J. Phys. B 1, 718 (1968); O. Bely and P. Faucher, Astron. and Astrophys. 1, 37 (1969).

6. G. W. F. Drake, University of Windsor (to be published).

7. C. Schwartz, University of California, private communication.

8. M. Lipeles, R. Novick, and N. Tolk, Phys. Rev. Letters 15, 690 (1965).

9. C. J. Artura, N. Tolk, and R. Novick, Astrophys. J. 157, L181 (1969).

10. R. C. Elton, L. J. Palumbo, and H. R. Griem, Phys. Rev. Letters 20, 783 (1968).

11. A. H. Gabriel and C. Jordan, Nature 221, 947 (1969); W. M. Neupert and M. Swartz, Astrophys. J. 160, L189 (1970).

12. R. Marrus and R. W. Schmieder, Phys. Letters 32A, 431 (1970).

13. R. W. Schmieder and R. Marrus, Phys. Rev. Letters 25, 1689 (1970).

14. R. Marrus and R. W. Schmieder, Phys. Rev. Letters 25, 1245 (1970).

15. A. S. Pearl, Phys. Rev. Letters 24, 703 (1970); R. S. Van Dyke, Jr., C. E. Johnson, and H. A. Shugart, University of California (to be published).

Observation of the Magnetic-Quadrupole Decay ($2^3P_2 \rightarrow 1^1S_0$) of Heliumlike Ar XVII and Lifetime of the 2^3P_2 State †

Richard Marrus and Robert W. Schmieder

In 1964, Mizushima[1] called attention to the possibility of magnetic-quadrupole (M2) transitions for spectral lines for which $\Delta S = \pm 1$. Subsequently, Mizushima[2] and Garstang[3] carried out numerical calculations of the lifetimes associated with M2 transitions that are of astrophysical significance. In recent publications Garstang[4] and Drake[5] have considered the decay of the level $(1s2p)2^3P_2$ of heliumlike atoms. In the neutral helium atom, the 2^3P_2 state decays to the 2^3S_1 state with a lifetime[6] of 10^{-7} sec. Since this is a fully-allowed electric-dipole (E1) transition, this mode might be expected to be dominant throughout the helium isoelectronic sequence. However, the rate that is associated with this mode, $A_{E1}(2^3P_2)$, can be shown to scale roughly as Z for high Z, whereas the rate associated with the M2 decay mode $A_{M2}(2^3P_2)$ scales roughly as Z^8. On the basis of numerical calculations, both Garstang and Drake conclude that, for the heliumlike ions beyond chlorine (Z = 17) the dominant decay mode is magnetic-quadrupole emission. For argon (Z = 18), the calculated rate is $A_{M2}(2^3P_2) = 3.14 \times 10^8$ sec^{-1}.

We report the first observation of the M2 transition $(1s2p)2^3P_2 \rightarrow (1s^2)1^1S_0$ in the heliumlike atom Ar XVII, and the measurement of the lifetime of the 2^3P_2 state using the beam-foil time-of-flight technique. The result is $\tau(2^3P_2) = (1.7 \pm 0.3) \times 10^{-9}$ sec (95% confidence).

Although magnetic-quadrupole transitions have been observed abundantly in nuclear physics, it has so far not been possible to reliably compare a measured rate with a theoretical rate that is calculated from first principles. Since highly accurate rate calculations are possible in hydrogenlike and heliumlike systems, we believe that this is the first experimentally measured M2 rate which is directly comparable with a theoretical rate derived from first principles.

A description and schematic diagram of the apparatus used in this work have been presented previously[11] and will be reviewed only briefly here. Ions of ^{40}Ar in the +14 charge state are obtained from the Berkeley Hilac with energy 10.3 MeV/nucleon ($\beta \equiv v/c = 0.148$). The beam passes through a thin (10 μg/cm^2) carbon foil and emerges distributed among the +15 (lithiumlike), +16 (heliumlike), +17 (hydrogenlike), and +18 (fully-stripped) charge states. In this nonequilibrium distribution, about 15% appear as +16 and a few percent as +17. The +15 and +18 ions produce no observable effects in our detectors. Initially the atoms may have large electronic excitation, but they decay rapidly ($\sim 10^{-14}$ sec) to the ground and long-lived levels, with a sizable fraction of the heliumlike ions appearing in the $(1s2p)2^3P_2$ state. The subsequent decay of these long-lived states is observed downstream from the foil with a high-resolution Si(Li) x-ray detector, and the count rate is normalized to the integrated beam current. The foil is mounted on a movable track, and varying the foil-detector separation makes it possible to plot the

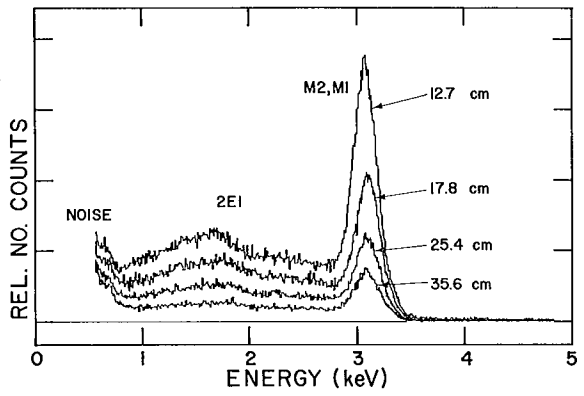

Fig. 1. Typical spectra obtained for several foil-detector separations. The shape of the two-photon spectrum has not been corrected for detector efficiency, so exhibits a large silicon absorption edge near 1.8 keV. The total number of counts within the right-hand half of the 3.1 keV peak was taken as a measure of the intensity of the peak. About half the line width is due to doppler broadening.
(XBL 709-6513)

decay curve over the range 15 - 200 cm. By fitting the observed decay with an exponential and knowing the beam velocity, we determine the lifetime.

Typical x-ray spectra taken with several foil-detector distances are shown in Fig. 1. They consist of a peak at an energy of 3.1 keV, and a continuous spectrum at energies between the noise level of the detector and the peak. Coincidence measurements reported elsewhere[8] have established the continuous spectrum as arising from the two-photon transitions $2^2s_{1/2} \rightarrow 1^2s_{1/2}$ of hydrogenlike atoms and $2^1S_0 \rightarrow 1^1S_0$ of heliumlike atoms. Within the doppler-broadened width of the peak, it is possible to have contributions from several transitions, but we now give arguments which indicate that the M2 transition $(1s2p)2^3P_2 \rightarrow (1s^2)1^1S_0$ dominates the observed decay at small distances.

The only decays of hydrogenlike and heliumlike atoms with sufficient energy to account for the 3.1 keV peak observed here are transitions to ground states, $1^2s_{1/2}$ and 1^1S_0, respectively. Moreover, with our apparatus geometry and the beam velocity of $4.4(1)\times10^9$ cm/sec, the lifetime of a transition must be $\gtrsim 3\times10^{-10}$ sec in order to be observable. The only decays satisfying these conditions are listed in Table I. The 2E1 decays give rise to the continuous spectra characteristic of two-photon emission, with intensities falling to zero at the end-point energies (3.1, 3.3 keV). Consequently, only a small fraction of the 2E1 decays overlap the peak width, and this fraction can be estimated and subtracted as a small correction. The M1 decay from the hydrogenlike $2^2s_{1/2}$ state gives a line at 3.3 keV, and is a potential source of error, since the $2^2s_{1/2}$ state lifetime is comparable to the

Table I. Forbidden decays in hydrogenlike and heliumlike argon.

Ion	Transition	Mode	Approximate Transition Probability	Ref.
Ar XVII	$(1s2p)2^3P_2 \rightarrow (1s^2)1^1S_0$	M2	$\approx 3\times10^8$ sec^{-1}	5
(E ≅ 3.1 keV)	$(1s2s)2^3S_1 \rightarrow (1s^2)1^1S_0$	2E1	$\approx 3\times10^3$	12
		M1	$\approx 6\times10^6$	10
	$(1s2s)2^1S_1 \rightarrow (1s^2)1^1S_0$	2E1	$\approx 4\times10^8$	13
Ar XVIII	$(2s)2^2s_{1/2} \rightarrow (1s)1^2s_{1/2}$	2E1	$\approx 3\times10^8$	14
(E ≅ 3.3 keV)		M1	$\approx 8\times10^6$	10

Note: Only transitions to ground states are listed. E is the total energy available in the transition. The rate of the spin-orbit induced E1 transition, $(1s2p)2^3P_1 \rightarrow (1s^2)\,1^1S_0$ is $\approx 10^{12}$, is too fast to be observable in the present apparatus. Nuclear spin inducement[15] of the E1 transitions, $(1s2p)2^3P_{2,0} \rightarrow (1s^2)1^1S_0$ is not present for the isotope ^{40}Ar.

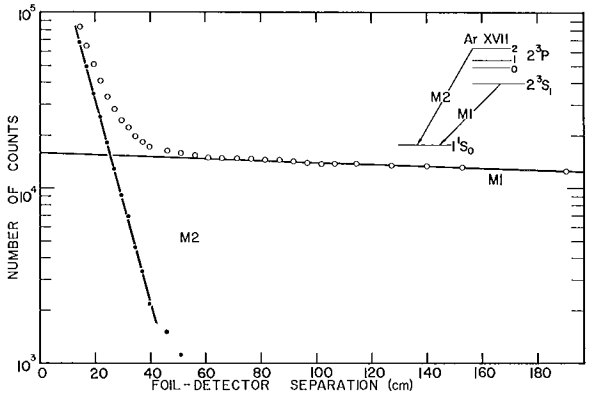

Fig. 2. Typical decay curve obtained by plotting the intensity of the peak vs foil-detector separation. By removing M1 contribution from the curve, we obtain the single exponential decay representing the M2 transition $2^3P_2 \rightarrow 1^1S_0$ in Ar XVII. (XBL 709-6514)

2^3P_2 state lifetime. However, our observation of a "single" line at 3.1 keV shows that this contribution is small. Furthermore, the actual contribution to the peak can be estimated from the 2E1 decay, and substracted as another small correction. The other M1 decay, from the heliumlike 2^3S_1 states, overlaps closely the M2 line, but because this state has such a long mean lifetime ($\tau \cong 172$ nsec),[11] this decay can be separated easily in the time-of-flight measurements. We conclude that the observed peak will decay with a fast and a slow component, the fast one being due to the $2^3P_2 \rightarrow 1^1S_0$ transition in Ar XVII.

That the observed peak actually consists of two unresolved components is evident from the decay curve taken by varying the foil position. This decay curve, shown in Fig. 2, exhibits the fast mode associated with the M2 transition and the slow mode associated with the M1 transition. Our association of the slow mode with the M1 decay is based on recent calculations[10, 16] and our measurement[11] of the M1 lifetime.

The lifetime of the 2^3P_2 state was extracted from the data in the following steps: First, the small 2E1 and M1 contributions to the total counts under the right-hand half of the peak were subtracted for each point in the decay curve. Second, the long-M1 component was removed leaving the single exponential decay. Third, a least-squares fit was made to an exponential, thus determining the mean decay length. Finally, dividing by the known velocity we obtain the mean (1/e) lifetime, $\tau(2^3P_2) = (1.7 \pm 0.3) \times 10^{-9}$ sec.

The main contributions to the error are errors in beam velocity (2%), count-rate normalization (3%), 2E1 and M1 corrections (3%), and instrumental effects such as background, beam and detector drifts, foil tracking error, etc. (5%). Although it is currently impossible to accurately correct the data for cascading effects, there is evidence that these effects are quite small.

Recently, Drake[16] has computed the electric dipole rate, with the result $A_{E1}(2^3P_2) = 3.55 \times 10^8$ sec^{-1}. Combining this with the value $A_{M2}(2^3P_2) = 3.14 \times 10^8$ sec^{-1} in the relation.

$$\frac{1}{\tau} = A_{E1} + A_{M2} ,$$

yields the predicted value $\tau = 1.49 \times 10^{-9}$ sec, which agrees with our measurements within the experimental error.

Footnote and References

†Condensed from UCRL-19968, September 1970; to be published in Phys. Rev. Letters

1. M. Mizushima, Phys. Rev. 134, A883 (1964).

2. M. Mizushima, J. Phys. Soc. Japan 21, 2335 (1966).

3. R. H. Garstang, Astrophys. J. 148, 579 (1967).

4. R. H. Garstang, Publ. Astron. Soc. Pac. 81, 488 (1969).

5. G. W. F. Drake, Astrophys. J. 158, 1199 (1969).

6. D. A. Landman, Bull. Am. Phys. Soc. II 12, 94 (1967).

7. R. Marrus and R. W. Schmieder, Phys. Letters 32A, 431 (1970).

8. R. Marrus and R. W. Schmieder, Bull. Am. Phys. Soc. 15, 794 (1970).

9. R. E. Knight and C. E. Scherr, Rev. Mod. Phys. 35, 431 (1963).

10. C. Schwartz, University of California, Berkeley, private communication.

11. R. W. Schmieder and R. Marrus, Phys. Rev. Letters 25, 1245 (1970).

12. O. Bely and P. Faucher, Astron. & Astrophys. 1, 37 (1969).

13. G. W. F. Drake, G. A. Victor, and A. Dalgarno, Phys. Rev. 180, 25 (1969).

14. J. Shapiro and G. Breit, Phys. Rev. 113, 179 (1959).

15. R. H. Garstang, J. Opt. Soc. Am. 52, 845 (1962).

16. G. W. F. Drake, University of Windsor, private communication.

Hyperfine Structure of ^{69}Ga in Crossed Electric and Magnetic Fields†

Joseph Yellin

In recent years several experiments have been reported in which electric fields were used in the C region of an atomic beam apparatus.[1] Most atomic beam experiments involving electric fields have been on $J = \frac{1}{2}$ states (e.g. alkalis) whose interaction with an electric field is a scalar and therefore independent of the field direction. More recently atomic beam electric field experiments involving gallium, indium and thallium have been reported.[2] Atomic beams of gallium and indium usually contain both the ground $^2P_{1/2}$ state and the metastable $^2P_{3/2}$ state and thus, regardless of which state is the object of study, both are present. The $^2P_{3/2}$ state possesses a tenor polarizability, and consequently the direction as well as magnitude of the electric field is important in determining the combined Zeeman-Stark effect. We examine the influence of crossed fields on the $^2P_{3/2}$ state taking ^{69}Ga as an example.

The hyperfine Hamiltonian including external electric and magnetic fields was diagonalized by machine for different values of the electric and magnetic fields as well as for different relative orientations of the fields.[3] The z axis was taken along the direction of the magnetic field. For the tensor polarizability we used the value $\alpha_2 = -2.76$ kHz/(kV/cm)^2 reported by Petersen.[2]

The result for E parallel to H is shown in Fig. 1a for the F = 3 hyperfine state.[4] Nine crossings occur between magnetic levels for which $\Delta m = 1, 2, 3, 4$ or 5. When E is rotated, the Stark operator is no longer diagonal in m but rather levels for which $\Delta m = 1$, 2 are now directly coupled, while levels for which $\Delta m > 2$ interact in higher order perturbations. The coupling leads to a repulsion of the levels removing the degeneracy at the crossing points. This is shown in Fig. 1b for an angle of $\phi = 5°$. When $\phi \to 90°$ all crossings become "anticrossing". Of particular interest is the crossing of the m = -1 and m = -2 levels, since transitions between these lead to a refocusing of the atomic beam. Application of degenerate perturbation theory shows that for $\phi(\text{rad}) \ll 1$, the degeneracy is removed by $\nu \approx 3/5\sqrt{5}\,\alpha_2 E_0^2 \phi$, where E_0 is the value of E at the crossing. This amounts to ≈ 7kHz/1° for the example shown in Fig. 1. Thus the coupling between the levels is strong and the alignment of E is very critical.

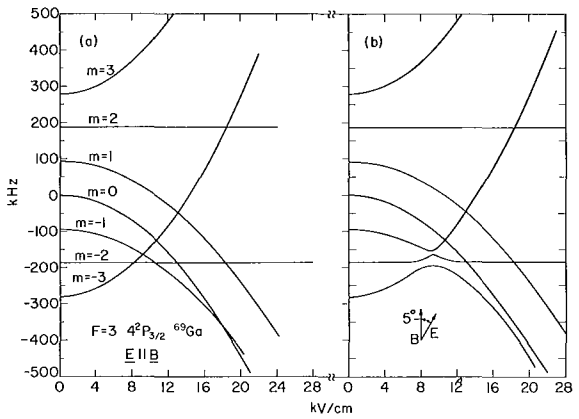

Fig. 1. Combined Zeeman-Stark effect in the F = 3 $4^2P_{3/2}$ state of ^{69}Ga. The calculations were performed for a magnetic field of 0.100 G. (a) E is parallel to B. (b) E is inclined 5° to B. (XBL-703-2573)

At the point where levels m and m + 1 would cross in the absence of perturbation, the wavefunction oscillates with frequency $\nu = \langle Fm+1|\mathcal{H}|Fm\rangle \sim \alpha_2 E^2 \phi$ between the levels $|Fm\rangle$, $|Fm+1\rangle$, so that transitions take place[5] between the levels m = -1 and m = -2. Such transitions, induced by static fields, are known from anticrossing experiments in excited states, and their connection with zero frequency rf transitions has been discussed by Series.[6] The observation of antilevel crossing in ground and low lying metastable states should be possible by the atomic beam method provided transitions between the crossing levels lead to a refocused beam. Detection of anticrossing by atomic beams would have the advantage that no light is required, in addition to the usual advantage of beams.

The author would like to thank Dr. E. Geneux for a number of stimulating discussions.

Footnote and References

†Condensed from Phys. Letters 32A, 337 (1970).

1. R. D. Haun and J. R. Zacharis, Phys. Rev. 107, 107 (1957); P. G. H. Sandars and E. Lipworth, Phys. Rev. Letters 13, 718 (1964); R. Marrus, D. McColm, and J. Yellin, Phys. Rev. 147, 556 (1966).

2. F. R. Petersen, Bull. Am. Phys. Soc. 14, 833 (1969); T. R. Fowler and J. Yellin, Bull. Am. Phys. Soc. 14, 832 (1969).

3. J. R. P. Angel, and P. G. Sandars, Proc. Roy. Soc. A305, 125 (1968).

4. UCRL-19569, 1970.

5. D. Bohm, Quantum Theory (Prentice-Hall, Inc., 1951), Ch. 19.

6. T. G. Eck, J. J. Foldy, and H. Wieder, Phys. Rev. Letters 10, 239; (1963); in this experiment the anticrossing is caused by an internal perturbation.
For a discussion see G. W. Series, Phys. Rev. Letters 11, 13 (1963); J. J. Forney and E. Geneux, Phys. Letters 20, 632 (1966).

The Use of Polarized Light in the Measurement of Differential Stark Shifts by the Atomic Beam Method†

Joseph Yellin

The observation of Stark splitting in optical transitions by the atomic beam method[1] utilizes unpolarized light. The nature of the detection is such that it is unnecessary to establish a population difference among the magnetic sublevels of either the excited state or the ground state. Nevertheless, a considerable advantage can be gained from selective excitation of magnetic sublevels by the use of polarized light. For example, by use of a linear polarizer only, it is possible to eliminate the need for the alkali D-line filters. Furthermore, the breakdown of hyperfine coupling by the electric field can be explored by use of polarized light. Cesium is a particularly attractive system in which to study the above effects. Due to the large fine structure interaction, two resonances — one due to the $^2P_{1/2}$ state and the other to the $^2P_{3/2\pm3/2}$ state — overlap so that is has been necessary to use D-line filters to measure the differential Stark shift in the $6^2P_{3/2}$ state.[2] Moreover, the large electric fields which have to be employed for cesium result in a complete breakdown of the hyperfine coupling in the $^2P_{3/2}$ state.

The intensity of the atomic beam reaching the detector depends on the rate at which ground state atoms are flopped from $m_J = -1/2$ to $m_J = 1/2$, as a result of the absorption and reemission of photons. This rate is determined by the electric-dipole matrix elements $P_\mu = \langle \psi(^2P_{1/2}) | rY_{1\mu} | \psi(^2S_{1/2}) \rangle$, where ψ are the perturbed (by the applied electric field) eigenfunctions, and μ the polarization. P_μ depends on the strength of hyperfine interaction relative to the electric field interaction which breaks down the hyperfine coupling. When the electric field strength, E, is such that $\alpha_2 E^2 \ll \Delta\nu_{hf}$, where α_2 is the tensor polarizability and $\Delta\nu_{hf}$ the hyperfine structure of the $^2P_{3/2}$ state, $P_\mu = \langle {}^2P_{3/2}\ F'm'_F | rY_{1\mu} | {}^2S_{1/2}\ Fm_F \rangle$. In this case the selection rules $\Delta F = 0, \pm 1$ and $\Delta m_F = 0, \pm 1$ are not favorable for selective excitation since, regardless of the polarization, many F levels may be excited. Hence polarization of the light is of limited use here. At the other extreme, when $\alpha_2 E^2 >> \Delta\nu_{hf}$, the electronic moment J is decoupled from the nuclear spin I and hence $P_\mu = \langle {}^2P_{3/2}\ m_J\ m_I | rY_{1\mu} | {}^2S_{1/2}\ Fm \rangle$. Now the selection rule is $\Delta m_J = 0, \pm 1$ and $\Delta m_I = 0$, and the polarization makes it possible to pick out a particular m_J level.

In order to take advantage of polarization effects it is necessary to propagate the light

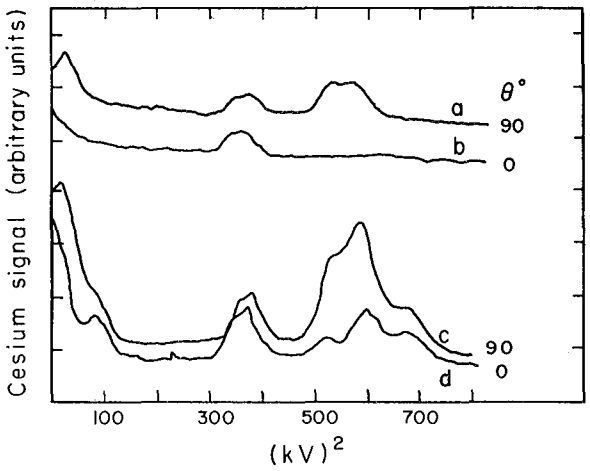

Fig. 1. Stark scan of the cesium lamp line. For (a) and (b) only the D_2 line is present, whereas for (c) and (d) the lamp is unfiltered. θ is the angle which the plane of polarization makes with the spin direction. The structure in the high field resonance of (d) is due to the hyperfine splitting of the $6^2P_{1/2}$ state.
(XBL-712-2925)

perpendicularly to the axis of quantization. The results of a preliminary investigation on cesium are shown in Fig. 1. When the light is linearly polarized perpendicularly to the quantum axis, (a) the selection rule $\Delta m_J = \pm 1$ connects the ground $^2S_{1/2}$ state with both $^2P_{3/2 \pm 1/2}$ and $^2P_{3/2 \pm 3/2}$, and consequently we observe the differential Stark shift. When the polarization is parallel to the axis (b) $\Delta m_J = 0$ and only the $^2P_{3/2 \pm 1/2}$ state can be excited. In (c), the unfiltered cesium lamp is scanned with the light polarized perpendicular to the axis and in (d) parallel to the axis of quantization. In the former case the high field resonance is due to both the $^2P_{3/2 \pm 3/2}$ and $^2P_{1/2}$, whereas in the latter it is only the $^2P_{1/2}$.

Thus the two resonances may be separated. The technique should prove especially useful when the differential Stark shifts are comparable to the line width of the exciting radiation or when optical filters may not be used without great loss of intensity (e.g. when the fine structure splitting is small).

Footnote and References

†UCRL-19575 Abstract; Second International Conference on Atomic Physics, Oxford, England, 21-24 July 1970.

1. R. Marrus and D. McColm, Phys. Rev. Letters 15, 813 (1965).

2. R. Marrus, D. McColm, and J. Yellin, Phys. Rev. 147, 55 (1966).

Alignment of ^{7}Li Atoms Formed by Charge-Capture Collisions with Crossed Atomic Beams and Carbon Foils

T. Hadeishi, R. D. McLaughlin, and M. C. Michel

We have observed the alignment of the $2\ ^2P_{3/2}$ and $2\ ^2D_{3/2}$ states of the ^{7}Li atom by sending $^7Li^+$ ions with energies varying from 20 to 70 keV through either cadmium vapor or a thin ($\approx 10\,\mu g/cm^2$) carbon foil. Level crossing was observed in both cases, and quantum beats[1] were observed in the case of the foil for the two transitions $\lambda = 6708$ Å ($2\ ^2P_{3/2} \rightarrow 2\ ^2S_{1/2}$) and $\lambda = 6103$ Å ($2\ ^2D_{3/2} \rightarrow 2\ ^2P_{3/2}$).

The experiments were performed with the apparatus shown in Fig. 1. A mass-analyzed beam of singly charged $^7Li^+$ ions was supplied by the Chemistry Cascade Isotope Separator, passed through either the cadmium atomic beam or the carbon foil, and the surviving ions were measured in the Faraday cup. Light resulting from the desired transitions could be detected by the monochromator-photomultiplier system and recorded in a multiscaler, stepped in synchronism with the externally applied magnetic field. Continuous rapid sweeping helped to eliminate the effect of small beam variations. The entire detector system could be moved to scan more than one mean life (27 nsec)[2] of the state behind the foil.

From the level crossing signal in the cadmium vapor case (see Fig. 2), we measured the polarization ratio $\pi = (I_{\parallel} - I_{\perp})/(I_{\parallel} + I_{\perp})$ to be 0.20 ± 0.02 for the $2\ ^2P_{3/2}$ level over the energy range of 20 to 60 kV, essentially independent of energy. $I_{\parallel}$ and $I_{\perp}$ are the intensities of the emitted light which are polarized parallel to and perpendicular to the axis of the lithium beam. If one assumes that only $m_\ell = 0$ for lithium atoms excited to the $2\ ^2P_{3/2}$ state, where the axis of quantization is along the beam axis, the maximum theoretical polarization ratio including the effects of nuclear spin and hyperfine structure,[3] is 0.213. Thus we conclude that the

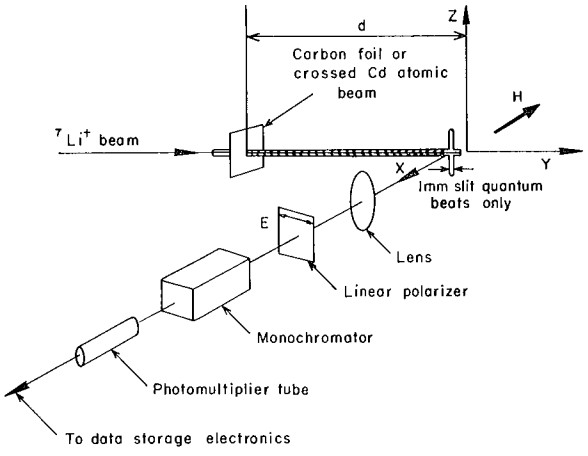

Fig. 1. Experimental arrangement. Detector assembly movable along beam direction for quantum beats experiment. (XBL-712-2930)

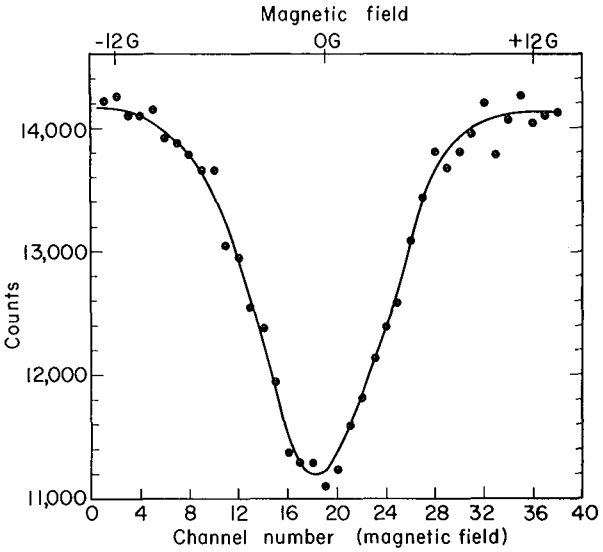

Fig. 2. Typical zero-field level-crossing signal at 40 keV Li^+ beam; linear polarizer perpendicular to beam with λ = 6708 Å ($2\,^2P_{3/2}$ - $2\,^2S_{1/2}$). (XBL-712-2956)

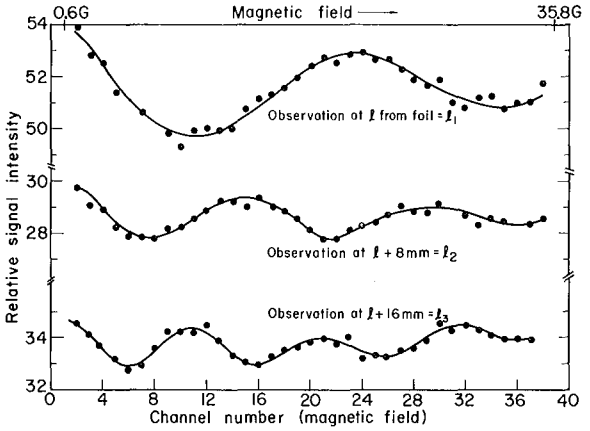

Fig. 3. Quantum beats signal with 40-keV-incident $^7Li^+$ ions. (XBL-712-2957)

electron capture collision between lithium and cadmium vapor puts almost all of those lithium atoms which have been left in the $2\,^2P_{3/2}$ level into the $m_\ell = 0$ sublevel. This can be understood by a simple argument involving the amount of angular momentum transfered in such a charge-transfer collision; the result being that for collisions giving very small angular deflections, as is the case here, only the $m_\ell = 0$ state can be populated with any probability.[4]

A single experiment with n-heptane vapor at a system pressure of $\approx 5 \times 10^{-5}$ torr gave easily demonstrated alignment of the ^7Li atoms, but no measure of π was possible because of the extended interaction region. Possibly all collisions of this type can lead to significant alignment.

Similar work with thin carbon foils gave a polarization ratio π=0 at 20 keV to π=0.07 at 60 keV — the measurements being made by observing quantum beats. (See Fig. 3.) In addition, the value of π was observed to decrease over the lifetime of the foil and to be dependent on foil thickness and, to some extent, on its previous history. In spite of the complexity of the system we believe that the following relatively simple model can explain most of the observations.

We suspect that the mechanism for alignment is essentially the same as for the isolated collisions in the case of free vapor, with the reservation that alignment can result only if electron capture occurs in the last collision the ion would have made in the foil, since an atom aligned by a previous collision would not be likely to retain its alignment after subsequent collisions. This means that only a very thin region near the exit side of the foil contributes to the observed alignment. This region includes any adsorbed gases which may contribute significantly to alignment and perhaps be responsible for the sensitivity to past history of the foil. Experimental observations show, for a typical foil, 98% and 95% of the beam is neutralized at 40 keV and 60 keV respectively. Thus the primary effect of energy is to change the value of the ion-beam flux at the sensitive exit region of the foil, completely masking any true energy dependence of the alignment. In addition, there is evidence that at least some of the neutral atoms leaving the foil are still in the $2\,^2P_{3/2}$ state (although no longer aligned), contributing to the total light observed and reducing the apparent polarization.

Refer to Fig. 4. The signal measured is I_a' and the polarization is I_a'/I_a (actually $\pi = (1/2)(I_a'/I_a)$ because of the nature of the quantum beat signal). However the additional light, I_0, from neutrals formed in earlier captures and subsequently quenched by collision cannot be distinguished from I_a, and a measurement of π using the total light I_t would obviously result in underestimating π. To complicate matters further, I_0, which is about equal to I_a, varies with both foil thickness and energy. These facts coupled with the sharp change with energy of the effective ion current surviving at the alignment region of the foil, result in completely obscuring the slight positive energy dependence of the polarization expected from theory.[5]

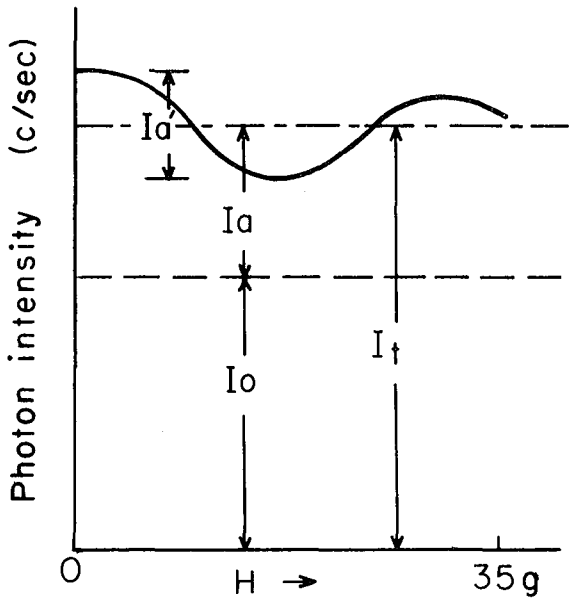

Fig. 4. Quantum beats signal from carbon foil (schematic). (XBL-712-2929)

Semiquantitative analysis of this treatment agrees with the experimental results within the accuracy of the measurements.

References

1. J. N. Dodd and G. W. Series, Proc. Phys. Soc. A213, 353 (1961); T. Hadeishi and W. A. Nierenberg, Phys. Rev. Letters 14, 891 (1965); J. N. Dodd, R. D. Kaul, and D. M. Warrington, Proc. Phys. Soc. 84, 176 (1964).

2. K. C. Brog, J. G. Eck, and H. Wieder, Phys. Rev. 153, 91 (1967).

3. M. J. Seaton, Colloques Internationaux du Centre National de la Recherche Scientifique 162, 21 (1966).

4. R. H. Hughes, Beam Foil Spectroscopy, edited by S. Bashkin (Gordon and Breach, New York, 1968).

5. J. Van Den Bos and F. J. DeHeer, Physica 34, 333 (1967).

Ab Initio Calculations of the Electronic Structure of Small Molecules

Henry F. Schaefer III

The purpose of this report is to summarize theoretical work carried out during the past year[1-13] on the electronic structure of diatomic and triatomic molecules. The distinguishing feature of our calculations[1-13] is that they go beyond the Hartree-Fock approximation, that is, electron correlation is explicitly included in the wave functions. Three papers[14-16] discussed in the Nuclear Chemistry Annual Report for 1969 (see page 199) have since appeared in print.

Theoretical Treatment of Penning Ionization[1]

The potential curves involved in the Penning ionization of the hydrogen atom by helium metastables have been computed by a large-scale configuration interaction. These are the potentials of the He-H system which dissociate to a ground-state H atom and He atom in the four states 1s2s ^{1}S, ^{3}S, 1s2p ^{1}P, ^{3}P; the ground-state He-H$^+$ potential curve is also required. A simplified description of the ionizing collision is introduced, which permits the determination of approximate cross sections (total ionization cross sections, associative ionization cross sections, the energy distribution of the ionized electron, etc.), without knowledge of the autoionization rate; numerical applications to the He*+H system are presented.

SiO Excited States[2]

Ab initio quantum mechanical calculations have been carried out at ten internuclear separations for those 72 molecular states of silicon monoxide which dissociate to a Si atom in ^{3}P, ^{1}D, ^{1}S, or ^{5}S state plus an oxygen atom in ^{3}P, ^{1}D, or ^{1}S state. Full configuration interaction calculations were made from a minimal basis set of Slater-type orbitals, with the restriction that the core orbitals (1s, 2s, 2p Si and 1s O) were fully occupied. The results were strikingly similar to those obtained for CO in an analogous theoretical study.[4] Ten bound states were found to dissociate to ground state Si plus ground state O; five of these states have been observed experimentally in SiO, but eight have experimentally known counterparts in CO. The predicted ordering of states is X $^1\Sigma^+$, a $^3\Pi$, a' $^3\Sigma^+$, $^3\Delta$, e $^3\Sigma^-$, I $^1\Sigma^-$, A $^1\Pi$, $^1\Delta$, $^5\Sigma^+$, and $^5\Pi$.

Molecular orbital configurations are assigned to each of these 10 states. Among 15 higher predicted bound states, the $^1\Pi$ III state, with calculated D_e = 1.32 eV, is perhaps the most likely to be observed experimentally. The tentative assignment of the I $^1\Sigma^-$ state by Verma and Mulliken[17] is considered unlikely on the basis of the present calculations. The A $^1\Pi$ potential curve is very flat as it approaches the dissociation limit, but, unlike CO, there is no maximum in this curve for SiO.

Symmetric Potential Surfaces for Methylene[3, 10]

Theoretical calculations have been carried out at 28 C_{2v} geometries for the lowest $^1A_1$, $^1A_2$, $^3A_2$, $^1B_1$, $^3B_1$, $^1B_2$, and $^3B_2$ states of CH_2. The basis set used was of the contracted gaussian type with four s and two p functions on carbon and two s functions on hydrogen. In all calculations except $^1A_1$, the SCF configuration plus all singly- and doubly-excited configurations were included (holding the K shell frozen), and the iterative natural orbital procedure was used to obtain an optimum set of orbitals. For the $^1A_1$ state a two-configuration SCF calculation was used as the starting point for the configuration interaction calculations. In a preliminary communication[3] we predicted the triplet ground state of CH_2 to be bent, and this prediction has since been justified experimentally by Bernheim, et al.,[18] and by Wasserman, et al.[19] For the $^1A_1$ state the ab initio geometry is r = 1.13 Å, θ = 104°, compared with experiment, r = 1.11 Å, θ = 102°. For the $^1B_1$ state the predicted geometry is r = 1.09 Å, θ = 144°, as opposed to experiment, r = 105 Å, $\theta \approx 140°$. The four other states investigated, $^1A_2$, $^3A_2$, $^1B_2$, and $^3B_2$ are all unstable with respect to a carbon atom plus a hydrogen molecule, and it is concluded that there are only four bound non-Rydberg states of CH_2. The $^3B_1$ - $^1A_1$ splitting, unknown experimentally, is predicted to be 7770 cm^{-1} (0.96 eV). The calculated $^1A_1$ - $^1B_1$ splitting is 7860 cm^{-1} (0.97 eV) compared to the experimental value of 7100 cm^{-1} (0.88 eV). The wave functions are discussed and three-dimensional plots of the potential surfaces are presented. Figure 1 shows the theoretical potential surface for the CH_2 ground state.

Valence-Excited States of Carbon Monoxide[4]

Calculations analogous to those described above for SiO[2] have been performed on CO. Seventeen bound states ($D_e \geq 0.27$ eV) were obtained, eight of which have been observed experimentally. The theoretical ordering of known bound states agrees with experiment except for the a $^3\Pi$ and A $^1\Pi$ states. This fact is rationalized by noting that these two states have much smaller r_e values than do the other excited states. The most interesting of the unobserved predicted bound states are the $^5\Sigma^+$ and $^5\Pi$ states, which dissociate to $^3PC + {}^3PO$, and the third $^1\Pi$ state, with a relatively large calculated dissociation energy. A dominant molecular-orbital configuration is associated with each of the first eleven bound states. Calculated spectroscopic constants are compared with available experimental data. Potential curves are presented and discussed for both bound and repulsive molecular states. The A $^1\Pi$ state has a calculated maximum of 1135 cm^{-1}, in good agreement with the experimentally based estimate (950 ± 150 cm^{-1}) of Simmons, Bass, and Tilford.[20] Calculations were also carried out on the X $^1\Sigma^+$, a $^3\Pi$, and a' $^3\Sigma^+$ states using 1s atomic Hartree-Fock orbitals and 2s and 2p STO's optimized for the X state at the experimental r_e. These calculations correctly placed the a $^3\Pi$ state below the a' $^3\Sigma^+$ state and resulted in improved D_e and r_e values for all three states.

Electronic Structures and Potential Energy Curves for the Low-Lying States of the CN Radical[5, 9]

At 11 internuclear separations, calculations have been carried out on those 59 molecular states of CN which dissociate to atomic limits up to ^1D C + ^2D N. Four electrons are held frozen in carbon and nitrogen 1s Hartree-Fock atomic orbitals, and a full configuration

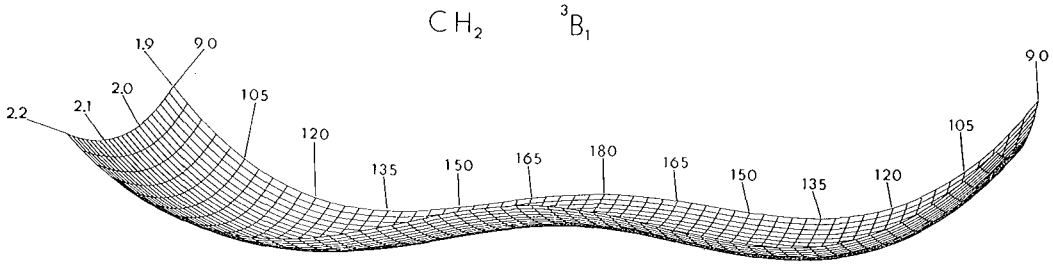

Fig. 1. Potential energy surface for the ground $^3B_1$ state of CH_2. (XBL-713-3044)

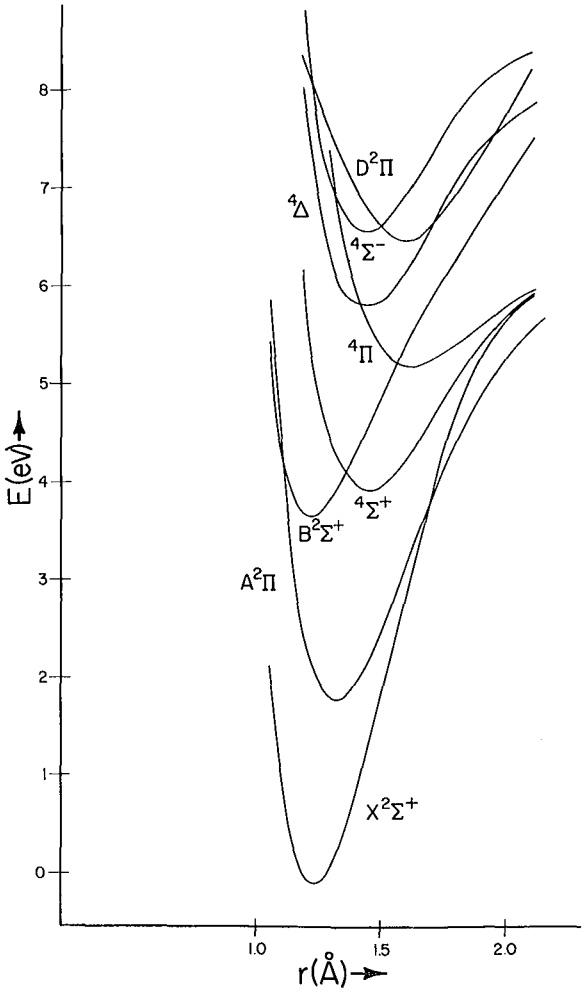

Fig. 2. Predicted potential curves for the eight lowest electronic states of the CN radical. (XBL-713-3045)

interaction is carried out for the remaining nine electrons using optimized 2s and 2p Slater-type orbitals on each atom. The $^2\Pi$ calculations, which include 486 configurations, are the most complicated. Eighteen significantly bound states ($D_e \geq 0.84$ eV) were obtained, nine of which have been observed spectroscopically. Our potential energy curves for the eight lowest states of CN are seen in Fig. 2. With the exception of the third $^2\Pi$ state, the theoretical ordering of states agrees with experiment. Three of the states never observed experimentally, ($^4\Sigma^+$, $^4\Pi$, and $^4\Delta$) lie below all but three of the known states of CN. Calculated spectroscopic constants are compared with experiment. The potential curves show many interesting features, including potential maxima in the $^4\Sigma^-$, $^2\Sigma^-$, J $^2\Delta$, and $^2\Pi$ IV bound states. By performing natural orbital analyses, dominant molecular-orbital configurations have been unambiguously assigned to the lowest 18 bound states. The second, third and fourth $^2\Pi$ states experience numerous avoided crossings among themselves, and natural orbitals have been used to follow the changes in electron configuration as a function of internuclear separation. The question of the approximate validity of the quantum numbers g and u is discussed.

Ground and First Excited States of CH_2^+ and BH_2[6]

Ab initio quantum mechanical potential surfaces were completed for the ground and first excited states of the CH_2^+ molecular ion. The natural orbital configuration interaction calculations employ a "double-zeta" contracted gaussian basis set. The ground state is of $^2A_1$ symmetry, arises from the $1a_1^2\ 2a_1^2\ 1b_2^2\ 3a_1$ configuration, and the ab initio geometry is r = 1.12 Å, θ = 141°. The first excited state is of $^2\Pi$ symmetry, arises from the $1\sigma_g^2\ 2\sigma_g^2\ 1\sigma_u^2\ 1\pi_u$ configuration, and the predicted bond length is about 0.02 Å less than 1.10 Å. The $^2A_1$ state is predicted to lie $\approx$1060 cm^{-1} below the $^2\Pi$ state. From analogous work on methylene, the calculated ionization potential of CH_2 is 10.01 eV, versus Herzberg's experimental value[21] of 10.40 eV. The relationship between these calculations and the dissociation energy of the CH_3 radical is discussed. The potential surfaces are displayed graphically.

The above theoretical results are qualitatively similar to those found experimentally by Herzberg and Johns[22] for the $^2A_1$ and $^2\Pi$ states of BH_2. To test the reliability of our predictions, parallel calculations were carried out on BH_2. For the $^2A_1$ state the ab initio geometry was r = 1.21 Å, θ = 129°, versus the experimental values r = 1.18 Å, θ = 131°. For the $^2\Pi$ state the predicted bond length was r = .19 Å, compared with the experimental r = 1.17 Å. The $^2\Pi$ state is calculated to lie 2260 cm^{-1} above the ground $^2A_1$ state, as opposed to the experimental splitting of 4300 cm^{-1}.

Multiconfiguration Wave Functions for the Water Molecule[7]

Configuration interaction (CI) wave functions have been calculated for H_2O using basis sets ranging from minimum Slater-type orbital to Dunning's 4s2pld contracted gaussian oxygen set[23] and 2slp set on the two hydrogen atoms. An iterative natural orbital procedure is used throughout. Three different types of CI functions are examined: (a) first natural configuration (FNC) plus single and double excitations to other valence orbitals; (b) the first-order wave function;[24] (c) FNC plus all

Table I. Spectroscopic constants for the three lowest states of NH

		D_e(eV)	D_0(eV)	r_e(Å)	ω_e(cm^{-1})	$\omega_e x_e$(cm^{-1})	B_e(cm^{-1})	α_e(cm^{-1})	T_e(eV)
$X^3\Sigma^-$	Hartree Fock[a]	2.10	1.88	1.018	3556	66.7	17.32	0.572	0
	Separated pair[b]	2.65	2.35	1.038	4910	78.3	16.63	0.466	0
	Small Basis CI[c]	2.62	2.42	1.12	3224	117	14.28	0.564	0
	This work	3.058	2.858	1.041	3300	120	16.56	0.760	0
	Experiment	3.41±0.16	3.21±0.16[e]	1.038[f]	3125.6[d]	78[g]	16.65[f]	0.646[d]	0
$a^1\Delta$	Hartree Fock[i]								1.83
	Small basis CI[c]	4.01	3.80	1.13	3557	132	14.16	0.563	1.9
	This work	3.965	3.760	1.037	3362	116	16.68	0.732	2.00
	Experiment			r_0 = 1.044[f]	3314[h]	63[h]	16.78[h]	0.67[2]	X
$b^1\Sigma^+$	Hartree Fock[i]								3.57
	Small basis CI[c]	4.28	4.06	1.12	3628	126	14.31	0.538	2.8
	This work	4.131	3.924	1.035	3396	113	16.73	0.712	2.79
	Experiment			r_0 = 1.046[f]	≈3480[f]				X + 1.05[f]

[a] P. E. Cade and W. M. Huo, J. Chem. Phys. 47, 614 (1967).

[b] D. M. Silver, K. Ruedenberg, and E. L. Mehler, J. Chem. Phys. 52, 1206 (1970).

[c] J. Kouba and Y. Ohrn, J. Chem. Phys. 52, 5387 (1970).

[d] R. N. Dixon, Can. J. Phys. 37, 1171 (1959).

[e] Reference 26.

[f] G. Herzberg, Spectra of Diatomic Molecules (D. Van Nostrand Company, Inc., Princeton, New Jersey, 1950).

[g] H. Guenebaut, Bull. Soc. Chim. France, 962 (1959).

[h] R. Florent and S. Leach, J. Phys. Radium 13, 377 (1952).

[i] W. M. Huo. J. Chem. Phys. 49, 1482 (1968).

singly- and doubly-excited configurations, holding the $1a_1$ orbital doubly occupied. It is found that correlation effects seen in the minimum basis set calculation continue to dominate in CI 2 as the size of the basis is increased. The importance of difference orbitals and configurations is discussed in light of the occupation numbers and wave functions. The most extensive calculation includes 1027 $^1A_1$ configurations and slightly more than 50% of the correlation energy of the water molecule.

Our most accurate first-order wave function yielded a dissociation energy of 8.2 eV, with respect to two exact hydrogen atoms and a very accurate O-atom wave function of the same general form. For comparison, the SCF dissociation energy of H_2O is 6.8 eV and the experimental value is 10.1 eV.

Accurate Potential Curve for the $X\ ^3\Sigma_g^-$ State of O_2[8]

Using a 4s2pld set of contracted Slater functions on each atom, configuration interaction (CI) wave functions have been calculated at eight points to determine a potential curve for the ground state of O_2. The approximate first-order wave functions[24] include 128 configurations of three basic types, and convergence to an optimum set of orbitals is attained using the Bender-Davidson iterative natural orbital procedure. Using this approach, the molecule dissociates properly to two oxygen atoms of slightly better than Hartree-Fock accuracy. The ab initio dissociation energy is 4.72 eV, compared with the Hartree-Fock value 1.43 eV and the experimental value 5.21 eV. Other computed spectroscopic constants (with experimental values in parentheses) are also in good agreement with experiment: r_e = 1.220 Å (1.207), ω_e = 1614 cm^{-1} (1580), and B_e = 1.417 cm^{-1} (1.446). Some general conclusions are drawn on the ab initio calculation of bond lengths.

$^3\Sigma^-$, $^1\Delta$, and $^1\Sigma^+$ State of NH[11]

Using a (3s, 2p, 1d/2s, 1p) basis set of contracted Slater-type functions and an iterative natural orbital scheme, valence configuration interaction studies have been done on the lowest three states of the imidogen radical at eight internuclear separations. Included in the CI were those configurations differing by zero, one or two space-orbitals from the Hartree-Fock configuration, except that the 1σ orbital was held doubly occupied. The size of the CI varied from 259 ($^1\Delta$) to 418 ($^3\Sigma^-$). For the ground state the computed total energy lies below that reported in any previous calculation, except the 3379 configuration wave function of Bender and Davidson.[25] From the potential curves thus obtained the spectroscopic constants r_e, ω_e, $\omega_e X_e$, B_e, and α_e are calculated, and compare well with the available experimental constants as shown in Table I. The molecular splittings are calculated to be 2.00 eV ($X^3\Sigma^- - a^1\Delta$) and 0.79 ($a^1\Delta - b^1\Sigma^+$), but when the discrepancy between calculated and experimental atomic limits is taken into account these splittings are estimated as 1.47 eV and 1.02 eV; the latter being close to the experimental value of 1.05 eV. Dissociation energies (D_e) for the $X^3\Sigma^-$, $a^1\Delta$, and $b^1\Sigma^+$, states are calculated as 3.06 eV, 3.97 eV, and 4.13 eV, respectively. For comparison, the Hartree-Fock dissociation energy for the $X^3\Sigma^-$ state is 2.10 eV and Seal and Gaydon's experimental value[26] is 3.41 ± 0.16 eV. The occupation numbers and most important configurations are given at several internuclear distances for each state.

Interaction Potential Between Ground State Helium Atom and the B $^1\Sigma_u^+$ State of the Hydrogen Molecule[12]

In order to aid in the interpretation of the energy transfer experiments of Moore and coworkers,[27] ab initio quantum mechanical calculations have been carried out on the four electron system ^1S He + B $^1\Sigma_u^+$ H_2. Nine C_{2v} geometries were considered, all involving a fixed H-H separation of 2.43 bohr. A contracted gaussian basis of three s and two p functions on each atom was used, and calculations were performed including 1, 416, and 706 configurations. The 416-configuration calculation was designed to include only the electron correlation between He and H_2 and should yield the most reliable results. The 416-configuration calculation predicts a large van der Waals interaction between He and the lowest $^1\Sigma_u^+$ state of H_2. The potential curve has a well depth of 401 cm^{-1} (0.05 eV) and this minimum occurs for a distance 3.72 bohr (1.97 Å) between He and the H_2 center of mass. SCF calculations using the same basis and geometries were done on the He + X $^1\Sigma_g^+$ H_2 and He + b $^3\Sigma_u^+$ systems. The potential curves for these two states lie well below that of He + B $^1\Sigma_u^+$ H_2 for thermal energies, and it is suggested that curve crossing with the two lower surfaces is not responsible for the observed quenching of the B $^1\Sigma_u^+$ H_2 fluorescence by He.

Electron Correlation in the Lowest $^1\Sigma^+$ State of Beryllium Oxide[13]

Ab initio first-order wave functions,[24] which include electron correlation, were computed for the lowest $^1\Sigma^+$ state of BeO. A contracted Slater-function basis of better than double zeta plus polarization accuracy was used, resulting in 157 configurations, constructed from 569 distinct Slater determinants. Considerable emphasis is placed in obtaining the correct dissociation behavior; in the present case to a two-configuration ($1s^2 2s^2$ and $1s^2 2p^2$) wave function for ^1S Be plus a slightly better than Hartree-Fock wave function for the ^1D state of oxygen. The calculated dissociation energy is 6.58 eV, compared with the Hartree-Fock value, 4.13 eV, and the spectroscopic value recommended by Gaydon,[28] 6.69 ± 0.4 eV. The other spectroscopic constants represent a substantial improvement over the Hartree-Fock values and are all within 10% of experiment. The dominant configurations in the wave function are presented, and it is seen that, contrary to the suggestion of previous workers, the $1\sigma^2 2\sigma^2 3\sigma^2 4\sigma^2 5\sigma^2 1\pi^2$ is not particularly important near the equilibrium internuclear

separation. The natural orbital occupation numbers complete our picture of the electronic structure of $^1\Sigma^+$ BeO.

I wish to thank William H. Miller, Charles F. Bender, Daniel Wallach, Timothy G. Heil, and Stephen V. O'Neil for their contributions to the work reviewed herein.

References

1. W. H. Miller and H. F. Schaefer, J. Chem. Phys. 53, 1421 (1970).

2. T. G. Heil and H. F. Schaefer, J. Chem. Phys. (in press).

3. C. F. Bender and H. F. Schaefer, J. Am. Chem. Soc. 92, 4984 (1970).

4. S. V. O'Neil and H. F. Schaefer, J. Chem. Phys. 53, 3994 (1970).

5. T. G. Heil and H. F. Schaefer, Astrophys. J. 163, 425 (1971); UCRL-19935.

6. C. F. Bender and H. F. Schaefer, J. Mol. Spectroscopy (in press).

7. H. F. Schaefer and C. F. Bender, J. Chem. Phys. (in press).

8. H. F. Schaefer, J. Chem. Phys. 54, 2207 (1971).

9. H. F. Schaefer and T. G. Heil, J. Chem. Phys. (in press); UCRL-19983.

10. S. V. O'Neil, H. F. Schaefer, and C. F. Bender, J. Chem. Phys. (in press).

11. S. V. O'Neil and H. F. Schaefer (to be published); UCRL-20401.

12. H. F. Schaefer, D. Wallach, and C. F. Bender, J. Chem. Phys. (in press).

13. H. F. Schaefer (to be published); UCRL-20417.

14. H. F. Schaefer, J. Comput. Phys. 6, 142 (1970).

15. H. F. Schaefer, J. Chem. Phys. 52, 6241 (1970).

16. T. G. Heil, S. V. O'Neil, and H. F. Schaefer, Chem. Phys. Letters 5, 253 (1970).

17. R. D. Verma and R. S. Mulliken, Can. J. Phys. 39, 908 (1961).

18. R. A. Bernheim, H. W. Bernard, P. S. Wang, L. S. Wood, and P. S. Skell, J. Chem. Phys. 53, 1280 (1970).

19. E. Wasserman, W. A. Yager, and V. J. Kuck, Chem. Phys. Letters, 7, 409 (1970).

20. J. D. Simmons, A. M. Bass, and S. G. Tilford, Astrophys. J. 155, 345 (1969).

21. G. Herzberg, Can. J. Phys. 39, 511 (1961).

22. G. Herzberg and J. W. C. Johns, Proc. Roy. Soc. (London) A298, 142 (1967).

23. T. H. Dunning, J. Chem. Phys. 53, 2823 (1970).

24. H. F. Schaefer and F. E. Harris, Phys. Rev. Letters 21, 1561 (1968).

25. C. F. Bender and E. R. Davidson, Phys. Rev. 183, 23 (1969).

26. K. E. Seal and A. G. Gaydon, Proc. Phys. Soc. (London) 89, 459 (1966).

27. D. L. Akins, E. H. Fink, and C. B. Moore, J. Chem. Phys. 52, 1604 (1970); and further work to be published.

28. A. G. Gaydon, Dissociation Energies and Spectra of Diatomic Molecules (Chapman and Hall Ltd., London, 1968).

Preliminary Level Analysis of the First and Second Spectra of Dysprosium†

John G. Conway and Earl F. Worden*

The preliminary work on Dy I and II has been completed and the publication of the results is now in press. Our wavelengths and spectral assignments were combined with the data of the late A. S. King and published as "Temperature Classification of the Spectra of Dysprosium (Dy I, Dy II)."[1] This paper contains 4584 lines, together with their temperature and furnace classifications.

The level analysis has been published as UCRL-19944. This report contains all the levels of both the first and second spectra. For the first spectra there are assigned 141 even and 197 odd levels which lead to a classification of 1952 lines. For the second spectra there are 14 even and 214 odd levels assigned, leading to a classification of 1000 lines. In addition, this report lists 22858 lines of the spectrum of dysprosium. The levels, the classified lines and the parameter fits have been accepted for publication in the Journal of

the Optical Society of America.

The work on Dy will now be done jointly with a group at Laboratoire Aime Cotton, and to some extent with Oak Ridge National Laboratory.

Footnotes and Reference

†Condensed from UCRL-19944, August 1970; to be published in J. Opt. Soc. Am.

*Lawrence Radiation Laboratory, Livermore, California 94550.

1. Arthur S. King, John G. Conway, Earl F. Worden and Charlotte Moore, J. Res. Nat. Bur. Stand. 74A, 355 (1970).

Optical Spectra of Einsteinium†

John G. Conway and Earl F. Worden*

The spectrum of einsteinium has been photographed and 53 lines have been observed. For Es II the interval between the ground level, $^5I_8$, and the first excited level, $^3I_7$, has been found to be 938.66 cm^{-1}. Analysis of the hyperfine structure confirms the nuclear spin of ^{253}Es as I = 7/2. A value of a_{7s} = 1.527 ± 0.001 cm^{-1} is obtained. From this analysis it is possible to derive the nuclear magnetic dipole moment, $\mu_1 = +5.1 \pm 1.3\ \mu_N$. There are several factors in the hyperfine analysis which had to be assumed and caused the large error.

Footnotes

†Condensed from J. Opt. Soc. Am. 60, 1297 (1970).

*Lawrence Radiation Laboratory, Livermore, California 94550.

The First and Second Spectra of Californium†

John G. Conway and Earl F. Worden*

Californium iodide was incorporated into an electrodeless discharge lamp, excited at a frequency of 2450 MHz, and the spectrum photographed. From the observation of the reversal of several lines and studies of the Zeeman effect, we have been able to characterize the ground state of Cf I as a J=8 state with a g value of 1.213. We therefore assign this state to the $^5I_8$ of the $5f^{10}7s^2$ configuration. For Cf II, two levels have been found: the ground state with $J=8\frac{1}{2}$ and g = 1.27, and the first excited level at 1180.54 cm^{-1} with $J=7\frac{1}{2}$ and g = 1.20. We assign the ground state of Cf II to a $^6I_{8\frac{1}{2}}$ state, and the first excited state to a $^4I_{7\frac{1}{2}}$ of the configuration $5f^{10}7s$.

This work is preliminary and it will take several years before a complete understanding can be obtained.

Footnotes

†Condensed from J. Opt. Soc. Am. 60, 1144 (1970).

*Lawrence Radiation Laboratory, Livermore, California 94550.

Electron Impact Excitation Functions Using the RPD Time-of-Flight Method†

Amos S. Newton and G. E. Thomas*

It is well known that the collision of an energetic free electron with an atom or molecule can cause transitions to electronically excited states. If the electron has an energy well in excess of the energy of the transition, then the excitations observed are those normally observed in optical spectroscopic studies. That is, the permitted transitions are described by the familiar optical selection rules. However, when the kinetic energy of the colliding electron is equal to the transition energy or exceeds it by typically a few tenths of electron volts, then optically forbidden transitions can occur with a high probability. One consequence of this fact is that normally forbidden states can be populated by electron impact and these states cannot emit radiation (in the absence of perturbing collisions, etc.) to return to the ground state. Such excited species are termed metastable atoms or molecules and can have free-space lifetimes of 10^{-4} sec or longer.

Experiments to study the relative efficiency of production of such metastable species, as a function of incident electron energy, have been carried out for several years at the Lawrence Radiation Laboratory.[1,2] A high-resolution electron beam from an RPD-type electron gun[3] is crossed with an atomic or molecular beam. The metastables produced are detected via their ability to eject an electron from the first dynode of a nude electron multiplier placed downstream from the excitation region. Perturbing collisions are kept to a minimum by performing the experiments in high vacuum, and with a well-collimated beam.

One difficulty with such experiments has been that ultraviolet photons (produced from the excitation of allowed levels or from allowed transitions between directly forbidden levels) also register on the multiplier. Previously, high-resolution metastable excitation efficiency curves have included a small inseparable contribution from such photons.

Figure 1 shows the detector signal as a function of time for the excitation of a neon atomic beam by a 10 μsec pulse of electrons. The photons are emitted promptly during the period in which the electron beam is on. The metastables arrive at later times because of the low thermal velocity of the neutral beam. They are also spread out in time, reflecting the thermal velocity distribution of particles

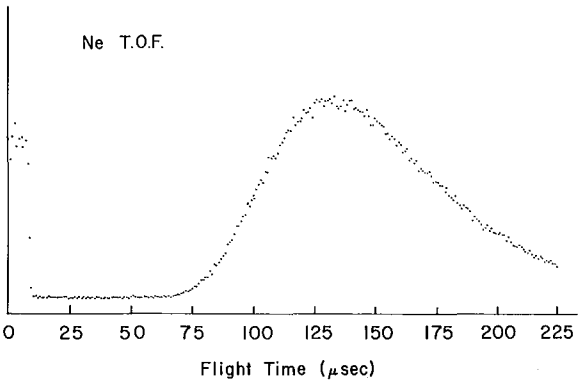

Fig. 1. Time-of-flight spectrum of a neon atomic beam excited by a 10 μsec pulse of electrons. (XBL 706-1053)

in a gas. Thus, the detector could be gated open so as to detect only photons (0-10 μsec from the start of the electron pulse in Fig. 1), or to detect only metastables (75 μsec and later). Reference 2 gives a more complete description of these time-of-flight techniques.

However, only recently has a technique been developed which permits using the RPD gun in such time-gated studies.[4] With this development, pure excitation efficiency curves for the production of uv photons and of metastables have been recorded for a variety of species.

In Figs. 2-4, such curves are shown for neon, argon and krypton respectively. In all three figures, the upper curve corresponds to metastable production and the lower to photon production. In the metastable curves, structure arising from the excitation of metastable levels of the $np^5(n+1)s$ and $np^5(n+1)p$ configurations (n = 2, 3, 4 for Ne, Ar, and Kr respectively) is seen just above threshold. In all three photon curves, photons are produced from allowed levels of the $np^5(n+1)s$ configuration. In argon and krypton, an upward break in the photon curve is seen at the energy of the np^5nd states.

Figure 5 shows similar curves for nitrogen molecular metastables (upper curve) and for photons from nitrogen. In N_2 the lowest metastable state is the $A^3\Sigma_u^+$, situated 6.2 eV above the ground state. However, this state is not accessible to a Franck-Condon transition from the ground state until somewhat

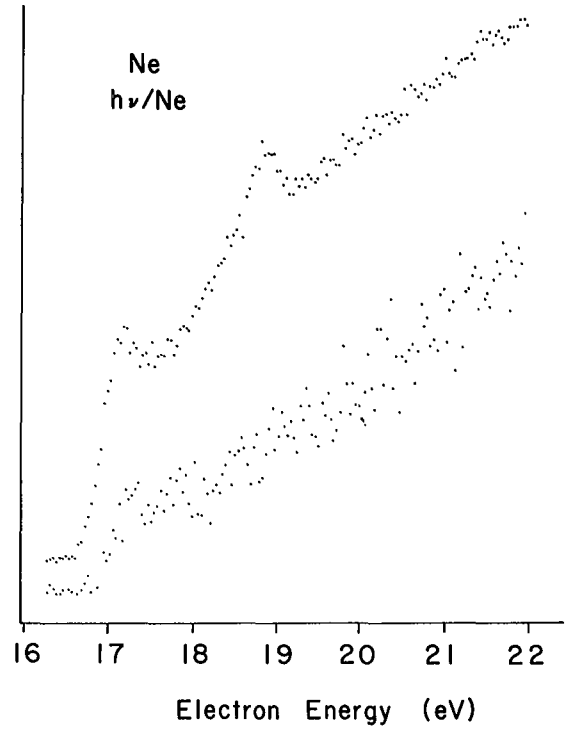

Fig. 2. The upper curve is the electron impact excitation efficiency curve for the production of metastable atoms in neon. The lower curve is the electron impact excitation efficiency curve for the production of uv photons in neon. (XBL 706-1067)

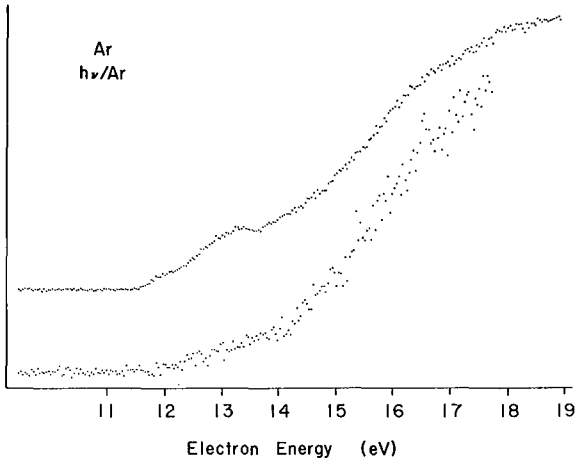

Fig. 3. The upper curve shows the production of metastable atoms in argon; the lower curve shows the production of uv photons in argon. (XBL-706-1058)

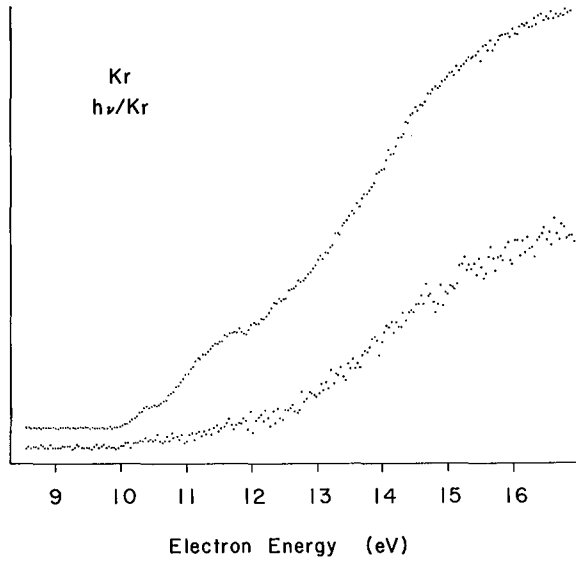

Fig. 4. The upper curve shows the production of metastable atoms in krypton; the lower curve shows the production of uv photons in krypton. (XBL 706-1066)

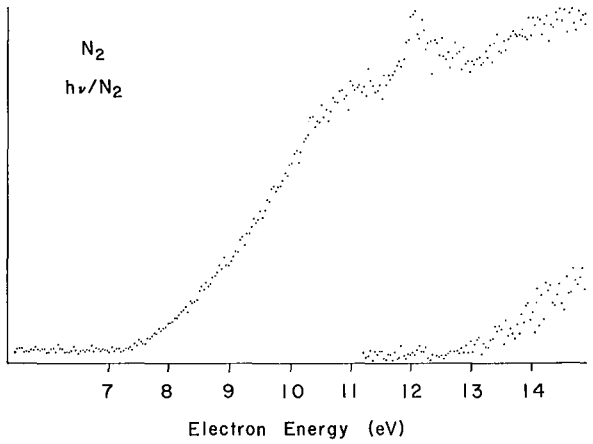

Fig. 5. The upper curve shows the production of metastable molecules in nitrogen; the lower curve shows the production of uv photons in nitrogen. (XBL 706-1060)

higher energies. The appearance potential 7.2 eV measured here would correspond to this transition. The $B^3\Pi_g$ state lies slightly higher in energy. The outstanding feature of the nitrogen metastable curve is the appearance of the $E^3\Sigma_g^+$ state peaking near 12 eV. The photons from nitrogen have an appearance potential of 12.6 ± 0.2 eV. This value, and the knowledge that the light is sufficiently energetic to eject an electron from the multiplier, strongly suggest that the well-known Birge-Hopfield System is the source of the light.

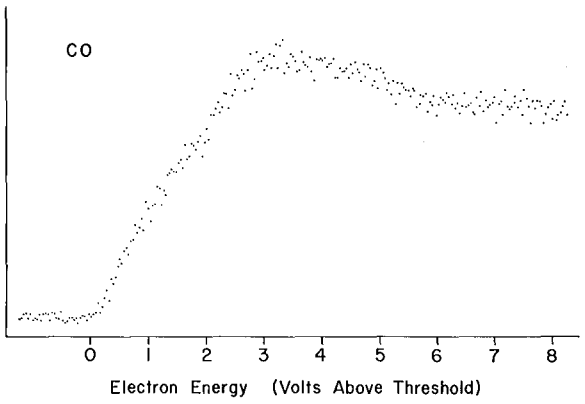

Fig. 6. Production of metastable molecules in carbon monoxide. (XBL 706-1055)

Figure 6 shows the excitation efficiency curve for the production of metastables in carbon monoxide. The measured appearance potential is 6.0 ± 0.2 eV, which corresponds to excitation of the $a^3\Pi$ state. The photon curve for CO (Fig. 7) shows the curious feature of a sharp peak near 8 eV. This peak is apparently not associated with the allowed $A^1\Pi$ state, as its onset is below the energy needed to reach this state. As yet, no assignment of this unusual structure has been made.

In addition to these results, a time-of-flight survey of a variety of molecular gases has been made, and in many of them, metastable dissociation products have been observed. These can be recognized by their fast flight times from the excitation region to the detector. Figure 8 shows, as an example, fast fragments produced in oxygen by 45 eV electrons. The flight time is much shorter than that expected for the parent molecular metastable. The reason for the fast flight time is that the fragment gains kinetic energy in the dissociation process. Similar fast fragments have been observed in CO, CO_2, SO_2, N_2O, H_2S, and CS_2.

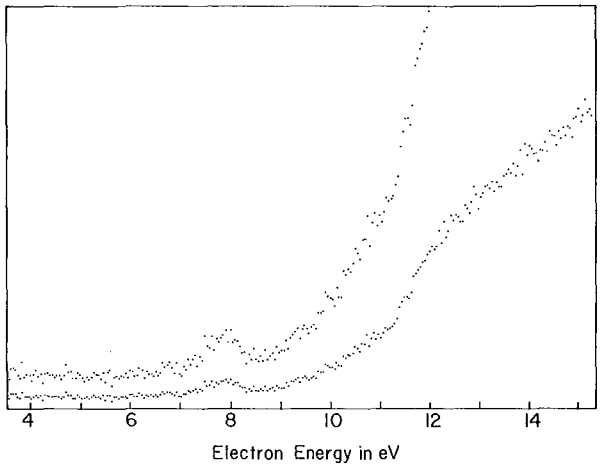

Fig. 7. Production of uv photons in carbon monoxide. (XBL-712-2870)

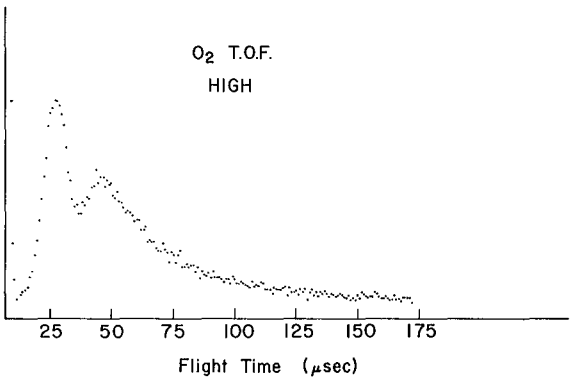

Fig. 8. Time-of-flight spectrum showing fast fragments produced in oxygen at an electron energy of 45 eV. (XBL 706-1054)

Footnotes and References

†Condensed from a paper presented at 18th Annual Conference on Mass Spectrometry and Allied Topics, San Francisco, June 14-19, 1970.

*Present address: Philips Research Laboratories, WY4, N. V. Philips' Gloeilampenfabrieken, Eindhoven, The Netherlands

1. John Olmsted III, Amos S. Newton, and K. Street Jr., J. Chem. Phys. 42, 2321 (1965).

2. R. Clampitt and Amos S. Newton, UCRL-18032, 1967.

3. R. E. Fox, W. M. Hickam, D. J. Grove, and T. Kjeldaas Jr., Rev. Sci. Instrum. 26, 1101 (1955).

4. G. E. Thomas and F. E. Vogelsberg, UCRL-19934, 1970; Rev. Sci. Instr. 42, 161 (1971).

The Occurrence of the H_3^+ Ion in the Mass Spectra of Organic Compounds †

Amos S. Newton, A. F. Sciamanna, and G. E. Thomas*

Smith[1] showed that H_3^+ ions, formed by a unimolecular dissociation process with an appearance potential, AP, of 25.3 ± 1 eV, were one of the normal components of the mass spectrum of methane. Because of the low intensity of H_3^+ ions in mass spectra, no further work on the occurrence of these ions is recorded. The present work shows that H_3^+ ions occur as a normal component of low yield in the mass spectra of most (if not all) organic compounds containing three or more atoms.

The experiments described here were performed with a Consolidated Electrodynamics Corp. Model 21-103B mass spectrometer, modified to increase the analyzer-tube pumping speed and to increase the detector sensitivity.[2,3] Initial kinetic energies with which H_3^+ ions are formed in the ion source were measured by use of negative repeller voltage-cutoff of the H_3^+ ion beam,[4] and by comparison of the metastable suppressor cutoff voltage of the H_3^+ ion beam with the cutoff voltage of the beam of an ion with thermal initial kinetic energy.[5]

The yields of H_3^+ ions from various organic compounds, as determined under standard operating conditions of the mass spectrometer, are shown in Table I. The H_3^+ ion current from each compound was shown to be a linear function of pressure. These yields (expressed as the percentage the H_3^+ ion current contributes to the total ion current in the mass spectrum of each respective compound) are only relative. The exact values are highly dependent on the mass spectrometer operating parameters because of the high initial kinetic energy, KE, with which the H_3^+ ions are formed in the ion source. This is illustrated for H_3^+ from CH_4 and C_2H_6 in Fig. 1, where the intensity of H_3^+ is shown to be a rapidly varying function of the ion accelerating voltage in each case. The intensity of an ion with only thermal initial KE is almost invariant over this range of ion accelerating voltage.

In Fig. 2, the yields of H_3^+ and H_2^+ are plotted as a function of carbon number for the normal alkanes and 1-alkenes. In Fig. 3, a similar plot is made for the methyl halides. In Fig. 3, the yield of H_2X^+ ions is included for comparison. The yields of H_3^+ and H_2^+ appear unrelated in both Figs. 2 and 3, but in Fig. 3 the variance of H_3^+ and H_2X^+ appears to follow a similar pattern.

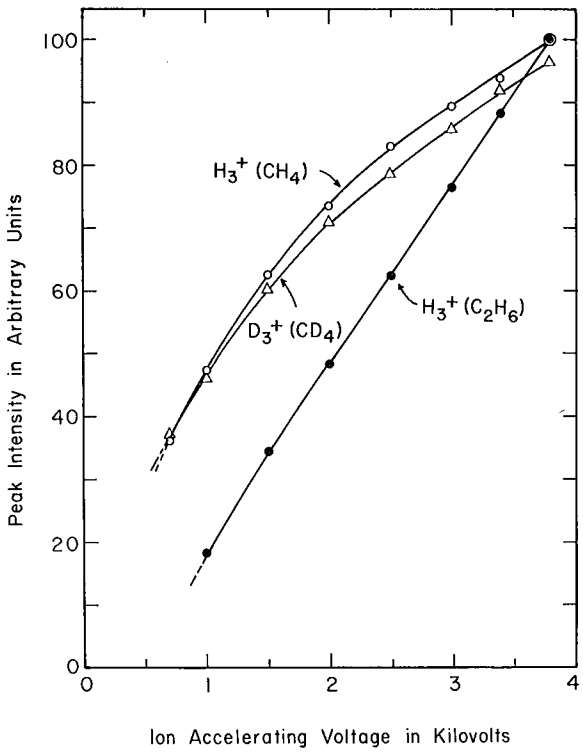

Fig. 1. Ion accelerating voltage discrimination curves of H_3^+ ions from CH_4 and C_2H_6, and D_3^+ ions from CD_4. (XBL 706-1091)

The compounds CD_4, C_2H_6, and CH_3Cl were studied in detail. Considerable thermodynamic data on these species and their fragmentation products are available.[6,7] The heat of formation of H_3^+ was calculated to be 11.12 eV from the proton affinity of H_2 equal to 4.73 eV, as derived from theoretical calculations of Conroy[8] on the potential energy surface of H_3^+.

In Figs. 4, 5, and 6 are shown metastable suppressor cutoff curves of the H_3^+ ion compared with the cutoff curve of an ion with thermal initial KE. The curve for D_3^+ ion from CD_4 (Fig. 4) shows that at an ionizing electron energy of 81 eV, most of the D_3^+ is formed with near thermal KE. There is only a small contribution of high initial KE

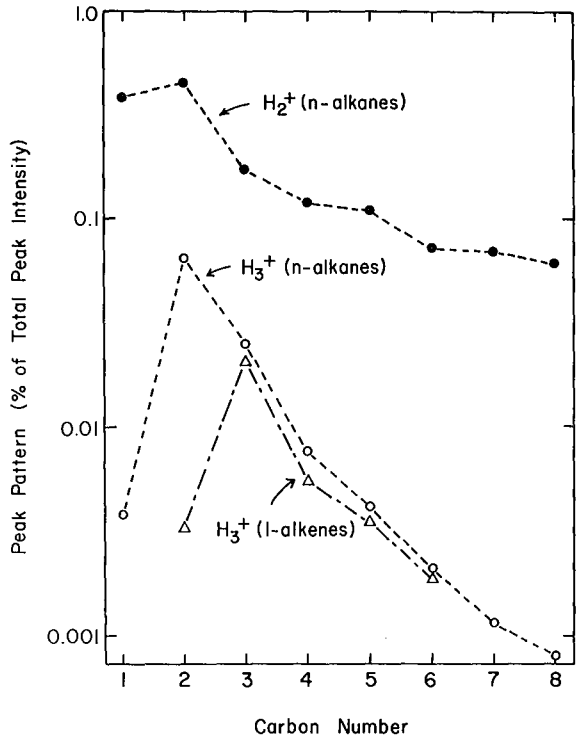

Fig. 2. Variation of yields of H_2^+ and H_3^+ in the n-alkanes and of H_3^+ in the 1-alkenes with carbon number. (XBL 706-1089)

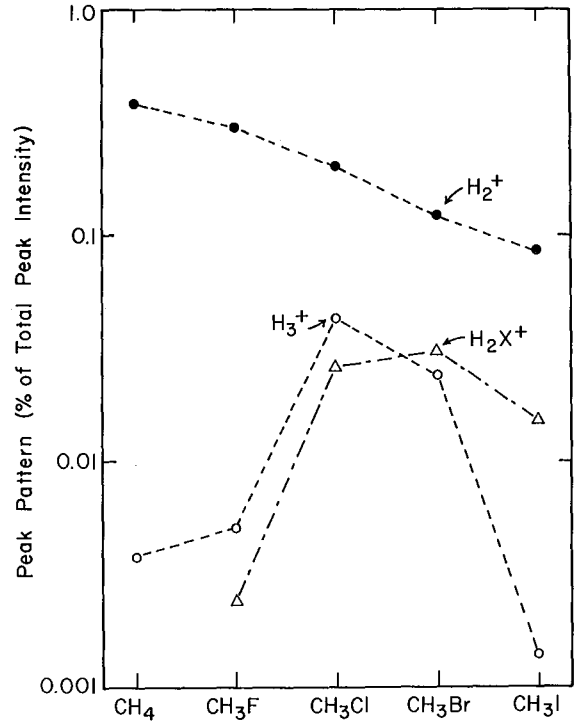

Fig. 3. Variation of yields of H_2^+, H_3^+, and H_2X^+ in the methyl halides. (XBL 706-1092)

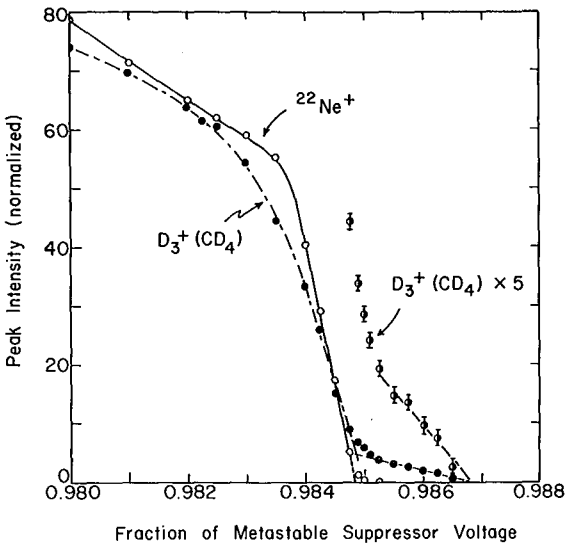

Fig. 4. Metastable suppressor cuttoff curves of $^{22}Ne^+$ ions and D_3^+ ions from a mixture of ^{22}Ne and CD_4. Conditions: V_A = 2000 V, repellers equal at 0.008 V_A, 1.000 V_{mss} = 2097 V, V_e = 81 V, magnetic scan. (XBL 708-1939)

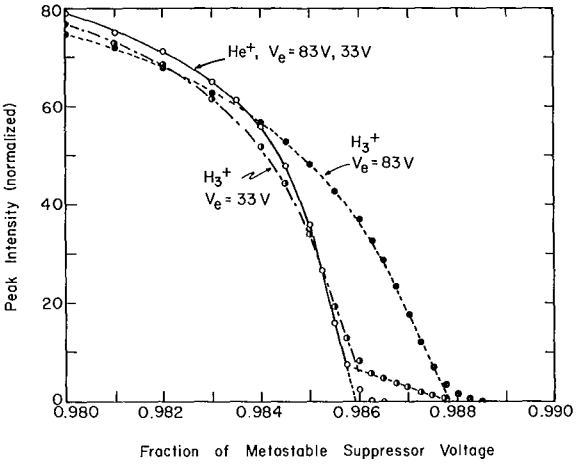

Fig. 5. Metastable suppressor cutoff curves of He^+ ions and H_3^+ ions from a mixture of 1% He gas in C_2H_6 at corrected ionizing electron energies of 83 eV and 33 eV. Conditions: V_A = 2000 V, repellers equal at 0.01 V_A, 1.000 V_{mss} = 2097 V, magnetic scan. (XBL 708-1936)

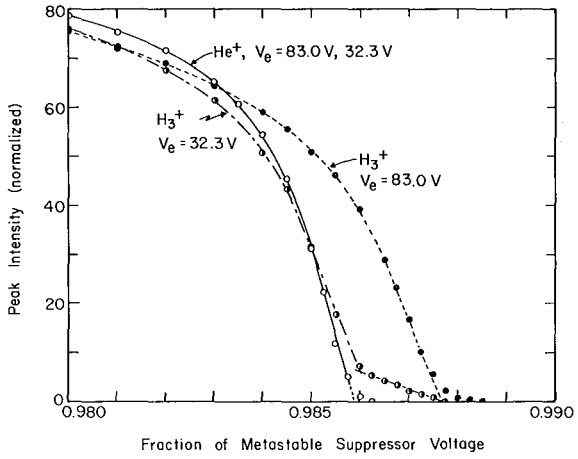

Fig. 6. Metastable suppressor cutoff curves of He^+ ions and H_3^+ ions from a mixture of 1% He gas in CH_3Cl at corrected ionizing electron energies of 83 eV and 32.3 eV. Conditions: V_A = 2000 V, repellers equal at 0.01 V_A, 1.000 V_{mss} = 2097 V, magnetic scan. (XBL 708-1940)

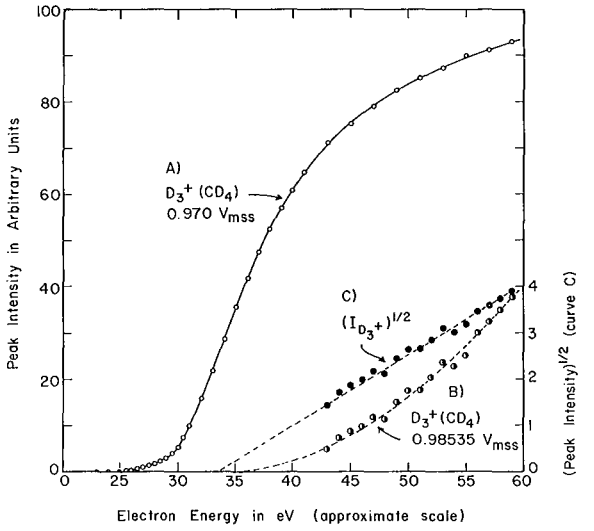

Fig. 7. Ionization efficiency curves for formation of D_3^+ ions from CD_4. Variation of curves with fraction of metastable suppressor voltage applied at collector. Conditions: V_A = 2000 V, repellers equal at 0.008 V_A, 1.000 V_{mss} = 2097 V, magnetic scan. Electron energy scale corrected to first appearance of D_3^+ at 25.5 eV with f_{mss} = 0.970. (XBL 708-1935)

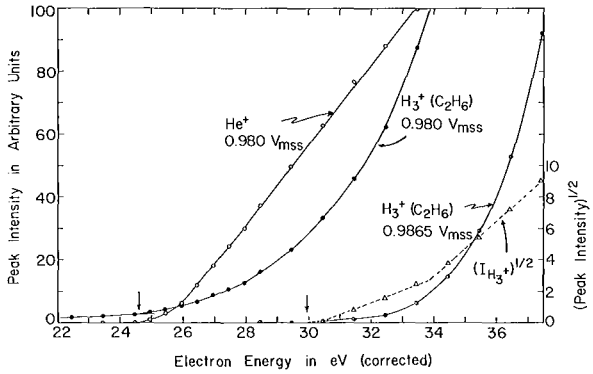

Fig. 8. Ionization efficiency curves for formation of He^+ and H_3^+ ions from a mixture of 1% He in C_2H_6. Variation of H_3^+ curves with fraction of metastable suppressor voltage applied at collector. Conditions: V_A = 2000 V, repellers equal at 0.01 V_A, 1.000 V_{mss} = 2097 V, magnetic scan. Electron energy scale corrected to first appearance of He^+ at 24.6 eV with f_{mss} = 0.980. (XBL-708-1937)

ions. On the other hand in Figs. 5 and 6, curves for H_3^+ from C_2H_6 and CH_3Cl, respectively, show the majority of the H_3^+ to be of high initial KE at an ionizing voltage of 83 eV. At an ionizing electron energy of 33 eV, however, most of the H_3^+ ions are near thermal with only a small contribution of a component with high initial KE. It is concluded that H_3^+ ions are formed by two mechanisms, one leading to ions of low initial KE and one to ions of high initial KE, and the high initial KE ions are the result of charge repulsion from dissociation of doubly-charged molecular ions.

Appearance potentials of D_3^+ from CD4 and H_2^+ from C_2H_6 and CH_3Cl were determined at a metastable suppressor setting where both high and low KE ions are collected, and at a higher setting where only high initial KE ions are collected. These ionization efficiency curves are shown in Figs. 7 and 8. The high initial KE ions have, in each case, an AP several volts higher than do the ions of low initial KE.

In Table II are shown the calculated and observed appearance potentials for formation of D_3^+ from CD_4 and H_2^+ from C_2H_6 and CH_3Cl by each of two mechanisms: (1) the dissociation of a singly-charged ion, and (2) the dissociation of a doubly-charged ion. The observed total kinetic energy release in each type dissociation is included. In each case the lowest AP for the singly-charged mechanism is several volts above the calculated AP. The observed and calculated AP's for formation of H_3^+ by the doubly-charged mechanism agree quite well. The AP of H_3^+ with high

Table I. Observed yields of H_3^+ ion from various compounds.

Compounds	$H_3^+/H_2^{+(a)}$	Pattern $H_3^{+(d)}$	Pattern $H_2X^{+(e)}$
Alkanes			
CH_4	0.0088[b]	0.0038	
CD_4	0.0086[c]	------	
C_2H_6	0.143	0.064	
C_3H_8	0.146	0.025	
n-C_4H_{10}	0.065	0.0076	
i-C_4H_{10}	0.067	0.0072	
neo-C_5H_{12}	0.037	0.0026	
i-C_5H_{12}	0.033	0.0033	
n-C_5H_{12}	0.038	0.0041	
n-C_6H_{14}	0.029	0.0021	
n-C_7H_{16}	0.017	0.0012	
n-C_8H_{18}	0.013	0.0008	
2, 2, 4-trimethyl-pentane	0.016	0.0012	
Alkenes, polyolefins, and aromatics			
C_2H_4	0.0097[b]	0.0032	
C_3H_4 (methyl acetylene)	0.029	0.0049	
C_3H_6	0.076	0.021	
1, 2-C_4H_6	0.025	0.0046	
1, 3-C_4H_6	0.018	0.0033	
1-C_4H_8	0.030	0.0055	
2-C_4H_8(cis)	0.036	0.0079	
2-C_4H_8(trans)	0.036	0.0075	
i-C_4H_8	0.030	0.0061	
2-methylbutene-2	0.025	0.0036	
hexene-1	0.017	0.0019	
2, 2, 4-trimethyl-pentene-1	0.013	0.0014	
benzene	0.037	0.0025	
Miscellaneous compounds			
CH_3F	0.017	0.0051	0.0024 (H_2F^+)
CH_3Cl	0.215	0.043	0.026 (H_2Cl^+)
CH_3Br	0.200	0.024	0.031 (H_2Br^+)
CH_3I	0.016	0.0014	0.015 (H_2I^+)
CH_3OH	0.053	0.028	0.11 (H_3O^+)
C_2H_5OH	0.076	0.025	1.3 (H_3O^+)
C_2H_5Cl	0.075	0.016	0.12 (H_2Cl^+)
CH_3CF_3	0.024	0.0054	0.038 (H_2F^+)

[a] The H_3^+ peak scanned at 2000 V ion accelerating voltage, the H_2^+ peak at 3000 V; each at 70 V nominal ionizing voltage, normal repellers of ≈0.01 V_A, 0.5 mm collector slit.

[b] Corrected for contribution of HD^+ from the H_2^+ peak.

[c] D_3^+/D_2^+ ratio.

[d] Patterns are expressed as the percentage the H_3^+ peak intensity contributes to the total peak intensity.

[e] H_2X^+ peak intensity as percentage of total peak intensity.

Table II. Comparison of calculated and observed appearance potentials for the formation of D_3^+ from CD_4 and H_3^+ from C_2H_6 and CH_3Cl.

	CD_4[a]		C_2H_6		CH_3Cl	
Products	$D_3^+ + CD$	$D_3^+ + CD^+$	$H_3^+ + C_2H_3$	$H_3^+ + C_2H_3^+$	$H_3^+ + CCl$	$H_3^+ + CCl^+$
$-\Delta H_f(CH_3X)$[b]	0.78	0.78	0.88	0.88	0.84	0.84
$\Delta H_f(CX)$	6.17		2.82		5.29	
$\Delta H_f(CX^+)$		17.30		11.67[c]		13.70[d]
$\Delta H_f(H_3^+)$[e]	11.12	11.12	11.12	11.12	11.12	11.12
Σ = Min A.P. at T=0	18.07	29.20	14.82	23.67	17.25	25.66
T	≤0.2	5.7	≤0.1	4.2	≤0.2	3.9
Calc A.P.	≤18.3	34.9	≤14.9	27.9	≤17.4	29.6
Obs A.P.	25.5±0.5	35.5±2	25.0±0.5	30.0±0.5	25.5±0.5	29.9±1
ΔA.P. (Obs-Calc)	7.2±0.5	0.6±2	10.1±0.5	2.1±0.5	8.1±0.5	0.3±1

[a] Assuming heats of formation of deuterated species equal to those given in Ref. 15 for protonated species.

[b] All heats of formation expressed in eV/molecule.

[c] Assuming $\Delta H_f(C_2H_3^+)$ = 269 kcal/mole (Ref. 15).

[d] Assuming $\Delta H_f(CCl^+)$ = 316 kcal/mole. Listed values range from 316 to 420 kcal/mole (Ref. 15).

[e] Calculated assuming the proton affinity of H_2 to be 4.73 eV.

initial KE from C_2H_6 of 30.0±1 eV also agrees quite well with AP of 30.3±0.3 eV for the AP of CH_3^+ ions with high initial KE from C_2H_6 (Ref. 9). The agreement suggests the same electronic state of $C_2H_6^{+2}$ can dissociate by at least two independent mechanisms.

Footnotes and References

†Condensed from UCRL-19916 Rev., September 1970; to be published in Intern. J. Mass Spectrom. Ion Phys.

*Present address: Philips Research Laboratories, WY4, N. V. Philips' Gloeilampenfabrieken, Eindhoven, The Netherlands

1. L. G. Smith, Phys. Rev. 51, 263 (1937).

2. A. S. Newton, A. F. Sciamanna, and R. Clampitt, J. Chem. Phys. 46, 1779 (1967); 47, 4843 (1967).

3. A. S. Newton and A. F. Sciamanna, J. Chem. Phys. 50, 4868 (1969); 44, 4327 (1966).

4. J. Olmsted III, "Formation of Energetic Fragment Ions by Bombardment of Organic Molecules with Slow Electrons," Dissertation, University of California, 1963; UCRL-10687, TID-4500, p. 21. Available from Office of Technical Services, U. S. Department of Commerce, Washington, D. C.

5. R. J. Kandel, J. Chem. Phys. 22, 1496 (1954).

6. J. L. Franklin, J. G. Dillard, H. M. Rosenstock, J. T. Herron, K. Draxl, and F. H. Field, Nat. Std. Ref. Data Ser., Natl. Bur. Std. (US), 26, U. S. Govt. Printing Office, 1969.

7. V. I. Vedeneyev, L. V. Gurvich, V. N. Kondrat'yev, V. A. Medvedev, and Ye. L. Frankevitch, Bond Energies, Ionization Potentials and Electron Affinities, (Edward Arnold Publishers Ltd., London, 1966).

Hyperfine Interactions

Nuclear Orientation of ^{253}Es in Neodymium Ethylsulfate†

A. J. Soinski, R. B. Frankel,* Q. O. Navarro,‡ and D. A. Shirley

Einsteinium-253 nuclei were oriented at low temperatures in a neodymium ethylsulfate (NES) lattice by means of the hyperfine interaction between the orbital and spin moments of the unpaired f-electrons and the nuclear magnetic-dipole moment. The angular distribution of α particles emitted by oriented nuclei can be written in terms of Legendre polynomials as

$$W(\theta) = 1 + Q_2 A_2 B_2 P_2(\cos\theta) + Q_4 A_4 B_4 P_4(\cos\theta) . \quad (1)$$

The A_k terms reflect the characteristics of the decaying nucleus and depend, in part, upon the relative amplitudes and phases of the alpha waves. The relative amplitudes can be calculated either by the semiempirical method of Bohr, Fröman, and Mottelson (BFM)[1] or through the application of Mang's shell-model theory of alpha decay.[2] The latter method also yields the relative phases of the alpha waves. The orientation parameters, B_k, depend on both the hyperfine interaction of the nucleus with its environment and the temperature. The Q_k terms are solid-angle correction factors which are smaller than unity for a finite-sized source and detector.

The experimental angular distribution of α particles from oriented ^{253}Es nuclei is plotted against the inverse temperature for one series of adiabatic demagnetizations in Fig. 1. From the values of the angular distribution function at the lowest temperatures, it is possible to determine A_2 and A_4. The experimental values are compared with the theoretical values in Table I. We also tabulate values for $W(0)$ and $W(\pi/2)$ at saturation; i.e., for T approaching zero. At sufficiently low temperatures only one nuclear magnetic substate is appreciably populated, and B_2 and B_4 approach a limiting value: $B_2(1/T \to \infty) = 1.528$ and $B_4(1/T \to \infty) = 0.798$.

The positive experimental value for A_2 given in Table I implies that the S and D (corresponding to orbital angular momenta 0 and 2) alpha partial waves are in phase. The negative experimental value for A_4 confirms the prediction of Mang and Rasmussen[3] that the S and G (L = 4) waves are out of phase. Mang and Rasmussen predicted that the S and G waves would be in phase for nuclei with a mass number lower than 244 but

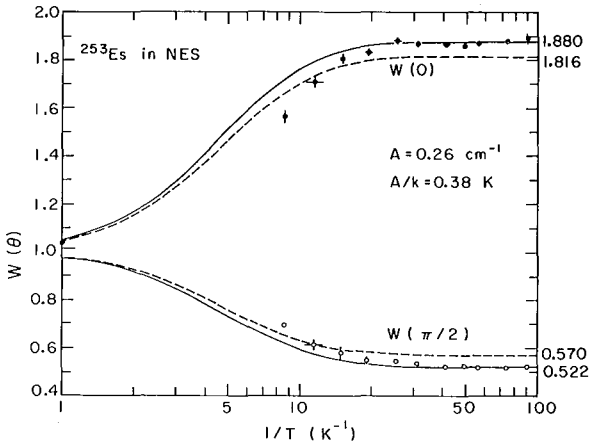

Fig. 1. Experimental angular distribution of α particles from ^{253}Es in NES as a function of the inverse temperature. The curves shown are theoretical, based on different estimates for the relative intensities of the alpha partial waves. (XBL705-2772)

would be out of phase for heavier nuclei. Detailed shell-model calculations by Poggenburg, Mang, and Rasmussen[4] confirm this general behavior.

Neither the BFM theory nor the Mang theory accurately reproduces the experimental A_2 and A_4. Both underestimate the G-wave intensity, as reflected in the small theoretical values for A_4. The dashed curve in Fig. 1 is the angular distribution obtained from the Mang theory predictions for the relative amplitudes and phases. The predicted relative intensities (which are proportional to the amplitudes squared) for the S, D, and G waves are 1.000:0.179:0.0052,[5] whereas the relative intensities that best fit the experimental angular distribution are 1.000:0.216:0.0078. In order to reproduce the experimental angular distribution, the Mang-theory-predicted intensities for decays to the ground-state band of ^{249}Bk were modified as follows: The S-wave intensity was decreased by 6%; the D-wave intensity was increased by 22% (mainly to fit the $P_2(\cos\theta)$ term); and the G-wave intensity was increased by 220% (mainly to fit the $P_4(\cos\theta)$ term). The resulting angular distribution would be

$$W(\theta) = 1 + 0.632\, Q_2 B_2 P_2(\cos\theta) - 0.054\, Q_4 B_4 P_4(\cos\theta) \quad (2)$$

Table I. Coefficients A_2 and A_4 for the ^{253}Es in NES angular distribution function $W(\theta) = 1 + A_2Q_2B_2P_2(\cos\theta) + A_4Q_4B_4P_4(\cos\theta)$.

	A_2	A_4	$W(0, 1/T \to \infty)$	$W(\pi/2, 1/T \to \infty)$
Experiment	0.630(5)	-0.059(7)	1.872(7)	0.521(4)
BFM (S and G waves out of phase)	0.594	-0.006	1.854	0.561
BFM (S and G waves in phase)	0.698	+0.138	2.102	0.523
Mang theory (S and G waves predicted to be out of phase)	0.576	-0.0248	1.816	0.570
Mang theory but with modified partial wave intensities	0.632	-0.0502	1.880	0.522

which is plotted as the solid curve in Fig. 1. The fit to the lowest temperature data is greatly improved. The poor fit at higher temperatures is due to the rapid warmup of the NES crystal. Immediately after demagnetization, the small active volume of the NES crystal is warmed at an appreciable rate by radioactive heating. This can lead to a spurious apparent temperature dependence, with the high temperature points showing a reduced effect. Hyperfine structure constants derived in such cases are anomalously small.[6] The temperature dependences of $W(0)$ and $W(\pi/2)$ are affected by different variables than those that affect their saturation values. The stronger the source and the shallower its distribution in from the surface (two conditions conducive to reliable measurement of saturation values of $W(0)$ and $W(\pi/2)$), the worse will be the self-heating effect. Therefore several series of demagnetizations were performed on NES crystals containing less activity in order to obtain a value for the magnetic hyperfine structure constant, A, of 0.26 ± 0.03 cm^{-1}.

The nuclear magnetic moment can be derived from A if both the ground crystal field state and the radial integral $\langle r^{-3} \rangle_{5f}$ are known. Since neither is known accurately, our derived value for μ has limited accuracy. We report a nuclear magnetic moment for ^{253}Es of $|\mu| = 2.7 \pm 1.3\ \mu_N$. Two estimates of the ^{253}Es nuclear magnetic moment have been made by Lamm.[7] Assuming $g_s = g_s^{free}$, $\mu = +4.239\ \mu_N$. However, better agreement with the moments of odd-mass nuclei is obtained with the semiempirical quenching factor $g_s = 0.6 g_s^{free}$. Then $\mu = +3.50\ \mu_N$, in better agreement with our value.

Footnotes and References

†Condensed from Phys. Rev. C 2, 2379 (1970).

*Permanent address: National Magnet Laboratory, Massachusetts Institute of Technology, Cambridge, Massachusetts.

‡Permanent address: Philippine Atomic Research Center, Diliman, Quezon City, The Philippines.

1. A. Bohr, P. O. Fröman, and B. R. Mottelson, Kgl. Danske Videnskab. Selskab, Mat.-Fys. Medd. 29, No. 10 (1955).

2. H. J. Mang, Z. Physik 148, 582 (1957); Phys. Rev. 119, 1069 (1960); Ann. Rev. Nucl. Sci. 14, 1 (1964).

3. H. J. Mang and J. O. Rasmussen, Kgl. Danske Videnskab. Selskab, Mat.-Fys. Medd. 2, No. 3 (1962).

4. J. K. Poggenburg, H. J. Mang, and J. O. Rasmussen, Phys. Rev. 181, 1697 (1969).

5. J. K. Poggenburg, Jr., UCRL-16187, 1965.

6. M. Kaplan, J. Blok, and D. A. Shirley, Phys. Rev. 184, 1177 (1969).

7. I.-L. Lamm, Nucl. Phys. A125, 504 (1969).

^{59}Co Nuclear Quadrupole Interaction in $CoCl_2 \cdot 2H_2O$

H. Haas

Recently the ^{59}Co NMR spectrum has been observed[1] in the antiferromagnetic state of $CoCl_2 \cdot 2H_2O$ at 4.2°K. From the magnetic structure of the material the internal field of 419.1 kG is expected to lie along the b axis of the monoclinic structure (z in Fig. 1a). The nuclear quadrupole splitting in this field shows a slightly unequal spacing. A program used earlier to analyze ^{59}Co NMR in single crystals[2] can account quantitatively for this second-order effect. Table I gives the calculated and observed frequencies, assuming that the major axis of the field gradient is oriented perpendicular to the b axis. The best fit is obtained for $eQ_q/h = 140 \pm 15$ MHz $\eta = 0.24 \pm 0.08$, with the b axis having the smallest component.

Obviously the field gradient is primarily due to the unfilled electron shell of the Co^{2+} ion, as was found[3] for Fe^{2+} in $FeCl_2 \cdot 2H_2O$. The observed orientation may be qualitatively understood when the splitting of the d orbitals shown in Fig. 1b is considered. All contributions cancel except for that of the hole in the d_{xz} orbital, resulting in a cylindrically symmetric field gradient along the y axis.

The wave functions for the lowest states ($^4T_{1g}$) of Co^{2+} in the rhombic field have been determined for the parameters obtained from the magnetic susceptibility,[4] using the effective Hamiltonian

$$\mathcal{H} = k\lambda \left[-\frac{3}{2} \vec{L} \cdot \vec{S} + \frac{2}{3} \frac{D}{k\lambda} (L_y^2 + kL_x^2 - L_z^2) \right]$$

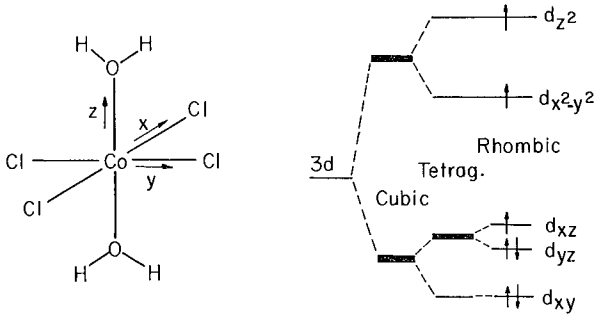

Fig. 1. Local environment (a) and rhombic field splitting (b) of Co^{2+} in $CoCl_2 \cdot 2H_2O$. (XBL712-2937)

with L = 1 ($\frac{D}{k\lambda} = -7.0$, k = 0.0). The expectation values of $\langle 3L_i^2 - L(L+1) \rangle$ determine the components of the electronic field gradient[5] along the three major axes. In Table II these have been calculated for the six lowest electronic states. For the lowest state (the only one populated at 4.2°K) this treatment correctly gives the major field gradient tensor component along the y axis, but the computed asymmetry parameter ($\eta = -0.20$) does not agree well with experiment ($\eta = +0.24$).

From the measured nuclear quadrupole interaction in the ^4F (d^7s^2) state of the cobalt atom[6] the magnitude of the electronic contribution to the field gradient may be calculated. For the pure $L_z = 0$ state, with $\langle 3L_z^2 - 2 \rangle = -2$, one can obtain from these data the nuclear quadrupole coupling constant for one d electron as eQ_q/h (3d) = $4/7 b_{3d}$ = 275 MHz. Neglecting minor changes in $1/r^3$ and the effect of covalency, the electronic contribution to the field gradient alone would give (at 0°K) $eQq_{yy}/h = \langle 3L_y^2 - 2 \rangle / -2 \times eQ_q/h$ (3d) = 200 MHz, in rough agreement with experiment. If one assumes 18% d-electron delocalization and an ionic field

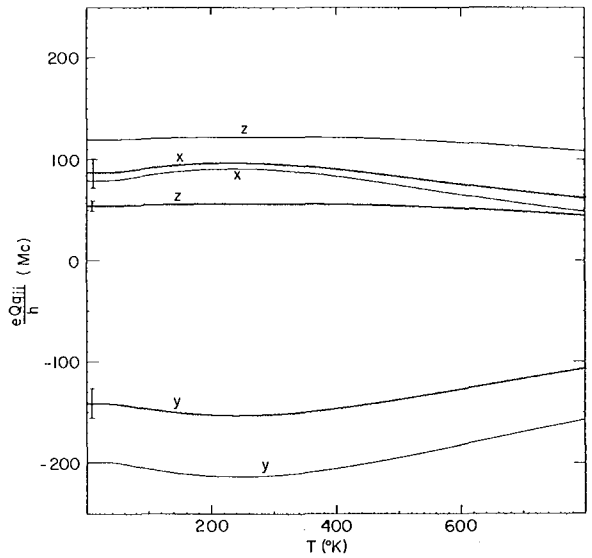

Fig. 2. Predicted temperature dependence of the nuclear-quadrupole interaction in $CoCl_2 \cdot 2H_2O$. Not adjusted to experiment (——) and corrected for covalency and ionic contribution (oooo). (XBL712-2943)

gradient contribution from the tetragonal field of eQq_{zz}/h (ionic) = 22 MHz, both quite reasonable numbers, the measured nuclear-quadrupole interaction is obtained. The temperature dependence of the three components of the nuclear quadrupole interaction tensor predicted from this model is shown in Fig. 2. An experimental measurement in the paramagnetic region would be particularly interesting.

Table I. Calculated and observed ^{59}Co NMR frequencies (MHz) in antiferromagnetic $CoCl_2 \cdot 2H_2O$ at 4.2°K.

Observed		Calculated	
ν	$\delta\nu$	ν	$\delta\nu$
411.8 ± 0.5		411.74	
	4.1		4.07
415.9 ± 0.5		415.81	
	3.9		3.95
419.8 ± 0.5		419.76	
	3.8		3.85
423.6 ± 0.5		423.61	
	3.7		3.74
427.3 ± 0.5		427.35	
	3.6		3.65
430.9 ± 0.5		431.00	
	3.6		3.55
434.5 ± 0.5		434.55	

Table II. Energies and $\langle 3L_i^2 - 2 \rangle$ expectation values for the low-lying electronic states in $CoCl_2 \cdot 2H_2O$ ($k = 0.9$, $\lambda = -176\ cm^{-1}$).

Energy (cm^{-1})	$\langle 3L_x^2-2 \rangle$	$\langle 3L_y^2-2 \rangle$	$\langle 3L_z^2-2 \rangle$
0	0.577	-1.448	0.871
136	0.892	-1.829	0.937
850	-1.547	0.889	0.658
1073	-1.478	0.523	0.955
1760	0.907	0.898	-1.805
1838	0.649	0.967	-1.616

References

1. H. Nishihara, A. Hirai, and H. Yasuoka, Phys. Letters 32 A, 355 (1970).

2. H. W. Spiess, H. Haas, and H. Hartmann, J. Chem. Phys. 50, 3057 (1969).

3. C. E. Johnson, Proc. Phys. Soc. (London) 88, 943 (1966).

4. A. Narath, Phys. Rev. A140, 552 (1965).

5. B. Bleaney, Hyperfine Interactions, edited by A. J. Freeman and R. B. Frankel (Academic Press, New York 1967), pp. 14-20.

6. W. J. Childs and L. S. Goodman, Phys. Rev. 170, 50 (1968).

Nuclear Quadrupole Moments of the Deformed $3/2^+$ States in ^{115}In and ^{117}In

H. Haas and D. A. Shirley

It has been postulated,[1] that there are excited states of the spherical nuclei ^{115}In and ^{117}In that show a considerable static deformation. States at 829 and 864 keV in ^{115}In and at 659 and 749 keV in ^{117}In (see Fig. 1) were assigned to be the I = 3/2 and I = 1/2 members of a K = 1/2 rotational band. The lower lying $3/2^+$ state has a fairly long half-life in both cases. The perturbed angular correlation (PAC) technique may therefore be used to measure the nuclear moments of these states. A PAC measurement of the magnetic moment in ^{117}In has been reported.[2] Since the electric quadrupole moments are

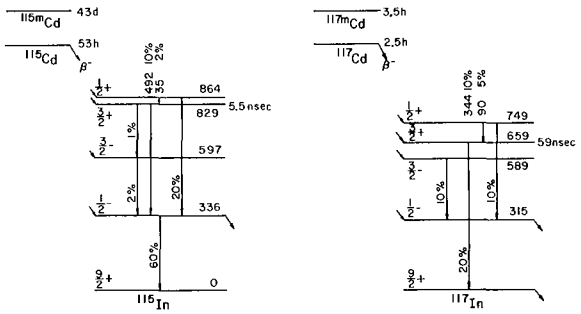

Fig. 1. Partial decay scheme of ^{115}Cd and ^{117}Cd. (XBL712-2936)

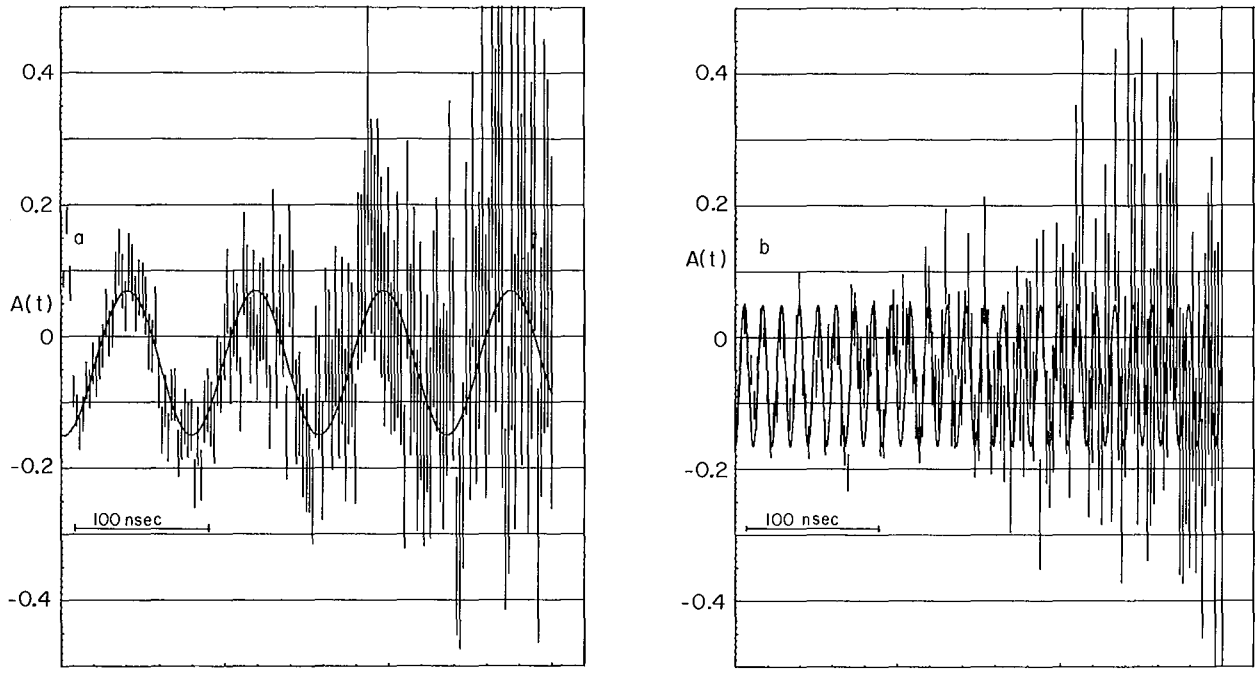

Fig. 2. Perturbation of angular correlation for ^{117}In in In (a) and Cd (b).
(XBL712-2935)
(XBL712-2934)

directly related to the nuclear deformation, their determination was thought to be of interest in this case.

In a number of studies of the nuclear quadrupole interaction by PAC a 4-detector system has been found very convenient, since the angular correlation as a function of time is obtained directly from the experiment. Sources were prepared by irradiating enriched ^{114}CdO and ^{116}CdO with reactor neutrons. The Cd metal sources were obtained by irradiating enriched metal foil that was used without further treatment.

The ^{117}In experiments could be performed with the standard setup of 2-in. ×3-in. NaI crystals on all detectors. Figure 2 shows the PAC data for some representative sources. The experimental conditions had not been optimized in this case and an improvement of counting statistics would be easily feasible. The perturbation frequency can, however, be obtained from the data shown with considerable accuracy. The fitted parameters are included in Table I.

The γ cascades through the 5-nsec 829-keV state are only very weak branches in

Table I. Nuclear quadrupole interaction constants ($\sqrt{1+\eta^2/3}\, eQ_q/h$) in MHz)
(ox = oxalate, oq = oxiquinolate)

Lattice	^{115}In	^{115}In (829 keV)	^{117}In (659 keV)
In (RT)	30.0		21.0 ± 0.5
Cd (RT)		148.5 ± 6.0	143.5 ± 3.0
$Cd(NO_3)_2 \cdot 4H_2O$			48.2 ± 2.0
$Cdox \cdot 3H_2O$		104.0 ± 8.0	89.2 ± 3.0
$Cdoq_2$		242.5 ± 10.0	

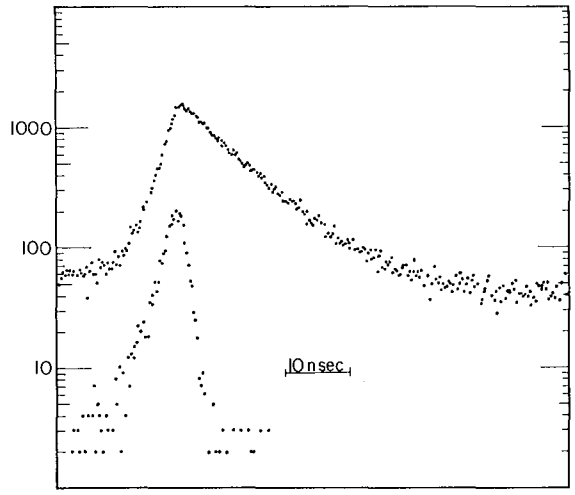

Fig. 3. Time resolution for 35-492 cascade and example of time-differential data. (XBL712-2944)

the ^{115}Cd decay (Fig. 1). Therefore, it was especially difficult to obtain sufficient counting statistics. For the time-differential measurement the 35 keV transition was observed with 1-mm NaI crystals. Figure 3 shows the time resolution reached with this setup and a representative data set. In solution the previously determined unperturbed angular correlation was found.[3] Figure 4 shows the perturbation observed in solids. The interaction frequencies fitted to these data are included in Table I.

From the PAC of ^{117}In in In (Fig. 2a) one can conclude unambiguously that the state involved must have I = 3/2, because for other values the perturbation would not have the simple sinusoidal form. The ratio of the nuclear quadrupole moments of the 659 keV state and ^{115}In can be obtained by comparison with NQR data.[4] One calculates

$$\frac{Q^{117}(659\ \text{keV})}{Q^{115}} = 0.70 \pm 0.02 .$$

The quadrupole moment of ^{115}In, however, is known with some accuracy from atomic-beam measurements as Q^{115} = 0.83 b, leading to $Q^{117}(659\ \text{keV})$ = 0.58 ± 0.06 b.

To determine the nuclear quadrupole moment of the 829 keV state in ^{115}In, the ratio

$$\frac{Q^{115}(829\ \text{keV})}{Q^{117}(659\ \text{keV})} = 1.04 \pm 0.05$$

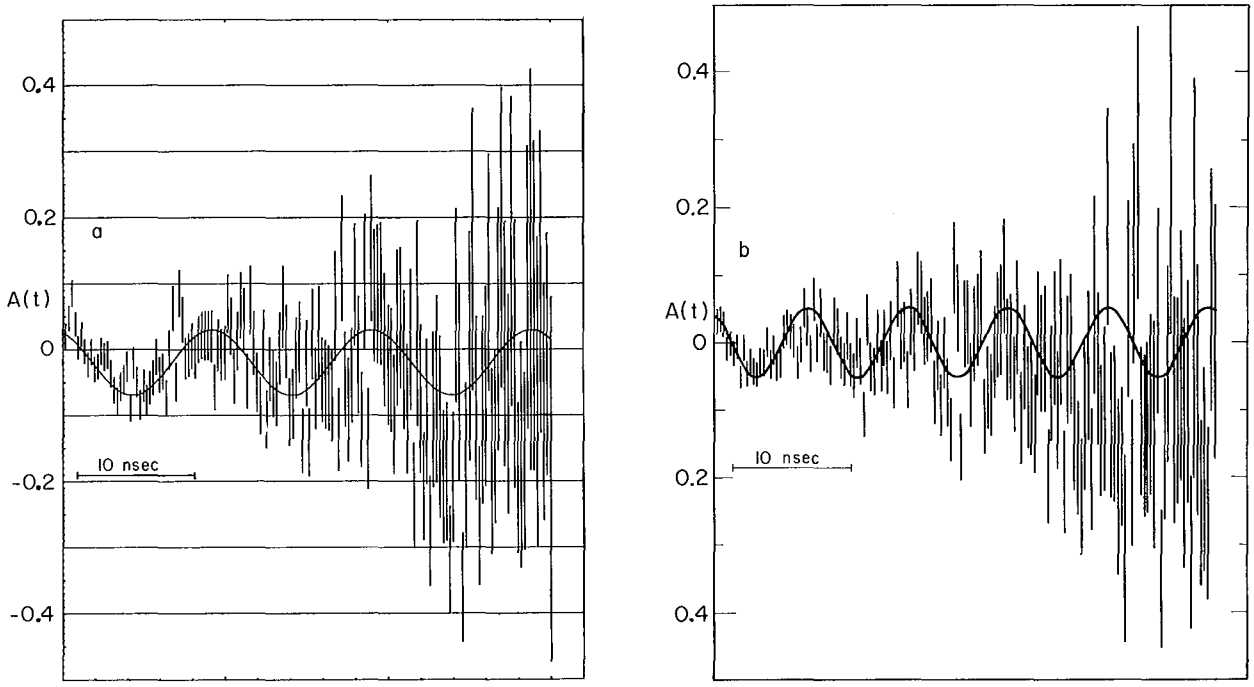

Fig. 4. Perturbation of angular correlation for ^{115}In in Cd (a) and $Cdoq_2$(b). (XBL712-2933) (XBL712-2942)

Table II. Intrinsic quadrupole moments of the $K = 1/2^+$ bands in ^{115}In and ^{117}In.

	PAC	B(E2)
^{115}In	3.0 ± 0.4 b	2.67 b
^{117}In	2.9 ± 0.3 b	3.18 b

is calculated from the measured interactions in Cd metal. This leads directly to Q^{115} (829 keV) = 0.60 ± 0.08 b. The fact that the excited states of ^{115}In and ^{117}In are probably deformed has been pointed out by several authors. The size of the measured nuclear-quadrupole moments lends strong support to this view. In the rotational model, the quadrupole moment of a deformed nucleus is given as

$$Q = \frac{3K^2 - I(I+1)}{(I+1)(2I+3)} Q_o ,$$

neglecting single-particle contributions. In Table II the intrinsic quadrupole moments Q_0 (calculated for $K = 1/2$) are compared with those determined from γ-ray transition probabilities.[1] The agreement is surprisingly good. Using $Q_0 = 0.8\, Z\, R^2 \delta(1+0.5\delta + \cdots)$, a deformation of $\delta = 0.20$ is computed for the excited states in both cases.

References

1. A. Backlin, B. Fogelberg, and S. G. Malmskog, Nucl. Phys. A96, 539 (1967).

2. V. R. Pandharipande, K. G. Prasad, and R. P. Sharma, Nucl. Phys. A104, 525 (1967).

3. M. M. Bajaj, S L. Gupta, and N. K. Saha, Aust. J. Phys. 21, 317 (1968).

4. R. R. Hewitt and T. T. Taylor, Phys. Rev. 125, 524 (1962).

5. G. F. Koster, Phys. Rev. 86, 148 (1952).

Perturbed Angular Correlations in RuNi and RuFe

T. A. Koster, S. Koički, and D. A. Shirley

As a tool in solid state physics, time-differential perturbed angular correlations (TDPAC) has proved very useful, because it permits microscopic observation of a variety of magnetic systems. With this technique, we may observe the precession of nuclear spins in a magnetic field by measuring the time variation of the intensity of radiation from the nuclei along some chosen direction. In this way we may study nuclear magnetism and, through the nucleus-electron interaction, electronic magnetism as well.

In these particular experiments, we have investigated the magnetic hyperfine interaction in the dilute alloy systems RuFe and RuNi at room temperature. Previous measurements[1] on 1 percent RuNi showed an attenuation of the angular correlation in time which was believed to be attributable either to a field distribution at the nucleus or to the existence of several different impurity lattice sites. We undertook these experiments 1) to clarify the origin of this damping in RuNi and to look for it in RuFe, 2) to further demonstrate the possibilities for using plastic scintillators for fast-timing TDPAC work, and 3) to demonstrate the usefulness of the TDPAC technique for measuring large fields by observing precession in ^{99}RuFe.

The ^{99}Rh parent is produced with 13-MeV protons from the Berkeley 88-inch cyclotron from isotopically enriched ^{99}Ru powder via the $^{99}Ru(p,n)\,^{99}Rh$ reaction. We then prepare carrier-free ^{99}Rh by digesting the target with $NaOH$-$NaNO_3$ and oxidizing the ruthenium to RuO_4 with $NaBrO_3$-H_2SO_4. The volatile tetroxide distills off and can be recovered. Fe^{3+} carrier is added, the ruthenium-free ^{99}Rh coprecipitated with $Fe(OH)_3$, and the hydroxide mixture dissolved in 6M HCl. Most of the iron is extracted into diethyl ether, while the remaining iron is column-separated, yielding carrier-free 15-day ^{99}Rh.

The 529-90 keV cascade was used for all these measurements. The relevant part of the decay scheme $^{99}Rh \rightarrow {}^{99}Ru$ is shown in Fig. 1. The detectors consisted of one PILOT plastic scintillator, 1.75 inches in diameter by 2 inches high, for the high-energy Compton edge from the 529 keV transition, and one 5 percent Sn-doped plastic scintillator (NE140) for the 90 keV gamma, each mounted on RCA 8850 photomultiplier tubes. Standard fast-slow coincidence electronics were used. The resolving time for this combination at these energies was generally around 0.7 nsec FWHM.

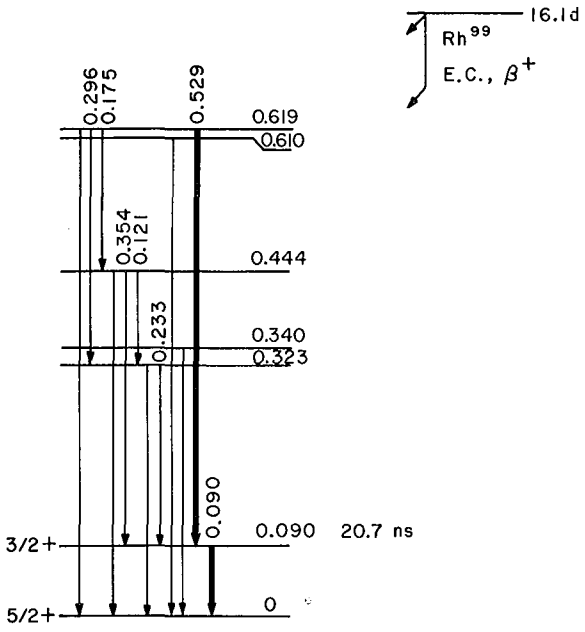

Fig. 1. Decay scheme for $^{99}Rh \rightarrow {}^{99}Ru$. (XBL6711-5668)

The time spectrum for RuNi is shown in Fig. 2. In the time range observed, there is no appreciable attenuation. We can therefore attribute the previously observed damping to the 1 percent ruthenium impurity present. Such effects caused by even very small amounts of impurity, possibly via a change in the conduction electron polarization, have been observed, for example, in spin-echo[2] and NMR/PAC[3] studies of various dilute alloy systems.

For the RuFe system, the time-differential spectrum also shows no damping for essentially zero-concentration ruthenium. The magnetic hyperfine frequency is measured to be 69.8(7) MHz, giving a magnetic hyperfine field at ruthenium nuclei in iron of H_{hf} = 484(10)kG at T = 296(1)°K. The error is largely due to the uncertainty in the

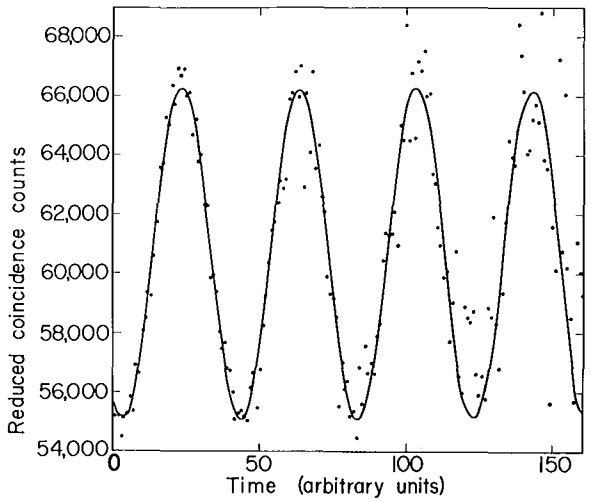

Fig. 2. Time-differential PAC spectrum for ^{99}RuNi. (XBL712-2939)

g factor, g = 0.189(4).[4] This field value is in agreement with earlier Mössbauer measurements[5] giving H_{hf} = - 500(10) kG at 4.2°K.

We gratefully acknowledge the help of Mrs. Winnifred Heppler in the preparation of the ^{99}Rh activity.

References

1. D. A. Shirley, S. S. Rosenblum, and E. Matthias, Phys. Rev. 170, 363 (1968).

2. J. I. Budnick, T. J. Burch, S. Skalski, and K. Raj, Phys. Rev. Letters 24, 511 (1970).

3. S. Koički, T. A. Koster, R. Pollak, D. Quitmann, and D. A. Shirley, Phys. Letters 32B, 351 (1970).

4. E. Matthias, S S. Rosenblum, and D. A. Shirley, Phys. Rev. 139, B532 (1965).

5. O. C. Kistner, Phys. Rev. 144, 1022 (1966).

Nuclear Spin Relaxation Rates by NMR on Oriented Nuclei; Co ^{60}Co †

J. A. Barclay* and H. Gabriel‡

The measurement of nuclear spin-lattice relaxation times, T_1, is essential to an understanding of heat transfer from nuclei to electrons or lattice. The mechanisms of this energy change are basic to hyperfine interactions, and a knowledge of them can add to our understanding of these interactions.

Although nuclear magnetic resonance (NMR) has been used to measure spin-lattice

relaxation rates (T_1) for some time, Templeton and Shirley[1] first illustrated the measurement of T_1 by NMR on oriented nuclei (NMR/ON). Here the resonance of oriented radioactive nuclei is detected by observing the resulting perturbation of the γ-ray anisotropy. With this method, spin-lattice relaxation can be studied in very dilute alloys in the temperature region 0.1 - 0.004°K. However, the interpretation of the observed signal in NMR/ON is complicated because one observes a nuclear radiation pattern whose directional intensity is described by kth rank statistical tensors, B_k.

Gabriel[2] has developed a theory describing the relaxation of these tensors in terms of a unique T_1 defined exactly as in previous NMR work. He also has given guidelines for calculating his relaxation factors, $G^{q\ q'}_{k\ k'}(t)$, at low temperatures. We present a numerical method for any spin at low temperatures and apply it to ^{60}Co in Co.

For a system with axial symmetry the angular distribution perturbed by the presence of relaxation effects can be written as:

$$W_{axial}(k;t) \equiv W(\theta;t) = \sum_k U_k F_k P_k(\cos\theta) B_k(t), \tag{1}$$

where the $U_k F_k$ depend on the decay scheme, $P_k(\cos\theta)$ is a Legendre polynomial, and the $B_k(t)$ are time-dependent orientation parameters. The latter can be given the form

$$\Delta B_k(t) = B_k(t) - B_k(eq) = \sum_{k'} G^{o\ o}_{k\ k'}(t) \Delta B_{k'}(t=0)$$

$$= \sum_{k'} (U^k_o | \exp\left\{-(iL' + \overline{M})t\right\} | U^{k'}_o) \Delta B_{k'}(t=0). \tag{2}$$

The perturbation factors $G^{o\ o}_{k\ k'}(t)$ (the same used in perturbed angular correlation theory) are the matrix elements of an evolution operation with respect to Fano's multipole representation. The Liouville operator, L', describes all static extranuclear interactions, whereas the relaxation operator $\overline{M}$ contains the properties of the surroundings into which the nuclei are embedded.

The matrix elements, $(U^k_o | \exp(-\overline{M}t) | U^{k'}_o)$, are nondiagonal in the low-temperature region. Therefore, diagonalization of the relaxation operator is required yielding (under certain conditions) a complete set of eigenvectors, $|\kappa)$ belonging to the eigenvalues Λ_κ. Equation (2) (with L' = 0) can be given the form

$$\Delta B_k(t) = \sum_{k'\kappa} (U^k_o | \kappa) e^{-\Lambda_\kappa t} (\kappa | U^{k'}_o) \Delta B_{k'}(t=0) \tag{3}$$

where the transformation matrix $a_{k\kappa} \equiv (\kappa | U^k_o)$, and obeys the relation

$$\sum_\kappa a_{k\kappa} a^*_{k'\kappa} = \delta_{kk'} . \tag{4}$$

In the numerical calculations the initial conditions have been used to normalize the eigenvectors in an appropriate way. The various perturbation factors $G^{o\ o}_{k\ k'}(t)$ are easily obtained from Eq. (8) by choosing a set of special initial conditions: $\Delta B_{k'=\alpha}(t=0) = 1$, $\Delta B_{k' \neq \alpha}(t=0) = 0$ for all possible choices of $\alpha = 1, 2, \cdots 2I$. The result can be cast into the form

$$G^{o\ o}_{k\ k'}(t) = \sum_\kappa (U^k_o | \kappa)\ (\kappa\ |\ U^{k'}_o)\ e^{-\Lambda_\kappa t}$$

$$= \sum_\kappa A^\kappa_{kk'}\ e^{-\Lambda_\kappa t}$$

$$(k, k' = 1, 2, \cdots (2I). \tag{5}$$

Numerically, $G^{o\ o}_{k\ k'}(t)$ will be a function of x and must be evaluated for each x. The method finds application in its ease of extension to higher spins.

As an example, we have chosen I = 5 at x = 0.3. In Fig. 1 we present $G^{o\ o}_{1k'}$, $G^{o\ o}_{2k'}$, and $G^{o\ o}_{4k'}$ as a function of t/T_1.

^{60}Co in Co fcc was used as an example of the application of this theory. The sample was a single crystal of Co grown by electrodeposition onto a Cu single crystal.[3] ^{60}Co was codeposited with ^{59}Co from a plating bath to which ^{60}Co had been added. There was a few percent of hcp Co in the original sample according to x-ray diffractometer measurements, but this was removed by heating to 500°C for approximately 30 sec and then quenching in H_2O immediately. The thickness of the single crystal foil was about 6000 Å which is less than the skin depth in Co at 125 MHz. After cooling the sample to 0.006°K, using adiabatic demagnetization of a cerium magnesium nitrate slurry, the resonance was found at 125.10 MHz with H_o = 600 Oe. This is in good agreement with the NMR value for single domain particles by Gossard et al.[4] The best linewidth (small modulation) was 1.26 MHz which indicates that there probably was considerable stress

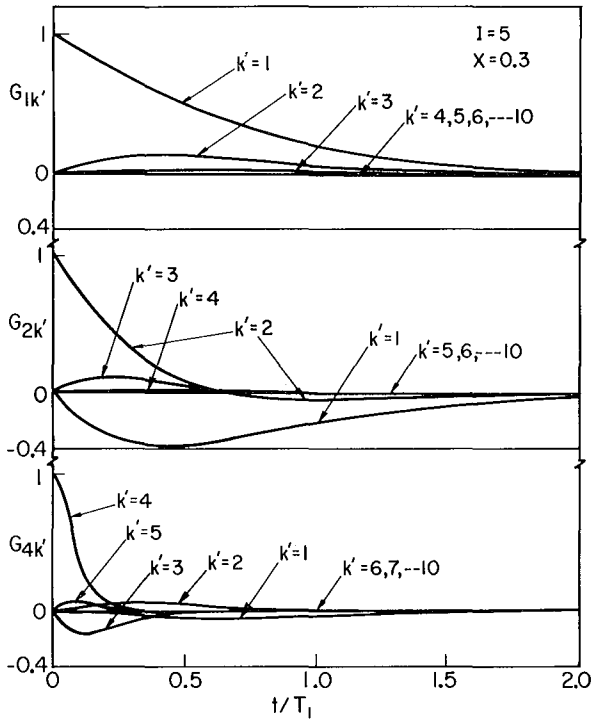

Fig. 1. Relaxation factors $G_{1k'}$, $G_{2k'}$, and $G_{4k'}$, vs t/T_1 for several values of k' at X = 0.3 and I = 5. (XBL712-2940)

in the Co foil. T_1 measurements were made by modulating over the line with H_1 as high as experimentally possible in order to maintain the same conditions over the entire temperature range.

The anisotropy curve vs time included a baseline and a warmup contribution. The theory gives the ratio of Λ_1 to Λ_2, Λ_3, Λ_4, so this constraint can be added, yielding the final function which was least-squares fitted to the data

$$F(t) = P_1 + P_2 t + \Sigma_1 e^{-\Lambda_1 t} + \Sigma_2 e^{-K_1\Lambda_1 t} + \Sigma_3 e^{-K_2\Lambda_1 t} + \Sigma_4 e^{-K_3\Lambda_1 t}, \quad (6)$$

where P_1 = baseline (equilibrium anisotropy),
P_2 = small warmup contribution,
$\Sigma_1 = U_2F_2\beta_{21} + U_4F_4\beta_{41}$, etc. and
$K_1 = \Lambda_2/\Lambda_1$ etc. The betas come from the summations in Eq. (3). The initial conditions used to calculate the betas were taken as the average of the observed anisotropy during the time H_1 was applied. The results of the data fitted by Eq. (5) with these initial conditions are shown in Fig. 2.

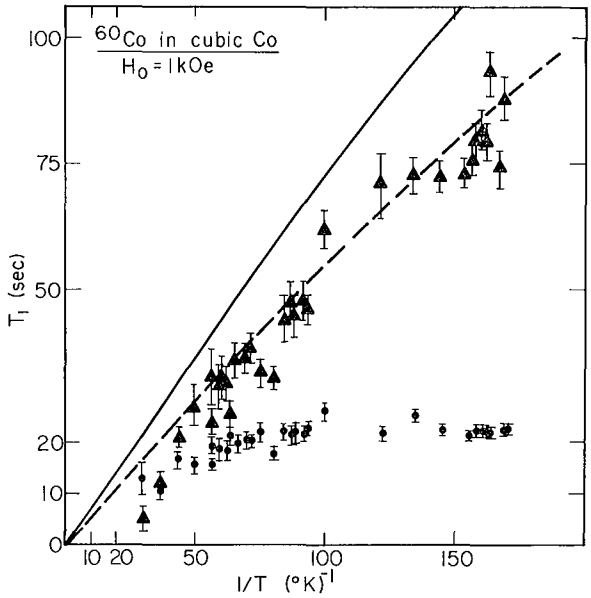

Fig. 2. Experimental relaxation times for ^{60}Co in fcc Co. The solid line represents the extrapolated ^{59}Co in Co NMR results (K = 0.75)[5] and the dashed line is for K = 0.55 sec °K. The triangles are the data fitted with a sum of exponentials and the dots are the data fitted with a single exponential. (XBL712-2941)

One comparison with our data can be made by using the high-temperature, high-field T_1 measurement of ^{59}Co in Co[5] which gave a Korringa constant K = 0.25 sec °K. After multiplying K by $[\gamma_n(^{60}Co)/\gamma_n(^{59}Co)]^2$ we can plot

$$\frac{1}{T_1} = \frac{\gamma\hbar H}{2kK} \coth\left(\frac{\gamma\hbar H}{2kT}\right)$$

for the extrapolated value at low temperature. This is shown as the solid line in Fig. 2. The discrepancy may indicate a systematic error in the initial conditions or a deviation from the Korringa law before reaching our temperatures. We obtain a value of K = 0.55 sec °K which corresponds to the dashed line in Fig. 2. Also in Fig. 2 we have shown a fit to the same data with a single exponential which yields T_1' rather than T_1. The deviation from T_1T = constant is still observed in the present theory as expected in a system obeying Fermi statistics.

Footnotes and References

†Condensed from UCRL-20433, January 1971.

*Present address: Department of Physics, Monash University, Clayton, Victoria, Australia.

‡Present address: I. Physikalisches Institut, Freie Universität Berlin, Berlin, Germany.

1. J. E. Templeton and D. A Shirley, Phys. Rev. Letters 18, 240 (1967).

2. H. Gabriel, Phys. Rev. 181, 506 (1969).

3. J. Goddard and J. G Wright, Brit. J. Appl. Phys. 15, 807 (1964); Brit. J. Appl. Phys. 16, 1251 (1965).

4. A. C. Gossard, A. M. Portis, M. Rubinstein, and R H. Lindquist, Phys. Rev. A 138, 1415 (1965).

5. V. Jaccarino, N. Kaplan, R. E. Walstedt, and J. H. Wernick, Phys. Letters 23, 514 (1966).

Mössbauer Spectroscopy with the 6.25-keV γ Transition of Tantalum-181†

D. Salomon and G. Kaindl*

The 6.25-keV El γ transition of ^{181}Ta is one of the sharpest transitions suitable for Mössbauer spectroscopy. Despite many advantageous features of this transition, including 100% natural abundance of ^{181}Ta and the easily preparable source activity of ^{181}W($T_{1/2}$ = 140 d), it was only recently that a successful application of this resonance was reported.[1] Inhomogeneous line broadening due to quadrupole interaction and isomer shift make it quite difficult to observe the resonance absportion. This is especially critical because the electric quadrupole moment of the $I = 7/2^+$ ground state is very large [$Q(7/2^+) = +3.9$ b], as well as the change of the mean-square nuclear charge radius during the intrinsic transition.

We have further improved the technique for measuring the Ta resonance, including source preparation method and velocity spectrometer. For the first time, the magnetic splitting of the 6.25-keV line in a longitudinal external magnetic field was fully resolved. The large asymmetries observed in both single-line and magnetically-split spectra are found to be due entirely to an interference between nuclear resonance absorption, followed by internal conversion, and photoelectric absorption.[2,3,4]

Velocity spectra were measured using a sinusoidal electromechanical drive as described in Ref. 5. The 6.25-keV γ rays were detected by an argon-filled proportional counter. The ^{181}W activity was obtained by irradiation of highly enriched ^{180}W (93%) with thermal neutrons. To prepare the source, a solution of the ^{181}W activity in concentrated HF-HNO_3 was dropped on the electropolished surface of a 99.999% pure, single-crystalline W metal disk, reduced under 1/2 atm of H_2 at 1100°C for 1/2 h and subsequently diffused for 1 h at 2600°C under high vacuum (10^{-6} Torr). The Ta absorber foil (purity: 99.996%) was rolled to a thickness of 4.1 mg/cm^2 and annealed for 10 h at 2000°C in high vacuum (10^{-8} Torr).

The velocity spectra measured in this work are shown in Fig. 1. For the magnetically-split velocity spectrum, the source was attached onto the flat surface of a cylindrically-shaped Sm-Co permanent magnet, producing a longitudinal magnetic field of 2.93 ± 0.03 kOe at the position of the source. The spectra were fitted with dispersion-modified Lorentzian lines of the form

$$N(v) = N(\infty)\left\{1 - \frac{A(W/2)^2}{(v-S)^2 + (W/2)^2}\left[1 + 2\xi\frac{(v-S)}{W/2}\right]\right\}$$

(N = number of counts, W = experimental linewidth (FWHM), A = maximum resonance effect, v = Doppler velocity, S = isomer shift). The amplitude of the dispersion term is according to Trammel et al.[2] given by

$$\xi = \epsilon\left(\frac{\alpha\sigma_e'}{6\pi\lambda^2}\right)^{1/2},$$

where σ_e' is the electronic absorption cross section for E1 absoprtion, α is the internal conversion coefficient, and λ is the wavelength of the incident γ rays. The coefficient ϵ is introduced to account for the fact that α and σ_e' are proportional to the sum of the squares of the amplitudes for the individual processes, whereas ξ is proportional to the sum of the products of these amplitudes (see Ref. 2).

Table I. Summary of experimental results

	Velocity spectra		
	Unsplit	Magnetically split	Magnetic drive spectrum
Halfwidth W/2	0.057 ± 0.001	0.066 ± 0.002	0.069 ± 0.003
Dispersion amplitude 2ξ	0.31 ± 0.01	0.31 ± 0.02	0.35 ± 0.07
Isomer shift S [mm/s]	0.857 ± 0.005	0.854 ± 0.005	----
g-factor ratio g(9/2)/g(7/2)	----	1.78 ± 0.02	1.76 ± 0.04

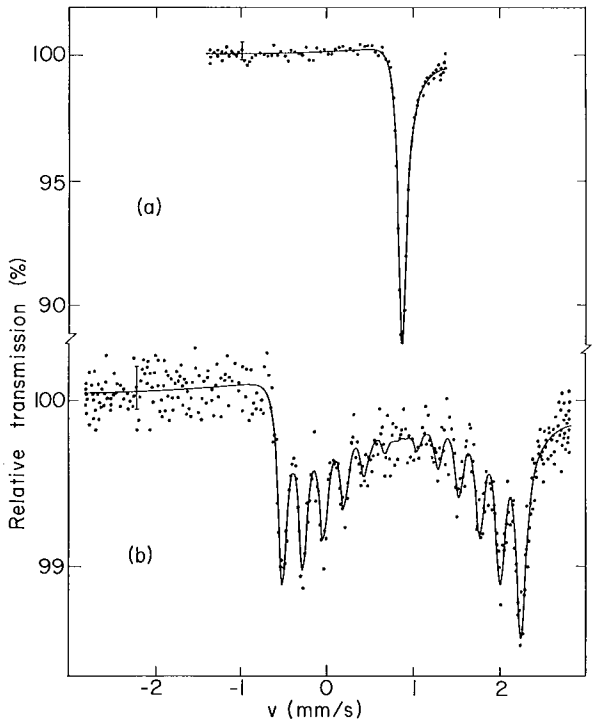

Fig. 1. Velocity spectra of the 6.25-keV γ transition: (a) unsplit source, (b) source in a longitudinal magnetic field of 2.93 ± 0.03 kOe. (XBL-712-2945)

The magnetic splitting was additionally measured with a "magnetic drive," where the resonance absorption is observed as a function of the magnetic field at the source, with no field at the absorber, and both source and absorber at zero relative velocity. The source was situated in a transverse magnetic field, generated by an electromagnet. The spectrum obtained is shown in Fig. 2.

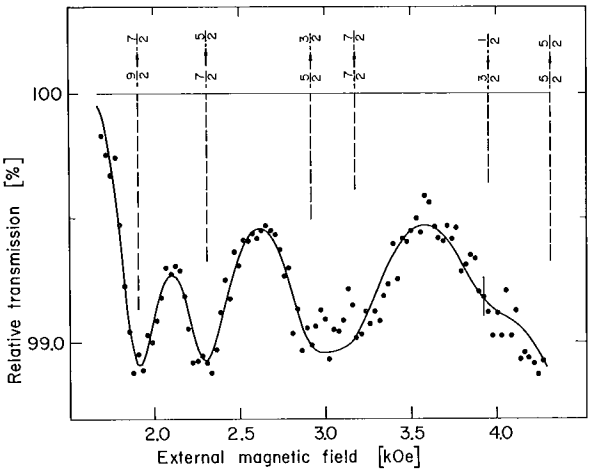

Fig. 2. Absorption spectrum of the 6.25-keV γ transition, measured with a "magnetic drive." (XBL-704-2686)

The results obtained from the analysis of the different spectra are summarized in Table I. The best experimental halfwidth obtained (W/2 = 0.057 ± 0.001 mm/s), uncorrected for finite absorber thickness, corresponds to about 17 times the natural linewidth. However, a maximum resonance effect of 11% uncorrected for background has been observed, indicating that a considerable amount of the broadening is due to the very thick Ta metal absorber (effective absorber thickness t = 23).

The experimental value for 2ξ may be compared with theory. Using $\alpha = 46 \pm 8$ [6] and $\sigma_e' = 9.8 \cdot 10^4$ b, [7] we obtain 2ξ = 0.31, indicating that ϵ is very close to 1 in the present case.

As a final result for the g-factor ratio we give the weighted average of both measurements

$$g(9/2)/g(7/2) = 1.77 \pm 0.02$$

With $\mu(7/2) = +2.35 \pm 0.01\ \mu_N$,[8] we obtain for the magnetic moment of the 6.25-keV state

$$\mu(9/2) = 5.35 \pm 0.09\ \mu_N$$

This value agrees with our earlier result,[9] but is slightly larger than that of Ref. 1.

We would like to thank Prof. D. A. Shirley for valuable discussions.

Footnotes and References

†Condensed from Phys. Letters 32B, 364 (1970).

*Miller-Fellow 1969-1971.

1. C. Sauer, E. Matthias, R. L. Mössbauer, Phys. Rev. Letters 21, 961 (1968).

2. G. T. Trammel and J. P. Hannon, Phys. Rev. 180, 337 (1969).

3. Yu. M. Kagan, A. M. Afanas'ev, and V. K. Voitovetskii, JETP Letters 9, 91 (1969).

4. A. M. Afanas'ev and Yu. Kagan, Phys. Letters 31A, 38 (1970).

5. G. Kaindl, M. R. Maier, H. Schaller and F. Wagner, Nucl. Instr. Methods 66, 277 (1968).

6. A. H. Muir, Jr., Nucl. Phys. 68, 305 (1965).

7. Table of Mass Absorption Coefficients, Norelco Report, May-June (1962).

8. L. H. Bennett and J. I. Budnick, Phys. Rev. 120, 1812 (1960).

9. G. Kaindl and D. Salomon, Phys. Letters 32B, 364 (1970).

Analysis of the Electron Paramagnetic Resonance Spectrum of Divalent Es in CaF_2 †

N. Edelstein

Dipositive lanthanide ions (Xe core, $4f^n$) stabilized in the alkaline earth fluorides have been intensively studied by optical and magnetic resonance techniques. Comparisons with atomic beam data on the corresponding free atom ground states (Xe core, $4f^n$, $6s^2$), which have similar electronic properties but no crystalline field effects, have proved fruitful. From the lowering of the Landé g value (g_J) in the dipositive ion with respect to the free atom, covalency has been determined,[1] and from differences in the hyperfine structure constants, core polarization effects have been found.[1,2] Dipositive Am (Ra core, $5f^7$) has until recently been the only dipositive actinide ion stabilized in alkaline earth fluorides. The analyses of the hyperfine structure of this ion and of Pu IV (spectroscopic notation) have shown much larger core polarization effects for the 5f series than for the 4f series.[4] Dipositive Es (Ra core, $5f^{11}$) has been stabilized in CaF_2 and identified by its electron paramagnetic resonance spectrum.[3] Although atomic beam data are not yet available for Es I (Ra core, $5f^{11}$, $7s^2$) a reasonable estimate of g_J from extrapolated parameters can be made. An analysis of the spin-Hamiltonian parameters of dipositive Es is described in this paper. A limit is placed on the ratio of the crystalline field parameters, the importance of covalent bonding is estimated by use of the orbital reduction factor, and a value for the nuclear moment of ^{252}Es ($I = 7/2$) is obtained.

The electron paramagnetic resonance spectrum at 4.2°K consisted of eight isotropic lines which were fitted to the spin Hamiltonian

$$\mathcal{H} = g\beta \vec{H} \cdot \vec{S}' + A \vec{I} \cdot \vec{S}' \qquad (1)$$

with $S' = 1/2$ and $I = 7/2$. The values of the parameters are listed in Table I. The agreement between the measured g value with that calculated for a Γ_6 state of a pure $^4I_{15/2}$ multiplet ($g_{calc} = -6.0$) in cubic symmetry was close enough to enable this spectrum to be assigned to dispositive ^{253}Es.

Table I. Spin hamiltonian parameters for ^{253}Es III.

$\lvert g \rvert$	5.809 ± 0.005
$\lvert A \rvert$	$(0.1216 \pm 0.002)\,cm^{-1}$

Since we have determined the crystalline field state that has the lowest energy, we may set a limit on the ratio B_6/B_4, which are crystalline field parameters. Graphs of the crystalline field energy levels vs a parameter related to the ratio of B_6/B_4 have been given for cubic symmetry by Lea, Leask, and Wolf[5] for all J states between 2 and 8 in half-integral steps. A similar graph has been specifically for the f^{11} system in eight-fold coordination by Weakliem and Kiss[6] (Fig. 7 in their paper), and since our convention for the crystalline field Hamiltonian is the same as these authors, we have used their graph to determine $-B_6/B_4 < 0.21$ for the Γ_6 state to be lowest. If the ratio $-B_6/B_4 > 0.21$, the Γ_7 state would be lowest, which is contrary to the experimental result. This result for Es III in CaF_2 is the same as that found for Ho III in the alkaline earth fluorides.[6]

We have estimated the value of $g_{J\ EsIII}$ for the free ion from reasonable estimates of the electrostatic parameters and the spin orbit coupling constant. We then parametrize covalency effects in terms of an orbital reduction factor k and find $(1 - k) = 0.033 \pm 0.005$. This value is compared with various lanthanide ions in CaF_2 in Table II.

From the analysis of the hyperfine coupling constant and tabulated values of $(1/r^3)$, the nuclear moment of ^{253}Es is found to be $(+)\ 3.62 \pm 0.5\ \mu_N$ where the sign is obtained from nuclear systematics.[7]

Table II. Orbital reduction factors for various ions in CaF_2

Ion	Configuration	(1-k)
Ho^{2+}	$4f^{11}$	0.016 ± 0.001
Tm^{2+}	$4f^{13}$	0.009 ± 0.001
Yb^{3+}	$4f^{13}$	0.016 ± 0.001
Es^{2+}	$5f^{11}$	0.033 ± 0.005

Footnote and References

†Condensed from UCRL-19936, July 1970; to be published in J. Chem. Phys.

1. B. Bleaney, Proc. Roy. Soc. (London) A277, 289 (1964).

2. B. Bleaney, Proceedings of the Third International Symposium on Quantum Electronics (Columbia University Press, New York, 1964).

3. N. Edelstein, J. Conway, D. Fujita, W. Kolbe, and R. McLaughlin, J. Chem. Phys. 52, 6425 (1970).

4. N. Edelstein and R. Mehlhorn, Phys. Rev. B 2, 1225 (1970).

5. K. R. Lea, M. J. M. Leask, and W. P. Wolf, J. Phys. Chem. Solids 23, 1381 (1962).

6. H. A. Weakliem and Z. J. Kiss, Phys. Rev. 157, 277 (1967).

7. A. J. Soinski, R. B. Frankel, Q. O. Navarro, and D. A. Shirley, Phys. Rev. C 2, 2379 (1970).

The Hyperfine Structure Anomaly of ^{241}Pu and ^{239}Pu and the Nuclear Moment of ^{241}Pu †

N. Edelstein

The hyperfine structure (hfs) constants for a number of levels in the Pu I and Pu II optical spectra have been measured by Fabry-Perot interferometry for the isotopes ^{241}Pu (I = 5/2, Z = 94, A = 147) and ^{239}Pu (I = 1/2, A = 145).[1]

The measured ratio of the hfs constants differed from that found earlier by Bleaney et al.[2] in electron paramagnetic resonance (EPR) experiments of $^{241,239}PuO_2^{++}$ (Pu VII) diluted in a crystal of $UO_2Rb(NO_3)_3$. In the course of ENDOR and EPR measurements on $^{241,239}Pu^{3+}$ (Pu IV) in CaF_2[3] this ratio has been remeasured. The data from the various measurements are collected in Table I.

In a recent analysis of the hfs of Pu IV in CaF_2[4] it was shown that approximately 5% of the total hyperfine interaction comes from unpaired s electrons through the mechanism of core polarization. The ground configuration of Pu II, f^6s, is fairly pure, and can be described by coupling the two lowest levels

Table I. Hfs constants for various levels of Pu ions.

Ion	Level (cm^{-1})	A (10^{-3} cm^{-1})	$\frac{A(^{241}Pu)I(^{241}Pu)}{A(^{239}Pu)I(^{239}Pu)}$	Reference
^{241}Pu I	23766	-58.25 ± 0.2	-3.367 ± 0.02	1
^{239}Pu I	23766	86.5 ± 0.2		
^{241}Pu II	0	-167.3 ± 0.5	-3.362 ± 0.02	1
^{239}Pu II	0	248.8 ± 0.5		
^{241}Pu II	22038	-32.7 ± 1	-3.41 ± 0.2	1
^{239}Pu II	22038	48 ± 1		
^{241}Pu IV	0	|4.807| ± 0.010	|3.590| ± 0.010	3
^{239}Pu IV	0	|6.695| ± 0.003		
^{241}Pu VII	0	|245| ± 1 G	|3.53 ± 0.02	2
^{239}Pu VII	0	|347| ± 1 G		

of the f^6 core ($^7F_{0,1}$) with an s electron and then mixing these two J = 1/2 states.[5,6] The hfs of the J = 1 level of Pu I (f^6s^2) has been shown to be extremely small[7] so almost all the hfs of the ground state of Pu II can be attributed to the s electron. Therefore the difference in the hfs ratios between the optical measurement of the lowest level of Pu II and the resonance measurements of Pu IV is attributed to the hfs anomaly $^{241}\Delta^{239}$ of the s electron.[8] The hfs splittings of the excited states of Pu I and Pu II listed in Table I also are probably due to s and $p_{1/2}$ electrons, but since many close lying configurations interact, further discussion is dependent upon the detailed analysis of the optical spectra.[6] Varying the percentage s-electron contribution to the total hfs constant will cause changes in the hfs ratio of ^{241}Pu to ^{239}Pu. This may be the reason for the discrepancy in the ratio between Pu VII and Pu IV.

Since the s-electron contribution to A(Pu IV) is small,

$$\frac{A(^{241}\text{Pu IV})}{A(^{239}\text{Pu IV})} \simeq \frac{g_I(^{241}\text{Pu})}{g_I(^{239}\text{Pu})} \quad : \qquad (1)$$

Then the hfs anomaly is

$$^{241}\Delta^{239} = \frac{A(^{241}\text{Pu II})}{A(^{239}\text{Pu II})} \times \frac{A(^{239}\text{Pu IV})}{A(^{241}\text{Pu IV})} - 1$$

$$= -6.3 \pm 0.2\% \, . \qquad (2)$$

The Bohr-Weisskopf theory[8] allows an estimate of $^{241}\Delta^{239}$, assuming g_s = g (neutron), g_ℓ = Z/A, and the coefficient b = 5.5% extrapolated from their table. Then

$$^{241}\Delta^{239} \simeq 0.3b \frac{g_s g_\ell}{g_s - g_\ell} \left(\frac{1}{g_I(^{241}\text{Pu})} - \frac{1}{g_I(^{239}\text{Pu})} \right)$$

$$= -5.4\%. \qquad (3)$$

The agreement between theory and experiment is surprisingly good, which was not true for the stable odd-neutron isotopes of Yb(Z = 70, A = 101, 103).[9]

A better value for μ_N of ^{241}Pu may be calculated from the hfs ratio, Eq. (1), and $\mu_N(^{239}\text{Pu}) = +0.200 \pm 0.004$ μ_N.[10] The new

value for $\mu_N(^{241}Pu) = -0.718 \pm 0.017\ \mu_N$, where the sign is obtained from the optical data.

I wish to thank J. Conway and M. Fred for many valuable discussions on the optical spectra of Pu I and Pu II, and W. Kolbe and G. Kaindl for their help and advice.

Footnote and References

†Condensed from Phys. Letters 33A, 233 (1970).

1. S. Gerstenkorn and F. S. Tomkins, Physica 42, 581 (1969).

2. B. Bleaney, P. M. Llewellyn, M. H. L. Pryce, and G. R. Hall, Phil. Mag. 45, 991 (1954).

3. W. Kolbe and N. Edelstein, (unpublished results).

4. N. Edelstein and R. Mehlhorn, Phys. Rev. B 2, 1225 (1970).

5. B. R. Judd, Phys. Rev. 125, 613 (1962).

6. M. Fred, private communication.

ENDOR of Pu^{3+} in CaF_2

W. Kolbe and N. Edelstein

The interactions between rare earth ions in cubic symmetry sites in CaF_2 and the surrounding fluorine ligands have been studied extensively by ENDOR (electron nuclear double resonance) spectroscopy.[1] Interpretations of the experimental results in terms of molecular orbital theory have been attempted, although for the most part only qualitative explanations of the empirical results have been obtained.

In the actinide series, the first di- or trivalent ion found in cubic sites in CaF_2 with an isotropic ground state is Pu^{3+} (Ac core, $5f^5$). The free-ion ground state for Pu^{3+} is a J = 5/2 state, which in eightfold cubic coordination decomposes into a Γ_7 doublet lying lowest and an excited Γ_8 quartet. The large crystalline field mixes the J = 7/2 excited state into the ground state and the resulting g value measured by electron paramagnetic resonance (EPR) enabled the crystalline field to be estimated.[2] Subsequently, the Pu^{3+} hyperfine structure was interpreted on the basis of a similar model.[3] The EPR spectrum of ^{239}Pu (I = 1/2) consists of two hyperfine lines, each characterized by an almost isotropic superhyperfine structure of 9 lines, as shown in Fig. 1. This structure is interpreted as being due to interactions of the Pu^{3+} ion with the eight nearest neighbor fluorine ions. In order to obtain quantitative information, we have measured these interactions using the ENDOR technique. Measurements of both the fluorine ENDOR and the plutonium (self) ENDOR are reported.

The experimental apparatus consisted of a microwave cavity containing an rf coil, and was similar in construction to that described by Davies and Hurrell.[4] A Nuclear Data

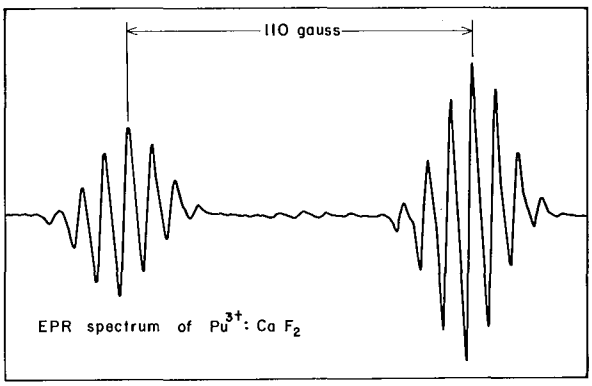

Fig. 1. EPR derivative spectrum of Pu^{3+} in CaF_2. The general appearance of the spectrum, which is shown here for an unoriented sample, is independent of the direction of the external magnetic field. (XBL-7012-4174)

multichannel analyzer attached to the output of a Varian microwave spectrometer was used to record the ENDOR signals. Single crystals of CaF2 containing approximately 0.05% $^{239}Pu^{3+}$ were grown as described earlier[2] and mounted in the microwave cavity. A worm gear drive was provided to rotate the crystal about a [110] axis making possible measurements with the external magnetic field parallel to the [100], [110], and [111] directions.

The Pu^{3+} self ENDOR frequencies were isotropic and were fitted to the following spin Hamiltonian.

$$\mathcal{H} = g\beta\vec{H}\cdot\vec{S}' + A\vec{I}\cdot\vec{S}' - g_n'\beta H\cdot I \qquad (1)$$

with S' = I = 1/2. The results are shown in

Table I. Spin hamiltonian parameters of Pu^{3+} in CaF_2.

g	1.2975 ± 0.002[a]
A	200.45 ± 0.1 MHz
g'_n	$(0.81 \pm 0.05) \times 10^{-4}\ \mu_B$
g_n	$(2.18 \pm 0.04) \times 10^{-4}\ \mu_B$[b]

[a] Ref. 2.
[b] Ref. 6.

Table II. Fluorine hyperfine parameters

Shell	A_s(MHz) (obs.)	A_p(MHz) (obs.)	A_D(MHz) (calc.)
1	-13.391 ± 0.01	-0.135 ± 0.01	+3.68
2	-0.59 ± 0.02[a]	$+0.16 \pm 0.02$[a]	+0.53

[a] The absolute signs of these quantities are not established.

Table III. Experimental and calculated nearest neighbor fluorine ENDOR frequencies.

Magnetic field orientation	$\cos^2\theta$	Freq. calc. (MHz)	Freq. obs. (MHz)	Magnetic field
[100]	1/3	14.144	14.168	5202.5
		27.536	27.540	5202.5
		14.584	14.597	5312.1
		27.975	27.980	5312.1
[110]	0	14.191	14.183	5197.3
		27.447	27.441	5197.3
		14.634	14.616	5308.0
		27.890	27.887	5308.0
[110]	2/3	14.057	14.057	5197.3
		27.582	27.579	5197.3
		14.500	14.487	5308.0
		28.025	28.025	5308.0
[111]	1	14.004	14.010	5201.2
		27.665	27.666	5201.2
		14.457	14.449	5314.3
		28.118	28.113	5314.3
[111]	1/9	14.184	14.177	5201.2
		27.485	27.473	5201.2
		14.637	14.626	5314.2
		27.938	27.916	5314.2

Table I. The g factor and hyperfine parameter are in agreement with previously reported values. The measured nuclear g factor, g_n', is found to differ from the true nuclear g factor by an amount Δg_n. This pseudo-nuclear g factor results from a second-order effect in which cross terms between the electron Zeeman interaction and the hyperfine coupling give a term proportional to $H \cdot I$. Δg_n depends upon the energy separation, $W_2 - W_1$ between the Γ_7 ground state and the Γ_8 excited state. For the values of g_n' and g_n given in Table I, $W_2 - W_1$ is found to be 348 ± 25 cm^{-1} in agreement with earlier estimates of this splitting.[2]

The fluorine ENDOR spectrum consisted of three well-separated groups of lines occurring in the vicinity of 14 and 28 MHz and near the free fluorine frequency of 21 MHz (for the field of 5400 G used). The ENDOR lines near 14 and 28 MHz can be attributed to hyperfine interactions of the Pu^{3+} ion with the first shell of 8 nearest neighbor fluorine ions surrounding it, while the remaining portion of the spectrum results from interactions with more distant fluorine ions.

The interactions of a magnetic ion with a fluorine ligand can be represented by the following spin Hamiltonian.[1]

$$\mathcal{H}_F = [A_s + A_p(\cos^2\theta - 1)] S_z I_z^F + 3 A_p \sin\theta \cos\theta \, S_z I_x^F - g_F \beta_n H_z I_z^F , \quad (2)$$

where I^F is the fluorine nuclear spin, g_F is the fluorine nuclear g factor, and θ is the angle between the applied magnetic field and the internuclear axis. A_s is a parameter describing the contact interaction through the fluorine s orbitals, and A_p is a dipolar term which includes the dipole-dipole interaction $A_D = g\beta g_n \beta_n / R^3$ between the two nuclei as well as interactions with the fluorine p orbitals.

The experimental results for A_s and A_p for the first and second fluorine shells surrounding the Pu^{3+} ions are given in Table II. Table III shows the experimental and calculated ENDOR frequencies for the nearest neighbor fluorine ligands.

The measured values of A_s and A_p for the actinide ion Pu^{3+} can be compared with results obtained for lanthanide series ions in CaF_2. For example, for Yb^{3+} $A_s = 1.67$ MHz and $A_p = 17.57$ MHz.[5] The large value for the isotropic contribution, A_s, indicates that the effects of covalency in Pu^{3+} are much more pronounced than in the lanthanides. This large value for A_s and the fortuitous near cancellation of terms contributing to A_p lead to a superhyperfine structure in the EPR spectrum which is well resolved for all orientations of the external magnetic field as shown in Fig. 1.

The signs of A_s and A_p are not uniquely determined by the Hamiltonian of Eq. (2), but were measured by means of a double ENDOR experiment and found to be negative. This information should be useful in future calculations of the bonding parameters. Other double ENDOR experiments were performed which provided information about the relaxation times of the spin system.

References

1. A. Abragam and B. Bleaney, Electron Paramagnetic Resonance of Transition Ions (Oxford, London, 1970), Chap. 4.

2. N. Edelstein, H. F. Mollet, W. C. Easley, and R. J. Mehlhorn, J. Chem. Phys. 51, 3281 (1969).

3. N. Edelstein and R. Mehlhorn, Phys. Rev. B 2, 1225 (1970).

4. E. R. Davies and J. P. Hurrell, J. Sci. Instr. 1, 847 (1968).

5. U. Ranon and J. S. Hyde, Phys. Rev. 141, 259 (1966).

6. J. Faust, R. Marrus, and W. A. Nierenberg, Phys. Letters 16, 71 (1965).

Theoretical Studies of Atomic and Molecular Hyperfine Structure

Henry F. Schaefer III

Three studies discussed in last year's Annual Report have since been published.[1-3] During the past year we have completed work on a) the molecular properties of SO_2[4] b) the magnetic hyperfine structure[5] and other properties[6] of the NO_2 radial, and c) the correlation energy and hyperfine structure of the nitrogen atom.[7]

Rigorous quantum mechanical calculations[4] were carried out for the $^1A_1$ ground state of the SO_2 molecule using the self-consistent-field (SCF) molecular orbital approximation. A large contracted gaussian basis set of s, p and d orbitals was used and the calculated energy, -547.2089 hartrees, is estimated to lie no more than 0.1 hartrees above the true Hartree-Fock energy. An interesting point discovered was that d functions on sulfur are much more important in SO_2 than found previously[1] in the H_2S molecule. This was ascribed to the oxygen atom's greater ability to destroy the spherical symmetry of the S atom. Calculated molecular properties were in good agreement with experiment. Of particular importance is the fact that the calculated elements of the molecular-quadrupole moment tensor were close to the values recently determined experimentally by Pochan, Stone and Flygare.[8] Values of the third moments, octupole moment tensor, diamagnetic shielding tensor, electric field gradient tensor, and O^{17} quadrupole coupling constants were predicted. On the basis of ab initio electric field gradients[1,4,9] and experimental S^{33} quadrupole coupling constants[10-12] for OCS, H_2S and SO_2, we deduce nuclear electric-quadrupole moments: $Q(S^{33}) = -0.062$ b and $Q(S^{35}) = 0.043$ b. To these values we attach a reliability of 10%.

Microwave spectroscopists have studied the hyperfine structure (hfs) of NO_2 in great detail.[13-15] We have carried out the first

Table I. Calculated and experimental magnetic hfs parameter for NO_2. All entries are in units of 10^{24} cm^{-3}.

Hyperfine parameters at the nitrogen nucleus	SCF no d functions	SCF with d functions	Experiment
$\|\psi(0)\|^2$	2.597	3.101	3.08[a]
$(3\hat{r}_a - 1)/r^3$	-4.125	-4.122	-3.88[a]
$(\hat{r}_b - i\hat{r}_c)/r^3$	4.360	4.211	3.36[a]
Hyperfine parameters at the oxygen nucleus			
$\|\psi(0)\|^2$	0.230	0.300	0.71[b]
$(3\hat{r}_a^2 - 1)/r^3$	-3.462	-3.178	-4.71[b]
$(\hat{r}_b - i\hat{r}_c)/r^3$	3.843	3.585	5.04[b]
$3\hat{r}_a\hat{r}_b/r^3$	1.524	1.579	--

[a] Reference 14

[b] Reference 15

ab initio calculations[5] of the magnetic hfs parameters of NO_2. In the Hartree-Fock approximation, these magnetic hfs parameters depend only on the form of the unpaired $6a_1$, molecular orbital. Our calculated SCF energy, -204.0679 hartrees, was much lower than the best previous calculation[16] on NO_2; the resulting molecular properties should be rather close to the Hartree-Fock values. The theoretical results (with and without d functions on N and O) are compared with experiment[14] in Table I. The notation used to define the hfs parameters is that of Bird et al.[13] For the off-diagonal parameter $3\hat{r}_a \hat{r}_b/r^3$, there is no experimental value.

It is seen that the inclusion of d functions does not qualitatively change the sp results. The agreement with experiment is very good for the parameters with respect to the ^{14}N nucleus. The near perfect agreement for the nitrogen spin density $|\psi(0)|^2$ must be considered somewhat fortuitous in light of the great importance[3] of correlation effects in atomic spin densities. However, the excellent agreement can be partially understood by the fact that the NO_2 nitrogen spin density is five times larger than that of the free nitrogen atom. The O^{17} parameters are in qualitative agreement with experiment, but are all of insufficient magnitude.

From previous comparisons[1] with very accurate SCF results,[17] it is reasonable to assume that our calculated parameters $(3\hat{r}_a^2 - 1)/r^3$ and $(\hat{r}_b - i\hat{r}_c)/r^3$ are within 10% of the true HF values. Thus our logical conclusion is that it is the single configuration HF approximation itself which is primarily responsible for the disagreement between calculated and experimental hfs parameters with respect to the oxygen nucleus. To summarize, the present NO_2 results seem to indicate that accurate SCF calculations can yield at least qualitatively correct magnetic hfs parameters for polyatomic free radicals. However, the present results also imply that the effects of electron correlation may be significant.

The correlation energy[18] of a closed-shell atom or molecule can be approximated as a sum of pair correlation energies.[19] We have previously formulated a symmetry-adapted pair correlation theory for open-shell systems,[20] and have recently[7] applied it to the ^4S ground state of the nitrogen atom. Using a very large basis set of Slater-type orbitals, we have accounted for about 95% of the correlation energy by considering 1633 ^4S configurations, constructed from 19,530 distinct Slater determinants.

It is also possible to approximate an expectation value f in terms of pair correlations.[19] In our formulation,[20] such an expectation value is given by

$$f \approx f\,(\text{first-order}) + \sum_{ij} f(i,j)\,,$$

where f (first-order) is the expectation value obtained from the variational first-order wave function,[20] which includes the Hartree-Fock configuration plus other configurations arising from the fact that the nitrogen 2p orbital is not fully occupied. The term f(i, j) is the effect on the expectation value of electron correlation involving orbitals i and j.

We have carried out this analysis for the hyperfine structure of ^4S N, which is solely determined by the Fermi contact interaction or spin density $|\psi(0)|^2$. Table II summarizes our results. The effects of single excitations are included in the first-order wave

Table II. Electron correlation and the hyperfine structure of ^4S N. Spin densities $|\psi(0)|^2$ are given in atomic units.

Type Configuration	$\lvert\psi(0)\rvert^2$
$1s^2\ 2s^2\ 2p^3$	0.0
$1s \rightarrow s_i$	-0.4969
$1s \rightarrow d_i$	0.0030
$2s \rightarrow s_i$	0.5106
$2s \rightarrow d_i$	0.1026
Sum of above	0.1193
Variational first-order result	0.0714
$1s^2$ correlation	-0.0346
1s 2s correlation	+0.0042
1s 2p correlation	+0.0106
$2s^2$ correlation	+0.0600
2s 2p correlation	-0.0363
$2p^2$ correlation	-0.0187
Final result	0.0748
Experiment[a]	0.0972

[a] W. W. Holloway, E. Luscher, and R. Novick, Phys. Rev. 126, 2109 (1962).

function, and it can be seen that these effects are not additive. The true correlation effects, of which the $2s^2$ contribution is the largest, are much smaller than the "core polarization" effects included in the first-order wave function. Our final spin density is 77% of experiment, much more accurate than, for example, the unrestricted Hartree-Fock result.[2] The reasons for the remaining discrepancy with experiment could be either a) lack of completeness in our basis set, or b) nonadditivity of the summation procedure used. We intend to test both of these approximations on two simpler but nontrivial systems, the $1s^2 2s2p\ ^3P$ and ^1P states of Be.

References

1. S. Rothenberg, R. H. Young, and H. F. Schaefer, J. Am. Chem. Soc. 92, 3243 (1970).

2. P. S. Bagus, B. Liu, and H. F. Schaefer, Phys. Rev. A 2, 555 (1970).

3. H. F. Schaefer and R. A Klemm, Phys. Rev. A 1, 1063 (1970).

4. S. Rothenberg and H. F. Schaefer, J. Chem. Phys. 53, 3014 (1970).

5. H. F. Schaefer and S. Rothenberg, J. Chem. Phys. 54, 1421 (1971).

6. S. Rothenberg and H. F. Schaefer, Mol. Phys. (in press).

7. O. R. Platas and H. F. Schaefer, Phys. Rev. (in press).

8. J. M. Pochan, R. G. Stone, and W. H. Flygare, J. Chem. Phys. 51, 4278 (1969).

9. A. D McLean and M. Yoshimine, reported by M. Krauss, Nat. Bur. Std. Technical Note 438 (U. S. Government Printing Office, Washington, D. C., 1967).

10. J. R. Eshbach, R. E. Hillger, and M. W. P. Strandberg, Phys. Rev. 85, 532 (1952).

11. C. A. Burrus and W. Gordy, Phys. Rev. 92, 274 (1953).

12. G. R. Bird and C. H. Townes, Phys. Rev. 94, 1203 (1954).

13. G. R. Bird, J. C Baird, A. W. Jache, J. A Hodgeson, R. F. Curl, A. C. Kunkle, J. W. Bransford, J. Rastrup-Andersen, and J. Rosenthal, J. Chem. Phys. 40, 3378 (1964).

14. R. M. Lees, R. F. Curl, and J. G. Baker, J. Chem. Phys. 45, 2037 (1966).

15. P. D Foster, J. A Hodgeson, and R. F. Curl, J. Chem. Phys. 45, 3760 (1966).

16. C. R Brundle, D. Neumann, W. C. Price, D. Evans, A W. Potts, and D. G. Streets, J. Chem. Phys. 53, 705 (1970).

17. A. D. McLean and M. Yoshimine, J. Chem. Phys. 47, 3256 (1967).

18. P. O. Löwdin, Adv. Chem. Phys. 2, 207 (1959).

19. R. K. Nesbet, Adv. Chem. Phys. 14, (1969).

20. H. F. Schaefer, Ph. D. thesis, Stanford University, April 1969.

III. Physical, Inorganic, and Analytical Chemistry

X-Ray Crystallography

The Crystal and Molecular Structure of the Monohydrated† Dipyridinated Magnesium Phthalocyanin Complex

Mark S. Fischer,* David H. Templeton, Allan Zalkin, and Melvin Calvin

Several phthalocyanin (Pc) structures have been determined previously, notably those by Robertson and his coworkers,[1-5] by Brown,[6,7] and Vogt, Zalkin and Templeton.[8] The phthalocyanin ring was found to be roughly planar with the central metal atom in the plane of the molecule. One of the metallophthalocyanin structures studied by Robertson was the magnesium derivative[3] (MgPc). Through a comparison of cell parameters and qualitative intensity data, Robertson showed that MgPc, when synthesized and crystallized in an anhydrous environment, was isomorphous with the other β-Pc's. In the course of an investigation of several porphyrin crystals, we observed that MgPc, when crystallized from an uncovered pyridine solution, i.e., a nonanhydrous environment, had different cell dimensions from the other Pc's studied. We were interested in obtaining a Pc structure of high accuracy, because this would be an important ingredient in the calculation of molecular orbitals and the related chemical ground and excited-state properties. A detailed structure of a magnesium porphyrin, particularly if solvated, would help in understanding the chemistry of magnesium porphyrin complexes[9-11] and of chlorophyll.[12]

The MgPc used in this structural analysis was obtained from E. I. duPont Code No. DD 1383. The violet-colored powder was recrystallized from an air-exposed solution in pyridine by slow evaporation to dryness. The deep violet crystals which remained were well formed.

Weissenberg photographs indicated Laue symmetry 2/m, and the observed systematic absences corresponded to the monoclinic space group $P2_1/n$. A General Electric XRD-5 x-ray diffractometer equipped with a copper x-ray tube, a manual quarter-circle Eulerian-cradle goniostat, and a scintillation counter was used to measure both the cell dimensions and the intensity data. The cell dimensions are $\underline{a} = 17.098 \pm 0.003$ Å, $\underline{b} = 16.951 \pm 0.003$ Å, $\underline{c} = 12.449 \pm 0.003$ Å, and $\beta = 105.88 \pm 0.03°$. The observed density of 1.368 ± 0.015 g-cm^{-3}, which was determined by flotation in an aqueous $ZnBr_2$ solution, agrees well with the calculated density of 1.364 for a formula weight of 713.1 of one MgPc, one water, and two pyridine molecules, for $Z = 4$, and for a unit cell volume of 3470 Å^3.

The data were taken on a crystal of approximate dimensions $0.1 \times 0.1 \times 0.15$ mm. All of the independent reflections lying within one quadrant of a sphere in reciprocal space corresponding to spacings ≥ 1.006 Å ($2\theta \leq 100°$) were counted for 10 sec, with both crystal and counter stationary. Of the 3558 reflections measured, 3323 were above background.

Normalized structure factors were calculated using Wilson's method,[13] and the phases of the highest 181 E values ≥ 2.0 were estimated from Long's sign determination program.[14] Fourier maps were calculated from the phased $\underline{E}$ values and showed all but six atoms of the Pc molecule with the magnesium atom at the fractional coordinates (.30, .00, .55). The positions of the hydrogen atoms were found in a later difference map and, when included in the least-squares refinement with isotropic-temperature factors, resulted in an R of 0.07. An extinction correction was applied, and the final discrepancy values were R = 0.050 for 3323 nonzero data, and R = 0.056 for all 3558 data. The standard deviation of an observation of unit weight was 1.02. In a Fourier synthesis of ΔF based on the final structure, no peak was higher than 0.18 e Å^{-3}.

The asymmetric unit contains one MgPc,

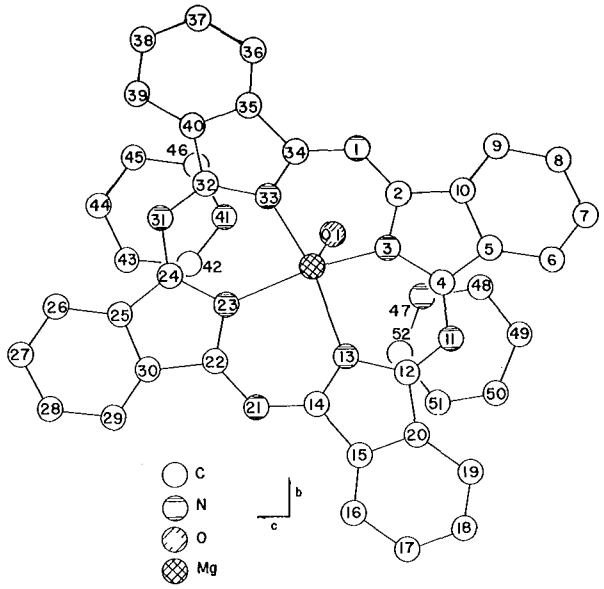

Fig. 1. The molecular structure projected on the bc plane. (XBL 691-18)

one water and two pyridine molecules. Figure 1 shows the atoms in the asymmetric unit projected on the bc plane and indicates the numbering system. The MgPc molecule itself is nonplanar, and the magnesium atom is 0.496 Å out of the plane of the central nitrogen atoms directed towards the water molecule. The two hydrogen atoms of the water molecule are hydrogen-bonded to the two pyridine molecules of crystallization. The intramolecular bond distances and bond angles are the same as those in other Pc's[1-8] to within the respective standard deviations. The precision, however, is greater by at least a factor of two for the MgPc in this work than for the other Pc's. The environment around the central

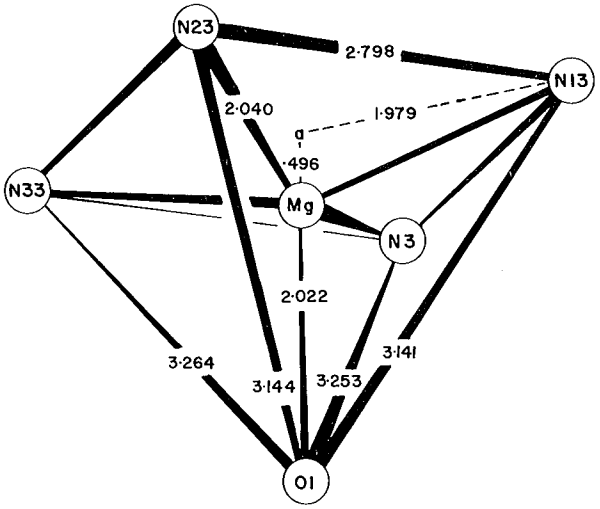

Fig. 2. The central region of the MgPc molecule. The equivalent Mg-N and N ··· N distances have been averaged. (XBL 691-15)

magnesium atom is depicted in Fig. 2. The O·· N distances of 2.739±0.004 Å to N(41) and 2.753±0.004 Å to N(47) are somewhat shorter than the average hydrogen-bonded O ·· N distance of 2.80 Å. The O-H-N angles to the N(41) and N(47) atoms are 172±4° and 167±4°, respectively. The relatively short O ·· N distances and the stability of the air-exposed crystals indicate that the hydrogen bonds are relatively strong. Chemically equivalent bond lengths and angles for the Pc averaged in accordance with C_{4v} (4mm) symmetry are shown in Fig. 3. Because of the deviations from planarity, the atomic positions in MgPc do not conform to C_{4v} symmetry, and they differ from even mirror symmetry by more than 30 times the standard deviations for some atoms. However, each pyrrole and benzene ring is planar within 0.02 Å.

The packing arrangement of the unit cell is shown in Fig. 4. The MgPc molecules are close together in pairs about the centers of

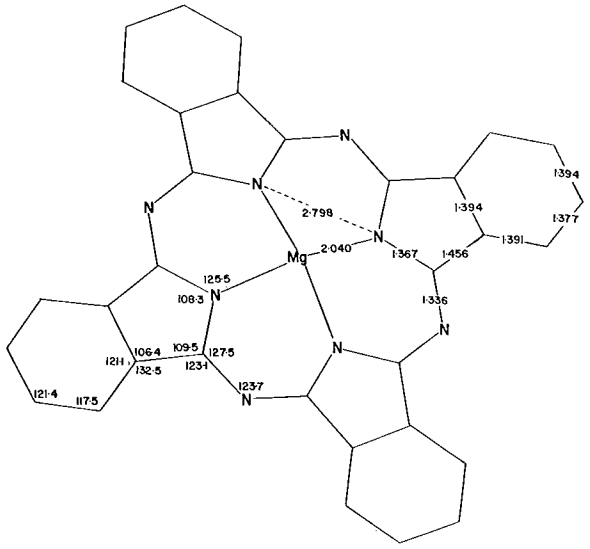

Fig. 3. Averaged bond distances (in Å) and bond angles (in °) of MgPc. Standard deviations of the bond distances and angles are 0.006 Å and 0.4°. (XBL 691-17)

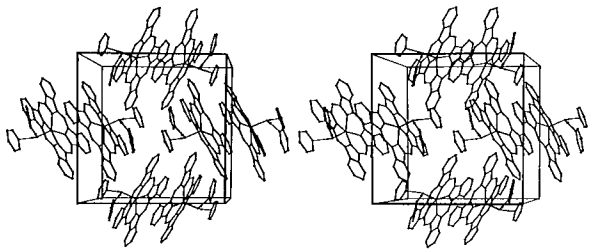

Fig. 4. Stereoscopic view of the contents of the unit cell looking down the c axis. All C, N, O, and Mg atoms, as well as the two hydrogens of the water molecule, are shown. The hydrogen bonds connecting the water molecule to the two pyridine molecules are drawn in. (XBL 691-162)

symmetry at $(\frac{1}{2}0\frac{1}{2})$ and $(0\frac{1}{2}0)$. The planes through the pyrrole nitrogens are separated by only 3.506 Å, a distance only slightly greater than the 3.354 Å interplanar spacing of graphite[15] and the 3.34 Å spacing of β-CuPc.[6] The closest atomic approach between molecules not involving hydrogen atoms is 3.239 Å. In comparison, the shortest non-H-atom intermolecular contacts in some other porphyrin structures are 3.43 Å in porphine,[16] and 3.38 Å in H_2Pc[2] and NiPc,[4] which are all longer than the shortest distance in MgPc. Packing forces can explain qualitatively some of the deviations from planarity of the Pc ring. The ruffling is in the proper direction to maximize the distance between overlapping groups in the "dimer."

The existence of hydrated pentacoordinate magnesium atoms may help to explain the role of water in both the pyridine-Mg porphyrin complexing reported by Seely[9] and the biosynthesis of Mg porphyrins. Seely has reported at least a twofold enhancement of poly(vinyl pyridine) complex formation when 0.016% H_2O was added to the nitromethane solutions of the Mg porphyrins or MgPc. The water molecules might act as a pivot between the polymer and porphyrin molecules. This would allow more movement of the porphyrin molecules so that other pyridine molecules would be available for complexing.

Plane et al.[11] have studied the effect of pyridine as a catalyst in the insertion and removal of magnesium atoms in water solutions of deuteroporphyrins. When pyridine or some other catalyst is present, a complex similar to the $MgPc \cdot H_2O \cdot 2C_5H_5N$ might be formed. The hydrogen-bonding of the bridging water molecule, with its donation of positive charge to the pyridines, would leave the oxygen more electronegative. The more electronegative oxygen, in turn, would attract the magnesium atom to form a stable complex with the magnesium atom halfway out of the plane. This would be in contrast to a more nearly planar molecule when pyridine is not present. From steric considerations alone, it would be more difficult to insert and remove the magnesium atom from the more planar configuration. In the biosynthesis of chlorophyll, a similar Mg coordination compound might be involved with the imidazole of a histidine, for example, replacing the pyridine molecules. In fact, Baum and Plane[17] found that the imidazole, as well as several other nitrogen bases, can act as catalysts similar to pyridine.

Footnotes and References

†Condensed from UCRL-19554.

*Present Address: Dept. of Physiological Chem., Medical School, University of Wisconsin, Madison, Wisconsin.

1. J. M. Robertson, J. Chem. Soc. 1935, 615.

2. J. M. Robertson, J. Chem. Soc. 1936, 1195.

3. R. P. Linstead and J. M. Robertson, J. Chem. Soc. 1936, 1736.

4. J. M. Robertson and I. Woodward, J. Chem. Soc. 1937, 219.

5. J. M. Robertson and I. Woodward, J. Chem. Soc. 1940, 36.

6. C. J. Brown, J. Chem. Soc. A1968, 2488.

7. Ibid., p. 2494.

8. L. H. Vogt, A. Zalkin, and D. H. Templeton, Inorg. Chem. 6, 1725 (1967).

9. G. R. Seeley, J. Phys. Chem. 71, 2091 (1967).

10. N. A. Magwiyoff and H. Taube, J. Am. Chem. Soc. 90, 2796 (1968).

11. R. Snellgrove and R. A. Plane, J. Am. Chem. Soc. 90, 3185 (1968).

12. K. Sauer, E A. Dratz, and L. Coyne, Proc. Nat. Acad. Sci. U. S., 61, 17 (1968); K. Ballschmiter and J. J. Katz, J. Amer. Chem. Soc. 91, 2661 (1969).

13. A. J. C. Wilson, Nature 150, 152 (1942).

14. R. E. Long, Ph. D. thesis, University of California, Los Angeles, 1965.

15. J. B. Nelson and D. P. Riley, Proc. Roy. Soc. 57, 477, 486 (1945).

16. L. E. Webb and E. B. Fleischer, J. Chem. Phys. 43, 3100 (1965).

17. S. J. Baum and R. A. Plane, J. Amer. Chem. Soc. 88, 910 (1966).

The Crystal Structure of $POBr_3$: Space Group and Refinement by Least Squares†

Lieselotte K. Templeton and David H. Templeton

Olie and Mijlhoff[1] (referred to below as OM) reported a crystal structure for phosphoryl bromide, $POBr_3$, which had been refined in space group $Pn2_1a$, but which deviated from Pnma by no more than 0.08 Å. OM stated that refinement by least squares in Pnma "proved to be disastrous" and that "R did not drop below 36%," whereas (with ani-

sotropic thermal parameters) R was reduced to 11.3% in $Pn2_1a$. We found it incredible that one could not get approximately as good agreement in space group Pnma as in $Pn2_1a$ with such slight deviations from the higher symmetry. Indeed, calculations we have made with the data of OM have reduced R below 11.3% in both space groups. We must conclude that there was some defect in the program used by OM or some error in using it.

Dr. Olie kindly gave us a list of 432 nonzero structure factors. We refined the structure using the CDC-6600 computer and the full-matrix least-squares program of Dr. Allan Zalkin of this laboratory.

Starting with coordinates similar to those reported by OM (but naturally with Br(1) and Br(3) equivalent), four cycles of refinement in Pnma with individual isotropic thermal parameters reduced $R = \Sigma | \Delta F | / \Sigma | F_o |$ to 0.192. Further cycles yielded no significant improvement. With individual anisotropic thermal parameters, eight cycles reduced R to 0.110 and $R_2 = (\Sigma (\Delta F)^2 / \Sigma F_o^2)^{1/2}$ to 0.128.

In space group $Pn2_1a$, one expects strong correlation between the parameters of Br(1) and Br(3), especially when these atoms are given independent anisotropic thermal parameters, and refinement difficulty would not be unexpected. However, refinement in this space group (with 45 independent parameters rather than the 28 used in Pnma) reduced R to 0.103 and R_2 to 0.119 without incident, other than considerably slower convergence than we achieved in Pnma. The resulting coordinates correspond to bond distances and angles less symmetrical than those found in space group Pnma, and the thermal parameters correspond to more asymmetric motion. We regard these results to be unacceptable as a plausible model of the molecular structure.

An examination of the discrepancies among the observed and calculated structure factors (for Pnma) revealed 11 that were larger than 15 electrons. Refinement in Pnma after removal of these 11 reflections resulted in R = 0.097, R_2 = 0.106, and a bond distance P - O = 1.49(2) Å. This sensitivity of the result to deletion of data suggests that more detailed analysis of this data set is unjustified without more specific knowledge of the accuracy of individual measurements, and that the standard deviations reported in this note are not to be taken too literally. The 11 reflections in question include the 10 which also gave the worst agreement in space group $Pn2_1a$, and therefore their poor agreement in Pnma cannot be taken as evidence for the noncentric group.

We conclude that there is no reason to reject Pnma as the correct space group, and that this description should be used unless and until some better evidence to the contrary is found.

Footnote and Reference

†Condensed from UCRL-20430, January 1970; submitted to Acta. Cryst.

1. K. Olie and F. C. Mijlhoff, Acta Cryst. B25, 974 (1969).

The Crystal Structure of 2, 4, 4-Triphenyl-1, 2-Diazetidine-3-One-1-Carboxylic Acid, Ethyl Ester

Helena Ruben, Hans Bates,† Allan Zalkin, and David H. Templeton

The structural formula of 2, 4, 4-triphenyl-1, 2-diazetidine-3-one-1-carboxylic acid, ethyl ester is

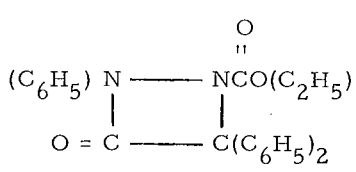

The compound was synthesized by Dr. Robert Kerber,[1] and an x-ray diffraction study of it was undertaken to verify the postulated structure.

The original material was recrystallized from ethanol. X-ray diffraction powder patterns of the material before and after recrystallization were identical. The triclinic crystals are yellow, well formed and stable in air. X-ray diffraction data were obtained with a Picker FACS-1 automatic diffractometer and copper radiation for a crystal of approximate dimensions 0.1×0.2×0.4 mm. A total of 6599

intensities were measured yielding 3279 independent structure factors.

The space group is $P\bar{1}$ with cell dimensions $a = 9.877 \pm 0.005$, $b = 14.037 \pm 0.005$, $c = 8.420 \pm 0.005$ Å, $\alpha = 94.45 \pm 0.01°$, $\beta = 108.97 \pm 0.01°$, and $\gamma = 112.67 \pm 0.01°$.

The structure was found by application of the $\Sigma 2$ relation[2] to various arbitrary combinations of signs for seven strong normalized structure factors. The first set used failed to give a solution. A second set of starting reflections yielded one combination of signs for which the E-map (based on 395 independent terms) showed all 28 nonhydrogen atoms.

Least-squares refinement gave an R factor: $R = \Sigma(|F_0| - |F_c|)/\Sigma|F_0|$ of 0.150 after three refinements with isotropic temperature factors. With anisotropic temperature factors on all of the nonhydrogen atoms, the R factor went to 0.084. A difference Fourier showed all 20 hydrogen atoms, which were then included in the least-squares refinement with isotropic temperature factors.

After an extinction-type correction was applied, the final R value for 2688 data with nonzero weights was 0.036. The R value for all 3279 data was 0.045.

The dimensions of the four-membered diazetidine ring are shown in Fig. 1. The ring deviates from planarity by about 0.03 Å for each atom. The interatomic distances in the molecule are comparable to the distances found in other compounds with similar type chemical arrangements. The complete unit cell is shown in a sterographic view in Fig. 2.

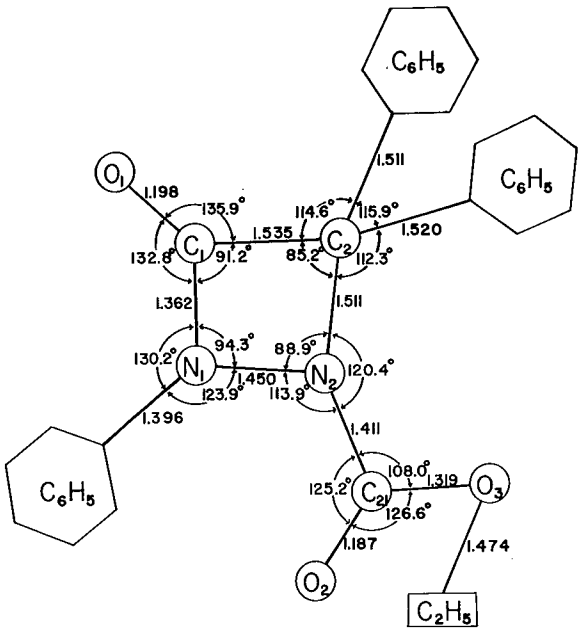

Fig. 1. Schematic drawing showing distances in Å and angles in degrees. (XBL 706-1220)

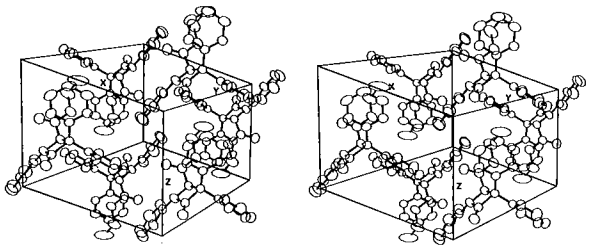

Fig. 2. Stereoscopic view of a unit cell showing the packing. (XBL 706-1218)

Footnote and References

†Summer student, 1969.

1. Dr. Robert Kerber, Dept. of Chem. S. U. N. Y. at Stony Brook, N. Y.

2. H. Hauptman and J. Karle, Solution of the Phase Problem I. The Centrosymmetric Crystal. A. C. A. Monograph No. 3. (Brooklyn: Polycrystal Book Service 1953).

The Crystal Structure of Tris-(2-aminoethyl)aminochlorozinc(II) Tetraphenylborate†

Rodney J. Sime,* Richard P. Dodge,‡ Allan Zalkin, and David H. Templeton

Although the coordination number five is generally regarded as an unusual one for first-row transition metals, a steadily increasing number of five-coordinated complexes are being described in the literature. In particular, the quadridentate ligands, tris(2-dimethylaminoethyl) amine and tris(2-aminoethyl) amine appear to form a variety of five-coordinated complexes with the first-row transition metal ions from manganese(II) to zinc(II). These ligands are more conveniently designated Me_6tren and tren, respectively. In general, these may be formulated as $[M^{II}(Me_6tren)X]Y$ or $[M^{II}(tren)X]Y$. The relative stability of five coordination among these metals is favored in the order (Co, Cu, Zn) > (Fe, Ni) > Mn.[1] Because of the increased bulkiness of Me_6tren, it forms more stable five-coordinated complexes than tren. Me_6tren complexes have been described, for which M = Mn, Fe, Co, Ni, Cu and Zn, and for which X = Y = Cl, Br, I, NO_3, and ClO_4.[2,3] Much physical evidence, including conductivity, spectral and magnetic measurements, indicated that these complexes are five-coordinated. In addition, crystal structure determinations of $[Cu(tren)(NCS)]SCN$[4] and $[Co(Me_6tren)Br]Br$[5] reveal that the copper and cobalt ions are indeed five-coordinated, and situated nearly at the center of a slightly distorted trigonal bipyramid. A recent report[6] on the structure of Zn(tren)(NCS)(SCN) also shows trigonal bipyramidal symmetry. More recently, a series of complexes have been prepared, $[Zn(tren)X]Y$, for which X = Cl, Br and I, and Y = X, ZnX_3, and $B(C_6H_5)_4$.[7] We report here the crystal structure of the five-coordinated complex $[Zn(C_2H_4NH_2)_3NCl]B(C_6H_5)_4$.

Dr. L. V. Interrante kindly supplied us with some well-formed, colorless, prisms of $[Zn(tren)Cl]B(C_6H_5)_4$, which were suitable for the structural analysis. The determination of the space group and cell dimensions was made using the precession technique with molybdenum radiation. A General Electric XRD-5 x-ray diffraction apparatus equipped with a molybdenum x-ray tube, a scintillation counter, a pulse-height discriminator, and a quarter-circle Eulerian-cradle type of goniostat was used to collect the intensity data. A total of 2692 independent intensities were measured, of which 233 were recorded as having zero intensity. A stationary-crystal, stationary-counter technique with a 10-sec count for each reflection was used. Lorentz and polarization corrections were made, but no correction was made for either absorption or extinction.

The monoclinic unit cell contains four formula units and has cell dimensions; $\underline{a} = 13.76 \pm 0.04$, $\underline{b} = 10.33 \pm 0.03$, $\underline{c} = 20.35 \pm 0.06$ Å, and $\beta = 95.0 \pm 0.2°$. The extinctions observed were consistent with space group $P2_1/c$. The density calculated from the x-ray data is 1.304 g/cm^3. The crystals were observed to float readily in carbon tetrachloride (d = 1.58 g/cm^3).

Trial coordinates for the zinc and chlorine atoms were derived from the Patterson function. A three-dimensional electron density map revealed the locations of the remaining 35 nonhydrogen atoms. Three cycles of least-squares refinements with isotropic temperature factors gave a value of R = 0.12, and several more cycles of least-squares calculations with anisotropic thermal parameters reduced R to 0.077. All the hydrogen positions were located from a difference Fourier and included in the least-squares refinements with isotropic temperature factors. Due to the limitation of the memory size of our computer, ≈ 120,000 words, it was necessary to divided the structure into two parts and refine them alternately. We arbitrarily divided the structure into the cation and anion, and refined one group while the other was kept fixed. All atoms with the exception of the hydrogen atoms were treated with anisotropic temperature factors. For the very last two cycles of refinement, the scheme was changed and the parameters of all 37 heavy atoms were refined in one pass; and the 40 hydrogen atoms were included but not refined. The final R value for 2193 nonzero weighted data is 0.041, and 0.059 for all 2692 data. The standard deviation of an observation of unit weight is 1.02.

In the cation, the zinc is surrounded by four nitrogen atoms--from the tren molecule--and one chlorine atom. A view of the structure down the Cl-Zn bond reveals the nearly threefold symmetry of the coordinated tren molecule neatly coiled about the zinc atom (Fig. 1). The zinc atom lies 0.38 Å out of the plane of the three nitrogen atoms (N2, N3, and N4) and toward the chlorine atom. The Cl-Zn-N1 angle is 176.4 ± 0.2° and indicates some of the deviation from true C_3 symmetry. It is of interest to note that the N(1)-Zn-N(5) angle reported in Zn(tren)(NCS)(SCN)[6] is

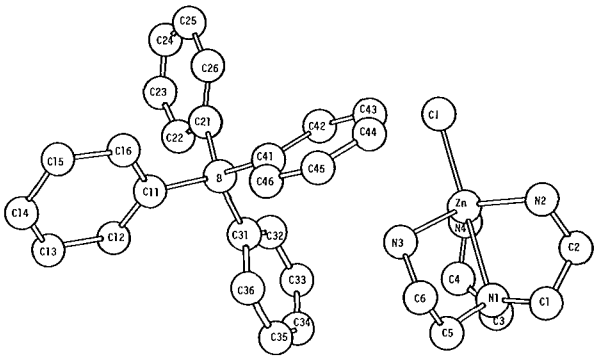

Fig. 1. The $Zn(C_2H_4NH_2)_3NCl$ cation drawn to indicate the nearly threefold nature of the cluster. (XBL 6910-5729)

176.8 ± 0.2°. The Zn-Cl distance of 2.308 Å is well within the range of distances, 2.223 to 2.358 Å, reported in the $[Co(NH_3)_6][ZnCl_4]Cl$ structure.[8]

The structure of the tetraphenylborate anion and its position relative to one of its cation neighbors is shown in Fig. 2. The molecular packing can be described in terms of a distorted sodium chloride type structure. The positions of the bulky anions are near a cubic-closest-packing based on a pseudo-cubic pseudo-cell with axes a, b + c/2, b - c/2. The cations are in octahedral holes in this anion packing, as in the sodium chloride structure, with atoms N1 close to the centers of the holes.

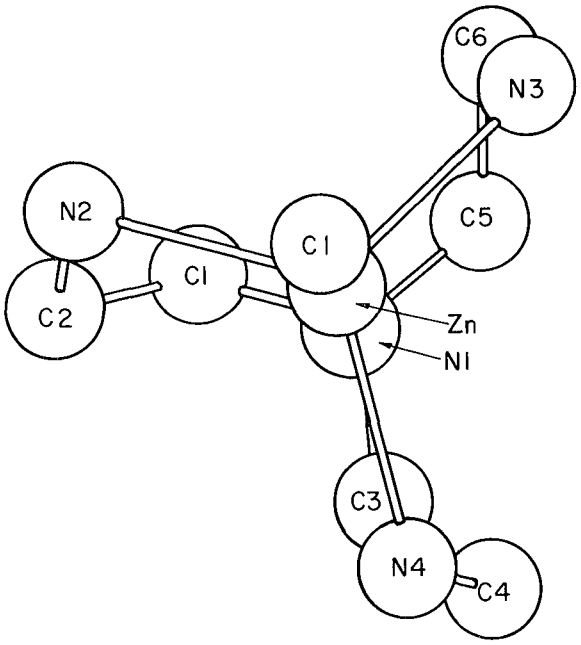

Fig. 2. Structure of the anion and its relation to one of its cation neighbors. (XBL 712-2938)

Footnotes and References

†Submitted to Inorg. Chem.

*Present Address: Department of Chemistry, Sacramento State College, Sacramento, California.

‡Present Address: Department of Chemistry, College of the Pacific, Stockton, California.

1. M. Ciampolini and P. Paoletti, Inorg. Chem. 6, 1261 (1967).

2. M. Ciampolini and N. Nardi, Inorg. Chem. 5, 41 (1966).

3. M. Ciampolini and N. Nardi, Inorg. Chem. 5, 1150 (1966).

4. P. C. Jain and E. C. Lingafelter, J. Am. Chem. Soc. 89, 724 (1967).

5. M. DiVaira and P. L. Orioli, Inorg. Chem. 6, 955 (1967).

6. G. D. Andreetti, P. C. Jain, and E. C. Lingafelter, J. Am. Chem. Soc. 91, 4112 (1969).

7. L. V. Interrante, Inorg. Chem. 7, 943 (1968).

8. D. W. Meek and J. A. Ibers, Inorg. Chem. 9, 465 (1970).

The Crystal and Molecular Structure of Sodium Gold(I) Thiosulfate Dihydrate†

Helena Ruben, Allan Zalkin, M. O. Faltens, and David H. Templeton

One of the authors, Faltens,[1] had been studying aurous (Au^I) and auric (Au^{III}) compounds to elucidate their internal bonding. Auric and aurous compounds are textbook examples of dsp^2 (square planar) and sp (linear) hybridization respectively. Similar electric-field gradients about the gold atoms might be expected, which would result in similar elec-

tric-quadrupole splittings as observed via the Mössbauer effect. Instead the quadrupole splitting for the aurous chloride was observed to be an order of magnitude larger than that for the auric chloride. In addition to the gold halides (AuCl and $AuCl_4$), other gold compounds including sodium gold(I) thiosulfate dihydrate[2] were investigated, and the quadrupole splitting was observed to be consistently larger for the aurous compounds. This crystal structure investigation of $Na_3Au(S_2O_3)_2 \cdot 2H_2O$ was undertaken to remove any doubt of its identity, and to establish the nature of the environment of the gold atom.

Sodium gold(I) thiosulfate[3] was prepared from $HAuCl_4 \cdot 4H_2O$ and $Na_2(S_2O_3) \cdot 5H_2O$. The compound was recrystallized from a water-ethanol solution in the dark. A clear thin crystal plate approximately .17×.07 ×.02 mm was mounted along the c axis on the end of a thin Pyrex glass fiber. The crystal was aligned on our G. E. XRD-5 hand operated diffractometer equipped with a quarter-circle Eulerian cradle, scintillation counter, pulse-height discriminator, and a molybdenum anode tube. Some 1965 independent reflections were observed and counted for 10 sec each, using the stationary-crystal stationary-count technique.

The space group is $P2_1/a$ and contains four formula units per monoclinic unit cell. The cell dimensions at 23° are $a = 18.206 \pm .006$, $b = 11.355 \pm .006$, $c = 5.436 \pm .004$ Å and $\beta = 97.87 \pm .05°$. The errors are subjective estimates. The volume is 1113 Å^3. With four formula units per unit cell, the density calculated from the x-ray data is 3.14 g/cm^3, compared with the literature value of 3.09 g/cm^3.[8]

The gold atom location was deduced from a three-dimensional Patterson function. A Fourier phased by the gold atom revealed the locations of the sodium and sulfur atoms. A least-squares refinement of this partial structure using isotropic temperature factors resulted in $R = \Sigma(|F_o| - |F_c|)/\Sigma|F_o| = 0.21$. With anisotropic thermal parameters on the gold atom, the R factor went to 0.19. A difference Fourier revealed the oxygen atom locations. Final full-matrix, all atoms anisotropic, refinement brought R to 0.078 after several cycles. After making an absorption correction, the final R = 0.055. Attempts at locating the hydrogen atoms were unsuccessful. This is not surprising considering the large absorption correction and the presence of such a heavy atom as gold.

The most significant structural feature in this compound is the $Au(S_2O_3)_2^{-3}$ anion. A schematic drawing is shown in Fig. 1. The S - Au - S angle is short of linearity by about 3.5°. The variation of the Au - S(3) and

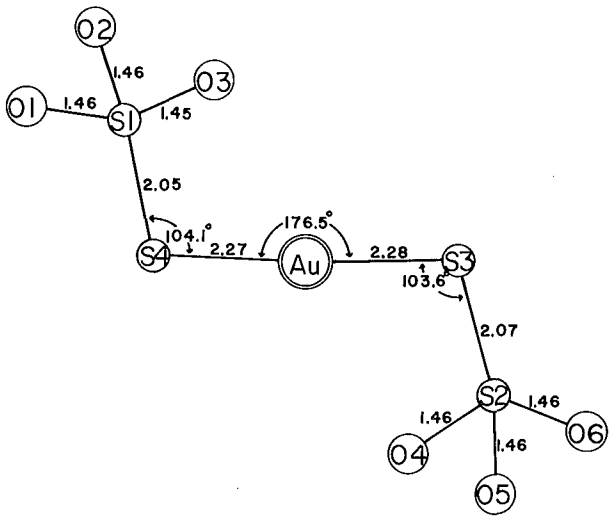

Fig. 1. Schematic drawing of $Au(S_2O_3)_2^{-3}$ anion. (XBL 707-1307)

Au - S(4) bond distances are less than 3σ, and is not considered to be significant. The Au - S - S bond angles are somewhat intermediate between a right and a tetrahedral angle, being somewhat closer to the latter. Each terminal sulfur atom has a tetrahedral configuration of a sulfur and three oxygen atoms, and is consistent with thiosulfate in sodium thiosulfate pentahydrate.[4] The two S-S distances in the anion are different by 3 to 4° from each other, but this difference is not considered by the authors to be significant. The average S - O bond distance of all six such bonds is 1.458 Å, and no individual value is greater than one σ from this average. The dihedral angle between the two planes defined by atoms Au - S(3) - S(2) and Au - S(4) - S(1) is 67°.

The three sodium ions are well encapsulated in irregular coordination spheres of oxygen atoms ranging in distances of 2.36 to 2.63 Å. Two of these oxygen atoms come from the two waters of hydration. Na(2) is also coordinated by six oxygen atoms at distances from 2.35 to 2.54 Å, only one of which comes from a water of hydration. Na(3) is coordinated by five oxygen atoms ranging in distance from 2.34 to 2.53 Å, with one water of hydration involved.

Of the four hydrogen atoms, only one appears to be involved in a "conventional" O - H ····· O hydrogen bond within this structure; that would be the donor water oxygen O(8) to O(5) at a distance of 2.75 Å. Hydrogen bonding to sulfur is not particularly a well-documented effect, and if it does exist, must certainly be fairly weak. Bonds of this type have been suggested[5] in S - H ····· S at

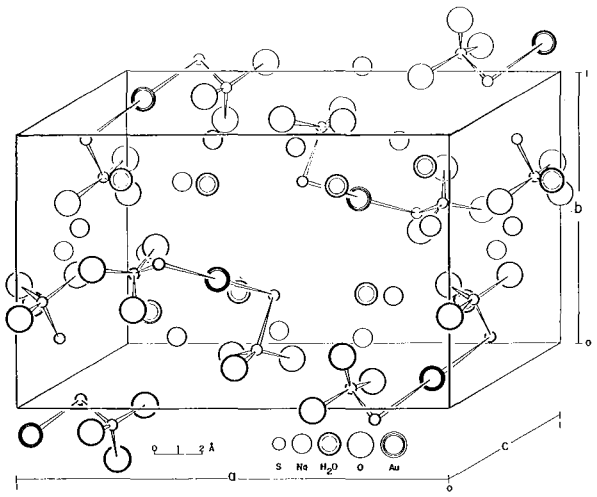

Fig. 2. Molecular packing in the unit cell of sodium gold (I) thiosulfate dihydrate. (MUB-11229)

Fig. 3. Stereo view of sodium gold(i) thiosulfate dihydrate showing examples of the bonding of the sodium atoms. (XBL697-959)

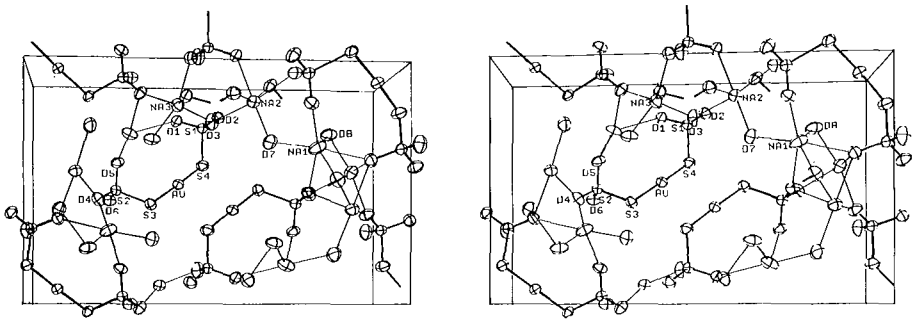

3.86 Å and N - H ····· S at 3.35 Å. In this context, water O(7) in this structure offers a possibility of O - H ····· S hydrogen bonding. O(7) is centered in an irregular tetrahedron consisting of Na(1), Na(2), S(3), and S(4). The S(3) - O(7) - S(4) angle is approximately 104° and the O - S distances are 3.24 and 3.33 Å respectively.

Footnote and References

†Condensed from UCRL-19985.

1. M. O. Faltens, Ph. D. thesis, UCRL-18706, January 1969.

2. Gold sodium thiosulfate, long known clinically as Sanocrycin, has been and is presently being used in some medical circles for the treatment of illnesses including arthritis, tuberculosis and leprosy.

3. H. Brown, J. Am. Chem. Soc. 49, 958 (1927).

4. P. G. Taylor and C. A. Beevers, Acta Cryst. 5, 341 (1952).

5. W. C. Hamilton and J. A. Ibers, Hydrogen Bonding in Solids (W. A. Benjamin Inc., New York, 1968), p. 167.

Structure Determination of 5-Methyl-2, 2, 4-Triacetyl-1, 3-Oxathiole†

Helena Ruben, David Kaplan,* Allan Zalkin, and David H. Templeton

Professor Edward C. Taylor and co-workers at Princeton University synthesized a material which they suggested contained one sulfur atom with two double bonds. We undertook the structure determination to check this possibility. The results of the determination showed the material to be 5-methyl-2, 2, 4-triacetyl-1, 3-oxathiole which does not contain the postulated sulfur bonding, but rather is a cyclic compound with normal bond geometry.

The colorless crystals sent to us by Dr. Taylor were recrystallized from hexane. X-ray powder diffraction patterns of the material before and after recrystallization were identical. Our initial irradiation of some of these crystals in air resulted in a degradation

of the x-ray patterns during exposure to x rays, and encapsulation in glass capillaries seemed to stabilize the crystals. Initially we studied two crystals with different orientations using the Weissenberg film technique. The resulting photographs indicated monoclinic symmetry with systematic absences characteristic of space group $P2_1/c$. A XRD-5 x-ray diffraction apparatus equipped with a molybdenum x-ray tube, a scintillation counter, a pulse-height discriminator, and a quarter-circle Eulerian-cradle type of goniostat was used. A stationary-crystal stationary-counter technique, with a 10-sec count for each reflection, was used to measure a total of 1119 independent intensities, of which 193 were recorded as having zero intensity.

The primitive cell contains four formula units of $C_{10}H_{12}O_4S$. It is monoclinic with dimensions $a = 9.817 \pm 0.004$, $b = 9.089 \pm 0.03$, $c = 13.776 \pm 0.002$ Å, and $\beta = 114.35°$. The calculated density is 1.35 g/cm^3 which corresponds to 1.3 ± 0.2 g/cm^3 measured by flotation.

The positions of four carbons and a sulfur atom were estimated from a three-dimensional Patterson function. A least-squares refinement was run on these atoms, followed by a three-dimensional Fourier calculation. Even though one of the original carbon atoms was found to be incorrect, this map showed all of the atoms except hydrogen. A least-squares refinement of the structure with isotropic temperature factors resulted in R = 0.13. With anisotropic temperature factors on all of the nonhydrogen atoms, the R factor went to 0.10. Hydrogen atom positions

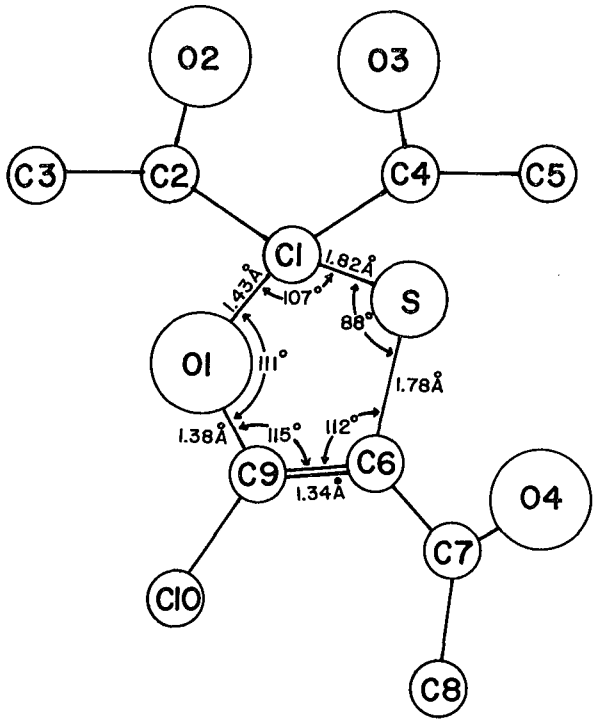

Fig. 1. Schematic drawing showing bonds and angles in the ring. (XBL 708-1791)

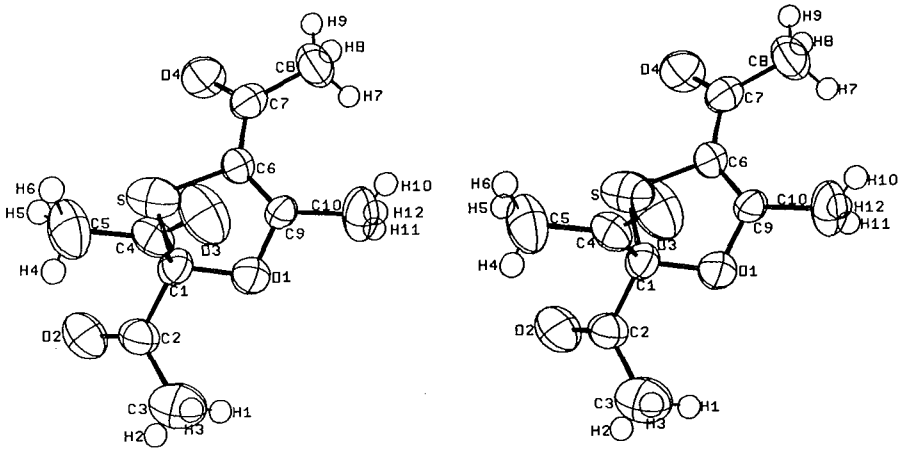

Fig. 2. Stereoscopic view of the 5-methyl-2, 2, 4-triacetyl-1, 3-oxathiole molecule. (XBL 693-325)

Physical and Inorganic Chemistry

were estimated from geometric considerations and a difference Fourier, and were included in the least-squares refinement with isotropic thermal parameters. Since these thermal parameters refined poorly, the hydrogen thermal parameters of each methyl group were tied together. The final R value for 824 data with nonzero weights is 0.06. The R value for all 1119 data is 0.105. The standard deviation of an observation of unit weight is 0.99.

The 1, 3 oxathiole ring is shown in Fig. 1. The C1-O1 and C1-S distances are typical of bond lengths found in paraffinic and saturated heterocyclic type compounds.[1] C6-C9 is a typical double bond at 1.34 Å. C9-O1 and C6-S are shorter by 0.05 and 0.04 Å respectively than the C1-O1 C1-S distances, probably because of their proximity to the double bond. The ring itself is puckered, with the sum of the internal angles being 533° opposed to a theoretical 540° for a planar model. This puckering is evident in the stereoscopic view of the molecule shown in Fig. 2.

Footnotes and Reference

†Condensed from UCRL-19982, November 1970.

*Summer student, 1968.

1. Table of Interatomic Distances and Configurations in Molecules and Ions, Supplement 1956-1959, edited by L. E. Sutton (Chemical Society, Burlington House, London W1).

Trigonal Californium Trifluoride

B. B. Cunningham and Paul Ehrlich†

From measurements of the lattice parameters of the actinide trifluorides through berkelium, and radius-ratio considerations analogous to those used by Thoma and Brunton[1] for the lanthanide halides, Peterson[2] predicted that californium trifluoride would exhibit the trigonal LaF_3 structure type above 700°C. In a number of preparations of CfF_3, initially subject to temperatures of about 700° and then cooled to room temperature in about 30 minutes, Fujita[3] observed only the orthorhombic-structure space group $Pnma(D_{ah}^{16})$ for CfF_3.

In connection with attempts to prepare californium metal, a 1 μg sample of CfF_3 was accidentally heated to about 800°C and cooled rapidly. An x-ray powder diffraction pattern of this material was obtained at room temperature. The pattern indicated that the trifluoride possessed trigonal-symmetry space group $P3C1(D_{3d}^4)$ (isostructural with LaF_3), and this showed that the prediction of inversion temperatures may be made with as much confidence from radius-ratio considerations in the actinide trifluorides as in the lanthanide trifluorides.

The identification of the high-temperature CfF_3 structure is based on measurement and indexing of 35 diffraction lines from $2\theta = 25.16°$ to $2\theta = 146.66°$, with good agreement between observed and calculated 2θ values. Additionally, satisfactory agreement was obtained between visually estimated and calculated intensities. A least-squares fit of the diffraction data gave $a = 6.922 \pm 0.001$ Å and $c = 7.085 \pm 0.002$ Å.

Footnote and References

†Participant in 1970 Summer Undergraduate Program.

1. R. E. Thoma and G. D Brunton, Inorg. Chem. 5, 1937 (1966).

2. Joseph Richard Peterson, Ph. D. thesis, UCRL-17875, October 1967.

3. Dennis Ken Fujita, Ph. D. thesis, UCRL-19507, November 1969.

Preparation and Determination of the Crystal Structures of Californium and Einsteinium Metals

B. B. Cunningham and T. C. Parsons

Both californium and einsteinium metals have been prepared on a microgram scale and their crystal structures determined.

The metals were made first by distilling metallic lithium in vacuo onto unheated samples of californium or einsteinium trifluoride, and then quickly raising the temperature of the lithium-coated trifluoride to ≈800°C to promote the reaction:

$$CfF_3 + 3\ Li = Cf + 3LiF$$

or

$$(EsF_3 + 3Li = Es + 3LiF).$$

It is essential that the reduction be completed quickly, because both metals have such high volatilities that they are rapidly vaporized even at temperatures as low as 800°C.

The reaction products, consisting of californium or einsteinium metals mixed with lithium fluoride, were transferred to thin-walled quartz capillary tubing for x-ray study. Diffraction lines from lithium fluoride were not observed in relatively short exposures, because these elements have lower scattering power for x rays than the actinide metals. In the case of californium, a total of 11 diffraction lines were obtained from the best sample. Except for a weak line at $2\theta = 82.70°$, all lines could be indexed on the basis of a face-centered cubic structure with a lattice parameter of 5.40 Å. Other preparations of californium metal yielded similar fcc phases with lattice parameters within ±0.02 Å of the 5.40 value from the best preparation. This variation may be outside experimental error and represents a slight variable contamination of the actinide metal with residual metallic lithium.

Only enough einsteinium was available for a single preparation on a 1 μg scale. The technique of preparation was the same as that used for californium metal. The reaction product formed by heating EsF_3 with Li metal yielded four diffraction lines, which also could be indexed on the basis of an fcc structure with a lattice parameter of 5.41 Å.

Metallic radii calculated for californium and einsteinium metals in the observed face-centered cubic structures are 1.86 ± 0.02 Å. This value is closer to the radius observed for ytterbium in the metallic state (1.94 Å) than to the metallic radius of curium (1.74 Å). Since ytterbium exhibits a metallic valence of two and curium a metallic valence of three, the data suggest that the average number of electrons per atom which participate in bonding in californium and einsteinium metals is substantially below three. This conclusion is consistent with the much greater ease of vaporization of these elements as compared with the preceding metals of the actinide series.

The ready volatility of californium and einsteinium metals may eventually form the basis for fast and efficient methods of separation and purification of these elements from the lighter and less volatile actinides.

After initial preparation of californium metal at Berkeley as described above, it was made at Los Alamos Scientific Laboratory by L. B. Asprey, who vaporized the metal onto a quartz-collecting plate from a mixture of californium oxide and molten lanthanum metal.

Californium metal has been produced by essentially the same technique in this laboratory, except that the vapor was collected on a thin film of lithium fluoride on a tantalum backing. Mixtures of the metal and lithium fluoride were scraped from the plate into x-ray capillaries. Diffraction patterns are those of a face-centered phase with a lattice parameter similar to that observed in the low-temperature reductions.

Bis(cyclooctatetraenyl)neptunium(IV) and Bis(cyclooctatetraenyl)plutonium(IV)†

D. G. Karraker,* J. A. Stone,* E. R. Jones, Jr.,‡ and N. Edelstein

The reduction of cyclooctatetraene in tetrahydrofuran (THF) solution produces the planar $C_8H_8^{2-}$ anion (COT), which can react with the anhydrous metal chlorides of transition metals to form M(COT), $M_2(COT)_3$, or $M(COT)_2$ complexes. The preparation of $U(COT)_2$ extended these complexes to actinide-(IV) ions.[1] Crystallographic studies[2] show that the $U(COT)_2$ molecule has a "sandwich" structure, with planar eight-member COT rings above and below the U^{4+} ion in D_{8h} molecular symmetry. An electronic configuration has been proposed[1] for $U(COT)_2$ that involves participation of the 5f orbitals in the bonding of the complex, with the orbitals of the two 5f electrons of the U^{4+} ion mixing with the degenerate E_{3u} orbitals of the ligands in essentially a nonbonding combination.

$Np(COT)_2$ and $Pu(COT)_2$ were prepared to allow a more thorough investigation of the nature of the actinide(IV)-COT compounds. Mössbauer measurements on $Np(COT)_2$ provide information on the shielding of s orbitals by outer electrons, and thus on the participation of ligand electrons in the bonding. Magnetic susceptibility measurements on $U(COT)_2$, $Np(COT)_2$, and $Pu(COT)_2$ (U^{4+}, $5f^2$; Np^{4+}, $5f^3$; Pu^{4+}, $5f^4$) narrow the choice of applicable molecular models.

The x-ray diffraction patterns for $U(COT)_2$, $Np(COT)_2$, and $Pu(COT)_2$ are identical within the precision of the measurements. A diffraction pattern calculated from the single-crystal structure of $U(COT)_2$ agreed with the experimental diffraction patterns of $Np(COT)_2$ and $Pu(COT)_2$; from this evidence all three actinide(IV)-COT compounds are isomorphous.

The Mössbauer spectrum of $Np(COT)_2$ at 4.2°K is similar to the spectrum of $NpCl_4$ (except for isomer shift), with combined magnetic and quadrupole splitting. Analysis of the spectrum to extract the hyperfine parameters and the isomer shift is straightforward. Table I gives the isomer shift relative to NpO_2, the magnetic splitting parameter $g_0\mu_N H_{eff}$, and the quadrupole coupling constant $eqQ/4$ for $Np(COT)_2$ at 4.2°K. Velocity spectra were also taken between 4.2 and 80°K in a search for possible magnetic transitions. Above ≈ 40°K, the recoilless absorption became too

Table I. $Np(COT)_2$ isomer shift and hyperfine parameters at 4.2°K, from Mössbauer spectra.

Isomer shift,[a] (cm/sec)	$g_0\mu_N H_{eff}$, (cm/sec)	eq Q/4, (cm/sec)
+ 2.50 ± 0.05	6.0 ± 0.1	-0.5 ± 0.1

[a] Relative to NpO_2.

weak to observe; magnetic splitting was present in all spectra below this temperature. No magnetic transitions were observed between 4.2 and 40°K.

Powdered samples of $U(COT)_2$ and $Np(COT)_2$ were paramagnetic from 4.2 to 45°K; $Pu(COT)_2$ was diamagnetic over the same temperature range. The susceptibility of $Pu(COT)_2$ in the low-temperature region was unusually large, and showed a strong increase with decreasing temperature. Room-temperature measurement of the $Pu(COT)_2$ diamagnetic susceptibility yielded $(-218 \pm 92) \times 10^{-6}$ emu/mol, which agrees with the -187.5×10^{-6} emu/mol calculated from the susceptibilities of the aromatic COT ligands (-73.4×10^{-6} emu/mol) and the diamagnetism of the Pu^{4+} ion (-40.8×10^{-6} emu/mol). The low-temperature magnetic susceptibilities of $U(COT)_2$ and $Np(COT)_2$ follow a Curie-Weiss law, $\chi = C/(T + \theta)$. A least-squares fit of the data to a Curie-Weiss law gives $\mu_{eff} = 2.43$ μ_B for $U(COT)_2$ and $\mu_{eff} = 1.81$ μ_B for $Np(COT)_2$.

The magnetic data for actinide(IV)-COT compounds can be interpreted qualitatively from a simple crystal-field model with suitable approximations. The interpretation is based upon these assumptions: (a) Only the lowest crystal-field state is populated within the temperature range of the magnetic measurements. Because the first excited state is $>> kT$, the paramagnetic susceptibilities should follow a Curie-Weiss law, as observed experimentally. (b) There is no mixing of J states by the crystal field. (c) The effects of intermediate coupling are assumed to be small and therefore neglected.

Because of the C_8 rotational axis in these molecules, the off-diagonal terms in the crystal-field Hamiltonian for the 5f electrons are all zero. The crystal-field potential may be written as $V_c = V_2^0 + V_4^0 + V_6^0$. The crystal field states are pure J_z states, doublets of $\pm J_z$ for $J_z \neq 0$, and a singlet state for $J_z = 0$. Assuming a point-charge model is valid, then $V_2^0 >> V_4^0 >> V_6^0$, and $V_c \approx V_2^0$. The energy matrix involves matrix elements of the type

$$\langle J, J_z | V_2^0 | J, J_z \rangle = [3J_z^2 - J(J+1)]B_2^0$$

which are tabulated in the literature. Considering the J = 4 ions, U^{4+} ($^3H_3$) and Pu^{4+} ($^5I_4$), the lowest state will be either the doublet $J_z = \pm 4$ or the singlet $J_z = 0$, depending upon whether the crystal-field parameter B_2^0 is positive or negative. A similar calculation for Np^{4+} ($^4I_{9/2}$) shows that the lowest state is either $J_z = \pm 9/2$ or $J_z = \pm 1/2$.

The crystal-field parameter B_2^0 is defined as $B_2^0 = \alpha_J A_2^0 \langle r^2 \rangle$, where α_J is the second-degree operator equivalent factor and is a function of L and S; A_2^0 is a parameter that depends upon the lattices and charges of the ions; and $\langle r^2 \rangle$ is the expectation value for the magnetic (5f) electrons. The parameter A_2^0 may be calculated exactly in the limit of a point-charge model, and is approximately constant for the three isomorphous actinide(IV)-COT compounds. $\langle r^2 \rangle$ is necessarily positive, so the algebraic sign of B_2^0 depends on the signs of α_J and A_2^0. α_J is negative for U^{4+} and Np^{4+} and positive for Pu^{4+}. Assuming A_2^0 is positive, $J_z = \pm 4$ is the lowest state for U^{4+}, $J_z = \pm 9/2$ for Np^{4+}, and $J_z = 0$ for Pu^{4+}. Experimentally, $U(COT)_2$ and $Np(COT)_2$ are paramagnetic, therefore, the assumption of $A_2^0 > 0$ must be correct.

Calculating the magnetic moments from $\mu_{eff} = g |J_z| \beta$, $\mu_{eff} = 3.20$ μ_B for $U(COT)_2$ and 3.27 μ_B for $Np(COT)_2$, and $Pu(COT)_2$ is diamagnetic.

These calculated values for paramagnetic susceptibilities are larger than the experimental values, but may be brought to agree by correcting for the reduction in orbital size caused by covalent contributions to the metal-ligand bonding. Introducing the orbital reduction factor k, and replacing the conventional Zeeman operator

$$\vec{L} + 2\vec{S}$$

with

$$k\vec{L} + 2\vec{S},$$

The Landé g_J becomes $g_J - (1 - k)(2 - g_J)$. A value of $k = 0.8$ agrees with experimental results.

The value of $k = 0.8$ required to achieve a satisfactory fit with experiment appears quite low for actinide compounds, and corresponds to values found for d transition metal compounds. However, this value of k can be interpreted to imply a strong interaction between the actinide ions and the COT orbitals, and is qualitatively consistent with the pronounced covalency inferred from the Mössbauer results of $Np(COT)_2$.

Footnotes and References

†Condensed from J. Am. Chem. Soc. 92, 4841 (1970).

*Savannah River Laboratory, E. I. du Pont de Nemours & Co. Aiken, S. C. 29801

‡ORAU Research Participant, Summer 1969.

1. A Streitwieser, Jr. and U. Müller-Westerhoff, J. Amer. Chem. Soc. 90, 7364 (1968).

2. A. Zalkin and K. N. Raymond, ibid., 91, 5667 (1969).

Electron-Probe Microanalysis of Pottery Materials

B. B. Cunningham and T. C Parsons

Electron-probe microanalysis equipment recently has become available in the Nuclear Chemistry Division. It seems to us that this technique could be of great value in helping to classify sherd materials in terms of the composition of clay used in the manufacture of the original objects, of which the sherds are the remains.

The capability of the microprobe technique to give rapidly the elemental compositions of particles as small as about $1\ \mu m^3$, providing rapid identification of mineral components which are almost invariably present in clays, would greatly increase the specification of these materials over that provided by neutron-activation analysis alone. It has long been known to mineralogists that the majority of mineral species is subject to all least small variations in composition as a consequence of localized conditions of formation or alteration. Study of mineral species would therefore help to localize possible points of origin of the clay materials.

In preparation for extended study of potsherd materials, we have photographed x-ray spectra of almost all of the elements up through uranium at various ranges of energy, to obtain reference spectra as they appear when produced with our microprobe equipment. We also have obtained reference spectra from different mineral species purchased from commercial suppliers, as well as spectra of two samples of modern clays sold by ceramics supply stores.

The results have been quite encouraging of the value of this technique to help solve problems in archaeology. Mislabeling of three of the commercial samples of mineral species was apparent after only a few minutes' examination with the microprobe. Samples of the same mineral species obtained from different geographical localities gave readily distinguishable spectra, because of differences in minor components. A sample of labradorite (a sodium-calcium aluminosilicate) was found to contain minute inclusions of a hitherto-unreported mineral species composed of equal amounts of chromium and nickel--surely, a geographically localized association of a common mineral with a very uncommon one.

The two modern clay samples gave distinctly different spectra, although one might expect modern clay materials to be more refined and thus more homogeneous in composition than the clays used by ancient potters. Very little application of the method to potsherd materials has been possible as yet.

However, some initial observations have been made on three potsherds of an age estimated as 3000 years, collected from the island of Cyprus. One of these sherds had been found, by neutron-activation analysis, to have an almost unbelievably high content of silver--namely about 0.3%. We found this same sherd to contain a high percentage of phosphorous, and to show correlation between abundances of silver and phosphorous in different localities within the same small fragment of the clay.

Another sherd consisted of clay of exceptional homogeneity, except for well-crystallized particles, some of which approached 0.5 mm in size. The mineral was quickly identified as fluoropatite, with a small amount of chloride as a substitutional impurity.

However, intensive use of the microprobe equipment will not be possible for some months yet, until equipment becomes available for storage of output data on magnetic tape and a program has been prepared for computer processing of the analytical information.

We are indebted to Joe Jaklevic, Donald Landis, Donald Malone, and members of the Nuclear Chemistry Electronic Instrumentation Group for construction and installation of the x-ray detection and energy analysis system.

We also wish to thank Mrs. Lillian Hill and Miss Lilly Goda for their careful work in preparing many of the element and mineral standards that we have used.

An Introductory Study of Mycenaean IIIC1 Ware from Tel Ashdod

F. Asaro, M. Dothan,† and I. Perlman

Introduction

Tel Ashdod lies in the southern coastal region of Israel about 4.5 km from the sea and 15 km northeast of Ashkelon. Excavations at Tel Ashdod[1,2] in the summer of 1968 turned up an early Philistine stratum (1300-1000 BC)[3] in which were found derivative MycIIIC1 sherds of style and fabric closely similar to pottery found mainly in Cyprus, for example at Sinda[4] and Enkomi.[5] Though the parallels between the Ashdod and the Cypriota MycIIIC1 (including additional sites such as Palaepaphos) are, until now, the closest, comparisons to Ashdod MycIIIC1 also exist on the Greek mainland and in Tarsus.

Analytical Method

The system of neutron-activation analysis employed for determining a large number of elements in pottery has been described in some detail in an earlier publication.[6] Since that article appeared, a number of substantial changes have been introduced to improve the accuracy for certain elements and to measure some elements not previously determined. However, within the accuracies cited, data obtained before and after the changes are of equal value and may be compared with each other. This article is not concerned with methodology, so little further will be said about how the data were obtained. The purpose is to show how such arrays of analytical data may be used to establish the provenience of this particular pottery.

Results

In the system of analysis presently used, calibrations and computer programming have been set to produce analytical data for more than forty elements. The levels for some of these which have so far been encountered in pottery are too low to produce useful information, but there is no added labor in carrying them along in the program once calibrations have been made. For other elements good numbers are obtained, but for a number of reasons we do not use them for general diagnostics. For diagnosing provenience, we choose 18 or 20 elements which, experience has shown, exhibit changes in level more or less independently of each other.

A. Mycenaean IIIC1 Ware - Individual results for 20 elements are given in Table I for this ware. The numbers in Table I are expressed in parts-per-million except for those elements which display the % sign. The error limit shown for each element expresses the precision of the measurement, which is determined by the counting statistics of the radioactivity in the particular measurement. (In most cases the true errors of the determinations are somewhat larger because of a number of factors which will not be explained here.) The numbers in parentheses ending each column are the mean value (M) for the five sherds and the dispersion of compositions expressed as the standard deviation (σ). It is the array of these mean values and standard deviations which establish a group profile for this particular ware. To the extent that a group of only five sherds may be considered a valid statistical array, and that the elements may be considered as independent variables, standard statistical methods may be employed to judge whether any other piece of pottery belongs to this group. For example, two out

of three elements should lie within one standard deviation, and only one in 20 should fall outside of two standard deviations.

Although the entire profile of elements must be used in matching potteries, sometimes a single element or two provides a strong signal that one is dealing with a particular area. In this case, high hafnium values are thus far, in our experience, unique to Tel Ashdod, but probably will also be found for those parts of the general area which share a common geochemical history. The question of provenience in this particular problem is not so much concerned with distinctions between different sites in southern coastal Israel, but whether the pottery came from overseas.

Turning to the spread of abundances among the five sherds, we note that for a number of elements the dispersions are unusually small. The standard deviations, expressed as percentages, are about 2% or less for chromium, iron, lanthanum, tantalum, and titanium. This probably means that we are dealing with a more discrete assemblage than is representative of the site of manufacture as a whole. Only if a much larger collection of sherds were to display such small dispersions could one be confident that such behavior is to be expected from the particular site. We shall return to this point when we compare these five sherds with other materials.

B. Comparison Pottery - The reference material we take to represent local Ashdod sources is also quite scanty. The collection analyzed consists of but five sherds, all of typical Philistine style and fabric. In Table II, under the designation "Tel Ashdod Phil.," we list the mean values and standard deviations for the group of five. At the time these numbers were obtained, we were not measuring aluminum; values for barium, uranium and titanium were less accurate than those now obtainable and represented by the Tel Ashdod MycIIIC1 ware.

If we accept the group of Tel Ashdod Philistine ware as the reference group for that site, then the Tel Ashdod MyCIIIC1 ware, piece by piece, may be compared by statistical analysis to see if they belong to the site. A reference group of only five sherds is likely to be unrepresentative and, as already mentioned, one may expect to find the spread in the composition of some elements to be distorted. For those elements which have unusually small spread, it becomes difficult for other pieces to fall within one standard deviation. If we arbitrarily do not accept standard deviations smaller than 5%, then each of the Tel Ashdod MycIIIC1 pieces is indeed local to Tel Ashdod. In the light of all of the pottery we have analyzed to date, we consider this agreement excellent, but we could not have changed our conclusions on provenience even if the two stylistic groups had differed somewhat. Different pottery technology was obviously employed, and it would not be surprising if the different potters had introduced some composition variance by different practices in refining the raw clay.

The other three columns in Table II give results on groups of MycIIIC1 ware from three sites on Cyprus.[7] It takes no detailed analysis to show that none of the Tel Ashdod MycIIIC1 pieces belong to any of these groups.

Table I. Tel Ashdod MycIIIC1 ware.

Serial number	Run number	Al (%)	Ba	Ca (%)	Co	Cr	Cs	Fe (%)	Hf	La	Lu
ASH 13	275V	5.83±0.20	445±11	5.6±0.2	16.5±0.2	133±2	1.44±0.15	3.64±0.05	15.96±0.15	30.90±0.37	0.492±0.013
ASH 14	275W	5.52±0.21	449±11	6.9±0.3	17.1±0.2	131±2	1.98±0.16	3.49±0.04	14.91±0.14	29.42±0.36	0.488±0.012
ASH 15	275X	5.89±0.29	565±12	5.7±0.3	18.8±0.3	132±2	1.68±0.19	4.19±0.05	12.66±0.13	30.78±0.37	0.453±0.012
ASH 16	275Y	4.87±0.24	504±11	6.7±0.4	17.5±0.2	129±2	1.71±0.17	3.79±0.05	15.04±0.15	29.53±0.36	0.485±0.012
ASH 17	275Z	5.80±0.29	508±11	6.1±0.2	16.1±0.2	127±2	1.51±0.16	3.56±0.05	13.84±0.14	29.26±0.37	0.449±0.012
(M±σ)		(5.58±0.39)	(494±47)	(6.2±0.6)	(17.2±1.0)	(130±2)	(1.67±0.19)	(3.73±0.26)	(14.48±1.23)	(29.82±0.62)	(0.473±0.023)

Serial number	Run number	Mn	Na (%)	Ni	Rb	Sb	Sc	Ta	Th	Ti (%)	U
ASH 13	275V	784±8	0.683±0.009	35±10	72±9	0.40±0.06	12.43±0.04	1.318±0.005	8.58±0.07	0.711±0.008	2.06±0.02
ASH 14	275W	816±9	0.671±0.009	54±12	59±9	0.30±0.05	12.03±0.03	1.333±0.006	8.46±0.07	0.723±0.010	2.02±0.02
ASH 15	275X	877±10	0.702±0.009	29±13	70±11	0.27±0.07	13.38±0.05	1.378±0.006	8.70±0.08	0.747±0.010	1.88±0.02
ASH 16	275Y	819±9	0.605±0.008	66±12	68±10	0.58±0.07	12.61±0.04	1.341±0.006	7.85±0.07	0.720±0.012	1.90±0.02
ASH 17	275Z	744±9	0.640±0.008	42±12	73±9	0.39±0.06	12.08±0.04	1.325±0.006	8.38±0.07	0.726±0.008	1.86±0.02
(M±σ)		(808±44)	(0.660±0.038)	(45±15)	(68±5)	(0.39±0.10)	(12.51±0.49)	(1.339±0.020)	(8.39±0.28)	(0.725±0.011)	(1.94±0.10)

Numbers are in ppm unless designated by % sign. Error limits represent precision of measurement in terms of "standard error." Beneath each column, in parentheses, is the mean value (M) and the standard deviation (σ) for the group of 5 sherds. Note that the spread of values, given by σ, is generally considerably larger than the precision of the measurement.

Table II. Group profiles of Tel Ashdod ware and Cypriote MycIIIC1 wares. [a]

	Tel Ashdod MycIIIC1 (5 pc)	Tel Ashdod Phil. (5 pc)	Enkomi MycIIIC1 (10 pc)	Palaephophos MycIIIC1 (13 pc)	Kition MycIIIC1 (6 pc)
Al(%)	5.58±0.39	–	5.96±0.34	6.17±0.60	6.11±0.31
Ba	494±47	382±121	462±164	590±100	222±21
Ca(%)	6.2±0.6	4.3±1.7	11.3±0.8	7.1±1.6	11.6±2.2
Co	17.2±1.0	19.1±0.8	28.0±4.1	19.9±1.6	20.5±3.6
Cr	130±2	122±5	323±25	100±13	336±26
Cs	1.67±0.19	1.64±0.12	4.38±0.86	3.87±0.26	2.86±0.61
Fe(%)	3.73±0.26	3.99±0.06	4.92±0.15	3.90±0.22	4.14±0.33
Hf	14.48±1.23	13.44±1.94	3.11±0.18	3.17±0.19	2.67±0.26
La	29.82±0.62	29.26±1.20	24.46±0.88	28.12±1.84	18.3±0.73
Lu	0.473±0.023	0.427±0.032	0.337±0.018	0.303±0.023	0.282±0.030
Mn	808±44	806±55	1118±216	932±189	766±94
Na(%)	0.660±0.038	0.624±0.018	1.070±0.240	0.351±0.061	1.094±0.045
Ni	45±15	59±8	272±39	88±15	156±29
Rb	68±5	53±5	79±18	75±8	52±10
Sb	0.39±0.10	0.39±0.09	0.96±0.06	0.52±0.08	0.73±0.17
Sc	12.51±0.49	12.67±0.28	19.98±0.60	14.18±1.01	18.01±1.39
Ta	1.339±0.020	1.295±0.060	0.772±0.023	1.049±0.063	0.586±0.010
Th	8.39±0.28	8.07±0.74	8.68±0.38	7.45±0.41	5.38±0.28
Ti(%)	0.725±0.011	0.697±0.066	0.499±0.066	0.423±0.019	0.395±0.018
U	1.94±0.10	2.13±0.22	3.74±0.59	1.59±0.23	2.18±0.34

(a) The numbers are in ppm unless designated by % sign. Listed are mean values for the group and standard deviations from the mean.

If one does compute by statistical analysis the probability that the Tel Ashdod MycIIIC1 ware does not belong to any of the three Cypriote groups, the numbers become astronomical. Similarly the three Cypriote groups are distinctly different from each other.

The deduction that the Tel Ashdod MycIIIC1 ware is local to Tel Ashdod stems from the fact that it matches the Philistine ware, not from a process of elimination. The question of the provenience of the Cypriote ware is a separate problem that will not be dealt with here. The data on these three groups are presented simply to show how other pottery groups of the same type appear.

To provide visual expression for the data already presented, a bar graph is shown in Fig. 1. The hatched region spanning the bar top represents the standard deviation.

Conclusions

We have already seen that the two groups of Tel Ashdod wares (Philistine and MycIIIC1) match each other in chemical profile as well as can be expected. In form, design, and fabric the MycIIIC1 pieces adhere closely to MycIIIC1 ware from other places, particularly with those found on Cyprus. Contrariwise, the Tel Ashdod MycIIIC1 ware looks distinctly different from the local Philistine ware, yet the clays are the same. These latter facts point strongly to particular pottery-making techniques (kiln conditions) which are different for the two types of wares. It is logical to ascribe the techniques which produced the MycIIIC1 ware as traditional for the potters, and hence that we are dealing with a recently transplanted people. It will be necessary to encounter remnants of pottery which they brought with them before we can hope to tell by our analytical methods where they came from.

Despite our assertion that the pottery under discussion was made locally, the question should properly be asked whether there can possibly be another area of the world whose clays are identical with those of Ashdod. There can never be an unequivocal answer to

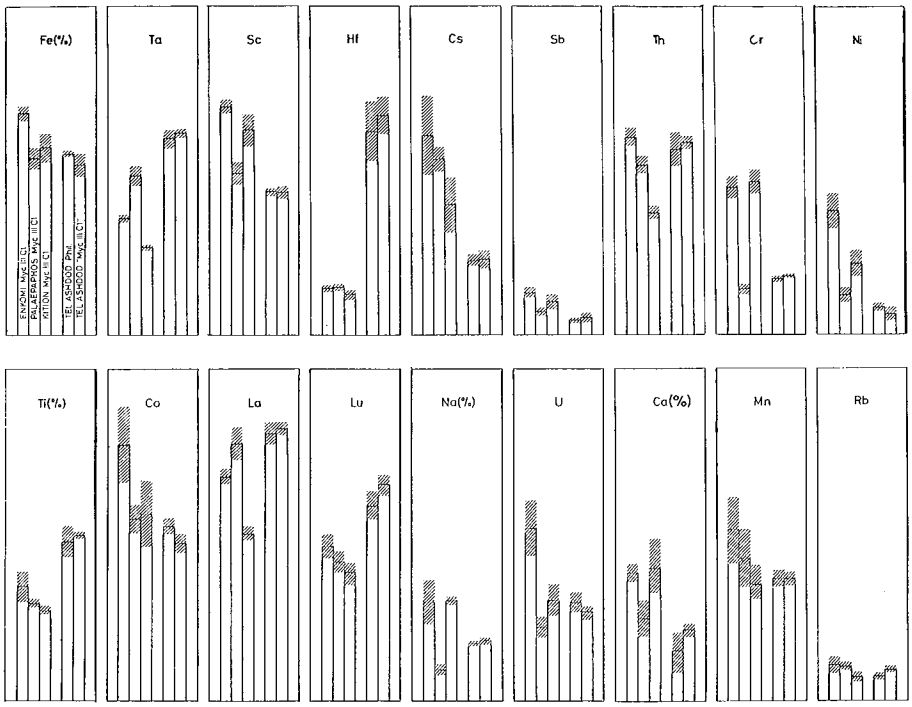

Fig. 1. Bar graph of pottery groups. The top of each bar represents the mean value for the abundance of the element, and the hatched zone is the standard deviation for the group. The identification of each group is shown only in the first box, for the element iron. The bars are drawn to scale in each box, but the different elements are drawn to different scales. (See Table II for numerical values.) (XBL712-2962)

this question, because it is clearly impossible to analyze material from all possible pottery-making sites. All we know at present is that the Tel Ashdod composition is easily distinguished from compositions of pottery thus far analyzed, which have known provenience away from the Ashdod area. To suggest that these MycIIICl pieces were imported also implies the peculiar coincidence wherein people bearing pottery chose to settle in a place which had clay identical with that which they had left.

We have already expressed our debt to Professor Einar Gjerstad and Dr. Vasos Karageorghis for the sherds from Cyprus mentioned in this paper. The Ashdod excavations were sponsored jointly by Carnegie Museum in Pittsburgh, the Pittsburgh Theological Seminary, and the Israel Department of Antiquities. The laboratory work was carried out in Berkeley under the auspices of the U. S. Atomic Energy Commission.

Concerning the laboratory work and data processing, we give especial thanks to the following for their expert and painstaking assistance: Helen V. Michel, Duane Mosier, Susanne Halvorsen, and Edward Minassian. The neutron irradiations were made in the Berkeley Triga Research Reactor.

Footnote and References

†Israel Department of Antiquities and Museums, Jerusalem.

1. M. Dothan, Israel Exploration Journal 18, 253 (1968).

2. M. Dothan, Israel Exploration Journal 19, 243 (1969).

3. M. Dothan and D. N. Freedman, Atiqot, English Series VII (1967).

4. A. Furumark, Opuscula Atheniensia 6, 106 (1965).

5. P. Diakaios, Enkomi (Philipp Von Zabern, Mainz am Rhein, 1969), Vol. I, pp. 263, 267, 271, 272; Vol. IIIa, Pls. 80:34, 81:26, 95:13.

6. I. Perlman and F. Asaro, Archaeometry 11, 21 (1969).

7. We are indebted to Professor Einar Gjerstad and Dr. Vassos Karageorghis for placing at our disposal a large collection of Cypriote pottery, of which the MycIIIC1 pieces cited here make up a small part. Eventually, the results obtained on the analysis of all of these wares will be published in collaboration with these authorities on Cypriote pottery.

Chemical Variations in Obsidian

H. R. Bowman, F. Asaro, and I. Perlman

Introduction

The object of this study has been to make detailed chemical analyses of obsidian from several sources to determine the degree of uniformity and the nature of any irregularities. This information could prove valuable in understanding some of the geochemical and physical processes taking place in the formation of volcanic materials.

The method used was neutron-activation analysis in which over 40 elements were tested for in each sample. This method has been described earlier by Perlman and Asaro[1] along with a detailed analysis of the accuracies attainable.

The elemental compositions of the obsidian samples were determined by comparing the intensities of γ-ray peaks observed in obsidian with those of a calibrated composite standard irradiated with the obsidian. The accuracy of these analyses was therefore limited by the accuracy of the standard. The composite standard used in these measurements was a fired pottery clay (referred to hereafter as "standard pottery"). A detailed description of the preparation and calibration of standard pottery has been given,[1] and the results of chemical analysis of six U. S. G. S. standard rocks using this composite standard will be presented elsewhere.[2]

The three obsidian sources or flows studied were in the Napa, Mt. Konocti, and Borax Lake areas, all located in the central part of northern California.

Source Description

Geologically, the Napa rhyolitic obsidian has been classified as a Pliocene volcanic rock by Osmont.[3] This area, locally referred to as "Glass Mountain," is near St. Helena (Napa County), California and has been described by Heizer.[4]

The Mt. Konocti and Borax Lake areas are adjacent to Clear Lake in Lake County, California, and both of these obsidian flows have been classified by Anderson[5] as Pleistocene (and in part recent). Archaeologically these obsidians are important because they are assumed to be the source materials used in the construction of very ancient Indian artifacts uncovered by Harrington[6] in the Borax Lake region.

Sampling Procedure

The majority of the samples were taken from highway cuts or exposed banks, and were usually found embedded in what appeared to be sand or volcanic ash. Usually four or five samples were taken from a single site or location within a radius of about 10 m. A number of sites were examined along a flow or source. Large blocks of obsidian were broken open and smaller center chips were taken as samples.

A total of 19 samples were examined from Napa County. The Mt. Konocti flow is quite extensive and could be sampled readily for several miles. The samples were taken from highway cuts along Bottle Rock Rd, Lower Lake Rd, or Highway 29. Thirty-nine samples were examined from eight sites. The Borax Lake source is smaller (less than 1 sq mile) and is located south of Borax Lake at the southeast corner of Clear Lake. Thirty-three samples were examined from this area and were taken from exposed banks, as well as from a gravel-pit area at the southern tip of the flow.

Results

The chemical compositions (in ppm or %) of the Napa, Mt. Konocti, and Borax Lake obsidian are given in Tables I, II, and III, respectively. The compositions in Tables I and II are listed under individual sampling

Table I. The chemical composition of Napa (California) obsidian.

Location	Site 40	Site 41	Site 42	Site 43	Average composition	Jack and Carmichael[9]	Griffin & Gordus[10]
No. of samples	5	5	5	4	19	2	3
Element	Composition in ppm or %						
Th	18.0	17.9	18.0	17.8	17.9±0.5	(25), (15)	
Sm	5.98	5.93	5.86	5.95	5.9±0.1		1.1
U	6.89	6.84	6.80	6.86	6.8±0.6		
Na%	3.39	3.37	3.34	3.38	3.37±0.07		3.6±0.4
Sc	2.89	2.86	2.87	2.80	2.86±0.06		3.4±0.4
Mn	147	151	150	147	149±4	(190), (200)	170±20
Cs	15.5	15.4	15.4	14.9	15±1		
La	31.6	31.6	30.8	31.5	31.3±0.7	(40), (40)	57±3
Fe%	0.92	0.93	0.93	0.90	0.92±0.02		1.0±0.2
Al%	6.6	6.6	6.8	6.5	6.6±0.2		
Dy	7.5	7.7	7.8	7.4	7.6±0.4		
Hf	7.0	7.2	7.2	7.3	7.2±0.5		
Ba	450	430	420	430	432±24	(420), (430)	
Rb	200	200	200	210	202±20	(190), (200)	140±20
Ce	67	67	70	66	67±4	(80), (70)	
Lu	0.64	0.63	0.61	0.61	0.62±0.06		
Nd	28	28	29	30	29±4	(30), (25)	
Yb	4.7	4.8	5.0	4.6	4.7±0.6		
Tb	0.98	0.97	0.94	0.99	0.97±0.1		
Ta	0.93	0.90	0.92	0.97	0.93±0.07		
Eu	0.30	0.26	0.25	0.27	0.27±0.03		
K%	3.7	4.6	3.9	3.5	4.0±0.5	3.76	
Sb	1.3	1.3	1.2	1.1	1.2±0.2		
Zn	65	65	70	60	66±10	(55), (50)	
Cr	7.0	7.5	6.5	6.0	7±1		
Ti%					< 0.05	(0.052), (0.054)	
Co					< 40[12]	(15), (15)	
Ca%					< 2		
Ni					< 40	(5), (5)	
V					< 30		
As					< 60		
Cu					< 100	(10), (5)	
Ag					< 2		
Au					< 0.02		
Ir					< 0.01		
Sr					< 400		
Ga					< 100		
In					< 2		

Table II. The chemical composition of Mt. Konocti (California) obsidian.

Location	S1	S2	S3	S4	S5	S6	S7a	S7b	Average composition	Jack and Carmichael[9]	Becker[11]
No. of samples	4	5	4	4	5	5	5	5	37	2	
Element	Composition in ppm or %										
Th	23.3	23.3	23.2	23.0	23.0	22.4	22.0	21.8	22.6±1.0	(25), (30)	
Sm	5.33	5.36	5.28	5.28	5.28	5.37	5.31	5.28	5.3±0.1		
U	7.52	7.60	7.44	7.46	7.45	7.39	7.36	7.23	7.4±0.7		
Na%	2.68	2.66	2.69	2.67	2.65	2.71	2.72	2.79	2.70±0.07		3.96
Sc	5.07	5.07	5.06	5.03	5.12	5.27	5.20	5.23	5.15±0.13		
Mn	186	181	184	184	191	206	205	211	195±13	(230), (230)	
Cs	15.4	15.3	15.4	15.2	15.4	14.6	14.5	14.3	15±1		
La	31.6	32.5	31.8	31.8	31.6	31.8	31.6	31.6	31.7±0.7	(40), (40)	
Fe%	0.96	0.97	0.95	0.95	1.01	1.07	1.05	1.08	1.01±0.05		1.10
Al%	7.1	7.0	7.0	6.9	6.9	7.0	7.0	7.2	7.0±0.1		6.86
Dy	5.9	5.9	6.1	6.1	5.9	6.0	5.9	5.8	5.9±0.4		
Hf	5.7	5.7	5.8	5.7	5.8	6.1	5.7	5.7	5.8±0.4		
Ba	630	640	620	610	620	650	650	660	633±37	(610), (650)	
Rb	230	230	210	220	220	230	210	210	214±29	(215), (215)	
Ce	68	67	68	68	67	66	65	65	66.5±3.5	(80), (70)	
Lu	0.47	0.50	0.49	0.47	0.47	0.46	0.46	0.44	0.46±0.05		
Nd	29	31	29	28	28	28	28	28	28.4±3.7	(30), (30)	
Yb	3.5	3.6	3.5	3.5	3.5	3.4	3.5	3.5	3.5±0.5		
Tb	0.82	0.82	0.83	0.84	0.80	0.80	0.79	0.78	0.80±0.08		
Ta	1.2	1.1	1.2	1.2	1.2	1.2	1.0	0.96	1.1±0.1		
Eu	0.40	0.38	0.40	0.40	0.40	0.40	0.42	0.43	0.40±0.04		
K%	4.4	3.9	3.8	4.3	4.7	4.0	4.0	4.1	4.1±0.4	4.0	3.9
Sb	1.3	1.3	1.4	1.3	1.3	1.2	1.3	1.2	1.3±0.1		
Zn	35	35	35	33	35	35	34	37	35±9	(25), (20)	
Cr	8.3	9.3	5.7	6.8	8.3	7.7	8.6	8.8	7±2		
Ti%	0.13	0.12	0.12	0.12	0.12	0.15	0.16	0.14	0.13±0.02	(0.152), (0.154)	0.15
Co									<2	(15), (15)	
Ca									<2		0.71
Ni									<50	(5), (5)	
V									<30		
As									<50		
Cu									<100	(5), (5)	
Ag									<2		
Au									<0.1		
Ir									<0.01		
Sr									<500	(65), (65)	
Ga									<100	(10), (15)	
In									<3		

sites as well as number of pieces sampled. The compositions in Table III are listed in decreasing order of total iron content for reasons to be described later. The average compositions, in these tables, are absolute values and can be compared with the work of other investigators, some of which is shown on each table. Tables I, II, and III have been divided vertically into sections of decreasing experimental precision, based on Napa chemical compositions. For Napa obsidian Th, Sm, and U compositions are measured to better than 1%. Elements above La are obtained to better than 2%, whereas those above Yb are better than 5%. The chemical precision drops to about 15% by Cr, and the compositions of elements below Cr are given only as upper limits.

The chemical composition of Napa obsidian was found to be very uniform, and the scatter in composition was comparable with the experimental counting errors. The material from Mt. Konocti was found to be nearly uniform, but the scatter in composition was somewhat larger than that expected from counting errors.

The chemical variations observed in Borax Lake obsidian were quite large, and

Table III. The chemical composition of Borax Lake (California) obsidian.

No. of samples	1	2	2	1	4	3	3	6	1	10	Average composition 33	Jack and Carmichael[9] 1	Anderson[5] Several
Elements	Composition in ppm or %												
SiO_2%	71.7±0.1									75.7±0.4			76.53
Th	15.1	15.7	15.7	16.6	16.7	16.7	17.0	17.0	17.4	17.6	16.9±1.0	10	
Sm	5.71	5.73	5.70	5.77	5.76	5.71	5.76	5.81	5.64	5.87	5.8±0.2		
U	5.77	5.99	5.96	6.30	6.25	6.20	6.35	6.45	6.41	6.73	6.4±0.7		
Na%	2.77	2.75	2.73	2.68	2.75	2.76	2.72	2.77	2.75	2.75	2.75±0.7		2.70
Sc	10.48	9.12	8.73	7.41	7.03	6.68	6.19	5.83	5.20	4.71	5.9±1.6		
Mn	342	295	283	230	222	206	186	179	150	135	184±60	240	160
Cs	13.6	14.0	14.1	14.9	15.2	15.0	15.2	15.5	15.1	15.9	15.2±1.2		
La	22.0	21.6	21.6	21.9	22.3	21.9	22.3	22.1	22.1	22.6	22.1±0.7	40	
Fe%	1.88	1.58	1.52	1.25	1.15	1.09	0.97	0.89	0.77	0.67	0.88±0.33		0.86
Al%	6.9	6.8	6.7	6.5	6.8	6.9	6.6	6.7	6.5	6.6	6.7±0.2		6.79
Dy	3.9	3.7	3.8	3.8	3.8	3.7	3.7	3.7	3.7	3.8	3.8±0.3		
Hf	3.9	3.7	3.8	3.8	3.8	3.7	3.7	3.7	3.7	3.8	3.8±0.3		
Ba	140	90	90	70	80	70	60	65	50	60	70±60	80	
Rb	230	200	200	210	260	250	250	210	250	240	220±30	215	
Ce	50	50	49	53	52	51	52	51	52	53	52±3	60	
Lu	0.52	0.51	0.51	0.54	0.50	0.51	0.50	0.52	0.51	0.52	0.51±0.06		
Nd	26	25	24	25	25	27	27	27	27	26	26±4	25	
Yb	3.7	3.9	3.8	4.2	3.9	3.9	4.0	4.1	4.2	3.9	4.0±0.6		
Tb	1.00	1.01	1.02	1.02	1.05	1.06	1.08	1.00	1.06	1.05	1.04±0.10		
Ta	1.2	1.1	1.1	1.2	1.1	1.1	1.1	1.1	1.1	1.2	1.14±0.08		
Eu	0.35	0.30	0.26	0.24	0.19	0.20	0.15	0.15	0.12	0.09	0.15±0.08		
K%	3.3	3.6	4.2	4.1	3.8	4.2	4.2	3.9	4.1	4.5	4.1±0.5		3.9
Sb	1.0	1.5	0.95	1.0	1.0	1.0	0.93	1.1	1.0	1.2	1.1±0.1		
Zn	54	50	49	50	47	43	45	55	44	44	47±9	45	
Cr	40	35	31	26	20	18	15	16	9	10	0.16±9		
Ti%	0.20	0.15	0.14	0.10	0.09	0.08	0.07	0.06	0.03	0.03	0.07±0.05	0.083	0.07
Co	7.0	5.8	5.1	3.4	3.0	2.8	2.0	1.7	0.91	0.36	1.2±1.8	10	
Ca%	2.0	2.0	2.0	1.4	1.6	1.6	1.1	1.2	1.1	0.8	1.3±0.6		0.56
Ni											< 50	10	
V											< 60		
As											< 70		
Cu											< 100	< 5	
Ag											< 2		
Au											< 0.1		
Ir											< 0.01		
Sr											< 600	15	
Ga											< 100	20	
In											< 40		

plots of these variations are shown in Fig. 1 and Fig. 2. The variable elements Fe, Mn, Sc, Co, Ti, Cr, Eu, Cs, Th, and U are apparently interrelated, and the minor and trace element compositions are shown plotted against those of iron, the major variable. Least-squares fits to the data shown in Fig. 1 for Sc and Mn show that the variations from straight-line functions are within the experimental errors. The functional parameters relating the variable composition (in ppm, unless otherwise noted) to the total iron content (in %) are given in Table IV. No other definite correlations could be detected in the remaining elements shown in Table III. The Na content at Borax Lake, for example, was found to be constant within 1.1% . The SiO_2 compositions in Table III are wet chemical results of Ray G. Clem (from this laboratory) using duplicate samples.

Because of these variations, the Borax Lake data in Table III have been grouped (from right to left) according to decreasing iron content. Analysis of different parts of a single piece of obsidian from this area showed no detectable chemical variation. Large variations, however, were observed in different samples from a single sampling location. The linear correlation of compositions could be caused by the mixing in varying amounts of two components prior to solidification of the obsidian. If this is true, then the chemical composition of the obsidian shown in data column 10 of Table III, which is depleted in a number of elements, would closely parallel that of one of the components. We have calculated the admixture of a second component, with a SiO_2 content of 65.7% , which would be needed to give the SiO_2 composition (71.7%) shown in column 1 (the obsidian enriched in a number of elements). This value of the SiO_2 composition (65.7%) is that given by Anderson[5] for the dacite flow underlying the obsidian flow. In Table V, we show the calculated composition of the second component for all elements measured by Anderson and by us. The agreements are excellent and Anderson's values lie within our counting errors except for Na, where the disagreement is two standard deviations.

The fact that the europium composition

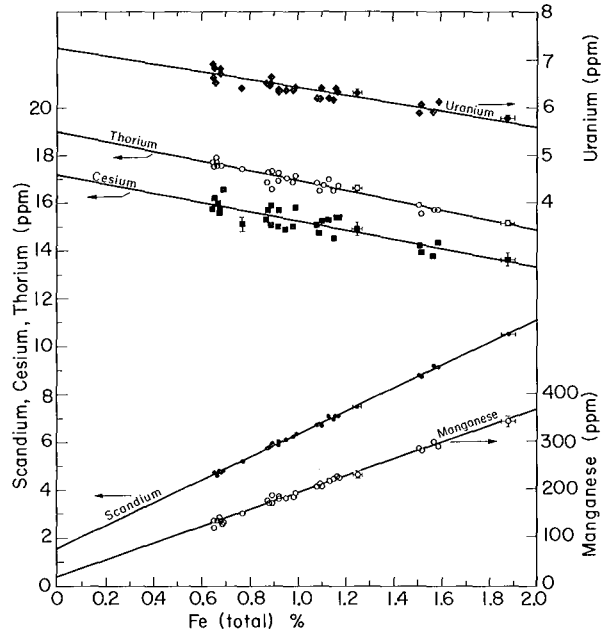

Fig. 1. The chemical abundances of Mn, Sc, Cs, Th, and U in Borax Lake obsidian relative to total iron. (XBL 7011-4158)

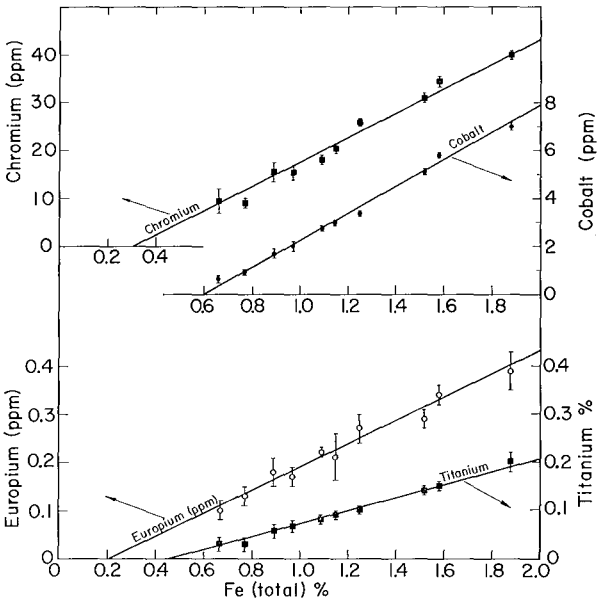

Fig. 2. The chemical abundances of Ti, Eu, Co, and Cr relative to total iron in Borax Lake obsidian for the 10 groups shown in Table III. (XBL7011-4160)

varies relative to the other rare earths is chemically very striking. The relative europium composition in these obsidians is rather depleted compared with other types of rocks. [7]

This europium depletion was found in lunar samples[8] and thought to be connected with fractional crystallization of europium in the 2^+ state. Figure 3 is a plot of these obsidian rare-earth distribution patterns (normalized to chronditic materials) similar to the lunar sample plots.[8] The europium composition used in the Borax Lake pattern is the minimum value and not the average value. One of the lunar rock analysis patterns is shown for comparison.

Summary of Results

The overall characteristics of Napa, Mt. Konocti, and Borax Lake obsidian are as follows:

1. The Napa obsidian is chemically uniform within the precision of these measurements. The Sm, Th, and U compositions are uniform to within 1%.
2. The Mt. Konocti obsidian is for the most part uniform. Some of the compositions

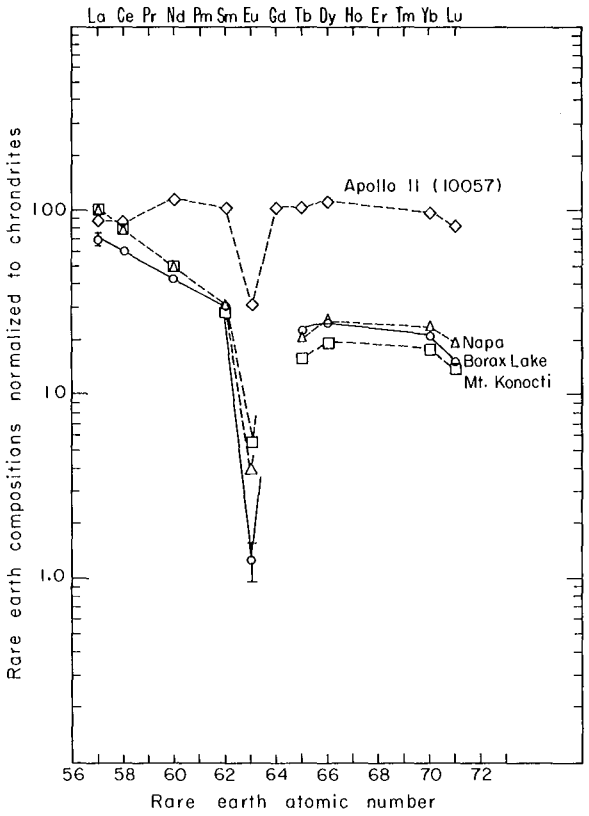

Fig. 3. The rare-earth element distribution patterns for three California obsidian materials normalized to the rare-earth abundances in chondritic materials. The europium depletion anomaly detected in lunar samples (Ref. 8) is shown for comparison. (XBL 711-2572)

Table IV. The functional parameters relating the variable elemental abundances (in ppm or %) to the total iron content (%) in Borax Lake obsidian in the form of M = S(Fe%) + b.

Elements	(Composition in ppm or %)	
(M)	(S)	(b)
Sc	4.76±0.04	1.54
Mn	173.6±3.2	19.3
Eu	0.212±0.013	-0.044
Cr	25.5±1.2	-7.95
Ti %	0.134±0.007	-0.062
Co	5.66±0.09	-3.41
Cs	-1.93±0.19	17.16
Th	-2.07±0.11	19.0
U	-0.84±0.07	7.25

Table V. The calculated compositions of a second component material (if Borax Lake variations are due to the mixing of two different materials) compared with the composition of the dacite flow which underlies the obsidian.

Elements	Calculated composition %	Borax Lake dacite[5] %
SiO_2	65.7*	65.7
Fe	3.69±0.07	3.62
Mn	0.065±0.003	0.07
Ti	0.45±0.05	0.46
K	1.5±1.0	2.47
Ca	3.3±1.3	3.39
Al	7.3±0.3	7.53
Na	2.8±0.1	2.60

*Normalized value

were found to be slightly variable. Real variations were detected in Th, U, Mn, Fe, and Cr and were of the order of 3% , 2% , 6% , 5% , and 20% respectively.

3. Variable chemical compositions were detected in Borax Lake obsidian and appear to be linearly related.

4. The europium compositions, in all obsidian samples that we measured, were found to be depleted relative to the other rare-earth compositions in a similar fashion to that detected in lunar samples.[8] The europium composition at Borax Lake was variable.

5. For archaeological studies, the measurements indicate that all three locations or flows can be used reliably for determining material sources used in the construction of obsidian artifacts. The variable chemical compositions at Borax Lake are predictably related and should be easy to handle.

6. Geochemically, the variable compositions at Borax Lake present an interesting problem. They can be explained in terms of the mixing of two magmatic materials.

Further experiments involving a more complete analysis of other volcanic material in the area and the dating of our obsidian samples may shed further light on the significance of the linear variability.

We gratefully acknowledge the continued help of Mr. Duane Mosier, Mrs. Helen V. Michel, Miss Susanne Halvorsen, Mr. Onnig Minasian, Mr. Edward Arnold, and Mr. Wally Chin. The arduous job of changing samples after hours was done by the Safety Services Department, and the reactor irradiations were made in the Berkeley Research Triga Reactor.

References

1. I. Perlman and F. Asaro, Archaeometry 11, 21 (1969).

2. H. R. Bowman, F. Asaro, and I. Perlman (to be published in Geochim. Cosmochim. Acta).

3. V. C. Osmont, Calif. Univ. Pub. Dept. Geol. Bull. 4, 39 (1904).

4. R. F. Heizer, A. E. Treganza, Calif. J. Mines Geol. 40, 291 (1944).

5. C. A. Anderson, Bull. Geol. Soc. Am. 47, 629 (1936).

6. M. R. Harrington, S. W. Mus. Pap. No. 16 (1948); C. W Meighan, Science 167, 1213 (1970).

7. L. A. Haskin and F. A. Frey, Science 152, 299 (1966).

8. L. A. Haskin, P. A. Helmke, and R. O. Allen, Science 167, 487 (1970); H. Wakita and R. A. Schmitt, Science 170, 969 (1970).

9. R. N. Jack, I. S. E. Carmichael, Calif. Div. of Mines and Geol., Short Contr. Calif. Geol. SR 100, 17 (1969).

10. J. B. Griffin et al., American Antiquity 34, No. 1 (1969).

11. G. F Becker, U. S. Geol. Surv. Mon 13, 238 (1888).

12. Co determinations in Napa obsidians were complicated by laboratory contamination.

A Rapid, Nondestructive Method of Fluorine Analysis by ^{3}He Activation†

Diana M. Lee, James F. Lamb,* and Samuel S. Markowitz

A sensitive, nondestructive means of determining fluorine by the $^{19}F(^3He, 2p)^{20}F$ reaction with the 1.63-MeV γ ray of 10.8-sec ^{20}F as the "signal" for fluorine is presented. Excitation functions for the $^{19}F(^3He, 2p)^{20}F$ and the ^{19}F $(^3He, \alpha)^{18}F$ reactions and the possible interfering reaction, $^{18}O(^3He, p)^{20}F$, are given. Thin samples of LiF, Teflon, and PbF_2, and thick samples of LiF and PbF_2 mixed in platinum were analyzed. Only milligram amounts of sample are required. The accuracy is about 3 to 5%. Under reasonable irradiation and counting conditions, the detection limit is approximately 0.2 μg/cm^2 corresponding to 2 ppm in a matrix 100 mg/cm^2 thick. With better care in shielding the NaI(Tl) scintillation detectors from the γ-ray background in the accelerator area, the detection limit could be lowered.

Fluorine determinations by activation analysis have been reported by several authors. Depending on the incident particle, fluorine can be measured with various degrees of success by thermal neutrons,[1] fast neutrons,[2,3] α particles,[4] protons,[5] and photons.[6] Ricci and Hahn,[7] using 5- and 10-MeV ^{3}He ions, determined detection limits for several light elements, including fluorine, normalized to a beam current of 100 μA; they considered only the reactions $^{19}F(^3He, \alpha n)^{17}F$ and $^{19}F(^3He, \alpha)^{18}F$. Yule[8] has estimated the limit of detection of F to be 0.55 μg using the $^{19}F(n,\gamma)^{20}F$ reaction with reactor-produced thermal neutrons at a flux of 4.3×10^{12} n/cm^2-sec.

In the present work, we have investigated the application of the reactions $^{19}F(^3He,2p)^{20}F$ and $^{19}F(^3He, \alpha)^{18}F$ to the analysis of fluorine. The absolute excitation functions for production of 10.8-sec ^{20}F and 110-min ^{18}F from ^{19}F have been determined and samples have been analyzed. We suggest a wide range of application to both organic and inorganic samples by using the 1.63-MeV γ ray of ^{20}F induced by ^{3}He reactions as a "signal" that is relatively free from interferences caused by other activities that may be present. A number of thin and thick samples were analyzed nondestructively to test the accuracy of the method.

The irradiation chamber and the beam-current measurement have been previously described;[9] activated samples were transferred to the counting chamber by a gravity track shown in Fig. 1. A typical γ-ray spectrum is shown in Fig. 2, and the gated 1.63-MeV γ from 10.8-sec ^{20}F is shown in Fig. 3.

Excitation Functions

The short-lived ^{20}F precluded the use of the stack-foil technique, so that each point in Fig. 4 of the ^{20}F excitation function represents a separate bombardment. The maximum cross section is about 70 mb at the ^{3}He energy of 19 MeV; it varies slowly from 12 to 22 MeV. Also shown in the same figure is the excitation function for the production of ^{18}F by the reaction $^{19}F(^3He, \alpha)^{18}F$. The data of the ^{18}F excitation function shown agree very well with values previously published.[10,11]

Sample Analyses

^{20}F activity from ^{3}He-activated fluorine samples was used for analyses. Each sample was irradiated for 10 seconds at a beam energy of 17 MeV. Decay of the 1.63-MeV γ ray

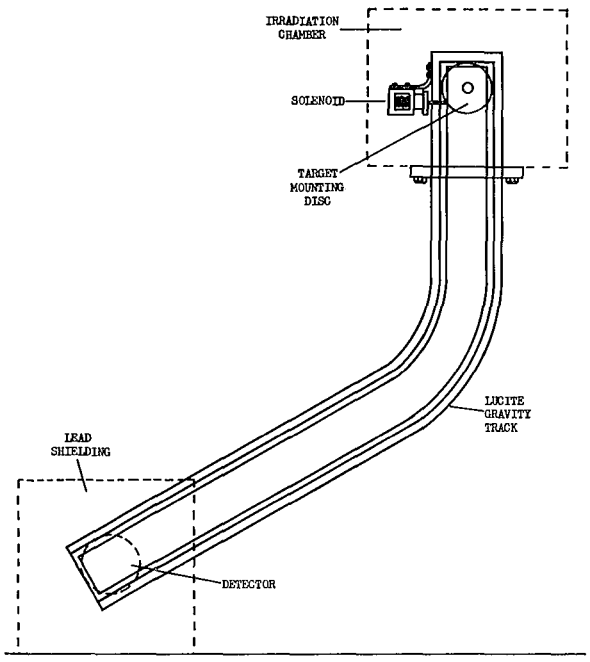

Fig. 1. Gravity-track sample holder for rapid retrieval of an activated target.
(XBL 697-1037)

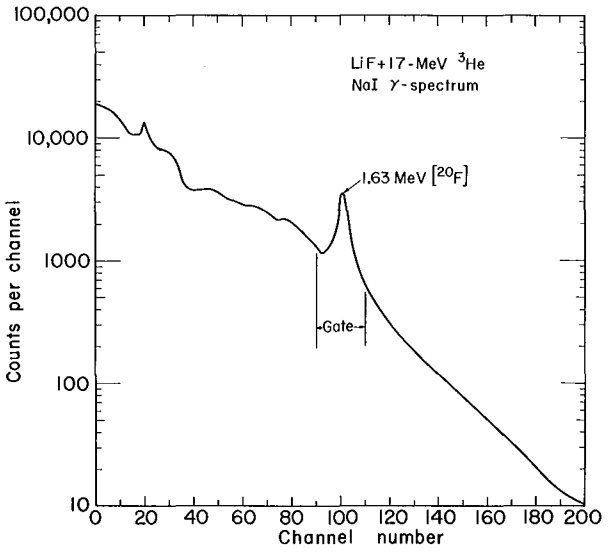

Fig. 2. Gamma-ray spectrum from LiF + 17-MeV ^{3}He. (XBL 709-3791)

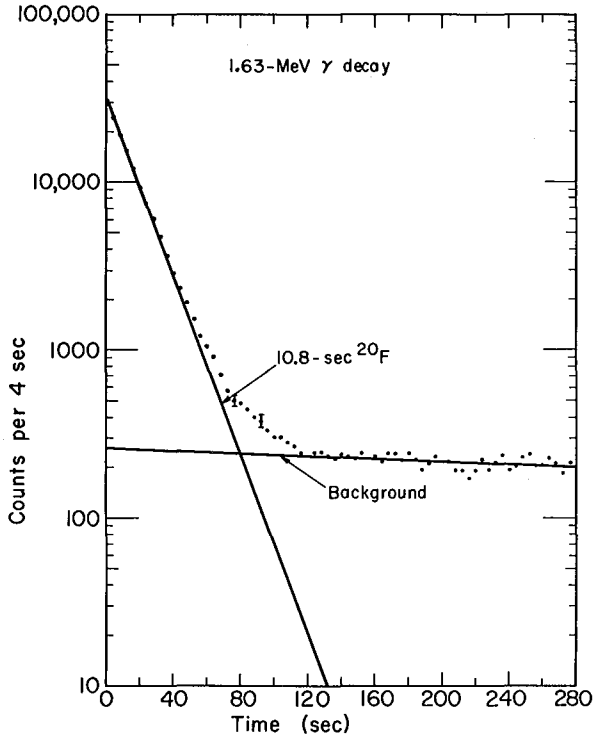

Fig. 3. Decay of the gated 1.63-MeV γ ray from ^{20}F. (XBL 709-3792)

(Fig. 3) was followed for 200 to 300 seconds. The amount of fluorine present was calculated by comparing the ratios of the A_0 values (activity at end of bombardment) of the samples to a thin LiF standard for thin samples, or to a thick LiF+ Pt standard for thick samples.

The results of the fluorine analyses for both thin and thick samples are shown in Table I and Table II, respectively. The error values (standard deviations) shown in both tables are based on counting statistics decay curve analysis only.

Interferences

By using ^{20}F activity, fluorine analyses

Table I. Fluorine analysis of thin samples[a]

Sample	F present (mg/cm^2)	F found (mg/cm^2)
LiF #13	1.68	standard
LiF #14	1.24	1.17±0.008[b]
LiF #12	1.03	1.02±0.007
LiF #16	0.82	0.82±0.007
LiF #21	0.77	0.73±0.007
LiF #19	0.54	0.53±0.007
LiF #22	0.25	0.23±0.007
Teflon #1 (CF_2)	1.85	1.90±0.010
Teflon #2	0.93	0.90±0.007
PbF_2 #1	0.29	0.26±0.007
PbF_2 #2	0.22	0.21±0.007

[a]Irradiated area of samples = 0.7 cm^2

[b]Standard deviation of decay-curve analysis. Average % difference = 4.7%

Table II. Fluorine analysis of thick samples[a,b]

Sample	F present (mg/cm^2)	F found (mg/cm^2)
Pt + LiF	1.02	standard
Pt + PbF_2 #1	1.53	1.54±0.016[c]
Pt + PbF_2 #2	0.33	0.32±0.010
Pt + PbF_2 #3	1.28	1.22±0.018

[a]Irradiated area of samples = 0.7 cm^2

[b]Total sample thickness ≈ 200 mg/cm^2. Average % difference = 2.8%

[c]Standard deviation of decay-curve analysis

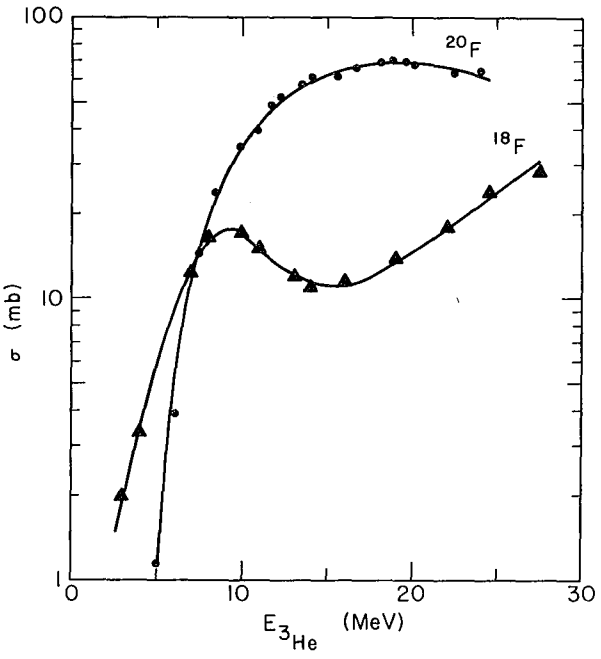

Fig. 4. Excitation functions for production of ^{20}F and ^{18}F from ^{19}F. (XBL 681-1733)

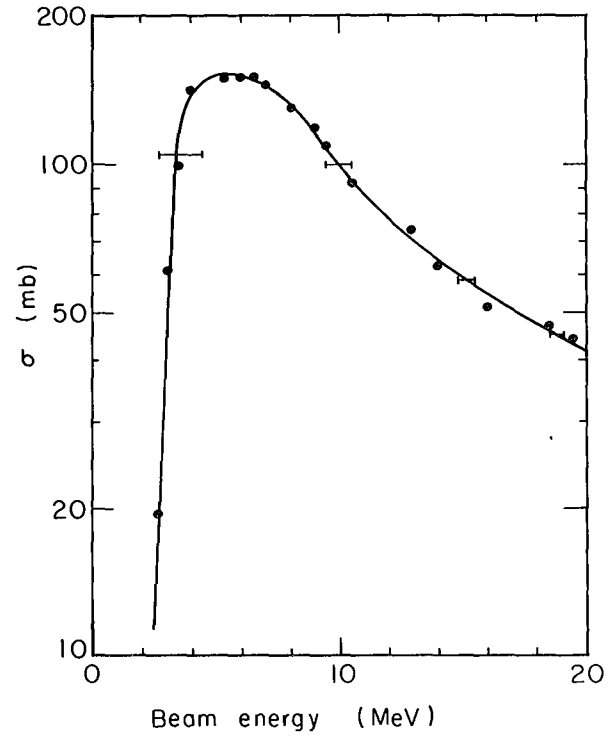

Fig. 5. Excitation function for the reaction ^{18}O(^{3}He, p)^{20}F. (XBL 671-330)

are relatively free from interferences produced either directly or indirectly by other elements present in the sample. The direct interference is caused by the same isotope (^{20}F) production; the only obvious interference would be ^{20}F activity produced in any ^{18}O present in the sample. The excitation function of ^{18}O(^{3}He, p)^{20}F is shown in Fig. 5; the cross section at 17 MeV is about 50 mb, rising to 100 mb at 10 MeV. The isotopic abundance, however, for ^{18}O in natural oxygen is only 0.2%. Because the ^{19}F(^{3}He,2p)^{20}F and ^{18}O(^{3}He,p)^{20}F cross sections are comparable between 12 and 17 MeV, at equal concentrations of fluorine and oxygen impurities in a given matrix, only 0.2% of the ^{20}F activity will have been caused by an interfering ^{18}O. An analysis based upon the production of ^{18}F is also feasible, in some cases, but the chances for interference are much greater with ^{18}F as the "signal" than with ^{20}F because ^{16}O would induce a direct interference. This possible interference would be caused by the ^{16}O(^{3}He,p)^{18}F reaction whose cross section below 10 MeV is about 20 times greater than the ^{19}F(^{3}He,2p)^{20}F reaction. Indeed, oxygen analysis via the former reaction has been previously described.[12] High atomic-number impurities or target matrices will not induce any radioactivities if the ^{3}He energy is controlled to be below the Coulomb barrier.

Estimate of Detection Limit

Under the following conditions--beam current 1 μA, cross section 70 mb, length of bombardment 10.8 sec--we found Do (disintegration rate at end of bombardment) to be 5.7×10^5 dps per mg/cm^2 of F. With our overall detection coefficient of only 1.6%, this gives about 10^4 counts per second in the γ photopeak. As the background was about 40 cps, this corresponds to a factor of about 250 times background. At equal signal and background rates, under our easy conditions, we could detect ≈ 4 μg/cm^2 of F. Because the beam intensity can be increased to 10 μA (or greater), and the detection coefficient can be easily doubled, the detection limit can be lowered to 0.2 μg/cm^2 of F. If the matrix in which the F is imbedded is 10 to 100 mg/cm^2 thick, the concentration limit would therefore be 20 ppm to 2 ppm, respectively. With more care for shielding, the background and therefore the detection limit could be lowered further. The sensitivity, of course, will depend upon the presence of interferences and the matrix.

Footnotes and References

†Condensed from Anal. Chem. 43, 000 (1971).

*Present address: Medi-Physics, Emeryville, California.

1. B. Van Zanten, D. Decat, and G. Leliaert, Intern. J. Appl. Radiation Isotopes 14, 105 (1963).

2. W. Leonhardt, Kernenergie 6, 45 (1963).

3. O. U. Anders, Anal. Chem. 32, 1368 (1960).

4. I. N. Plaskin, M. A. Belyakov, and L. P. Starchik, At. Energ. 13, 374 (1962).

5. T. B. Pierce, R. F. Peck, and D. R. A. Cuff, Analyst 92, 143 (1967).

6. L. Kosta and J. Slunecko, Anal. Chem. 42, 831 (1970).

7. E. Ricci and R. L. Hahn, Anal. Chem. 37, 742 (1965).

8. H. P. Yule, Anal. Chem. 37, 129 (1965).

9. J. F. Lamb, D. M. Lee, and S. S. Markowitz, Proc. 2nd Conf. on Practical Aspects of Activation Analysis with Charged Particles, Liege, Euratom, Brussels, 1967, 1, 225 (1968).

10. O. D. Brill, Soviet J. Nucl. Phys. 1, 37 (1966).

11. John D. Mahony, (Ph. D. thesis) UCRL-11780, 1965.

12. S. S. Markowitz and J. D. Mahony, Anal. Chem. 34, 329 (1962).

Anion Exchange in Aqueous-Organic Solvent Mixtures. II.

C. H. Jensen,† A. Partridge,* T. Kenjo,‡ J. Bucher, and R. M. Diamond

A previous paper[1] has discussed the anion-exchange selectivity shown by (organic) ion-exchange resins with water-dioxane solutions. Experimentally, the selectivity dropped markedly with an increase in dioxane content, so that by 50% mole fraction dioxane, the ratio of the distribution coefficients of I^- to F^- was only ≈ 4, instead of the ≈ 100 in water alone. This paper pointed out that, as was generally recognized,[2,3] water was a much better solvating agent for anions than was dioxane, for a number of reasons. Thus anions would compete to follow the distribution of water between the resin and external phases, and the smaller, more basic anion, which stood to gain the most in hydration energy, would win and push the other larger, less basic anion into the dioxane-rich phase. Since it was also found that the resin phase took up water in preference to dioxane, this meant that the smaller anions, which strongly favored the external phase with dilute aqueous solutions, should prefer that phase less and less as the proportion of dioxane increased. This is just what was observed.[1]

But if this idea has validity, it would be interesting to compare the behavior of the same anions and resin when using mixtures of water and a hydroxylic solvent, such as an alcohol. Certainly a less-marked decrease in selectivity with increasing organic-solvent mole fraction should be expected than was the case with dioxane, as the alcohol molecule can hydrogen bond to the anion and so offer it better solvation. Isopropyl alcohol was chosen for this study.

A plot of the resin-phase alcohol mole fraction for the Dowex 1-X4 resin vs the equilibrium external-phase alcohol mole fraction is shown in Fig. 1. Again, the strong-base resin in the Cl^- form preferentially takes up water from the water-organic mixture in the external phase, in agreement with the results of other investigations.[4,5] Thus, we might again expect the smaller halides to

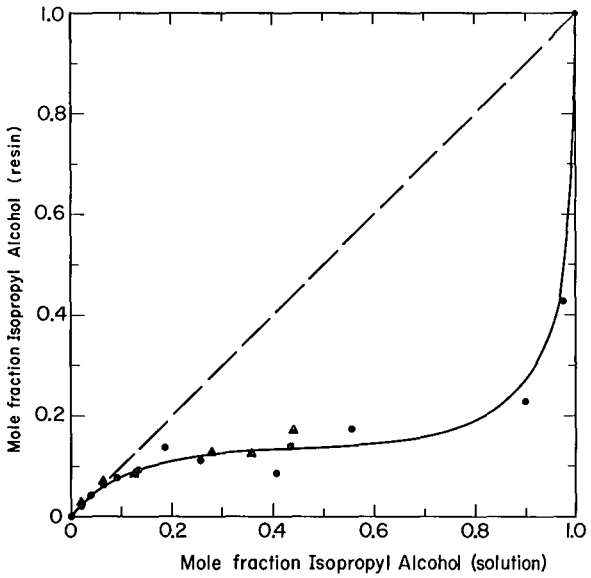

Fig. 1. The mole fraction of isopropyl alcohol in the resin phase for Dowex 1-X4 vs the mole fraction of alcohol in the external solution. (XBL 708-3659)

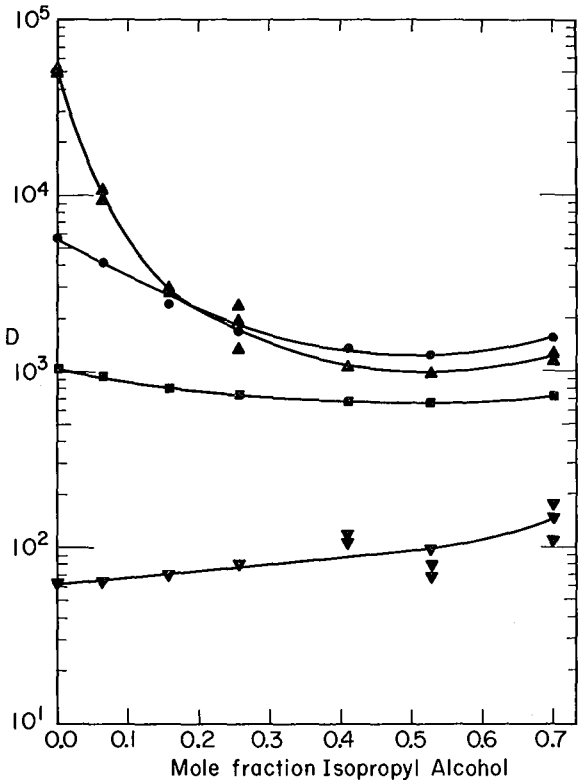

Fig. 2. Plot of D vs isopropyl alcohol mole fraction in the solution for 0.0100 M LiCl and Dowex 1-X4 resin and the tracer anion: F^-, ▼ ; Br^-, ■ ; I^-, ●; and ReO_4^-, ▲ . (XBL 708-3657)

increasingly favor the resin phase as the alcohol mole fraction increases, but moderated this time by the better solvation afforded the anions in the external phase by the isopropyl alcohol (hydroxyl groups). Figure 2 shows the distribution ratio,

$$D = \frac{\text{meq/g dry } Cl^-\text{-form resin}}{\text{meq/ml solution}}$$

for the tracers F^-, Br, I^-, and ReO_4^- as a function of the isopropyl alcohol mole fraction for an external solution 0.0100 M in LiCl.

The expected behavior does appear to occur, in that the curves of D for Br^-, I^-, and ReO_4^- do lie above the corresponding curves with dioxane as solvent, and that for F^- lies below. But it is not a large effect, a factor of about two at 0.5 mole fraction. Why is it so small? To study this further, some experiments were done using acetone-water mixtures; acetone is of similar size, form, and dielectric constant as isopropyl alcohol, but without the hydroxyl group of the latter. Thus, it cannot hydrogen bond to the anions and should be a poorer solvating agent for them. Figure 3 shows that, at least for tracer ReO_4^- and Br^- vs macro Cl^-, acetone solutions do appear to be poorer; the differences in the relative distribution ratios of ReO_4^- and Br^- between the two water-solvent mixtures are considerable. Those of the acetone mixtures go in the expected direction and show the least anion exchange selectivity. Although we cannot explain, as yet, why the water-dioxane mixtures are not more like the acetone-water ones, the following conclusions seem deducible from the previous paper and from this and other unpublished work.

1. There is a general tendency for anion selectivity to decrease markedly with the addition of organic diluent to the dilute aqueous external solution.
2. There does not appear to be a single reason for this general behavior, but several features contribute.

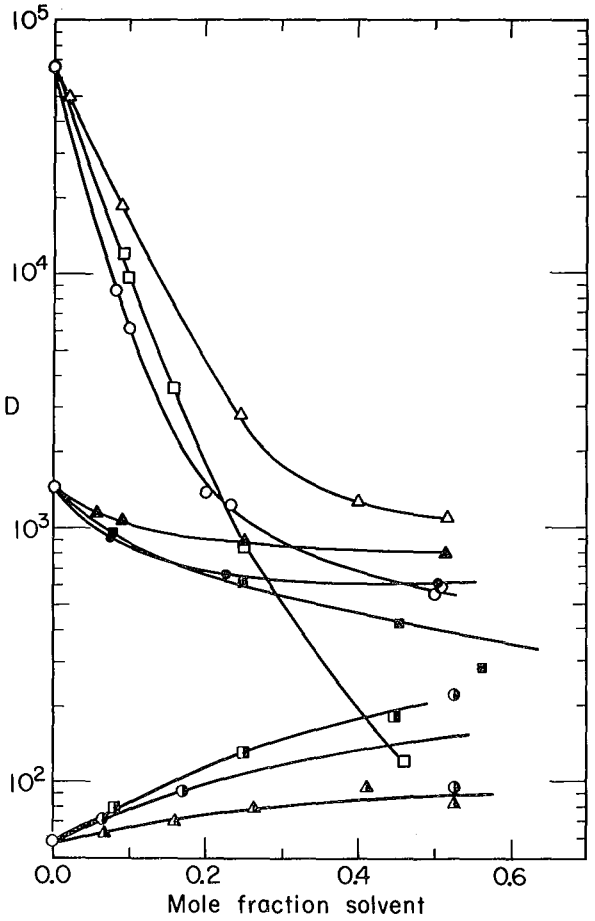

Fig. 3. Plot of D vs diluent mole fraction on the solution for 0.0100 M LiCl and Dowex 1-X4 resin for tracer ReO_4^-, open symbols; Br^-, filled symbols; F^-, half-filled symbols; and alcohol, △; dioxane, ○; and acetone, □ . (XBL 711-2568)

a. One of the most important is that the high charge density in the resin phase draws small molecules with large dipole moments into that phase to effectively neutralize that charge and lower the electrostatic free energy. The best combination of size and moments is usually furnished by the water molecule, and so water is usually taken up preferentially by the resin. The smaller, more basic anions increasingly seek out this phase and its water as the mole fraction of organic diluent increases.

b. Diluents incapable of hydrogen bonding to the anions provide an additional reason for the smaller more basic anions to leave the external solution and go into the resin phase (water) as the organic solvent mole fraction increases, leading to the most striking changes in selectivity.

c. The value of the diluent dielectric constant is not in itself a prime factor (e. g., dioxane with $\epsilon = 2.21$ does not show as marked an effect as acetone with $\epsilon = 20.7$ and isopropyl alcohol, $\epsilon = 18.3$, shows still less), although it is related indirectly through the effect of the diluent bond dipole moments in solvating the anions.

Footnotes and References

[†]Summer Visitor, 1967, NSF College Teachers Research Participation Program. Permanent address: Cabrillo College, Aptos, California.

[*]Undergraduate summer visitor from Bates College, Lewiston, Maine, 1970.

[‡]Permanent address: Department of Chemistry, Tokyo Institute of Technology, Tokyo, Japan.

1. Nuclear Chemistry Annual Report, 1969, p. 301; C. H. Jensen and R. M. Diamond, J. Phys. Chem. 75, 79 (1971).

2. E. Grunwald, G. Baughman, and G. Kohnstam, J. Am. Chem. Soc. 82, 5801 (1960).

3. D. Feakins and D. J. Turner, J. Chem. Soc. 1965, 4986.

4. Y. Marcus and J. Naveh, J. Phys. Chem. 73, 591 (1969).

5. H. Rückert and O. Samuelson, Acta Chem. Scand. 11, 703 (1957).

Radiation Chemistry

Reductive Deamination in the Radiolysis of Oligopeptides in Aqueous Solution and in the Solid State†

Winifred Bennett-Corniea, Harvey A. Sokol, and Warren M. Garrison

Radiolysis of the simpler α-amino acids such as gylcine and alanine leads to reductive deamination as a major chemical consequence both in aqueous solution and in the solid state.[1]

We now find that the linear di, tri, and tetra peptide derivatives of these amino acids undergo analogous chemistry.

In dilute aqueous solutions the ionization step[2]

$$H_2O \longrightarrow H^+,\ OH,\ e^-_{aq} \qquad (1)$$

leads to formation of the hydroxyl radical, OH, and the hydrated electron, e^-_{aq}. The yield for reductive deamination by e^-_{aq} can be measured directly through use of second solutes, which are highly reactive toward OH but relatively unreactive toward e^-_{aq}. Formate ion[3] is such a solute and the effects of increasing formate concentrations on product yields from 0.5 M glycine solution are shown in Fig. 1. We see that $G(NH_3)$ drops rapidly with increasing formate concentrations, and then levels off at a limiting value which is a measure of the reductive deamination reaction[1d]

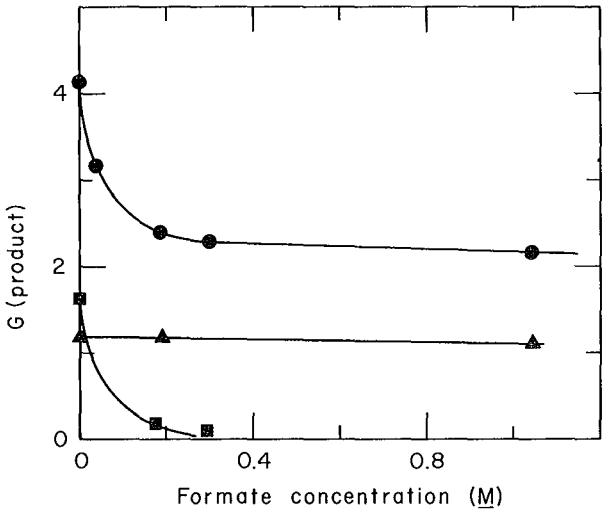

Fig. 1. Product yields from 0.5 M glycine as a function of sodium formate concentration in oxygen-free solution of pH 6.4 under γ radiolysis. Ammonia (●), acetic acid (▲), and glyoxylic acid (■). (XBL-673-2201)

$$e^- + NH_3^+CHRCOO^- \longrightarrow NH_3 + \dot{C}HRCOO^-. \qquad (2)$$

We find that the linear di, tri, and tetra peptide derivatives also undergo reductive deamination. In the γ radiolysis of these oligopeptides we find $G(NH_3) \approx 3$ at peptide concentrations above 0.05 M. Addition of formate ion to these systems results in a small decrease in $G(NH_3)$. The evidence is that essentially all of the free ammonia liberated in the γ radiolysis of these oligopeptide systems arises as a consequence of reductive deamination; i.e., for glycylglycine

$$e^- + NH_3^+CHRCONHCHR_2 \longrightarrow NH_3 + \dot{C}HRCONHCHR_2 \qquad (3)$$

In accordance with these formulations we find that acetylglycine and acteylglycylglycine are formed as major products from diglycine and triglycine. Data are summarized in Table I.

Table I. Product yields in the γ radiolysis of diglycine and triglycine in 0.1 M oxygen-free solutions.

	Yield, G	
Compound	Ammonia	Acetyl derivative
Diglycine	3.1	2.5
Triglycine	2.8	2.0

Radiolysis in the solid state also leads to the formation of ammonia and the corresponding acetyl derivative as shown in Table II. The products of Table II may be accounted for

Table II. Product yields in the γ radiolysis of diglycine and triglycine in the solid state (evacuated).

	Yield, G	
Compound	Ammonia	Acetyl derivative
Diglycine	4.5	3.4
Triglycine	3.1	3.2

in terms of the formulation

$$NH_3^+CHRCONHCHR_2 \xrightarrow{\sim\sim} NH_3^+CHRCONH\dot{C}R_2 + H^+ + e^- \quad (4)$$

$$e^- + NH_3^+CHRCONHCHR_2 \longrightarrow NH_3 + \dot{C}HRCONHCHR_2, \quad (5)$$

where (4) represents the ionization act in the solid state.

Footnote and References

†Condensed from UCRL-19504, January 1970. Presented at 18th Annual Meeting of the Radiation Research Society, Dallas, Texas, March 1-5, 1970.

1. a) G. Stein and J. Weiss, J. Chem. Soc. (1949), 3245; b) N. E. Sharpless, A. E. Blair, and C. R. Maxwell, Radiation Res. 2, 135 (1955); c) B. M. Weeks, and W. M. Garrison, Radiation Res. 9, 291 (1958); d) B. M. Weeks, Sibyl A. Cole, and W. M. Garrison, J. Phys. Chem. 69, 4131 (1965).

2. For a recent review of the radiation chemistry of water see M. S. Matheson, Adv. Chem. Ser. 50, 45 (1965).

3. $k(HCOO^- + OH) \simeq 2.5\times10^9\ M^{-1}\ sec^{-1}$, $k(HCOO^- + e^-_{aq}) = < 10^6\ M^{-1}\ sec^{-1}$; see the review by M. Anbar and P. Neta, Intern. J. Appl. Radiation Isotopes 18, 493 (1967).

Radiolytic Oxidation of the Polypeptide Main Chain in Dilute Aqueous Solution†

Mathilde Kland-English, Michael E. Jayko, Harvey A. Sokol, and Warren M. Garrison

In the γ radiolysis of peptides, $RCONHCHR_2$, in dilute oxygen-saturated solution, reaction of OH radicals at the main chain leads to formation of peroxy radicals, $RCONHC(\dot{O}_2)R_2$.[1-3] These react preferentially via

$$2RCONHC(\dot{O}_2)R_2 \longrightarrow 2RCONHC(\dot{O})R_2 + O_2. \quad (1)$$

The alkoxy radicals formed in Step (1) are then removed through

$$O_2 + RCONHC(\dot{O})R_2 \longrightarrow \text{products} + H_2O. \quad (2)$$

In the specific case of N-acetylalanine, reaction (2) is of the form

$$O_2 + RCONHC(\dot{O})RCOOH \longrightarrow RCONHCOR + CO_2 + HO_2. \quad (3)$$

This step yields carbon dioxide and diacetamide as major oxidation products. Mild hydrolysis of diacetamide in 1 N sodium hydroxide at room temperature for 15 min yields acetamide and acetic acid as major organic products.

Now, in the radiolysis of polyamino acids such as poly-DL-alanine (mol wt, 2000) in dilute oxygenated solution, we must assume that OH attack leads to the production of $RCONHC(\dot{O}_2)R_2$ radical sites at random along the polypeptide chain. There is the question, then, as to whether or not the chemistry of the radical removal, Steps (2) and (3), are also of importance in the radiolytic oxidation of the polyamino acid configuration. Yields of major degradation products formed in the radiolysis of oxygenated solutions of N-acetylalanine and polyalanine are compared in Table I. We see that carbon dioxide, amide, and acetic acid are the major oxidation products in both cases. In the case of polyalanine, we envisage the removal of the alkoxy radicals via Step (3) as involving the enol form of the peptide bond

$$O_2 + RCONHC(\dot{O})(R)C{=}C(OH){-}N{-}R \longrightarrow RCONHCOR + O{=}C{=}N{-}R + HO_2, \quad (4)$$

where the reaction

$$H_2O + O{=}C{=}N\text{-}R \longrightarrow CO_2 + RNH_2 \quad (5)$$

follows spontaneously.

Footnote and References

†Condensed from J. Phys. Chem. 74, 4506 (1970).

1. W. M. Garrison, M. E. Jayko, and W. Bennett, Radiation Res. 16, 483 (1962).

2. W. M. Garrison and B. M. Weeks, Radiation Res. 17, 341 (1962).

3. H. L. Atkins, W. Bennett-Corniea, and W. M. Garrison, J. Phys. Chem. 71, 772 (1967)

Table I. Product yields in the γ radiolysis of N-acetylalanine and polyalanine in oxygenated solution.

Product	Yield (G)[a] 0.05 M N-acetylalanine	0.5% polyalanine
NH_3[b]	2.9	3.9
CH_3COOH[c]	3.0	~3.9
CO_2	2.0	2.4
H_2O_2	2.2	2.2
ROOH[b]	0.5	---
$CH_3COCOOH$	~0.2	1.2
CH_3CHO	~0.2	0.4

[a]Product yields are independent of dose up to $\sim 2\times10^{19}$ eV/ml.

[b]After hydrolysis in 2 N NaOH for 24 hours at room temperature.

[c]After hydrolysis in 1 N NaOH for 15 minutes at room temperature.

Radiolytic Cleavage of the Peptide Main Chain in Concentrated Aqueous Solution: Energy Level of Excited-Molecule Intermediates †

Michael A. J. Rodgers, ‡ Harvey A. Sokol, and Warren M. Garrison

The radiation chemistry of N-acetylalanine and N-acetylglycine in dilute neutral solution in the absence of O_2 may be represented in terms of the radiation-induced step[1-4]

$$H_2O \sim\!\!\!\!\!\!\rightarrow H^+,\ OH,\ e^-_{aq}, \quad (1)$$

followed by[5-8]

$$e^-_{aq} + RCONHCHR_2 \longrightarrow R\dot{C}(O^-)NHCHR_2 \quad (2)$$

$$OH + RCONHCHR_2 \longrightarrow RCONH\dot{C}R_2 + H_2O. \quad (3)$$

The radical products of reactions (2) and (3) are subsequently removed mainly through the reconstitution reaction[8]

$$H_2O + R\dot{C}(O^-)NHCHR_2 + RCONH\dot{C}R \longrightarrow 2RCONHCHR_2 + OH^- . \quad (4)$$

In more concentrated solutions, however, other reactions become of importance. In the case of N-acetylalanine there is a very marked increase in the amide ammonia yield as the solute concentration is increased above 0.1 M, as shown in Fig. 1. Propionic acid is the principal concomitant product associated with the enhancement in the amide yield from N-acetylalanine.

The production of amide and fatty acid at the higher solute concentrations does not appear to be related in any significant way to the reactions of OH and e^-_{aq}. We have found[9]

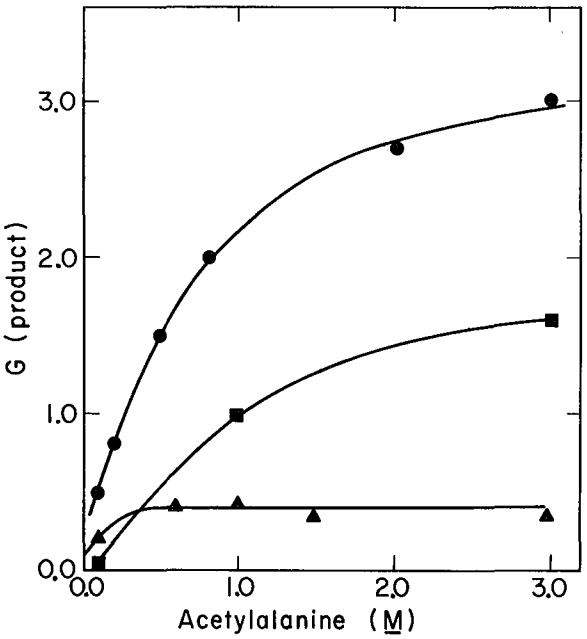

Fig. 1. Ammonia (●), propionic acid (■), and carbonyl (▲) yields as a function of N-acetylalanine concentration in oxygen-free solution at pH 7 under γ radiolysis.
(XBL-705-2908)

that addition of second-solutes at concentrations sufficient to quantitatively scavenge the products of water radiolysis has relatively little effect on the amide yield in concentrated aqueous solution. The evidence is that a new reaction mode sets in at concentrations above 0.1 M. We have suggested[9] that such reaction is of the form

$$e^- + RCONHCHR_2 \longrightarrow RCONHCHR_2^* + e \quad (5)$$

$$RCONHCHR_2^* + RCONHCHR_2 \longrightarrow RCONH\dot{C}R_2 + RCONH_2 + \dot{C}HR_2, \quad (6)$$

where $RCONHCHR_2^*$ represents an electronically excited state of the solute.

Now, aromatic compounds are, of course, known to be effective scavengers of excited states providing the energy level of the aromatic compound is lower than that of the excited species.[10] We find experimentally that naphthalene sulfonic acid, benzoic acid, and benzaldehyde are remarkably effective in quenching the formation of amide ammonia in 2M N-acetyalanine. Phenol and benzene sulfonic acid, on the other hand, are without effect even at the higher concentrations. Typical data are summarized in Fig. 2.

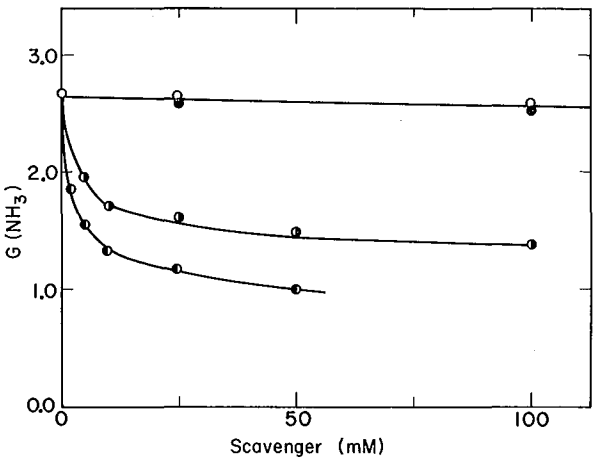

Fig. 2. Effects of excitation scavengers on ammonia yields in oxygen-free, 2M N-acetylalanine solutions under γ radiolysis; benzene sulfonic acid (O), phenol (◉), benzoic acid (◑), naphthalene sulfonic acid (◐).
(XBL-705-2906)

The reason that certain aromatic compounds are effective quenchers and others are not becomes evident on examination of the energy-level diagram given in Fig. 3. Data for the singlet and triplet levels of the aromatic compounds are taken from Calvert and Pitts.[11] The value of the singlet level of N-acetylalanine is from the work of Saidel.[12]

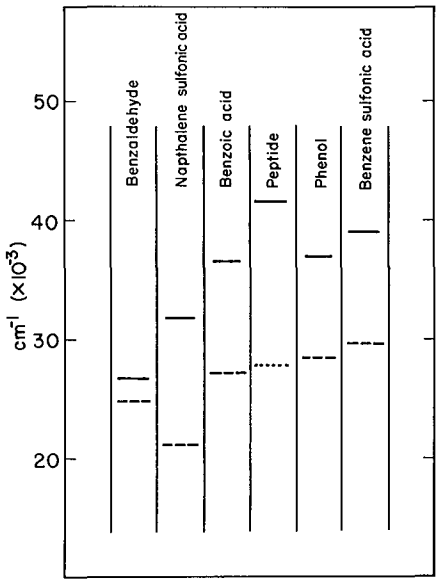

Fig. 3. Singlet (——) and triplet (---) energy levels of excitation scavengers used in the present study. The line (···) represents the energy level of $RCONHCHR_2^*$.
(XBL-705-2907)

We observe first that although all of the aromatic solutes studied here have singlet levels below the peptide upper singlet, all are not effective quenchers as we have noted. The correlation appears when the triplet levels are considered. We see that those compounds that are effective quenchers, such as benzaldehyde, naphthalene sulfonic acid, and benzoic acid, have the lower triplet levels as compared with phenol and benzene sulfonic acid. The change from quenching to nonquenching occurs between benzoic acid (27,200 cm^{-1}) and phenol (28,500 cm^{-1}). In other words, the energy of the excited state, $RCONHCHR_2^*$, in the case of N-acetylalanine must be between these two values at $\simeq$28,000 cm^{-1} $\simeq$ 80 kcal $\simeq$3.5 eV.

Footnotes and References

†Condensed from Biochem. Biophys. Res. Commun. 40, 622 (1970).

‡Present address: Chemistry Department, University of Manchester, Manchester, England.

1. N. F. Barr and A. O. Allen, J. Phys. Chem. 63, 928 (1959).

2. G. Czapski and H. A. Schwarz, J. Phys. Chem. 66, 471 (1962).

3. E. J. Hart and J. W. Boag, J. Am. Chem. Soc. 84, 4090 (1962).

4. B. H. J. Bielski and A. O. Allen, Intern. J. Radiation Phys. Chem. 1, 153 (1969).

5. H. L. Atkins, W. Bennett-Corniea, and W. M. Garrison, J. Phys. Chem. 71, 772 (1967).

6. W. M. Garrison, Radiation Res. Suppl. 4, 158 (1964).

7. W. M. Garrison, Current Topics in Radiation Research, edited by M. Ebert and A. Howard (North-Holland Publishing Co., Amsterdam, 1968) Vol. IV.

8. J. Holian and W. M. Garrison, J. Phys. Chem. 72, 4721 (1968).

9. M. A. J. Rodgers and W. M. Garrison, J. Phys. Chem. 72, 758 (1968).

10. F. Wilkinson, Advan. Photochem. 3, 241 (1964).

11. J. G. Calvert and J. N. Pitts, Jr., Photochemistry (John Wiley and Sons, New York, New York, 1967).

12. L. J. Saidel, Arch. Biochem. Biophys. 54, 184 (1955).

Chemical Engineering

Rate of Reaction of Gaseous Nitrogen Oxides with Water

C. Corriveau and R. L. Pigford

The two chemical reactions

$$2\ NO_2 + H_2O = HNO_2 + HNO_3 \qquad (1)$$

and

$$N_2O_3 + H_2O = 2\ HNO_2 \qquad (2)$$

occur in solution after the gaseous oxides dissolve at a gas-liquid interface. The rate of solution and reaction depends on the solubility of the unreacted oxide in water and on the homogeneous reaction rate. Knowledge of the solubility and rate coefficients is needed not only for chemical processes in which nitrous gases must be handled, but also for removal of the compounds from flue gases in power plants to effect pollution control. The coefficients have not been available heretofore because they can not be measured by conventional methods.

By measuring the rate of solution of NO_2 from gaseous mixtures with nitrogen into a stream of water flowing over a spherical surface, we have been able to show that the rate is proportional to the square of the partial pressure of NO_2 in the gas that is in contact with the liquid surface. Because of the gas-phase equilibrium

$$2\ NO_2 = N_2O_4\ , \qquad (3)$$

the partial pressure of N_2O_4 is proportional to the square of that of NO_2. The rate measurements show, consequently, that the rate of solution and reaction is proportional to pN_2O_4, as shown in Fig. 1. This indicates that the mechanism of the combined process is one in which NO_2 molecules first react in the gas to form the dimer, N_2O_4. This compound then dissolves and reacts with water by the bimolecular process,

$$N_2O_{4\,(aq)} + H_2O = HNO_2 + HNO_3 \qquad (4)$$

From such rate measurements, and with the aid of a calculation of the flow pattern in the laminar layer of liquid which runs over the spherical surface in the laboratory absorber, it has been possible to extract values of the Henry's Law coefficient for unreacted N_2O_4 in water and for the pseudo first-order reaction rate constant in reaction 4. The results show that the solubility is about twice that of carbon dioxide, and that the half-life of a molecule after it dissolves is about 0.01 sec at room temperature.

Measurements of the rate of the sesquioxide, N_2O_3, are being made with the same apparatus by observing the increment to the rate for NO_2-N_2O_4 when NO is added to the gaseous mixture. The hydration of N_2O_3 appears to be a comparatively rapid reaction, suggesting that the removal of NO from gaseous mixtures can be accomplished by the intentional addition of NO_2 to the gas before passing it through an absorption tower.

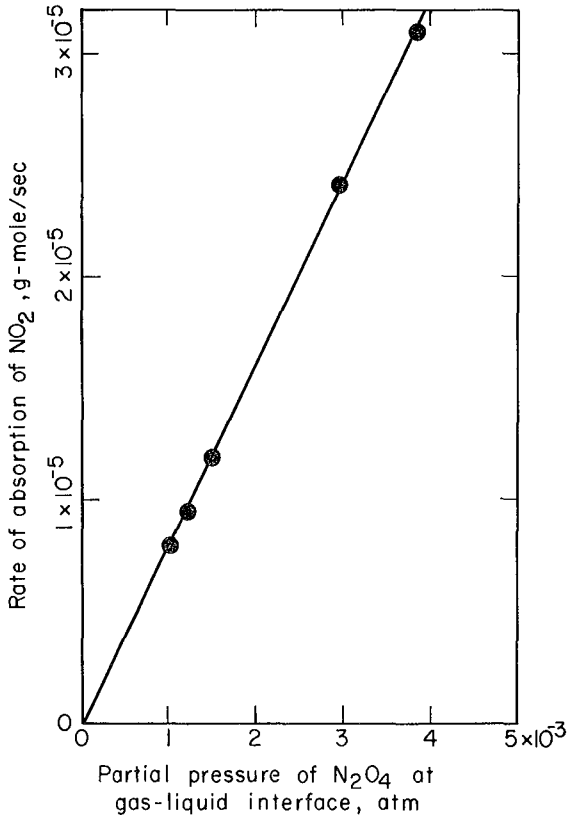

Fig. 1. Rate of absorption of nitrogen dioxide into water flowing over a sphere.
(XBL-713-3081)

The Behavior of Chlorella Pyrenoidosa in Steady-State Continuous Culture†

Joseph N. Dabes, Charles R. Wilke, and Kenneth H. Sauer

The unicellular alga Chlorella pyrenoidosa was grown in steady-state continuous culture at 25°C in a rectangular glass vessel (9.1 cm ×19.9 cm×2.8 cm thick). Growth was never limited by CO_2, minerals, pH, or temperature. The primary objective was an examination of the effects of the two remaining variables, specific growth rate and incident light intensity, on algal biomass productivity and algal physiology.

Total chlorophyll content (Fig. 1), ratio of chlorophyll a to chlorophyll b, light saturated rate of photosynthesis (Fig. 2), dark respiration rate, and RNA content were found to be strong functions of specific growth rate. On the other hand, maximum quantum efficiency of the quinone Hill reaction, and DNA content changed little, if at all, as a function of specific growth rate. Physiological changes in the cells as a function of incident light intensity were small.

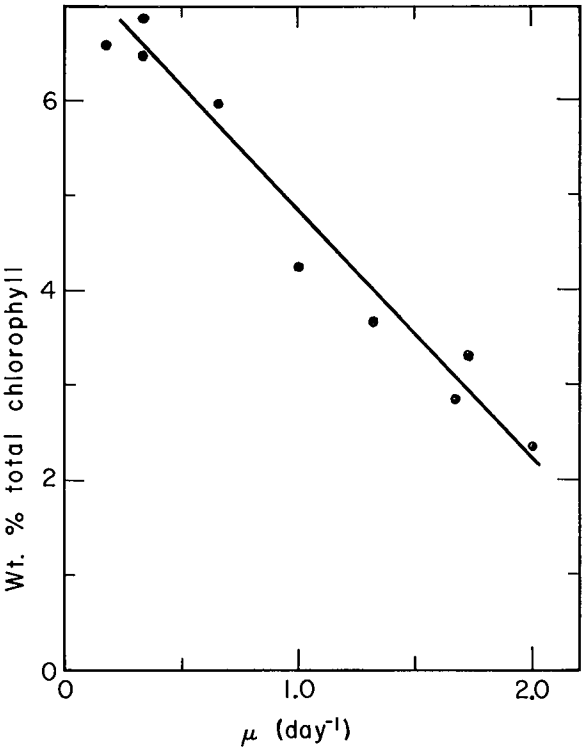

Fig. 1. Total chlorophyll content versus specific growth rate. (XBL-695-2706)

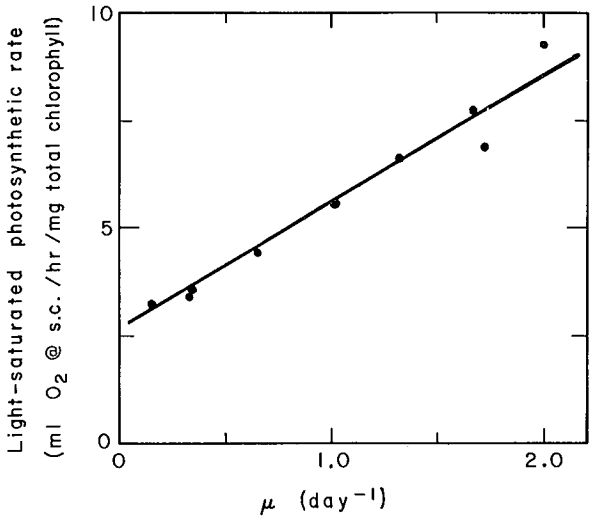

Fig. 2. Light saturated rate of photosynthesis at 25°C versus specific growth rate. (XBL-695-2708)

The Performance of Optically Dense Cultures of Algae

Optically dense cultures are of practical interest in the mass culture of algae. To mathematically model such systems, the manner in which light intensity changes as a function of distance into the culture must be known. If the rate of photosynthesis as a function of light intensity is also known, the local rate of photosynthesis at any point in the system may be calculated. By mathematically integrating the local rate of photosynthesis with respect to distance into the culture, the total rate of photosynthesis in the system may be found. Since photosynthesis results in growth, the productivity of algal biomass may be predicted.

These principles were incorporated into the system of Eqs. (1-4), which may be employed to describe the performance of dense cultures

$$\mu = \frac{1}{S}\int_0^S R_{O_2}(\mu,I)\,\big|_s\, C(\mu)B(\mu)ds - U(\mu)B(\mu), \quad (1)$$

$$R_{O_2}(\mu, I)\big|_s =$$

$$\int_{380}^{720} 2\Phi\epsilon(\lambda)I(\lambda)\big|_s S_M \, d\lambda \div \left\{2S_M + \Phi\epsilon(\lambda)I(\lambda)\big|_s + \sqrt{2\Phi\epsilon(\lambda)I(\lambda)\big|_s S_M + \left[\Phi\epsilon(\lambda)I(\lambda)\big|_s\right]^2}\right\} , \quad (2)$$

or, if it gives a smaller value,

$$R_{O_2}(\mu, I)\big|_s = S_A(\mu) , \quad (3)$$

$$I(\lambda)\big|_s = I_0(\lambda) \exp\left\{-Xs \; \epsilon(\lambda) \; C(\mu)\right\} , \quad (4)$$

where

μ = specific growth rate (1/h)

$R_{O_2}(\mu, I)\big|_s$ = local rate of photosynthesis in terms of O_2 evolution at any point s (moles O_2/h/mg chlorophyll) (Fig. 2)

$C(\mu)$ = weight fraction of chlorophyll in the cells (mg chlorophyll/mg dry weight) (Fig. 1)

$B(\mu)$ = factor for converting O_2 evolved to cell dry weight (mg dry weight/mole O_2)

$U(\mu)$ = uptake of O_2 due to respiration (mole O_2/h/mg dry weight)

ds = differential distance at any point s (cm)

S = total algal suspension thickness (cm)

Φ = maximum quantum yield, as I approaches zero (moles O_2/einstein)

$\epsilon(\lambda)$ = extinction coefficient of light expressed as a function of λ (cm^2/mg chlorophyll)

$I(\lambda)$ = light intensity at any point s expressed as a function of λ (einsteins/cm^2/h)

S_M = the saturated rate of O_2 evolution intrinsic to the photoelectron transport system (when no steps in the carbon fixation cycle limit) (mole O_2/h/mg chlorophyll)

$S_A(\mu)$ = the actual rate of O_2 evolution caused by a bottleneck in the carbon fixation cycle (mole O_2/h/mg chlorophyll)

X = concentration of algal biomass (mg dry weight/ml)

The light response curve, Eq. (2), developed in this study is consistent with the experimental data and current knowledge of the chemical kinetics of photosynthesis. Values of λ are limited to the region 380 to 720 nm, which is the region of importance. In addition to its use of Eq. (2), our model differs from earlier models in accounting for changes in cellular composition and physiology with specific growth rate.

The above four equations may be solved by substituting Eq. (4) into Eq. (2) and using Eq. (2) or Eq. (3), whichever is appropriate, in Eq. (1). Eq. (1) cannot be integrated analytically, except for monochromatic light, or if it is assumed that an average extinction coefficient will suffice. Therefore, a trial and error solution is generally necessary.

A detailed derivation of the model and methods of numerical solution are presented in the original report (UCRL-19958).

Once the algal biomass concentration, X, is known, productivity, p, may be found

$$p = X\mu S , \quad (5)$$

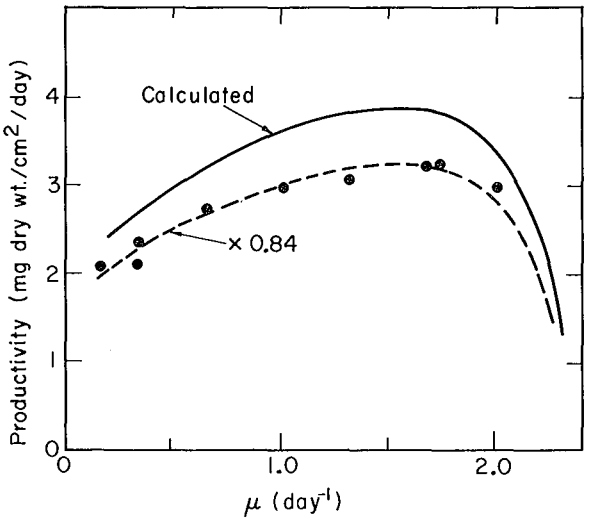

Fig. 3. Productivity of Chlorella pyrenoidosa in continuous culture as a function of the steady-state specific growth rate.
(XBL-713-3080)

where

p = the production of cellular dry weight (mg dry weight/h/cm^2).

Figure 3 presents our experimental data for biomass productivity of Chlorella pyrenoidosa. The solid curve is calculated by Eq. (1-4). It was found that optimum productivity was obtained at a specific growth of approximately 1.6 day^{-1}, when the incident light intensity was 8.05 mW/cm^2. This optimum, which is not expected to change significantly as a function of incident light intensity, results primarily from a high light saturated rate of photosynthesis and a low amount of light transmitted through the culture. The experimental data are about 14% lower than the computer calculated curve (dotted line). This result is reasonable because of the inaccuracy of some of the experimentally determined parameters used in the computer program, particularly the maximum quantum efficiency, Φ. No arbitrary fitting constants were used in the computer program.

The above mathematical model for optically dense cultures should be useful in designing and predicting the performance of algal systems.

Footnote

†Condensed from UCRL-19958, August 1970.

Optical Isomer Separations Through Stereospecific Molecular Interactions

John M. Krochta and Theodore Vermeulen

Stereospecific sorption has been investigated as a potentially valuable means of separating optical isomers, based on the requirement that only an asymmetric substance can separate a mixture of asymmetric isomers. This work has led to the study of amino acid interactions in aqueous solution, and has involved extensive chromatographic testing of two types of asymmetric sorbents.

An exploratory study on the resolution of optical isomers undertaken earlier in our laboratory[1] included solubility measurements on the optical isomers of aspartic acid in aqueous solutions of other amino acids. These data, supplemented with aspartic acid solubility data in glycine solution obtained in this study, appear in Table I. The differences in solubility found between the L- and D-isomers confirm the existence of stereoselective interactions between optical isomers.

Extensive work with Framework Molecular Models, in conjunction with the three-point-interaction model,[2,3,4] has been fairly successful in identifying the types of interactions causing the differences in solubility of aspartic acid optical isomers in the various amino acid solutions.

The increase in solubility of an aspartic acid optical isomer in a solution of another optical isomer, relative to its solubility in water, measures the extent of interspecies dimer formation. A minimum value of the equilibrium constant for interdimer formation can be obtained by assuming that no self dimers form. For aspartic acid, minimum interdimer equilibrium constants, $K_{L\text{-sol:D-asp}}$, calculated from solubility in the several amino acid (sol) solutions of Table I, range from 0.76 to 1.92. Furthermore, ratios between the dimerization constants for L- and D-aspartic acid with the several other amino acids studied yield a number of selectivity ratios different from 1.00, up to 1.33.

The dimerization constants given above provide an interesting comparison with those calculated from the data of other workers for different amino acids. The solubility data of Cohn et al.[5] give interdimer constants ≤ 0.53, whereas the data of Su and Shafer[6] yield constants ≤ 1.64. This comparison marks aspartic acid as especially capable of forming dimers with other amino acids.

The available data taken all together point to a probable value of only 0.24 for the non-selective part of the interdimer equilibrium constant (0.12 for self-dimer constant) that results from interaction of the NH_3^+ and COO^- groups on each member of a complexing pair of amino acids. This means than when large interdimer constants are found for amino acid pairs, they must result mainly from interactions involving the remainder of the molecule. Other data indicate the likelihood that in some cases diastereoisomers between amino acids pairs are stable and have lower solubility than either amino acid taken separately.

Table I. Excess solubility of L-aspartic acid over D-isomer in various solutions at 28°C.[a]

Aqueous solvent	Solubility of D-isomer, mmoles/g solution	Excess solubility of L-isomer, %	Minimum interdimer constant $K_{L\text{-sol:D-asp}}$ $(\text{mmoles/g solution})^{-1}$	Selectivity ratio $\frac{K_{L\text{-sol:L-asp}}}{K_{L\text{-sol:D-asp}}}$
Water	0.04147			
0.05M solutions				
Glycine	0.04462		1.63	
L-leucine	0.04385	0.4	1.21	1.07
L-serine	0.04385	-0.4	1.25	0.93
L-arginine·HCl	0.04514	0.0	1.92	1.00
L-glutamic acid	0.04295	1.3	0.76	1.33
D-glutamic acid	0.04344	-0.9		

[a]Excess solubility percentage is L-isomer solubility minus D-isomer solubility, divided by L-isomer solubility, times 100. Amino acids have the formula $^{+}NH_3CH(COO^{-})R$, with R having the following structures: aspartic acid, $-CH_2COOH$; glutamic acid, $-CH_2CH_2COOH$; leucine, $-CH_2CH(CH_3)_2$; serine, $-CH_2OH$; arginine hydrochloride, $-(CH_2)_3NHC(NH_2)=NH_2^{+}Cl^{-}$; glycine, -H.

Two different types of asymmetric sorbents were synthesized previously in our laboratory.[1] The first of these was an asymmetric ion exchanger. Chitin, poly(N-acetyl-D-glucoseamine), was hydrolyzed to chitosan, poly(D-glucoseamine), a weak base. This was followed by crosslinking with epichlorohydrin to preserve chitosan's structure in acidic solutions. Chitosan has shown a tendency to sorb only the acidic amino acids (aspartic acid and glutamic acid). Nonetheless, no optical isomer separation was detected in these cases. However, chitosan has displayed a striking ability to separate the optical isomers of N-acylated amino acids. Samples with isomer ratios of up to 2.30 were obtained in the partial separation of the optical isomers of N-acetyl-DL-phenylalanine on a short column in methanol shown in Fig. 1. The corresponding selectivity ratio is about 1.10.

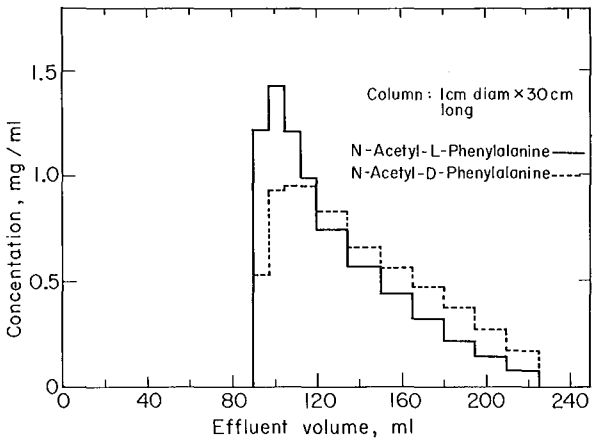

Fig. 1. Separation of N-acetyl-DL-phenylalanine on chitosan (MeOH)
(XBL-713-3079)

The second asymmetric sorbent previously synthesized is a material composed of amino acids attached to an insoluble matrix. The synthesis scheme consisted of three steps: (1) imine formation by reacting formylated polystyrene beads with an amino acid ester, (2) reduction of the imine with $NaBH_4$, and (3) hydrolysis of the attached ester. In separate chromatographic experiments using short columns containing L-tyrosine, L-glutamic acid, and L-aspartic acid resins, respectively, the optical isomers of DL-mandelic acid have been partially separated in methanol. Samples with isomer ratios up to 1.10 have been achieved using the L-tyrosine resin. Attempts to separate amino acid optical isomers on the amino acid resins, in both methanol and water, have not yet succeeded. The bound amino acid appears less accessible for complex formation, and shows effectively

zero retention of dissolved amino acids. However, because of the relative success in separating the optical isomers of DL-mandelic acid, the possibility of resolving N-acylated amino acids on the amino acid resins will be investigated as the next phase of this study. A full length report on this work is due for release.[7]

References

1. D. R. Buss, Ph.D. Dissertation in Chemical Engineering, University of California, Berkeley, 1966.

2. A. G. Ogston, Nature 162, 963 (1948).

3. C. E. Dalgliesh, J. Chem. Soc. 1952, 3940.

4. K. Amaya, Bull. Soc. Japan 34, 1689 (1961); ibid., 1803 (1961).

5. E. J. Cohn et al., J. Phys. Chem. 43, 169 (1939).

6. S. C. K. Su and J. A. Shafer, J. Am. Chem. Soc. 90, 3961 (1968).

7. J. M. Krochta and T. Vermeulen, UCRL-20429, 1971.

IV. Instrumentation and Systems Development

Construction and Use of the Gated Baseline Restorer for Anodic Stripping Analysis †

Ray G. Clem and William W. Goldsworthy

In addition to the equipment described last year, [1] a gated baseline restorer has been developed as an aid for anodic stripping analysis. This device was developed specifically for use on high-background, radioactive solutions, although its usefulness extends to any sample solution in which the background current is disproportionately high with respect to the sample current.

The operation of the module can best be understood by considering the sequence of events occurring during a gated stair-step-potential scan. This module uses a track-and-store amplifier to supply a baseline-restoration signal to the current amplifier. The track-and-store amplifier is in the track mode during the time in which the initial cell potential is applied. It thus charges up to an output potential necessary to restore the current-amplifier output baseline to zero. During the sampling period the track-and-store amplifier is switched to the hold mode, and during this same period the cell potential is stepped up to its new value. Two signals are sent to the current amplifier during the sample period--one being the inverted output of the track-and-store amplifier, the other being the cell current. If for example, the current at any sampling period were exactly equal to the current before it, then the output potential of the current amplifier would be zero. If, on the other hand, a different current flowed during the following sampling period, then the output of the current amplifier would be proportional to the difference between the currents of the two periods. Thus, one is in effect looking at the small changes in current occurring at different cell potentials, free of any continuous background current.

After each gated sampling period, the track-and-store amplifier is switched to the track mode; it is charged to an output potential proportional to the new value of the background current; and it is now ready to supply the necessary signal to compensate the current amplifier for the average background current during its next sampling period.

Figure 1 is a block diagram of this module. A comparison is given below between conventional anodic stripping and anodic stripping using the gated baseline restorer.

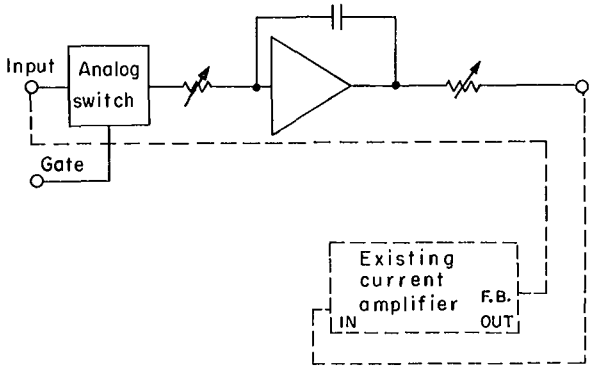

Fig. 1. Gated baseline restorer.
(XBL-7010-3949)

Several problems are attendant on performing conventional anodic-stripping analysis. A voltage scan rate--as high as is practical--is employed, because the peak current height--hence sensitivity--and the scan rate are directly related; unfortunately, the background current also increases with higher scan rates owing to the double-layer charging requirements of the electrode. Too high a scan rate results in severe tailing and loss of resolution between adjacent stripping peaks, since a finite time is necessary for the establishment of amalgam equilibrium at the electrode surface. The peak-height measurement must be made by extrapolating a generally nonlinear baseline, because accumulation of impurities in the mercury increases the background current relative to a blank scan, due to a decrease in the hydrogen overvoltage of the electrode.

Our instrumental approach eliminates these problems and improves the sensitivity of the method, while decreasing the time necessary for the accumulation step via the gated-baseline-restorer module. A stair-step ramp is employed to effect potential scanning. The step height used is usually 5 to 10 mV; the step width is generally 500 msec to give a better signal averaging of the continuous background current stored by the store amplifier in the gated baseline restorer. A 5-msec wait period, followed by a gate interval of 100 msec, is sufficient to record essentially all the faradaic current at the solution resistance levels encountered. These instrument settings have an effect on the shape of the stripping polarogram recorded. The

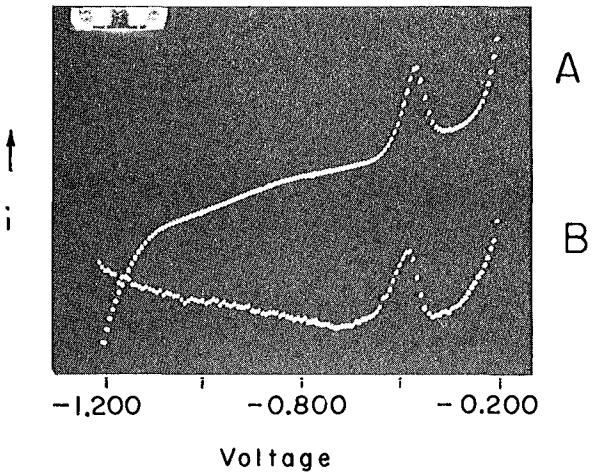

Fig. 2. Anodic stripping voltammogram of 23-ppb Pb^{2+}. Solution: 0.10 M KCl pH 4.0. Conditions: Accumulation time, 15 min; step width, 500 msec; step height, 5 mV.
A. Gated baseline restorer out.
B. Gated baseline restorer in.
(XBL-7010-4821)

height of the stripping peak is related to the potential height and, in the absence of baseline restoration, the magnitude of the background current depends upon the step width.

Figure 2A shows a stripping polarogram of 0.1 M KCl adjusted to pH 4.0 with HCl. Observe the sharp increase of anodic current as the cell potential decreases. This is due to a decrease in the electrolysis of hydrogen ion. Elements giving waves prior to reaching the plateau would be difficult to detect and measure, because of the nonlinearity of the background. Figure 2B shows a repeat of the same experiment, but now using the gated baseline restorer. The high continually-changing background present at more negative potentials in the first trace is now absent. The bowing of the baseline is due to the changing capacitive-charge requirements of the electrode about the electrocapillary maximum potential. These requirements are of a short-term nature, and are generated by the abrupt stair-stepping of the potential. Although the baseline is not strictly linear, measurement of the peak area is improved.

Footnote and References

†Condensed from UCRL-19956, August 1970.

1. Nuclear Chemistry Division Annual Report, 1969, Lawrence Radiation Laboratory Report UCRL-19530, p. 329.

Computerized Normalization of Coulometric Data

Ray G. Clem, Fredi Jakob, † and Ruth L. Hinkins

Meites and Moros[1] have described the phenomena that give rise to background currents in controlled-potential coulometry. The phenomena include charging current, faradaic currents, kinetic currents, and currents due to induced electrochemical reactions. Charging current is that which is associated with charging the electrical double layer, which surrounds the working electrode to the control potential. The magnitude of this charging current can be readily calculated and the appropriate correction applied to the coulometric titration data. Kinetic and induced reactions can be avoided, in many, but not all, coulometric determinations by judicious selection of experimental conditions. Faradaic currents, in contrast, can never be completely eliminated in a coulometric determination. These background currents are associated with the direct reduction or oxidation of impurities in the supporting electrolyte or the solvent, or an electron-transfer reaction involving the solvent or mercury. If the faradaic background current is due to the reduction of a trace impurity, such as adventitious heavy metals, then the current decays toward zero in accordance with the Lingane equation[2]

$$i = i_0 e^{-kt}, \qquad (1)$$

where i is the current at time t, i_0 is the initial value of the current, and k is the electrolytic rate constant. If the electron-transfer reaction involves the reduction or oxidation of a major component of the supporting electrolyte or solvent, e.g., hydrogen ion, then the background current may be constant with respect to time.

In this laboratory we have employed normalization procedures to correct our controlled-potential coulometric-determination data for background currents of the faradaic variety.

Equation (1) is also valid for the current associated with the reduction or oxidation of the major electroactive species. This equation written in logarithmic form becomes

$$\log i = \log i_0 - k't. \qquad (2)$$

Plots of log i vs time should thus be linear with a slope equal to k' (k' = k). Current data points, stored in memory of a multichannel analysis, are coverted to log current values with a Northern Scientific data processor. These values are in turn displayed vs channel number. The resulting plot of log i vs time generally exhibits a tail of different slope than that of the initial portions of the data. The same number of counts are removed from each data channel until the plot of log i vs time is linear. This procedure suffers from two shortcomings, viz., it is subjective, and it is based on the assumption that the faradaic background current is constant throughout the electrolysis process. As indicated above, the faradaic phenomena can, depending on their type, lead to constant or exponentially decaying background current. It is for these reasons that we have sought to develop computer methods for the resolution of the background and titration currents. Both analog and digital methods have been investigated. In both cases we assume that the total current is given by

$$i_t = i_p + i_b, \qquad (3)$$

where i_t, the total current, is the sum of i_p, the current due to the desired reaction and i_b is the faradaic background current. Each of these currents in turn is given by Eq. (1). Equation (3) is applicable in cases where the background current is constant or undergoes an exponential decay.

An analog computer was used to generate two exponentially decaying signals. These signals were added and the resulting curve was compared on an oscilloscope with the experimental data. Coefficient potentiometers were set to give the best observable fit of the experimental and computed curves. After an initial match of the curves with the oscilloscope, a final match of the computer-generated curves and the experimental data was obtained on an x-y plotter. Four coefficient potentiometers were employed, two for the initial current values and two for the respective electrolytic rate constants given in the expanded version of Eq. (3)

$$i_t = i_p e^{-k_p t} + i_b e^{-k_b t} \qquad (4)$$

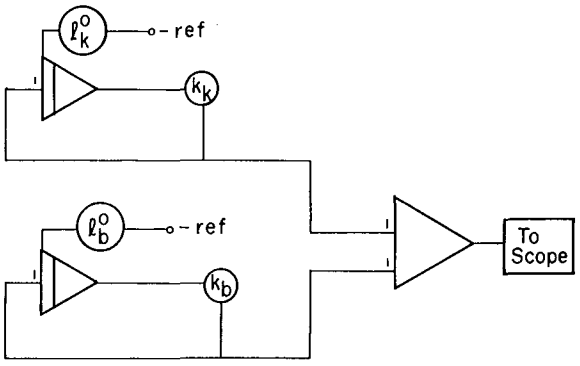

Fig. 1. Analogue computer simulation of a coulometric-titration curve.

(XBL-713-3058)

The relative number of coulombs associated with the primary and background currents was then obtained by integration of the respective currents for a fixed period of time. The quantity of electroactive sample was then calculated with the equation

$$\text{mg total} = \text{total counts} \frac{Q_p}{Q_p + Q_b}, \qquad (5)$$

where Q is the number of coulombs calculated for the given current.

Figure 1 shows the analog computer circuit that was employed in this work.

A digital computer program to fit the experimental data to Eq. (4) has also been developed. N values of current as a function of time are read from data cards. Parameters i_p^0, k_p, i_b^0, and k_b--redesignated x1, x2, x3, and x4, respectively--are determined by an iterative gradient method, so that the function F(t) = x1*exp(x2*t) + x3*exp(x4*t) is the "best" (in the least-squares sense) fit to a subset of data values obtained by deleting the first N1 of the N values. For certain input data the parameter x4 is forced by the user to be zero and the best values are determined for the other three parameters. This is done when the background current is believed to be constant. The value of N1 may be read from a data card.

During program development, we have used a program option which allows us to view the data points, fitted curve, and final values on the CRT as the program executes, and to input from the teletype various N1 values and observe the resulting changes. In the production version, the N1 value will be computer determined, within certain limits, to give the best parameter values. Pictures of the data and curves will probably be made on film for

later viewing only when requested specifically by the user, or when the computer determines that the data or fits seem "odd."

The parameters x1, x2, x3, x4, and the difference

$$D = \sum_{I=1}^{n} y_I - \int F(t)dt,$$

where the integral of F is taken over the whole t range, are the results which are returned to the user. The options for execution-time viewing and user interaction will remain in the code, but will probably be seldom utilized. In fact, when the input is put on magnetic tape, data values and results will most likely be kept on a tape in the computer-center tape library, and the program itself will be on the data cell. The only chore remaining for the user is to look at the printed results.

Footnote and References

†Permanent address: Department of Chemistry, Sacramento State College, Sacramento, California 95819.

1. L. Meites and S. A. Moros, Anal. Chem. 31, 23 (1959).

2. J. J. Lingane, Electroanalytical Chemistry (Interscience Publishers, Inc., New York, 1958), 2nd ed., pp. 224-229.

A Rotated Mercury Cell for Constant Potential Coulometry Titration Background Determination by Normalization

Ray G. Clem, Fredi Jakob, † Dane Anderberg, and Lawrence D. Ornelas

The rotated-cell design presented is, to our knowledge, the first successful conceptual departure from the stirred mercury-pool design introduced over 25 years ago by Ligane.[1] These conventional mercury cells employ a stationary pool of mercury, which is efficiently stirred at the solution-mercury interface by a glass stirrer driven by a high-speed motor. The probes--an isolated auxiliary electrode and a reference electrode--are also stationary. Prior to an electrolysis, the solution electrolyzed is sparged of electroactive dissolved oxygen by a strong jet of nitrogen gas directed at the solution surface, in the case of small cells, or it is bubbled through the solution, in the case of large cells. The minimum sparge times required are usually 7 to 10 min. The electrolysis times employed are generally 15 to 20 min. This time span is that required to reduce the initial cell current by three orders of magnitude.

In contrast to the foregoing, the rotated cell can be sparged within 20 sec and the electrolysis completed within less than 12 min. An exploded view of this cell and assembly are shown in Fig. 1. The present cell requires 2.0 ml of mercury and 2.0 ml of solution; however, the cell could be scaled down to hold 100 μl of mercury and sample or less, if a better bearing mount for the cell was developed.

The probe-tip design shown in Detail 3 of Fig. 1 permits contacting of the rotated solution without causing deleterious spray formation. Figure 2 shows the steps in the construction of a probe.

A time comparison between the rotated and conventional cell is given in Table I. The

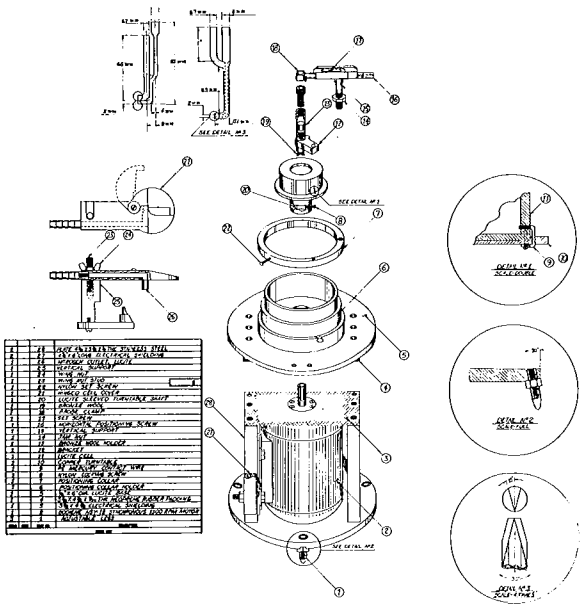

Fig. 1. Exploded view of the rotated cell assembly. (XBL-711-40)

Table I. Time comparison of the rotated cell with a conventional cell.

	Time, minutes	
Operation	Rotated cell	Conventional cell
Aliquot	1	1
Sparge	0.3	7 to 10
Pretitrate	1 to 3	1 to 3
Titrate[a]	12	15
Time Totals	14.3 to 16.3	24 to 29

[a]For U^{6+} in 1M H_2SO_4

titration-time disparity would have been greater had a diffusion-controlled system such as cadmium been used in the example. The rate of reduction of uranium is kinetically controlled and depends upon the rate of disproportionation of the U(V) species.[2,3] Even so, the total time to obtain the result is reduced by almost a factor of two.

Presented too for the first time is a technique we term "normalization," which permits the evaluation of the background current contribution in each individual determination. The ability to do this greatly improves the precision of the data. The variation of the average background current is the limiting factor as to how small a sample can be titrated. The following data will illustrate the point. Table II shows the results for cadmium and lead which were obtained by applying the average background current correction to the raw data; the uranium results were corrected by the normalization technique. Table III details this. Note that the average deviation of 0.2 μg is less by a factor of 4.5 than the average deviation which would have been obtained had the average correction been applied.

The normalization technique is applied in the following manner. The digital information is stored in the first half of the memory of the pulse-height analyzer, using a 3 sec/channel time dwell. When the titration is completed, the stored data are transferred to the last half of the memory using the data processor. The data processor is switched to its normalized mode of operation and the analyzer's storage sense is changed to subtract. While observing the 5-cycle log display of the data on the analyzer's oscilloscope, the normalization program is repeatedly initiated until all the data points of the curve in the second half of the memory fall on a straight line. The product of the number of memory channels used to record the data and the number of counts removed from each channel during the normalization process is the correction factor. Figure 3 illustrates the technique. Curve A is the original data; curve B is the data after normalization.

If very small samples are titrated, it becomes necessary to correct the results for the charging current. This value too is obtained by normalization of data obtained from a blank run.

Thanks are due Mr. F. T. McCarthy of this laboratory for helping build the prototype

Table II. Titration results.

μg Cd				μg Pb				μg U			
Taken	Found	Av.dev.	No. of analyses	Taken	Found	Av.dev.	No. of analyses	Taken	Found	Av.dev.	No. of analyses
1030[a]	1029.9	±1.4	5	1250[a]	1250.0	±0.9	6	1124[a,c,d]	1123.5	±0.2	5
258[b]	257.8	±0.3	5	500[b]	500.2	±0.4	5	562[a,c]	561.7	±0.1	5
26[b]	26.2	±0.2	5	100[b]	99.9	±0.1	5	281[a,c]	280.4	±0.5	6
				10[b]	9.9	±0.2	6	56[a,c]	57.0	±0.2	5

[a]Coaxial probes used.

[b]Parallel probe used.

[c]Normalization procedure used.

[d]Also see Table III.

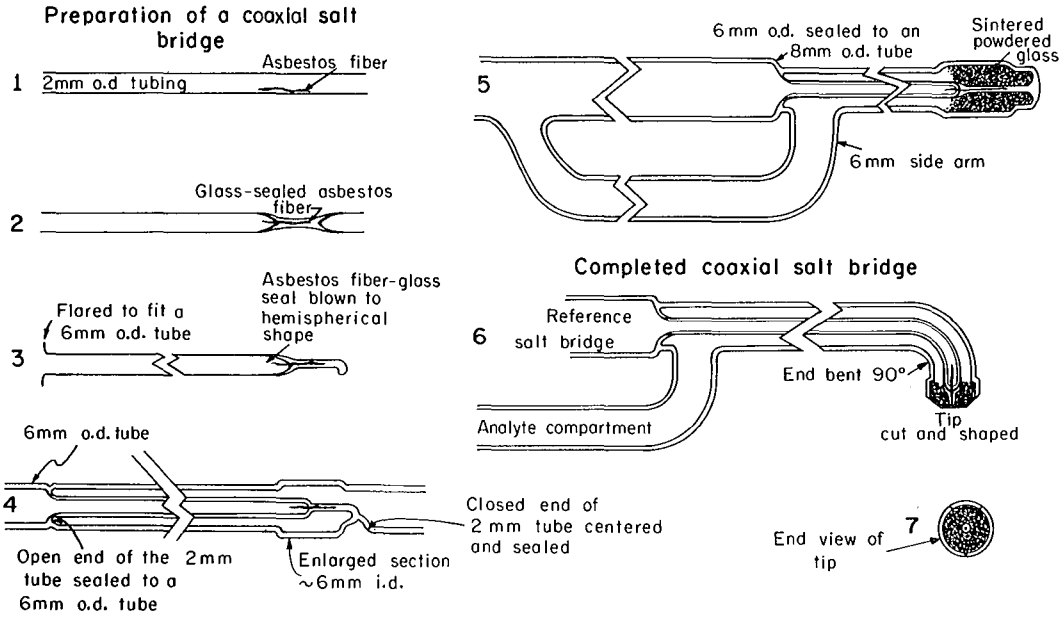

Fig. 2. Construction of coaxial probe.
(XBL-7011-4138)

Table III. Normalization of uranium results.

Run No.	1	2	3	4	5
Scaler counts	1128373	1128259	1129566	1126863	1126666
Correction	3400	3840	5120	2560	2048
Normalized value	1124973	1124419	1124446	1124303	1124618
Nominal value, μg	1125.0	1124.4	1124.4	1124.3	1124.6
Less charging current U equivalent (1.0 μg)	1124.0	1123.4	1123.4	1123.3	1123.6
Average			1123.5 ± 0.2		

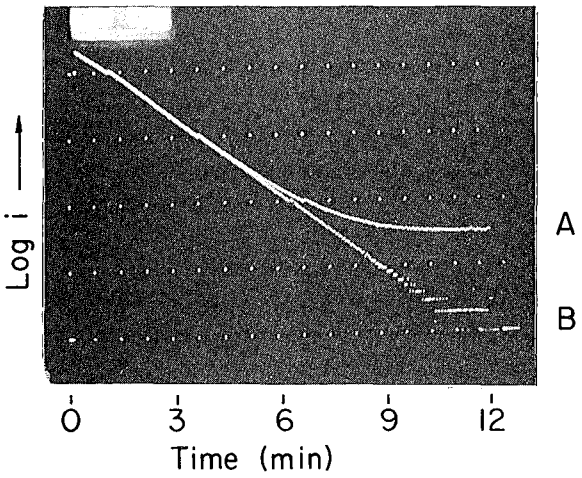

Fig. 3. Normalization of a constant potential coulometric titration for uranium.
A. Raw data 569.8 μg U^{6+} found
B. Normalized Data: 561.6 μg U^{6+} found. Uranium present 561.8 μg U^{6+}.
(XBB-711-145)

model of the cell and assembly upon which the present model is based.

Footnote and References

†Permanent address: Department of Chemistry, Sacramento State College, Sacramento Calif. 95819.

1. J. J. Lingane, J. Am. Chem. Soc. 67, 1916 (1945).

2. G. L. Booman, W. B. Holbrook, and J. E. Rein, Anal. Chem. 29, 219 (1957).

3. I. M. Kolthoff and W. E. Harris, J. Amer. Chem. Soc. 68, 1175 (1946)

Fumed-Silica Salt Bridges †

Ray G. Clem, Fredi Jakob,* and Dane Anderberg

This investigation was prompted by our need for rugged, highly conducting salt bridges of various geometries with low leakage which could be fabricated rapidly and at low cost. Although unfired Vycor tubes[1] have gained wide acceptance for use as salt bridges in coulometry, they shatter if allowed to dry with a salt solution inside, and strongly adsorb dye material. Also, they have a considerable chemical memory which necessitates a long washout operation when one wishes to change the filling solution. These drawbacks, in addition to the cost and delays associated with custom fabrication (a recent price increase to $85.00 per tube from $15.00 a few years ago, coupled with the fact that the tube must be custom fabricated, thus involving a long time delay) forced us to consider alternative materials. These problems were overcome very simply and inexpensively by the use of a supporting electrolyte gel, prepared from fumed silica, contained in a tube having a fritted

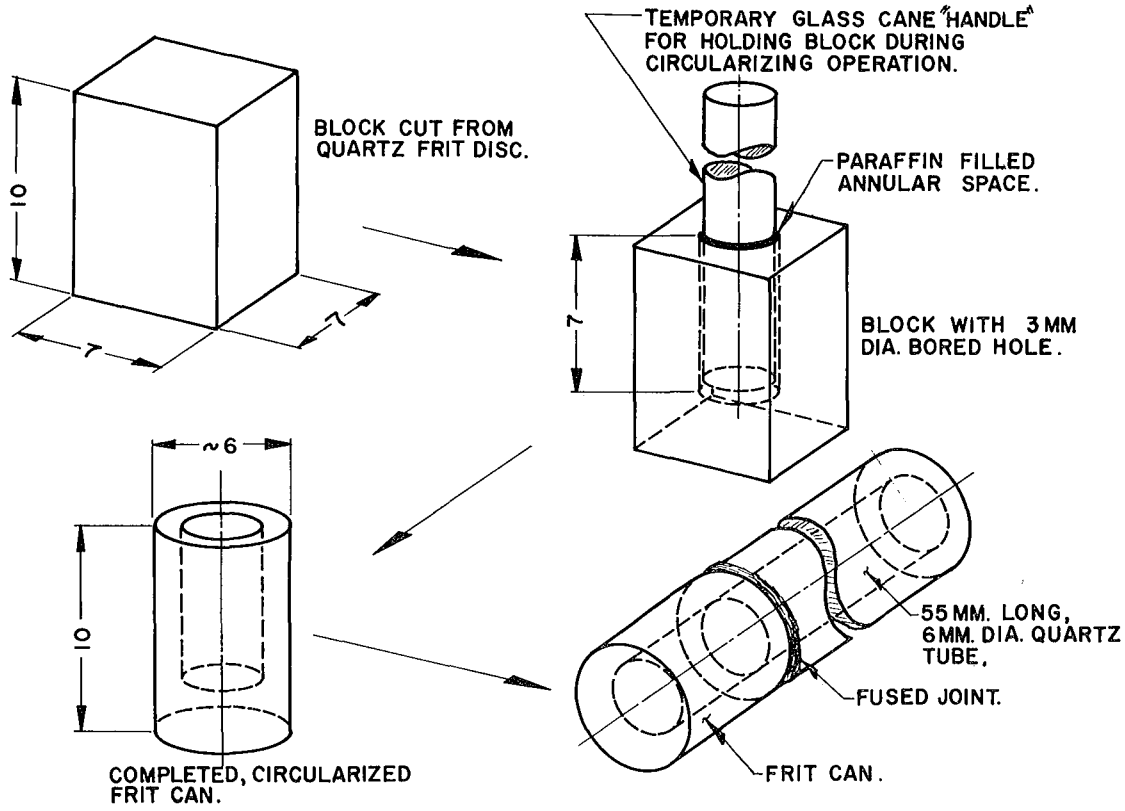

Fig. 1. Construction of a quartz frit. (XBL-709-6629)

lower section. The cost of these bridges is about $3.00 each, material and shop time included.

These bridges are characterized by a low leakage rate of 13.2 µl per hour and a very low resistance. High currents can therefore be passed without deleterious heating effects. Also, fumed silica gels can be formed with a wide variety of electrolytes, the only limitation being that the pH must not exceed 8 if the gel is to be stable. A salt bridge can be converted from one supporting electrolyte to another within minutes, and no harm is done to the frit if the silica gel is allowed to dry.

Figure 1 shows the steps in the construction of a frit.

The authors wish to thank Mr. Warren Harden of this laboratory for making the technical illustration.

Footnotes and References

†Condensed from UCRL-19950 Rev., August 1970.

*Permanent address: Department of Chemistry, Sacramento State College, Sacramento, Calif. 95819.

1. W. N. Carson, C. E. Michelson, K. Koyama, Anal. Chem. 27, 472 (1955).

Hot Bath for Samples in Volumetric Flasks †

U. Abed

It is often required to heat volumetric flasks containing liquid samples in a bath of a definite, uniform, and controllable temperature. For instance, many spectrophotometric analyses depend upon the proper color development, which should, furthermore, be reproducible. Care must be exercised not to overheat and thereby possibly destroy the reagent, particularly when organic chromogenic or volatile substances are present in the system. Such consequences often occur when the flasks are resting directly on a hot plate or are touching the bottom of a bath which is in contact with the heater. Suspending the flasks individually from clamps attached to ringstands is cumbersome, demanding unnecessary work, space, and equipment.

A simple, inexpensive bath was designed in our laboratory which fulfills the above-mentioned requirements. A perforated, stainless steel "table" top, consisting of a 14-in. ×8-in. stainless-steel sheet, is cut and supported at each corner by a 4-1/2 in. long screw "leg." Eighteen 5/8-in. holes, punched through the sheet, allow easy insertion and withdrawal of 25-ml and 50-ml volumetric flasks. The flasks are secured within the holes by retainer rings just below their ground-glass joint. Cut from hard nylon (or teflon) 3/32-in. sheeting, the o.d. of the ring equals 1 in. and the i.d. equals 7/16 in. A 1/2-in. section is cut out of the ring, permitting it to be slipped around, or removed from, the neck of a volumetric flask.

A thermometer is inserted vertically through one of the holes to the level of the bottom of the flasks. Either the entire table, or the flasks and thermometer alone, are suspended in the bath recommended in a given procedure.

The bath container may be of any appropriate size and material available. We used a 20-in. ×15-in. ×2.5-in. Pyrex pan filled with water, placed on top of a thermostatically-controlled heating unit, to maintain a sample temperature of 85°C for several hours. A constant bath level can be held against evaporation by use of a "chicken feeder."

The size of the table, the length of the supporting screw legs, and the number and diameter of the holes, are optional to suit individual needs. Greater versatility of the table can be obtained by using removable legs, i.e., screws of different, interchangeable lengths to accommodate 100-ml and 250-ml volumetric flasks also. If the holes were made to be 1 in. in diameter, retainers having a 1-1/2 in. o.d. but different i.d.'s would serve to secure a variety of volumetric-flask sizes.

The table is easily disassembled and can be stored in a minimum of drawer space.

Footnote

†UCRL-20410, November 1970; submitted to Anal. Chim. Acta.

88-Inch Cyclotron Operation and Development

J. Bowen, D. J. Clark, J. P. Meulders,† and J. Steyaert†

During 1970 the cyclotron operated continuously, except for shutdowns at the beginning of January and the end of December. The shutdown in the first two weeks of January was to straighten the dee and do general mechanical and electrical maintenance. The shutdown during the last week in December was part of a laboratory shutdown, and was used to get a start on the January 1971 shutdown. The distribution of operating hours during 1970 is shown in Table I. The breakdown of operating time according to the type of ion accelerated is shown in Table II. The operating time included 499 energy changes.

Table I. 1970 Time distribution.

Operating for experiments		
Tune-up	6%	
Beam optics	4%	
Run time	58%	
Beam development	10%	
Operating time		78% (6512 hours)
Shutdowns, planned maintenance	13%	
Unplanned maintenance	9%	
Total maintenance		22%
Total work time		100% (8336 hours)

Table II. 1970 particle distribution.

Internal ion source		
Protons	31%	
Deuterons	2%	
Helium 3	8%	
Helium 4	30%	
Nitrogen	4%	
Oxygen	14%	
Other	4%	
Total		93%
External polarized proton source		7%
Total operating time		100% (6512 hours)

During this year, heavy-ion beams were developed for scattering experiments. Nitrogen and oxygen beams of 50-70 MeV were run frequently. External-beam currents were several μA of N^{+3} and O^{+3}. Small beams of 160 MeV N^{+4}, 250 MeV N^{+5}, Ne^{+4}, Kr^{+4}, and Kr^{+5} were extracted. Fifth-harmonic acceleration was developed for the krypton beams. The best beams were obtained by use of an anode with water cooling around the top, in addition to the normal cooling around the base. This was done on an anode made of inconel for extra mechanical rigidity. However, other data indicate that copper would be a better material for thermal conductivity so a similar anode is being made of copper.

The polarized source continued to run reliably after a misalignment in the center region was corrected. This problem was caused by a drop of the dee of about 0.1 inch, giving the beam a strong vertical kick on the first turn between the dee and dummy dee, causing a factor of five beam loss. It was solved by realigning the dee with a transit. The source was operated with deuterons for the first time. The vector polarization was measured by the Cave 5 group as 57%, which is 85% of the maximum theoretical value of 67%, and is a good value for experiments. The intensity was 50-100 nA external beam, about the same as for protons. The proton polarization was increased from 75% to 80% by eliminating magnetic-field reversals in the rf-transition region.

An unusual dee motion was discovered late in the year. This was an effect which caused the north half of the front edge of the dee to drop slowly by about 0.050 inch during the first 45 minutes after the rf was turned on. It then rose back up in some 45 minutes after rf turnoff. From temperature and water flow measurements it appears that there is a cooling unbalance in the north part of the dee. Since this movement causes beam tuning problems, it will be corrected in the January 1971 shutdown.

An external heavy-ion source was constructed, and testing was started near the end

of the year. It is a copy of one of the Berkeley Hilac ion sources. It is a PIG source whose magnetic field is used both for trapping the electrons in the arc chamber and for analysis of the extracted beam. The water-cooled anode is copper and the two cathodes are tantalum, loosely attached to copper supports. These cathodes are hot enough to thermally emit electrons. The power supply contains a series-regulating triode, but the latter was not used for the initial trials. A 500-ohm resistor was the only series element. The source gases used were nitrogen, hydrogen, and neon. A typical source nitrogen output at 10 kV energy is: N^{2+} - 1500 μA, N^{3+} - 830 μA, N^{4+} - 60 μA, and N^{5+} - 2 μA. The arc parameters were .8 kV and 2.5 A. The gas is just enough to maintain the discharge. Some initial tests were performed for the ionization of lithium. We used a stainless-steel insert following an idea of Bennett.[1] For 10-kV accelerating voltage, the bending magnet was not powerful enough to bend ions with a charge/mass ratio below 1/3, so it was replaced by an electrostatic mirror. The initial overall transmission for protons between the PIG source and the extracted beam was 0.5%. This low yield will be increased by improved beam transport from source to injection line, and by the use of the buncher.

Studies were resumed on the modification of the downstream deflector electrodes to give radial electrostatic quadrupole focusing to the deflected beam. The deflected beam is defocused radially by the fringing magnetic field of the cyclotron as it crosses the main magnet pole edge. The phase space is distorted by the nonlinear field, increasing the effective phase space area and reducing the transmission to the caves. This study is using ray tracing through the electric and magnetic fields of the deflector region to determine the amount of focusing and the electrode shape required for the downstream deflector electrodes.

Footnote and Reference

†On leave of absence from University of Louvain, Ottignies, Belgium.

1. International Cyclotron Conference, Oxford, England, September 1969.

88-Inch Cyclotron Magnetic-Particle Spectrometer

D. L. Hendrie, J. R. Meriwether,† F. B. Selph, D. W. Morris, W. S. Flood, and B. G. Harvey

For the past few years, much of the staff of the 88-inch cyclotron has been involved in the construction of a heavy-particle magnetic spectrometer. This spectrometer is now mostly complete and is able to be used for experiments. This report will give a brief and preliminary description of its purpose, features, capabilities, and performance to date.

Since a spectrometer is necessarily a costly, complicated, and cumbersome device, one must consider its various and sometimes conflicting properties carefully to ensure that the advantageous features are maximum. It helps to remember that most of the experimental work at a cyclotron uses the high-energy particle beams to excite low-lying and closely spaced energy levels in the target nucleus. The scattered light particle is detected and its energy is measured with respect to the incident beam energy; we are usually less interested in the particle's absolute energy. By using the spectrometer in this "energy loss" mode of operation, one is permitted several techniques for improving resolution and rates of data accumulation that would not otherwise be available.

The main advantage of a spectrometer is its capability of improving energy resolution by at least a factor of two over the best available solid-state systems. This improvement is even more pronounced for light particles of high energy, where their long range makes them difficult to stop in present detectors. When the spectrometer is used in the energy-loss mode and with some simple manipulation of the apparatus, this resolution is not lost by experiments with large "kinematic broadening" effects, such as produced by heavy projectiles on light targets. Further, matching the dispersion of incident beam to that of the spectrometer in the energy-loss mode allows the delivery of several times as much beam on target as in counter experiments, again without loss of resolution. Since the typical solid angle of acceptance of the spectrometer is a factor of 5-10 larger than most detector apertures, improvements in counting rates of 15-50 are achieved.

A second major advantage is the capability of reducing backgrounds in the experimental spectra. This is especially important for weak reactions in which intense elastic scattering

causes "pile up" in detector spectra and obscures the weak reaction product peaks. The physical displacement of different reaction products almost entirely eliminates the backgrounds due to competing reactions, as it does more generally for backgrounds due to x rays, γ rays, and neutrons. An additional improvement is effected by the superior entrance slit geometry which can be used with a spectrometer.

Several other advantageous features are present. Different reaction products can be identified by comparing their magnetic rigidities with other easily measured quantities such as E, dE/dx, or time of flight, but always without loss of energy resolution. The ability to calibrate the magnet to make absolute energy measurements can be invaluable in some experiments. Finally the ability to conduct experiments at very small scattering angles, including zero, can sometimes be of great use.

A schematic layout of the final design is shown in Fig. 1 and a list of relevant spectrometer parameters is listed in Table I. Some of the more novel features will be described briefly. Because many of the cross sections obtained in high-energy experiments change rapidly with angle, it was considered important to obtain the large solid angle of acceptance in the vertical direction, i.e., perpendicular to the scattering plane. A typical operating aperture is 0.6° radially and 6° vertically, giving a solid angle of 10^{-3} sr. The quadrupole is used to focus the reaction products in the vertical direction to stay within the magnet gap; the entrance-edge angle of the sector magnet then provides a vertical focus at the focal plane. Since, for large solid

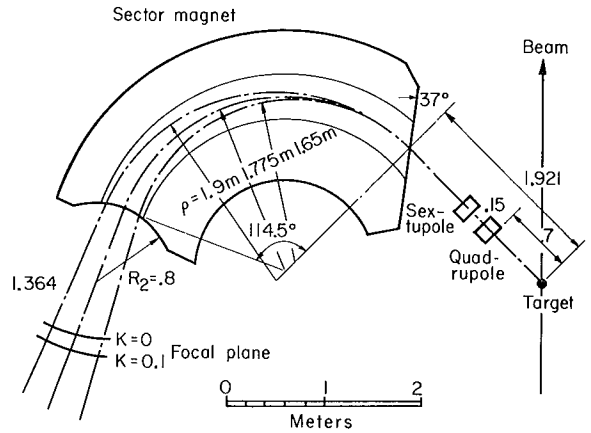

Fig. 1. Schematic representation of the 88-inch cyclotron magnetic-spectrometer system. (XBL-713-3068)

Table I. Parameters: 88-in. magnetic spectrometer.

Magnet iron	32 Tons
Magnet copper	1.8 Tons
Power at 13.5 kG	200 kW
Magnet gap	10.95 cm
Radius	1.65-1.90 m
Maximum dimension	5.5 m
Focal plane length	55 cm
Vertical acceptance	100 mrad
Radial acceptance	20 mrad
Solid angle (maximum)	2 msr
Energy range	30%
Maximum energy (triton)	90 MeV
Dispersion	3.3-4.2 m
Radial magnification	0.33-0.40
Vertical magnification	4.7
Angular range (total)	+125° to -180°
Angular range (ext. Faraday cup)	+15° to 125°
	-55° to -165°
Angle of incidence on focal plane	-11° to +10°
Resolving power $\frac{E}{\Delta E}$ at Ω = 1 msr	3,000
Maximum resolving power	10,000

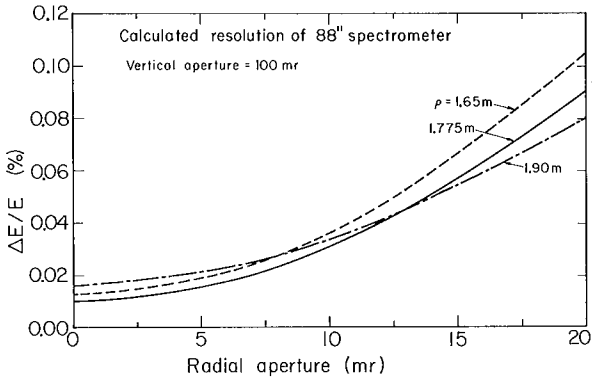

Fig. 2. Calculated resolution of the spectrometer with full vertical aperture of 100 mrad as a function of radial aperture, assuming a beam spot size of 0.5 mm×6.0 mm. (XBL-713-3069)

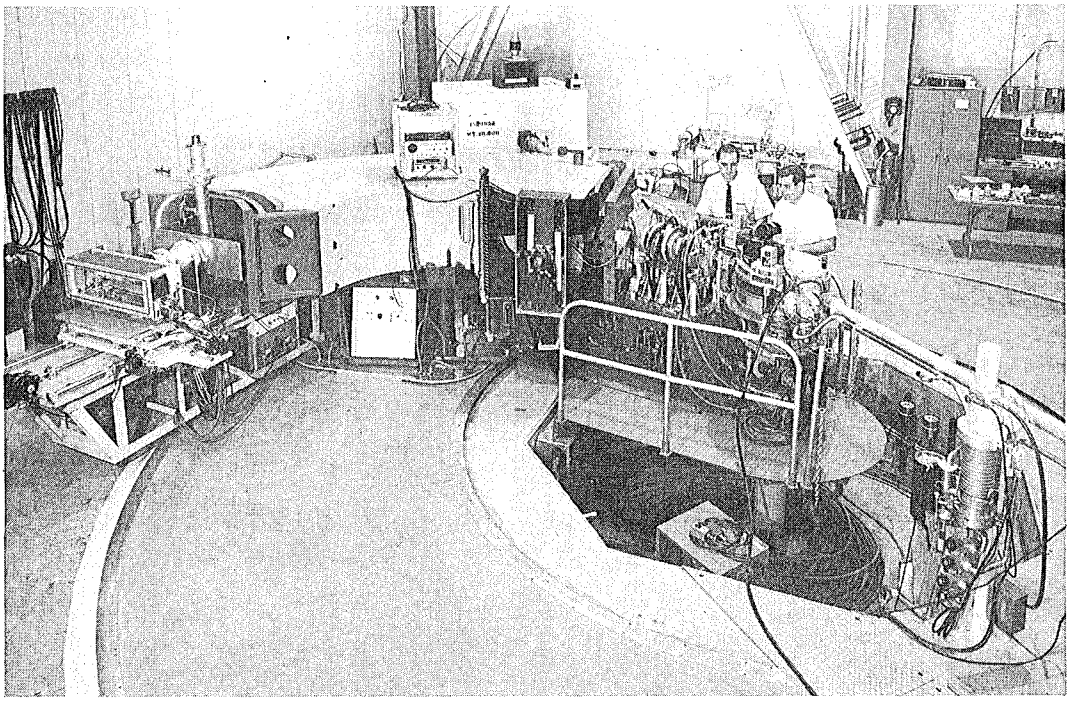

Fig. 3. Picture of the complete system, showing the beam line and scattering chamber to the right and the focal-plane-detector apparatus to the left. (BBC 709-4354)

angles, abberations limit the resolution obtainable, a sextupole magnet was devised to compensate for those most troublesome abberations which are due to the large vertical aperatures and beam-spot sizes. Since the sextupole is independently energized, it can be set to optimum value for the performance of each experiment.

Because it was decided to design the spectrometer for active focal-plane detectors, rather than the more typical nuclear emulsions, several features were incorporated specifically for this. The most unusual is the negative radius of curvature at the exit edge of the sector magnet, which is used to rotate the focal plane so that incident particles strike the detector almost perpendicularly. The dispersion was kept large in order to give maximum separation between peaks, although this was done somewhat at the expense of the total energy range of the spectrometer. A typical displacement of the focal surface for a kinematic broadening parameter K = 0.1 (alphas scattered from magnesium) is seen in Fig. 1. Figure 2 shows the calculated resolution of the spectrometer for full vertical aperture for a range of horizontal openings.

The spectrometer is held in alignment by a sturdy steel frame and tongue which rotates, using a 12-in. ball bearing, about a central post upon which the scattering chamber is affixed. While data are being taken, the magnet sits upon two carefully located flat steel rails, as shown in Fig. 3. To move the spectrometer, four air pads are inflated on the smoothly grouted area between the rails, and a small air motor is easily able to move the 40-ton apparatus. In Fig. 3, one can see the beam line entering the chamber and passing on to a heavily shielded Faraday cup. A sliding foil scattering chamber window gives a working range of 110° in scattering angle. The chamber is normally positioned to work from 15° to 125°; however, rotation of the chamber can provide access to all angles between +125° and -165°, including 0°. The magnetic field regulation is provided by a transductor-monitored series current supply. NMR measurements indicate stability to a few parts per million after the temperature of the magnet has stabilized.

Preliminary and limited tests of the system have shown no significant deviations from the design features, and experiments are being performed with the system. At least for the present, position-sensitive silicon detectors available commercially are being used for tests and experiments. A typical result would be that for a $^{238}U(\alpha, \alpha')$ experiment at 50 MeV.

A resolution of 16 keV, including target and beam preparation effects was maintained for 3 days, with a total beam delivered on target of 1 μA and with a solid angle of 0.7×10^{-3} sr.

Footnote

†Present address: Computer Science Department, University of Southwestern Louisiana, Lafayette, Louisiana 70501.

Computer Control System for the Field-Free Spectrometer

J. E. Katz

A computer control system was assembled to collect data and control the operation of the Field-Free Spectrometer in 1968.[1] The system has been in almost continuous operation for the past two years. In each year, more than 7000 hours of experiments have been performed. The computer and peripheral equipment, except for an ASR-33 teletype, have proved to be very reliable. The installation, in the near future, of a heavy-duty Model-35 teletype will provide a more reliable printer.

Until this year, the capability of this system has been limited by the small memory (4K, 12-bit words) of the Digital Equipment Corporation PDP-8 computer. Another major limitation has been the slow input and output via teletype and paper tape. Of course it has been very troublesome for the experimenters to convert their data by hand to punched cards for analysis by large fitting programs at the CDC-6600 computer center.

In the past year, the computer system has been substantially upgraded with little loss in experimental time. The system hardware is presently interconnected as shown in Fig. 1.

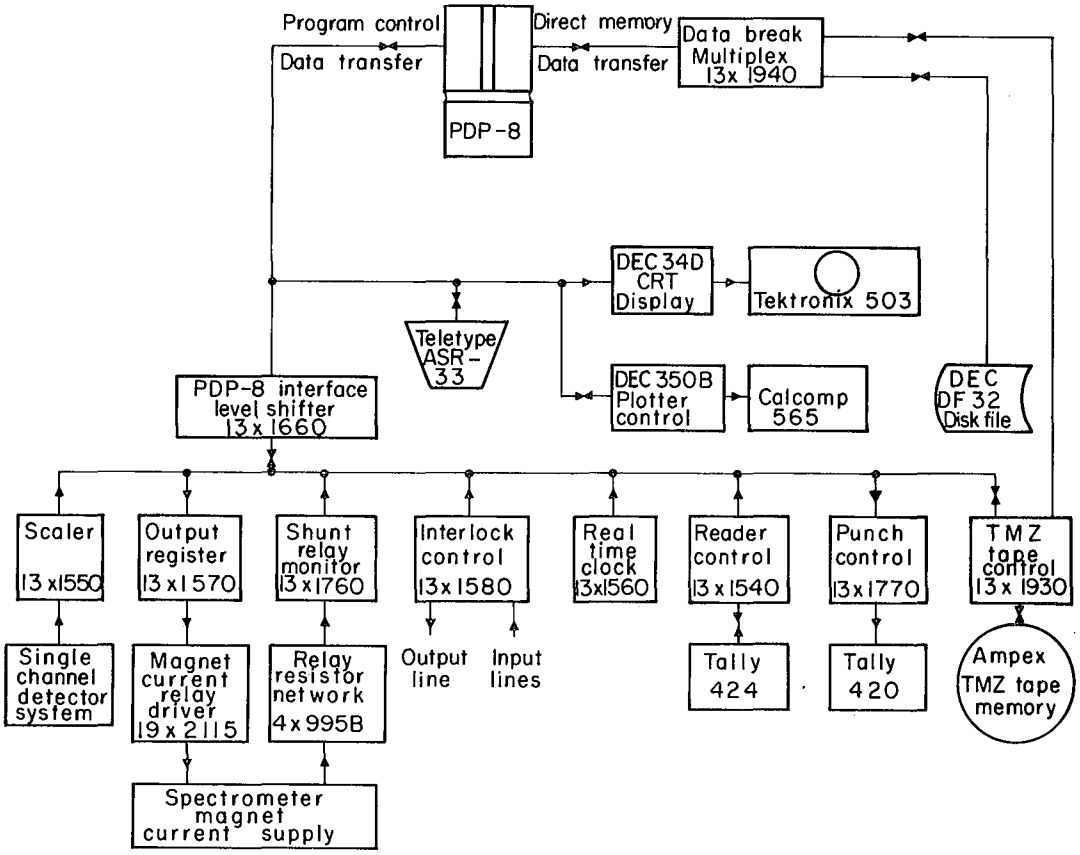

Fig. 1. (XBL-711-2655).

The program storage and data handling capabilities have been greatly expanded with the addition of a 32K, 12-bit word, disk file memory system. The magnetic tape memory system, installed this year, provides for very fast input and output of programs and data. Large amounts of experimental data may be stored and accessed conveniently on magnetic tape and may be transferred directly to the CDC-6600 computer center for analysis.

Reference

1. Ron Zane, R. L. LaPierre, and J. E. Katz, in Nuclear Chemistry Annual Report, 1968, UCRL-18667, p. 337.

Fast-Coincidence Timing at Low Gamma Energies with Tin-Loaded Scintillators

S. Koički, T. A. Koster, and D. A. Shirley

Fast-coincidence timing at photon energies below or in the vicinity of 100 keV is often required in lifetime determinations and perturbed angular correlation (PAC) experiments. Of particular interest is the $^{100}Pd \rightarrow {}^{100}Rh$ decay, where the 84.0-keV - 74.8-keV cascade offers several useful applications of the time-differential PAC method to solid-state investigations.

The difficulties usually encountered at low photon energies are twofold: 1) The response of NaI(Tl) is relatively slow, and 2) the energy absorbed in faster organic scintillators represents only a small fraction of the incident photon energy.

In this note we describe some advantages of commerically available Sn-loaded scintillators (Nuclear Enterprises NE-140 plastic and NE-316 liquid scintillators) in this area.

Energy Response

The 5% (by weight) tin content in the NE-140 plastic scintillator greatly enhances the overall detection efficiency at lower photon energies. More important, the nature of the absorption changes in favor of the photoelectric effect, and peaked energy spectra may be expected, similar to those obtained with NaI scintillators. The relatively high light output and good optical quality of NE-140 ensures reasonably good energy resolution, and both the full energy peak and the tin escape peak are observed in the energy spectrum.

Figure 1 shows the energy spectra obtained with the 1.5-in. × 1.5-in. NE-140 scintillator at a few representative low photon energies. Above an incident energy of 29.2 keV, the tin K escape peaks are observed. The weak Compton edge also appears at quite low energies. The absence of a full energy peak and an escape peak in ordinary, unloaded plastic

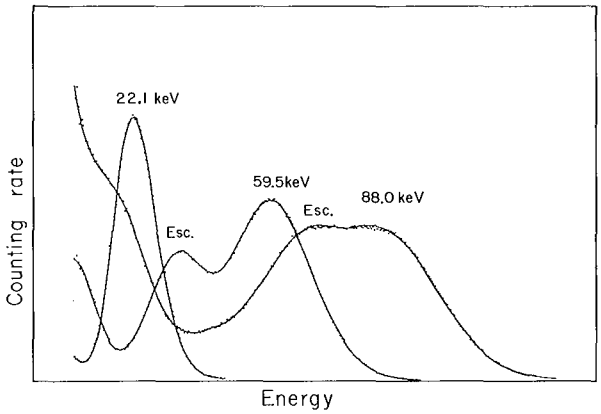

Fig. 1. Energy spectra of single-energy γ rays of 22.1 keV, 55.9 keV, and 88.0 keV, detected by the 1.5-in. × 1.5-in. NE-140 plastic scintillator. The spectra start at 5 keV of energy spent in the scintillator.
(XBL-713-3065)

scintillators is demonstrated in Fig. 2. Here the same phototube was used and plastic scintillators NE-111 (unloaded) and NE-140, of the same size, were interchanged. The incident photon energy was 88.0 keV.

The efficiency of absorption of the NE-140 phosphor is quite high at low energies. Thus, in a layer of 1.5 in., the Sn component alone absorbs about 50% of the photons in the 80-keV region.

Time Response

The manufacturer, Nuclear Enterprises, does not give the decay constant for NE-140, which is presumably dependent on the exact tin content and possibly other factors involved in phosphor preparation. Nevertheless, NE-140 has the fast properties of a plastic scin-

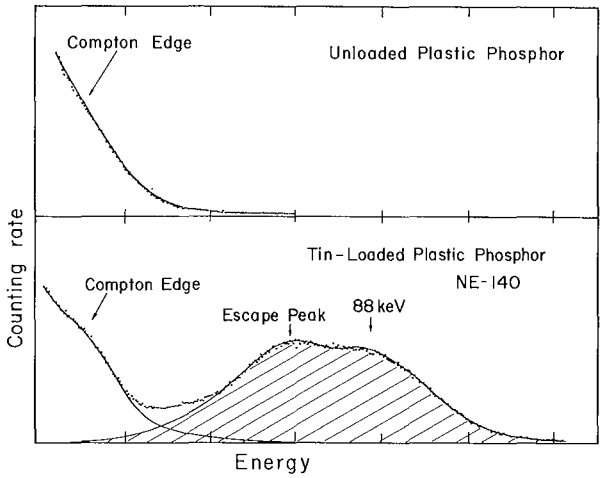

Fig. 2. Comparison of the energy response of unloaded and Sn-loaded plastic phosphors (both 1.5 in. × 1.5 in.) to photons of 88.0 keV. (XBL-713-3066)

tillator, though not so pronounced as in most unloaded phosphors. We did not attempt to determine the decay constant of our specimens, but rather tried to compare the time response of the NE-140 to that of NaI(Tl) in an arrangement similar to that used in most real experiments.

In a fast-slow coincidence arrangement consisting of two RCA C10001D photomultiplier tubes, we kept one side "as fast as possible," i.e., the fast NE-111 (1.5-in. × 1.5-in.) scintillator was used and the energy channel set permanently at the high energy edge of the Compton distribution of incident annihilation photons. The other annihilation photon was detected either in the NE-140 (1.5 in. × 1.5 in.) or in NaI(Tl) (1.5 in. × 3 mm). Energy channels were set at different energies in each run, but always in a way to accept the entire full energy peak corresponding to that incident energy in either phosphor. (Escape peaks were not accepted.)

Two families of coincidence curves were obtained: one for 1.5-in.-thick NE-140 and the other for 3-mm NaI(Tl). At lower energies the widths (FWHM) of the prompt peaks are mostly determined by the second side [NE-140 or NaI(Tl)], which detects lower energies in slower phosphors. The contribution of the fast side is smaller and constant in both families. Figure 3 presents the various FWHM time resolutions obtained. It can be seen that in our arrangement the 1.5-in. × 1.5-in. NE-140 phosphor gives coincidence curves about twice as narrow as the thin NaI(Tl) crystal. Remembering its relatively high detection efficiency, it then seems to be a

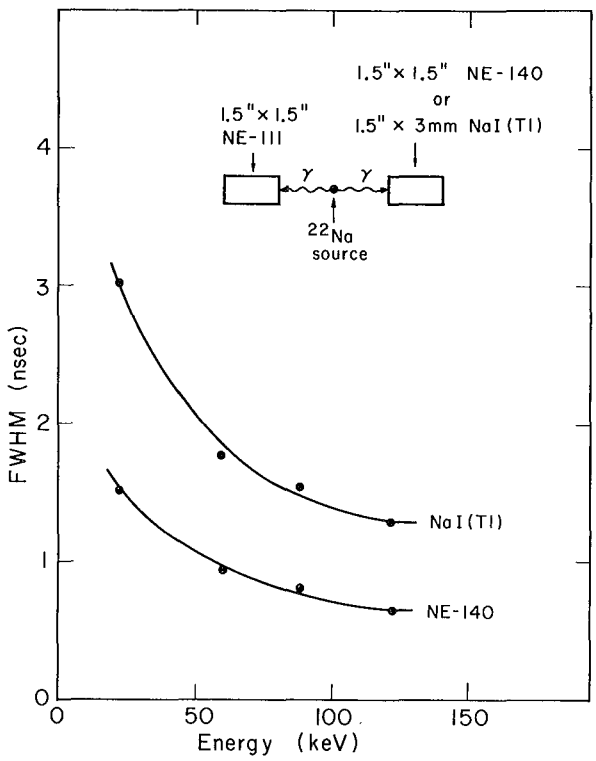

Fig. 3. Widths of coincidence curves vs energy for NaI(Tl) and NE-140 phosphors as one side of the coincidence system. The other side is very fast and provides constant timing. (XBL-713-3067)

useful phosphor when dealing with fast coincidences at low gamma energies. At higher gamma energies, the advantages of NE-140 are reduced, since the selection of the Compton edge in the considerably faster unloaded scintillators becomes more useful.

An example of a time-differential spectrum of ^{100}Rh (for the 84-keV - 75-keV cascade) dissolved in ferromagnetic Ni, at room temperature, is shown in Fig. 4. The time resolution at these energies, FWHM = 1.15 nsec, was achieved by a pair of 1.5-in. × 1.5-in. NE-140 plastics, mounted on RCA C10001D PM tubes. The Larmor modulation peaks separated by only 3 nsec could easily be resolved and the modulation frequency of 340 MHz detected. A Fourier analysis of the spectrum reveals clearly even the double frequency of 680 MHz, corresponding to details separated by only 1.5 nsec.

In all our experiments the NE-140 phosphors were painted with standard white plastic scintillator reflector paint and used in connection with the abovementioned tubes operating at -2700 V. No special care was taken to

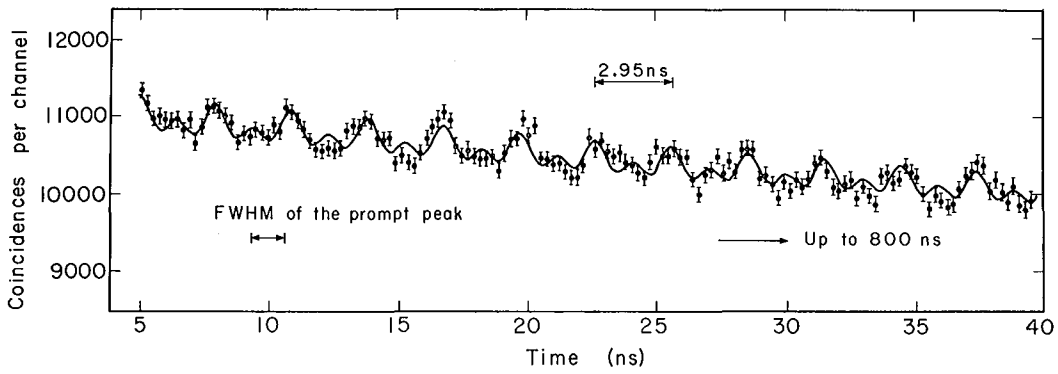

Fig. 4. One-twentieth of the time-differential coincidence spectrum of the 84-keV - 75-keV cascade of ^{100}Rh dissolved in ferromagnetic Ni. The spectrum was detected by two 1.5-in. ×1.5-in. NE-140 plastics. (XBL-703-2405)

provide optimal working voltages so our time resolution figures could probably be improved. The fast output signals were amplified 10 times, fed to EG&G fast discriminators, and then to an Ortec 437A time-to-amplitude converter. The fast discriminator levels were set to trigger to a single photoelectron. We have noticed that NE-140 phosphors coming from different batches may have somewhat different optical properties (transparency, fluorescence hue) noticeable by simple eye examination. Those more transparent showed better energy and time resolution.

Finally, we have also investigated the Sn-loaded liquid scintillator (NE-316, 10% tin content by weight, scintillation decay constant 4 nsec). As a consequence of the increased tin content, it has a still higher detection efficiency. Its light output is lower than that of NE-140, but this seems to be compensated for by a shorter decay constant. We judge its overall response to be just slightly poorer than that of NE-140. In experiments where the ultimate in time resolution is not really required, this phosphor seems to be superior to NE-140, because of its higher detection efficiency at low energies and consequently the reduced influence of the background which usually comes from higher energy gamma radiation.

We gratefully acknowledge the assistance of Mr. George Gabor during the course of this work.

A Computer Program for the Smoothing and Differentiation of Data from Multichannel Analyzers†

D. J. Gorman*

In the interpretation of spectra taken on multichannel analyzers it is frequently helpful, especially in cases where the statistics are poor, to smooth the data in order to reduce the statistical fluctuations. When presented with such a spectrum, one would normally draw through the points a smooth curve which best fits them. This can be done numerically when we define what we mean by best fit. The most common criterion is to minimize the sum of the squares of the residuals between the actual and fitted points.

The method used is that of Savitzky and Golay,[1] who fit a polynomial over a range of 2m+1 data points. The smoothed value at the midpoint of the range is the value of the polynomial at that point. The data points are then shifted by one, dropping the point at the left and picking up one at the right. This process is repeated to cover the entire spectrum.

Upon doing the least-squares analysis, one obtains a set of coefficients, one for each point over which the fit is performed. The value at the midpoint of one interval of 2m+1 points is found by summing the products of the

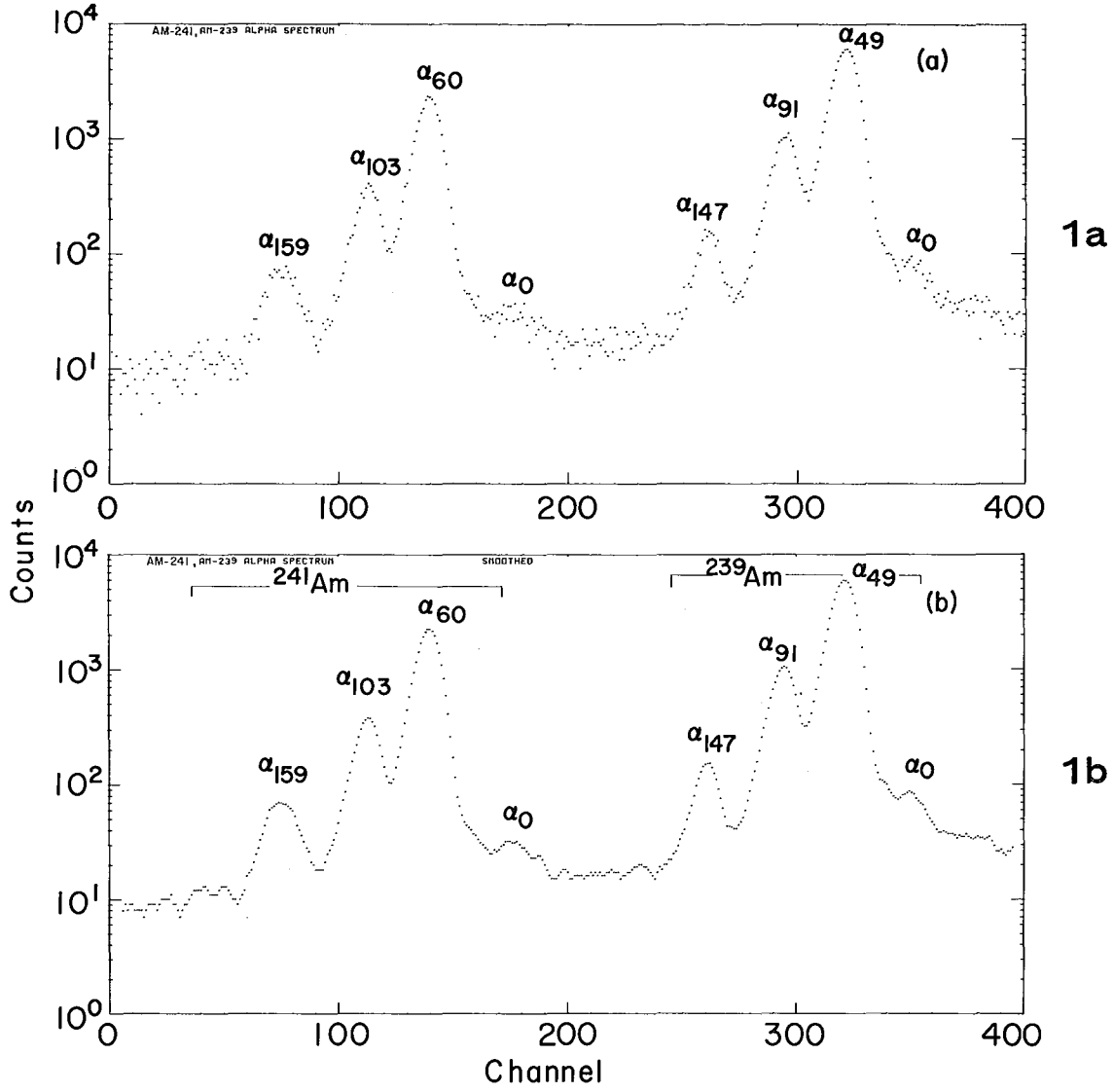

Fig. 1. Alpha spectrum of ^{239}Am and ^{241}Am. Raw data are shown in 1a; 1b shows spectrum after 11-point smoothing operation. (XBL705-3025)

counts in each channel and the particular coefficient for that channel, i.e.,

$$\overline{Y}_j = \sum_{i=-m}^{+m} C_i Y_{i+j},$$

where the Y_{i+j} are the counts in channel i+j, the C_i are a set of convoluting factors, and $\overline{Y}_j$ is the best calculated value for the number of counts in channel j; j is an index which runs over all of the channels in the spectrum.

The derivative of the spectrum can also be obtained by taking the derivative of the fitted polynomial. A set of convolution factors can also be derived to do this.

A computer program has been written to calculate these convolution factors C_i for any degree of polynomial and taking any number of points. The report from which this is condensed gives a listing of the program and some tables of the more commonly used convolution factors for polynomials up to degree 6 and number of points up to 23.

Figure 1 shows an alpha spectrum of ^{239}Am and ^{241}Am[2] taken with a 6 mm Au-Si detector and recorded in a 400-channel pulse-height analyzer. In 1a is plotted the raw data

and 1b is the spectrum after performing a smoothing operation using a quadratic polynomial and smoothing over 11 points at a time. The smoothing operation has not changed either the peak heights or the peak shapes, but it has particularly accentuated the two α_0's, which in the raw data are barely discernible above the statistical fluctuations of the background. It is much easier to perform a stripping operation on the smoothed spectrum than on the raw data.

Footnotes and References

†Condensed from UCRL-19903, June 1970.

*Present address: Bureau International des Poids et Mesures, Pavillon de Breteuil, 92 Sèvres, France.

1. Abraham Savitzky and Marcel J. E. Golay, Anal. Chem. 36, 1627 (1964).

2. D. J. Gorman and F. Asaro, Energy Levels in ^{235}Np, (UCRL-19946; 1970), submitted to Phys. Rev.

A Pulsed Electron Beam Retarding Potential Difference Technique†

G. E. Thomas* and F. E. Vogelsberg

Recently, Chantry described an automated retarding potential difference (RPD) technique using a multichannel scaler.[1] The method he developed permits the automatic accumulation of high-resolution electron-impact data using the RPD technique pioneered by Fox, Hickam, Grove and Kjeldaas.[2] Chantry's method has been applied to recording electron-impact ionization efficiency curves.[1,3]

In certain experiments it is advantageous or necessary to use a pulsed electron beam. That is, the electron beam is turned on for a short period of time and is then turned off.[2] Often, the products of the electron collisions are examined during this off time. One example of such an application is in molecular beam time-of-flight studies. It is possible to make low resolution efficiency measurements on time-resolved species by pulsing the electron beam and by appropriately gating the detector.[4,5] The purpose of this note is to point out that a slight modification of Chantry's scheme[1] permits the automated technique to be employed in such experiments.

The pulsing scheme is shown in Fig. 1. The times indicated on the figure are typical for an experiment being performed in this laboratory, but are not restrictive. A master clock-pulse triggers the sweep start of a Hewlett-Packard Model 5400A multichannel analyzer (MCA) operating in the multiscale mode, and after a short delay triggers a pulse train from a time-base oscillator (TBO). These TBO pulses trigger the channel advance of the MCA, establish zero time for the data count gate, and trigger an electron "on" pulse.

The electron "on" pulse is applied to the retarding grid of a 5-electrode RPD gun. The voltage during the "on" period is exactly enough to allow the appropriate truncated electron energy distribution to pass into the collision chamber. As in Chantry's scheme, the level of this voltage is changed on alternate sweeps of the MCA. When the "high" RPD pulse is applied, the MCA operates in the "add" mode. On the "low" RPD cycle, the MCA is automatically reset to operate in "subtract." The electron accelerating voltage is derived from the plotter X output of the Hewlett-Packard analyzer. In contrast to the voltage offered by the CAT-400C analyzer used by Chantry,[1] the X output of the Hewlett-Packard 5400A is suitable for this purpose. This voltage is appropriately amplified and biased before use. The dc voltages applied to the remaining electrodes in the RPD gun are conventional.[2] The data count gate allows data to be stored in the MCA only during a specified time slot referenced to the electron "on" pulse. The width and the delay of the data gate are variable. A description of the electronics used to generate the pulsing scheme is available elsewhere.[6]

This method has been used to record excitation efficiency curves for the production of photons and of neutral metastable species in an experiment similar to that described by Clampitt and Newton.[5] For cases where high time resolution has been required, the gun has been operated with an "on" pulse as short as 5 μsec. The experiment requires that an "off" time approaching 1 msec be used, although this is not a consequence of the pulsing scheme or of the electronics employed. With this ratio of "on" to "off" time, the RPD curves build up very slowly, and many scans

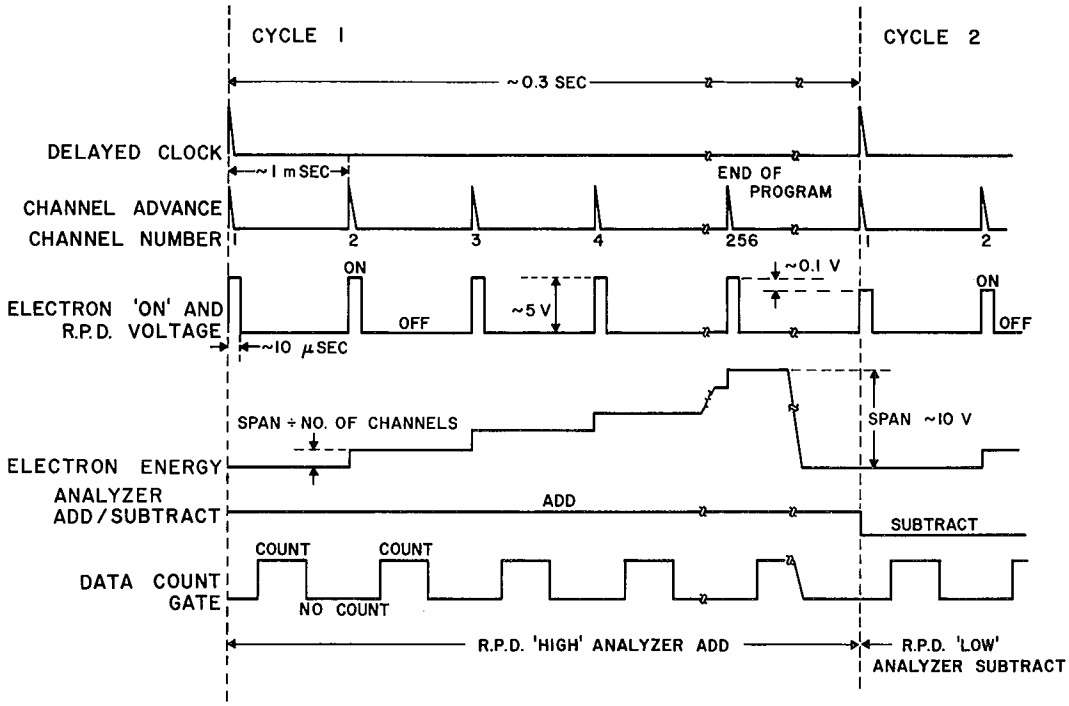

Fig. 1. Timing diagram for the pulse scheme used to make RPD measurements on time-resolved species. (XBL-708-1063)

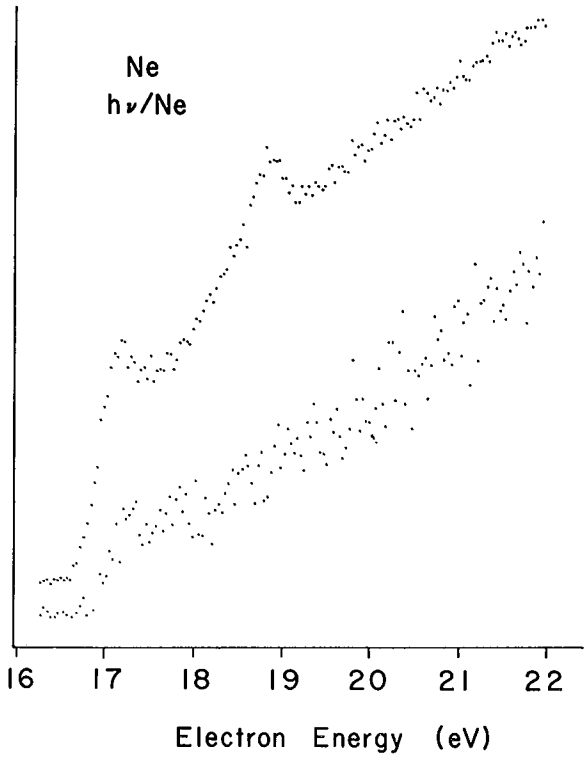

are required to achieve a satisfactory signal-to-noise ratio. However, as Chantry has pointed out,[1] this fact is not overly critical when the individual scans are short. The width of the electron "on" pulse does not affect the high resolution performance. This has been checked by performing the same experiment in the pulsed mode, and in the dc mode described by Chantry. Obviously an increase in the duty cycle of the gun reduces the time necessary to record acceptable efficiency curves. Mixing the "on/off" pulse with the RPD voltage on the retarding grid appears to be highly satisfactory. The operation of the gun is very stable, and no adverse effects from the beam pulsing have been noted in the high-resolution data.

Figure 2 shows some data obtained using this pulsing scheme on an instrument that has been described previously.[5] The upper curve in Fig. 2 shows an excitation efficiency curve for the production of metastable neon atoms. The lower curve is for uv photons from neon.

Fig. 2. Upper curve: Electron-impact excitation efficiency curve for the production of neutral metastable atoms in neon. Lower curve: Electron-impact excitation efficiency curve for the production of uv photons in neon. (XBL-706-1067)

Both were recorded using a 10 μsec electron-beam pulse. To record the photon curve, the data gate was opened only during the electron pulse. For the metastable curve, the data gate was delayed for 50 μsec, and then opened for ≈ 200 μsec in order to intercept a large fraction of the Ne^* time-of-flight distribution. The time period between electron pulses was 1 msec. These curves (and the corresponding time-of-flight spectrum) are discussed in Ref. 6. In our apparatus, the photon signal is approximately 1/12 of the metastable signal at electron energies just above 20 eV. These curves can be compared with a composite RPD curve (i.e., no separation of metastables and photons) obtained by Olmsted, Newton, and Street[7] on a similar apparatus.

Footnotes and References

†Condensed from UCRL-19934, July 1970; to be published in Rev. Sci. Instr.

*Present address: Philips Research Laboratories, WY4, N.V. Philips Gloeilampenfabrieken Eindoven, The Netherlands.

1. P. J. Chantry, Rev. Sci. Instr. 40, 884 (1969).

2. R. E. Fox, W. M. Hickam, D. J. Grove, and T. Kjeldaas Jr., Rev. Sci. Instr. 26, 1101 (1955).

3. P. J. Chantry, J. Chem. Phys. 51, 3369 (1969).

4. R. Clampitt, Entropie 30, 36 (1969).

5. R. Clampitt and Amos S. Newton, J. Chem. Phys. 50, 1997 (1969); UCRL-18032.

6. G. E. Thomas and F. E. Vogelsberg, UCRL-19934.

7. John Olmsted III, Amos S. Newton, and K. Street, Jr., J. Chem. Phys. 42, 2321 (1965).

Identification of Nuclear Fragments by a Combined Time-of-Flight ΔE-E Technique †

Gilbert W. Butler,* A. M. Poskanzer, and D. A. Landis

Time-of-flight techniques have been employed in past studies to identify particles produced in nuclear reactions. One particle identification method involves the combination of a particle time-of-flight technique and a ΔE-E technique.[1,3] In this method, particle flight times are determined between two ΔE detectors. The mass number is calculated from the nonrelativistic formula A = const. × $\mathcal{E}t^2$, where t is the fragment flight time between the two ΔE detectors and $\mathcal{E}$ is the fragment energy during flight. Experiments utilizing this technique have had to rely heavily on the isotopic resolution obtained from the ΔE-E method, because the time-of-flight mass resolution was slightly greater than one mass number. However, the technique was successful in establishing the identity of several neutron-rich light nuclei produced in the interaction of high-energy protons with heavy nuclei.[1-3]

We have made significant improvements in the combined time-of-flight ΔE-E technique. Modified electronic equipment was used to identify nuclear fragments of Z = 5-10 produced in the interaction of 5.5 GeV protons with uranium. Fragment flight times were determined between a ΔE and an E detector instead of between two ΔE detectors as in earlier experiments.[1-3] This made it possible to measure fragments that had lower energies and, consequently, longer flight times. The longer flight times greatly enhanced the time-of-flight determination, and the lower energies meant greater fragment yields, since the minimum energies measured were still above the peaks of the measured energy distributions for these high-energy reactions.[4] In this experiment the ΔE detector was thinner and provided only element resolution, but the time-of-flight determination provided adequate mass resolution by itself.

The experiment was performed by using the 5.5 GeV external proton beam of the Bevatron to bombard a uranium metal target of 27 mg/cm^2 thickness. Beam pulses 0.8 sec long and containing an average of 10^{12} protons occurred every six seconds. Many of the details of the experimental equipment that do not involve time-of-flight have been published elsewhere.[4]

A detector telescope consisting of three phosphorus-diffused silicon detectors was placed at 90° to the beam to view the fragments emitted from the target. The 22-μm ΔE detector was 14.5 cm from the center of the target, and the 112-μm E detector was 25.7 cm further away, with a rejection detector right behind it. The ΔE and E detectors had sensitive areas of 5×7 mm and were collimated to 4×6 mm by copper collimators 0.8 mm thick.

The electronic circuitry is illustrated schematically in Fig. 1. Fast rise-time linear preamplifiers of a special type were designed and built. These were integrally mounted with the ΔE and E detectors in the vacuum chamber. The electronic rise time was less than one nsec and the decay time constant was about 60 μsec. Signals from the preamplifiers were sent through 50-Ω coaxial cables to fast amplifiers located in the counting area. Details of the preamplifier design, the electronics circuitry, and of the walk of the timing signals as a function of pulse height in both detectors are provided in the full report.

During measurements of nuclear fragments from the uranium target in the 5.5-GeV proton beam, the fast discriminator outputs were sent to a Time-to-Amplitude Converter (TAC) that operated in the 0-100 nsec range. The TAC was started by the E discriminator signal and stopped by the signal from the ΔE discriminator delayed by 50 nsec. The time spectrum was thereby inverted so the flight time of a fragment was $(t_0 - t_{TAC})$, where t_0 was a zero-time reference whose value it was necessary to determine. The system was set up to measure flight times ranging from 10 to 30 nsec--adequate to cover flight times of all fragments from B to Ne in the energy range 10 to 40 MeV over a 25.7-cm flight path.

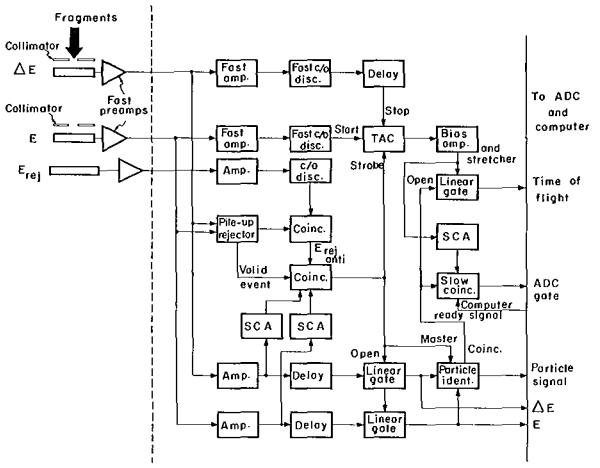

Fig. 1. Schematic diagram of the electronics. (XBL 705-2887)

The ΔE, E, TAC, and particle signals for each valid event were digitized and were then stored on magnetic tape. The computer performed an on-line calculation of the quantity $E(t_0 - t_{TAC})^2$ which is proportional to Et^2 (and thus to mass). This on-line calculation and the associated oscilloscope display were of considerable use for monitoring purposes during the long experiments, but the final data reduction was done with a CDC-6600 computer, where a Fortran program used the raw data tape to calculate a mass spectrum corrected for the walk of the timing signals with pulse height. This program also calculated a particle spectrum from a modified power-law equation.

The particle spectrum obtained during a 57-hour experiment is shown in Fig. 2. Because of the thinness of the ΔE detector, no isotopic separation was achieved, but elements were clearly resolved. The corrected mass spectrum containing all of the fragments that deposited from 15 to 30 MeV in the E detector is shown in Fig. 3. Each mass peak in this spectrum contains some contribution from more than one isobar. The mass resolution (FWHM) was 4.0% at mass 11 and 4.1% at mass 18. The time resolution of the pulser was 140 psec. The time resolution for the particles was about 250 psec. This was calculated from the measured mass resolution, with a correction for the contribution from the energy resolution.

A two-parameter contour plot of the number of events vs particle signal and mass signal is shown in Fig. 4. The element lines increase with mass simply because the particle signal is somewhat a function of the mass of the isotope as well as its charge. With the walk corrections that we used, the mass number lines are not all vertical, which means

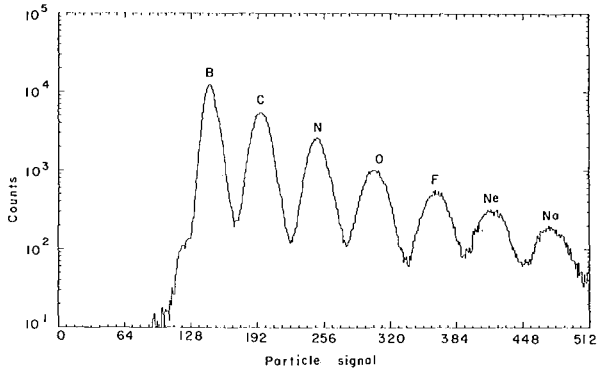

Fig. 2. Particle spectrum obtained in this experiment. The data shown in Figs. 2-5 represent only those valid events that deposited from 15 to 30 MeV in the E detector. (XBL-701-2182)

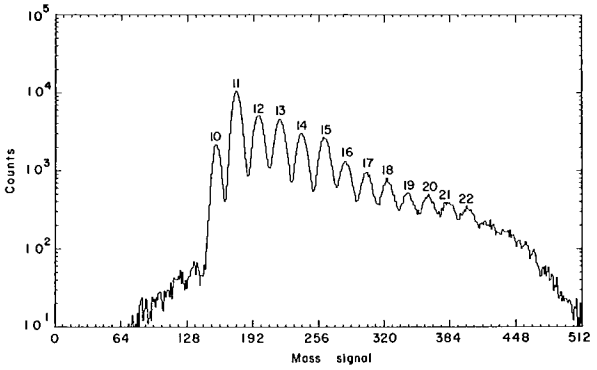

Fig. 3. Mass spectrum of Z = 5 to 11 fragments obtained in this experiment. (XBL-701-2183)

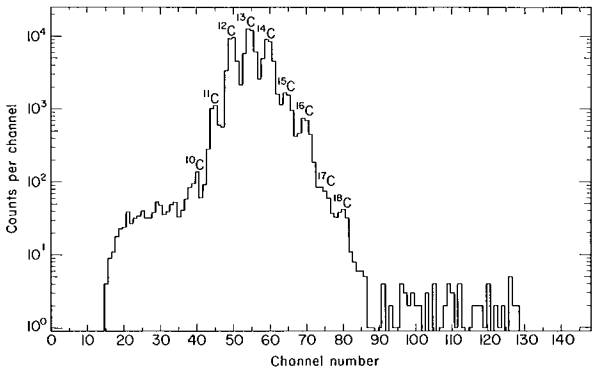

Fig. 5. Mass spectrum of carbon isotopes obtained by projecting carbon data from Fig. 4 onto the mass axis. (XBL-705-2833)

that the mass resolution was somewhat better than is indicated in Fig. 3. It is clear from this contour plot that the charge and mass resolution was sufficiently good to separate not only the major isotopes of the elements boron to neon, but also many of neutron-rich nuclides. This is illustrated more clearly in Fig. 5, which is the carbon mass spectrum obtained by projecting the carbon data in Fig. 4 onto the mass axis. In this experiment, ^{17}C was produced in much greater yield than in our earlier experiment.[1] Even ^{18}C is easily distinguishable in Fig. 5, and we thus confirm recent experiments[5] concerning the particle stability of this nuclide. Unfortunately, background problems prevent us from being able to say anything about the particle stability of nuclides of carbon heavier than ^{18}C, such as ^{19}C, which has been reported recently as being particle stable.[3] Also, as seen in Fig. 4, our data clearly confirm the recent work[5,6] in which the particle stability

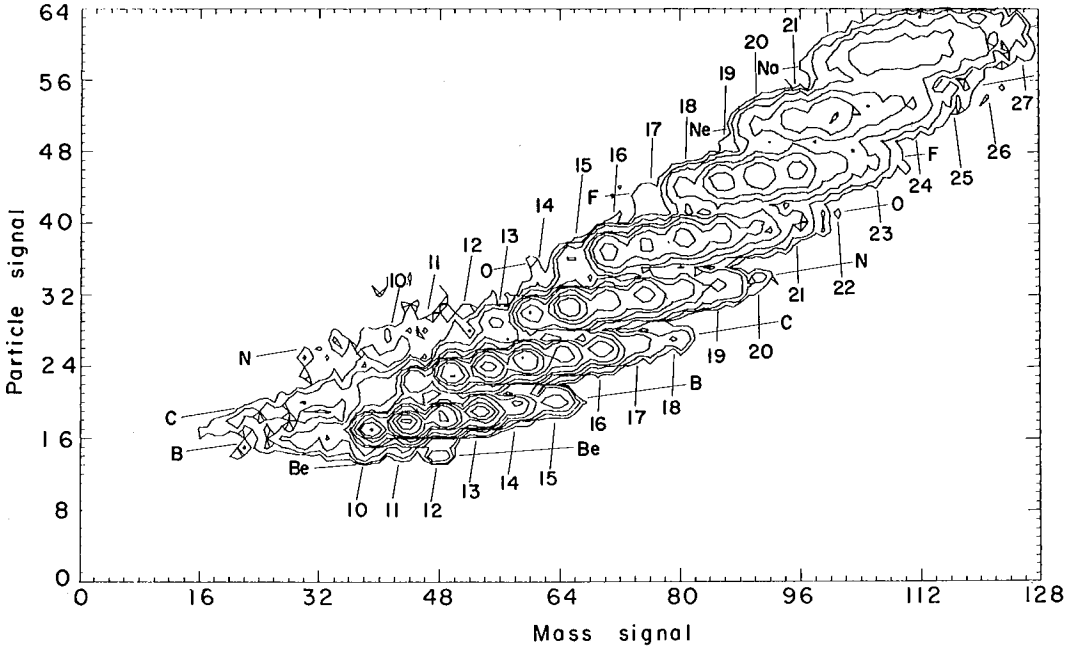

Fig. 4. Contour plot of mass signal and particle signal for this experiment. The contour levels are at 5, 10, 20, 50, 100, 200, 500, 1000, 2000, 5000, 10,000, and 20,000 events. The dimensions of the array are 128×64. The elements and mass numbers are indicated. (XBL-701-2181)

of the neutron-rich nuclei ^{20}N, ^{22}O, ^{23}F, and ^{25}Ne was established by observing these nuclei during a study of heavy-ion transfer reactions on a heavy nucleus.

Footnotes and References

†Condensed from UCRL-19952, August 1970; to be published in Nucl. Instr. Methods (1970).

*Present address: Chemistry Division, Argonne National Laboratory.

1. A. M. Poskanzer, G. W. Butler, E. K. Hyde, J. Cerny, D. A. Landis, and F. S. Goulding, Phys. Letters 27B, 414 (1968).

2. T. D. Thomas, G. M. Raisbeck, P. Boerstling, G. T. Garvey, and R. P. Lynch, Phys. Letters 27B, 504 (1968).

3. G. M. Raisbeck, P. Boerstling, P. Riesenfeldt, T. D. Thomas, R. Klapisch, and G. T. Garvey, in publication (1970).

4. A. M. Poskanzer, G. W. Butler, and E. K. Hyde, Phys. Rev. C 3, 882 (1971).

5. A. G. Artukh, G. F. Gridnev, V. L. Mikheev, and V. V. Volkov, Nucl. Phys. A137, 348 (1969).

6. A. G. Artukh, V. V. Avdeichikov, G. F. Gridnev, V. L. Mikheev, V. V. Volkov, and J. Wilczynski, Phys. Letters 31B, 129 (1970).

Improved Algorithm for Particle Identification †

Gilbert W. Butler* and A. M. Poskanzer

A widely used method of particle identification was developed some years ago by Goulding, Landis, Cerny, and Pehl.[1,2] The method makes use of the empirical-power-law formula $R=aE^b$, where R is the range of a particle of energy E, a is a constant which is characteristic of a given particle, and b is a constant with a value of approximately 1.6. In its original form, a thin transmission (ΔE) detector of semiconductor silicon was placed in front of a thicker (E) detector and the signals from the detector were manipulated in analog electronic circuitry to derive the function $(E+\Delta E)^b-E^b$, which can be shown to be equal to T/a, where T is the thickness of the ΔE detector. T/a has a characteristic value for each particle.

We have employed this particle identification system with considerable success in a study of fragments ejected from uranium bombarded with 5.5 GeV protons.[3] However, in this interaction a wide variety of fragments with a wide spread in kinetic energies is produced and the power-law parameters could not be chosen in such a way to obtain a good fit over wide ranges of energy or particle type. Consider the data shown in Fig. 1(a), which shows the output of the analog electronic system for a certain experiment in which a 20-μm ΔE detector was used. In this case no isotopic resolution was obtained, but elements up through sodium were separated.

The particle spectrum shown in Fig. 1(b) was calculated by an off-line computer from a magnetic tape record of the ΔE and E data. The same power-law expression and the same b parameter were used to simulate the analog-particle spectrum. A two-parameter contour plot of the number of events vs particle signal and total energy for this same experiment is shown in Fig. 2(a). It can be seen from Fig. 2(a) that the particle signal is not independent of energy for a given element. For the lighter elements, the decrease in particle signal with increasing energy could be corrected by raising the parameter b, but then the curvature at the lowest energies for the heavier elements would be considerably worse.

We have determined a modified power-law formula that is capable of automatically adjusting the exponent to obtain improved resolution for a broader spectrum of particles. It can be seen that the nuclei that deviate most from the original power-law formula are the heavier elements with the lowest energies. Since these nuclei are the ones that have the highest dE/dx values, we decided to make the exponent decrease with the value of dE/dx given by the energy deposited in the ΔE detector. The modified algorithm has the following form

$$\left[\left(\frac{E+\Delta E}{k}\right)^n - \left(\frac{E}{k}\right)^n\right]^{1/2},$$

where the exponent is $n = b - c\,\Delta E/T$. We have taken the units of c to be mg/cm^2-MeV. In this formula the two energy terms are divided by a large constant (we use $k = 300$ but the exact value is not critical). This is done because with a variable exponent it is necessary to normalize the spectra at a high energy, where the exponent is approximately

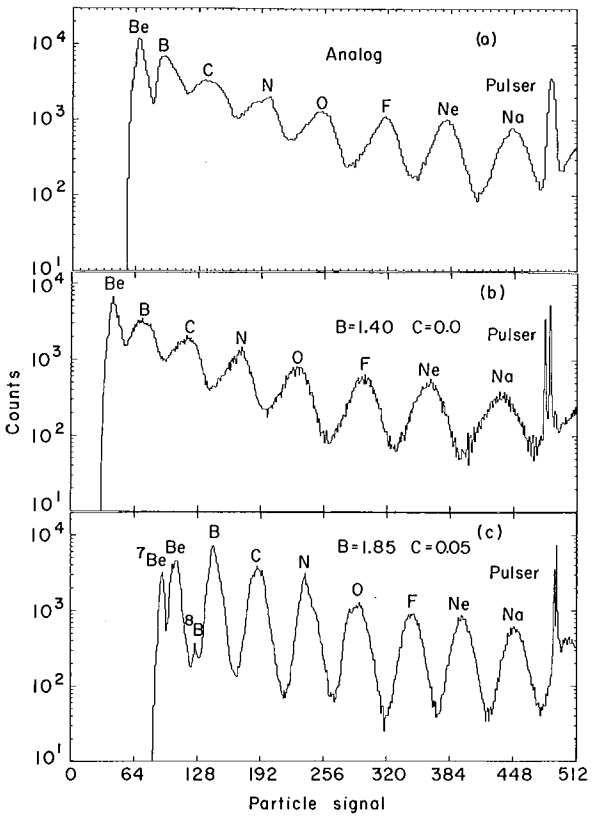

Fig. 1. Particle spectra resulting from the interaction of 5.5-GeV protons with a uranium target. The detector telescope consisted of a 20-μm ΔE detector and a 300-μm E detector. All three spectra are from the same experiment, but the data were processed in different ways, as discussed in the text. The pulser peak is split in (b) and (c) because the least significant bit of the ADC was not functioning during the experiment. The Li data were removed from the figure. (XBL-705-2885)

constant. The square root of the particle signal is used simply because it makes the signal proportional to Z instead of to Z^2. It should be mentioned that in the search for the best b and c values to use in this equation, we have relied on range-energy and energy-loss programs written at this laboratory.

The dramatic improvement in particle-spectrum resolution that results from the use of the modified power-law equation with the appropriate b and c parameters is illustrated in Figs. 1(c) and 2(b), which represent the same data reprocessed according to this modified equation. (The calculations to process each event took about 300 μsec on a Control Data Corporation 6600 computer.) The modified equation produces the desired effect of making the particle signal more independent of energy, and the resolution is improved to such an extent that the isotopes ^{7}Be and ^{8}B are

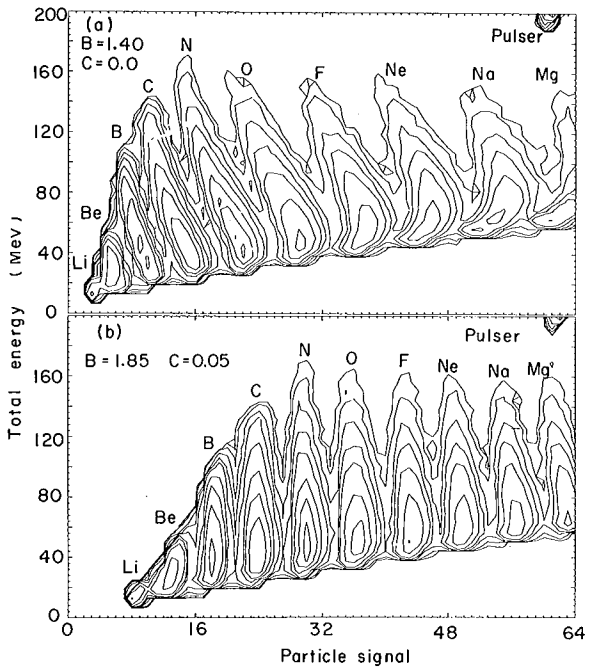

Fig. 2. Contour plots of particle signal and total energy corresponding to the data of Fig. 1(b) and 1(c). The contour levels are at 10, 20, 50, 100, 200, 500, 1000, 2000, and 5000 events. The array size was 64×32 which accounts for the coarseness of the plots. (XBL-705-2886)

clearly resolved in Fig. 1(c). (^{8}Be and ^{9}B do not appear in the spectra because their half-lives are too short to allow them to reach the detector.) The widths of the other peaks are mainly due to the high yields of the many unresolved isotopes of each element.[3] We have shown that it is possible to obtain element resolution up to argon (Z = 18) with a 20-μm ΔE detector[3] and this method could probably be extended to even heavier elements with the use of thinner ΔE detectors.

Footnotes and References

†Condensed from portion of UCRL-19952, August 1970; to be published in Nucl. Instr. Methods (1970).

*Present address: Chemistry Division, Argonne National Laboratory.

1. F. S. Goulding, D. A. Landis, J. Cerny, and R. H. Pehl, Nucl. Instr. Methods 31, 1 (1964).

2. F. S. Goulding, D. A. Landis, J. Cerny, and R. H. Pehl, IEEE Trans. Nucl. Sci. 13, 514 (1966).

3. A. M. Poskanzer, G. W. Butler, and E. K. Hyde, Phys. Rev. C 3, 882 (1971).

Computer Interpolation of Internal-Conversion Coefficients

C. M. Lederer

Computer programs for interpolation of theoretical internal-conversion coefficients and random-accessible tables of coefficients (Hager and Seltzer) have been placed on the data cell at the LRL-Berkley CDC-6600 computer. Interpolated values may be obtained by submission of a few simple cards specifying the desired atomic number, energies, and or α_{Total}) and ratios (such as K/L). The program may also be run on-line via a teletype console.

Details of the use of the programs and the method of computation are given in UCRL-19980.

Digital Nuclear Spectrometer †

William Goldsworthy

The direct rundown of the charge liberated by the interaction of radiation or charged particles in a nuclear detector is accomplished for direct conversion to a digital number, eliminating the need for separate restoration of input charge and further processing of the analog signal.

By applying digital feedback to the output of a nuclear detector so that charge balance can be maintained, charge liberated as a result of detecting nuclear events or accumulated from detector or input leakage are extracted and digitized.

This early conversion of charge into a number eliminates the necessity of converting event-produced charge to a voltage pulse, amplifying this pulse through an amplifier system having high stability, good linearity, and rigid control of band pass, and finally measuring the amplitude of the amplified pulse by means of an elaborate pulse-height analyzer.

Little dependence upon integrator or amplifier stability, linearity, or band pass results in the digital scheme described, since the integrator and amplifier serve solely as a means of sensing input-charge unbalance, and the familiar functions of integration and differentiation are handled digitally by controlling rebalance time, by time averaging, and by numerical background subtraction.

Application of this digital approach to remotely located scientific data-sensing monitors, such as would be used in space probes or unmanned pollution-monitoring stations, seems quite attractive due to its simplicity, low weight and power requirements, and greater compatibility with direct transmission of useful data.

Basic Digital Nuclear Spectrometer

In the block diagram of the basic digital nuclear spectrometer of Fig. 1, the output of the nuclear-event detector is attached to the input of a current integrator and also to a charge extractor. Connected to the output of the integrator is a logic circuit which continually maintains integrator input-charge balance on demand by controlling the amount of digital feedback applied to the integrator input by the charge extractor attached to it. A digital output proportional to extracted charge is also developed in this logic circuit and is sent along to a data processor for information extraction.

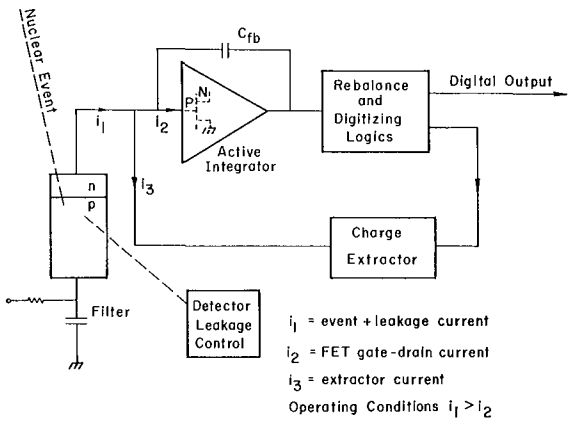

Fig. 1. Basic digital nuclear spectrometer. (XBL-712-2747)

At the input of the spectrometer, current flows out of the detector as a result of event-liberated charge and detector leakage. Current also flows out across the gate-drain junction of the integrator's input field-effect transistor (FET), since it is reverse biased with respect to the detector. Current can also flow out through the charge extractor upon command from the logic circuitry. Normally, current flow through the charge extractor is quite low, being only at a digital rate necessary for the extraction of the current surplus supplied by the detector which does not flow out through the FET.

Upon the interaction of a nuclear event in the detector, an abrupt change occurs in its charge level. This charge shift results in an output potential unbalance of the integrator. The logic circuit attached to the integrator senses this rapid change and allows digital rundown of input charge at the maximum rate of the local clock used to synchronize and originate rundown commands to the charge extractor. Real-event start, and rundown-terminate information are contained in the digital output signals, since only during the time of rundown will the digital rundown intervals have their minimum spacing. They will have a rate occurence equal to the clock frequency. During rundown a train of pulses proportional in number to the event-produced charge plus leakage charge will be developed and sent to the data processor. Since the digital output of the basic converter is continuous and contains all charge and time information, separate event, total event, and background information can be extracted in a separate data processor.

Data Processor

Information coming from the output of the basic digital nuclear spectrometer is in pulse and time form. The data processor must examine this information and convert it to useful data. Many types of information may be stripped from the available digital input data. These are total radiation data, individual event data, number of events, time relationships of events and background data.

The data processor used to demonstrate the feasibility of direct digital input conversion was designed only to determine individual nuclear-event energies. A block diagram showing the data processor used is shown in Fig. 2. This processor consists of a programmer, an up-down accumulator, and a memory and display unit. Digital signals from the basic digital nuclear spectrometer are delayed in a delay line before entering the up-down accumulator, allowing for the start of the accumulator programmer before arrival of digital information coming from a real event.

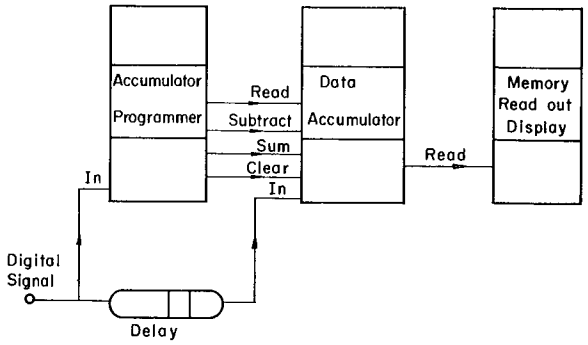

Fig. 2. Data accumulator.
(XBL-713-3062)

The same digital signals also enter the accumulator programmer to identify the start time of a real event. Upon the occurrence of a real event, the spacing between digital-feedback intervals synchronizes to the clock frequency and causes an accumulator program of accumulator reset, accumulator sum, accumulator subtract, and accumulator read-out to be initiated. This program is shown in Fig. 3 with integrator rundown. The subtract portion of the accumulator program ensues only after rundown termination has been sensed by an increase in the time spacing of the digital-feedback intervals. An equal time ensues following event rundown, where information relating only to background is numerically subtracted from the real event plus background information already accumulated during the sum portion of the cycle. A digital up-down scaler driven at the clock frequency is used to automatically equalize sum and subtract time by allowing countup during summing and countdown to zero during subtraction. Upon completion of the sum and subtract portions of the cycle, a read interval occurs where information contained in the accumulator is transferred to a readout device or memory. Visual display of the energy of the last events is also made for convenience.

Circuit Details

To handle the low charge levels developed from nuclear detectors, a low-leakage input integrator followed by a gain-of-20 amplifier was used to sense detector unbalance. The active input integrator uses an input FET to ensure low leakage, and employs a 0.2-pF integrator charge-storage capacitor to maximize its sensitivity.

Charge extraction from the input is by

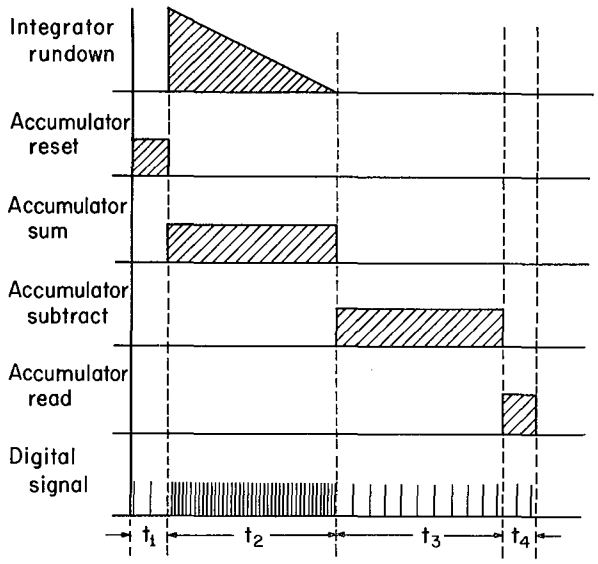

Conditions: t_1 = delay-line time; $t_2 = t_3$.

Fig. 3. Accumulator program.
(XBL-712-2749

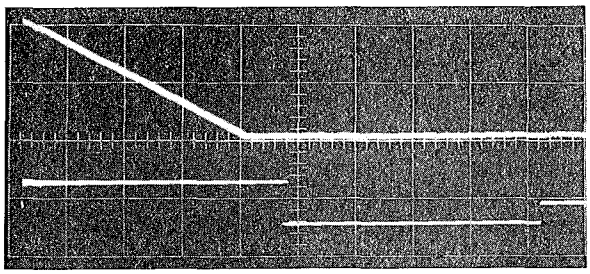

Fig. 4. Integrator run down.
(XBB-712-471)

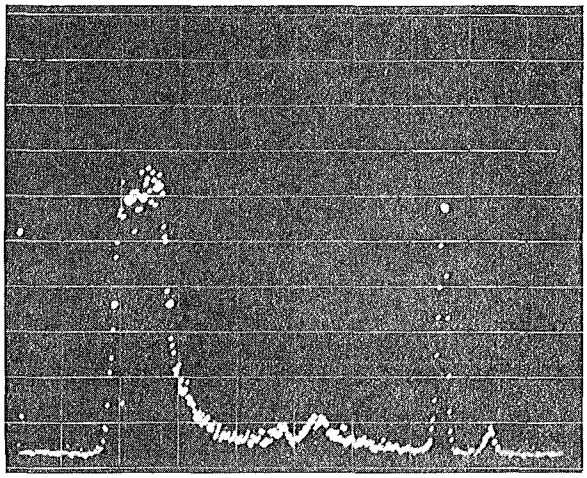

Fig. 5. Gamma spectrum of ^{57}Co.
(XBB-712-472)

means of light radiation stimulation of the input FET's gate-drain junction. This technique has been described earlier by Kandiah et al.[1] Light radiation stimulation by this same means is also applied to the nuclear-event detector to ensure a detector leakage greater than that of the input FET, so that continuous input balance is possible. Light radiation stimulation is by means of light-emitting diodes (LED), where light radiation induces charge-pair generation inside the p-n junctions of the detector or input FET in much the same manner in which charge pairs are generated by nuclear radiation. The LED employed for charge extraction is driven digitally at constant current by the rebalance logic circuitry, and the LED employed for average balance is driven from a direct-current source.

Rebalance commands to the impulse charge extractor occur whenever the comparitor sensing level of the rebalance logic is exceeded. When this occurs a synchronous gate operates, allowing operation of the extractor only during precise complete time periods. With background only, an occasional one of these time periods will be used for controlling digital feedback. When an event occurs, however, feedback intervals will occur at a clock-frequency rate.

A clock frequency of 500 kHz was used in running the test spectrum. It produced a rundown time of over 1 msec for each gamma event digitized. Since the timer described here was not working exactly as described at the time the spectrum was run, all rundowns were made with fixed sum and subtract times. These totalled about 1.6 msec and were independent of input energy.

The upper trace in Fig. 4 is the output waveform of the digital input integrator during actual rundown. The lower trace shows the periods of summing and subtracting used. The horizontal scale is 200 μsec/cm.

To make an actual performance test, a silicon x-ray detector was used to detect the γ-ray energies from a ^{57}Co source. The spectrum produced is shown in Fig. 5. Although the ≈ 2 keV resolution performance obtained for the 122-keV γ peak cannot be considered as excellent, it is certainly not bad for a first try. Improvements in techniques especially in more rapid digitization, greater extractor stability, and more accurate timing should certainly lead to better future resolution.

It should be apparent that the underlying principles of this new approach can be applied to any scientific study where current or charge

must be measured. In fact the technique described was developed originally for application to electrochemical studies. The application of the technique to environmental and space studies--where its advantages of simplicity, light weight, low power consumption, and data compatibility--is also attractive.

Footnote and Reference

†Condensed from UCRL-20434, January 1971.

1. K. Kandiah and A. Sterling, A Direct-Coupled Pulse Amplifying and Analyzing System for Nuclear Particle Spectroscopy, Nuclear Particle Detectors and Circuits (Nat. Academy of Sciences Pub. 1593 1969), p. 495.

NIM Packaging Modifications

W. W. Goldsworthy

From the standpoints of operator convenience, reduction of front panel connector and wiring clutter and for the ease of equipment maintenance, all front panel module-to-module cabling should be eliminated, all intermodule cabling should disconnect automatically upon removal of a module from a bin, and all necessary module inputs and outputs should be brought to a central location for easy patching.

By minor modification of the NIM system, it is easily possible to accomplish all of the aforementioned goals. The existing NIM bin and power supply has one serious drawback, that of the power supply blocking easy access to the multipin module receptacles provided. This has prevented almost everyone from utilizing the six coaxial positions and the 30 small pin positions not now used for power delivery that are available at each module position, and has forced an unnecessarily strong discipline upon the use of these largely unused pins. To expose these rear receptacles for easy use, it is only necessary to provide a pair of hinges like those shown in Fig. 1 that can be inserted between the bin and power supply. These hinges allow the power supply to be swung upwards exposing the rear of the module receptacles as shown in Fig. 2.

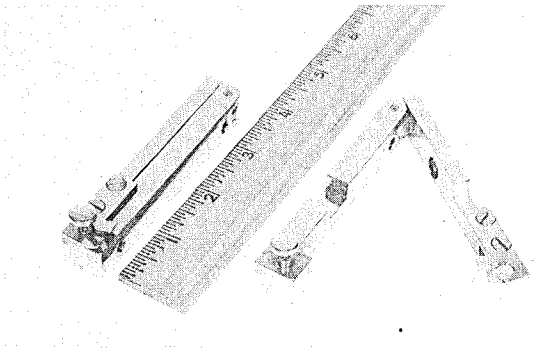

Fig. 1. NIM power supply hinge. (XBB-6910-6699)

Connection to a central patch panel can be made easily by utilizing prefab cables having AMP-coax-pokehome connectors on one end and bulkhead connectors, which mate to the patch panel, on the other end. Intermodule wiring can be accomplished by using prefab-coax or single-wires cables of various lengths with AMP pokehome connectors on each end.

Wiring to peripheral equipment can be made through a rear-mounted patch panel, where connection to a module is similar to that described for the central patch panel. With

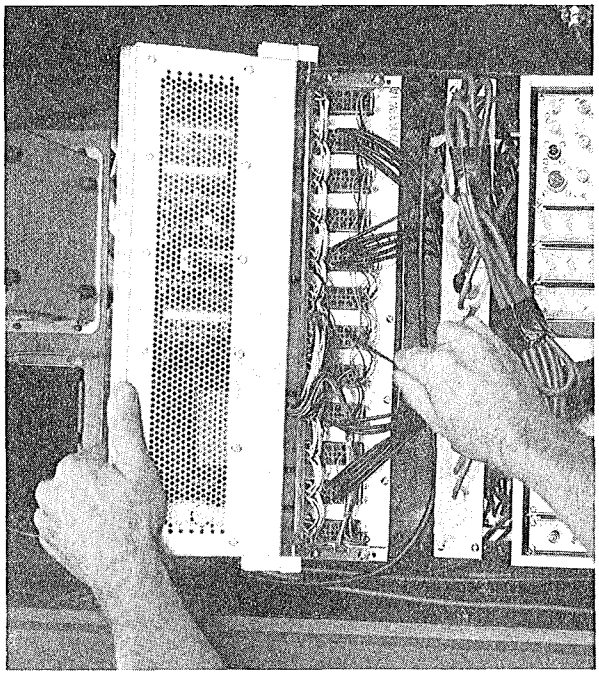

Fig. 2. Rear of module connectors exposed for cable insertion. (XBB-6910-6696)

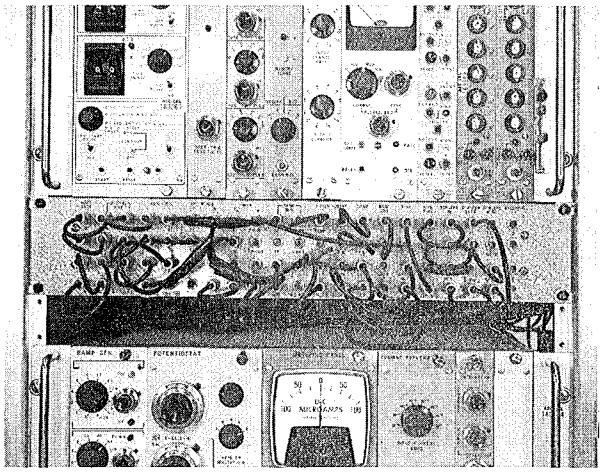

the exception of power supply positions on the multipin module receptacles, there are 30 small pins and 6 coax pins available for each module width, so that for a 3-unit module, 90 small pins and 18 coax connections could conceivably be used.

Figure 3 shows the central patch panel of a digital polarograph-coulometer utilizing this modified NIM system.

Fig. 3. Patch panel used in digital polarograph-coulometer. (XBB-711-98)

Pulsed-Feedback Techniques for Semiconductor-Detector Radiation Spectrometers †

D. A. Landis, F. S. Goulding, R. H. Pehl, and J. T. Walton

The charge-sensitive capacitive feedback loop shown in Fig. 1a, with a parallel resistive-feedback path (Fig. 1b), is commonly used with semiconductor detectors. The virtues of a charge-sensitive configuration compared with the older voltage-sensitive circuit include relative insensitivity of the output signal to capacity changes in the detector, stabilization of output signal against changes in the elements within the loop, and ease of testing by application of a voltage step, via a small capacitor to the virtual ground point at the input of the preamplifier.

A penalty in the signal-to-noise ratio results from the feedback capacity C_F increasing the total capacity in the input circuit, but the degradation can be made insignificant by using a relatively small capacitor. The parallel resistive-feedback path (R_F) serves two purposes; it provides dc feedback to stabilize the operating point of the elements in the feedback loop, and acts as a path for charge deposited on C_F to leak away. The decay time constant of the feedback path is nominally $R_F C_F$, so charge impulses from the detector produce voltage steps at the output of the preamplifier that decay with this time constant.

It has also become common in recent years to dc-connect the detector to the preamplifier, thereby keeping stray capacities at the input to a minimum. This method has also eliminated damage problems in the FET input stage resulting from voltage breakdown in the coupling capacitor. With dc coupling, the detector leakage current flows into the input of the preamplifier producing a voltage drop across the feedback resistor--which can be used as a convenient monitor of detector leakage current. When the detector is in a high radiation field, insufficient time is available between the individual radiation-induced pulses for the voltage steps across C_F to decay, so voltage is present across R_F continuously.

Fundamental noise sources include the FET channel noise, detector leakage-current noise, and thermal noise of the feedback resistor. Also an additional source of noise (current noise) may be expected to be present in the high-valued feedback resistor when the voltage across it exceeds thermal fluctuation values. This becomes important only at high counting rates where appreciable average currents flow in the feedback resistor.

The feedback resistor is a source of many additional problems. Due to its large physical size, a substantial amount of capacity is added to ground on the input of the preamplifier, thereby degrading the signal-to-noise ratio. Furthermore, high-valued resistors rarely behave as well as would be indicated by fundamental considerations. They act as sources of noise far larger than would be expected theoretically, and their value changes both as a function of voltage and frequency in the range

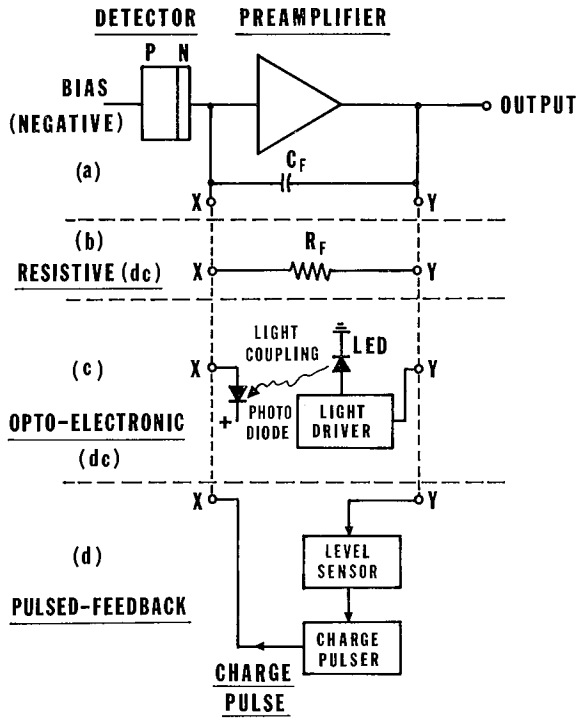

Fig. 1. Generalized feedback configurations used in charge-sensitive preamplifiers. (XBL-7010-6739)

of interest. The poor frequency behavior of R_F produces a complex decay in the voltage across C_F that is not amenable to correction by pole-zero cancellation techniques. This is a major factor in the degradation of high-resolution systems at high counting rates.

The optoelectronic feedback system[1,2] was devised to overcome the frequency sensitivity of high-valued resistors. As shown in Fig. 1c, the feedback resistor is replaced by a light-emitting diode (LED), which feeds light into a photodiode connected to the input of the preamplifier. In practice, the gate junction of the FET is used as the photodiode, thereby avoiding any degradation of resolution due to the photodiode leakage current and its capacity. The combination of LED and photodiode behaves as a pure resistor up to quite high frequencies, but nonlinearity in the input current vs light output characteristic of the LED causes the effective value of the feedback resistor to change in sympathy with the average voltage level at the output of the preamplifier. The feedback time constant therefore changes, pole-zero cancellation is made ineffective, and the high counting-rate performance is degraded. Furthermore, random current fluctuations in the photodiode act as a noise source that becomes significant at high counting rates.

The noise and counting-rate problems associated with the dc-feedback path can be eliminated by using a pulsed-feedback system similar to that shown in Fig. 1d. Here a measurement of the output level of the preamplifier (or of a later point in the amplifier) is made, and when the voltage excursion at this point exceeds prescribed limits, charge is fed to the input point to restore the output to its fiducial level.

In the example shown in Fig. 1, the current flow in the detector circuit causes the output to move in a positive direction. When the output voltage crosses an upper discriminator level, the charge pulser is turned on to feed charge into the input, thereby driving the output point in a negative direction. The charge pulser is turned off when the output reaches a lower discriminator level. During the recharge operation, analysis of the pulses in the later electronics is stopped, thereby imposing a dead time--which can be made suitably small by recharging quickly.

The most important single choice to be made in a pulsed-feedback system is the technique used to inject the resetting charge into the input point of the preamplifier. The ideal recharging element would:

(1) introduce no additional noise in the system;

(2) reset the system in a very short time;

(3) produce no additional signals due to the switching operations; in particular,

(4) produce no long-term aftereffects to interfere with real signals following the recharge period; and

(5) operate satisfactorily at liquid-nitrogen temperature to be compatible with the cooled-detector-FET systems used in high-resolution spectroscopy. The pulsed-light feedback system in Fig. 2 offers the best promise for very high-resolution work.

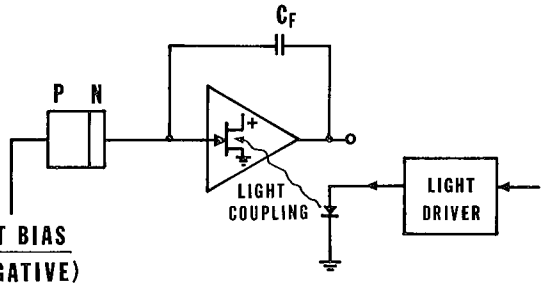

Fig. 2. Pulsed-light feedback via FET drain-gate diode. (XBL-7010-6743)

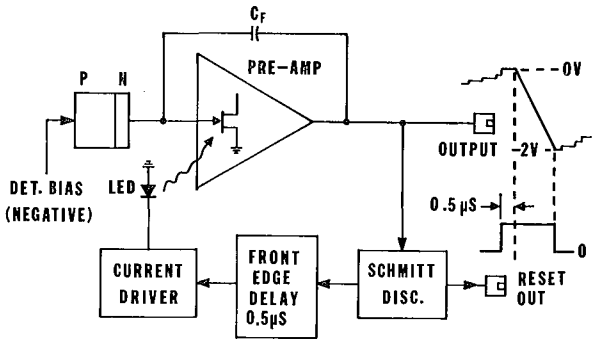

Fig. 3. Pulsed-light feedback preamplifier block diagram. (XBL-710-6801)

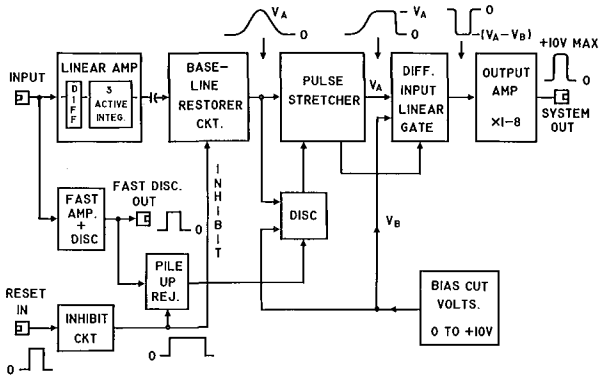

Fig. 4. Pulsed-light feedback amplifier system block diagram. (XBL-711-75)

Figures 3 and 4, respectively are block diagrams of the preamplifier and amplifier used in low-energy photon spectrometer employing pulsed-light feedback. The amplifier unit, containing a pileup rejector and a biased amplifier, performs amplification and signal processing operations, and provides a 2 μsec-wide output pulse suitable for a pulse-height analyzer. At low counting rates, the performance of this system is only slightly better than than that of dc-coupled optoelectronic feedback systems. As expected, the main advantages of the system are exhibited at high counting rates.

Figure 5 is an illustration of the performance at very high-input counting rates (260,000 per second) from ^{55}Fe, with and without the use of the pileup rejector. In this case, the Gaussian peak was at 4.5 μsec. The output rate when using the pileup rejector was 4,000 counts per second, whereas it was 32,00 counts per second with no pileup rejector. The accidental double, triple and even quadruple coincidences between the Mn x rays, within the discrimination time of the pileup rejector (≈250 nsec), are clearly seen when

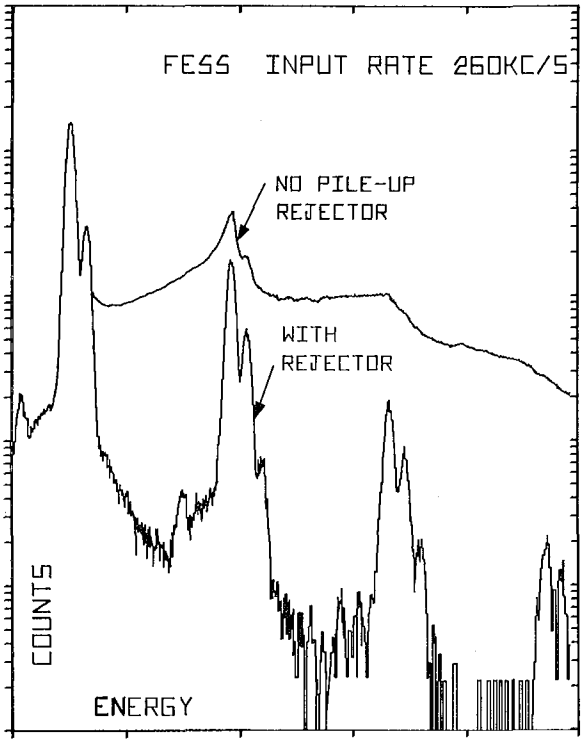

Fig. 5. Spectrum of ^{55}Fe illustrating the effect of pileup rejection on a Mn x-ray spectrum taken at an input rate of 260,000 counts per second. (XBL-7010-6802)

the pileup rejector is operating, but these features are almost hidden by background when the pileup rejector is not used. Moreover, the primary peak, and even secondary pileup peaks, exhibit very good resolution at this high-counting rate when the pileup rejector is employed. It is interesting to note than even the very weak silicon K x-ray escape peak is clearly visible in the pileup as well as in the singles spectra.

Footnote and References

†Condensed from UCRL-20151, October 1970; presented at 1970 Nuclear Science Symposium, New York, Nov. 4-6, 1970; also to be published in IEEE Trans. Nucl. Sci. NS-18, 1, (1971).

1. F. S. Goulding, J. Walton, D. Malone, Nucl. Instr. and Methods, 71, 273 (1969).

2. F. S. Goulding, J. T. Walton, R. H. Pehl, IEEE Trans. Nucl. Sci., NS-17, 1, 218 (1970).

Detection of Low-Energy X Rays with Si(Li) Detectors †

J. M. Jaklevic and F. S. Goulding

The continuing improvement in energy resolution of semiconductor-detector x-ray spectrometers has led to interest in the use of these devices at energies less than 2 keV. This is an energy region of potential analytical interest since the K x rays of several elements of biological and chemical importance occur at these energies. Using a windowless x-ray spectrometer system and electron beam excitation on low-Z targets, we have performed measurements of characteristic K x rays of elements down to and including carbon (277 eV).

Experimental Apparatus

The modified x-ray spectrometer system used in the measurements is shown schematically in Fig. 1. It consists of an experimental chamber with access ports for mechanical motion feedthroughs, electron-gun electrodes, and vacuum pumpout. A two-position gate valve is mounted in place of the usual window on top of the detector holder and is actuated by means of a mechanical feedthrough to the outside of the sample chamber. In one position of the gate valve, a 0.005-in. beryllium window isolates the detector from the sample chamber, enabling operation of the chamber at atmospheric pressure without disturbing the detector cryostat. In the other position, a thin self-supporting aluminum foil, typically of 25 $\mu gm/cm^2$ to 60 $\mu gm/cm^2$ thickness, is present. In addition to serving as a vacuum baffle, these foils prevent light from reaching the detector while transmitting x rays.

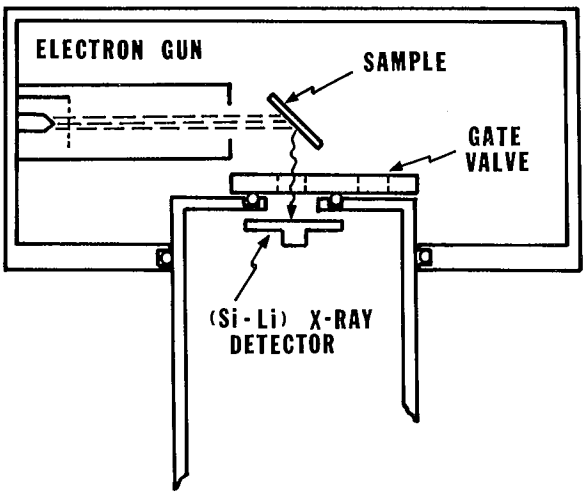

Fig. 1. Schematic diagram of modified x-ray spectrometer and sample chamber.
(XBL-7010-6814)

An electron gun was used to generate characteristic x rays in the light element samples. The detector was 3 mm deep by 5 mm diameter Si(Li), included in a system employing pulsed-light feedback electronics.[1] The electronic resolution was 118 eV when using a Gaussian pulse-shape peaking at 35 μsec.

Linearity and Energy Resolution

The response of the spectrometer to fluorescence x rays in the energy range below 2 keV has been measured and the system linearity and energy resolution determined. The maximum observed deviation of the measured energies from a straight line fitted to the data between 500 eV and 2 keV was less than the minimum estimated error of 4 eV. The rms deviation over the entire range was less than 3 eV. These limits were established by uncertainty in locating the midpoint of peaks from the graphical spectra and might be reduced by the application of more sophisticated curve fitting techniques; the system nonlinearity could be less than the numbers quoted, but we cannot eliminate the possibilities of minor nonlinearities[2] below our limits.

Energy-resolution data were also obtained and are summarized in the plot of resolution squared vs energy given in Fig. 2. The data are reasonably consistent with statistical summing of electronic noise and detector charge fluctuations. The straight line shown in this figure was calculated using the measured electronic resolution of 118 eV, assuming a mean energy-per-hole electron pair (ϵ) of 3.81 eV and a Fano factor (F) of 0.132. There appear to be systematic departures from the straight line below 1 keV, which can be attributed to the effect of tailing on the peaks. Measurements of the full-width at 1/10 maximum show an increased tailing effect at low energies, and at low bias voltages, suggesting window-related charge collection problems. Typical resolution (FWHM) are 137 ± 3 eV for Al K x rays (1480 eV), and 126 ± 8 eV for oxygen (525 eV).

Detection of Carbon X Rays

The region below 500 eV warrants separate discussion because of the special techniques that have been used in these experiments

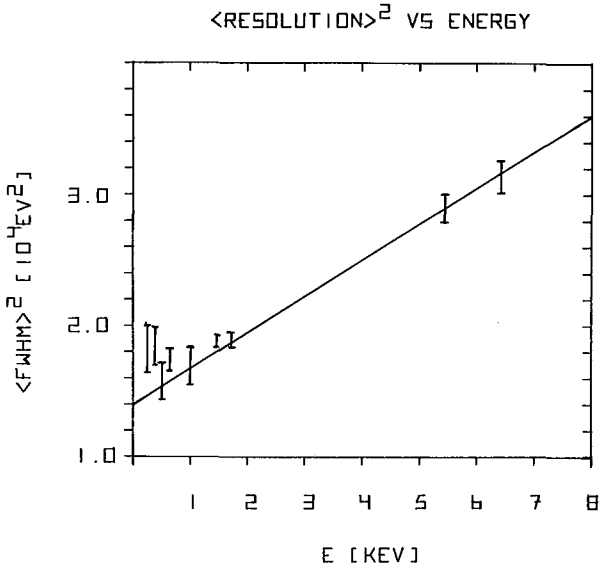

Fig. 2. Resolution squared vs energy. (XBL-7010-6808)

to observe x rays in this range, specifically carbon and nitrogen K x rays at 277 eV and 392 eV, respectively.

To reduce noise counts at low energies by a large factor relative to the fluorescent x-ray signal, we have employed a pulse-excitation source generated by pulsing the grid on the electron-gun, then gating the electronics for only a brief time when we know that fluorescent x-ray pulses would be at their peak value. By sampling the system output only when there is a very high probability of an x ray being present, we increase the ratio of x-ray events to noise pulses by the off-on ratio of the sampling pulses. Preliminary experiments using a 1-μsec-wide pulse with a 150-μsec period have yielded sufficient noise suppression to permit observation of carbon x rays. Figure 3 is a spectrum obtained with a graphite target using the pulse technique; we also show an Al_2O_3 spectrum for comparison.

The energy resolution of carbon and nitrogen x rays under the pulsed operation are 136 ± 8 eV and 131 ± 10 eV (FWHM) respectively, which is consistent with our previous discussion of the departure from statistical behavior at low energy. We have also consistently observed departures from linearity for these x rays, which we have attributed to the detector itself. The carbon peak position, defined as the point midway between the half-height values, lies approximately at 0.7 of the expected value extrapolated from the linearity curves for higher energy, whereas the nitrogen line is at 0.9 of its expected value. Linearity measurements on the electronics, using a

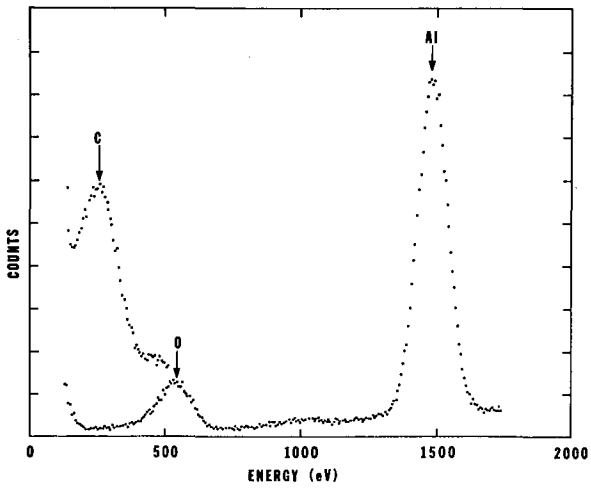

Fig. 3. Spectrum of carbon x rays from graphite target observed in the pulsed mode. An Al_2O_3 spectrum is shown for comparison. (XBL-7010-6815)

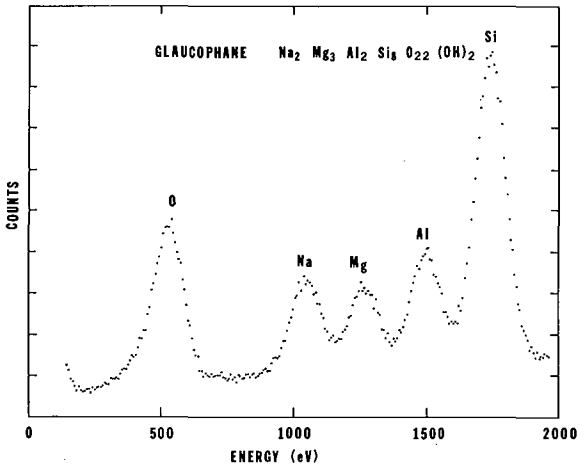

Fig. 4. Spectrum of fluorescence x rays from electron excitation of glaucophane. The composition of this mineral sample is indicated on the graph. (XBL-7010-6816)

pulser, exhibit no nonlinearity; we have therefore concluded that it is most likely due to charge collection in the detector. At 277 eV approximately, 10% of the photoelectric events occur within 2×10^{-6} cm of the surface. In addition to being less than the estimated window thickness, this distance is also less than the range for the photoelectrons produced in the silicon. A sizable fraction of the ionization will therefore be produced outside the intrinsic volume and will not appear in the signal.

As an illustration of the potentialities for fluorescence analysis at these low energies,

Fig. 4 shows a spectrum obtained by bombardment of mineral targets with 7.5-keV electrons. The characteristic x rays at the light element constituents are labeled.

Footnote and References

†Condensed from IEEE Trans. Nucl. Sci., NS-18, 187 (1971).

1. D. A. Landis, F. S. Goulding, R. H. Pehl and J. T. Walton, IEEE Trans. Nucl. Sci., NS-18, 115 (1971).

2. H. R. Zulliger, L. M. Middleman, and D. W. Aiken, IEEE Trans. Nucl. Sci., NS-16, 47 (1969), and references cited therein.

Low Cost Lock-In Amplifier

Michiyuki Nakamura

We have built a low cost lock-in amplifier using linear integrated circuits. The lock-in amplifier consists of 7 operational amplifiers, 2 comparators, 2 voltage followers, 1 hex-inverter digital integrated circuit, and 6 transistors. The total cost of components and hardware is less than $150.

The reference section of the amplifier uses a gain-controllable operational amplifier and a comparator as a Schmitt trigger to square the incoming reference signal. Double integration is used to produce a parabolic waveform from the squared reference signal. The parabolic wave is enough like a sine wave that we could use a phase-splitter and an RC network for a phase shifter. A second comparator is used to square the phase-shifted reference signal, and the squared signal is used in the demodulating section of the amplifier.

The signal-amplifier section uses a voltage-follower integrated circuit at its input stage. The input impedance is 10 megohms. The last stage has a twin-tee filter network in the feedback section tuned to the incoming-signal frequency and has a gain of 20. Additional amplifiers can be switched in and out to acquire the desired amount of gain. A maximum gain of 100,000 was designed into this lock-in amplifier, but we see that an additional gain of 10 could have been used without exceeding the noise margins we had set for ourselves.

The demodulating section uses an operational amplifier suggested by the Fairchild Semiconductor Linear Integrated Circuits Applications Handbook, 1967. We had to modify the switching network used to ensure the same gain for both positive- and negative-going signals.

RC integration follows the demodulator with selectable 6 or 12 db/octave rolloff. A meter shows the amount of output signal, and a signal is available for driving a chart recorder.

A 100-MHz Digital Stabilizer

R. LaPierre and R. Strudwick

During the past year we have upgraded some of our digital stabilizers[1] to operate with multichannel analyzers that use a 100 MHz digitizing clock rate in their analog-to-digital converter. The modification incorporates MECL-II logic elements in the design of the first decade of the stabilizer's address scaler. The design changes are limited to one printed-circuit board. The modified units will operate with all types of analyzers which have been previously interfaced for stabilization.

Reference

1. M. Nakamura and R. LaPierre, Nucl. Instr. Methods 32, 277 (1965).

Computer Control of a Quadrupole Mass Spectrometer System

R. LaPierre and R. Strudwick

A system utilizing a Digital Equipment Corporation PDP-8L computer has been assembled to control the operation of an EAI mass spectrometer. The spectrometer system is being used by Mr. Norman Milleron's group to study the feasibility of analyzing air, breath, and skin respiration as a means of diagnosing and prognosing states of health and disease.

The computer was obtained from the Mathematics and Computing Group on a short-term loan basis. The operation of the controller is depicted in the block diagram of Fig. 1. The quadrupole's sweep circuitry is operated under program control via a 12-bit digital-to-analog (DAC) converter. The staircase sweep voltage from the DAC may be programmed to prevent ions of the highly abundant peaks, such as nitrogen and oxygen, from ever reaching the exit port of the mass filter and swamping the ion detector. The controller is also able to turn off the ion source in the EAI between steps of the sweep voltage.

The experimental data are accumulated in a RIDL multichannel analyzer operating in the multiscale mode. The operation of the analyzer is under program control and is operated in synchronization with the staircase

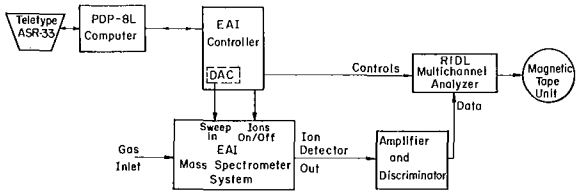

Fig. 1. Mass spectrometer system block diagram. (XBL-713-3060)

sweep voltage applied to the mass spectrometer. The analyzer, rather than the computer, was used for data storage because it was already interfaced to a magnetic tape unit. The magnetic tape output allows the experimenter to record the data in a format suitable for further analysis at the computer center.

The staircase sweep voltage applied to the mass filter produces a significant improvement in stability when compared with the results obtained with a normal sawtooth sweep voltage. Signal-to-noise was improved from 5×10^5 for the unmodified EAI quadrupole to 5×10^8 for the modifications in conjunction with LHe pumping.

Extended Core Storage for a PDP-9 Computer

R. LaPierre

The core memory of a Nuclear Data Model 160 analyzer has been used extensively over the past year as auxiliary storage for a PDP-9 computer. The 4K memory of the ND is very compatible with the computer as both have an 18-bit word size.

At the present time, all data transfers are under computer control, and occur via programmed data transfer. (We are considering putting the auxiliary memory on the API bus.) The design of the hardware interface unit allows the following modes of operation for the transfer of data between the computer and the ND memory:

(a) "Read" into the computer, commencing at location X in the analyzer, the contents of m successive locations.

(b) "Write" into the analyzer, commencing at location X, m successive words.

(c) "Add-1" to the contents of location X in the analyzer.

All of the signal levels and timing required by the ND memory are incorporated into the hardware design of the interface and are "invisible" to the programmer.

The operation of the ND as a stand-alone multiparameter analyzer has not been affected by its interface to the PDP-9. Additionally, the interface permits operation of the analyzer in its normal fashion under program control. The availability of the ND for multiparameter analysis has been somewhat affected, however, as the extended-core feature has been utilized in several of the programs used by the Fission Research Group. The hardware display feature of the memory is utilized by one program in which the spectral data of an on-line experiment is transferred to the ND for storage and display.

There has been no known failure in the interface and (or) memory storage since its initial checkout. Since many of the routines use the extended core for program storage as well as data storage, it can be assumed that the system is error-free.

On-Line Mass Determination of ^{252}Cf Fission Fragments

R. C. Jared, E. K. Quigg,† J. B. Hunter, E. Cheifetz,*
J. B. Wilhelmy, and S. G. Thompson

Correlations of fission fragment masses with γ-ray or x-ray emission have been studied extensively in multiparameter fission experiments in which the masses of the fragments were obtained from the measured kinetic energies of the two fragments. It is common in such experiments to record 10^7 - 10^8 multidimensional events and then to be faced with the problem of sorting the massive amounts of data to obtain meaningful correlations. The programs that reduce the data involve complex data handling procedures and require lengthy preparation. Even when the programs are available, it takes months to sort the data. It has been our experience that six months to two years pass before meaningful physical results are derived from the raw data. To overcome this difficulty, a program which determines fission fragment masses has been incorporated in an on-line PDP-9 computer system. This program sorts γ rays into spectra correlated with different ranges of fragment masses during the experiment.

The procedure of determining the fragment masses from their measured kinetic energies has been described in detail by Watson[1] and is summarized here briefly. The pulse-height responses of the solid-state detectors of each fragment are digitized into 256 channels, such that the light-fragment peak falls at channel 104 and the heavy-fragment peak falls at about channel 75. The useful single-fragment pulse-height spectrum in the case of spontaneous fission of ^{252}Cf extends from channels 31 to 130. The energy calibration is obtained from the centroids of the two peaks of the single-fragment spectra. The masses corresponding to all possible pulse-height-response combinations in the useful region are calculated and placed in a 100×100 table. Each location in this table is generated by an iterative procedure that involves the Schmitt calibration procedure and the known corrections for neutron emission as a function of fragment masses and total kinetic energy. In practice, the fragment pulse heights were digitized into 12-bit numbers (corresponding to 4096 channels), of which the eight most significant bits were used to obtain the 256-channel spectrum. The four least-significant bits were used for interpolation between adjacent values of the masses in the table. The mass of one of the fragments in each sorted event was obtained by referring the pulse heights of the fragments in each event to the mass table described above and interpolating within the table.

Immediate determination of the masses in the PDP-9 system follows basically the above procedure. The PDP-9 computer consists of a 16K-word memory, a disk with a capacity of 250K words, magnetic tape output, display oscilloscope, a teletype unit, and three DEC tapes. The memory holds the mass table. It has been found that only 3500 memory locations out of the 100×100 mass table are referred to in any significant frequency, so that the mass table is reduced to that size. The mass table is calculated in advance by the CDC-6600 computer and is fed into the PDP-9 before the experiment. Since the mass table is based on a predetermined calibration equation, a two-point gain-stabilization system similar to that described by Nakamura[2] has been incorporated in the program to maintain the exact positions of both the light- and heavy-fragment peaks. There are 32 γ-ray spectra, each of 4096 channels, in the disk storage. Each γ-ray spectrum corresponds to a particular mass interval, which is usually 2 amu in range, but can be varied if necessary.

Figure 1 shows the flow of the multidimensional events. Each event consists of

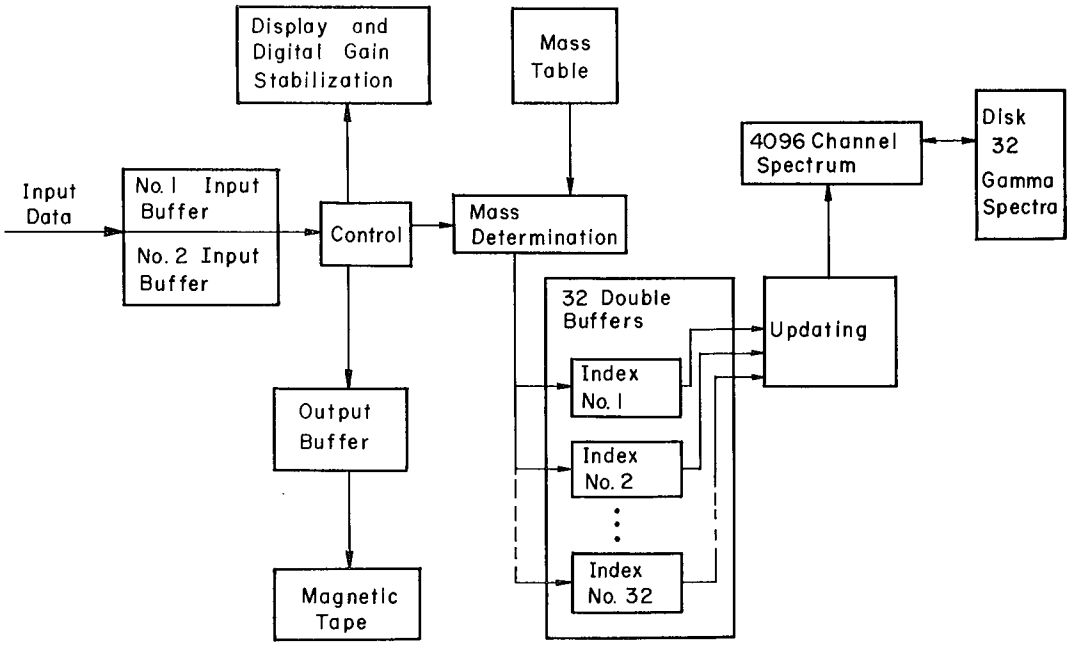

Fig. 1. Block diagram of the computer "on-line" data processing of γ-ray events associated with fission-fragment masses.
(XBL-713-3059)

digital values for the two fragment pulse heights, the γ-ray pulse height, and a signal identifying the nature of the event (e.g., two-fragment coincidence used for stabilization, fission γ-ray coincidence, γ-ray stabilization event, etc.) These events are initially placed in double-input buffers. Each buffer can hold 30 multidimensional events and requires 120 PDP-9 words. The two input buffers allow for sorting of one buffer as the other one is filled with new events. When a buffer is filled, sorting commences and the events go to any or all of the following places: (1) a subroutine that controls the variable-gain amplifiers which stabilize the various detectors and display the single-detector pulse-height distributions on the oscilloscope, (2) an output double buffer that is written, when filled, on a magnetic tape (this step is equivalent to the output stage of past experiments), and (3) the mass-sorting part of the program.

In the mass-sorting sequence, an index between 1 and 32 corresponding to the mass range is determined for each event by first referring the fragment channel numbers to the mass table and then converting the derived mass value to an appropriate index. The γ-ray channel number of the event is then placed in one of 32 double buffers, each corresponding to a mass interval. When one of these buffers is filled, the corresponding γ-ray spectrum is read from the disk to the memory and is updated with the events in the buffer. At the end of the updating process, the γ-ray spectrum is rewritten on the disk. During the updating sequence the second buffer continues to be filled.

The system can handle up to 5000 events/min. At the end of an experimental run, the 32 γ-ray spectra are stored on a DEC magnetic tape for analysis. By using this system, collection of many events is reduced to a manageable number of spectra which can yield meaningful physical results within a short time.

Footnotes and References

†Present address: Department of Earth and Space Sciences, State University of New York, Stony Brook, L. I., New York 11790.

*On leave from the Weizmann Institute of Science, Rehovoth, Israel.

1. R. L. Watson, J. B. Wilhelmy, R. C. Jared, C. Rugge, H. R. Bowman, S. G. Thompson, and J. O. Rasmussen, Nucl. Phys. A141, 449 (1970).

2. M. Nakamura and R. L. LaPierre, Nucl. Instr. Methods 32, 277 (1965).

Analysis of Prompt Gamma and X-Ray Radiations of ^{252}Cf Fission Fragments

R. C. Jared, E. Cheifetz,† S. G. Thompson, J. B. Wilhelmy, E. K. Quigg,* and T. H. Strong

A series of multiparameter experiments have been performed to study the correlations of promptly emitted γ rays and x rays with specific fission fragments. The mass of the fragment associated with a γ transition was determined from the measured kinetic energy of a pair of fragments. The atomic number of the fragment was determined from the particular K x ray emitted in coincidence with the γ rays.

Prompt K x rays and (or) γ rays in coincidence with pairs of fission fragments were measured using the detector arrangement indicated in Fig. 1. Three separate experiments using different photon detectors were performed: (1) recording γ rays with a 1-cm^3 Ge(Li) detector (resolution 1 keV at 122 keV) in position γ_2, (2) recording γ rays and (or) x rays in coincidence using a 6-cm^3 Ge(Li) detector in position γ_1 and a 2-cm^2 Si(Li) detector in position γ_2, and (3) recording γ-γ coincidences with a 35-cm Ge(Li) coaxial detector in position γ_2 and a 6-cm^3 Ge(Li) detector in position γ_1. In all the experiments a nominal 10^5-fission/min source of ^{252}Cf was electrodeposited onto the surface of fragment detector F_1. Thus Doppler shifting and broadening problems were eliminated for transitions from the fragments stopped in that detector. This technique, which simplified the spectra, applies to transitions with lifetimes longer than the stopping time of the fragments ($\approx 10^{-12}$ sec).

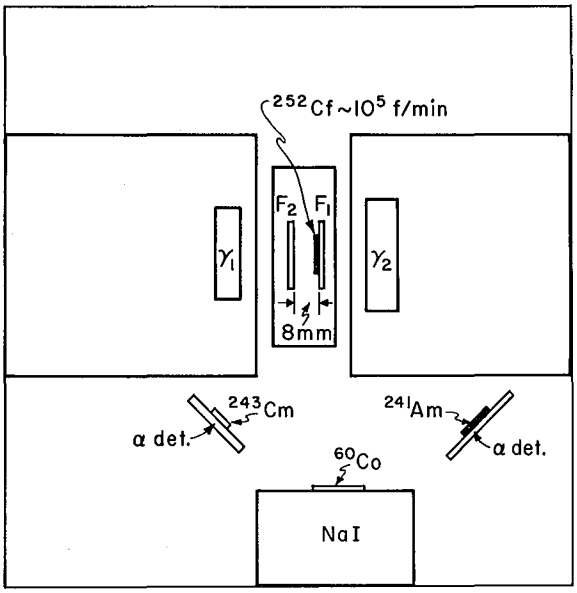

Fig. 1. Schematic representation of detector system. Detectors F_1 (with electrodeposited ^{252}Cf) and F_2 measured energies of fragments. Detectors γ_1 and γ_2 measured energies of γ rays and (or) x rays. External sources for stabilization of the photon detectors were ^{243}Cm (α-γ coincidence), ^{60}Co (γ-γ coincidence), and ^{241}Am (α-γ coincidence).
(XBL-703-2403)

Due to the large acceptance angle of the fragment detectors, all of the transitions above ≈ 100 keV that were emitted by the fragments in flight were broadened enough so that they did not appear as lines in the spectrum. Lifetime determinations in the time region 0.1 - 2.0 nsec were obtained from the ratio of the non-Doppler-shifted γ-ray intensity observed when the fragment stopped in the plated detector F_1 relative to the intensity observed when the fragment stopped in the second detector F_2, which was separated from the plated detector by 8 mm.

Each multidimensional event consisted of five pulse heights, four of which were the analog signals from the individual detectors (F_1, F_2, γ_1, γ_2), and the fifth was a marking signal to specify the nature of the coincidence between the various detectors (e.g., F_1F_2 stabilization, $F_1F_2\gamma_1$, $F_1F_2\gamma_1\gamma_2$, γ_1 gain stabilization, etc.). The events were fed to an analog multiplexer[1] that stored the analog information until a 4096-channel ADC[2] consecutively digitized each dimension and presented the information to the computer. The digital information of each event was transferred to one of two input buffers in a PDP-9 computer. When a buffer was filled the events were processed according to the event type, as specified in the fifth dimension, and used for any of the following purposes: (1) storage in a display buffer for visual monitoring of the various γ-ray, x-ray and fission-fragment spectra, (2) digital gain stabilization of the various detectors, and (3) calculation of fission-fragment detector responses, i.e., peak-to-valley ratios that are sensitive to the detector deterioration. All of the events were also placed in one of two output buffers that were written on magnetic tape after they had been filled. Double buffers were used in

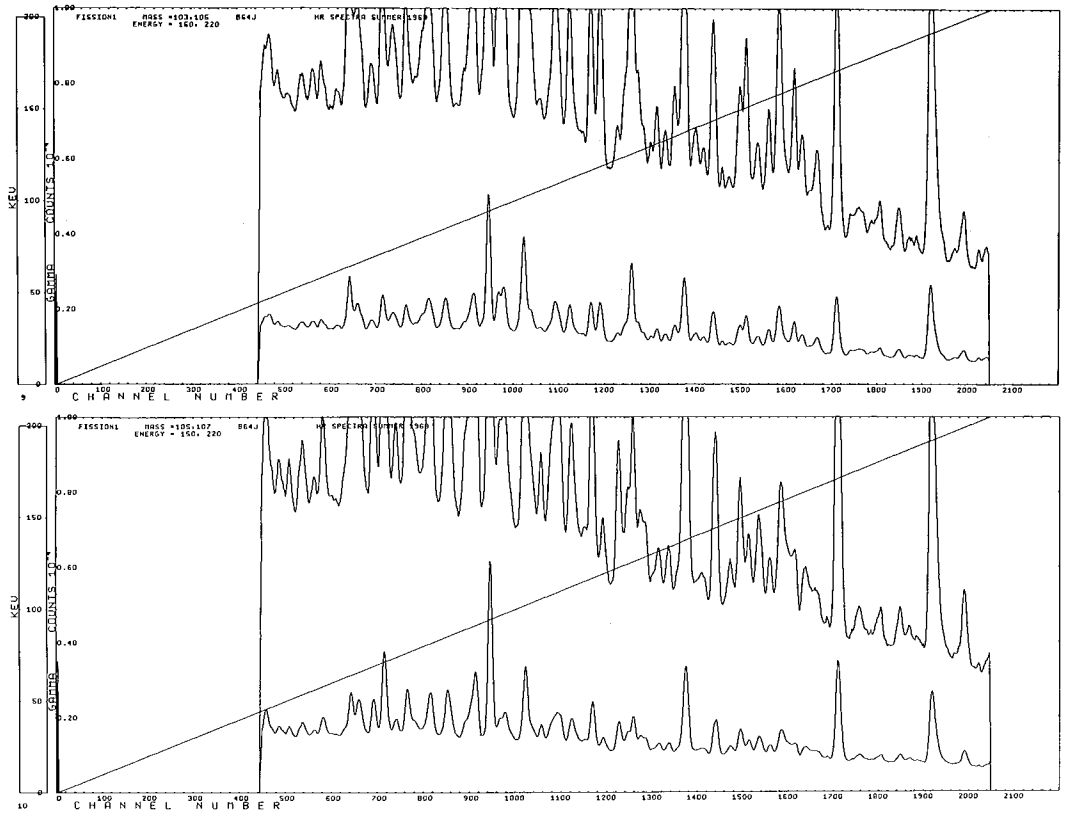

Fig. 2. Gamma-ray spectra recorded using a 1-cm^3 high-resolution Ge(Li) detector. Results shown are for fission fragments that were stopped in the plated detector having masses 103 - 105 and 105 - 107.
(XBL-708-1785)

both the input and output stages to facilitate uninterrupted data collection.

In the experiments, 2.5×10^8 multidimensional events were recorded on 150 magnetic tapes. The tapes were sorted in the CDC-6600 computer. First the various event types were separated onto different tapes, and the fission-fragment energy calibration equation for each PDP-9 output tape was determined from the F_1F_2 stabilization coincidence events. (Events corresponding to one of every 100 F_1F_2 coincidences were recorded.) In the second step all the events of γ_1 or γ_2 in coincidence with a pair of fragments were sorted. The masses of the fragments in such events were calculated[3] and the spectra of γ rays in coincidence with mass intervals of 2 amu were produced. Examples of such spectra are shown in Fig. 2. These γ-ray spectra were then analyzed using the on-line photopeak analysis code of Routti and Prussin[4] to obtain quantitative energies and intensities of individual transitions. The average mass associated with specific γ-ray transitions was

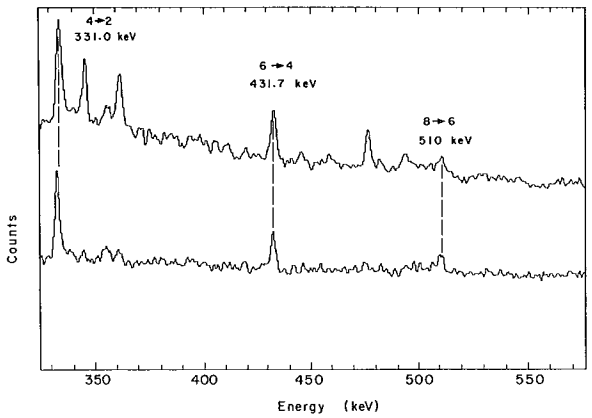

Fig. 3. Prompt γ-ray spectrum from ^{252}Cf observed using a 35-cm^3 coaxial Ge(Li) detector (a) in coincidence with fragments having experimental masses between 143 and 145, (b) in coincidence with fragments having experimental masses between 139 and 149, and also with the 199.4-keV γ ray ($2 \rightarrow 0$ in ^{144}Ba) detected by a 6-cm^3 planar Ge(Li) detector.
(XBL-707-3280)

obtained from the distribution of the transition intensity over the mass intervals.

The events consisting of two photon coincidences with a pair of fragments ($\gamma_1\gamma_2F_1F_2$) were analyzed by first calculating for each event the mass of fragment 1 and the total fragment kinetic energy, and rewriting them event by event on magnetic tapes. These tapes were later sorted in the PDP-9 computer in the following manner. The γ-ray, x-ray coincidence events were sorted into γ-ray spectra in coincidence with specific K x-ray energies and fragment masses corresponding to ± 8 amu about the expected most probable mass of any given element. The x-ray detector resolution was equivalent to roughly one atomic number so that for many intense transitions, the Z identity of the emitting fragment or its complement was easily observed. The γ-ray, γ-ray coincidence events were sorted by setting windows corresponding to intense lines in one photon detector and windows around the mass values of that line (obtained from γF_1F_2 analysis) and observing the spectrum of the second γ-ray detector. An example of a γ-ray spectrum in coincidence with one γ-ray transition is shown in Fig. 3. By combining such an analysis with several considerations of known properties of ground-state bands, it was possible to determine level structure for specific even-even isotopes produced from the spontaneous fission of ^{252}Cf.

Footnotes and References

†On leave from the Weizmann Institute of Science, Rehoboth, Israel.

*Present address: Department of Earth and Space Sciences, State University of New York, Stony Brook, L. I., New York 11790.

1. L. B. Robinson, F. Gin, and H. Cingolani, Nucl. Instr. Methods 75, 121 (1969).

2. L. B. Robinson, F. Gin, and F. S. Goulding, Nucl. Instr. Methods 62, 237 (1968).

3. R. L. Watson, J. B. Wilhelmy, R. C. Jared, C. Rugge, H. R. Bowman, S. G. Thompson, and J. O. Rasmussen, Nucl. Phys. A141, 449 (1970).

4. J. T. Routti and S. G. Prussin, Nucl. Instr. Methods 72, 125 (1969).

V. Thesis Abstracts

Rates of Growth of Crystals from Solutions

Cheng T. Cheng

(UCRL-19518)

Studies of the rates of crystal growth from undercooled binary liquid mixtures of organic substances were conducted in two systems, a simple eutectic mixture of salol and thymol, and bibenzyl and transstilbene which form nearly complete solid solubility.

The newly designed temperature-gradient microscope stage, which incorporates facilities for a quantitative determination of the interfacial liquid and solid compositions and temperature through the use of interferometric techniques, has been successfully used for the first time to study the interfacial rate phenomena of crystallization.

A new theory is developed by modifying the Eyring's absolute-rate-theory concept to interpret the experimental results for the growth of mixed crystal from the binary mixture in terms of a separation factor. This factor, representing the deviation from equilibrium, is found to depend on the growth and interface conditions.

The experimental results have shown that considerable departures of interfacial compositions and temperatures from the phase diagram can occur. The results suggest that the assumption of instantaneous phase equilibrium usually should not be used in design calculations for crystallization equipment.

The adaptation of Eyring-type theory in the prediction of rates of crystal growth by Kirwan and Pigford has been further tested, and its application to crystal growth for various molecules of different structural complexity has been found to be good for an order-of-magnitude estimate.

The Behavior of Chlorella Pyrenoidosa in Steady-State Continuous Culture

Joseph N. Dabes

(UCRL-19958)

Chlorella pyrenoidosa was grown in steady-state continuous culture. Algal growth was never limited by CO_2, minerals, pH, or temperature. The effects of the two remaining independent variables, specific growth rate and incident light intensity, on algal biomass productivity and algal physiology were examined.

It was found that optimum algal biomass productivity was obtained at a specific growth rate of approximately 1.6 day^{-1}, when the incident light intensity was 8.05 mW/cm^2. This optimum specific growth rate is not expected to change significantly as a function of incident light intensity. This optimum specific growth rate for cell biomass production results primarily from a high light saturated rate of photosynthesis and a low amount of light transmitted through the culture.

Total chlorophyll content, chlorophyll a/chlorophyll b ratio, light saturated rate of photosynthesis, dark respiration rate, and RNA content were found to be strong functions of specific growth rate. On the other hand, maximum quantum efficiency of the quinone Hill reaction, and DNA content changed little, if at all, as a function of specific growth rate. Physiological changes in the cells as a function incident light intensity were small.

A mathematical expression for the light response curve of photosynthesis was formulated, which is consistent with both experimental data and current knowledge of the chemical kinetics of photosynthesis.

A mathematical model for the performance of optically dense algal systems, which are of interest for the mass culture of algae, is presented. This model differs from previous models, since it uses the abovementioned light response curve to describe the local rate of photosynthesis and also accounts for changes in the physiology of the algae. This model for optically dense cultures was found to give a reasonable fit of our continuous culture experimental data, and should be useful in designing and predicting the performance of algal systems.

Decay Studies of Neutron-Deficient Isotopes of Astatine, Polonium, and Bismuth

Janis M. Dairiki

(UCRL-20412)

Alpha particle and gamma ray studies were made of the decay of neutron-deficient isotopes of astatine, polonium, and bismuth. Astatine isotopes were produced in Au(^{12}C,xn) reactions at the Berkeley Heavy-Ion Linear Accelerator (Hilac). Polonium and bismuth sources were obtained as products of astatine decay.

Three kinds of experiments were performed: 1) α-particle energies and branching ratios, 2) high resolution γ-ray singles studies, and 3) γ-γ coincidence measurements. In the γ-ray studies, measurements were made on a source containing a mixture of isotopes with no previous chemical separation, primarily due to the short half-lives involved. Computer codes were developed to analyze the resulting complex multicomponent γ spectra.

Decay schemes were constructed for even-mass At isotopes, A = 202-206. Confirming evidence was obtained in α measurements for an isomeric state of ^{202}At. Partial decay schemes were deduced for ^{205}At and ^{203}At, characterized by intense direct population of a $9/2^-$ excited level in the Po daughters followed by a γ transition to the $5/2^-$ ground states. For ^{202}Po-^{205}Po, tentative decay schemes were proposed. The odd-mass polonium nuclei exhibit substantial decay to positive parity states in their Bi daughters. In addition, an α group at 5.37 ± 0.15 MeV was attributed to ^{203}Po. Finally, a systematic series of energy levels (0+, 4+, 4+, and 5-) were observed in the even-even Pb nuclei produced in the electron-capture decay of ^{198}Bi-^{204}Bi.

Core and Valence Electronic States Studied with X-Ray Photoelectron Spectroscopy

Charles Sherwood Fadley

(UCRL-19535)

X-ray photoelectron spectroscopy (XPS) is applied to two separate studies of electronic structure: (1) Experimental and theoretical results are presented for metal-atom electron binding-energy splittings due to multiplet effects in the final-hole state of the measurement. Such splittings are observed in several solid compounds containing Mn and Fe, as well as in Fe metal, Co metal, and Ni metal. The 3s electron binding energy is split into two components with a separation as large as 7.0 eV. The instrumental resolution is ≈ 1.0 eV. Theoretical predictions are in good agreement with these 3s results, provided that the effects of covalency in chemical bonding are taken into account; 2p and 3p electron energies also appear to exhibit such splittings. XPS results for monatomic Eu also give evidence for multiplet effects. Photoelectron peaks due to the Eu 4d and 4f electrons show certain anomalies in shape and width that are consistent with multiplet splittings. (2) The application of XPS to studies of the valence-band densities of states of solids is discussed. A comparison is made with the closely related experimental technique, ultraviolet photoelectron spectroscopy. XPS results are presented for the fifteen solids: Fe, Co, Ni, Cu, ZnS, Ru, Rh, Pd, Ag, $CdCl_2$, Os, Ir, Pt, Au, and HgO. Where possible, comparisons are made with the results of other experiments and theory. Systematic trends are observed in the XPS-derived densities of states for these solids. In particular, the d bands of Ag, Ir, Pt, Au, and HgO all show a similar two-component structure. With the present resolution, XPS results appear to represent a good description of the overall shape of the density-of-states function.

Special experimental equipment and data analysis techniques necessary for these studies are also discussed. A procedure for least-squares fitting of analytic peak shapes to XPS spectra is presented. Also, a technique is developed to correct XPS spectra for the effects of inelastic scattering and a non-monochromatic x-ray source.

The Theoretical Analysis of Nuclear Reactions Involving Strongly Deformed Nuclei Using Phenomenological Models

Raymond Stuart Mackintosh

(UCRL-19529)

Stripping reactions, A(d, p) A+1, are studied for the case where A is a strongly deformed nucleus. In the standard treatment, using DWBA, the possibility that the projectiles d and p can set the nucleus in rotational motion is ignored. We have studied in detail the importance of these inelastic processes using the coupled-channel source-term technique of Ascuitto and Glendenning. We have shown this to be equivalent to the coupled-channel Born approximation written down by Penny and Satchler. We have also generalized a formal derivation of DWBA given by Greider and Dodd. We have discovered that for A $\approx$ 25 and for 10- and 12-MeV deuterons, inelastic processes are of vital importance -- that relative strengths of levels may be greatly changed by their inclusion and that angular distributions may be significantly improved, although the detailed shape is still not reproduced for these light nuclei. This latter failing, therefore, seems to be characteristic of any generalization for zero-range DWBA to include rotational excitations. For 12-MeV deuterons in the deformed rare earth region, the inclusion of inelastic processes will, in general, lead to substantial differences in values, extracted by comparison with experiment, of the amplitudes with which particular angular momenta occur in the various Nilsson states. Angular distributions of weaker levels in a band are often changed substantially, and the change in stripping strengths of various levels is quite comparable to that which is a result of coriolis mixing (not included in our calculations). Our calculations involve purely macroscopic rotational excitations, and we further ignore transitions between members of different bands of the odd-A residual nucleus.

Electrochromatographic Separations of Rare Earths

Louie Nady

(UCRL-19526)

Electrochromatography has been investigated as a possible separation process for ions, particularly for lanthanides and actinides. Following a review of previous work, two new advances were developed. One is a proposed new device in which a stable broad-band concentration gradient is developed by applying a dc voltage to a packed bed of ion-exchange resin confined by ion-exchange membranes. The resulting separation depends on solution-phase and resin-phase mobilities of the ions and on the resin selectivity for the ions.

Because resin-phase mobilities play an important part, bed-conductivity measurements were made for Dowex 50W-X4 resin in equilibrium with solutions of NaCl, $AgNO_3$, $La(NO_3)_3$, $Ce(NO_3)_3$, $Nd(NO_3)_3$, $Ho(NO_3)_3$, and mixtures of $AnNO_3$-$La(NO_3)_3$, and $AgNO_3$ - $Ce(NO_3)_3$. Particle conductivities were then calculated by use of Bruggeman's equation. Electrolyte sorption for these same ions into Dowex 50W-X4, and of $La(ClO_4)_3$ into Dowex 50W-X2, X4, X8, X12 were investigated. The resulting identification of all species in the resin phase made it possible to determine resin-phase mobilities for the individual ions.

The second advance is the development and operation of a continuous preparative-scale ligand electrochromatograph. Continuous separation is achieved in this unit as a result of transverse electrophoretic migration of uncomplexed rare earth ions across a laminar flow of complexing agent in a packed bed. Selective complex formation with the ion mixture (with a resultant marked mobility change for the complexed species) causes the net electrophoretic migration rates to differ for each component, hence separates them. Zones of relatively pure Ce^{+++} and La^{+++}, in different runs, have been achieved from mixtures of the two ions, using EDTA as the ligand.

X-Ray Structure Investigation of Some Substituted Indoles, and the X-Ray Structure of 1, 1'-Bishomocubane

William G. Quarles

(UCRL-19906)

The crystal structures of 5-methoxytryptamine, melatonin, and the p-bromobenzoate of 1, 1'-bishomocubane have been solved by x-ray diffraction methods. A computer program for the trial-and-error solution of crystal structures is also described here.

The molecular structure of 1, 1'-bishomocubane has been solved to an R-factor accuracy of 5.5% using 990 independent manual diffractometer data, of which 865 were nonzero. Standard deviation on bond lengths is ± .02 Å. The compound crystallizes in space group $P2_1/c$ with a = 6.379 ± .001 Å, b = 26.07 ± .005 Å, c = 8.443 ± .002 Å, β = 96.87 ± .01°, λ = 1.54051 Å, and Z = 4. Density calculated on these cell dimensions is 1.575 g/cm^3, and density measured by floatation in ethylene bromide and ethylene chloride is 1.560 g/cm^3. The compound is sensitive to x rays, and decomposes anistropically. Addition of two extra carbons into one of the cubane cyclobutane rings causes two of the remaining cyclobutane rings to pucker by 27° from a planar configuration, whereas the other two cyclobutane rings stay planar within the standard deviations of the determination.

The crystal structure of 5-methoxytryptamine has been solved using a trial-and-error computer program which is also outlined in this thesis. The compound crystallizes in the noncentric monoclinic space group Pc, and a = 6.110 ± .002 Å, b = 9.532 ± .003 Å, c = 8.831 ± .003 Å, β = 98.72 ± .01°, λ = 1.54051 Å, and Z = 2. The density calculated on the basis of these cell dimensions is 1.242 g/cm^3. The density measured by floatation at room temperature in ethyl acetate and ethylene chloride is 1.245 g/cm^3. The structure was refined against the 759 independent θ-2θ scan automatic diffractometer data, of which 17 were zero to an R factor of 2.5%. Standard deviations on bond lengths are .003 Å. Within the standard deviations of the determination, the indole ring is not planar. Two carbons of the benzene portion are warped above the plane of the ring at an angle of 1.6°. Short bonds correlate with high-π electron density as calculated by molecular orbital theory. One of the shortest N-H-N hydrogen bonds yet reported, 2.916 Å, is formed between the primary amine nitrogen of the aliphatic chain and the nitrogen of the indole ring, which donates its hydrogen for the formation of this bond.

The crystal and molecular structure of melatonin has been solved using statistical methods and automatic diffractometer θ-2θ scan data. This compound crystallizes into space group $P2_1/c$, with a = 7.707 ± .002 Å, b = 9.252 ± .002 Å, c = 17.007 ± .004 Å, β = 96.78 ± .03°, λ = .709261 Å, and Z = 4. Density calculated on the basis of these cell constants is 1.276 g/cm^3, and the density measured by floatation in ethylene chloride, ethylene bromide, and ethyl acetate is 1.272 g/cm^3. The structure was refined to a 3.5% R value against the 1140 independent data, of which 808 were nonzero weight. The indole ring is not planar within the standard deviation of the structure determinations. The carbons C(3) and C(10) of the pyrrole ring are warped above the ring by 1.8°.

The findings of the x-ray work are entirely consistent with the dual conformation theory of serotonin.

VI. 1970 Publications

1970 Publications

Papers Published and UCRL Reports Issued, 1970

ABED, U.
Hot bath for samples in volumetric flasks
UCRL-20410, November 1970
Submitted to Anal. Chim. Acta

ABED, U. (See McLaughlin, R., UCRL-18999)

ANDERBERG, D. (See Clem, R. G., UCRL-19950 Rev.)

ANDERSON, O. A. (See Halbach, K., Plasma Phys. 12, 207 (1970))

APONICK, A. A., Jr., C. M. Chesterfield, D A. Bromley, and N. K. Glendenning
Quadrupole and hexadecapole deformations in rare earth nuclei
Nucl. Phys. A159, 367 (1970)

ASARO, F. (See Perlman, I., Nobel Symposium 12)

ASARO, F. (See Gorman, D. J., UCRL-19900)

ASARO, F. (See Gorman, D. J., UCRL-19946)

ASARO, F. (See Gorman, D J., UCRL-19953)

ASCUITTO, R. J., and N. K. Glendenning
Assessment of two-step processes in (p,t) reactions
UCRL-19574, March 1970
Phys. Rev. C 2, 1260 (1970)

ASCUITTO, R. J., N. K. Glendenning, and B. Sorenson
Confirmation of strong second-order processes in (p,t) reactions on deformed nuclei
UCRL-20402, October 1970
Submitted to Phys. Letters

BACHER, A. D., R. de Swiniarski, G. R. Plattner, F. G. Resmini, D. L. Hendrie, A. U. Luccio, and J. Sherman
Inelastic scattering of 24.5-MeV polarized protons from ^{20}Ne and ^{22}Ne
UCRL-19550 Abstract, February 1970
Meeting of the American Physical Society, Washington, D. C., 27-30 April 1970

BACHER, A. D., G. R. Plattner, H. E. Conzett, D. J. Clark, H. Grunder, and W. F. Tivol
Polarization and cross-section measurements in p-^{4}He scattering from 20 to 40 MeV
UCRL-19943, July 1970
Third International Symposium on Polarization Phenomena in Nuclear Reactions, Madison, Wisconsin, 31 August - 4 September 1970

BACHER, A. D., R. de Swiniarski, D. L. Hendrie, A. Luccio, G R. Plattner, F. G. Resmini, and J. Sherman
Hexadecapole deformation and asymmetry in inelastic scattering of 24.5-MeV polarized protons from ^{20}Ne and ^{22}Ne
UCRL-19976 Abstract, August 1970
3rd International Symposium on Polarization, Madison, Wisconsin, 29 August - 4 September 1970

BACHER, A. D., and G. R. Plattner
Absolute calibration of spin-1/2 polarization
UCRL-19995 Abstract, October 1970
Meeting of the American Physical Society, Stanford, California, 28-30 December 1970

BACHER, A. D. (See Plattner, G. R., UCRL-19548 Abstract)

BACHER, A. D. (See Hardy, J. C., UCRL-19549 Abstract)

BACHER, A. D. (See Hardy, J C., UCRL-19912)

BACHER, A. D. (See Mendelson, R., UCRL-19929)

BAKER, B., III, and R. L. Pigford
Cycling zone adsorption: quantitative theory and experimental results
UCRL-19945, August 1970
To be published in Ind. Eng. Chem. Fund.

BALDESCHWIELER, J. D. (See Meares, C. F., Proc. Natl. Acad. Sci. 64, 1155 (1969))

BARTUNIK, H. D., W. Potzel, R. L. Mössbauer, and G. Kaindl
Study of gold compounds by nuclear gamma resonance spectroscopy
UCRL-19933, July 1970
Submitted to Zeitschrift für Physik

BASSICHIS, W. A., A. K. Kerman, C. F. Tsang, D. R. Tuerpe, and L. Wilets
A study of deformation energy surfaces obtained from single particle energies
UCRL-73044
"Festschrift for J. A. Wheeler"

BENNETT-CORNIEA, W., H. A. Sokol, and W. M. Garrison
Reductive deamination in the radiolysis of oligopeptides in aqueous solution and in the solid state
UCRL-19504, January 1970
18th Annual Meeting of the Radiation Research Society, Dallas, Texas, 1-5 March 1970

BERNTHAL, F. M., J. O. Rasmussen, and J. M. Hollander
The decays of ^{176}Ta, ^{176}Lu, and ^{176m}Lu to levels in ^{176}Hf
UCRL-19587, April 1970
Submitted to Phys. Rev.

BJØRNHOLM, S., J. Borggreen, and E. K. Hyde
Search for new islands of fission isomerism
UCRL-19905, June 1970
To be published in Nucl. Phys.

BORGGREEN, J., K. Valli, and E. K. Hyde
Production and decay properties of protactinium isotopes of mass 222 to 225 formed in heavy-ion reactions
UCRL-19539, January 1970
Phys. Rev. C 2, 1841 (1970)

BORGGREEN, J., and E. K. Hyde
Alpha decay of neutron deficient osmium isotopes
UCRL-19596, June 1970
Submitted to Nucl. Phys.

BORGGREEN, J. (See Bjørnholm, S., UCRL-19905)

BOWMAN, H. R. (See Frierman, J. D., Science 164, 588 (1969))

BOWMAN, H. R. (See Cheifetz, E., UCRL-19957)

BOWMAN H. R. (See Cheifetz, E., UCRL-19988)

BOWMAN, H. R. (See Wilhelmy, J. B., UCRL-20405 Abstract)

BREWER, W. D., and D. A. Shirley
Beta-particle and gamma-ray angular distributions from ^{186}Re, ^{188}Re, and ^{194}Ir polarized in iron at low temperatures
UCRL-19536, January 1970
Nucl. Phys. A149, 392 (1970)

BREWER, W. D. (See Thorp, T. L., UCRL-19650)

BROMLEY, D. A. (See Aponick, A. A., Jr., Nucl. Phys. A159, 367 (1970))

BRUGE, G. L., R. F. Leonard, and M. S. Zisman
The $^{58}Ni(p, ^{3}He)^{56}Co$ reaction at 45 MeV
UCRL-19545 Abstract, February 1970
Meeting of the American Physical Society, Washington, D. C., 27-30 April 1970

BRUGE, G. L., and R. F. Leonard
$^{58}Ni(p, ^{3}He)^{56}Co$ and $(p,t)^{56}Ni$ reactions at 45 MeV
UCRL-19915, June 1970
Phys. Rev. C 2, 2200 (1970)

BRUGE, G. (See Loiseaux, J. M., UCRL-19558)

BRYANT, R. G. (See Meares, C. F., Proc. Natl. Acad. Sci. 64, 1155 (1969))

BUCHER, J. J., T. J. Conocchioli, and R. M. Diamond
Extraction of $HReO_4$ by trioctyl phosphine oxide in nitrobenzene and in 1,2-dichloroethane
UCRL-19556, February 1970
Submitted to J. Phys. Chem.

BUCHER, J. J., E. R. Held, J. A. Labinger, B. A. Sudbury, and R. M. Diamond
Extraction of HBr, HCl, and HNO_3 by trioctylphosphine oxide in nitrobenzene and in 1,2-dichloroethane
UCRL-19599, May 1970
Submitted to J. Phys. Chem.

BUCHER, J. J., M. Zirin, R. C. Laugen, and R. M. Diamond
Extraction of $HReO_4$ and $HAuCl_4$ by trioctylphosphine oxide in benzene, 1,3,5-triethylbenzene and chloroform
UCRL-19920, September 1970
Submitted to J. Phys. Chem.

BUTLER, G. W.
Identification of nuclear fragments by a combined time-of-flight, dE/dx-E technique
UCRL-19913 Abstract, May 1970
160th National Meeting of the American Chemical Society, Chicago, Illinois, 13-18 September 1970

BUTLER, G. W. (See Poskanzer, A. M., UCRL-18996)

CALVIN, M. (See Fischer, M. S., UCRL-19554)

CALVIN, M. (See Pohlit, H. M., UCRL-19703)

CARDINAL, C. U. (See Cerny, J., Phys. Rev. Letters 24, 1128 (1970))

CARDINAL, C. U. (See Jackson, K. P., UCRL-19963)

CARDINAL, C. U. (See Cerny, J., UCRL-19971)

CERNY, J., C. U. Cardinal, H. C. Evans, K. P. Jackson, and N. A. Jelley
^{49}Fe: a new $T_Z = -3/2$ delayed-proton emitter
Phys. Rev. Letters 24, 1128 (1970)

CERNY, J. ,C. U. Cardinal, K. P. Jackson, D. K. Scott, and A C. Shotter
Heavy-ion reactions as a technique for direct mass measurements of unknown Z > N nuclei
UCRL-19971, July 1970
Phys. Rev. Letters 25, 676 (1970)

CERNY, J. , J. E. Esterl, R. A. Gough, and R. G. Sextro
Confirmed proton radioactivity of $^{53}Co^{m}$
UCRL-19973, September 1970
Phys. Letters 33B, 284 (1970)

CERNY, J. (See Mendelson, R., UCRL-19929)

CERNY, J. (See Esterl, J. E., UCRL-19947)

CERNY, J. (See Hardy, J. C., UCRL-19951)

CERNY, J. (See Hardy, J. C., UCRL-19954)

CERNY, J. (See Jackson, K. P., UCRL-19963)

CERNY, J. (See Fleming, D. J., UCRL-19966)

CERNY, J. (See Esterl, J. E., UCRL-19989 Abstract)

CERNY, J. (See Wozniak, G. J., UCRL-19992 Abstract)

CERNY, J. (See Maples, C., UCRL-19996 Abstract)

CERNY, J. (See Sextro, R. G., UCRL-19998 Abstract)

CERNY, J. (See McGrath, R. L., UCRL-20416)

CHEIFETZ, E., R. C. Gatti, R C. Jared, S. G. Thompson, and A. Wittkower
Acceleration of fission fragments
UCRL-19516, November 1969
Phys. Rev. Letters 24, 148 (1970)

CHEIFETZ, E., R. C. Jared, S. G Thompson, and J. B. Wilhelmy
Experimental information concerning deformation of neutron-rich nuclei in the A≈100 region
UCRL-19584, April 1970
Phys. Rev. Letters 25, 38 (1970)

CHEIFETZ, E., E. R. Giusti, and S. G. Thompson
Search for superheavy elements in nature by detection of events with large numbers of neutrons
UCRL-19589 Abstract, April 1970
Conference on the Properties of Nuclei Far from the Region of Beta Stability, Leysin, Switzerland, 31 August - 4 September 1970

CHEIFETZ, E., R. C. Jared, S. G. Thompson, and J. B. Wilhelmy
Excited state in even-even fission products
UCRL-19949, August 1970
Conference on the Properties of Nuclei Far from the Region of Beta Stability, Leysin, Switzerland, 31 August - 4 September 1970

CHEIFETZ, E., E. R. Giusti, H. R. Bowman, R. C. Jared, J. B Hunter, and S. G. Thompson
Search for superheavy elements in nature by detection of events with large numbers of neutrons
UCRL-19957, August 1970

CHEIFETZ, E., H. R. Bowman, J. B. Hunter, and S. G. Thompson
Prompt neutrons from spontaneous fission of ^{257}Fm
UCRL-19988, December 1970
To be published in Phys. Rev.

CHEIFETZ, E. (See Wilhemy, J. B., UCRL-19931)

CHEIFETZ, E. (See Wilhelmy, J. B., UCRL-20405 Abstract)

CHESTERFIELD, C. M. (See Aponick, A. A., Jr., Nucl. Phys. A159, 367 (1970))

CLARK, D. J.
An external heavy-ion source for the Berkeley 88-inch cyclotron
UCRL-20406 Abstract, November 1970
Meeting of the American Physical Society, Chicago, Illinois, 1-3 March 1971

CLARK, D. J. (See Plattner, G. R., UCRL-19548 Abstract)

CLARK, D. J. (See Bacher, A D., UCRL-19943)

CLARKSON, J. E. (See Sikkeland, T., UCRL-19928)

CLEM, R. G , F. Jakob, and D. Anderberg
Fumed silica salt bridges
UCRL-19950 Rev., August 1970
Anal. Chem. 43, 292 (1971)

CLEM, R. G., and W. W. Goldsworthy
A modularized digitizing time-synchronizing current-sampling system for electroanalytical studies
UCRL-19956 Rev., February 1971
To be published in Anal. Chem.

CONOCCHIOLI, T. J. (See Bucher, J. J., UCRL-19556)

CONWAY, J. G., and E. F. Worden
Preliminary level analysis of the first and second spectra of dysprosium, Dy I and Dy II
UCRL-19944, August 1970
To be published in J. Opt. Soc. Am.

CONWAY, J. G. (See King, A. S., J. Res. Natl. Bur. Std. A 74A, 355 (1970))

CONWAY, J. G. (See McLaughlin, R., UCRL-18999)

CONWAY, J. G. (See Edelstein, N., UCRL-19568)

CONZETT, H. E. (See Plattner, G. R., UCRL-19548 Abstract)

CONZETT, H. E. (See Bacher, A. D., UCRL-19943)

DABES, J. N., C. R Wilke, and K. H. Sauer
The behavior of Chlorella pyrenoidosa in steady-state continuous culture
UCRL-19958, August 1970
Ph. D. Thesis

DABES, J. N., R. K. Finn, and C. R. Wilke
The growth rate of microorganisms as a function of the concentration of a single limiting substrate
UCRL-19959, August 1970
Submitted to Biotech. Bioeng.

DAIRIKI, J. M.
Decay studies of neutron-deficient isotopes of astatine, polonium, and bismuth
UCRL-20412, November 1970
Ph. D. Thesis

De BOER, B. G., A. Zalkin, and D H. Templeton
The crystal and molecular structure of phosphorus trifluoride-tris(difluoroboryl) borane, $B_4F_6 \cdot PF_3$
Inorg. Chem. 8, 836 (1969)

De BOER, J. (See Stephens, F S., UCRL-19571)

de SWINIARSKI, R. (See Bacher, A. D., UCRL-19550 Abstract)

de SWINIARSKI, R. (See Bacher, A. D., UCRL-19976 Abstract)

DIAMOND, R. M., F. S Stephens, K. Nakai, and R. Nordhagen
Lifetimes of ground-band states in $^{148,150,152}Sm$
UCRL-19517 Rev., October 1970
Phys. Rev. C 1, 344 (1971)

DIAMOND, R. M.
Heavy-ion in-beam spectroscopy
UCRL-19961, August 1970
Conference on the Properties of Nuclei Far from the Region of Beta Stability, Leysin, Switzerland, 31 August - 4 September 1970

DIAMOND, R. M. (See Jensen, C. H., UCRL-19540)

DIAMOND, R. M. (See Nakai, K., UCRL-19544)

DIAMOND, R. M. (See Quebert, J. L., UCRL-19555)

DIAMOND, R. M. (See Bucher, J. J., UCRL-19556)

DIAMOND, R. M. (See Stephens, F S., UCRL-19571)

DIAMOND, R. M. (See Stephens, F. S , UCRL-19588 Abstract)

DIAMOND, R. M. (See Bucher, J. J., UCRL-19599)

DIAMOND, R. M. (See Bucher, J. J., UCRL-19920)

DIAMOND, R. M. (See Nakai, K., UCRL-19923)

DIAMOND R. M. (See Leigh, J. R., UCRL-19955)

DIAMOND, R. M. (See Stephens, F. S., UCRL-20422)

DODGE, R. P. (See Sime, R. J., UCRL-19941)

DREW, M. G. B., D. H. Templeton, and A. Zalkin
The crystal and molecular structure of cembrene
Acta Cryst. B25, 261 (1969)

DUHM, H. H. (See Parkinson, W. C., Phys. Rev. 178, 1976 (1969))

EDELSTEIN, N., and R. Mehlhorn
Hyperfine structure in trivalent plutonium
UCRL-19563, March 1970
Phys. Rev. B 2, 1225 (1970)

EDELSTEIN, N., J. G. Conway, D. Fujita, W. Kolbe, and R. McLaughlin
Formation and characterization of divalent einsteinium in a CaF_2 crystal
UCRL-19568, March 1970
J. Chem. Phys. 52, 6425 (1970)

EDELSTEIN, N.
Analysis of the electron paramagnetic resonance spectrum of divalent Es in CaF_2
UCRL-19936, July 1970
To be published in J. Chem. Phys.

EDELSTEIN, N.
The hyperfine structure anomaly of ^{241}Pu and ^{239}Pu and the nuclear moment of ^{241}Pu
UCRL-19972, September 1970
Phys. Letters 33A, 233 (1970)

EDELSTEIN, N., G. N. LaMar, F. Mares, and A. Streitwieser, Jr.
Proton magnetic resonance shifts in bis(cyclooctatetraenyl)uranium(IV)
UCRL-20413, December 1970
To be published in Chem. Phys. Letters

EDELSTEIN, N. (See Karraker, D. G., J. Am. Chem. Soc. 92, 4841 (1970))

EDELSTEIN, N. (See McLaughlin, R., UCRL-18999)

ERWIN, W. R. (See Pohlit, H. M., UCRL-19703)

ESKOLA, K.
Recent studies of elements with $Z \geq 102$ at Berkeley
UCRL-19921 Abstract, June 1970
Nuclear Structure Symposium of the Thousand Lakes, Jousta, Finland, 3-7 August 1970

ESKOLA, K. (See Eskola, P., UCRL-19562)

ESKOLA, K. (See Ghiorso, A., UCRL-19565)

ESKOLA, K. (See Ghiorso, A., UCRL-19577)

ESKOLA K. (See Silva, R., UCRL-19938)

ESKOLA, K. (See Ghiorso, A., UCRL-19974)

ESKOLA, P., K. Eskola, M. Nurmia, and A. Ghiorso
Alpha decay of ^{255}No and ^{257}No
UCRL-19562, March 1970
Phys. Rev. C 2, 1058 (1970)

ESKOLA, P. (See Ghiorso, A., UCRL-19565)

ESKOLA, P. (See Ghiorso, A., UCRL-19577)

ESKOLA, P. (See Ghiorso, A., UCRL-19974)

ESTERL, J. E., J. C. Hardy, R. G. Sextro, and J. Cerny
Beta-delayed-proton decay of ^{13}O: a violation of mirror symmetry
UCRL-19947, August 1970
Phys. Letters 33B, 287 (1970)

ESTERL, J. E., J. C. Hardy, R. G. Sextro, and J. Cerny
Isospin purity and the delayed-proton-decay of ^{33}Ar
UCRL-19989 Abstract, October 1970
Meeting of the American Physical Society, Stanford, California, 28-30 December 1970

ESTERL, J. E. (See Hardy, J. C., UCRL-19951)

ESTERL, J. E. (See Cerny, J., UCRL-19973)

EVANS, H. C. (See Cerny, J., Phys. Rev. Letters 24, 1128 (1970))

EVANS, H. C. (See Jackson, K. P., UCRL-19963)

EWAN, G. T. (See Yamazaki, T., Nucl. Phys. A134, 81 (1969))

FADLEY, C. S.
Core and valence electronic states studied with x-ray photoelectron spectroscopy
UCRL-19535, April 1970
Ph. D. Thesis

FADLEY, C. S., and D. A. Shirley
Multiplet splitting of metal-atom electron binding energies
UCRL-19566, April 1970
Phys. Rev. A 2, 1109 (1970)

FALTENS, M. O., and D. A. Shirley
Mössbauer spectroscopy of gold compounds
UCRL-19559, February 1970
J. Chem. Phys. 53, 4249 (1970)

FALTENS, M. O. (See Ruben, H., UCRL-19985)

FINN, P., R. K. Pearson, J. M. Hollander, and W. L. Jolly
Chemical shifts in core electron binding energies for some gaseous nitrogen compounds
UCRL-19671, May 1970
Submitted to Inorg. Chem.

FINN, R. K. (See Dabes, J. N., UCRL-19959)

FISCHER, M. S., D. H. Templeton, A. Zalkin, and M. Calvin
Structure and chemistry of the porphyrins. The crystal and molecular structure of the monohydrated dipyridinated magnesium phthalocyanin complex
UCRL-19554, February 1970
To be published in J. Am. Chem. Soc.

FLEMING, D. J., J. C. Hardy, and J. Cerny
Spin dependence in the reactions $^{16}O(p,t)^{14}O$ and $^{16}O(p,\ ^{3}He)^{14}N$
UCRL-19966, August 1970
To be published in Nucl. Phys.

FRANKEL, R. B. (See Soinski, A. J., UCRL-19576)

FRIERMAN, J. D., H. R. Bowman, I. Perlman, and C. M. York
X-ray fluorescence spectrography: use in field archeology
Science 164, 588 (1969)

FUJITA, D. (See Edelstein, N., UCRL-19568)

FUSS, D. (See Halbach, K., Plasma Phys. 12, 207 (1970))

GARRISON, W. M., M. Kland-English, H. A. Sokol, and M. E. Jayko
Radiolytic degradation of the peptide main chain in dilute aqueous solution containing oxygen
UCRL-19926, June 1970
J. Phys. Chem. 74, 4506 (1970)

GARRISON, W. M.
Radiation-induced reactions of amino acids and peptides
UCRL-19984 Abstract, October 1970
161st National Meeting of the American Chemical Society, Los Angeles, California, 28 March - 2 April 1971

GARRISON, W. M. (See Bennett-Corniea, W., UCRL-19504)

GARRISON, W. M. (See Rodgers, M. A. J., UCRL-19595)

GARRISON, W. M. (See Makada, H. A., UCRL-19979)

GARSIDE, L., and M. Weigel
Single-particle resonances in the renormalized RPA-treatment of nucleon-nucleus scattering
UCRL-19538, January 1970
Phys. Rev. C 2, 374 (1970)

GARSIDE, L., M. Weigel, and P. K. Haug
Renormalization constants in the random-phase approach
UCRL-19940, August 1970
Phys. Rev. C 3, 563 (1971)

GATTI, R. C. (See Cheifetz, E., UCRL-19516)

GHIORSO, A.
The Berkeley Hilac heaviest element research program
UCRL-18633, April 1970
Proceedings of the Robert A. Welch Foundation Conferences on Chemical Research: XIII. The Transuranium Elements--The Mendeleev Centennial (Houston, Texas, November 17-19, 1969), pp. 107

GHIORSO, A., M. Nurmia, K. Eskola, and P. Eskola
^{261}Rf; new isotope of element 104
UCRL-19565, March 1970
Phys. Letters 32B, 95 (1970)

GHIORSO, A., M. Nurmia, K. Eskola, J. Harris, and P. Eskola
New element hahnium, atomic number 105
UCRL-19577, April 1970
Phys. Rev. Letters 24, 1498 (1970)

GHIORSO, A.
Two new elements--atomic numbers 104 and 105
UCRL-19585, August 1970
Yale Scientific, October 1970

GHIORSO, A., M. Nurmia, J. Harris, K. Eskola, and P. Eskola
In defense of the Berkeley work concerning the alpha-emitting isotopes of element 104
UCRL-19974, September 1970
Submitted to Nature

GHIORSO, A. (See Silva, R. J., UCRL-18296)

GHIORSO, A. (See Silva, R., UCRL-18713)

GHIORSO, A. (See Eskola, P., UCRL-19562)

GHIORSO, A. (See Silva, R., UCRL-19938)

GILBERT, G. W., A. M. Poskanzer, and D. A. Landis
Identification of nuclear fragments by a combined time-of-flight, ΔE-E technique
UCRL-19952, August 1970
Nucl. Instr. Methods 89, 189 (1970)

GIUSTI, E. R. (See Cheifetz, E., UCRL-19589 Abstract)

GIUSTI, E. R. (See Cheifetz, E., UCRL-19957)

GLASHAUSSER, C., D. L. Hendrie, and E. A. McClatchie
Single-particle proton admixtures in core-excited states of ^{207}Bi
UCRL-19993, October 1970
Submitted to Phys. Letters

GLASHAUSSER, C. (See Hendrie, D. L., UCRL-19547 Abstract)

GLENDENNING, N. K., and R. S. Mackintosh
Study of inelastic processes on (d, p) reactions in deformed nuclei
UCRL-20404, November 1970
Submitted to Nucl. Phys.

GLENDENNING, N. K. (See Aponick, A. A., Jr., Nucl. Phys. A159, 367 (1970))

GLENDENNING, N. K. (See Stephens, F. S., UCRL-19571)

GLENDENNING, N. K. (See Ascuitto, R. J., UCRL-19574)

GLENDENNING, N. K. (See Ascuitto, R J., UCRL-20402)

GOLDSWORTHY, W. W. (See Clem, R. G., UCRL-19956 Rev.)

GORMAN, D. J., and F. Asaro
Tables of the Clebsch-Gordon coefficients for odd- and even-mass deformed nuclei
UCRL-19900, May 1970
Submitted to Nucl. Data

GORMAN, D. J.
A computer program for the smoothing and differentiation of data from multichannel analyzers
UCRL-19903, June 1970

GORMAN, D. J., and F. Asaro
Energy levels in ^{235}Np
UCRL-19946, August 1970
Phys. Rev. C 3, 746 (1971)

GORMAN, D. J., and F. Asaro
The alpha decay of ^{240}Am
UCRL-19953, August 1970
Phys. Rev. C 2, 2406 (1970)

GOUGH, R. A. (See Cerny, J., UCRL-19973)

GRUNDER, H. (See Plattner, G. R., UCRL-19548 Abstract)

GRUNDER, H. (See Bacher, A. D., UCRL-19943)

HALBACH, K., O. A. Anderson, and D. Fuss
Systematic shaping of $|B|$ on flux surfaces in axisymmetric toroidal systems
Plasma Phys. 12, 207 (1970)

HALBACH, K.
Effect of drift tube tolerances on the elastic field distribution along the length of an Alvarez cavity
UCRL-19932, September 1970
Proton Linear Accelerator Conference, Batavia, Illinois, 28 September - 2 October 1970

HARDY, J. C., A. D. Bacher, G. R. Plattner, J. A. Macdonald, and R. G. Sextro
Two-nucleon transfer reactions using polarized protons
UCRL-19549 Abstract, February 1970
Meeting of the American Physical Society Washington, D. C., 27-30 April 1970

HARDY, J. C., A. D Bacher, G. R. Plattner, J. A Macdonald, and R. G. Sextro
Two-nucleon transfer reactions induced by polarized protons
UCRL-19912, June 1970
Phys. Rev. Letters 25, 298 (1970)

HARDY, J. C., J. E. Esterl, R. G. Sextro, and J. Cerny
Isospin purity and delayed-proton decay: ^{17}Ne and ^{33}Ar
UCRL-19951, August 1970
Phys. Rev. C 3, 700 (1971)

HARDY, J. C., J. M. Loiseaux, and J. Cerny
The reactions $^{11}B(p, {}^{3}He)^{9}Be$ and $^{11}B(p,t)^{9}B$: Is there strong isospin mixing in mass 9?
UCRL-19954, August 1970
To be published in Nucl. Phys.

HARDY, J. C. (See Esterl, J. E., UCRL-19947)

HARDY, J. C. (See Fleming, D. J., UCRL-19966)

HARDY, J. C. (See Esterl, J. E., UCRL-19989 Abstract)

HARDY, J. C. (See Sextro, R. G , UCRL-19998 Abstract)

HARRIS, J. (See Ghiorso, A., UCRL-19577)

HARRIS, J. (See Silva, R., UCRL-19938)

HARRIS, J. (See Ghiorso, A., UCRL-19974)

HARVEY, B. G. (See Zisman, M. S., UCRL-19914)

HARVEY, B. G. (See Sherman, J. D., UCRL-19997 Abstract)

HARVEY, B. G. (See McGrath, R. L., UCRL-20416)

HAUG, P. K. (See Garside, L., UCRL-19940)

HEIL, T. G., and H. F. Schaefer III
Four new bound, low-lying states of cyanogen: $^{4}\Sigma^{+}$, $^{4}\Sigma^{-}$, $^{4}\Pi$, $^{4}\Delta$
UCRL-19935, July 1970
Astrophys. J. 163, 425 (1971)

HEIL, T. G. (See Schaefer, H. F., III, UCRL-19983)

HELD, E. R. (See Bucher, J. J., UCRL-19599)

HENDRICKSON, D. N., J. M. Hollander, and W. L. Jolly
Core-electron binding energies for compounds of boron, carbon, and chromium
UCRL-19083
Inorg. Chem. 9, 612 (1970)

HENDRIE, D. L., J. R. Meriwether, F. Selph, D. Morris, and C. Glashausser
Design features of a magnetic spectrometer
UCRL-19547 Abstract, February 1970
Meeting of the American Physical Society, Washington, D. C., 27-30 April 1970

HENDRIE, D. L. (See Parkinson, W. C., Phys. Rev. 178, 1976 (1969))

HENDRIE, D. L. (See Meriwether, J. R., UCRL-19546 Abstract)

HENDRIE, D. L. (See Bacher, A. D., UCRL-19550 Abstract)

HENDRIE, D. L. (See Bacher, A. D., UCRL-19976 Abstract)

HENDRIE, D. L. (See Glashausser, C., UCRL-19993)

HENDRIE, D L. (See Sherman, J. D., UCRL-19997 Abstract)

HENDRIE, D. L. (See McGrath, R. L., UCRL-20416)

HOLLANDER, J. M., and W. L. Jolly
X-ray photoelectron spectroscopy
UCRL-19158, January 1970
Accounts of Chemical Research 3, 193 (1970)

HOLLANDER, J. M , and D. A. Shirley
Chemical information from photoelectron and conversion electron spectroscopy
UCRL-19592, May 1970
Ann. Rev. Nucl. Sci. 20, 435 (1970)

HOLLANDER, J. M. (See Hendrickson, D. N., UCRL-19083)

HOLLANDER, J. M. (See Bernthal, F. M., UCRL-19587)

HOLLANDER, J. M. (See Finn, P., UCRL-19671)

HOLLANDER, J. M. (See Lederer, C. M., UCRL-19986)

HOWERY, D. (See Vermeulen, T., UCRL-19981)

HUFFMAN, E. H. (See McLaughlin, R., UCRL-18999)

HULET, E. K. (See Silva, R. J., UCRL-18296)

HUNTER, J. B. (See Cheifetz, E., UCRL-19957)

HUNTER, J. B. (See Cheifetz, E., UCRL-19988)

HUNTZICKER, J. J., and D. A. Shirley
A proposed absolute temperature scale for cerium magnesium nitrate below 0.003 K
UCRL-19541, January 1970
Phys. Rev. B 2, 4420 (1970)

HYDE, E. K. (See Poskanzer, A. M., UCRL-18996)

HYDE, E. K. (See Borggreen, J., UCRL-19539)

HYDE, E. K. (See Borggreen, J., UCRL-19596)

HYDE, E. K. (See Bjørnholm, S., UCRL-19905)

JACKSON, A. D., A. Lande, and P. U. Sauer
Triton binding energy calculations in a harmonic oscillator basis
UCRL-19557, February 1970
To be published in Nucl. Phys.

JACKSON, K. P., H. C Evans, C. U. Cardinal, N. A. Jelley, and J. Cerny
$^{53}Co^{m}$: a proton-unstable isomer
UCRL-19963, August 1970
Phys. Letters 33B, 281 (1970)

JACKSON, K. P. (See Cerny, J., Phys. Rev Letters 24, 1128 (1970))

JACKSON, K. P. (See Cerny, J., UCRL-19971)

JAKLEVIC, J. M. (See Lederer, C. M., UCRL-19986)

JAKOB, F. (See Clem, R. G., UCRL-19950 Rev.)

JARED, R. C. (See Cheifetz, E., UCRL-19516)

JARED, R. C. (See Cheifetz, E., UCRL-19584)

JARED, R. C. (See Wilhelmy, J. B., UCRL-19931)

JARED, R. C. (See Cheifetz, E., UCRL-19949)

JARED, R. C. (See Cheifetz, E., UCRL-19957)

JARED, R. C. (See Wilhelmy, J. B., UCRL-20405 Abstract)

JAYKO, M. E. (See Garrison, W. M., UCRL-19926)

JELLEY, N. A. (See Cerny, J., Phys. Rev. Letters 24, 1128 (1970))

JELLEY, N. A. (See Jackson, K. P., UCRL-19963)

JENSEN, C. H., and R. M. Diamond
Anion exchange in mixed organic-aqueous solutions. I. Dioxane-water
UCRL-19540, January 1970
J. Phys. Chem. 75, 79 (1971)

JOLLY, W. L. (See Hendrickson, D. N., UCRL-19083)

JOLLY, W. L. (See Hollander, J. M., UCRL-19158)

JOLLY, W. L. (See Finn, P., UCRL-19671)

JONES, E. R., Jr. (See Karraker, D. G., J. Am. Chem. Soc. 92, 4841 (1970))

KAINDL, G., and D. Salomon
Interference of photoelectric and nuclear resonance absorption, and magnetic splitting of 6.25-keV γ rays of ^{181}Ta
UCRL-19579, April 1970
Phys. Letters 32B, 364 (1970)

KAINDL, G.
Mössbauer effect study of hyperfine interactions in ^{145}Nd
UCRL-19942, July 1970
Submitted to Zeitschrift für Physik

KAINDL, G.
Chemical shifts of core electron binding energies in osmium
UCRL-19975 Abstract, September 1970
Meeting of the American Physical Society, New Orleans, Louisiana, 23-25 November 1970

KAINDL, G. (See Bartunik, H. D., UCRL-19933)

KAPLAN, D. (See Ruben, H., UCRL-19982)

KARRAKER, D. G., J. A. Stone, E. R. Jones, Jr., and N. Edelstein
Bis(cyclooctatetraenyl) neptunium(IV) and bis(cyclooctatetraenyl) plutonium(IV)
J. Am. Chem. Soc. 92, 4841 (1970)

KERMAN, A. K. (See Bassichis, W. A., UCRL-73044)

KING, A. S., J. G. Conway, E. F. Worden, and C. E. Moore
Temperature classification of the spectra of dysprosium (Dy I, Dy II)
J. Res. Natl. Bur. Std. A 74A, 355 (1970)

KLAND-ENGLISH, M. (See Garrison, W. M., UCRL-19926)

KOIČKI, S., T. A. Koster, R. Pollak, D. Quitmann, and D. A. Shirley
Perturbed angular correlations in ferromagnets: the ^{100}RhNi case
UCRL-19561, February 1970
Phys. Letters 32B, 351 (1970)

KOLBE, W. (See Edelstein, N., UCRL-19568)

KOSSANYI-DEMAY, P. (See Loiseaux, J. M., UCRL-19558)

KOSTER, T. A., and D. A. Shirley
Table of hyperfine fields
UCRL-20411, November 1970
International Conference on Hyperfine Interactions Detected by Nuclear Radiation, 6-11 September 1970, Rehovoth-Jerusalem, Israel

KOSTER, T. A. (See Koički, S., UCRL-19561)

KROCHTA, J. M. (See Vermeulen, T., UCRL-19981)

LABINGER, J. A. (See Bucher, J. J., UCRL-19599)

LaMAR, G. N. (See Edelstein, N., UCRL-20413)

LAMB, J. F. (See Lee, D. M., UCRL-19967)

LAMB, J. F. (See Lee, D M., UCRL-19967 Abstract)

LANDE, A. (See Jackson, A. D., UCRL-19557)

LANDIS, D. A. (See Gilbert, G. W., UCRL-19952)

LAUGEN, R. C. (See Bucher, J. J., UCRL-19920)

LEDERER, C. M.
Computer interpolation of theoretical internal conversion coefficients
UCRL-19980, September 1970

LEDERER, C. M., J. M. Jaklevic and J. M. Hollander
In-beam gamma-ray spectroscopy of even Mo and Ru isotopes
UCRL-19986, November 1970
Submitted to Nucl. Phys.

LEE, D. M., C. V. Stauffacher, and S. S. Markowitz
Determination of oxygen in copper by ^{3}He activation analysis
UCRL-19532, January 1970
Anal. Chem. 42, 994 (1970)

LEE, D. M., J. F. Lamb, and S. S. Markowitz
A rapid, nondestructive method of fluorine analysis by ^{3}He activation
UCRL-19967, September 1970
To be published in Anal. Chem.

LEE, D. M., J. F. Lamb, and S. S. Markowitz
A rapid, nondestructive method of fluorine analysis by ^{3}He activation
UCRL-19967 Abstract, November 1970
Meeting of the American Chemical Society, Division of Nuclear Chemistry, Los Angeles, California, 28 March - 2 April 1971

LEIGH, J. R., F. S. Stephens, and R. M. Diamond
Rotational bands in odd-odd holmium isotopes
UCRL-19955, August 1970
Phys. Letters 33B, 410 (1970)

LEIGH, J. R. (See Stephens, F. S., UCRL-19588 Abstract)

LEIGH, J. R. (See Stephens, F. S., UCRL-20422)

LEMMON, R. M. (See Pohlit, H. M., UCRL-19703)

LEONARD, R. F. (See Bruge, G. L., UCRL-19545 Abstract)

LEONARD, R. F. (See Bruge, G. L., UCRL-19915)

LOISEAUX, J. M., P. Kossanyi-Demay, Ha Duc Long, G. Bruge, and R. Schaeffer
Study of the $^{40}Ca(He^3,t)^{40}Sc$ reaction at 30.2 MeV
UCRL-19558, February 1970
ANL Meeting on (He^3,t) Reactions, Chicago, Illinois, 25 January 1970

LOISEAUX, J. M. (See Mendelson, R., UCRL-19929)

LOISEAUX, J. M. (See Hardy, J. C., UCRL-19954)

LOISEAUX, J. M. (See Wozniak, G. J., UCRL-19992 Abstract)

LONG, Ha Duc (See Loiseaux, J. M., UCRL-19558)

LUCCIO, A. U. (See Bacher, A. D., UCRL-19550 Abstract)

LUCCIO, A. (See Bacher, A. D., UCRL-19976 Abstract)

MACDONALD, J. A. (See Hardy, J. C., UCRL-19549 Abstract)

MACDONALD, J. A. (See Hardy, J. C., UCRL-19912)

MACKINTOSH, R. S.
The theoretical analysis of nuclear reactions involving strongly deformed nuclei using phenomenological models
UCRL-19529, March 1970
Ph. D. Thesis

MACKINTOSH, R. S. (See Glendenning, N. K., UCRL-20404)

MAHONEY, J. (See Parkinson, W. C., Phys. Rev. 178, 1976 (1969))

MAIN, R. M.
Modification of the Berkeley Hilac
UCRL-19919, September 1970
Proton Linear Accelerator Conference, Batavia, Illinois, September 28 - October 2, 1970

MAKADA H. A., and W. M. Garrison
Radiolysis of liquid N-ethylacetamide
UCRL-19979, September 1970
To be published in Int. J. Radiat. Phys. Chem.

MANG, H. J. (See Poggenburg, J. K., Phys. Rev. 181, 1697 (1969))

MAPLES, C., and J. Cerny
Systematics of direct (p, ^4He) reactions in the 1p shell
UCRL-19996 Abstract, October 1970
Meeting of the American Physical Society, Stanford, California, 28-30 December 1970

MARES, F. (See Edelstein, N., UCRL-20413)

MARKOWITZ, S. S. (See Lee, D. M., UCRL-19532)

MARKOWITZ, S. S. (See Lee, D. M., UCRL-19967)

MARKOWITZ, S. S. (See Lee, D. M., UCRL-19967 Abstract)

MARRUS, R., and R. W. Schmieder
Observation of the magnetic-dipole decay of the 2^3S_1 state of heliumlike Si XIII, S XV, and Ar XVIII
UCRL-19483, February 1970
Phys. Letters 32A, 431 (1970)

MARRUS, R., and R. W. Schmieder
Observation of the two-photon decay of the $2^2S_{1/2}$ states of hydrogenlike Si XIV, S XVI, and Ar XVIII
UCRL-19748 Abstract, April 1970
Meeting of the American Physical Society, Winnipeg, Canada, 22-24 June 1970

MARRUS, R., and R. W. Schmieder
Observation of the magnetic quadrupole decay ($2^3P_2 \rightarrow 1^1S_0$) of heliumlike Ar XVII and lifetime of the 2^3P_2 state
UCRL-19968, September 1970
Phys. Rev. Letters 25, 1689 (1970)

MARRUS, R., and R. W. Schmieder
Lifetime of the $2^2s_{1/2}$ state of hydrogenlike Ar XVIII
UCRL-19978, September 1970
Phys. Rev. Letters 25, 1692 (1970)

MARRUS, R. (See Schmieder, R. W., UCRL-19948)

MARRUS, R. (See Schmieder, R. W., UCRL-19965 Abstract)

McCLATCHIE, E. A. (See Meriwether, J. R., UCRL-19546 Abstract)

McCLATCHIE, E. A. (See Zisman, M. S., UCRL-19914)

McCLATCHIE, E. A. (See Glashausser, C., UCRL-19993)

McCLATCHIE, E. A. (See McGrath, R. L., UCRL-20416)

McGRATH, R. L., D. L. Hendrie, E. A. McClatchie, B. G. Harvey, and J. Cerny
The (d, ^{6}Li) reaction on light nuclei
UCRL-20416, December 1970
To be published in Phys. Letters

McLAUGHLIN, R., U. Abed, J. G. Conway, N. Edelstein, and E. H. Huffman
Oxidation states and site symmetries of CaF_2: U crystals
UCRL-18999, April 1970
J. Chem. Phys. 53, 2031 (1970)

McLAUGHLIN, R. (See Edelstein, N., UCRL-19568)

MEARES, C. F., R. G. Bryant, J. D. Baldeschwieler, and D. A. Shirley
Study of carbonic anhydrase using perturbed angular correlations of gamma radiation
Proc. Natl. Acad. Sci. 64, 1155 (1969)

MEHLHORN, R. (See Edelstein, N., UCRL-19563)

MENDELSON, R., G. J. Wozniak, A. D. Bacher, J. M. Loiseaux, and J. Cerny
Mass of ^{13}O and the isobaric multiplet mass equation
UCRL-19929, July 1970
Phys. Rev. Letters 25, 533 (1970)

MENDELSON, R. A., Jr., (See Wozniak, G. J., UCRL-19992 Abstract)

MERIWETHER, J. R., D. L. Hendrie, E. A. McClatchie, and F. Resmini
A dynamic detector for the focal plane of a magnetic spectrometer
UCRL-19546 Abstract, February 1970
Meeting of the American Physical Society, Washington, D. C., 27-30 April 1970

MERIWETHER, J. R. (See Hendrie, D. L., UCRL-19547 Abstract)

MILLERON, N.
What is a vacuum?
Res./Develop. 21, 40 (1970)

MOORE, C. E. (See King, A. S., J. Res. Natl. Bur. Std. A 74A, 355 (1970))

MORRIS, D. (See Hendrie, D. L., UCRL-19547 Abstract)

MORSS, L. R.
Thermochemistry of some chlorocomplex compounds of the rare earths; third ionization potentials and hydration enthalpies of the trivalent ions
UCRL-19937, July 1970
J. Phys. Chem. 75, 392 (1971)

MÖSSBAUER, R. L. (See Bartunik, H. D., UCRL-19933)

MYERS, W. D., and W. J. Swiatecki
Average nuclear properties
UCRL-18214, December 1969
Anal. Phys. 55, 395 (1969)

NADY, L.
Electrochromatographic separation of rare earths
UCRL-19526, May 1970
Ph. D. Thesis

NADY, L. (See Vermeulen, T., UCRL-19981)

NAKAI, K., J. L. Quebert, F. S. Stephens, and R. M. Diamond
Quadrupole moments of first excited states in ^{28}Si, ^{32}S, and ^{40}Ar
UCRL-19544, January 1970
Phys. Rev. Letters 24, 903 (1970)

NAKAI, K., F. S. Stephens, and R. M. Diamond
Quadrupole moment of the first excited state in ^{36}Ar
UCRL-19923, November 1970
To be published in Phys. Letters

NAKAI, K.
An evidence for oblate deformation of the 9/2- isomeric state in ^{199}Tl
UCRL-19925, July 1970
To be published in Phys. Letters

NAKAI, K. (See Diamond, R. M., UCRL-19517 Rev.)

NAKAI, K. (See Quebert, J. L., UCRL-19555)

NAVARRO, Q. O. (See Soinski, A. J., UCRL-19576)

NEWTON, A. S., and A. F. Sciamanna
The metastable dissociation of the doubly charged carbon monoxide ion
UCRL-19531, January 1970
J. Chem. Phys. 53, 132 (1970)

NEWTON, A. S., and G. E. Thomas
Electron impact excitation efficiency curves for the formation of neutral metastable species
UCRL-19594, June 1970
Eighteenth Annual Conference on Mass Spectrometry and Allied Topics, San Francisco, California, 14-19 June 1970

NEWTON, A. S., A. F. Sciamanna, and G. E. Thomas
The occurrence of the H_3^+ ion in the mass spectra of organic compounds
UCRL-19916 Rev., September 1970
To be published in Intern. J. Mass Spec. Ion Phys.

NORDHAGEN, R. (See Diamond, R. M., UCRL-19517 Rev.)

NURMIA, M.
Investigations of transuranium elements at Berkeley, in Nuclear Reactions Induced by Heavy Ions, ed. by R. Bock and W. R. Hering (North-Holland Publishing Co., Amsterdam, 1970), p. 666.

NURMIA, M. (See Silva, R. J., UCRL-18296)

NURMIA, M. (See Silva, R., UCRL-18713)

NURMIA, M. (See Eskola, P., UCRL-19562)

NURMIA, M. (See Ghiorso, A., UCRL-19565)

NURMIA, M. (See Ghiorso, A., UCRL-19577)

NURMIA, M. (See Silva, R., UCRL-19938)

NURMIA, M. (See Ghiorso, A., UCRL-19974)

O'NEIL, S. V., and H. F. Schaefer III
A configuration interaction study of the $X^3\Sigma^-$, $a^1\Delta$, and $b^1\Sigma^+$
UCRL-20401, October 1970
To be published in Phys. Rev.

PARKINSON, W. C., D. L. Hendrie, H. H. Duhm, J. Mahoney, J. Saudinos, and G. R. Satchler
^{208}Pb(d,t) and (d, ^{3}He) reactions with 50-MeV deuterons
Phys. Rev. 178, 1976 (1969)

PEARSON, R. K. (See Finn, P., UCRL-19671)

PERLMAN, I., and F. Asaro
Neutron-activation analysis of pottery
Nobel Symposium 12, Radiocarbon Variations and Absolute Chronology, ed. by Ingrid U. Olsson (Almqvist and Wiksell, Stockholm, 1970), p. 141

PERLMAN, I. (See Frierman, J. D., Science 164, 588 (1969))

PHILLIPS, N. E. (See Thorp, T. L., UCRL-19650)

PIGFORD, R. L. (See Baker, B., III, UCRL-19945)

PLATTNER, G. R., A. D. Bacher, H. E. Conzett, D. J. Clark, H. Grunder, and W. F. Tivol
Polarization and cross-section measurements in p-α scattering from 20 to 40 MeV
UCRL-19548 Abstract, February 1970
Meeting of the American Physical Society, Washington, D. C., 27-30 April 1970

PLATTNER, G. R. (See Hardy, J. C., UCRL-19549 Abstract)

PLATTNER, G. R. (See Bacher, A. D., UCRL-19550 Abstract)

PLATTNER, G. R. (See Hardy, J. C., UCRL-19912)

PLATTNER, G. R. (See Bacher, A. D., UCRL-19943)

PLATTNER, G. R. (See Bacher, A. D., UCRL-19976 Abstract)

PLATTNER, G. R. (See Bacher, A. D., UCRL-19995 Abstract)

POGGENBURG, J. K., H. J. Mang, and J. O. Rasmussen
Theoretical alpha-decay rates for the actinide region
Phys. Rev. 181, 1697 (1969)

POHLIT, H. M., W. R. Erwin, F. L. Reynolds, R. M. Lemmon, and M. Calvin
A low-energy ion accelerator for hot atom chemical research
UCRL-19703
Rev. Sci. Instr. 41, 1012 (1970)

POLLAK, R. (See Koički, S., UCRL-19561)

POSKANZER, A. M., G. W. Butler, and E. K. Hyde
Fragment production from uranium by 5.5-GeV protons
UCRL-18996, October 1969
Phys. Rev. C 3, 882 (1971)

POSKANZER, A. M. (See Gilbert, G W., UCRL-19952)

POTZEL, W. (See Bartunik, H. D., UCRL-19933)

QUARLES, W. G.
X-ray structure investigation of some substituted indoles, and the x-ray structure of 1,1'-bishomocubane
UCRL-19906, May 1970
Ph. D. Thesis

QUEBERT, J. L., K. Nakai, R. M. Diamond, and F. S. Stephens
Lifetime measurement of the first excited state in ^{206}Pb
UCRL-19555, February 1970
Nucl. Phys. A150, 68 (1970)

QUEBERT, J. L. (See Nakai, K., UCRL-19544)

QUITMANN, D. (See Koički, S., UCRL-19561)

RASMUSSEN, J. O. (See Poggenburg, J. K., Phys. Rev. 181, 1697 (1969))

RASMUSSEN, J. O. (See Bernthal, F. M., UCRL-19587)

RASMUSSEN, J. O. (See Wilhelmy, J. B., UCRL-20405 Abstract)

RAVOO, E. (See Vermeulen, T., UCRL-19981)

RESMINI, F. (See Meriwether, J. R., UCRL-19546 Abstract)

RESMINI, F. G. (See Bacher, A. D., UCRL-19550 Abstract)

RESMINI, F. G. (See Bacher, A. D., UCRL-19976 Abstract)

REYNOLDS, F. L. (See Pohlit, H. M., UCRL-19703)

ROBINSON, C. W., and C. R. Wilke
Mass transfer coefficients and interfacial area for gas absorption by agitated aqueous electrolyte solutions
UCRL-19570, March 1970
Chemical Engineering Conference Australia 1970, Sydney and Melbourne, Australia, 18-26 August 1970

RODGERS, M. A. J., H. A. Sokol, and W. M. Garrison
Radiolytic cleavage of the peptide main-chain in concentrated aqueous solution: energy level of excited-molecule intermediates
UCRL-19595, May 1970
Biochem. Biophys. Res. Commun. 40, 622 (1970)

RUBEN, H., D. Kaplan, A. Zalkin, and D. H. Templeton
Structure determination of 5-methyl-2,2,4-triacetyl-1,3-oxathiole
UCRL-19982, November 1970

RUBEN, H., A. Zalkin, M. O. Faltens, and D. H. Templeton
The crystal and molecular structure of sodium gold(I) thiosulfate dihydrate
UCRL-19985, October 1970

SALOMON, D. (See Kaindl, G., UCRL-19579)

SATCHLER, G. R. (See Parkinson, W. C., Phys. Rev. 178, 1976 (1969))

SAUDINOS, J. (See Parkinson, W. C., Phys. Rev. 178, 1976 (1969))

SAUER, P. U. (See Jackson, A. D., UCRL-19557)

SAUER, K. H. (See Dabes, J. N., UCRL-19958)

SCHAEFER, H. F., III, and T. G. Heil
Electronic structures and potential energy curves for the low-lying states of the CN radical
UCRL-19983, September 1970
To be published in J. Chem. Phys.

SCHAEFER, H. F., III
Electron correlation in the lowest $^1\Sigma^+$ state of beryllium oxide
UCRL-20417, December 1970
To be published in J. Chem. Phys.

SCHAEFER, H. F., III (See Heil, T. G., UCRL-19935)

SCHAEFER, H. F., III (See O'Neil, S. V., UCRL-20401)

SCHAEFFER, R.
Exchange effects for composite particles
UCRL-19537, January 1970
Nucl. Phys. A158, 321 (1970)

SCHAEFFER, R.
Some new features in the microscopic theory of (He^3, t) reactions
UCRL-19551, February 1970
American Physical Society Meeting, Chicago, Illinois, 26-29 January 1970

SCHAEFFER, R.
The microscopic analysis of a charge-exchange reaction: $^{42}Ca(^3He, t)^{42}Sc$
UCRL-19927, June 1970
To be published in Nucl. Phys.

SCHAEFFER, R.
The recent explanation proposed for the $0^+(^3He, t)0^+$ anomalous transitions to antianalogue states is wrong
UCRL-20415, December 1970
Submitted to Phys. Rev. Letters

SCHAEFFER, R. (See Loiseaux, J. M., UCRL-19558)

SCHMIDT, P. H. (See Thorp, T. L., UCRL-19650)

SCHMIEDER, R. W.
Matrix elements of the quadratic Stark effect on hyperfine structure
UCRL-19560, February 1970
Submitted to Am. J. Phys.

SCHMIEDER, R. W.
A partition method for the quantum-mechanical equation of motion
UCRL-19582, April 1970
Submitted to Phys. Rev.

SCHMIEDER, R. W., and R. Marrus
Relativistic magnetic dipole emission: lifetime of the 1s2s $^3S_1$ state of heliumlike argon
UCRL-19948, August 1970
Phys. Rev. Letters 25, 1245 (1970)

SCHMIEDER, R. W., and R. Marrus
Magnetic quadrupole radiation by two-electron atoms: lifetime of the 1s2p $^3P_2$ state of heliumlike argon
UCRL-19965 Abstract, August 1970
Meeting of the American Physical Society, Seattle, Washington, 23-25 November 1970

SCHMIEDER, R. W.
Lifetime of the $2^2s_{1/2}$ state of hydrogenlike argon
UCRL-20421 Abstract, November 1970
Meeting of the American Physical Society, New York, New York, 1-4 February 1971

SCHMIEDER, R. W. (See Marrus, R., UCRL-19483)

SCHMIEDER, R. W. (See Marrus, R., UCRL-19748 Abstract)

SCHMIEDER, R. W. (See Marrus, R., UCRL-19968)

SCHMIEDER, R. W. (See Marrus, R., UCRL-19978)

SCIAMANNA, A. F. (See Newton, A. S., UCRL-19531)

SCIAMANNA, A. F. (See Newton, A. S., UCRL-19916 Rev.)

SCOTT, D. K. (See Cerny, J., UCRL-19971)

SELPH, F. (See Hendrie, D. L., UCRL-19547 Abstract)

SEXTRO, R. G., J. C. Hardy, and J. Cerny
T = 1 analogue states in mass 22 and mass 26 from the two-nucleon transfer reactions
UCRL-19998 Abstract, October 1970
Meeting of the American Physical Society, Stanford, California, 28-30 December 1970

SEXTRO, R. G. (See Hardy, J. C., UCRL-19549 Abstract)

SEXTRO, R. G. (See Hardy, J. C., UCRL-19912)

SEXTRO, R. G. (See Esterl, J. E., UCRL-19947)

SEXTRO, R. G. (See Hardy, J. C., UCRL-19951)

SEXTRO, R. G. (See Cerny, J., UCRL-19973)

SEXTRO, R. G. (See Esterl, J. E., UCRL-19989 Abstract)

SHERMAN, J. D., B. G. Harvey, M. S. Zisman, and D. L Hendrie
Spectroscopy of ^{140}Ce and ^{138}Ce via the ^{142}Ce(p, t), ^{140}Ce(p, p'), and ^{140}Ce(p, t) reactions
UCRL-19997 Abstract, October 1970
Meeting of the American Physical Society, Stanford, California, October 1970

SHERMAN, J. (See Bacher, A. D., UCRL-19550 Abstract)

SHERMAN, J. (See Bacher, A. D., UCRL-19976 Abstract)

SHIRLEY, D. A.
Estimates of correlation times of dissolved complexes from "rotational tracer" experiments
UCRL-19552, February 1970
J. Chem. Phys. 53, 465 (1970)

SHIRLEY, D. A.
Thermal equilibrium nuclear orientation: the present experimental situation
UCRL-19591 Abstract, April 1970
12th International Conference on Low Temperature Physics, Japan, 6-10 September 1970

SHIRLEY, D. A.
Comment on: Empirical correction to Hartree-Fock-Slater s-electron densities for calculation of contact hyperfine splittings
UCRL-19917, June 1970
Submitted to J. Chem. Phys.

SHIRLEY, D. A.
On the influence of molecular geometry, orientation, and dynamics on angular correlation patterns from rotationally labeled macromolecules
UCRL-20407, November 1970
To be published in J. Chem. Phys.

SHIRLEY, D. A. (See Meares, C F., Proc. Natl. Acad. Sci. 64, 1155 (1969))

SHIRLEY, D. A. (See Brewer, W. D., UCRL-19536)

SHIRLEY, D. A. (See Huntzicker, J. J., UCRL-19541)

SHIRLEY, D A. (See Faltens, M. O., UCRL-19559)

SHIRLEY, D. A. (See Koički, S., UCRL-19561)

SHIRLEY, D. A. (See Fadley, C. S., UCRL-19566)

SHIRLEY, D. A. (See Soinski, A. J., UCRL-19576)

SHIRLEY, D. A. (See Hollander, J. M., UCRL-19592)

SHIRLEY, D. A. (See Thorp, T. L., UCRL-19650)

SHIRLEY, D. A. (See Koster, T. A., UCRL-20411)

SHOTTER, A. C. (See Cerny, J., UCRL-19971)

SIKKELAND, T.
Effects of angular momentum on kinetic energy release in fission
UCRL-18991, January 1970
Phys. Letters 31B, 451 (1970)

SIKKELAND, T., J. E. Clarkson, N. H. Steiger-Shafrir, and V. E. Viola
Fission-excitation functions in interactions of ^{11}B, ^{12}C, ^{14}N, and ^{19}F with various targets
UCRL-19928, July 1970
Phys. Rev. C 1, 329 (1971)

SIKKELAND, T. (See Silva, R. J., UCRL-18296)

SIKKELAND, T. (See Silva, R., UCRL-18713)

SILVA, R. J., T. Sikkeland, M. Nurmia, A. Ghiorso, and E. K. Hulet
Determination of the No(II)-No(III) potential from tracer experiments
UCRL-18296
J. Inorg. Nucl. Chem. 31, 3405 (1969)

SILVA, R., T. Sikkeland, M. Nurmia, and A. Ghiorso
Tracer chemical studies of lawrencium
UCRL-18713
Inorg. Nucl. Chem. Letters 6, 733 (1970)

SILVA, R., J. Harris, M. Nurmia, K. Eskola, and A. Ghiorso
Chemical separation of rutherfordium
UCRL-19938, July 1970
Inorg. Nucl. Chem. Letters 6, 871 (1970)

SIME, R. J., R. P. Dodge, A. Zalkin, and D. H. Templeton
The crystal structure of tris-(2-aminoethyl)aminochlorozinc(II) tetraphenylborate
UCRL-19941, July 1970
Inorg. Chem. 10, 537 (1971)

SOINSKI, A. J., R. B. Frankel, Q. O. Navarro, and D. A. Shirley
Nuclear orientation of ^{253}Es in neodymium ethylsulfate
UCRL-19576, April 1970
Phys. Rev. C 2, 2379 (1970)

SOKOL, H. A. (See Bennett-Corniea, W., UCRL-19504)

SOKOL, H. A. (See Rodgers, M. A. J., UCRL-19595)

SOKOL, H. A. (See Garrison, W. M., UCRL-19926)

SORENSON, B. (See Ascuitto, R. J., UCRL-20402)

STARK, R. W. (See Thorp, T. L., UCRL-19650)

STAUFFACHER, C. V. (See Lee, D. M., UCRL-19532)

ST. CLAIR, D., A. Zalkin, and D. H. Templeton
The crystal structure of 3,3' -commo-Bis[undecahydro-1,2-dicarba-3-nickela-closo-3-dodecaborane], a nickel(IV) complex of the dicarbollide ion
J. Am. Chem. Soc. 92, 1173 (1970)

STEIGER-SHAFRIR, N. H. (See Sikkeland, T., UCRL-19928)

STEPHENS, F. S., R. M. Diamond, N. K. Glendenning, and J. de Boer
Electric hexadecapole moment in ^{152}Sm
UCRL-19571, March 1970
Phys. Rev. Letters 24, 1137 (1970)

STEPHENS, F. S., J. R. Leigh, and R. M. Diamond
How neutron deficient can we get?
UCRL-19588 Abstract, April 1970
Conference on the Properties of Nuclei Far From Beta Stability, Leysin, Switzerland, 31 August - 4 September 1970

STEPHENS, F. S.
E2 and E4 transition moments in ^{152}Sm and ^{154}Sm
UCRL-19909 Abstract, May 1970
Nuclear Structure Symposium, Joutsenlampi, Finland, 2-8 August 1970

STEPHENS, F. S., J. R. Leigh, and R. M. Diamond
Some limitations on the production of very neutron-deficient nuclei
UCRL-20422, December 1970
Submitted to Nucl. Phys.

STEPHENS, F. S. (See Diamond, R. M., UCRL-19517 Rev.)

STEPHENS, F. S. (See Nakai, K., UCRL-19544)

STEPHENS, F. S. (See Quebert, J. L., UCRL-19555)

STEPHENS, F. S. (See Nakai, K., UCRL-19923)

STEPHENS, F. S. (See Leigh, J. R., UCRL-19955)

STONE, J. A. (See Karraker, D. G., J. Am. Chem. Soc. 92, 4841 (1970))

STREITWIESER, A., Jr. (See Edelstein, N., UCRL-20413)

SUDBURY, B. A. (See Bucher, J. J., UCRL-19599)

SWIATECKI, W. J. (See Myers, W. D., UCRL-18214)

TEMPLETON, D. H. (See De Boer, B. G., Inorg. Chem. 8, 836 (1969))

TEMPLETON, D. H. (See Drew, M. G. B., Acta Cryst. B25, 261 (1969))

TEMPLETON, D. H. (See St. Clair, D. A., J. Am. Chem. Soc. 92, 1173 (1970))

TEMPLETON, D. H. (See Fischer, M. S., UCRL-19554)

TEMPLETON, D. H. (See Sime, R. J., UCRL-19941)

TEMPLETON, D. H. (See Ruben, H., UCRL-19982)

TEMPLETON, D. H. (See Ruben H., UCRL-19985)

TEMPLETON, J. E. (See Thorp, T. L., UCRL-19650)

THOMAS, G. E., and R. E. Vogelsberg
A pulsed electron beam retarding potential difference technique
UCRL-19934, July 1970
Rev. Sci, Instr. 42, 161 (1971)

THOMAS, G. E. (See Newton, A. S., UCRL-19594)

THOMAS, G. E. (See Newton, A. S., UCRL-19916 Rev.)

THOMAS, T. D.
X-ray photoelectron spectroscopy of carbon monoxide
UCRL-19542, December 1969
J. Chem. Phys. 53, 1744 (1970)

THOMPSON, S. G. (See Cheifetz, E., UCRL-19516)

THOMPSON, S. G. (See Cheifetz, E., UCRL-19584)

THOMPSON, S. G. (See Cheifetz, E., UCRL-19589 Abstract)

THOMPSON, S. G. (See Wilhelmy, J. B., UCRL-19931)

THOMPSON, S. G. (See Cheifetz, E., UCRL-19949)

THOMPSON, S. G. (See Cheifetz, E., UCRL-19957)

THOMPSON, S. G. (See Cheifetz, E., UCRL-19988)

THOMPSON S. G. (See Wilhelmy, J. B., UCRL-20405 Abstract)

THORP, T. L., B. B. Triplett, W. D. Brewer, N. E. Phillips, D. A. Shirley, J. E. Templeton, R. W. Stark, and P. H. Schmidt
Search for superconductivity in lithium and magnesium
UCRL-19650, August 1970
To be published in Low Temp. Phys.

TIVOL, W. F. (See Plattner, G. R., UCRL-19548 Abstract)

TIVOL, W. F. (See Bacher, A. D., UCRL-19943)

TRIPLETT, B. B. (See Thorp, T. L., UCRL-19650)

TSANG, C. F. (See Bassichis, W. A., UCRL-73044)

TUERPE, D. R. (See Bassichis, W. A., UCRL-73044)

VALLI, K. (See Borggreen, J., UCRL-19539)

VERMEULEN, T., L. Nady, J. M. Krochta, E. Ravoo, and D. Howery
Design theory and separations in preparative-scale continuous-flow annular-bed electrophoresis
UCRL-19981, October 1970
Ind. Eng. Chem., Process Design Devel. 10, 91 (1971)

VIOLA, V. E. (See Sikkeland, T., UCRL-19928)

VOGELSBERG, R. E. (See Thomas, G. E., UCRL-19934)

WEGMANN, G. (See Weigel, M., UCRL-19999)

WEIGEL, M.
Resonant approximation for single-particle resonances in the renormalized RPA-problem
UCRL-19578, April 1970
Z. Naturforsch. 25a, 1562 (1970)

WEIGEL, M., and G. Wegmann
The nuclear matter problem in the Green's function approach
UCRL-19999, October 1970
Submitted to Fortschritte der Physik

WEIGEL, M. (See Garside, L., UCRL-19538)

WEIGEL, M. (See Garside, L., UCRL-19940)

WILETS, L. (See Bassichis, W. A., UCRL-73044)

WILHELMY, J. B., S. G. Thompson, R. C. Jared, and E. Cheifetz
Ground-state bands in heavy even-even fission products
UCRL-19931, July 1970
To be published in Phys. Rev. Letters

WILHELMY, J. B., E. Cheifetz, S. G. Thompson, R. C. Jared, H. R. Bowman, and J. O. Rasmussen
Angular momentum of primary fission products
UCRL-20405 Abstract, December 1970
Meeting of the American Physical Society, New York, New York, 1-4 February 1971

WILHELMY, J. B. (See Cheifetz, E., UCRL-19584)

WILHELMY, J. B. (See Cheifetz, E., UCRL-19949)

WILKE, C. R. (See Robinson, C. W., UCRL-19570)

WILKE, C. R. (See Dabes, J. N., UCRL-19958)

WILKE, C. R. (See Dabes, J. N., UCRL-19959)

WITTKOWER, A. (See Cheifetz, E., UCRL-19516)

WORDEN, E. F. (See King, A. S., J. Res. Natl. Bur. Std. A 74A, 355 (1970))

WORDEN, E. F. (See Conway, J. G., UCRL-19944)

WOZNIAK, G. J., R. A. Mendelson, Jr., J. M. Loiseaux, and J. Cerny
Excited states of the neutron-deficient nuclei ^{17}Ne and ^{21}Mg
UCRL-19992 Abstract, October 1970
Meeting of the American Physical Society, Stanford, California, 28-30 December 1970

WOZNIAK, G. J. (See Mendelson, R., UCRL-19929)

YAMAZAKI, T., and G. T. Ewan
Level and isomer systematics in even tin isotopes from ^{108}Sn to ^{118}Sn observed in Cd(α,xn) reactions
Nucl. Phys. A134, 81 (1969)

YAMAZAKI, T.
Isomeric states of Po isotopes in the nanosecond range populated by Pb(α,xn) reactions
Phys. Rev. C 1, 290 (1970)

YELLIN, J.
Combined Zeeman and Stark effect in the hyperfine structure of the $6^2P_{3/2}$ state of thallium 205 and the $4^2P_{3/2}$ state of gallium 69
UCRL-19569, March 1970

YELLIN, J.
Hyperfine structure of the $^2P_{3/2}$ states of gallium, indium, and thallium in crossed electric and magnetic fields
UCRL-19573 Abstract, March 1970
Second International Conference on Atomic Physics, Oxford, England, 21-24 July 1970

YELLIN, J.
The use of polarized light in the measurement of differential Stark shifts by the atomic beam method
UCRL-19575 Abstract, April 1970
Second International Conference on Atomic Physics, Oxford, England, 21-24 July 1970

YELLIN, J.
Hyperfine structure of ^{69}Ga in crossed electric and magnetic fields
UCRL-19598, May 1970
Phys. Letters 32A, 337 (1970)

YORK, C. M. (See Frierman, J D., Science 164, 588 (1969))

ZALKIN, A. (See De Boer, B. G., Inorg. Chem. 8, 836 (1969))

ZALKIN, A. (See Drew, M. G. B., Acta Cryst. B25, 261 (1969))

ZALKIN, A. (See St. Clair, D. A., J. Am. Chem. Soc. 92, 1173 (1970))

ZALKIN, A. (See Fischer, M. S., UCRL-19554)

ZALKIN, A. (See Sime, R. J., UCRL-19941)

ZALKIN, A. (See Ruben, H., UCRL-19982)

ZALKIN, A. (See Ruben, H., UCRL-19985)

ZIRIN, M. (See Bucher, J. J., UCRL-19920)

ZISMAN, M. S., E. A. McClatchie, and B. G. Harvey
The ^{14}N(α,d)^{16}O reaction at 40 MeV
UCRL-19914, June 1970
Phys. Rev. C 2, 1271 (1970)

ZISMAN, M. S. (See Bruge, G. L., UCRL-19545 Abstract)

ZISMAN, M. S. (See Sherman, J. D., UCRL-19997 Abstract)

VII. Author Index

Author Index

Contributors to this Report